

RESONANCE MEETING
MAY 11-15, 1997
ASILOMAR CONFERENCE CENTER
PACIFIC GROVE, CA

VOLUME 2. TRANSPARENCIES

The Jamie Whitten National Center for Physical Acoustics

DISTRIBUTION STATEMENT A
Approved for public release;
Distribution Unlimited



*The
University of Mississippi*

19980713 002

**RESONANCE MEETING
MAY 11-15, 1997
ASILOMAR CONFERENCE CENTER
PACIFIC GROVE, CA**

VOLUME 2. TRANSPARENCIES

**Proceedings of a Symposium Sponsored by the
Office of Naval Research
Grant Number N00014-97-1-0270**

DISTRIBUTION STATEMENT A

**Approved for public release;
Distribution Unlimited**

**Compiled by
Elizabeth A. Cauthen
The National Center for Physical Acoustics
University, MS 38677**

19980713 002



The
University of Mississippi

NATIONAL CENTER FOR PHYSICAL ACOUSTICS

July 9, 1998

Defense Technical Information Center
8725 John J. Kingman Road
STE 0944
Ft. Belvoir, VA 22060-6218

Dear DTIC:

Enclosed please find proceedings for the Resonance Meeting held May 11-15, 1997 at the Asilomar Conference Center. This meeting was supported by the Office of Naval Research under grant N00014-97-1-0270. A Form 50 is also enclosed.

Regards,


Elizabeth A. Furr
Research Project Coordinator

EAF:lc

enclosures

PREFACE

The proceedings of the Resonance Meeting consist of two volumes. Volume 1 contains a verbatim transcript of each presentation. Volume 2 contains accompanying transparencies for each transcript. Anyone interested in obtaining more information on a particular presentation may contact the author(s). Volume 1 contains a complete list of participants and addresses.

COPIES OF THESE PROCEEDINGS MAY BE OBTAINED FROM THE

NATIONAL CENTER FOR PHYSICAL ACOUSTICS

UNIVERSITY OF MISSISSIPPI

UNIVERSITY, MS 38677

601-232-5889

NCPA@OLEMISS.EDU

TABLE OF CONTENTS

	PAGE
<i>Mini-tutorial on RUS</i>	Albert Migliori 1
<i>Elastic properties calculated from the high-temperature database found from RUS</i>	Orson L. Anderson 31
<i>RUS measurements of nickel alloys at high temperature</i>	J.D. Carnes, et al. 56
<i>Measurement of the complete elastic tensor of a single crystal of $\text{La}_{0.83}\text{Sr}_{0.17}\text{MnO}_3$ and its response to magnetic fields</i>	T.W. Darling, et al. 76
<i>Magnetic effects and RUS</i>	John L. Sarrao 90
<i>High temperature RUS and the elastic constants of steel</i>	T.W. Darling, et al. 103
<i>Resonant ultrasound spectroscopy study of texture in polycrystalline materials</i>	Robert G. Leisure and Keir Foster 119
<i>Comparison of RUS measurements with conventional methods</i>	C.M. Fortunko and H. Ledbetter 137
<i>Sampled cw investigation of vortex viscosity and phase transitions in YBCO single crystals</i>	D. Dasgupta, et al. 161
<i>Thin film characterization using resonant ultrasound spectroscopy</i>	Jason White and J.D. Maynard 181
<i>System identification alternatives to swept sine and curve fitting</i>	Ralph Muehleisen 188
<i>Resonant ultrasound spectroscopy measurements for spheres under pressure with different gases</i>	Donald G. Isaak, et al. 197
<i>Gas pressure dependence of radiation impedance of a resonating sphere</i>	Jeff Feller, et al. 214
<i>Determining the radiation impedance for arbitrarily shaped vibrating surfaces</i>	J.D. Maynard and Jason White 238
<i>Temperature dependence of elastic moduli of spinel, MgAl_2O_4 (Poster presentation)</i>	Isao Suzuki, et al. 253
<i>Resonant frequency of an elastic sphere at high pressure (Poster presentation)</i>	Hitoshi Oda, et al. 274
<i>Acoustical resonator frequency shift due to the migration of suspended particles</i>	Chris Kwiatkowski 292
<i>Resonances and other mechanisms for elastic contributions to the scattering of sound by objects in water</i>	Philip L. Marston, et al. 313
<i>Magnetic excitation and acoustic detection of spherical shell modes in air and in water</i>	Brian T. Hefner and Phillip L. Marston 340

		PAGE
<i>Material property measurements via GHz interferometry</i>	H. Spetzler, et al.	361
<i>Applications of ultrasonic interferometry</i>	Dipen N. Sinha, et al.	380
<i>RUS use in chemical weapons convention and resonant photoacoustic spectroscopy of aerosols</i>	Pat Arnott	403
<i>Resonant photoacoustic spectroscopy of optical materials</i>	J.D. Maynard	424
<i>Resonant bar acoustic spectroscopy</i>	David A. Brown and Qiushuang Guo	436
<i>Acoustic resonance techniques applied to metrology: The universal gas constant R and the thermodynamic temperature scale</i>	Michael R. Moldover	464
<i>Cheap acoustic gas analyzers</i>	Matthew Golden, et al.	502
<i>Measurements of relaxation processes in gases and liquids using resonance systems</i>	Henry E. Bass	512
<i>Design considerations for thermoacoustic resonators</i>	Tom Hofler	522
<i>Acoustic measurements of thermodynamic and transport properties in gases</i>	Michael R. Moldover, et al.	533
Report Documentation Page		561

Resonant Ultrasound Spectroscopy

Los Alamos

Los Alamos National Laboratory
Los Alamos, New Mexico 87545

Albert Migliori
Timothy W. Darling
John Sarrao
William M. Visscher
J.D. Thompson
Ray Dixon
U.F. Kocks
R.B. Schwartz
Stuart Trugman
David Mandrus

Bob Leisure
Z. Fisk

Colorado State University
Florida State University/NHMFL

George W. Rhodes

Hundreds of administrators, the IPC, the STC, Domenici, Bingamen, KOB, dozens of lawyers, the DOE, the New Mexico Highway and Transportation Dept., Quatrosonics Corp., George Rhodes, and many others but I ran out of space!

1. How to do it
2. What it does
3. Non-destructive testing

Why study ultrasound?

$$\Delta G = G_{hot} - G_{cold}$$

ΔG is the Gibbs free energy
change across a phase boundary

$$\Delta V = \frac{\partial}{\partial P} \Delta G$$

ΔV is the volume change across
the boundary, and is zero for second
order phase transitions

$$\frac{1}{K_{hot}} - \frac{1}{K_{cold}} = -\frac{1}{V} \frac{\partial \Delta V}{\partial P} = -\frac{1}{V} \frac{\partial^2 \Delta G}{\partial P^2}$$

ΔK is the discontinuity in bulk modulus
across the boundary, which ties directly
to the speed of sound, and which is not
zero for a second order transition

WHY STUDY ELASTIC CONSTANTS?

$$dF = -SdT + \sigma_{ik} du_{ik}$$

\uparrow EE ENERGY \uparrow STRESS (LIKE PRESSURE) \nwarrow STRAIN (LIKE VOLUME)

HOOKE'S LAW : STRESS "PROPORTIONAL" TO STRAIN

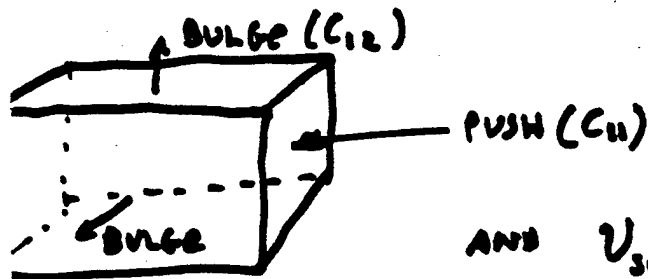
SYMMETRIES OF REAL OBJECTS

REDUCTION OF INDICES

FOR ORTHORHOMBIC SYMMETRY

$$= \begin{pmatrix} C_{11} & C_{12} & C_{13} & 0 & 0 & 0 \\ C_{12} & C_{22} & C_{23} & 0 & 0 & 0 \\ C_{13} & C_{23} & C_{33} & 0 & 0 & 0 \\ 0 & 0 & 0 & C_{44} & 0 & 0 \\ 0 & 0 & 0 & 0 & C_{55} & 0 \\ 0 & 0 & 0 & 0 & 0 & C_{66} \end{pmatrix} \begin{pmatrix} e_1 \\ e_2 \\ e_3 \\ e_4 \\ e_5 \\ e_6 \end{pmatrix}$$

} COMPRESSION
 } SHEAR
 STRAIN



$$\text{AND } v_{sound} = \sqrt{\frac{C_0}{\rho}} \text{ ETC.}$$

Signal/noise comparison of pulsed and resonant measurements

parameter	Impulse	Swept Sine
drive power per unit bandwidth	peak power/full bandwidth $10^6/10^9=.001$	peak power/sweep rate $1/100=0.01$
noise bandwidth for complete measurement using optimum receiver	10^9	number of modes x width of each mode x $10=10^4\text{Hz}$
drive duty cycle (typical)	10^{-3}	1
detect duty cycle	1	1
square root of all factors, which is a measure of S/N	3×10^{-7}	10^{-3}

Table I. Signal-to-noise comparison between impulse (pulse-echo) and swept-sine (RUS) resonance measurement methods for a measurement of a 1 cm sample with resonances having a $Q=10^4$, using 10 modes over 0.5 MHz-1.5MHz= 10^6 Hz bandwidth to obtain an elastic modulus. Note that the pulse-echo measurement provides about 0.1% absolute accuracy at best, compared with about 0.01% for the best RUS measurements.

John William Strutt, the Baron Rayleigh tried to do this computation. Without a 90MHz Pentium, he found that

In the case of a short rod and of a particle situated near the cylindrical boundary, this lateral motion would be comparable in magnitude with the longitudinal motion, and could not be overlooked without risk of considerable error.

226. The problem of a rectangular plate, whose edges are free, is one of great difficulty, and has for the most part resisted attack¹.

Even with a Pentium, if you try this using finite element methods, the computation time goes like the cube of the numerical accuracy and you can't compute as well as you can measure in a reasonable time on a reasonable computer. However, if you are careful, and smart, as were Orson Anderson and his postdoc Harold Demarest at Bell labs 30 years ago, then.....

12 ELASTIC MODULI AND SOLID-BODY RESONANCES

3.3 The problem with 3-D resonances in solids

As suggested above, the resonances of 3-dimensional solids with small aspect ratios (all the dimensions are comparable) are very difficult to compute. To see why, let's set up a problem that John William Strutt, Baron Rayleigh⁴, worked on his honeymoon. We will not solve the problem here, nor we will follow through with Rayleigh's approximate solution because, as Rayleigh notes "A more complete solution...has been given by Pochhammer..."⁵. Furthermore, in Chapter 4, we will set up all the machinery to solve this and other nasty problems to as high an accuracy as anyone might care about (6 digits is easy on a PC).

The problem here is to redo the computation that resulted in 2.2.7 but now with a short fat rod. When such a rod resonates, it alternately bulges and constricts at some places along its length but not at others.

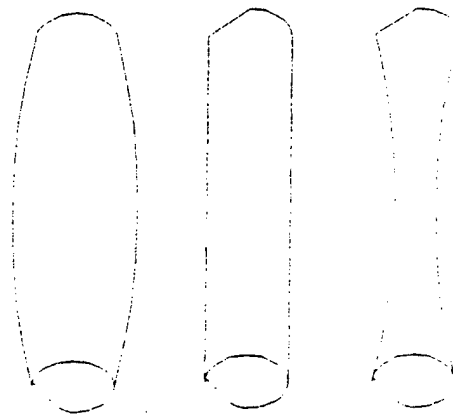


Fig. 3.3 A short fat bar undergoing a longitudinal oscillation. As the bar oscillates between being longer and shorter, it also alternately bulges and constricts near its middle.

Stresses along the bar associated with longitudinal oscillations, combined with the effect of the Lamé coefficient λ , cause lateral strains as depicted in Fig. 3.3. The problem is to understand completely all the strains and velocities of all the material in the bar. This is very difficult to do simply. What we can do is use σ to estimate the lateral motion of the bar, include this in the total kinetic energy, and then estimate the frequency shift. This approach relies on an oscillator alternating between brief moments when everything is stopped (think of the top of a pendulum's swing) to brief moments when all that moves is moving at its peak speed and no strains are present. Because we are not considering any dissipation to be present, the total kinetic energy at peak speeds equals the total potential energy when things stop briefly. If in the case of a short fat bar, more mass moves than in a long thin bar of equal mass, then

Seasons Greetings

It brightens the spirits
in times like these,
To know the Moon
is made of cheese.

Lunar rocks and cheeses	Sound Velocity, V_p (Kilometers/second)
Lunar Rock 10017	1.84
Gjetost (Norway)	1.83
Provelone (Italy)	1.75
Romano (Italy)	1.75
Cheddar (Vermont)	1.72
Emmenthal (Swiss)	1.65
Muenster (Wisconsin)	1.57
Lunar Rock 10046	1.25

(Science, 168, 1579, 1970)



MINERAL PHYSICS LABORATORY
LAMONT-DOHERTY GEOLOGICAL OBSERVATORY
OF COLUMBIA UNIVERSITY

Reprinted from

26 June 1970, volume 168, pages 1579-1580

SCIENCE

Properties and Composition of Lunar Materials: Earth Analogies

Abstract. *The sound velocity data for the lunar rocks were compared to numerous terrestrial rock types and were found to deviate widely from them. A group of terrestrial materials were found which have velocities comparable to those of the lunar rocks, but they do obey velocity-density relations proposed for earth rocks.*

Certain data from Apollo 11 and Apollo 12 missions present some difficulties in that they require explanations for the signals received by the lunar seismograph as a result of the impact of the lunar module (LEM) on the lunar surface (1). In particular, the observed signal does not resemble one due to an impulsive source, but exhibits a generally slow build-up of energy with time. In spite of the appearance of the returned lunar samples, the lunar seismic signal continued to ring for a remarkably long time—a characteristic of very high Q material. The lunar rocks, when studied in the laboratory, exhibited a low Q (2). Perhaps most startling of all,

however, was the very low sound velocity indicated for the outer lunar layer deduced from the LEM impact signal. The data obtained on the lunar rocks and fines agree well with the results of the Apollo 12 seismic experiment (2, 3). These rock velocities are startlingly low. The measured velocities on a vesicular medium grained, igneous rock (10017) having a bulk density of 3.2 g/cm³ were $v_p = 1.84$, and $v_s = 1.05$ km/sec. The results for a microbreccia (10046) with a bulk density of 2.2 g/cm³ were $v_p = 1.25$ and $v_s = 0.74$ km/sec for the compressional (v_p) and shear (v_s) velocities.

It was of some interest to consider

the behavior of these lunar rocks in terms of the expected behavior based on measurements of earth materials. Birch (4) first proposed a simple linear relation between compressional velocity and density for rocks. This relation was examined further by Anderson (5) who showed that this was a first approximation to a more general relation, derivable from a dependence of the elastic moduli with the density through a power function. Comparison of the results obtained from the returned lunar rocks with the predictions of these relationships expresses graphically the manner they deviate from the behavior of rocks found on earth. The velocities are remarkably lower than what would be predicted from either the Birch or Anderson relationships.

To account for this very low velocity, we decided to consider materials other than those listed initially by Birch (4) or more detailed compilation of Anderson and Liebermann (6). The search was aided by considerations of much earlier speculations concerning the na-

Table 1. Comparison of compressional velocities of lunar rocks and various earth materials.

Lunar rocks and chert	v_p (km/sec)	Sedimentary rocks	v_p (km/sec)	Metamorphic rocks	v_p (km/sec)	Igneous rocks	v_p (km/sec)	Minerals	v_p (km/sec)
Sapelo (Swiss)	2.12	Dolomite	5.6	Schist	5.1	Granite	5.9	Corundum	10.8
Lunar Rock 10017	1.84	Dolomite	4.69	Slate	5.39	Syenite	5.7	Periclase	9.69
Gjetost (Norway)	1.83	Limestone	5.06	Charnockite	6.15	Diorite	5.78	Spinel	9.91
Provolone (Italy)	1.75	Limestone	5.97	Gneiss	4.9	Oligoclase	6.40	Garnet	8.53
Romano (Italy)	1.75	Greywacke	5.4	Marble	6.02	Andesite	5.23	Quartz	6.05
Cheddar (Vermont)	1.72	Greywacke	6.06	Quartzite	5.6	Gabbro	5.8	Hematite	7.90
Emmenthal (Swiss)	1.65	Sandstone	4.90	Amphibolite	6.70	Gabbro	6.8	Olivine	8.42
Muenster (Wisconsin)	1.57			Eclogite	6.89	Norite	6.50	Tremolite	7.23
Lunar Rock 10046	1.25					Diabase	6.33	Lime	7.95

Computation of resonances

from Migliori et.al. Physica B **183**,1,1993

The procedure for solving the direct problem for an arbitrarily shaped elastic solid with volume V , elastic tensor c_{ijkl} , density ρ , and with a free surface S begins with the Lagrangian

$$L = \int_V (\text{KE} - \text{PE}) dV \quad (4)$$

where the kinetic energy, KE, is given by

$$\text{KE} = \frac{1}{2} \rho \omega^2 u_i^2, \quad (5)$$

and the potential energy, PE, by

$$\text{PE} = \frac{1}{2} c_{ijkl} u_{i,j} u_{k,l}. \quad (6)$$

Following Hamilton, we allow u_i to vary arbitrarily in the volume V and on the surface S ($u_i \rightarrow u_i + \delta u_i$) and calculate the variation δL in L . The result is

$$\begin{aligned} \delta L = & \int_V (\text{left side of eq. (8)})_i \delta u_i dV \\ & + \int_S (\text{left side of eq. (9)})_i \delta u_i dS \end{aligned} \quad (7)$$

The immediate results are two equations, the elastic wave equation and the vanishing of surface traction

$$\rho \omega^2 u_i + c_{ijkl} u_{k,lj} = 0, \quad (8)$$

$$n_j c_{ijkl} u_{k,l} = 0 \quad (9)$$

where $\{n_i\}$ is the unit outer normal to S .

Because of the arbitrariness of δu_i in V and on S , the u_i 's which correspond to stationary points of L (i.e. $\delta L = 0$) must satisfy eq. (8) in V and eq. (9) on S . There are no such u_i 's, of course, unless ω^2 is one of a discrete set of eigenvalues, the normal mode frequencies of free vibration of the system.

Following the Rayleigh–Ritz prescription, we expand the displacement vector in a complete set of functions $\{\Phi_\lambda\}$,

$$u_i = a_{\lambda i} \Phi_\lambda, \quad (10)$$

and choose as our basis functions powers of cartesian coordinates:

$$\Phi_\lambda = x^l y^m z^n, \quad (11)$$

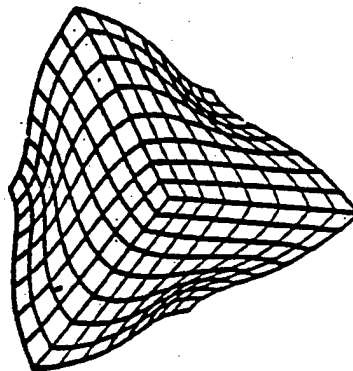
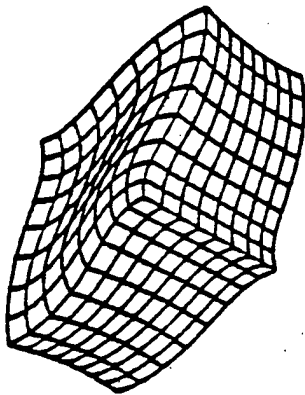
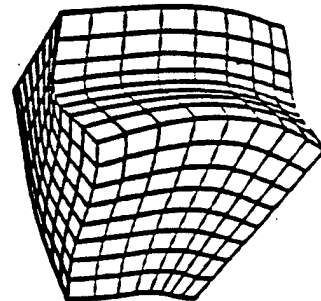
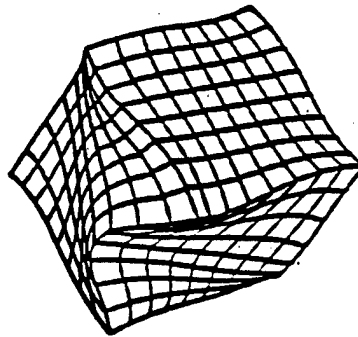
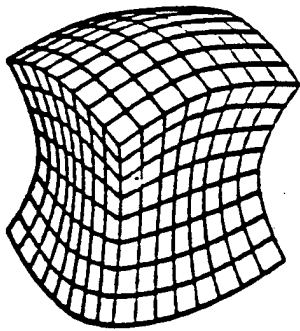
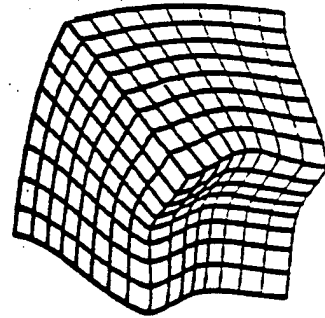
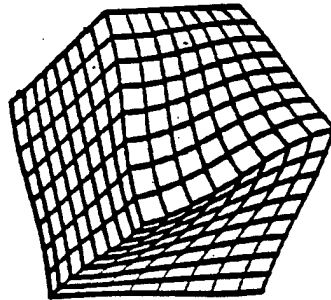
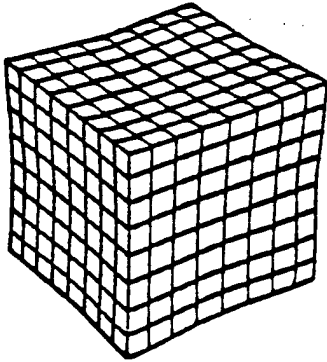
where $\lambda = (l, m, n)$ is the function label, a set of three nonnegative integers. After substituting eq. (10) into eq. (4), we obtain (\mathbf{a} becomes a column vector)

$$L = \frac{1}{2} \omega^2 \mathbf{a}^T \mathbf{E} \mathbf{a} - \frac{1}{2} \mathbf{a}^T \mathbf{\Gamma} \mathbf{a} \quad (12)$$

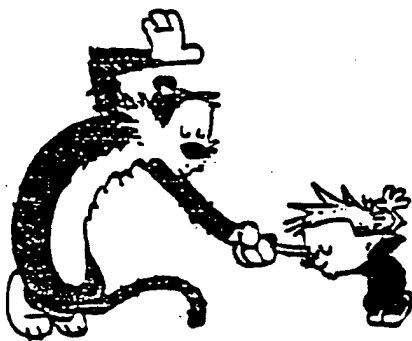
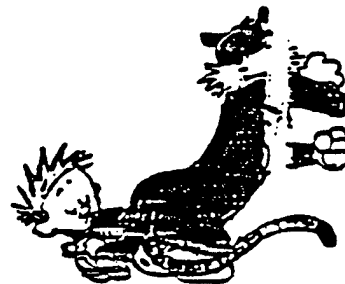
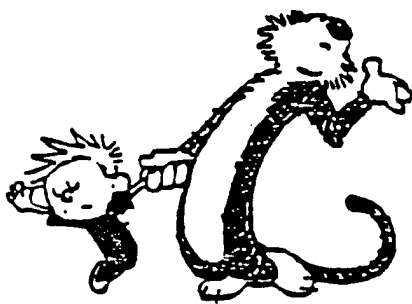
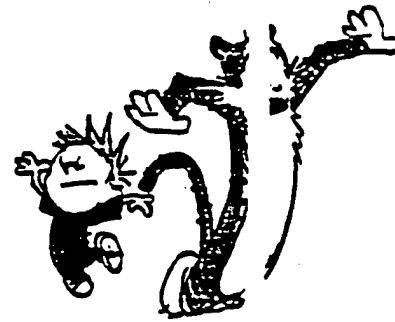
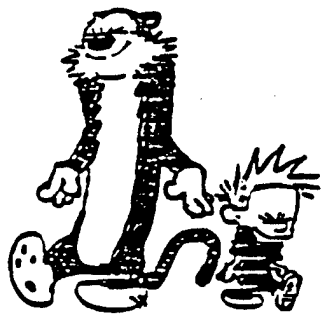
SAW
WAVE

Vibrations of a Rectangular Parallelepiped

- *Not a plane wave among them
- *Sufficiently complex to provide all the elastic moduli
- *Completely understood mechanics problem



The "Calvin and Hobbes" model of the vibrations of a rectangular parallelepiped



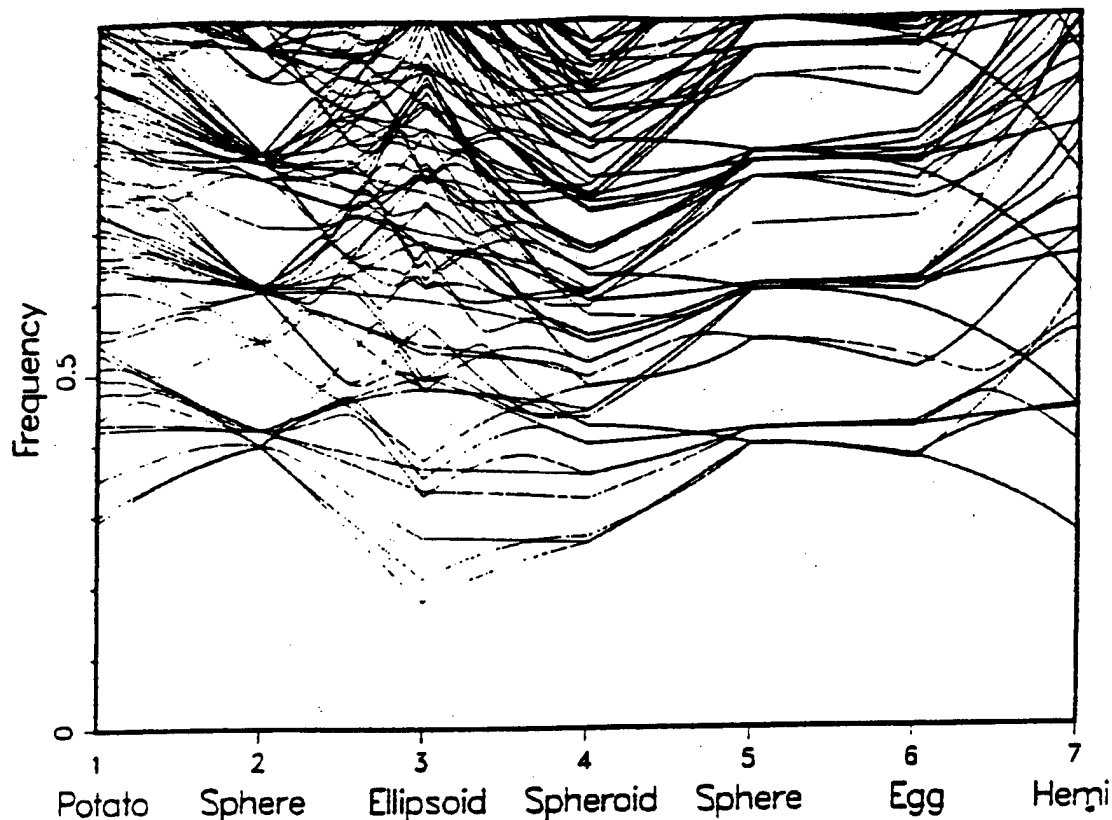
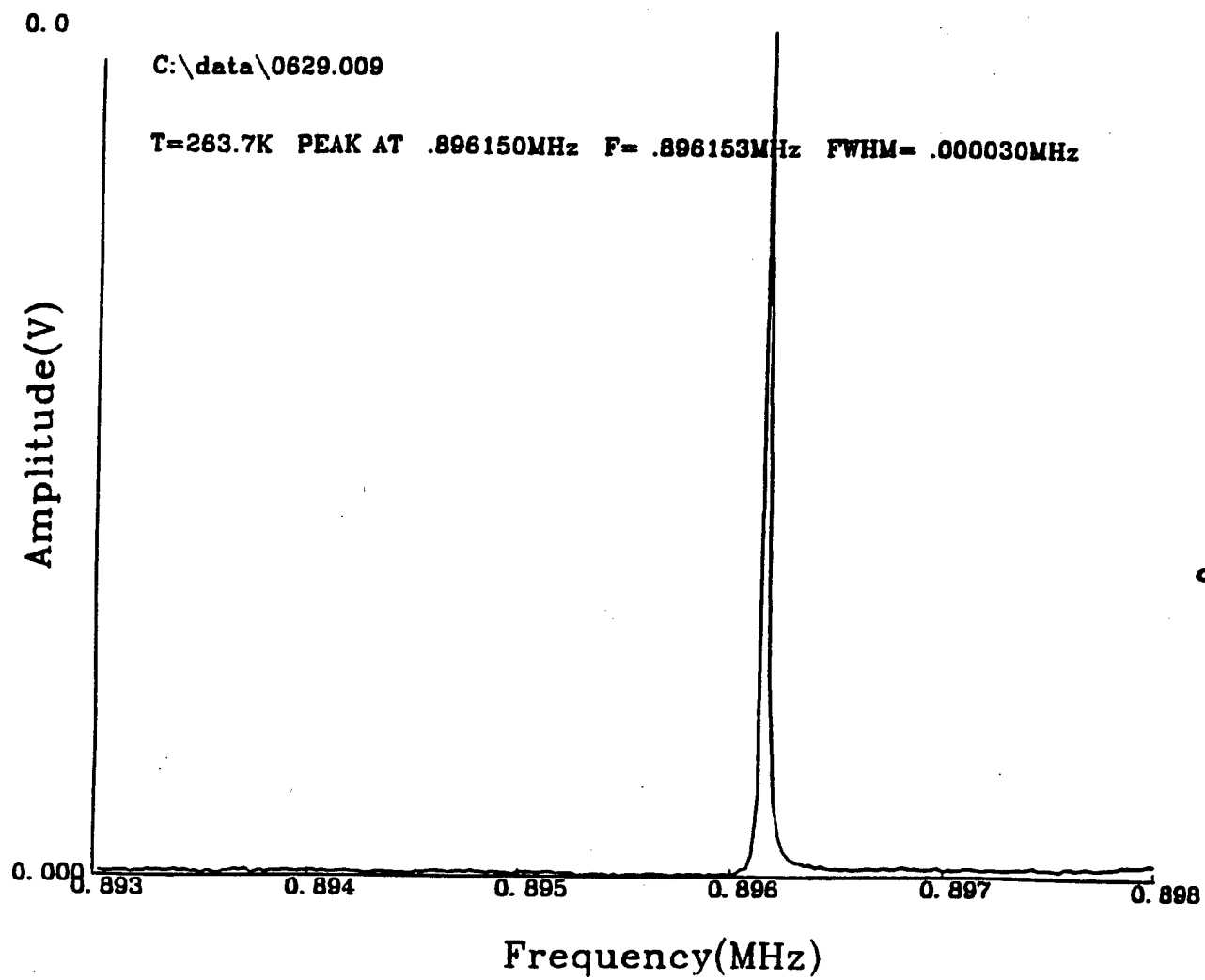
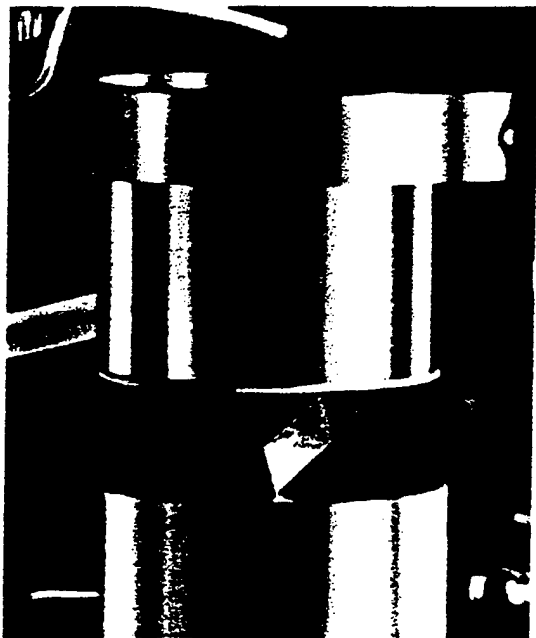
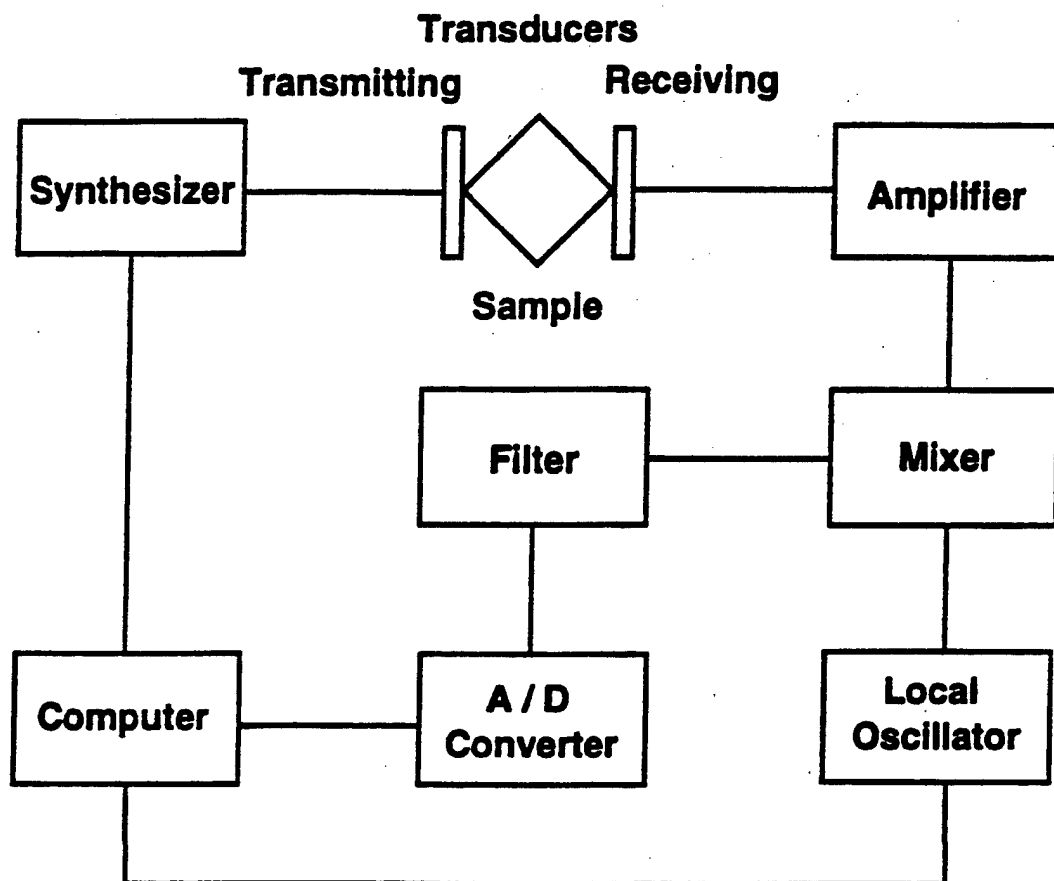


FIG. 8. Frequency spectra of a number of objects in the potato family. The seven stations correspond to shapes as labeled, with semiaxes as given in Table II. The sphere frequencies agree well with those in the literature for these material parameters (Poisson's ratio = $1/4$).²⁰ The dimensional parameters $d_{1+}, d_{1-}, \dots, d_{3-}$ are interpolated linearly between the seven stations here. Several interesting features invite comment. First, the potato has no degenerate lines, because of its low symmetry, and the sphere, conversely, has few lines that are nondegenerate. The ellipsoid has no degeneracies, and the spheroid, the egg, and the hemisphere (all being rotationally symmetric) do, but never more than doubly degenerate lines. Small deviations from the sphere in the egg direction do not change any of the frequencies to first order, because d_{3+} increases as much as d_{3-} decreases, compensating one another as far as affecting resonant frequencies is concerned. As in several other figures, apparent avoided crossings on this plot should be viewed with suspicion because the plotting program does not interchange line identities when physically the modes do, in fact, cross. Spectra are computed for 241 abscissa values here and elsewhere, which sets the scale on which avoided crossings may be spurious.



Instrumentation Block Diagram



Low temperature RUS cell with a 2mm rectangular parallelepiped sample set between 2 diamond/LiNbO₃ transducers using no coupling fluids. The force on the sample is equivalent to 1 gm weight. This cell operates between 1K and 400K.

Transducer construction

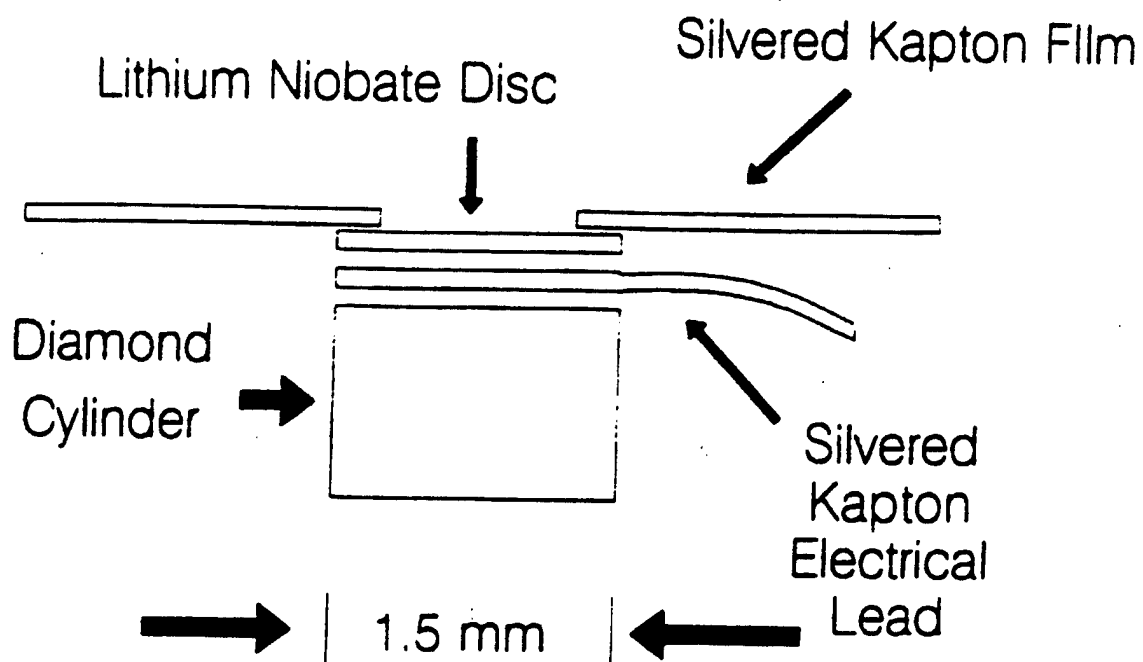
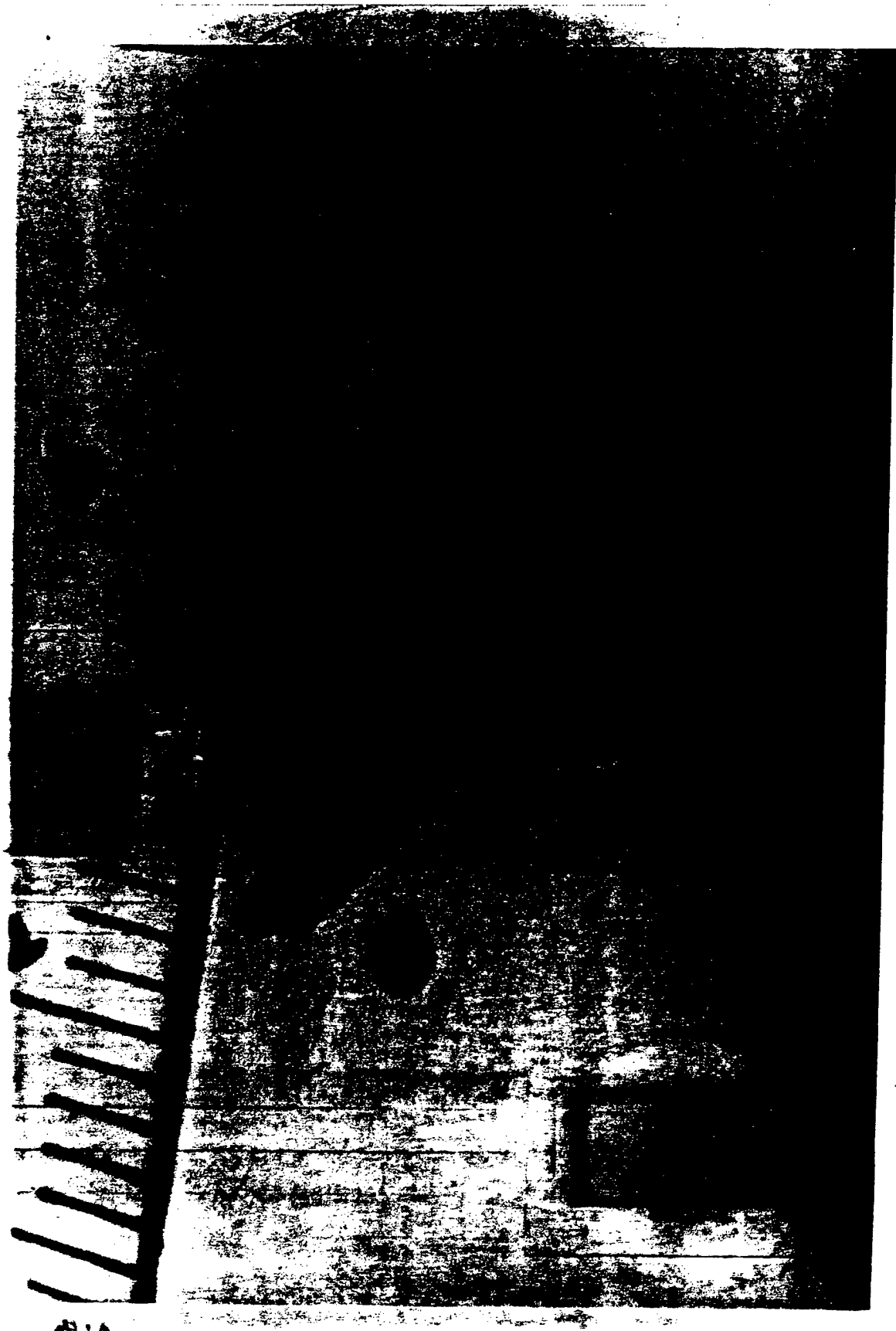


Fig. 3. Shown is a schematic of the diamond/polyimide/ LiNbO_3 composite transducer used for all the measurements.



The "Real" Figures

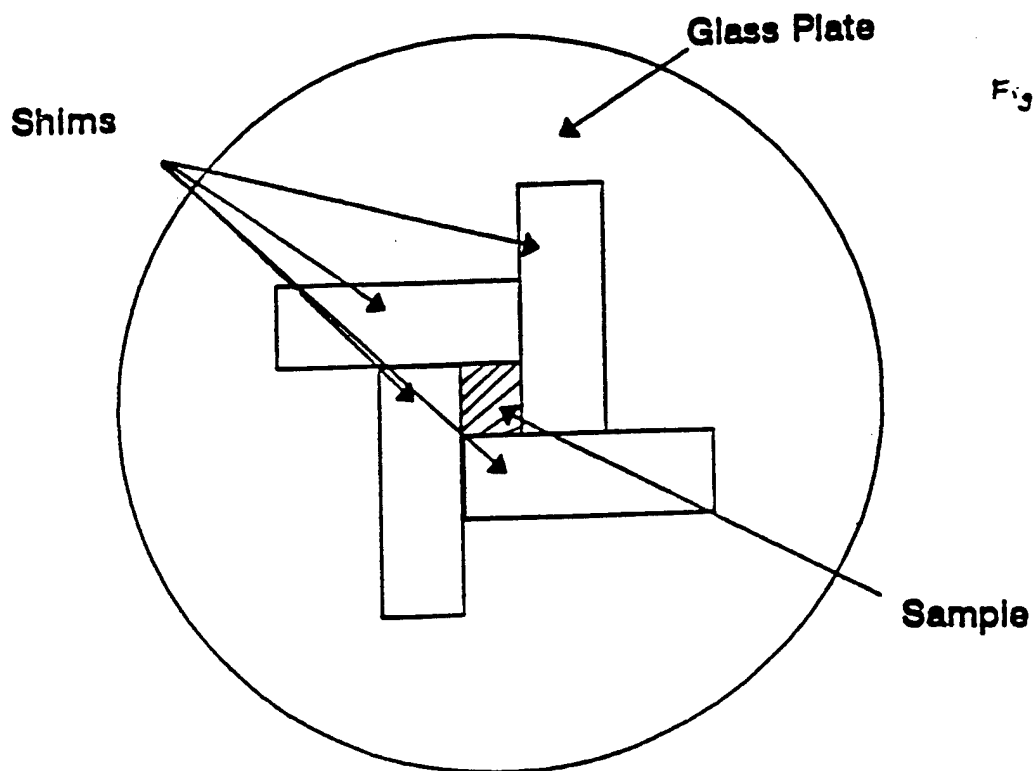
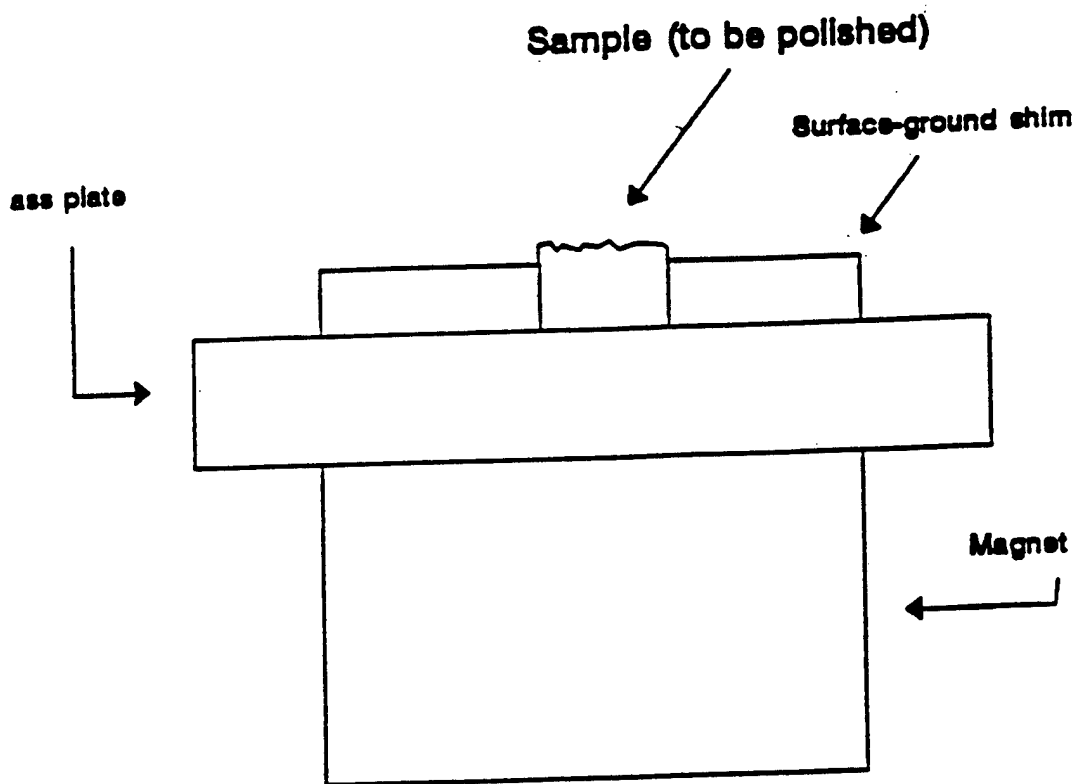
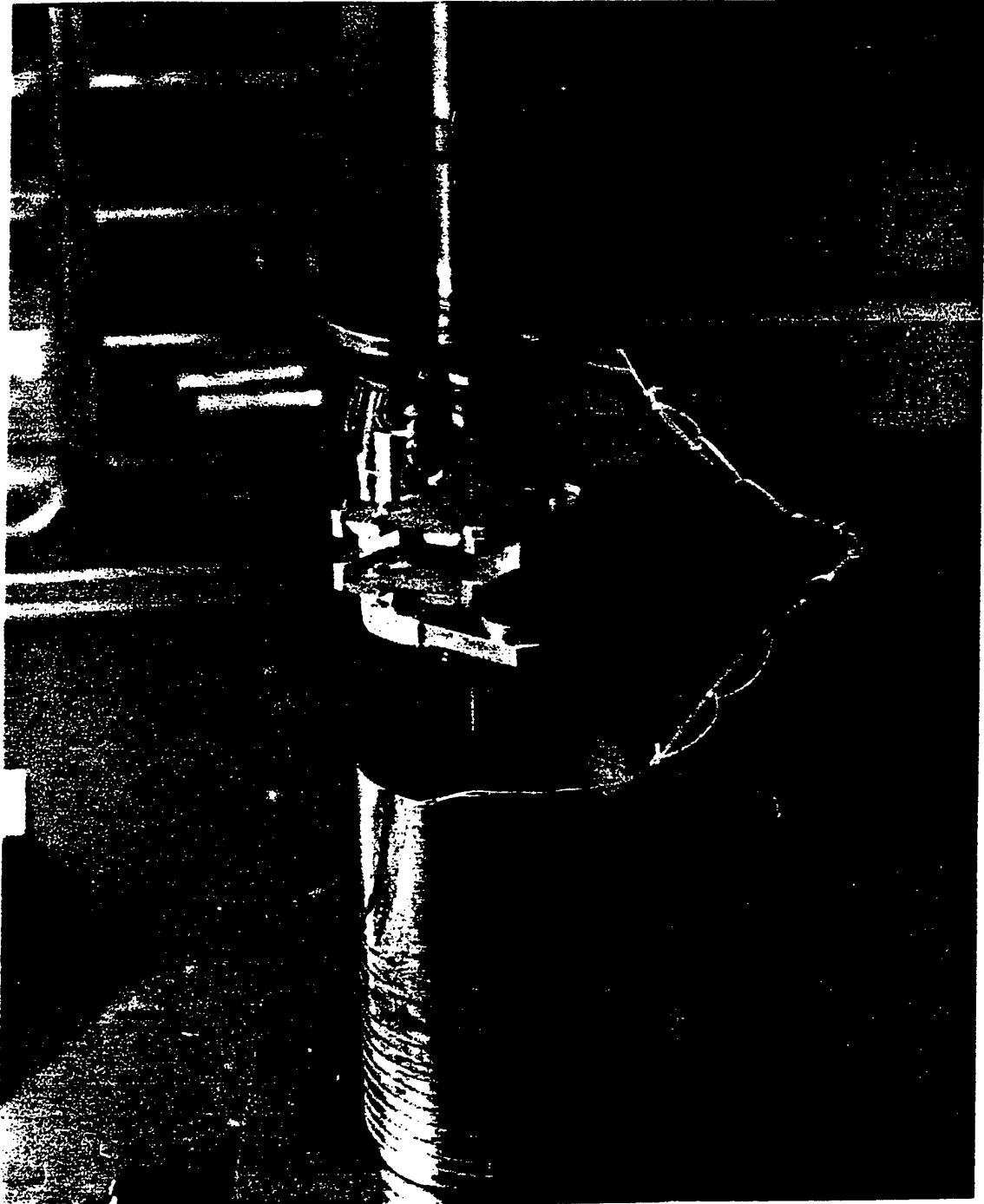
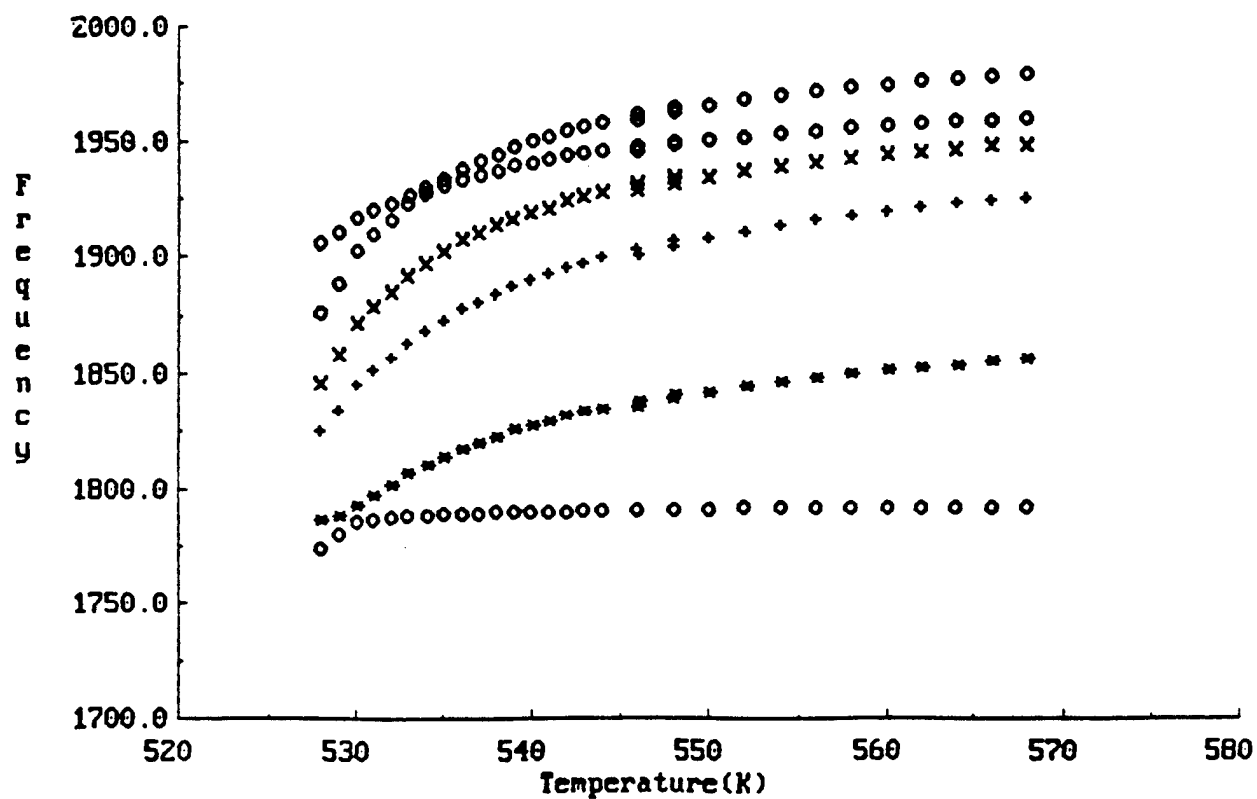
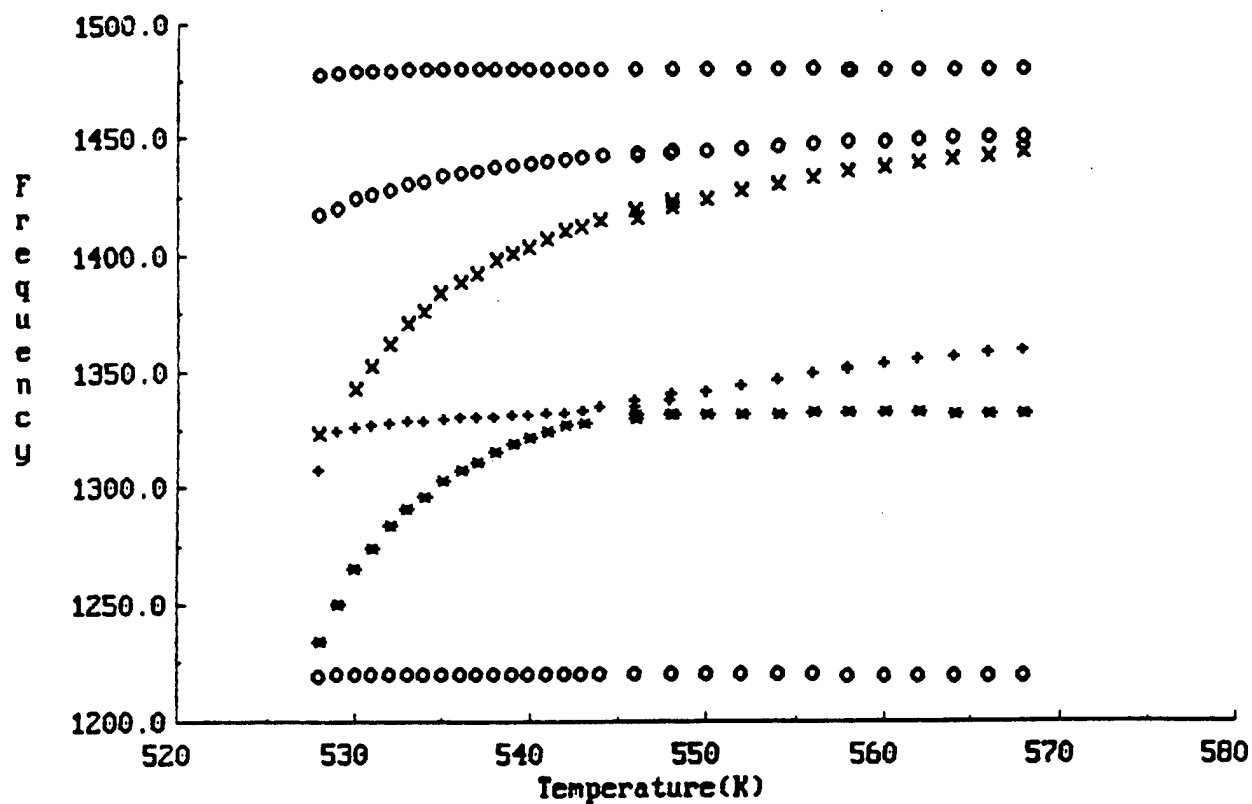
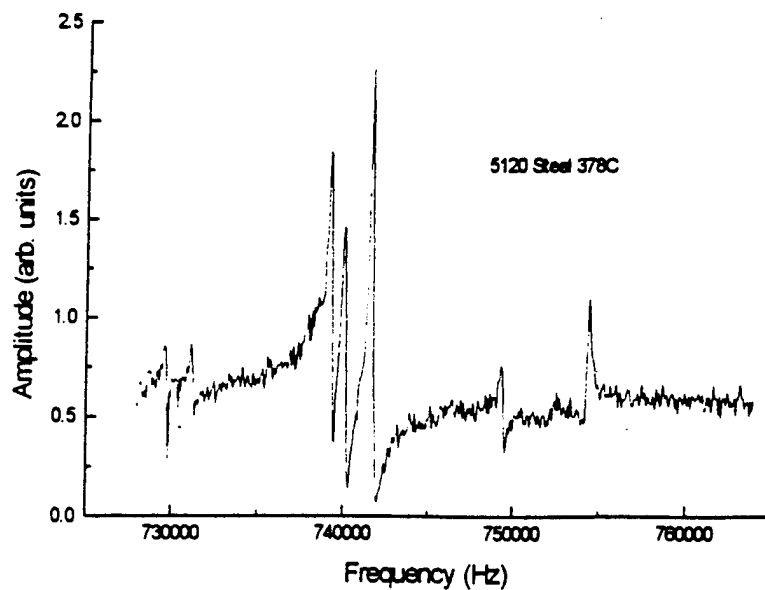
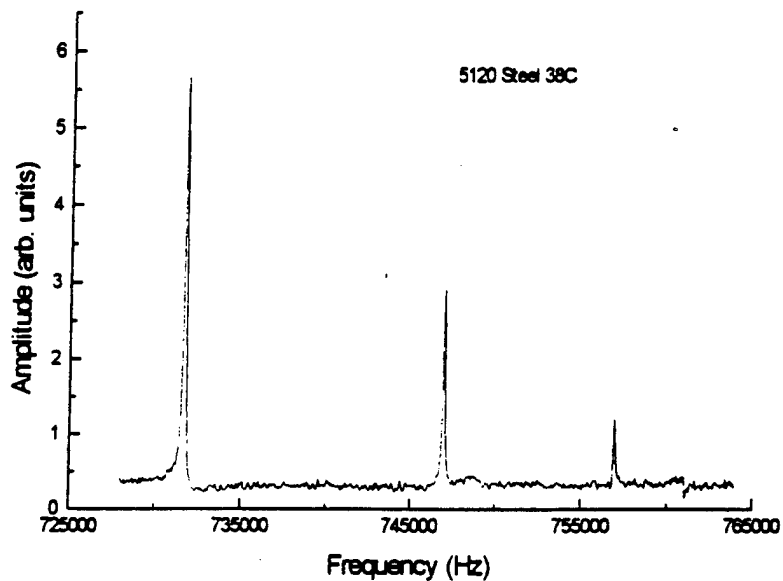


Figure 1 (polish. ch 3)





**Resonances of a 5120 steel RPR at 38C and 378C
measure using metal diffusion bonded LiNbO_3 /Alumina
transducers**



Ultimate accuracy determined by geometry-for a Si_3N_4 ball bearing, geometry errors are less than 1 part in 10^5 . So are the modulus errors!

Table 1

Resonant ultrasound measurement of a 0.63500 cm diameter Si_3N_4 ceramic sphere with a density of 3.2325 g/cm^3 . f_m are measured frequencies, f_f are fitted, n is the mode number, k is our designator (to be discussed below) for the symmetry of the mode and i is in essence the harmonic number of each symmetry type. Multiple entries indicate the mode degeneracy. The fit for $\mu = 1.2374 \times 10^{12} \text{ dyne/cm}^2$ and $\sigma = 0.2703$ has a $\chi^2 (\%) = 0.0124$. This is sufficient to determine μ to about 0.01% and σ to about 0.05%. There are no corrections so these values are absolute.

n	f_f (MHz)	f_m (MHz)	% error	(k, i)
1	0.775706	0.775707	-0.000138	(6, 1), (1, 1), (4, 1), (4, 2), (7, 1)
6	0.819567	0.819983	-0.050778	(5, 1), (3, 1), (5, 2), (8, 1), (2, 1)
11	1.075664	1.075399	0.024614	(1, 2), (7, 2), (6, 2)
14	1.198616	1.198505	0.009239	(5, 3), (2, 2), (3, 2), (8, 2), (3, 3), (8, 3), (2, 3)
21	1.217375	1.217850	-0.039042	(1, 3), (6, 3), (7, 3), (1, 4), (6, 4), (7, 4), (4, 3)
28	1.440760	1.440750	0.000712	(5, 4)
29	1.527080	1.526474	0.039695	(5, 5), (8, 4), (3, 4), (5, 6), (2, 4)
34	1.558358	1.558848	-0.031448	(5, 7), (5, 8), (5, 9), (3, 5), (8, 5), (2, 5), (3, 6), (8, 6), (2, 6)
43	1.580067	1.579871	0.012426	(6, 5), (7, 5), (7, 6), (1, 5), (4, 4), (1, 6), (6, 6), (4, 5), (4, 6)

Determination of high temperature moduli to support the broad DOE initiative in heat treatment distortion

5120 steel - ground parallelepiped

free dimensions are d1, d2, d3 (initial= 0.41205, 0.33973, 0.26380) cm

using 10 order polynomials mass= .2875 gm; density= 7.785 gm/cc

n	f-expt	f-calc	%err	C11 df/d(moduli)	C44
1	.340010	.339607	-.12	.00	1.00
2	.447200	.447109	-.02	.13	.87
3	.490240	.490366	.03	.16	.84
4	.541860	.541482	-.07	.02	.98
5	.557460	.556663	-.14	.00	1.00
6	.591740	.592306	.10	.05	.95
7	.608670	.608417	-.04	.31	.69
8	.615590	.615290	-.05	.02	.98
9	.623100	.622662	-.07	.07	.93
10	.642700	.642897	.03	.12	.88
11	.675510	.676384	.13	.10	.90
12	.683560	.683316	-.04	.05	.95
13	.690650	.690436	-.03	.16	.84
14	.746720	.747335	.08	.10	.90
15	.753860	.754125	.04	.05	.95
16	.827430	.827569	.02	.06	.94
17	.848300	.849153	.10	.03	.97
18	.855320	.854953	-.04	.08	.92
19	.870540	.870865	.04	.12	.88
20	.878390	.878891	.06	.11	.89
21	.882080	.881734	-.04	.33	.67
22	.884870	.884342	-.06	.21	.79
23	.887380	.887639	.03	.20	.80
24	.891190	.891892	.08	.04	.96
25	.916680	.916689	.00	.31	.69

rms error= .0680 %,

Fitted values for elastic constants and dimensions:

Young's Modulus = 30.39×10^6 psi (209.55 GPa)

Shear Modulus = 11.82×10^6 psi (81.50 GPa) Poisson's ratio= 0.285

d1 = 0.4121 cm d2 = 0.3395 cm d3 = 0.2639 cm

Perturbation analysis of error sensitivity : (goodness of fit)

χ^2 increased 2% by the following % changes in independent parameters

C11	C44	d1	d2	d3	
.48	.41	-.42	-.42	-.4	=> errors on fitted values ~ 0.5%

Elastic constants of copper. B represents bulk modulus.

	Single crystal		Polycrystal (wire-drawn)	
c_{ij} (GPa)	Literature average	Measured ^a	RP	Cylinder
c_{11}	168.75	170.88	193.61	194.25
c_{33}			205.88	203.98
c_{12}	122.14	124.63	105.65	106.84
c_{13}			95.00	95.93
c_{44}	75.48	74.01	39.35	39.46
c_{66}			43.98	43.71
B	137.68	140.05	131.65	132.84

^aCrystal rotated 45.4° about [100].

Elastic constants of tantalum at room temperature.

T (K)	ρ (g/cm ³)	c_{11} (GPa)	c_{12} (GPa)	c_{44} (GPa)
300 ¹	16.678	266.7	160.8	82.5
300 ¹	16.678	266.8	161.4	82.5
300 ²	16.633	260.9	157.4	81.8
298 ³	16.626	260.2	154.5	82.6
295 ⁴	16.641	266.3	160.5	82.8

¹D.I. Bolef, J. Appl. Phys. **33**, 2311 (1962).

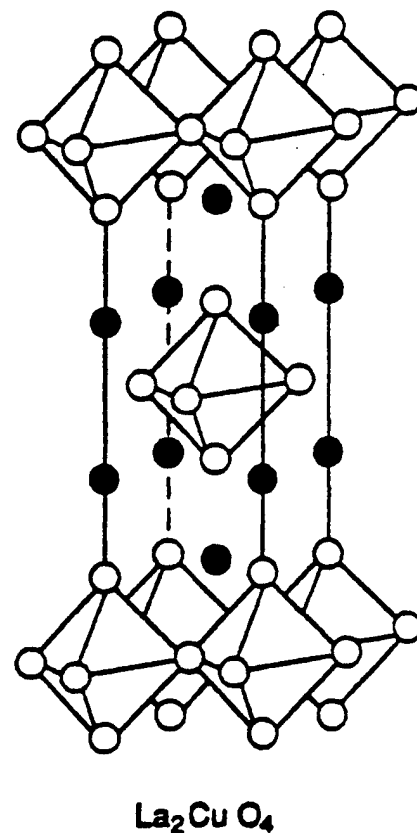
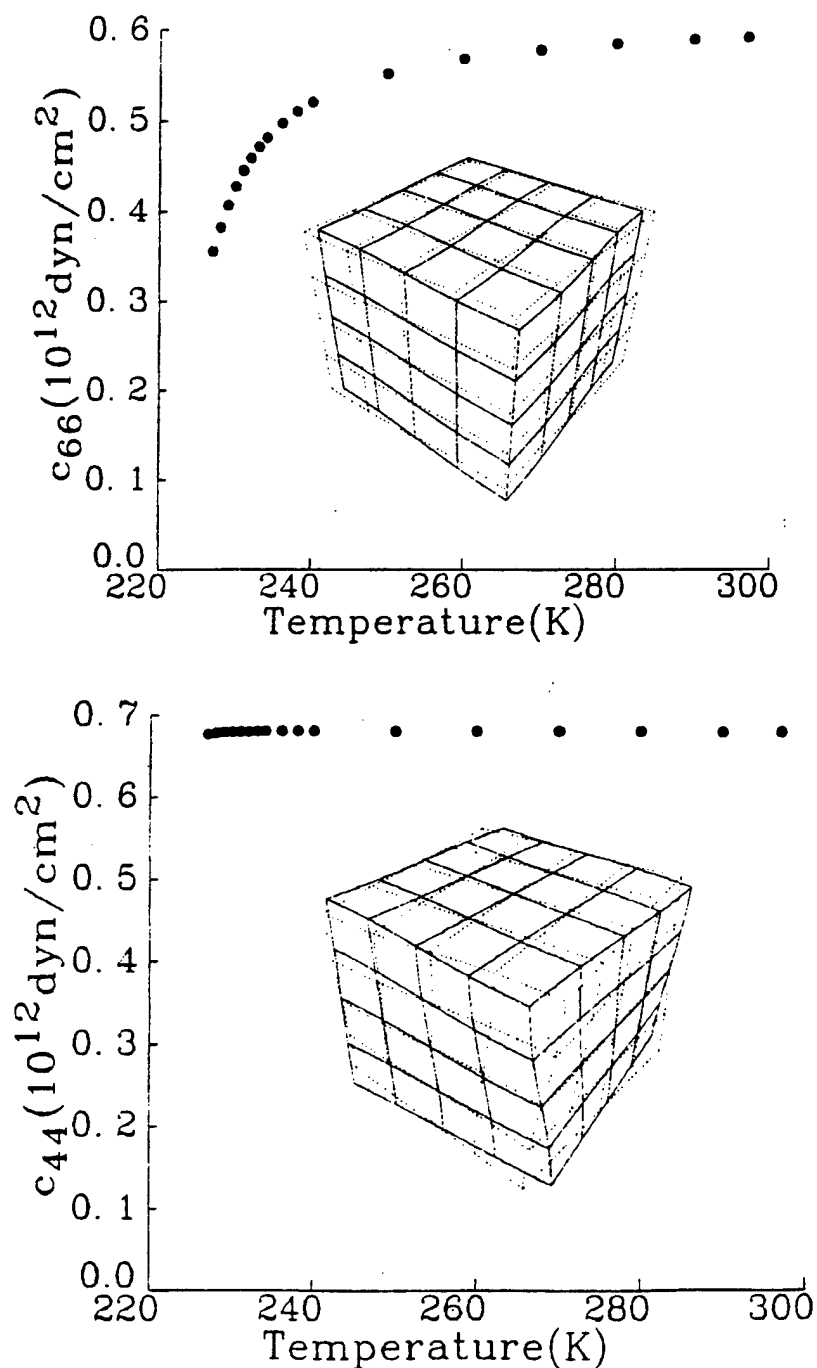
²F.H. Featherstone and J.R. Neighbours, Phys. Rev. **130**, 1324 (1963).

³N. Soga, J. Appl. Phys. **37**, 3416 (1966).

⁴Euler angles (defined in Roe's convention) were determined to be $\alpha = 138.3^\circ$, $\beta = 29.7^\circ$, and $\gamma = 155.1^\circ$ by RUS and $\alpha = 135^\circ$, $\beta = 33^\circ$, and $\gamma = 158^\circ$ by X-ray.

Structural phase transition in $\text{La}_{2-x}\text{Sr}_x\text{CuO}_4$

RUS simultaneously sees collapse of c_{66} and no effect on c_{44} in a 2mm single crystal



↓ lasrr3.p

La_{1.86}Sr_{1.14}CoO₇ 8/21/91
S.C.

nn	np	it	rho	6	10	1	6.946	i	11	33	23	12	44	66
1	0.550101	0.548752	-0.25	0.0	4	1	0.01	0.01	0.00	0.00	0.17	0.33		
2	0.655544	0.653127	-0.37	0.0	4	2	0.01	0.00	0.00	0.00	0.47	0.02		
3	0.767276	0.767542	0.03	1.0	3	1	0.02	0.01	-0.01	0.00	0.00	0.48		
4	0.840904	0.840137	-0.09	1.0	1	1	0.35	0.17	-0.18	0.01	0.01	0.15		
5	0.842859	0.840724	-0.25	1.0	8	1	0.02	0.01	0.00	0.00	0.48	0.00		
6	0.870588	0.872288	0.20	1.0	2	1	0.02	0.01	-0.01	0.00	0.48	0.00		
7	0.882324	0.882338	0.00	1.0	6	1	0.41	0.03	-0.05	-0.06	0.17	0.00		
8	0.914348	0.916268	0.21	1.0	7	1	0.31	0.27	-0.24	0.02	0.04	0.10		
9	0.962734	0.985844	0.32	1.0	6	2	0.35	0.06	-0.11	0.01	0.19	0.00		
10	1.017951	1.018350	0.04	1.0	5	1	0.40	0.45	-0.41	0.06	0.00	0.00		
11	1.031479	1.028883	-0.25	1.0	1	2	0.07	0.30	-0.09	0.00	0.14	0.09		
12	1.064057	1.062296	-0.17	1.0	2	2	0.36	0.04	-0.09	-0.01	0.19	0.01		
13	1.070964	1.071351	0.04	1.0	7	2	0.10	0.19	-0.04	-0.01	0.12	0.14		
14	1.071533	1.072243	0.07	1.0	5	2	0.47	0.31	-0.27	-0.01	0.00	0.00		
15	1.091915	1.091434	-0.04	1.0	3	2	0.09	0.45	-0.21	0.02	0.04	0.12		
16	1.101242	1.101298	0.01	1.0	2	3	0.05	0.02	-0.02	0.00	0.21	0.24		
17	1.119834	1.116659	-0.28	1.0	8	2	0.37	0.05	-0.08	-0.02	0.18	0.01		
18	0.000000	1.135942	0.00	0.0	5	3	0.63	0.04	-0.02	-0.14	0.00	0.00		
19	1.163975	1.164571	0.05	1.0	4	3	0.02	0.01	0.00	0.00	0.34	0.13		
20	1.186826	1.188038	0.10	1.0	8	3	0.08	0.03	-0.04	0.00	0.19	0.23		
21	1.237561	1.235048	-0.20	1.0	5	4	0.32	0.38	-0.26	0.05	0.00	0.01		
22	1.264551	1.261810	-0.22	1.0	3	3	0.07	0.06	-0.04	-0.01	0.40	0.01		
23	1.296307	1.294200	-0.16	1.0	1	3	0.26	0.33	-0.20	0.01	0.03	0.06		
24	1.317507	1.316531	-0.07	1.0	7	3	0.30	0.31	-0.20	0.00	0.03	0.06		
25	1.321605	1.320288	-0.10	1.0	5	5	0.46	0.11	-0.02	-0.07	0.02	0.00		
26	1.329940	1.326090	-0.29	1.0	6	3	0.45	0.11	-0.15	-0.02	0.11	0.00		
27	1.354530	1.354440	-0.01	1.0	1	4	0.26	0.07	-0.08	-0.02	0.11	0.16		
28	1.357242	1.358113	0.06	1.0	7	4	0.24	0.16	-0.15	0.01	0.15	0.09		
29	1.410719	1.410488	-0.02	1.0	6	4	0.27	0.09	-0.09	-0.02	0.24	0.00		
30	1.471757	1.474156	0.16	1.0	6	5	0.27	0.15	-0.15	0.01	0.21	0.01		
31	1.510419	1.508057	-0.16	1.0	3	4	0.16	0.02	-0.03	-0.01	0.03	0.34		
32	1.511018	1.515919	0.32	1.0	7	5	0.35	0.14	-0.04	-0.06	0.04	0.07		
33	1.512835	1.516014	0.21	1.0	6	6	0.13	0.04	-0.03	-0.01	0.27	0.11		
34	1.516509	1.518927	0.16	1.0	1	5	0.23	0.20	-0.09	-0.02	0.14	0.05		
35	1.564802	1.560320	-0.29	1.0	1	6	0.11	0.06	-0.03	-0.01	0.27	0.10		
36	1.566096	1.567781	0.11	1.0	5	6	0.23	0.21	0.01	0.02	0.03	0.00		
37	1.586001	1.585657	-0.02	1.0	8	4	0.15	0.09	-0.06	-0.01	0.31	0.01		
38	1.592957	1.590255	-0.17	1.0	4	4	0.14	0.06	-0.06	0.00	0.15	0.22		
39	1.599764	1.600863	0.07	1.0	2	4	0.16	0.10	-0.07	-0.01	0.19	0.13		
40	1.607484	1.610029	0.16	1.0	3	5	0.17	0.19	-0.16	0.03	0.22	0.06		
41	1.608641	1.611600	0.18	1.0	5	7	0.17	0.24	-0.14	0.01	0.07	0.16		
42	1.628330	1.628521	0.01	1.0	7	6	0.09	0.05	-0.03	0.00	0.27	0.12		
43	1.635094	1.639071	0.24	1.0	8	5	0.20	0.11	-0.08	-0.01	0.18	0.11		
44	1.672216	1.674642	0.15	1.0	2	5	0.15	0.11	-0.06	-0.01	0.30	0.01		
45	1.738091	1.735809	-0.13	1.0	4	5	0.13	0.08	-0.06	0.00	0.26	0.07		
46	1.740325	1.743251	0.17	1.0	5	8	0.28	0.04	-0.05	-0.02	0.25	0.01		
47	1.775364	1.775280	0.00	1.0	4	6	0.12	0.07	-0.03	-0.01	0.27	0.08		
48	1.782064	1.779391	-0.15	1.0	7	7	0.26	0.10	-0.10	-0.01	0.12	0.13		
49	0.000000	1.818747	0.00	0.0	3	6	0.07	0.02	-0.02	0.00	0.02	0.41		
50	0.000000	1.822177	0.00	0.0	5	9	0.28	0.06	-0.07	-0.01	0.07	0.17		
51	0.000000	1.826381	0.00	0.0	1	7	0.28	0.07	-0.08	-0.02	0.07	0.18		

orthorhombic elastic constants (c11,c22,c33,c23,c13,c12,c44,c55,c66):

2.65932 2.65932 2.58209 0.99080 0.99080 0.63820

0.67740 0.67740 0.58697

dimensions

0.11436 0.12371 0.10992

mass error = 0.00000e+00 %

rms = 0.16522 percent

chisquare increased 2% by % change in x's of

-0.25 -0.14 -0.66 -1.70 0.01 -0.01 0.00 0.00 0.00

chisquare increased 2% by % change in x's of

0.06 -0.31 -0.28 0.53 0.00 0.02 0.00 0.00 0.00

chisquare increased 2% by % change in x's of

-0.12 0.03 -0.13 0.39 0.05 0.00 0.00 0.00 0.00

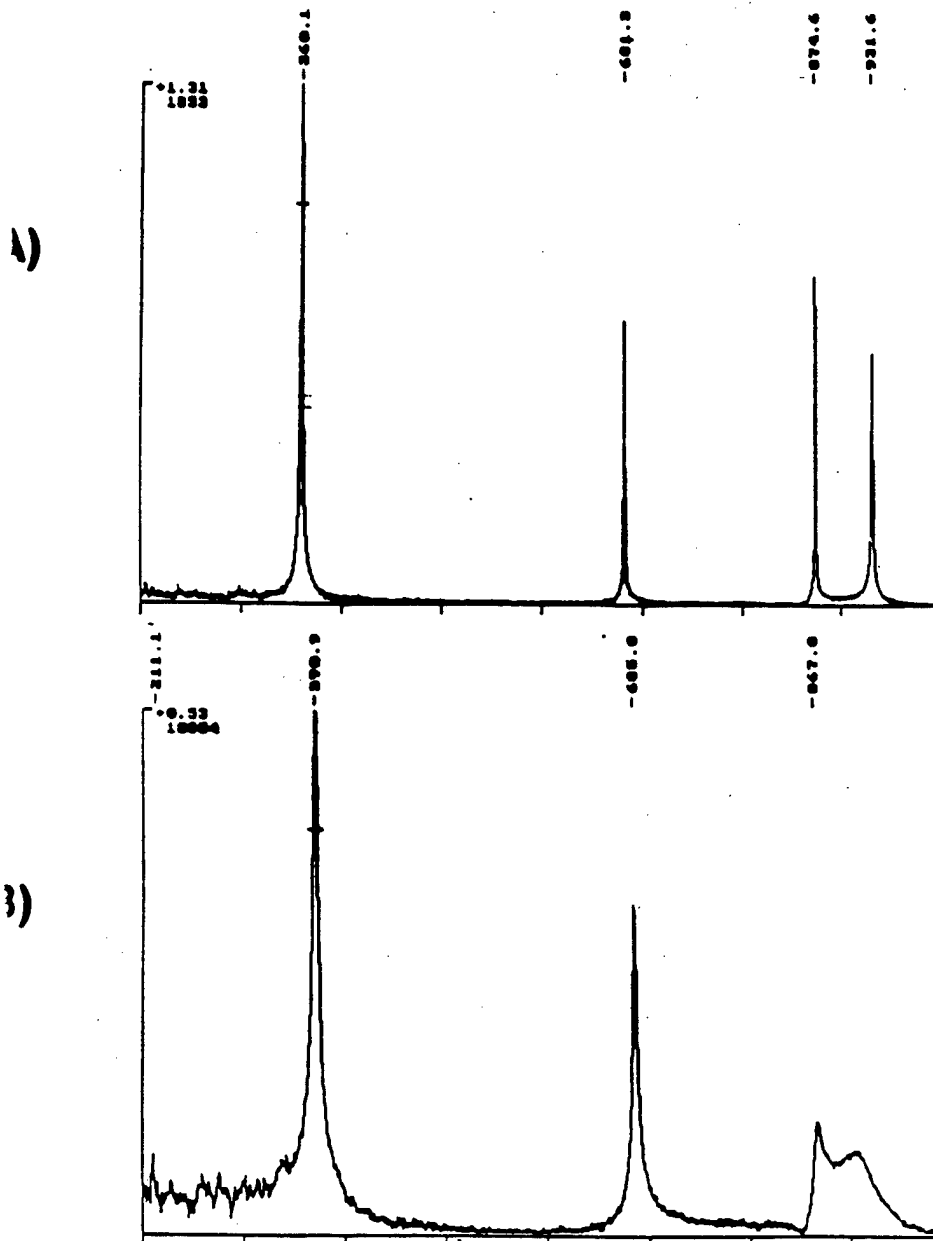
xohmrq61 ctss time 82.350 seconds

cpu = 66.355 i/o = 7.158 mem = 8.837

all done

Detection of microcracking in a single crystal sample of EuB_6

- A) Resonances of the pristine sample
 B) Resonances after a small stress has induced microcracking



We have not succeeded in answering all of our questions. Indeed, we sometimes feel that we have not completely answered any of them. The answers we have found only served to raise a whole new set of questions. In some ways we feel that we are as confused as ever, but we think we are now confused on a higher level, and about more important things.

-Author unknown



ELASTIC PROPERTIES CALCULATED FROM THE
HIGH-TEMPERATURE DATABASE FOUND FROM RUS

by

Orson L. Anderson

Supported by ONR

The vibrational part of the free energy of an ensemble of independent insulator oscillators obeying Bose-Einstein statistics is [Landau and Lifshitz, 1958]

$$\mathcal{F}_{VIB_i} = \left(\frac{\hbar\omega_i}{2kT} \right) \ln \left(1 - e^{\hbar\omega_i/kT} \right), \quad (1)$$

where there are $3pN$ modal energies given by $\omega_1, \omega_2, \omega_3 \dots 3pN$; N is Avogadro's number; p is the number of atoms in the formula unit; \hbar is Planck's constant; and k is the Boltzmann constant.

An important approximation to the above equation is provided by the assumption that all frequencies depend on V , but not explicitly on T . This is called the quasiharmonic approximation, defined by

$$\left(\frac{\partial\omega_i}{\partial V} \right)_T \neq 0, \quad (2)$$

and

$$\left(\frac{\partial\omega_i}{\partial T} \right)_V = 0, \quad (3)$$

where $i = 1, 2, 3 \dots 3pN$.

Assume that the acoustic normal modes, f_i , measured in RUS, follow the quasiharmonic approximation; that is

$$\left(\frac{\partial f_i}{\partial T}\right)_V = 0. \quad (4)$$

Expressing f_i as $f_i(P, T)$, we have from calculus

$$\left(\frac{\partial f_i}{\partial T}\right)_V = \left(\frac{\partial f_i}{\partial T}\right)_P + \left(\frac{\partial P}{\partial T}\right)_V \left(\frac{\partial f_i}{\partial P}\right)_T. \quad (5)$$

By means of a calculus equation involving P , V , and T , we have

$$\left(\frac{\partial P}{\partial T}\right)_V = \alpha K_T, \quad (6)$$

where α , the volume coefficient of thermal expansivity, is $(1/V)(\partial V/\partial T)_P$, and K_T , the isothermal bulk modulus, is $-V(\partial P/\partial V)_T$.

Therefore, within the quasiharmonic approximation, the pressure derivatives of frequencies are easily approximated from the temperature derivatives, being

$$\left(\frac{\partial f_i}{\partial P}\right)_T = -\frac{1}{\alpha K_T} \left(\frac{\partial f_i}{\partial T}\right)_P. \quad (7)$$

Then, assuming each f_i is linear in P , we can find

$$f_i(P)_T = f_i(P = 0, T) + \left(\frac{\partial f_i}{\partial P} \right)_T P. \quad (8)$$

The linear pressure dependencies of optic phonon frequency, including Raman and infrared vibration, are found in α - and β -olivine up to at least 14 GPa [*Chopelas, 1990, 1991; Hofmeister et al., 1989; Cynn and Hofmeister, 1994*].

Before we can confidently use the above equations to find elastic constants versus P , we must be sure of 3 conditions: (1) the thermal pressure (or αK_T) must be independent of V ; (2) $(\partial f_i / \partial T)_V = 0$ must be fulfilled; and (3) the mode frequencies must be linear in P . In principle, αK_T could vary with T and P (or V), implying that the $(\partial f_i / \partial P)_T$ obtained from $-(1/\alpha K_T)(\partial f_i / \partial T)_V$ is appropriate for only one coordinate of P, T space. Thus, the assumption that αK_T is independent of volume is necessary for condition 3 as well. We shall examine solids for which conditions 1 and 2 are fulfilled, or one or the other condition is fulfilled. The test of the first condition is whether αK_T is independent of V .

Is αK_T Independent of V ?

When P_{TH} is independent of V , αK_T is independent of V , as is now shown. The general form of the equation of state is

$$P(V, T) = P_1(V) + P_{TH}(V, T), \quad (9)$$

where the first term on the right, P_1 , refers to the isothermal equation of state (EoS), and the second term on the right, P_{TH} , refers to the thermal pressure. Since P_1 is independent of T , $(\partial P / \partial T)_V = (\partial P_{TH} / \partial T)_V$, and therefore

$$P_{TH} = \int \alpha K_T dT \text{ at constant } V. \quad (10)$$

Therefore, αK_T must vary with V in the same way P_{TH} varies with V . The thermodynamic identity relating αK_T and V is given by *Anderson [1995]*

$$\left(\frac{\partial \alpha K_T}{\partial V} \right)_T \equiv \left(\frac{\alpha K_T}{V} \right) (\delta_T - K'), \quad (11)$$

where δ_T is the Anderson-Grüneisen parameter, a dimensionless thermoelastic parameter defined as $-(1/\alpha K_T) (\partial K_T / \partial T)_P$.

Is There Anharmonicity in C_V at High T ?

The literature has several examples, e.g., for NaCl and MgO, $(\partial C_V / \partial T)_P = 0$ at high T .

Table 1. MgO: Physical Properties at High Temperature

T	ρ	α	K_S	G	C_P	γ	C_V	K_T
100	3.602	0.63	165.7	132.0	0.194	1.59	0.194	165.6
200	3.597	2.24	164.6	130.3	0.662	1.55	0.658	163.5
300	3.585	3.12	163.9	131.8	0.928	1.54	0.915	161.6
400	3.573	3.57	162.3	129.4	1.061	1.53	1.048	158.9
500	3.559	3.84	160.7	126.9	1.130	1.53	1.098	156.1
600	3.545	4.02	158.9	124.4	1.173	1.54	1.131	153.2
700	3.531	4.14	157.1	121.8	1.204	1.53	1.153	150.4
800	3.516	4.26	155.1	119.2	1.227	1.53	1.166	147.4
900	3.501	4.38	153.1	116.7	1.246	1.54	1.175	144.3
1000	3.486	4.47	151.1	114.1	1.262	1.54	1.181	141.4
1100	3.470	4.56	148.9	111.5	1.276	1.53	1.185	138.3
1200	3.454	4.65	146.7	109.0	1.289	1.53	1.188	135.1
1300	3.438	4.71	144.4	106.4	1.301	1.52	1.190	132.1
1400	3.422	4.80	142.0	103.8	1.312	1.52	1.191	128.1
1500	3.405	4.89	139.7	101.3	1.323	1.52	1.191	125.7
1600	3.388	4.98	137.3	99.0	1.334	1.51	1.191	122.5
1700	3.371	5.04	134.9	96.7	1.346	1.50	1.193	119.6
1800	3.354	5.13	132.7	94.5	1.358	1.50	1.193	116.6

To successfully predict $C_{ij}(P)$ from measured $(\partial C_{ij}/\partial T)_P$, we need three conditions satisfied:

$$1. \quad \left[\frac{\partial (\alpha K_T)}{\partial V} \right] = 0 \quad (12)$$

$$2. \quad \left[\frac{\partial f_i}{\partial T} \right]_V = 0 \quad (13)$$

$$3. \quad C_{ij}(P) = C_{ij}(P=0) + \left(\frac{\partial C_{ij}}{\partial P} \right)_T P \quad (14)$$

To test these three conditions:

$$1. \quad \text{Is } P_{TH} \text{ independent of } V \text{ or is } \delta_T = K', \quad (15)$$

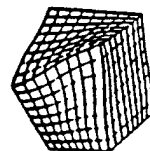
where $\delta_T = -\frac{1}{\alpha K_T} \left(\frac{\partial K_T}{\partial T} \right)_P$ and $K' = \left(\frac{\partial K}{\partial P} \right)_T$?

$$2. \quad \text{Is } \left(\frac{\partial C_V}{\partial T} \right)_P = 0 \quad (\text{Dulong and Petit limit})? \quad (16)$$

$$3. \quad \text{Is } \left(\frac{\partial^2 C_{ij}}{\partial P^2} \right) = 0 \quad (\text{beyond our resolution})? \quad (17)$$

Quasiharmonic theory is based on the assumptions,

$$\left(\frac{\partial \omega_i}{\partial T}\right)_V = 0 \quad \left(\frac{\partial \omega_i}{\partial V}\right)_T \neq 0,$$



where $i = 1, 2, 3 \dots 3pN$

Therefore, we assume that for the normal modes, f_i ,

measured in RUS,

$$\left(\frac{\partial f}{\partial T}\right)_V = 0. \quad (18)$$

Sodium chloride (NaCl), at ambient conditions.

dimension : 5.947x4.529x3.463 mm³

density : 2.160 g/cm³

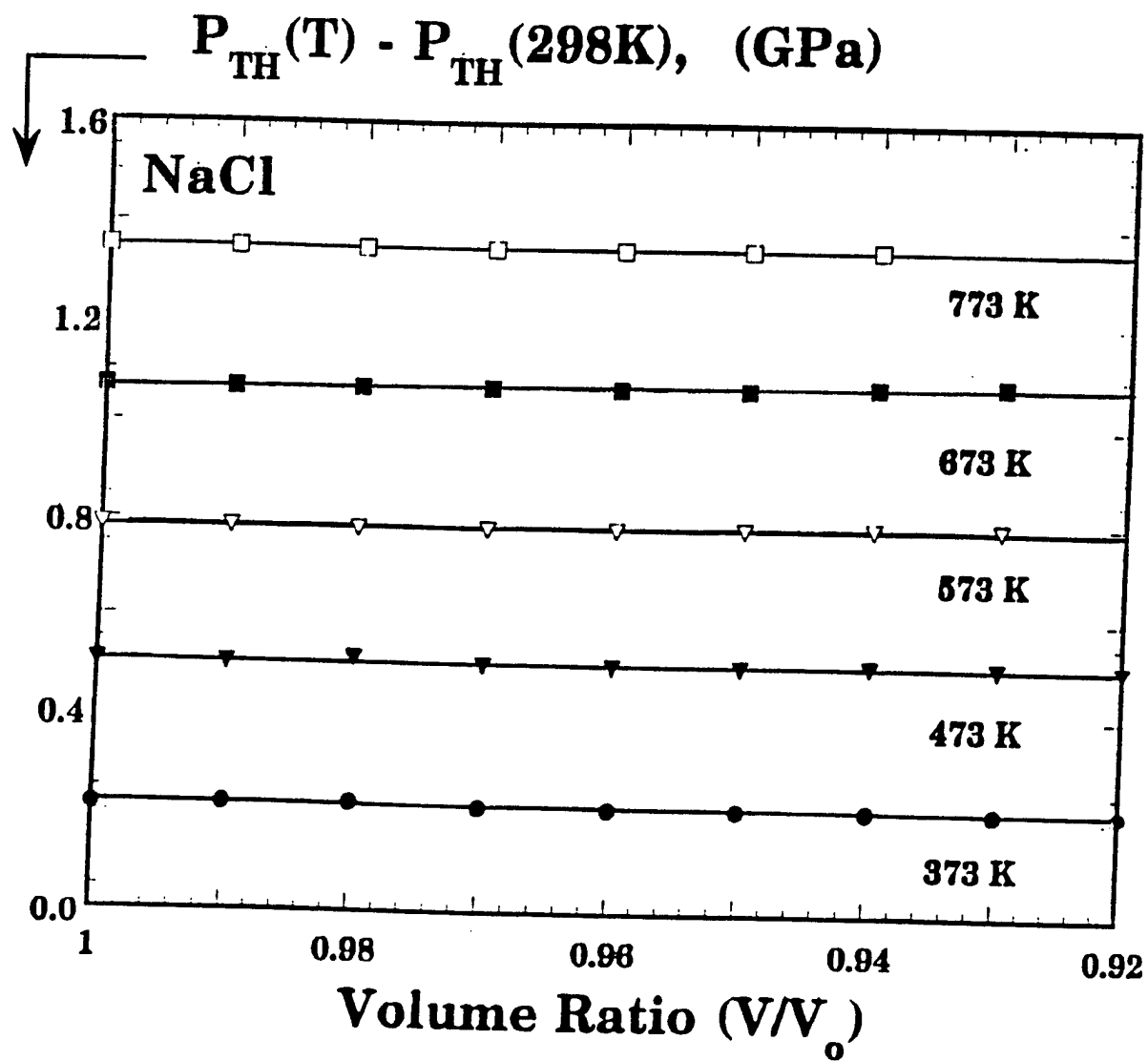
C₁₁ : 496.7 (3.7) kbar

C₁₂ : 131.8 (4.4) kbar

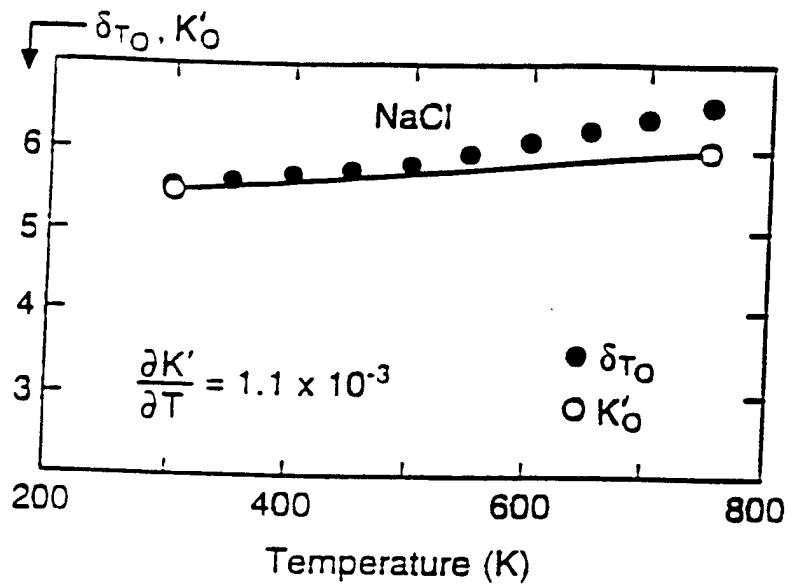
C₄₄ : 127.8 (0.2) kbar

$$\alpha K_T = (117 \times 10^{-6} / K) * (242 \text{ kbar}) = 0.028557 \text{ kbar/K}$$

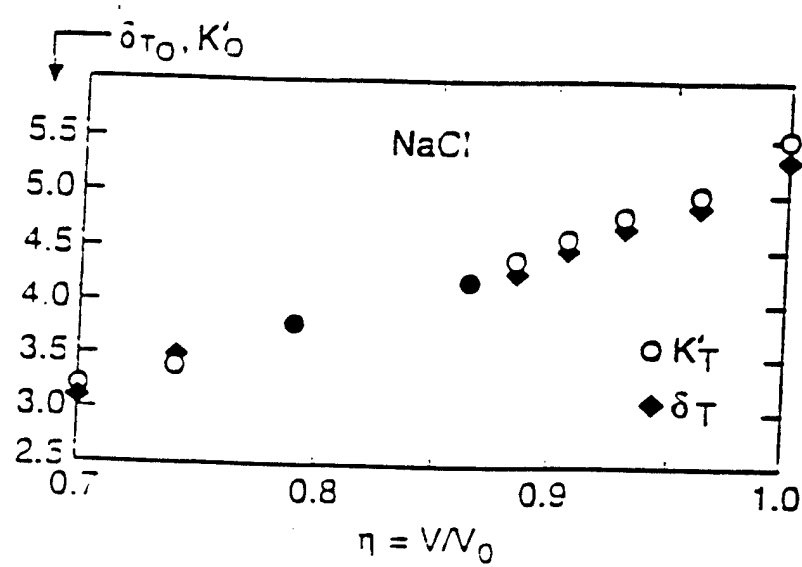
mode	294 K	571 K	($\partial f / \partial T$)	($\partial f / \partial P$)
	(Hz)	(Hz)	(Hz/K)	(Hz/kbar)
Au-1 (torsion) :	180600	176300	-15.5	543.6
Blu-1 (flexure):	255100	229100	-93.9	3286.9
Blg-1 (shear):	297300	286900	-37.5	1314.7
Ag-1 (dilation):	370600	320200	-181.9	6371.4

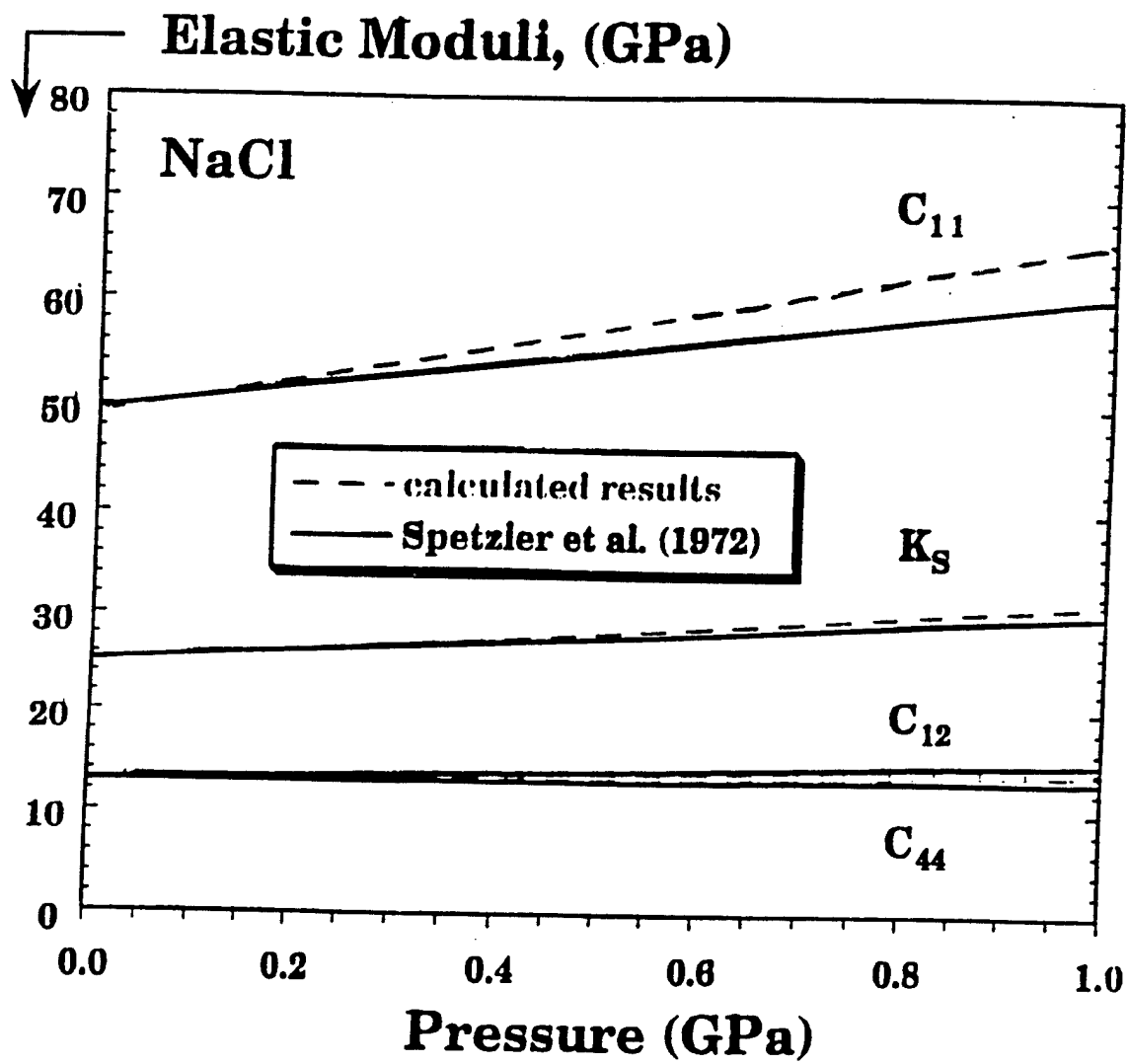


$$\frac{\partial \ln \alpha K_T}{\partial \ln V} = \delta_T - K'$$

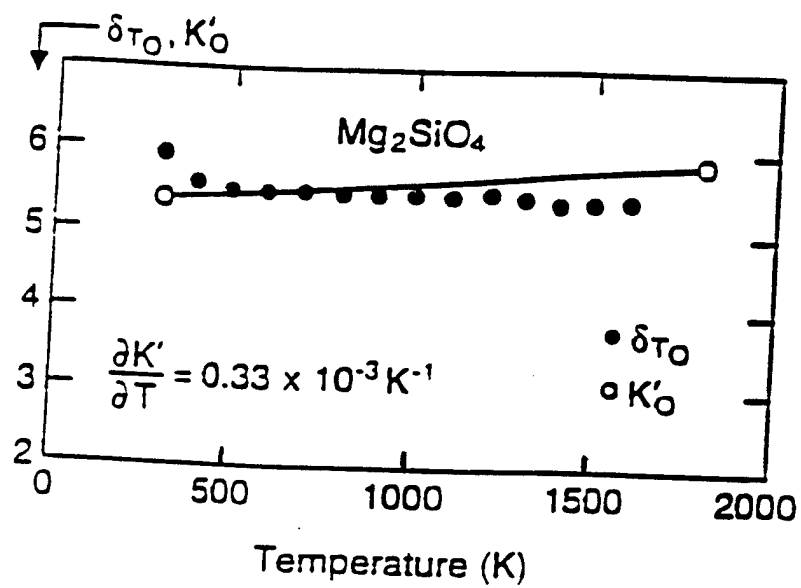


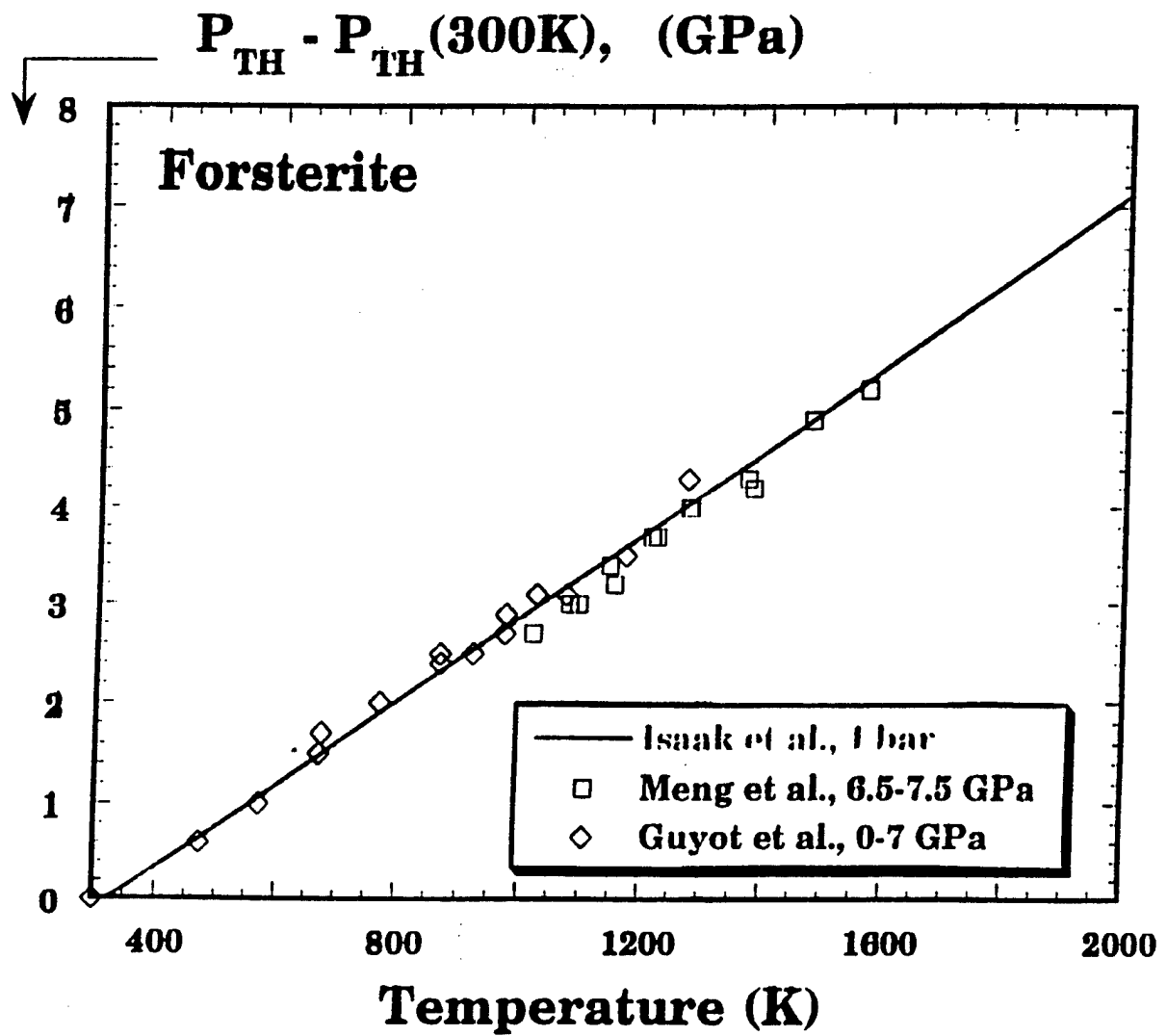
$$\frac{\partial \ln \alpha K_T}{\partial \ln V} = \delta_T - K'$$

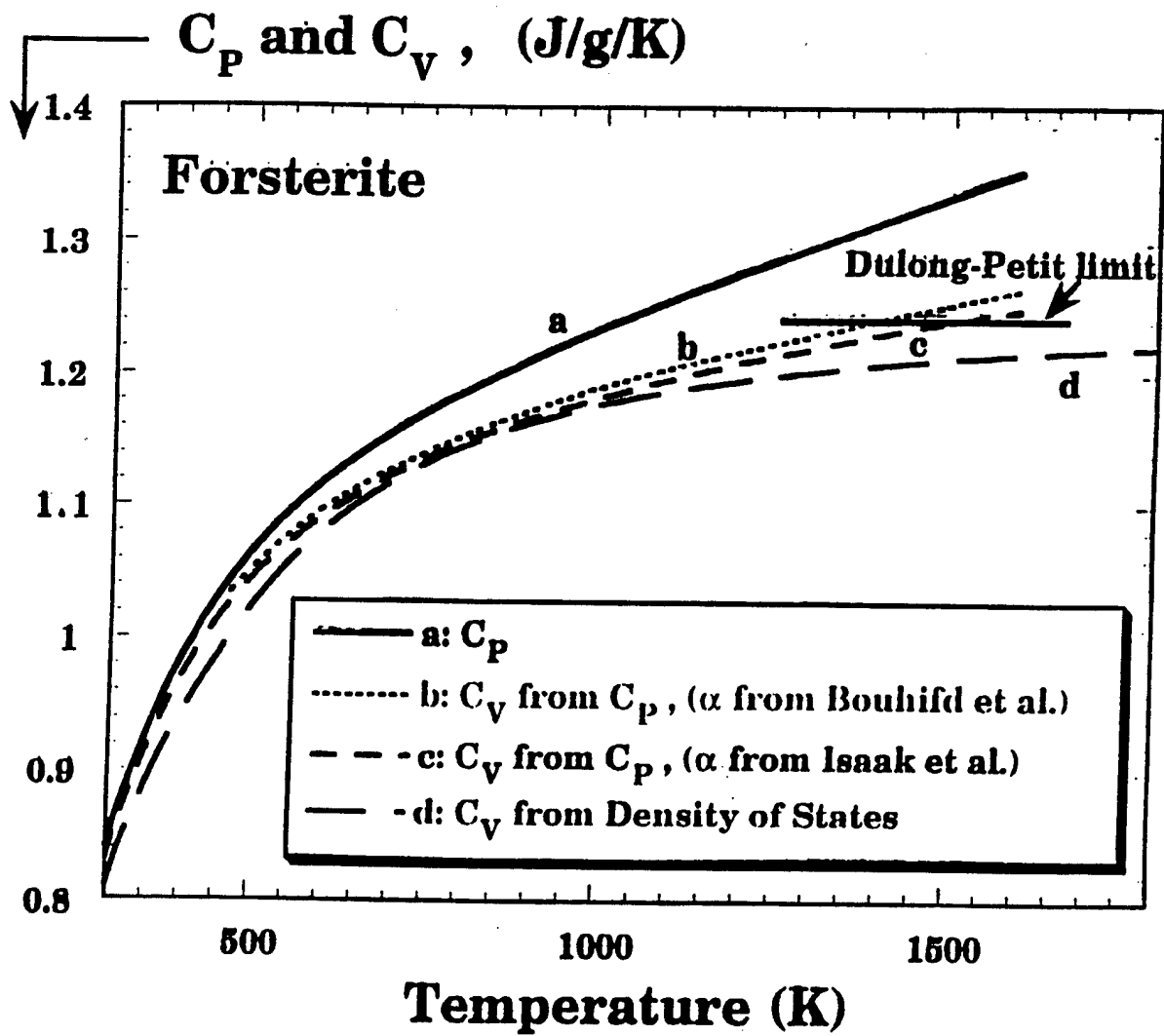


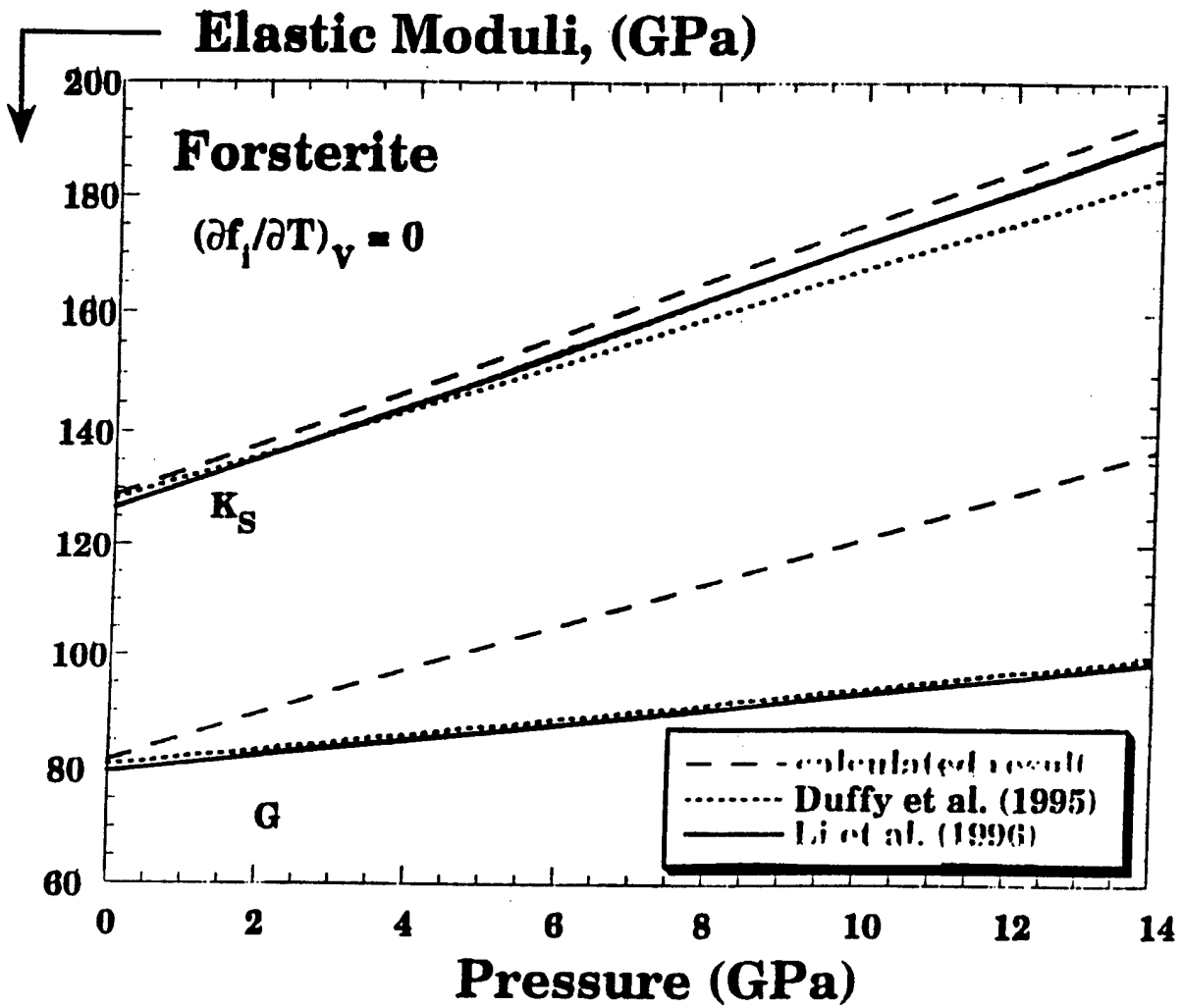


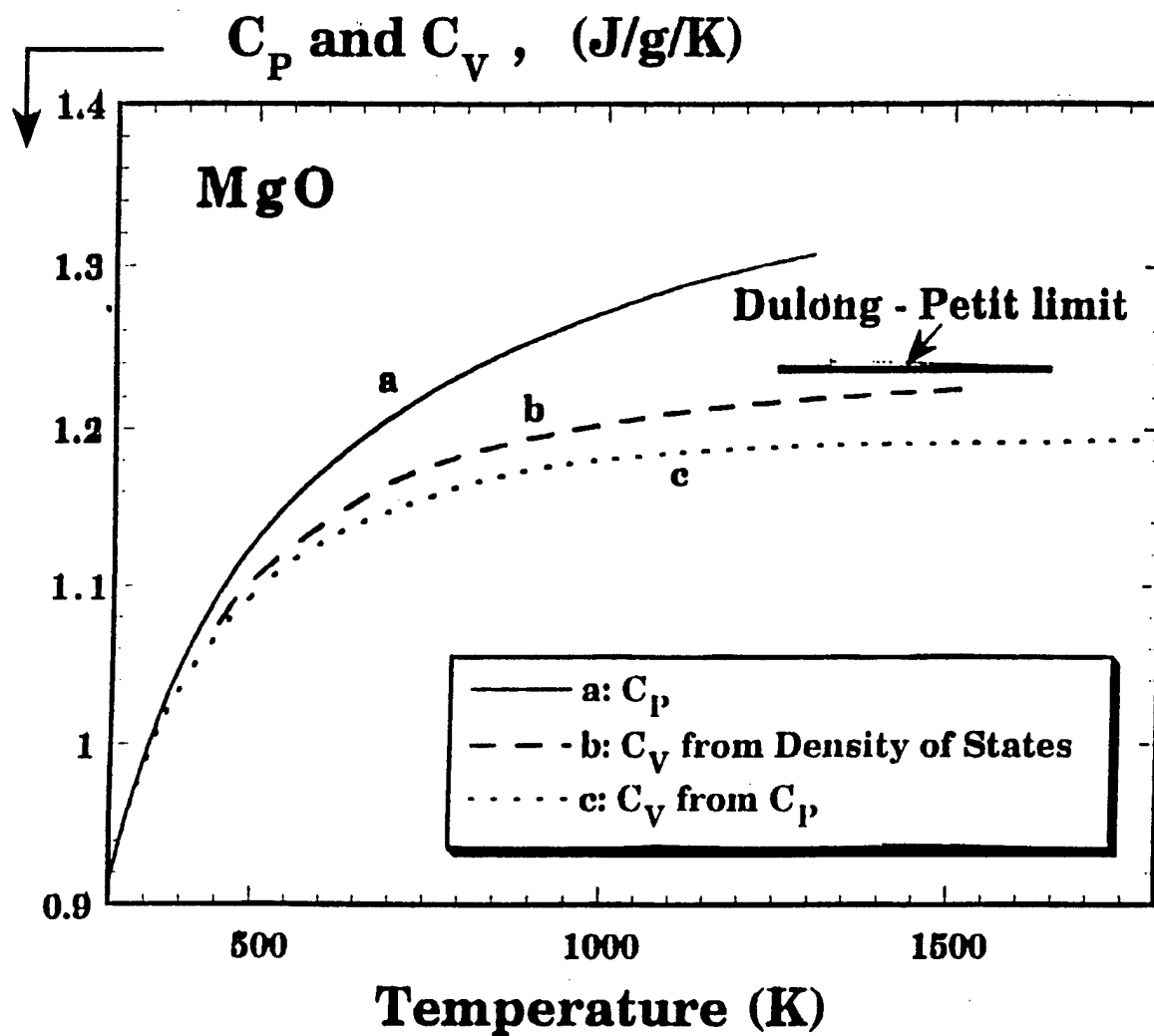
$$\frac{\partial \ln \alpha K_T}{\partial \ln V} = \delta_T - K'$$

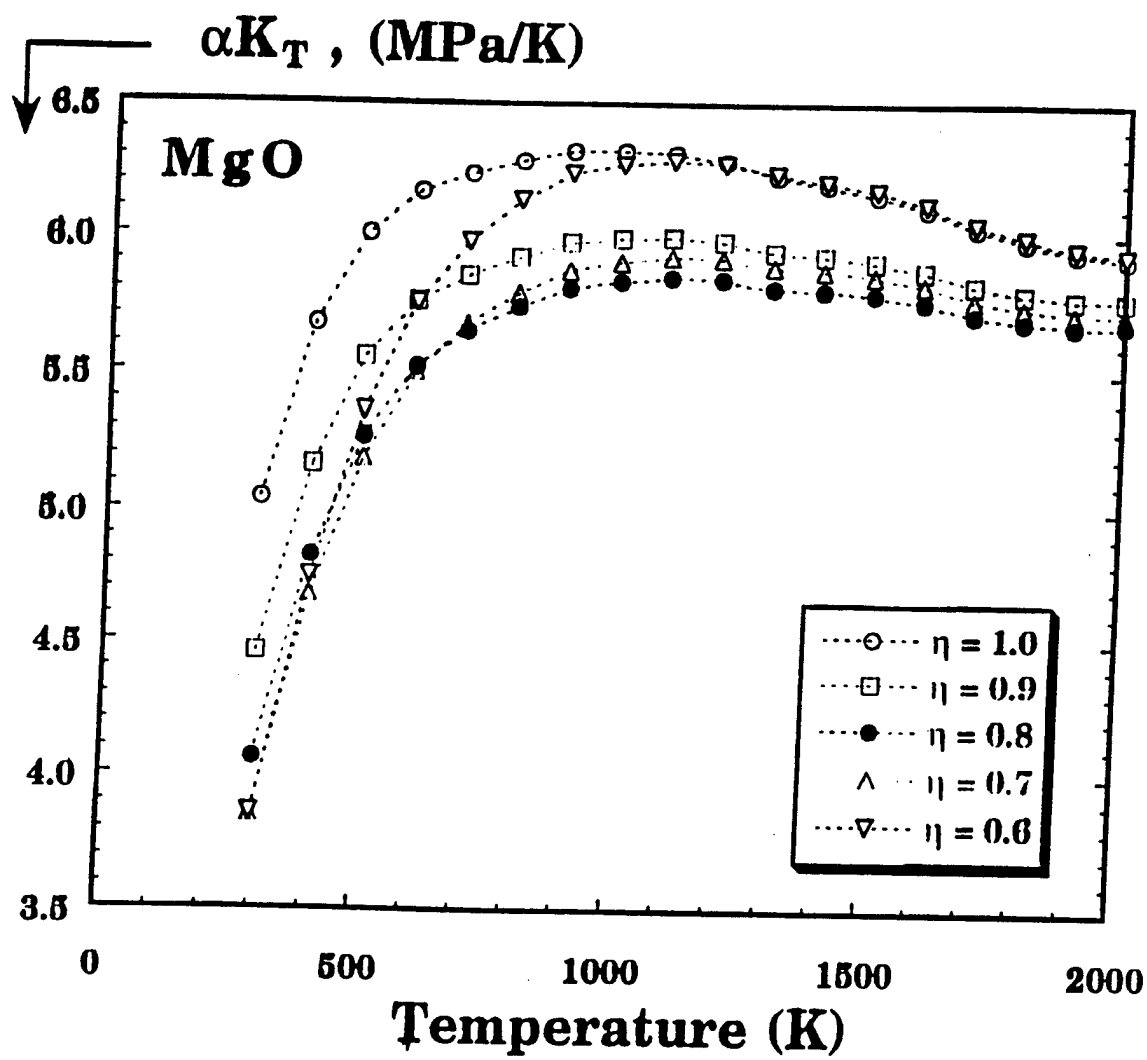


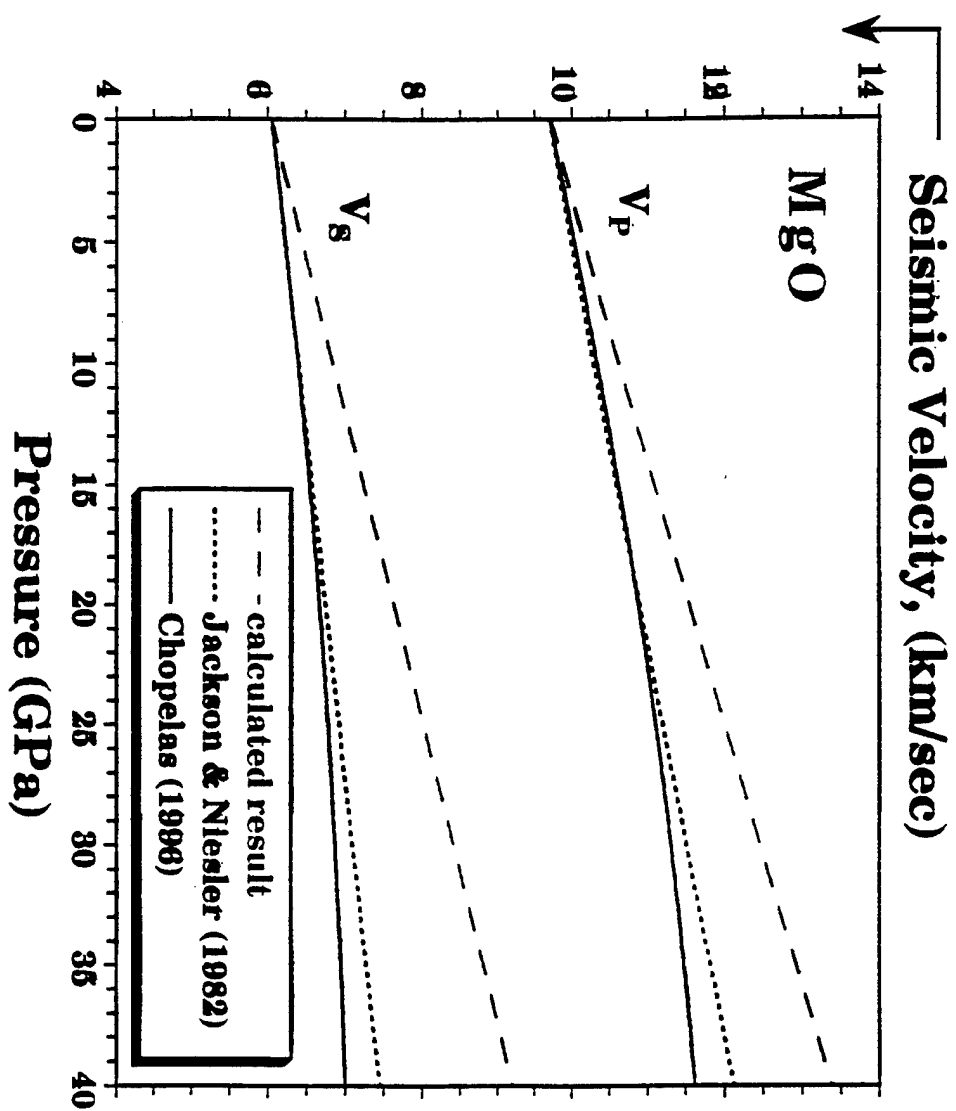


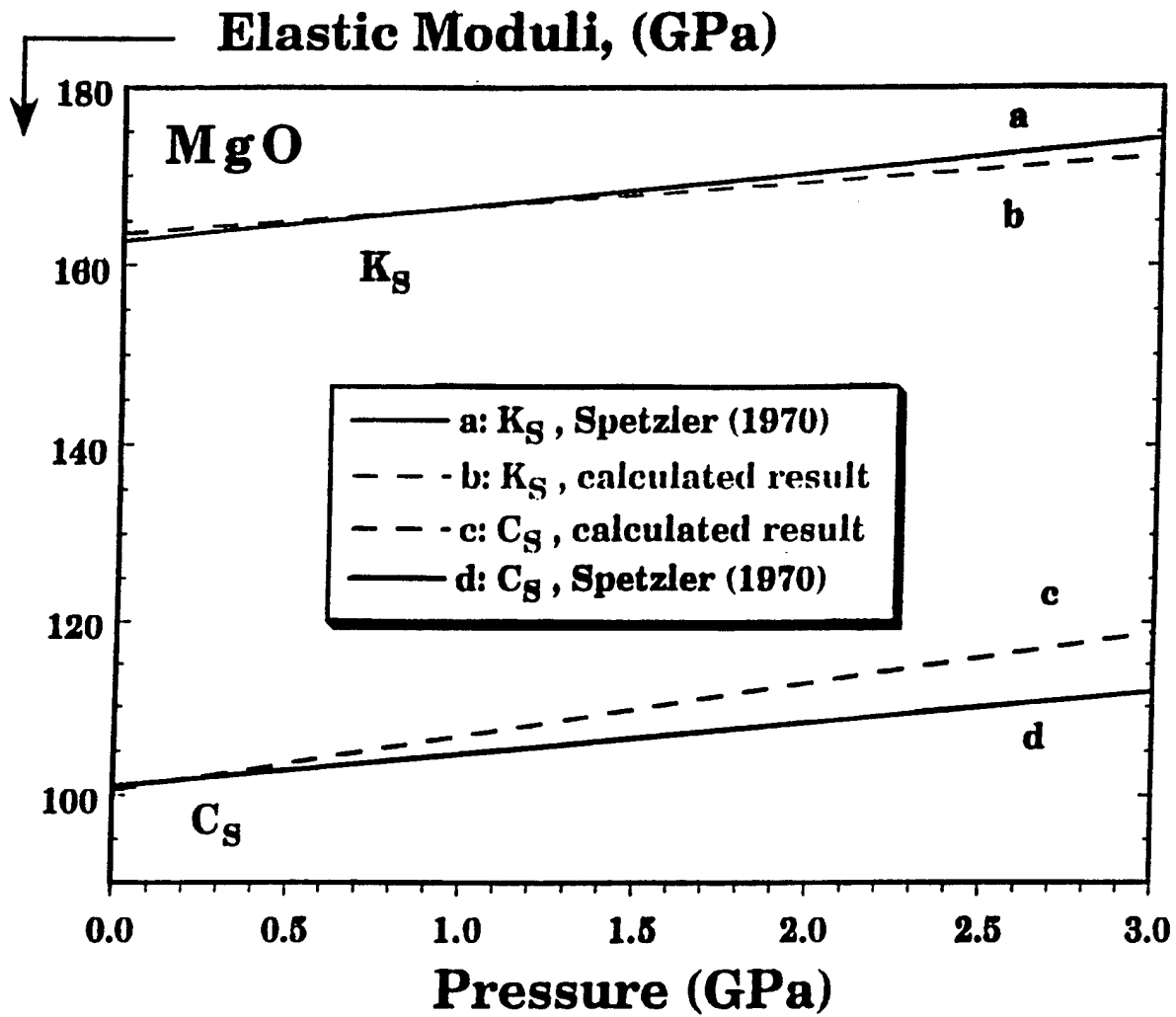












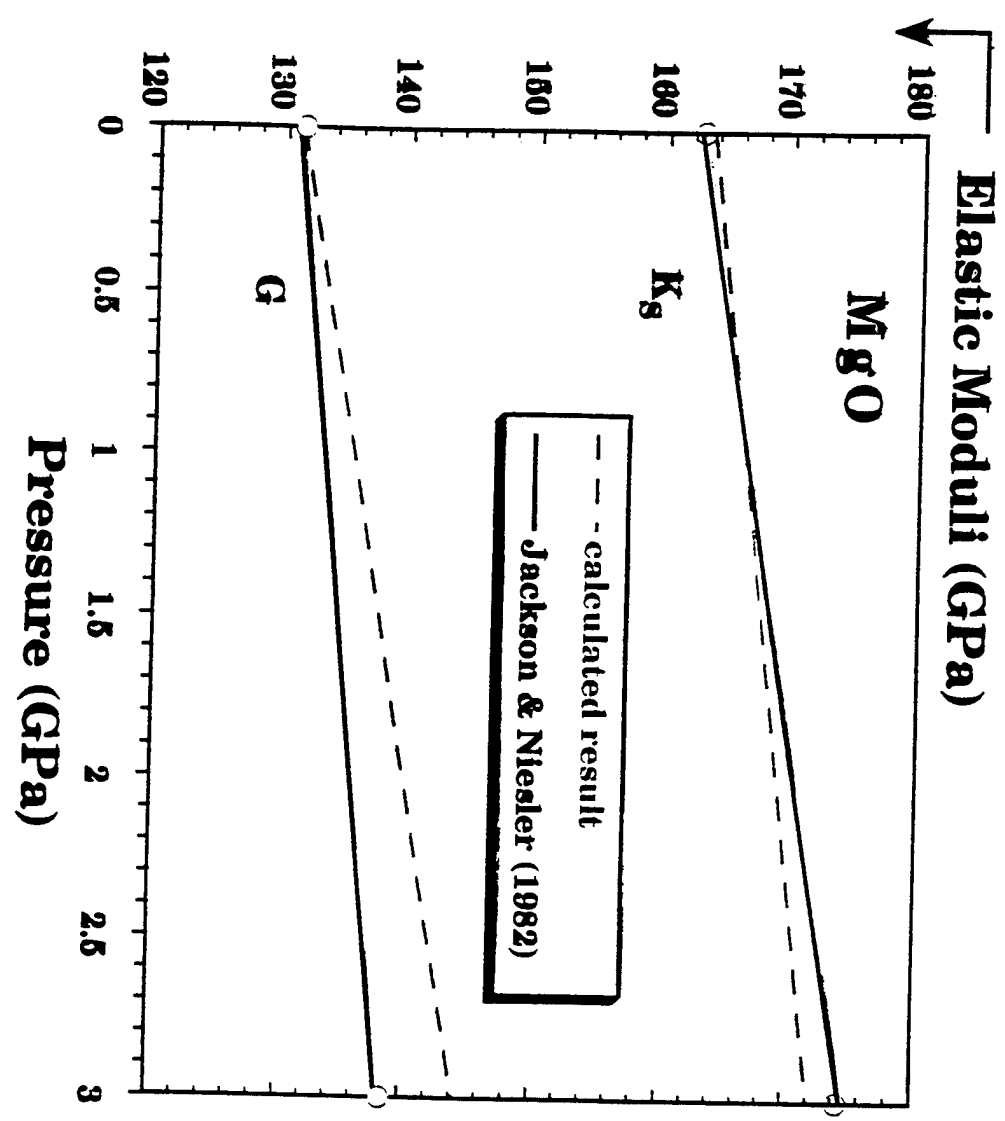


Table 5. Calculated RPR Frequencies for Forsterite at High Pressure

Mode	300 K Hz	$(\partial f_i / \partial T)$ Hz/kbar	$(\partial f_i / \partial P)$ Hz/kbar	10 kbar Hz
Au-1	647430	-55.3	1598.3	663412
Au-2	771500	-76.2	2202.3	793523
B2g-1	959190	-78.7	2274.6	981936
B3g-1	965260	-93.9	2713.9	992399
B2u-1	973720	-63.9	1845.4	992174
B1g-1	1001740	-95.2	2750.0	1029240
B1u-1	1004250	-61.7	1783.2	1022082
B3u-1	1018320	-80.8	2335.3	1041672
B2u-2	1061100	-78.3	2261.6	1083715
B1u-2	1120120	-88.4	2554.9	1145669
B1g-2	1194370	-91.2	2634.4	1220713
B2g-2	1211820	-93.0	2686.4	1238684
B3g-2	1219490	-86.0	2485.6	1244345
B3u-2	1225260	-85.9	2842.7	1250086
B3g-3	1302690	-105.9	3060.7	1333296
Ag-4	1331730	-96.2	2780.3	1359533
Au-3	1368250	-123.1	3557.8	1403828
B1g-3	1398060	-121.8	3520.2	1433262
B3u-3	1418260	-104.7	3024.6	1448505
Ag-5	1432110	-77.0	2225.4	1454364
B1u-3	1459700	-104.7	3026.0	1489960
B2g-3	1468400	-131.5	3799.1	1506391
B2u-3	1494980	-102.1	2949.4	1524474
B1u-4	1564840	-130.0	3757.2	1602412
B2u-4	1575170	-135.0	3900.3	1614172
Ag-6	1636520	-98.2	2836.7	1664887
B1u-5	1668710	-110.1	3180.6	1700516
B2u-5	1688220	-118.4	3422.0	1722439
B3u-5	1701340	-108.4	3132.9	1732669
B2u-6	1707460	-147.7	4267.3	1750133

Table 6. Pressure Dependence of the Elastic Constants of Forsterite

$(\frac{\partial C_{ij}}{\partial P})_T$	Pulse ¹ Superposition	Pulse ² Superposition	Brillouin ³	Pulse-Echo ⁴ Overlap	Brillouin ⁵	This Study ⁶	This Study ⁷
C_{11}	8.47	8.32	9.83	7.08	5.45	10.50	3.62
C_{22}	6.56	5.93	7.03	5.09	5.17	8.11	3.88
C_{33}	6.57	6.21	7.55	5.29	4.72	8.68	3.70
C_{44}	2.12	2.12	1.72	1.80	1.67	4.09	2.63
C_{55}	1.66	1.65	1.50	1.40	1.41	4.15	2.39
C_{66}	2.37	2.32	2.20	2.09	1.76	4.84	3.07
C_{23}	4.11	3.53	...	3.17	3.45	1.73	0.24
C_{31}	4.84	4.23	...	3.40	3.04	2.91	1.46
C_{12}	4.67	4.30	...	3.56	3.66	3.19	1.77

¹ Kumazawa and Anderson [1969].² Graham and Barach [1969].³ Shimizu et al. [1982].⁴ Yoneda and Morioka [1992].⁵ Duffy et al. [1995].⁶ $(\partial f_i / \partial T)_V = 0$.⁷ $(\partial f / \partial T)_V \neq 0$.

Summary

We have found that for a solid (such as NaCl) in which αK_T is independent of V and C_V is quasiharmonic, the inversion of the measured $(\partial f_i / \partial T)_P$ yields reliable values of $(\partial f_i / \partial P)_T$ modes. This provides an accurate calculation of $K_S(P)$ and shear moduli up to 1.5 GPa.

We have found that for a solid (such as MgO), where C_V is quasiharmonic up to very high T but αK_T is not independent of V at ambient conditions, the inversion leading to $K_S(P)$ yields good results, but $G(P)$ departs from experiment.

We have found that for a solid (such as Mg_2SiO_4), where αK_T is independent of V but C_V is not quasiharmonic, the inversion leading to $K_S(P)$ and $\Phi(P)$ yields good results, but $G(P)$ departs from experiment.

RUS Measurements of Nickel Alloys at High Temperature

J.D. Carnes

Don Isaak

Orson Anderson

Institute for Geophysics and Planetary Physics

UCLA

Overview of Topics

- Discussion of sources of funding and interest for these RUS projects
- Materials studied
- Resonant mode identification issues
- RUS spectra and resultant moduli determined as a function of temperature
- Results/conclusions

RUS Projects involving nickel alloys at UCLA

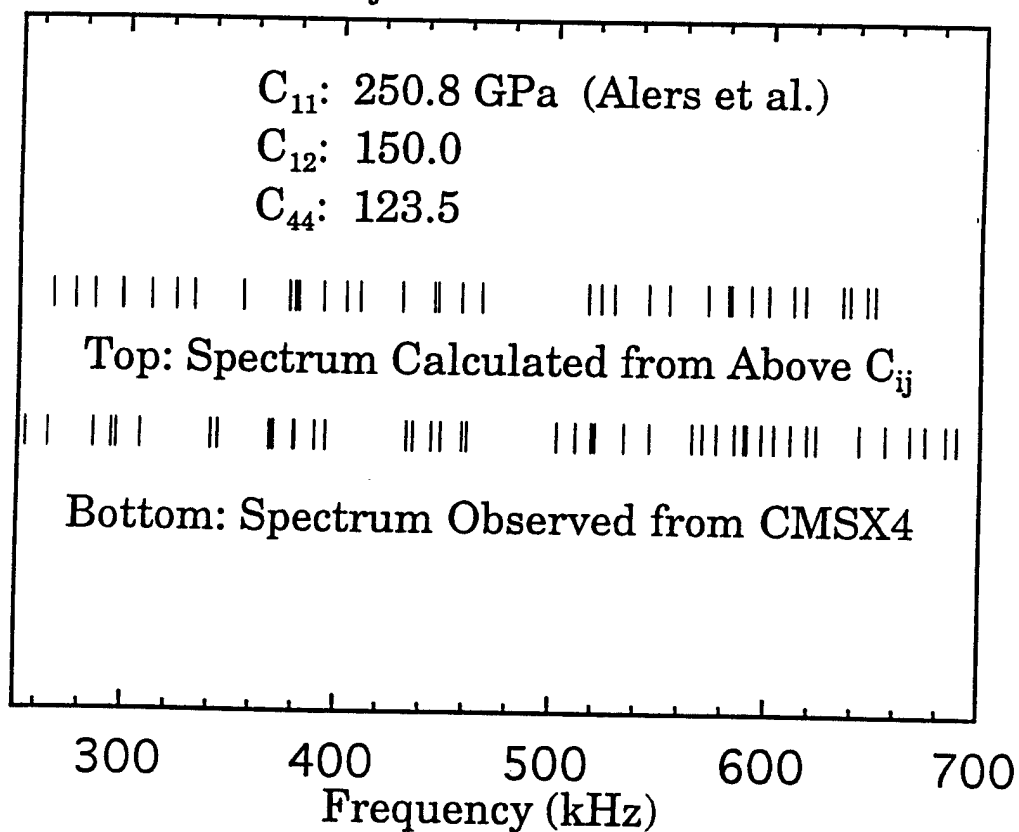
- Project in collaboration with Concurrent Technologies Corporation (CTC), an independent nonprofit organization, serves as a national resource to the industrial base
- Project in collaboration with Prof. Alan Ardell of the materials science dept., UCLA

CTC Alloy Composition (wt%, Ni balance)

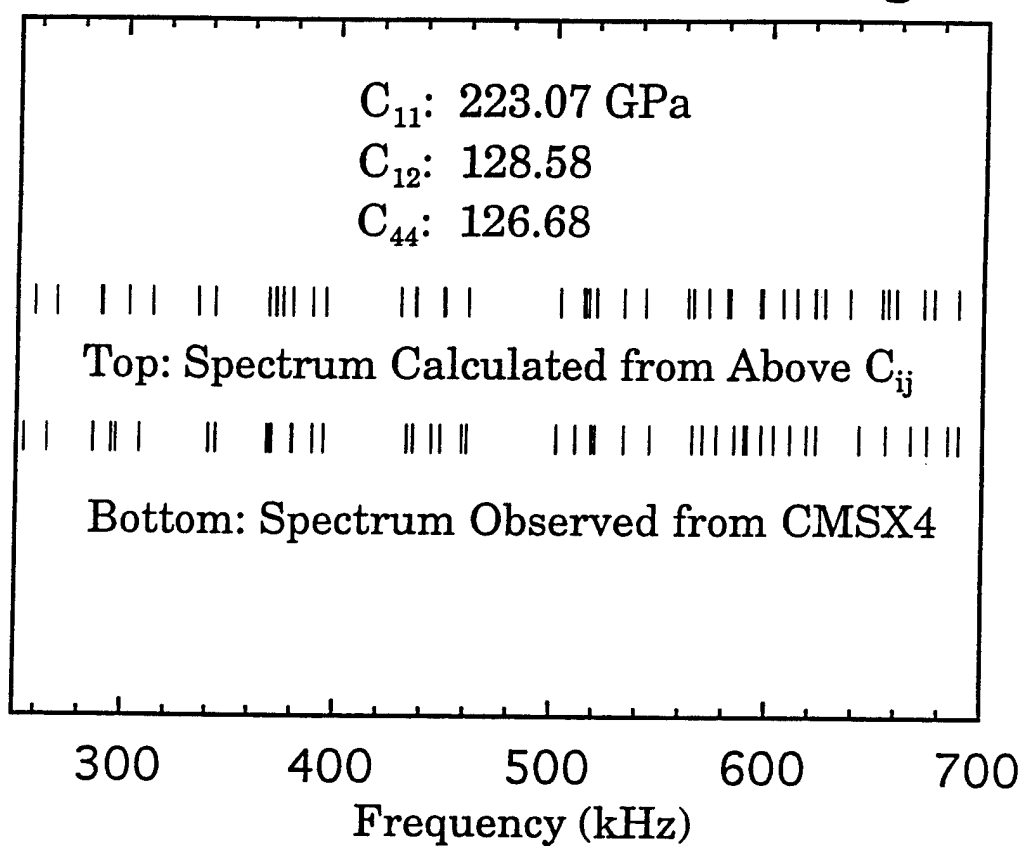
Alloy	Density (g/cm ³)	Cr	Co	Mo	W	Ta	Re	Al	Ti	Hf
CMSX-4	8.712	6.5	9	0.6	6	6.5	3	5.6	1.0	0.1
CMSX-6	8.043	10	5	3		2		4.8	4.7	0.1

Other Material Studied: SPEC2
(Ni-13.36%Al)

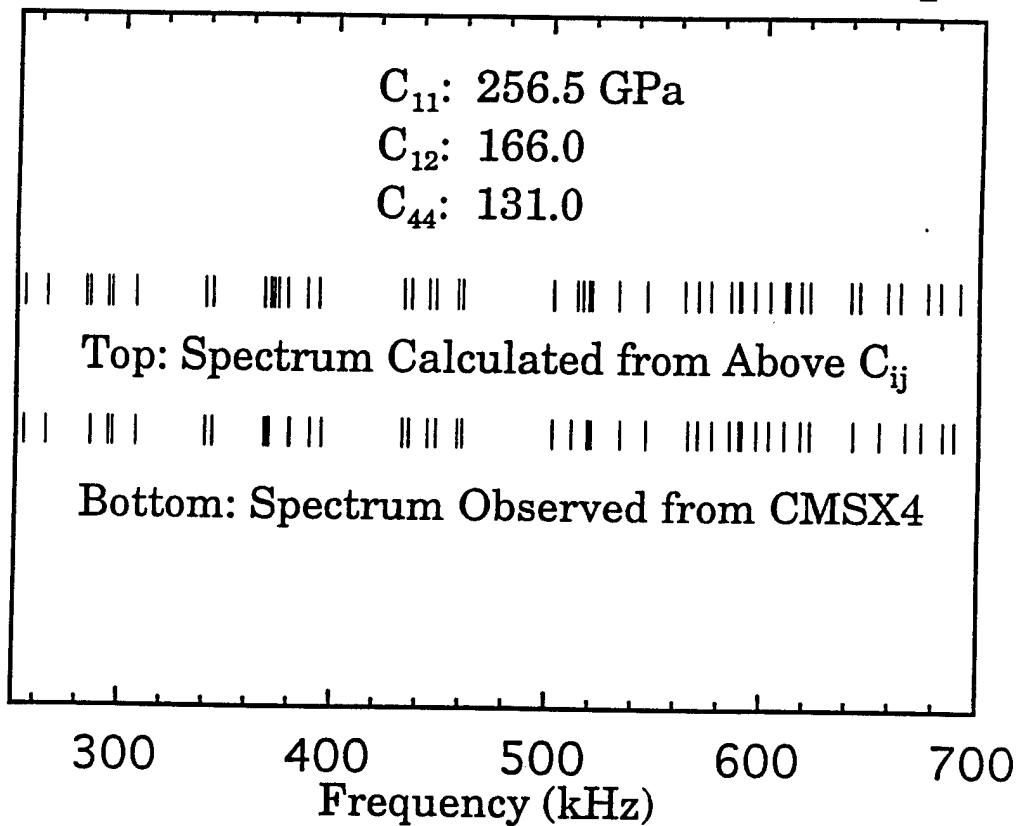
CMSX4 Mode ID Using C_{ij} from Nickel



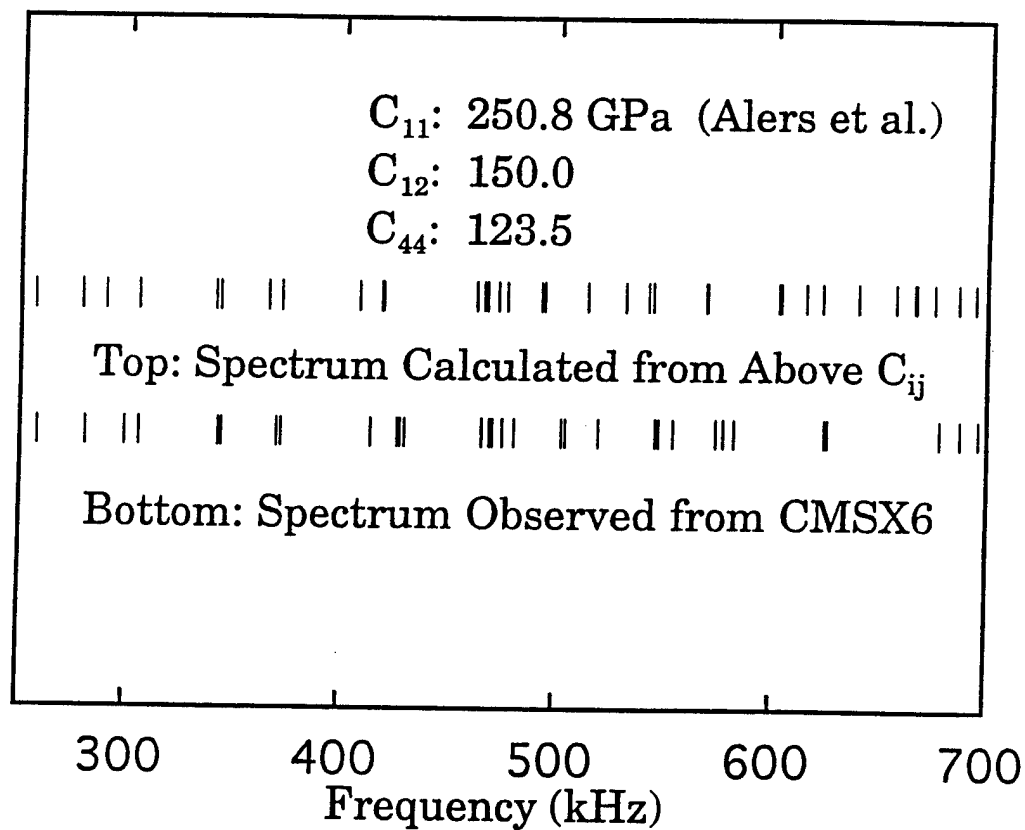
CMSX4 (Result of First Mode Assignments)



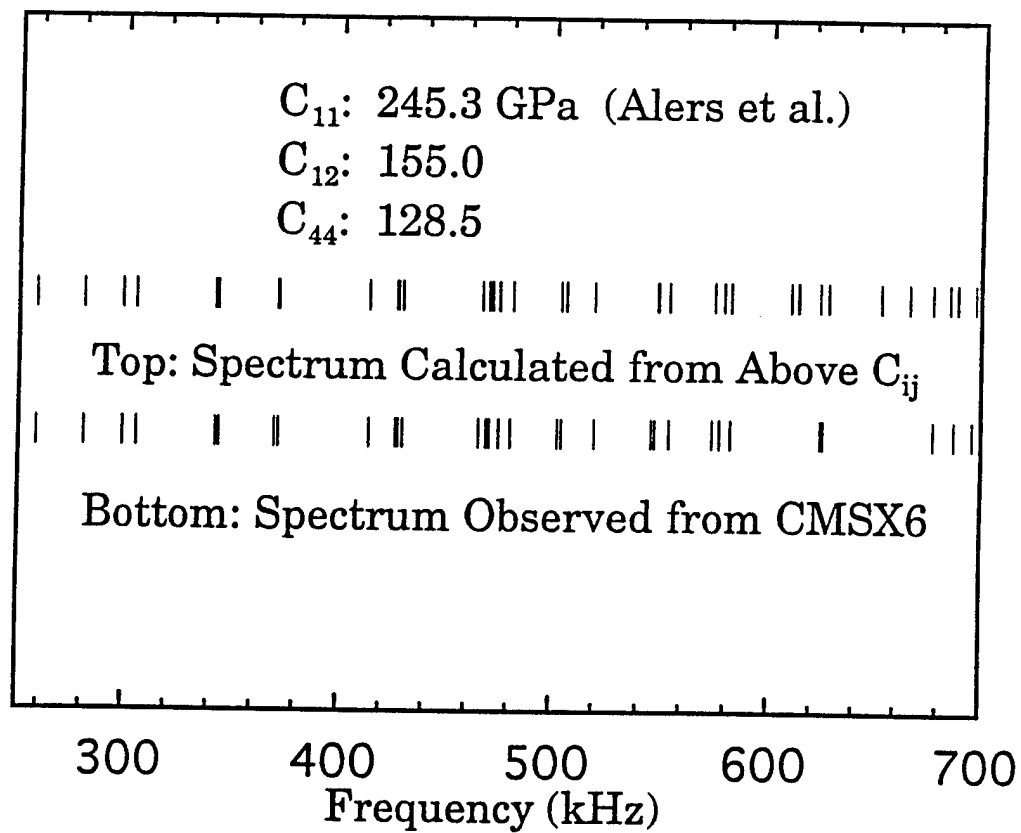
CMSX4 Mode ID (Final Calculated Spectrum)



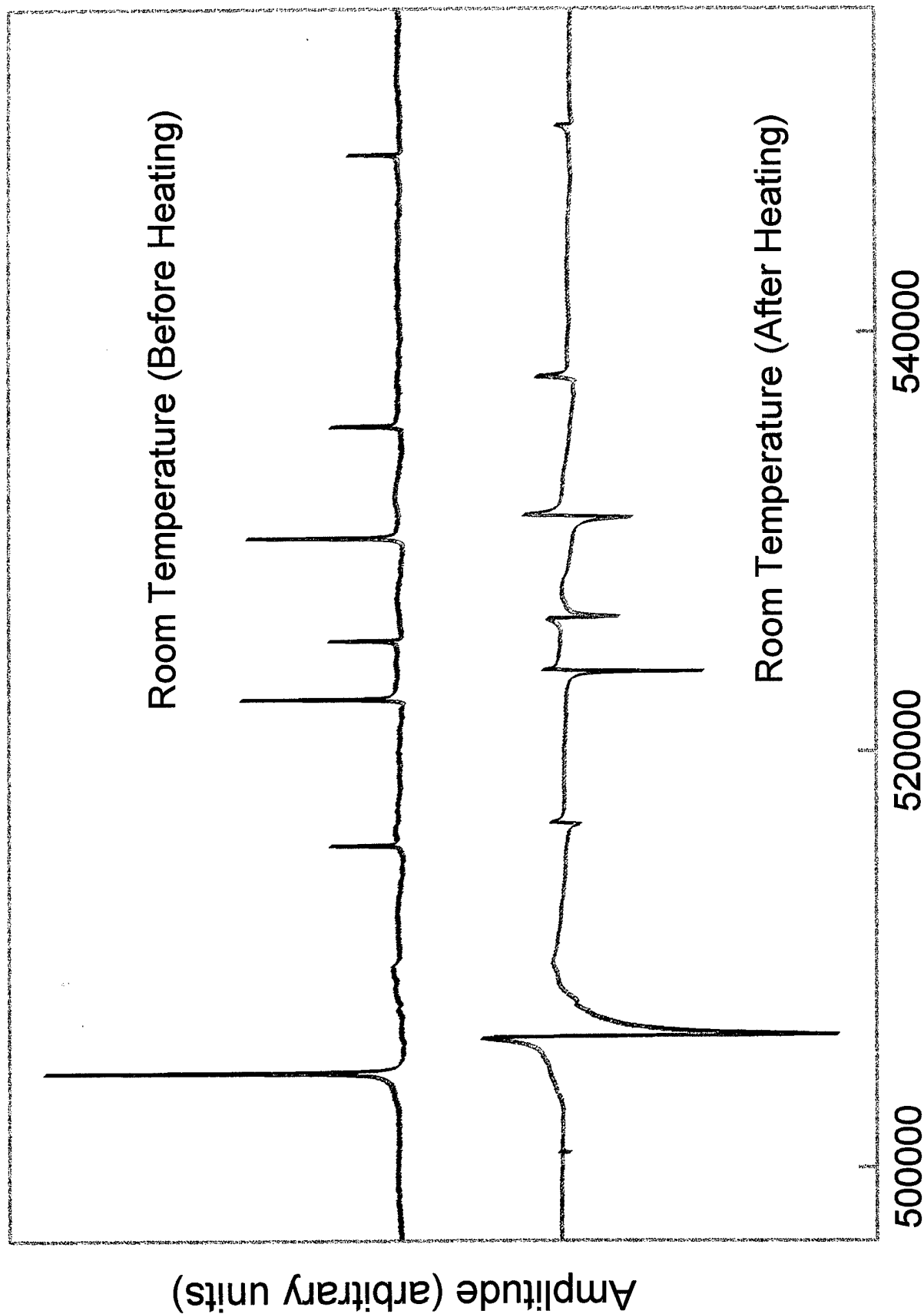
CMSX6 (Comparison with Nickel)



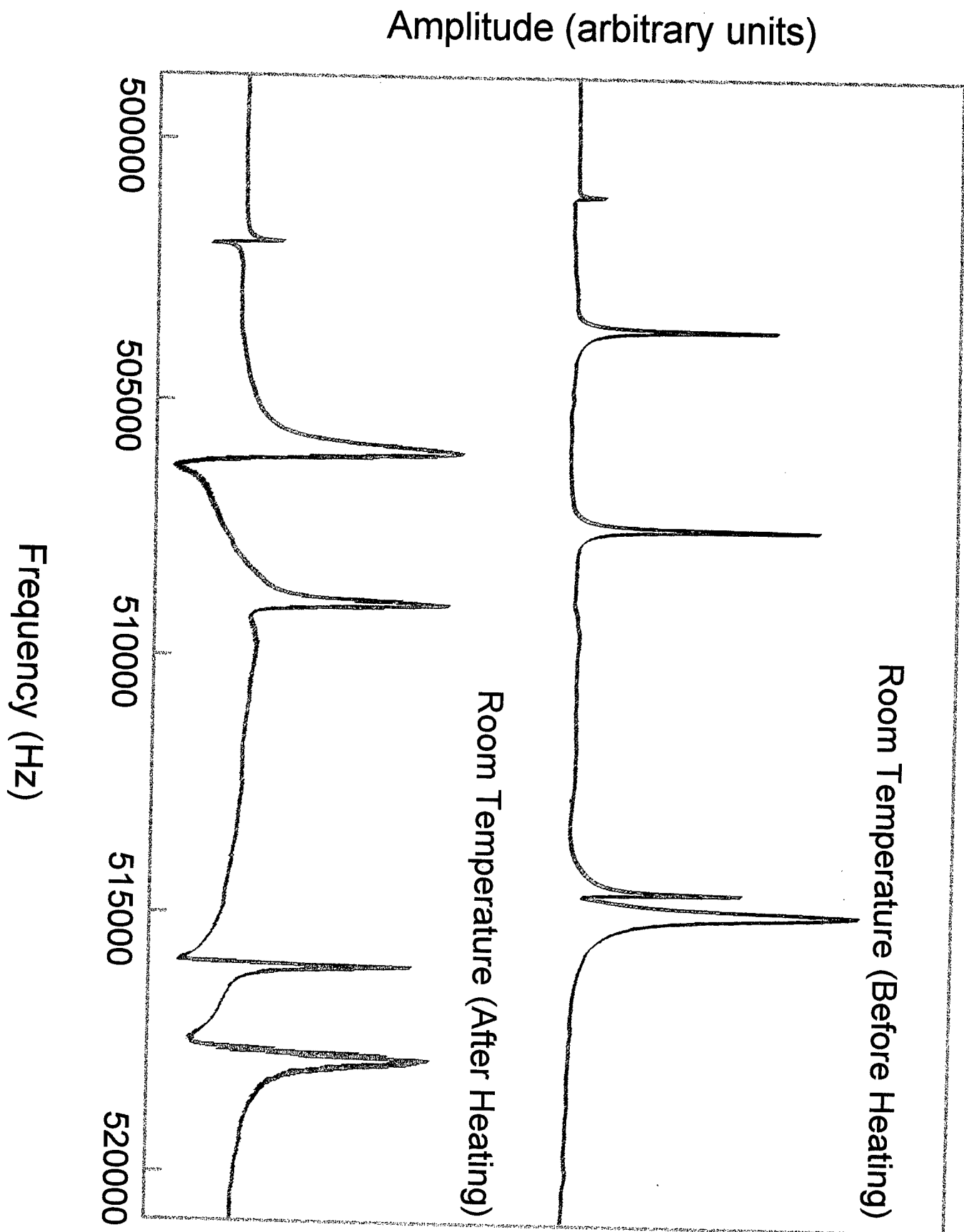
CMSX6 Mode ID (Final Calculated Spectrum)



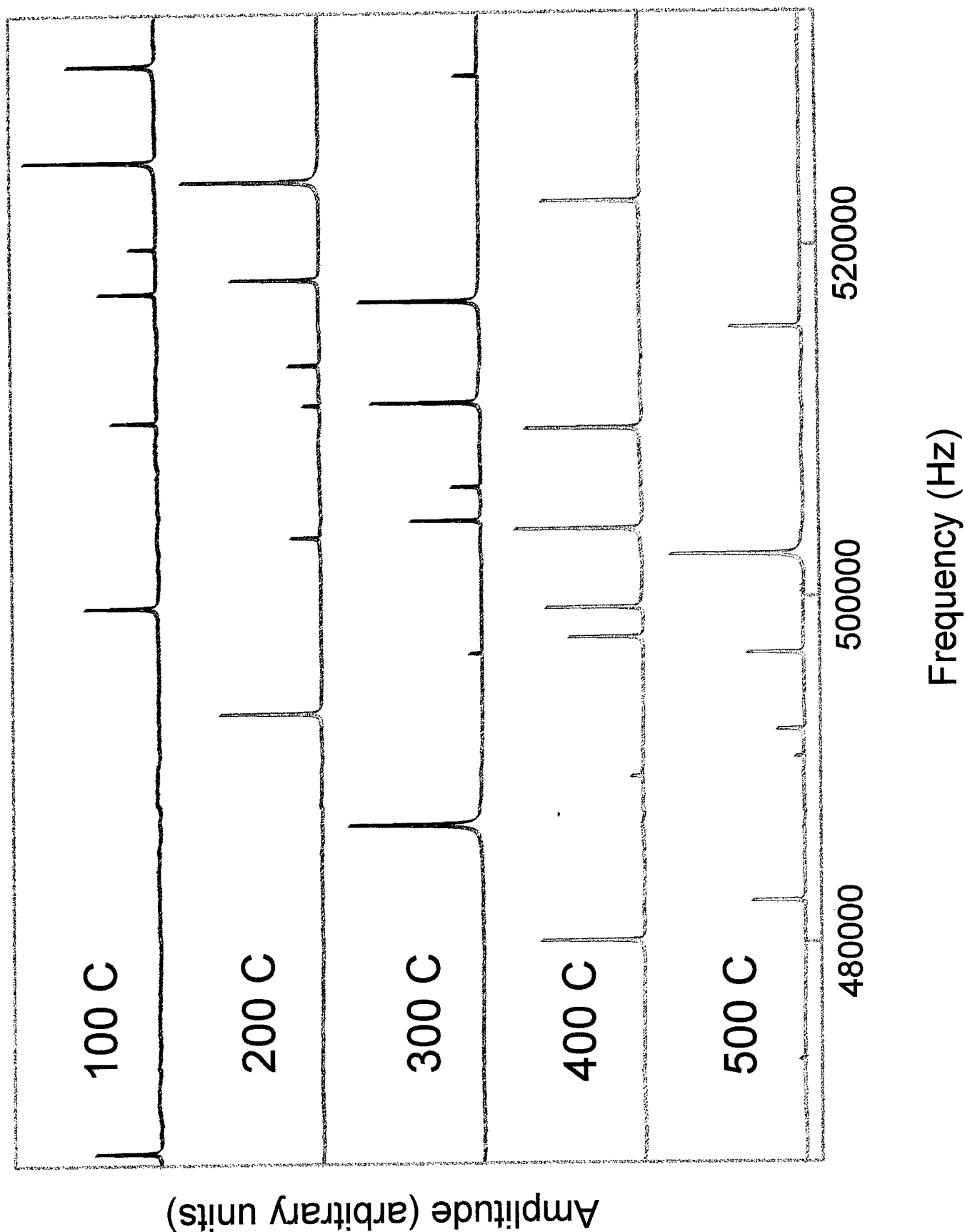
CMSX4



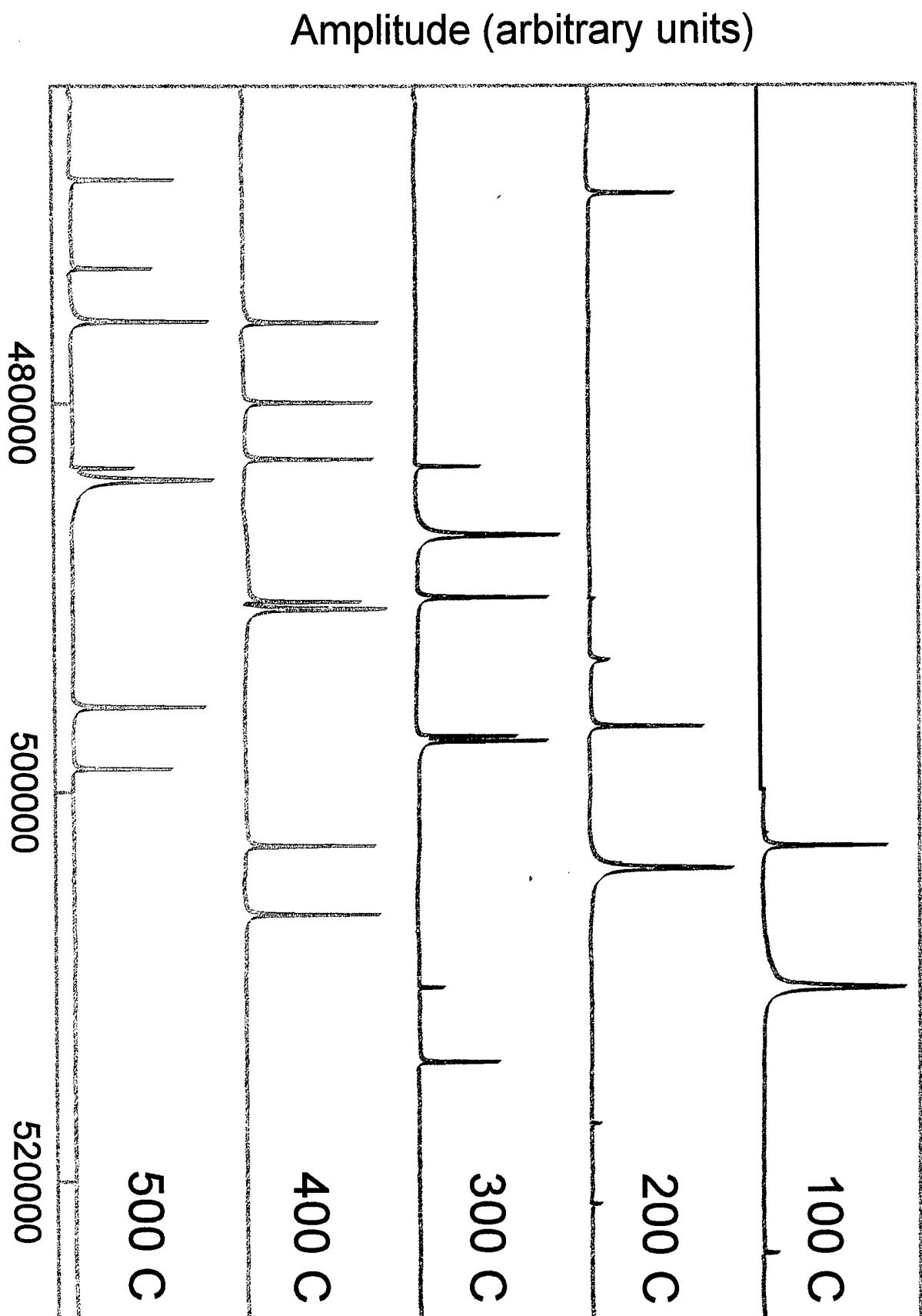
CMSX6



Frequency Shift with Temp. for CMSX4

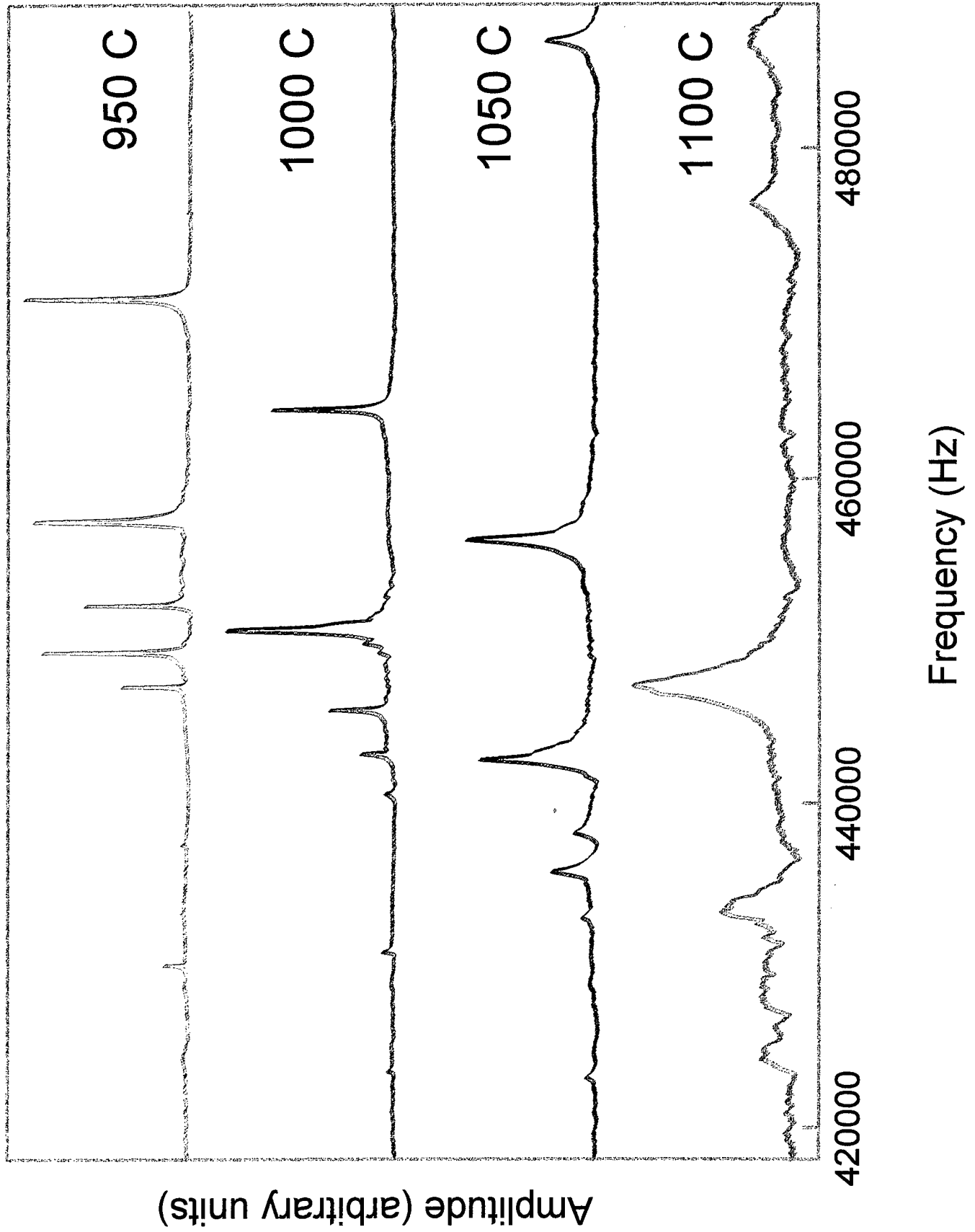


Frequency Shift with Temp. for CMSX6

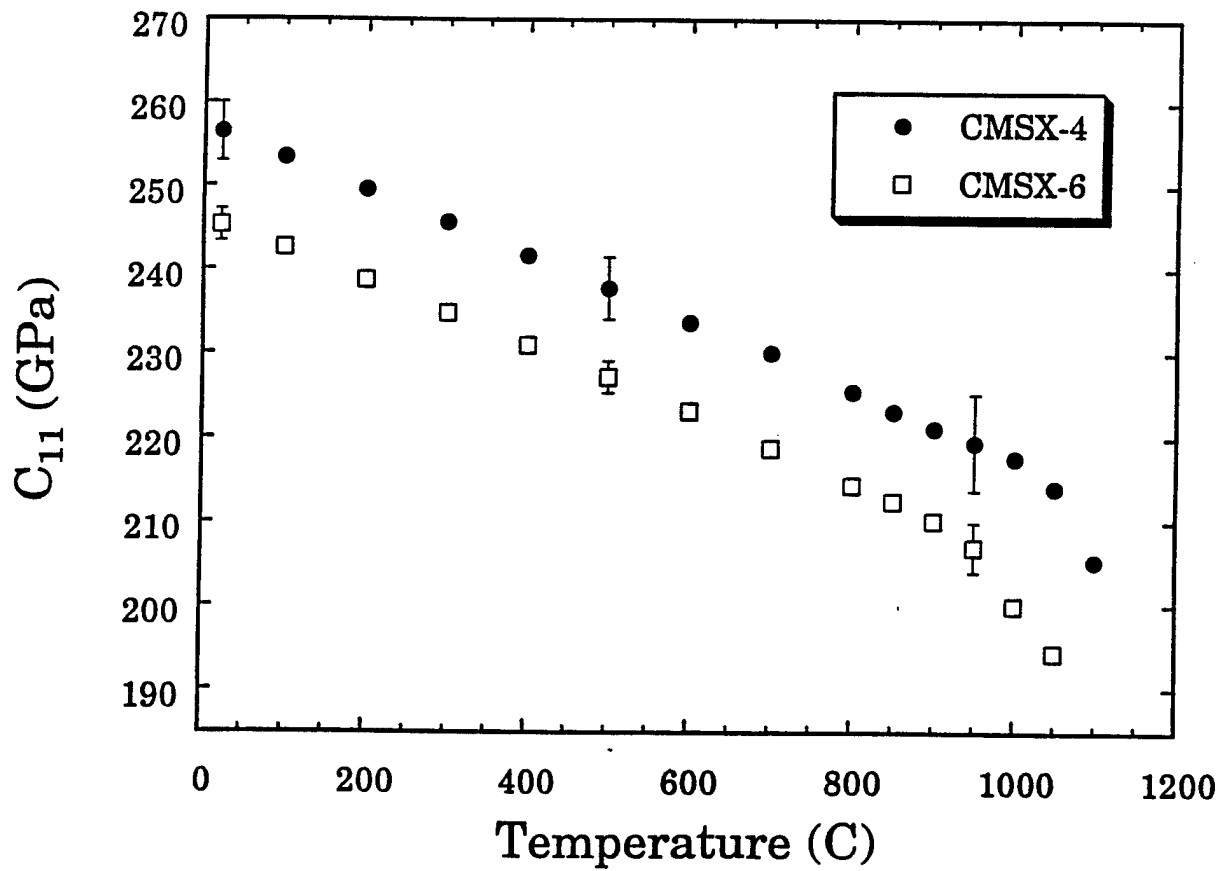


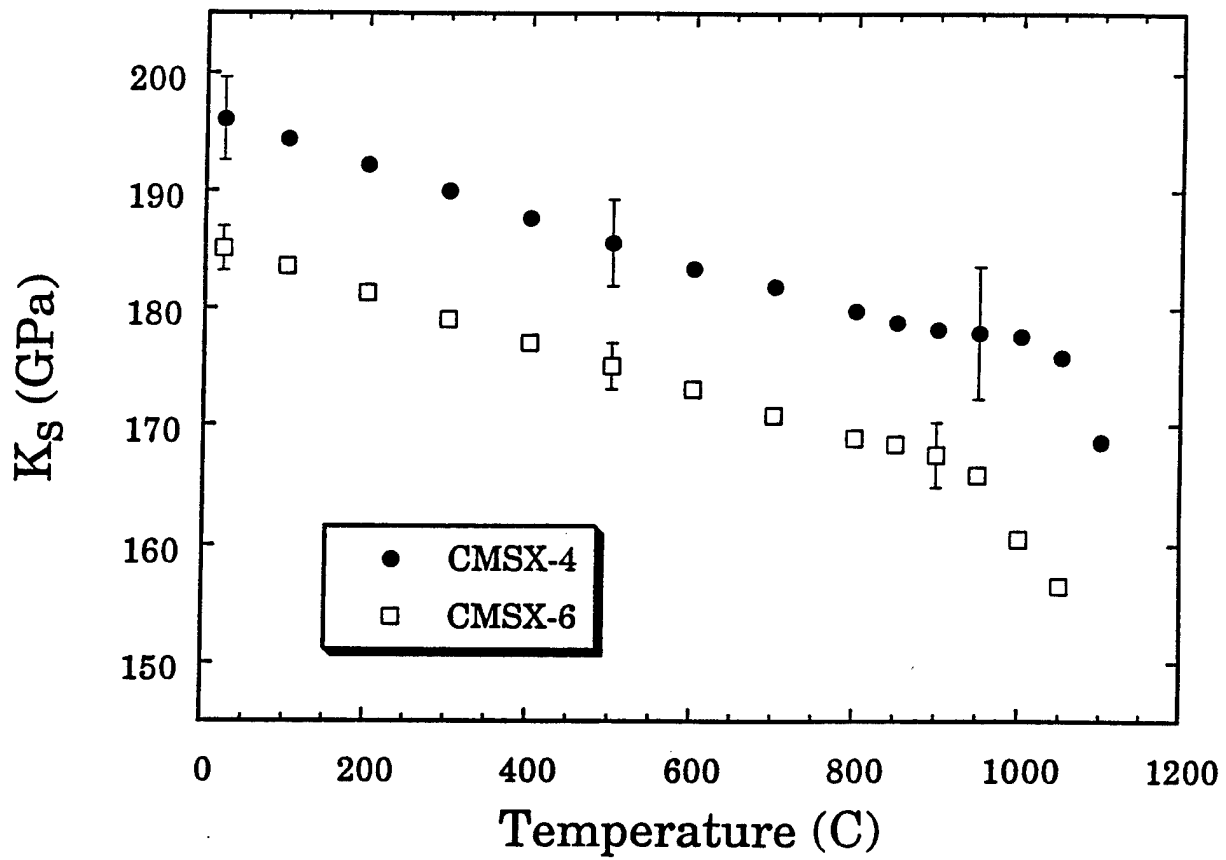
Frequency (Hz)

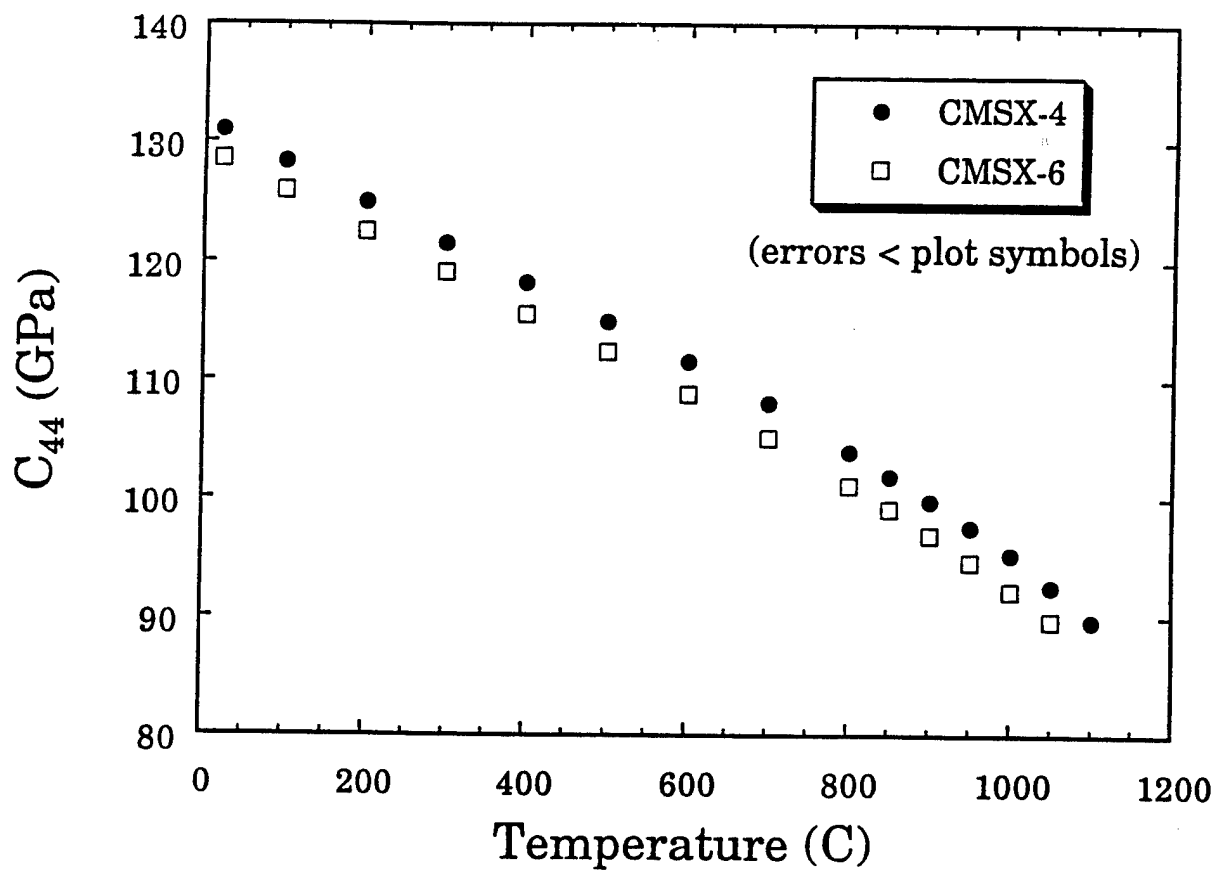
Deterioration of Acoustic Response, CMSX4



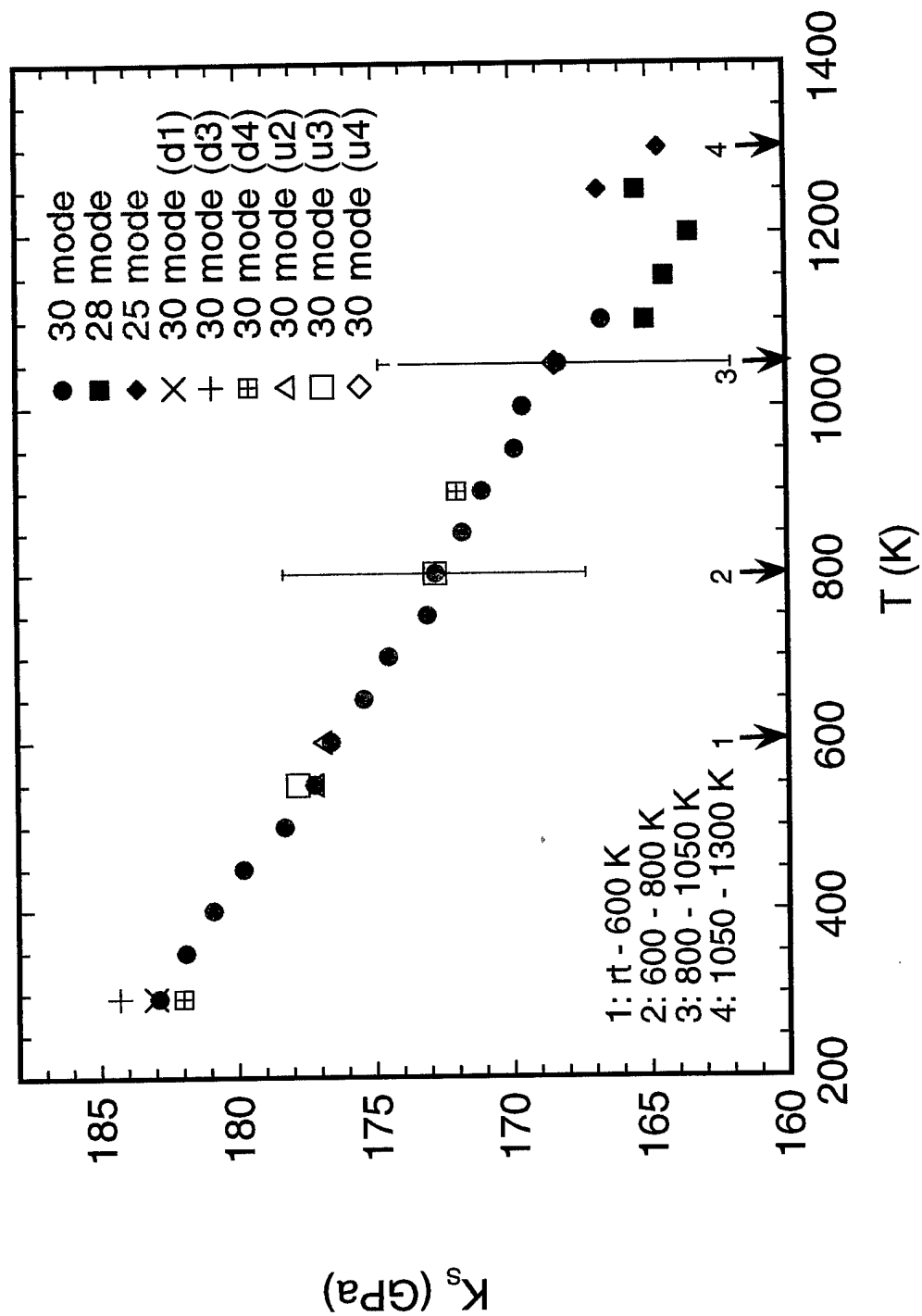
C_{11} for CTC Nickel Alloys



K_s for CTC Nickel Alloys

C_{44} for CTC Nickel Alloys

K_s versus Temperature Spec2: Ni-13.36%Al



Derivatives of Elastic Moduli of Nickel Alloys Studied

	CMSX-4	CMSX-6	SPEC2
dC_{11}/dT	-0.043	-0.045	-0.038
R^2	0.984	0.973	0.999
dC_{12}/dT	-0.010	-0.013	-0.010
R^2	0.863	0.882	0.974
dC_{44}/dT	-0.037	-0.037	-0.032
R^2	0.995	0.997	0.997
dC_s/dT	-0.016	-0.016	-0.014
R^2	0.986	0.986	0.998
dK_s/dT	-0.021	-0.024	-0.019
R^2	0.961	0.948	0.948

Result/conslusions

- Temperature derivatives determined
- RUS has proven useful in the characterization of materials whose initial C_{ij} 's were not well known.
- RUS studies are valued in the characterization of new metal alloys

Los Alamos

Los Alamos National Laboratory
Los Alamos, New Mexico 87545

Response of the Elastic Moduli of $\text{La}_{0.83}\text{Sr}_{0.17}\text{MnO}_3$ to Magnetic fields near the CMR Transition Temperature

T.W. Darling, A. Migliori, J.J. Neumeier, E.G. Moshopoulou,
J.D. Thompson, J.Sarrao*

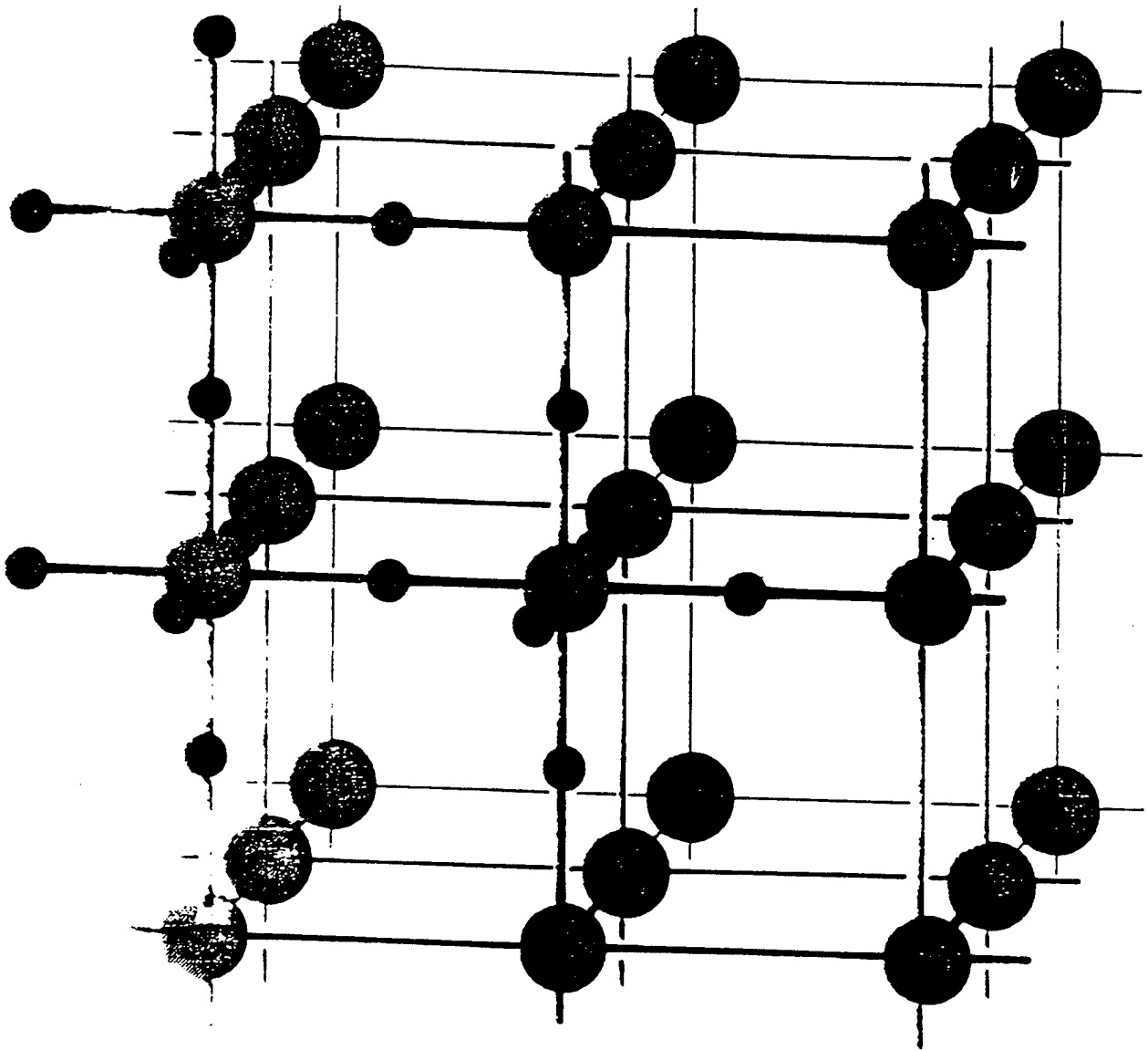
Los Alamos National Laboratory, Los Alamos, NM 87545

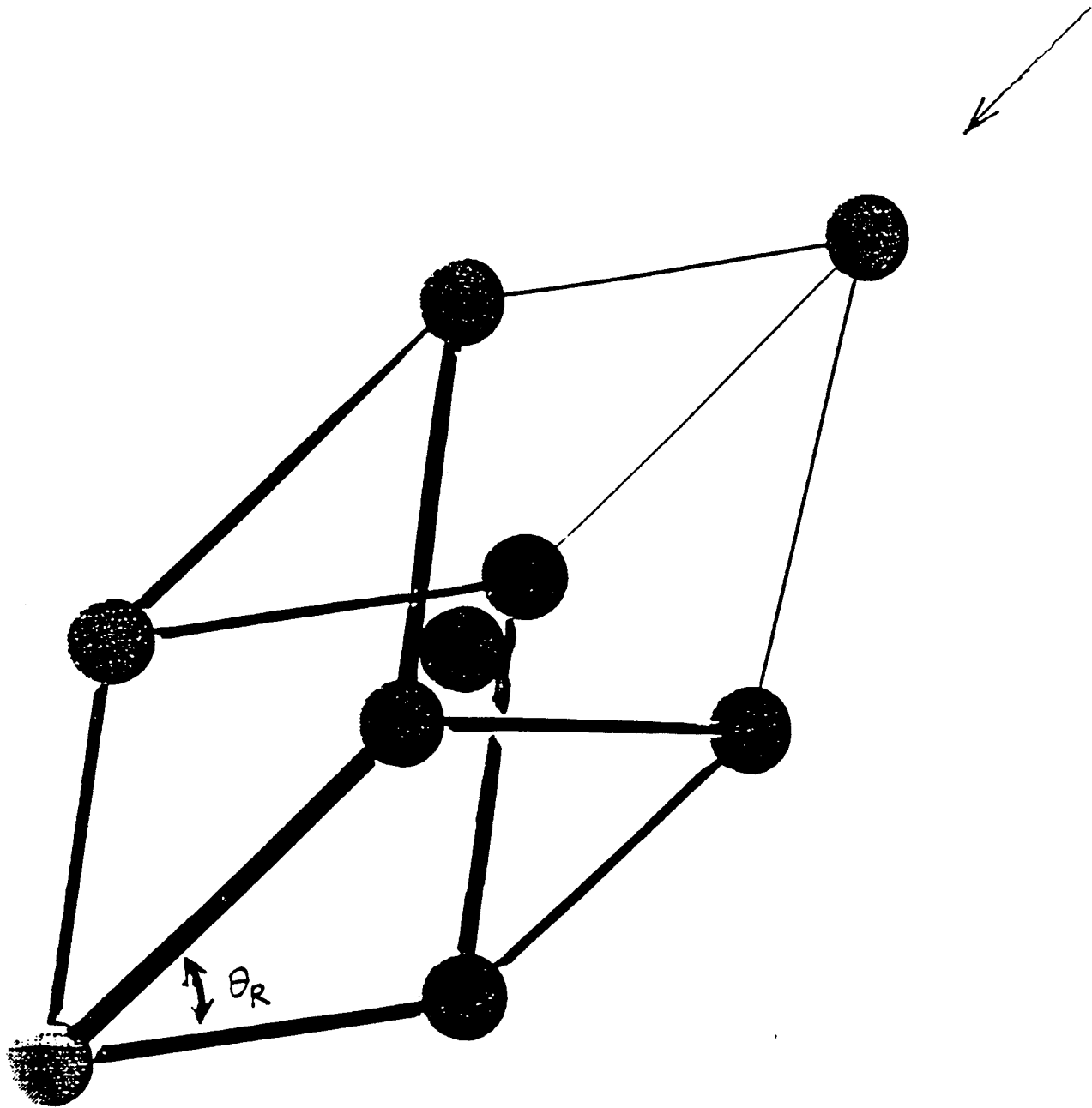
*NHMFL, Florida State University, Tallahassee, FL)

- C_{ij} couple to free energy by second strain derivative - sensitive to symmetry and coupling
- RUS measures the "complete" elastic tensor (as complete as the model)
- Strong electron-spin-lattice effects in CMR- Jahn-Teller etc

- 1 RUS primer
- 2 Sample - preparation and analysis
- 3 RUS data
- 4 Discussion

TRANSPARENCY 1





$$\theta_R = 60.997^\circ \Rightarrow \text{"}\theta_c\text{"} = 90.85^\circ$$

High Temperature phase Rhombohedral

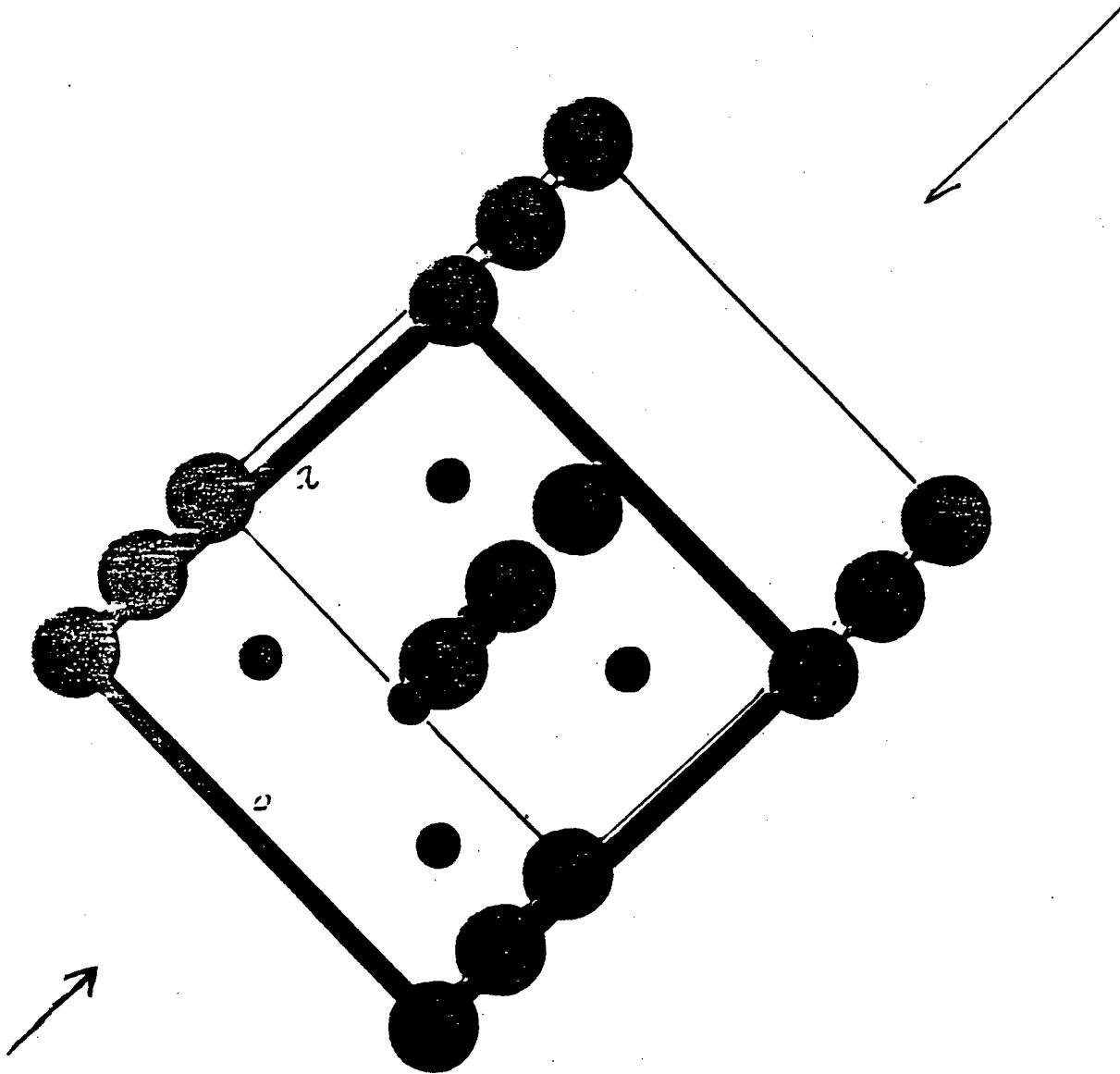
Asamitsu et al (Nature) 290K

Low Temperature phase Orthorhombic

$$a = 3.52 \text{ \AA}; b = 5.47 \text{ \AA}; c = 3.77 \text{ \AA}$$

Transition
280 K

$$\beta = 90.8^\circ \quad \gamma = 89.53^\circ$$



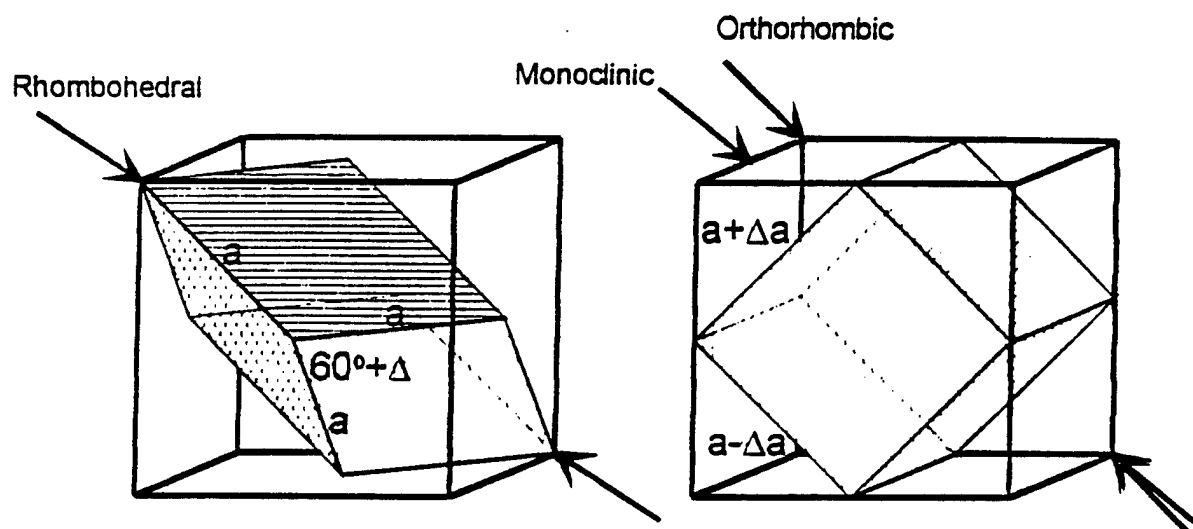


Figure 1. Shown are the parent FCC-like unit cell and the rhombohedral and orthorhombic derivative structures and their orientation with respect to cubic axes. The arrows on the left cube indicate the direction of the distortion that develops to take the cubic structure to rhombohedral. The two sets of arrows on the right cube show the distortion directions that can take a rhombohedral structure and deform it to monoclinic or to orthorhombic. Mn ions are at the corners, the center of the faces, the center of the edges and the body center of the large cube.

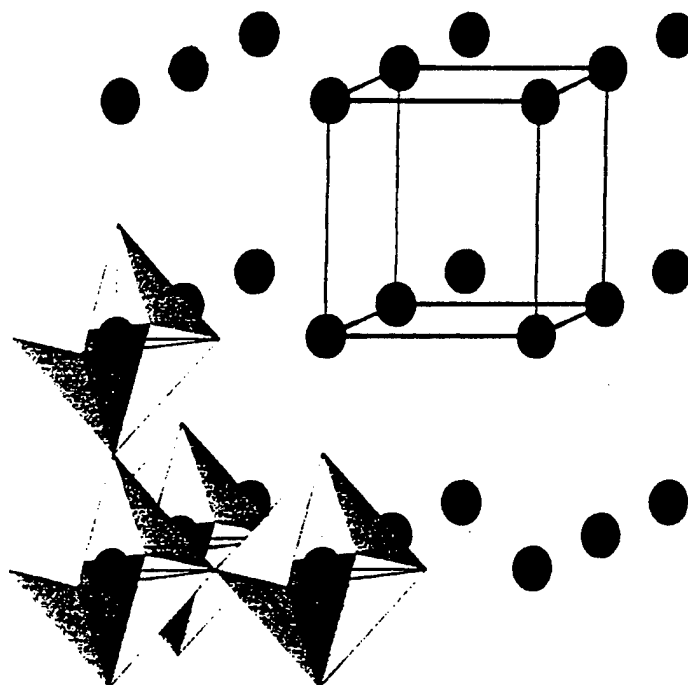
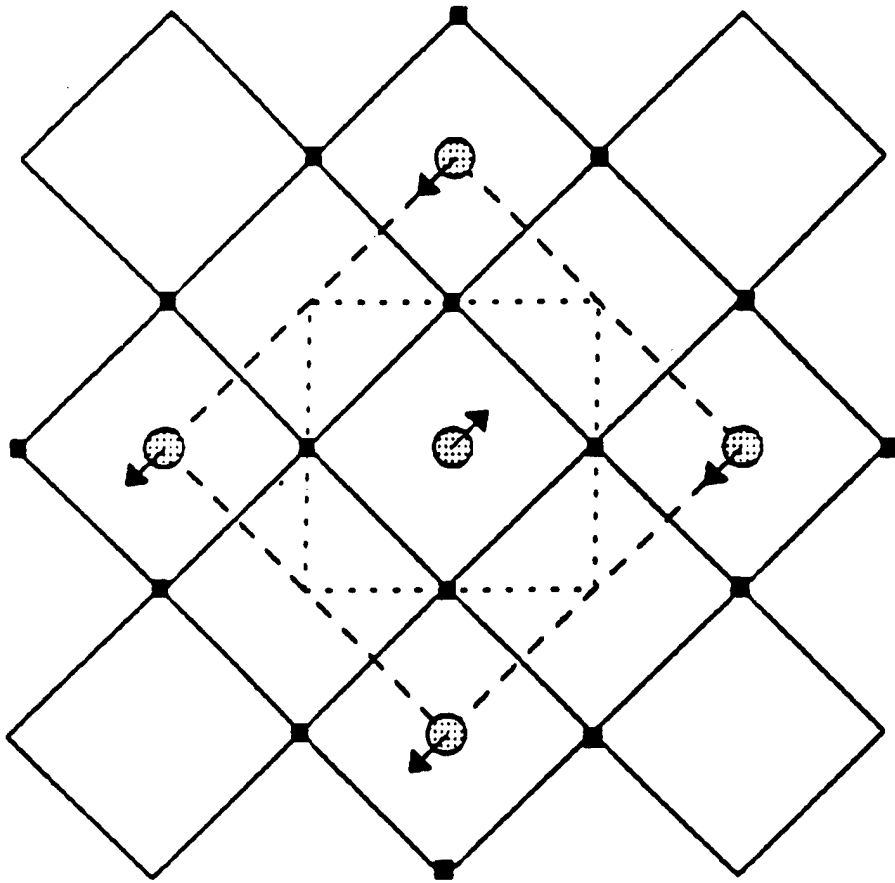
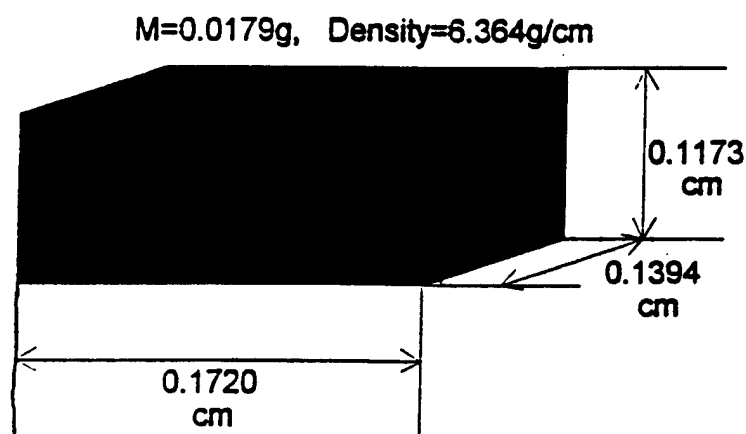


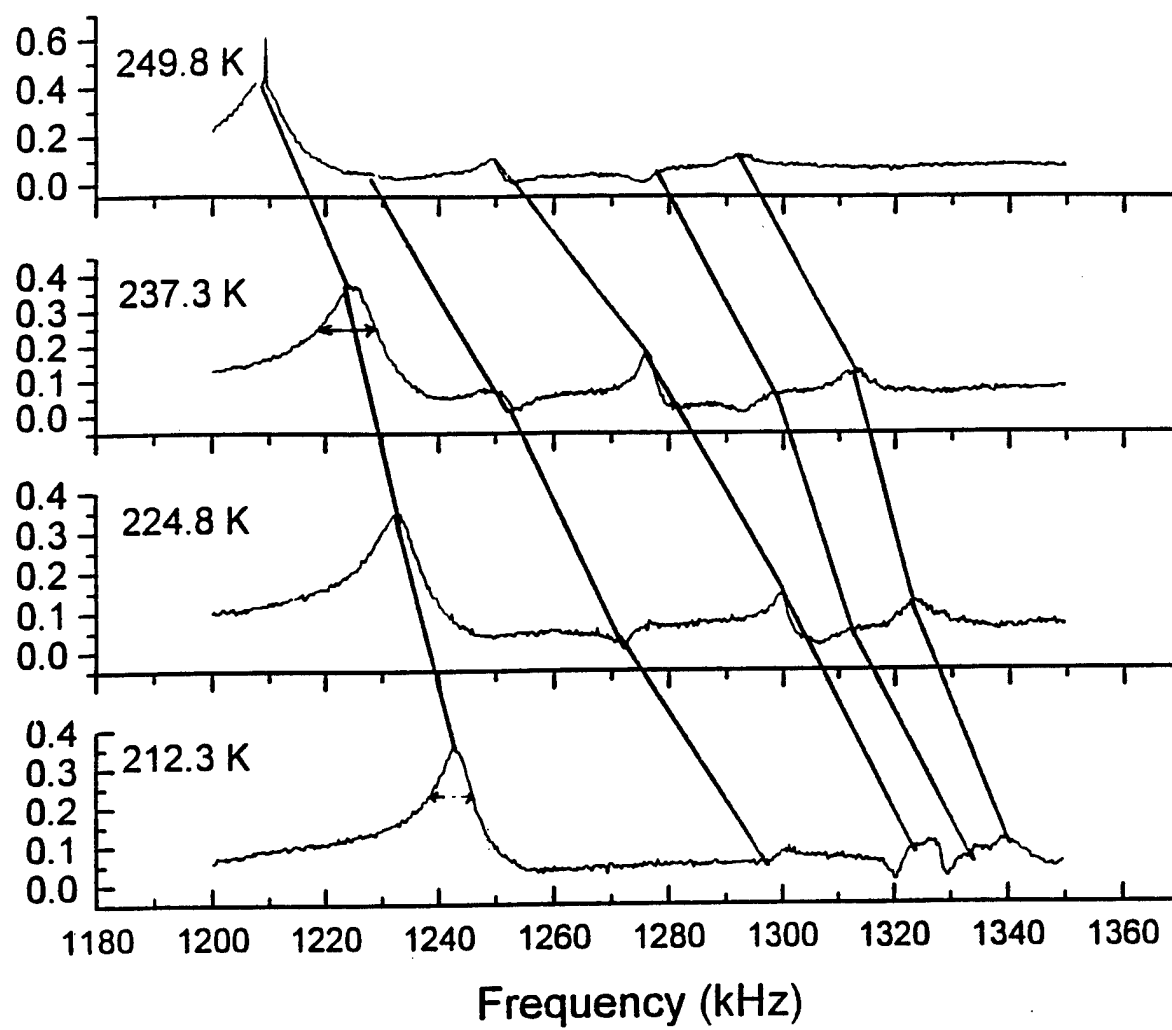
Figure 4. Shown are the Mn ions, a few of the oxygen octahedra and the simple cubic parent unit cell.



Sample preparation and characterization

- Optical-float-zone method used
- Starting materials La_2O_3 , SrCO_3 and MnO_2 mixed, ground and reacted at high temperature then isostatically pressed into rods
- The crystal was grown in air at a rate of 6 mm/hour
- Powder x-ray diffraction detected no second phase
Refined cell parameters (Hex) were: $a = 5.545(1) \text{ \AA}$ and $c = 13.382(2) \text{ \AA}$. The x-ray density was $6.51427 \text{ g cm}^{-3}$
- A single grain was cut and Laue diffraction was used to orient the single crystal to the almost cubic lattice planes.





$f_{\text{measured}}(\text{MHz})$	$f_{\text{fitted}}(\text{MHz})$	%error	k	i	$\partial \ln f / \partial \ln c_{11}$	$\partial \ln f / \partial \ln c_{12}$	$\partial \ln f / \partial \ln c_{44}$
0.835100	0.832982	-0.25	4	1	0.06	-0.04	0.98
0.849000	0.849199	0.02	6	1	2.77	-1.88	0.11
0.912100	0.911084	-0.11	7	1	2.75	-1.86	0.11
1.025500	1.028140	0.26	5	1	3.18	-2.18	0.00
1.178600	1.177794	-0.07	5	2	3.15	-2.15	0.01
1.184900	1.182407	-0.21	1	1	2.91	-1.99	0.07
1.242000	1.247010	0.40	4	2	0.30	-0.21	0.91
0.000000	1.265354	0.00	6	2	2.28	-1.47	0.19
1.268200	1.268338	0.01	3	1	0.62	-0.42	0.80
1.278100	1.280845	0.21	5	3	3.18	-2.18	0.00
1.299200	1.297507	-0.13	2	1	1.69	-1.15	0.47
1.323600	1.317075	-0.49	8	1	1.41	-0.96	0.55
1.491900	1.493765	0.13	2	2	0.77	-0.49	0.72
1.541500	1.542163	0.04	1	2	2.71	-1.86	0.15
1.561300	1.562077	0.05	7	2	2.47	-1.63	0.16
1.586500	1.588603	0.13	8	2	0.17	-0.09	0.93

RMS error = 0.2159%

$$c_{11}(10^{12} \text{ dynes/cm}^2) = 2.2006 \pm 2.28\%$$

$$c_{12}(10^{12} \text{ dynes/cm}^2) = 1.5142 \pm 3.35\%$$

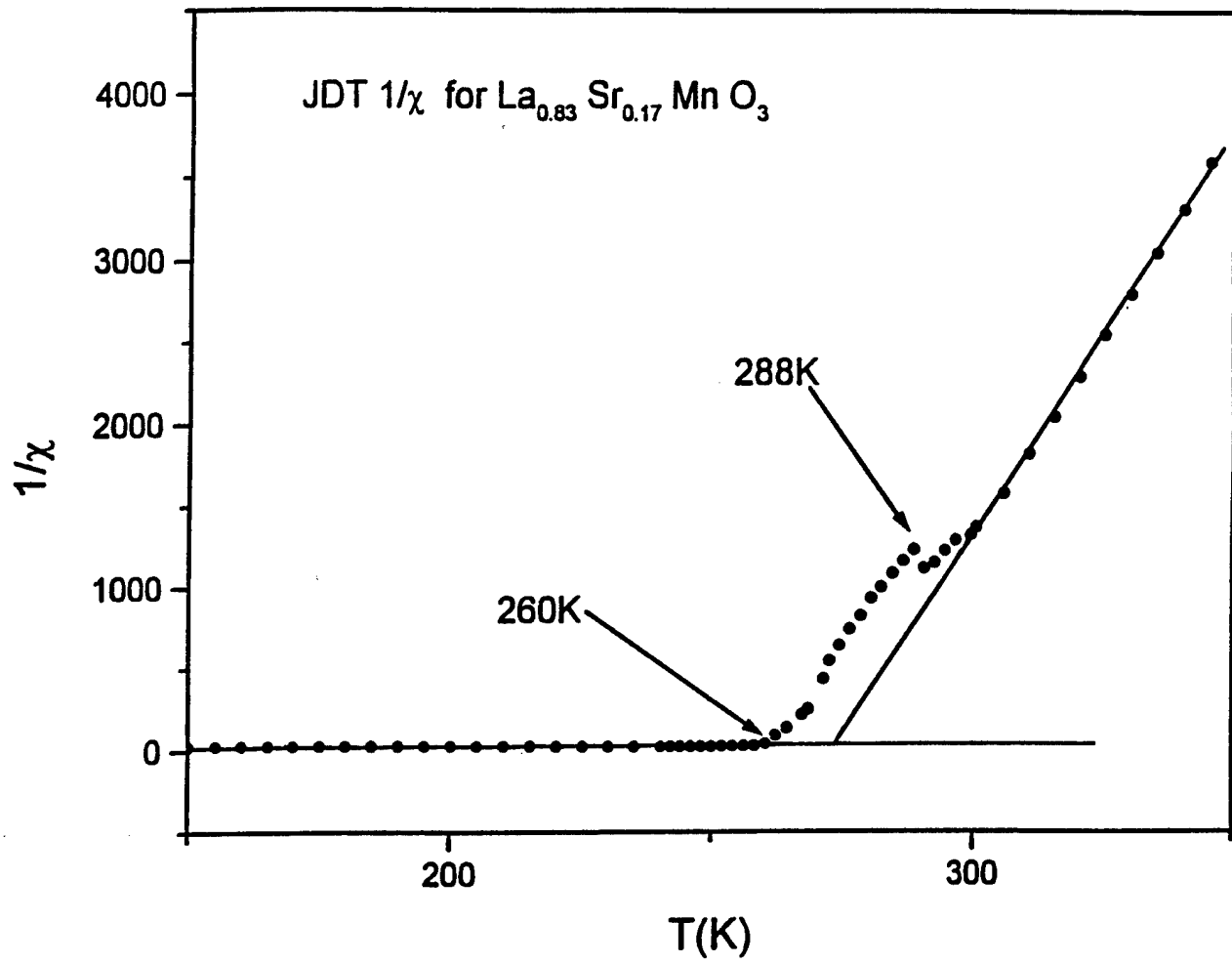
$$c_{44}(10^{12} \text{ dynes/cm}^2) = 0.6683 \pm 0.12 \%$$

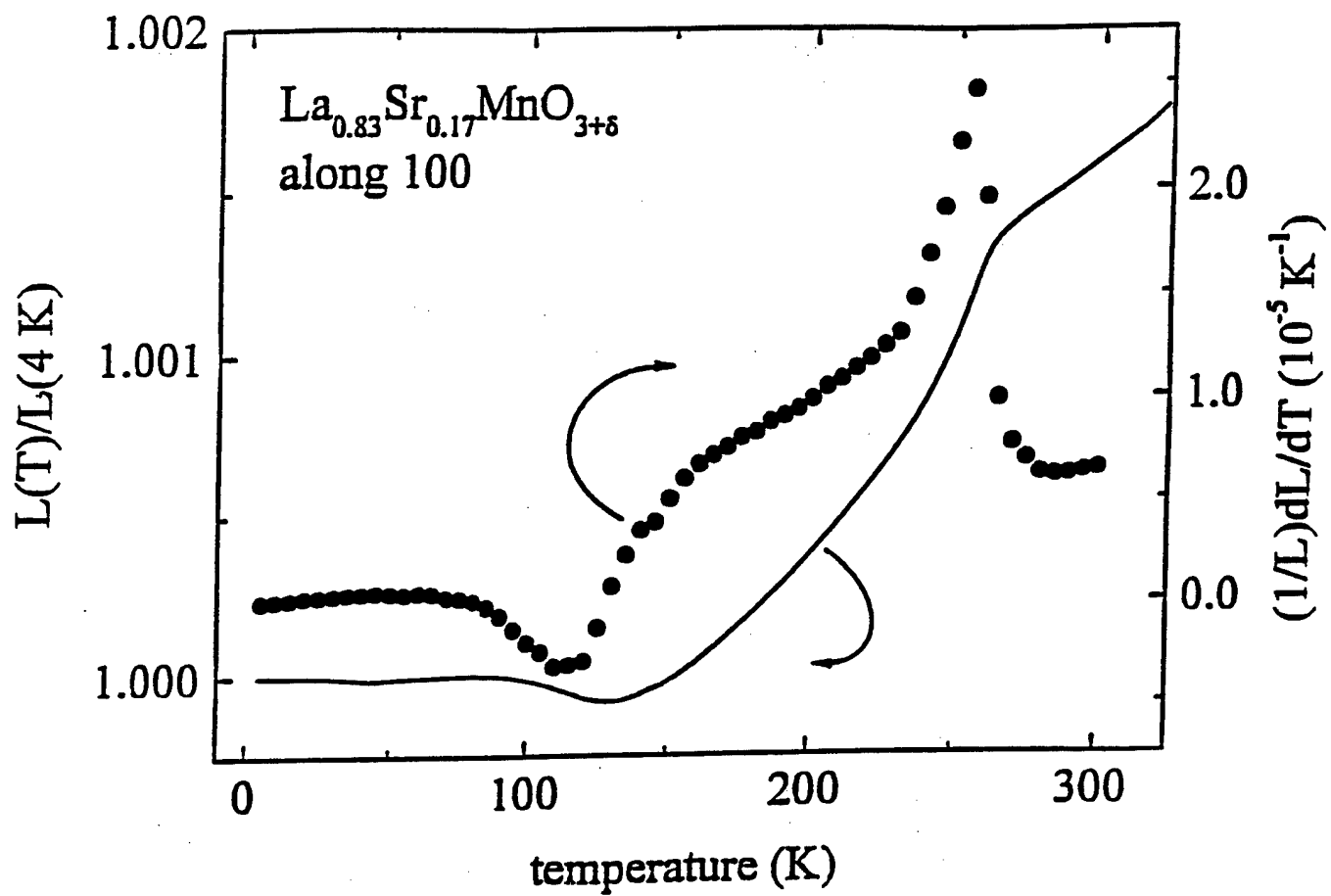
$$B(10^{12} \text{ dynes/cm}^2) = 1.743 \text{ (computed from the moduli)}$$

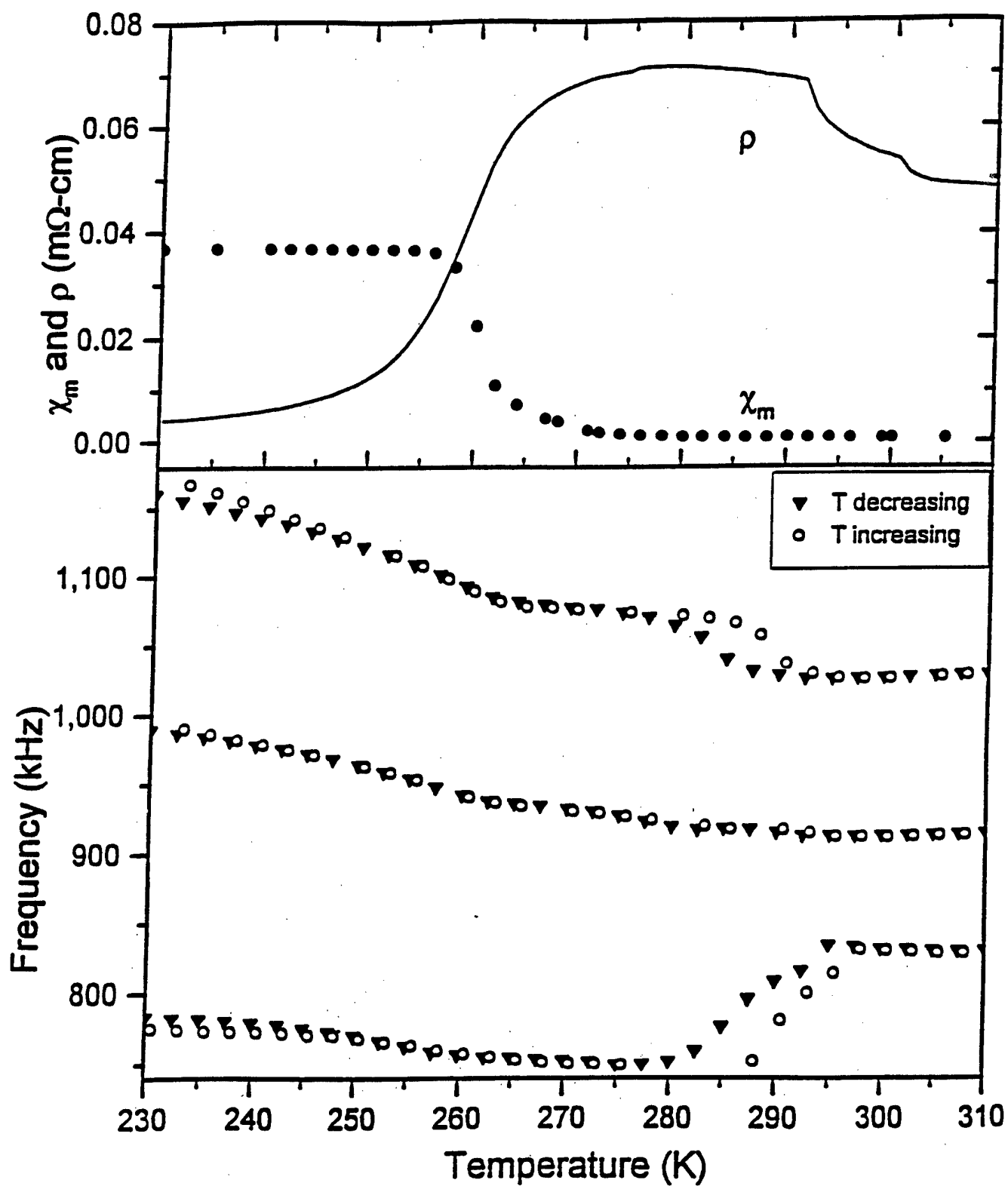
T=290K

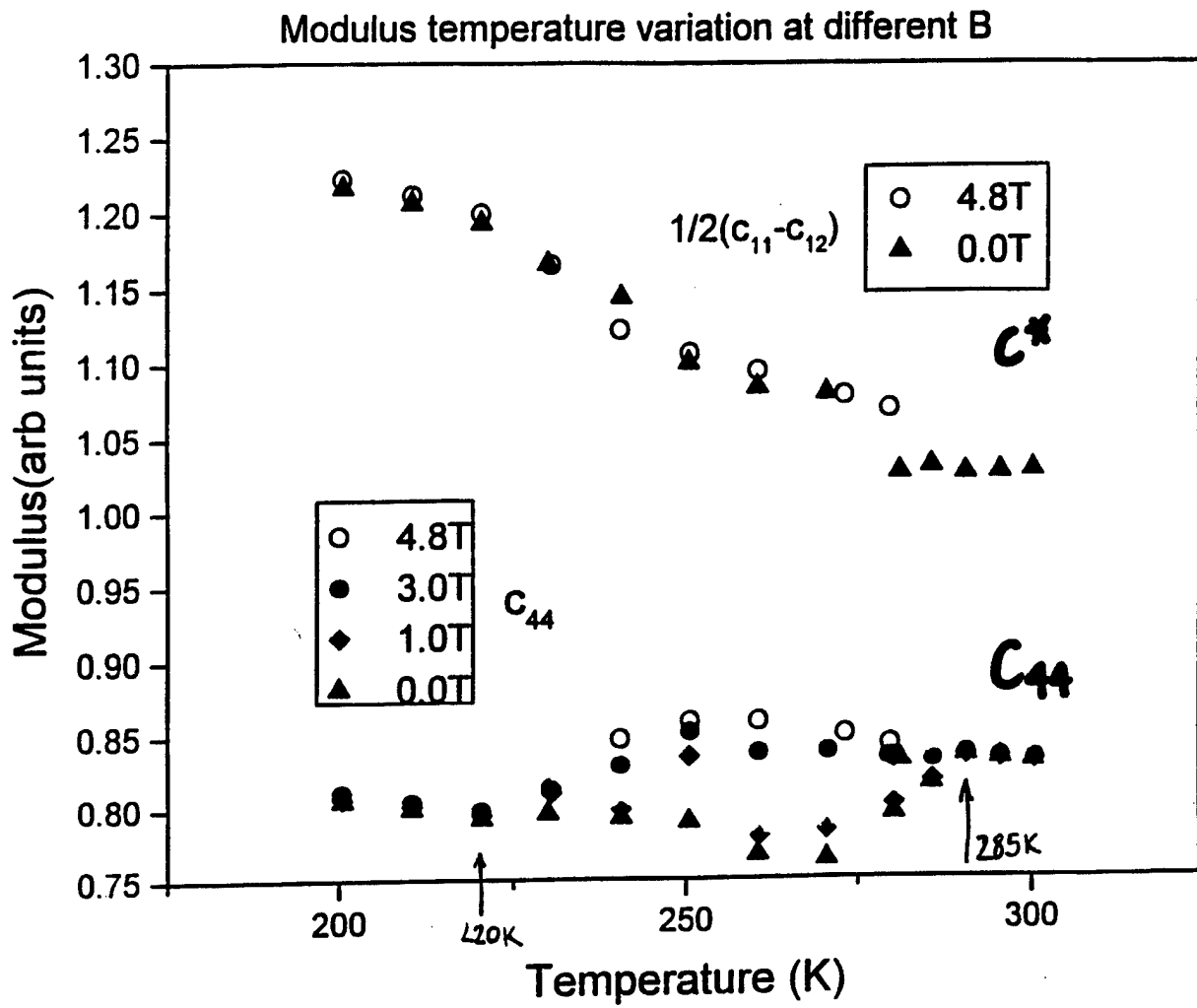
mass = 0.0179 gm ($\rho = 6.364 \text{ g/cm}^3$), dimensions: 0.17201 cm x 0.13944 cm x 0.11727 cm

Table 1. Shown are the measured and fitted resonance frequencies, the mode type (k), the mode harmonic (i), and the logarithmic derivatives of frequency with modulus. These derivatives describe accurately the fractional dependence of each mode frequency on each elastic modulus. Also shown are the fitting errors, the elastic moduli (B is the computed bulk modulus) and their (larger than the RMS) errors determined from the fit, and the sample size and mass.









Magnetic Effects and RUS

J.L. Sarrao
LANL

Collaborators:

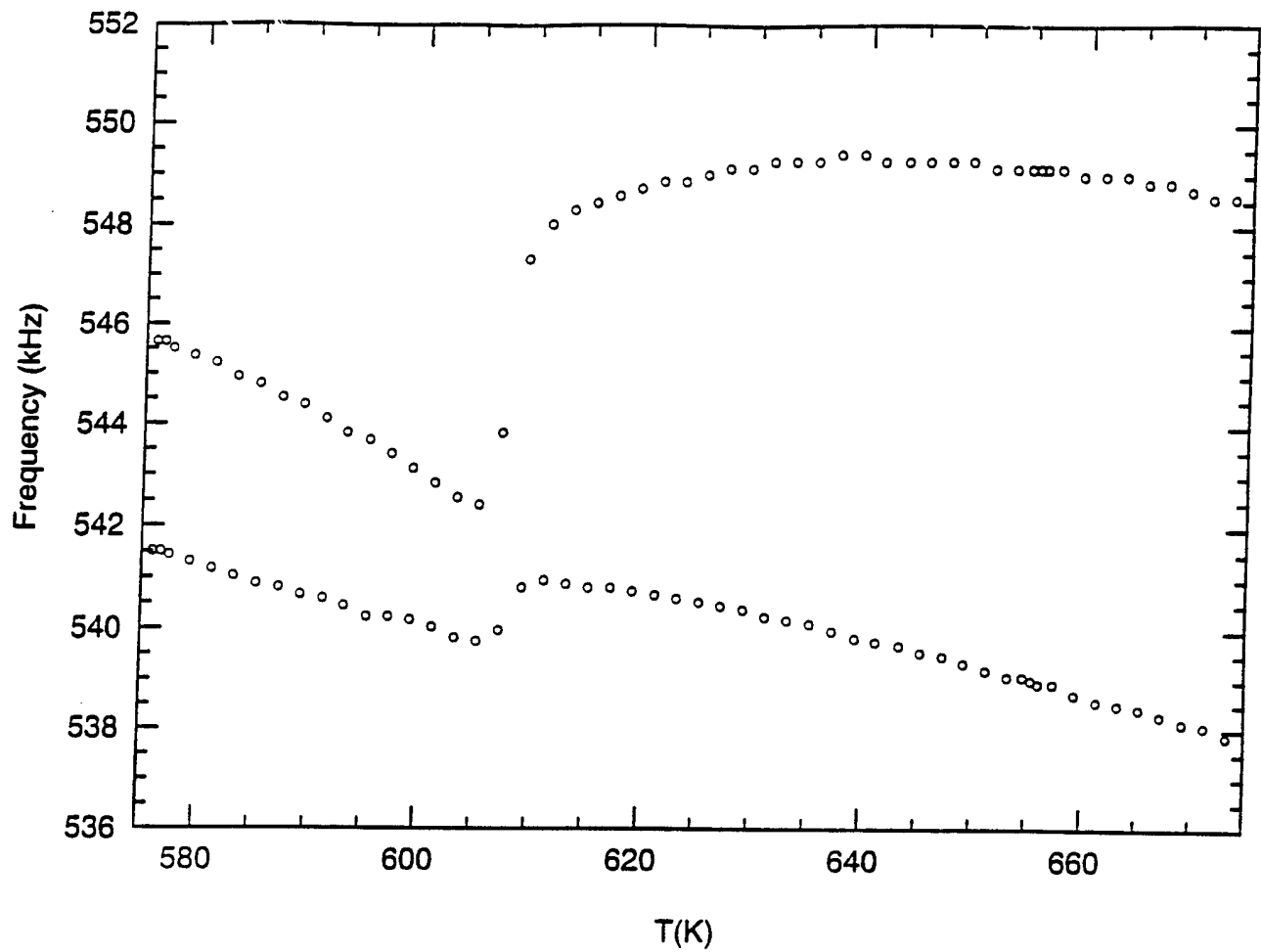
A. Migliori
T.W. Darling
D. Mandrus
Z. Fisk

I. Magneto-elastic effects

II. Field-dependent effects

III. Details and problems particular to RUS

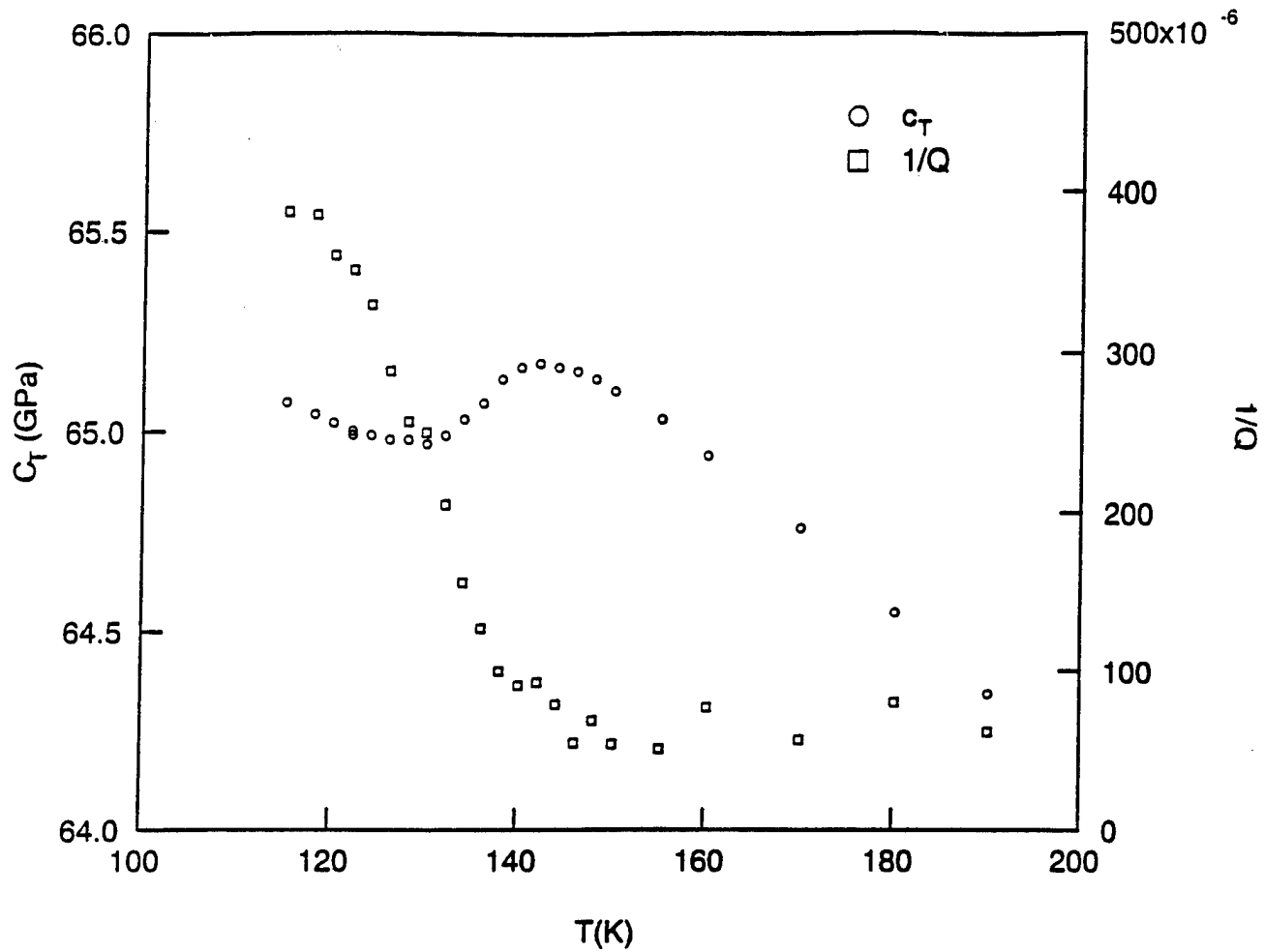
IV. Prospects for the future



$\text{Nd}_2\text{Fe}_{14}\text{B}$ (polycrystal)

$T_{\text{Curie}} \sim 610 \text{ K}$

thermodynamics : $\frac{\partial^2 \Delta G}{\partial P^2} = \frac{\partial \Delta V}{\partial P} = -\frac{1}{\Delta B}$



$\text{Nd}_2\text{Fe}_{14}\text{B}$ (polycrystal)

- Spin re-orientation transition
- magnetic easy axis cants from $\langle 001 \rangle$ to $\langle 110 \rangle$

$\langle 001 \rangle \rightarrow \langle 100 \rangle$
spin re-orientation

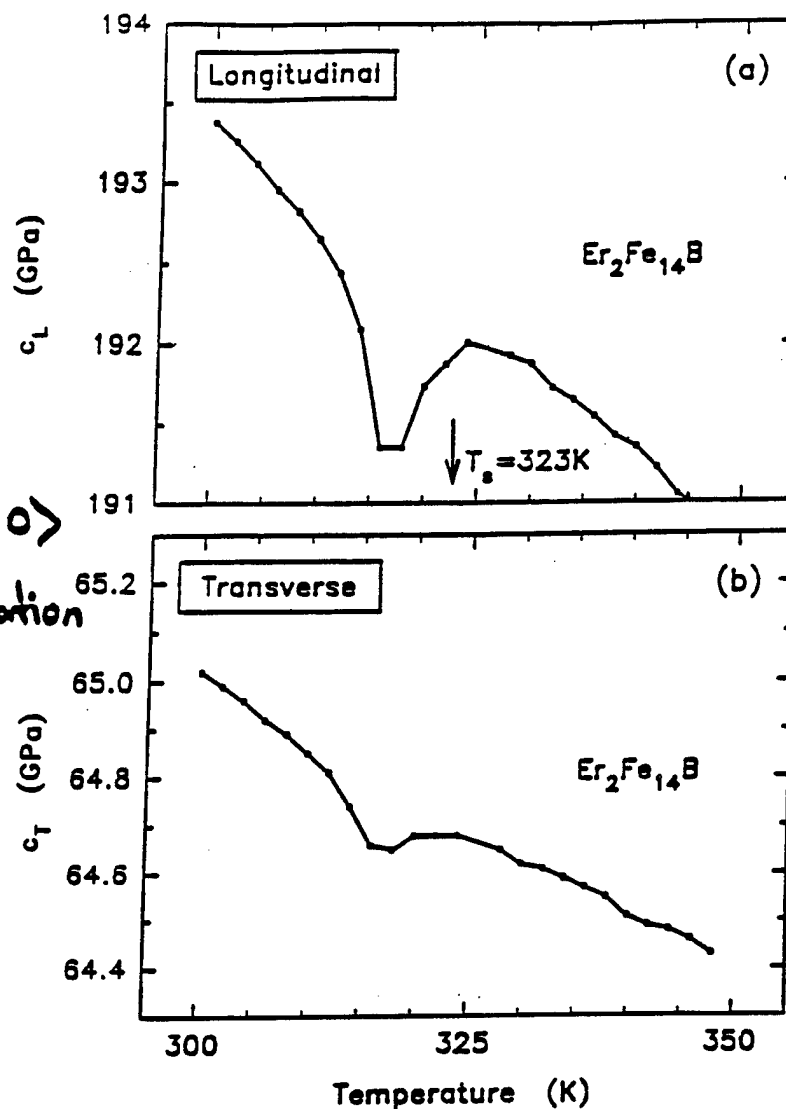
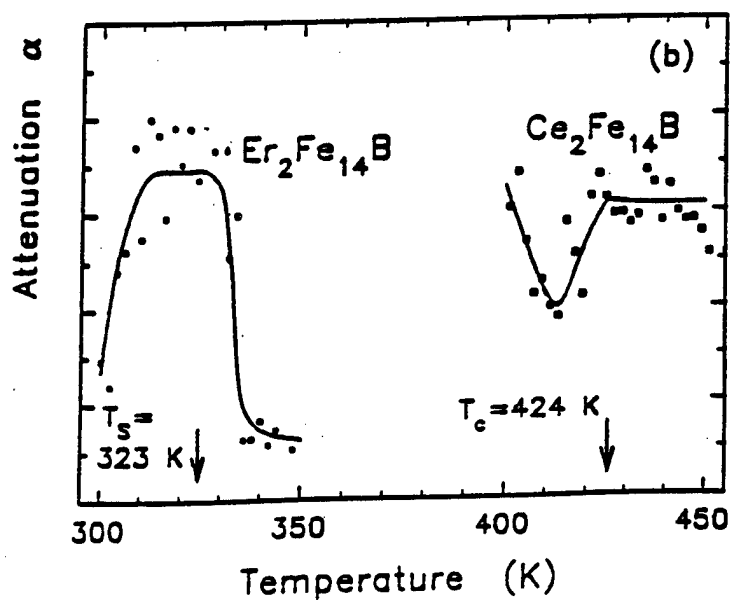
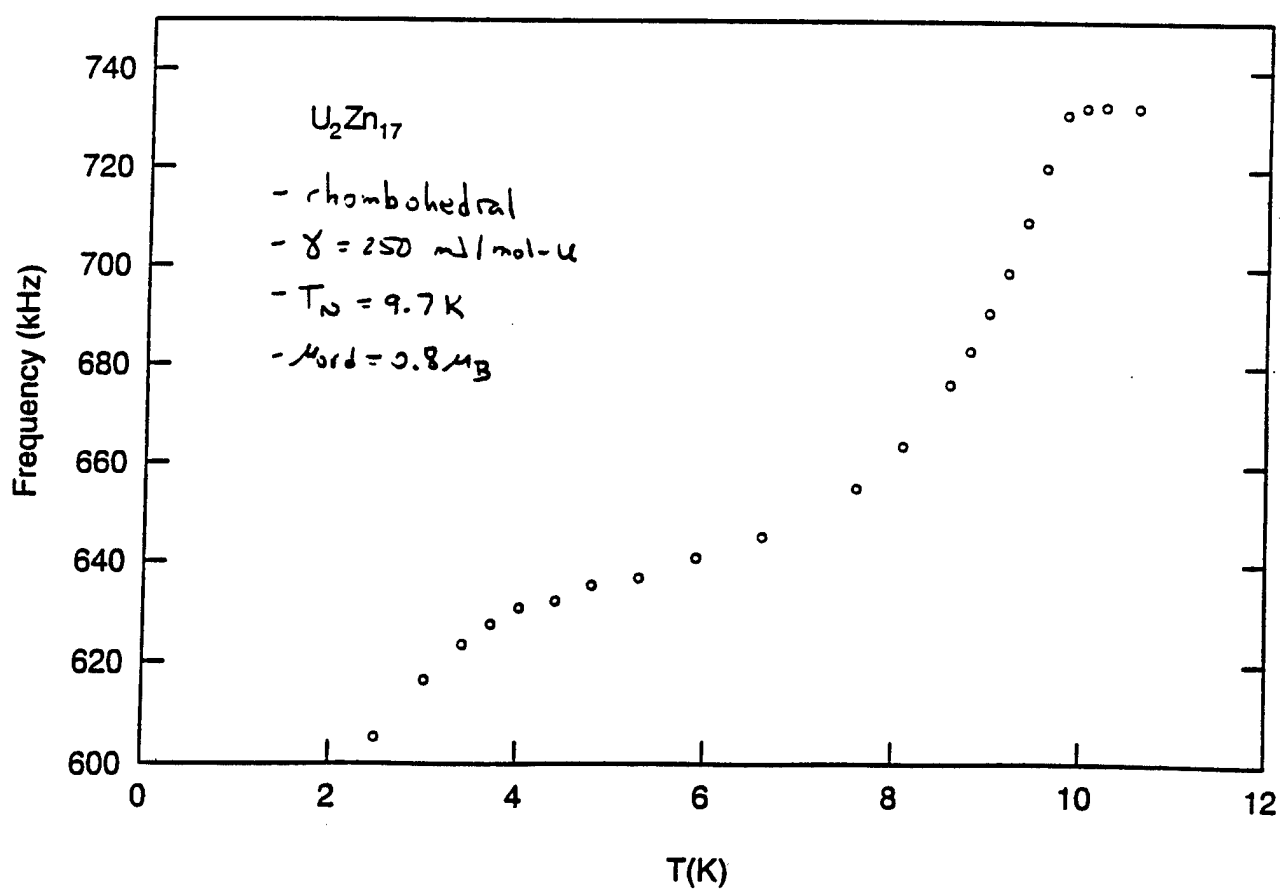
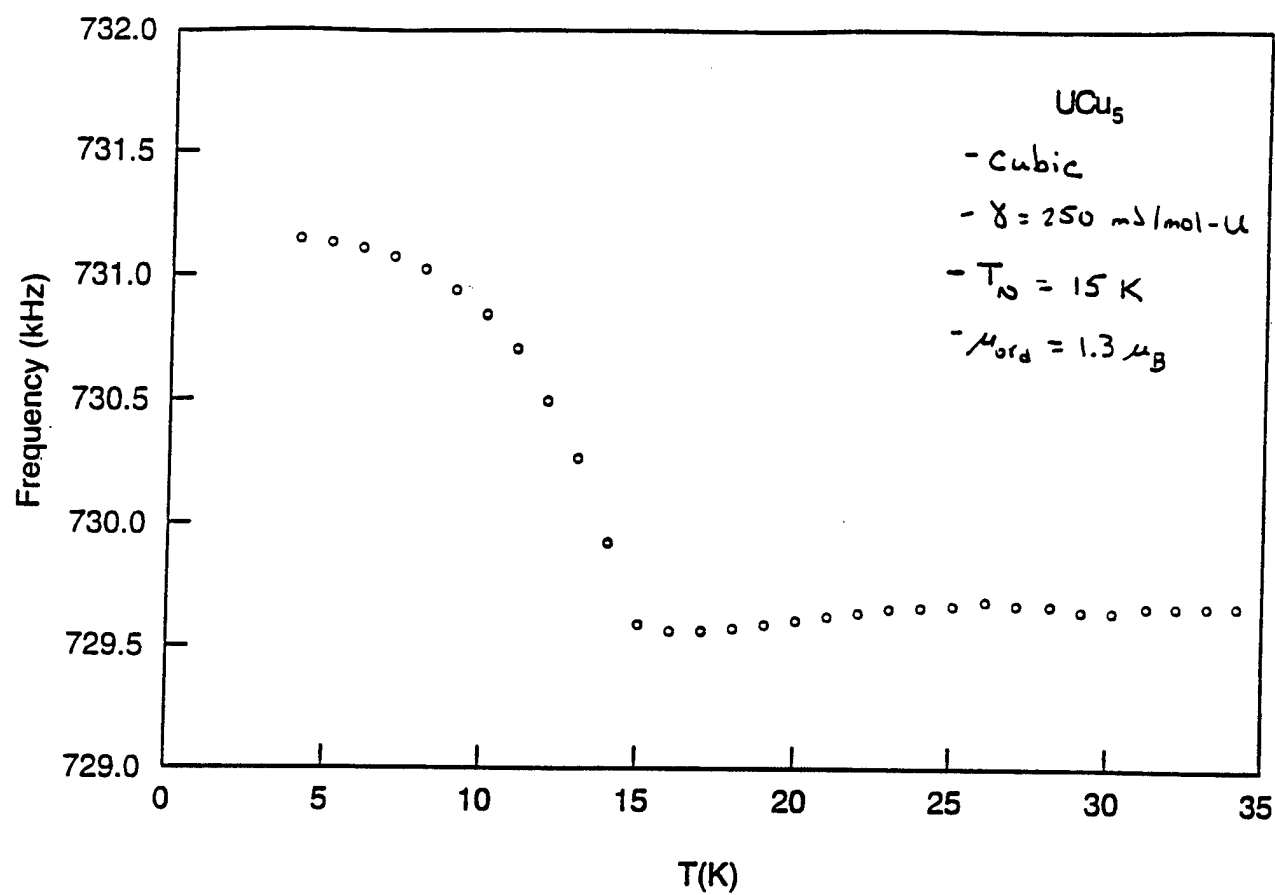


FIG. 2. (a) Longitudinal and (b) transverse elastic constants of $\text{Er}_2\text{Fe}_{14}\text{B}$ in the 300–350 K temperature range.

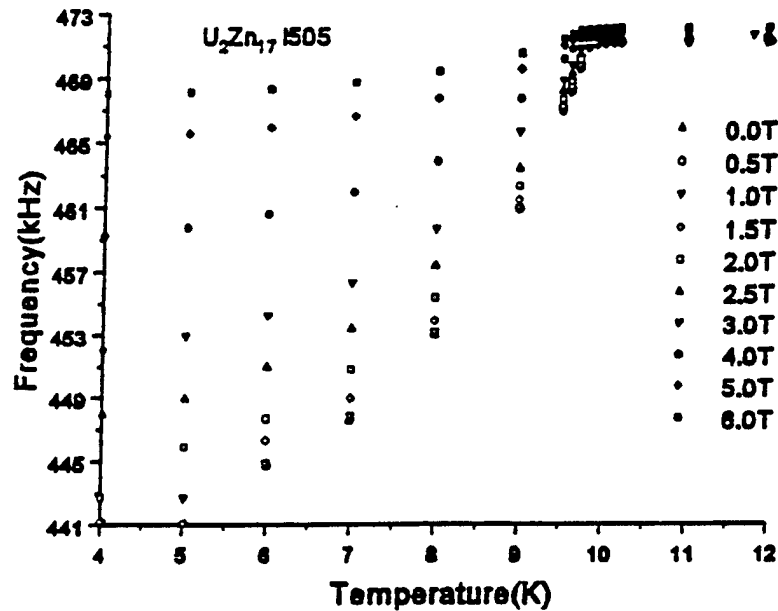




Resonant frequency of single-crystal fragment

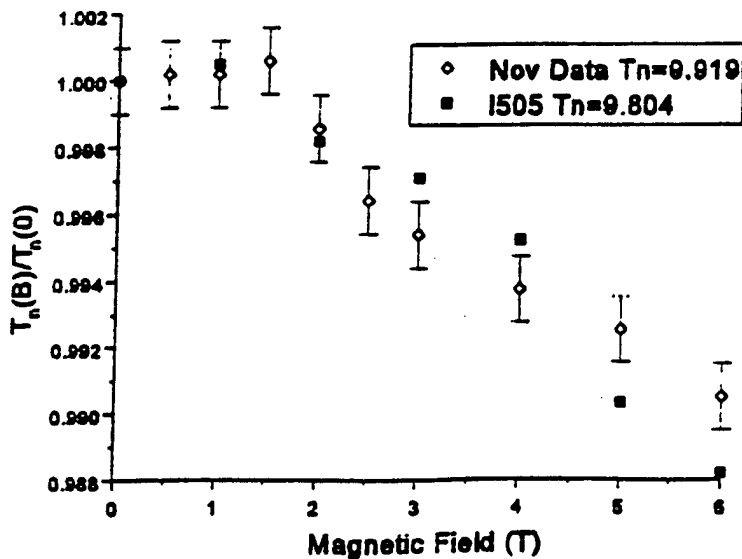
Undetermined mix of c_{44} and c_{66}

Undetermined orientation of field with crystal axes

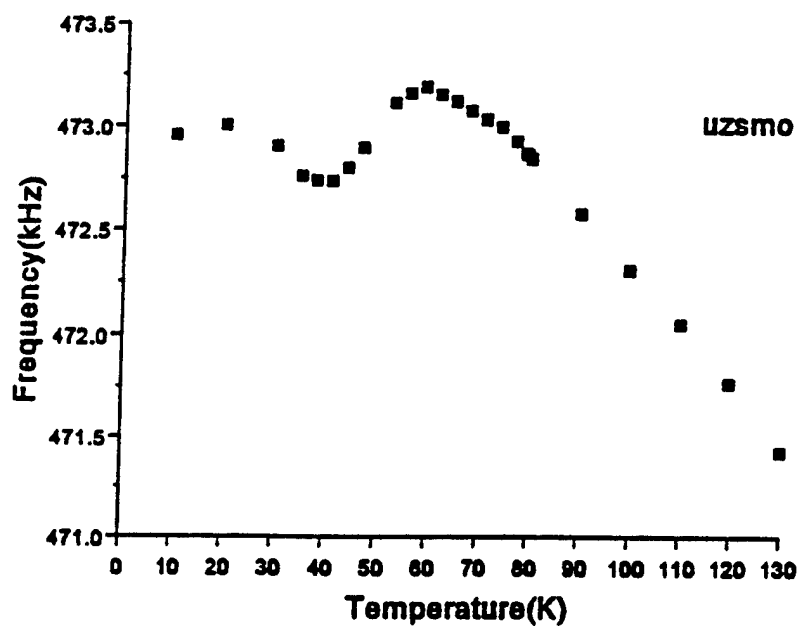


Variation of Neel temperature and softening with field and with c_{44}/c_{66} ratio (undetermined) on several samples with different mixes

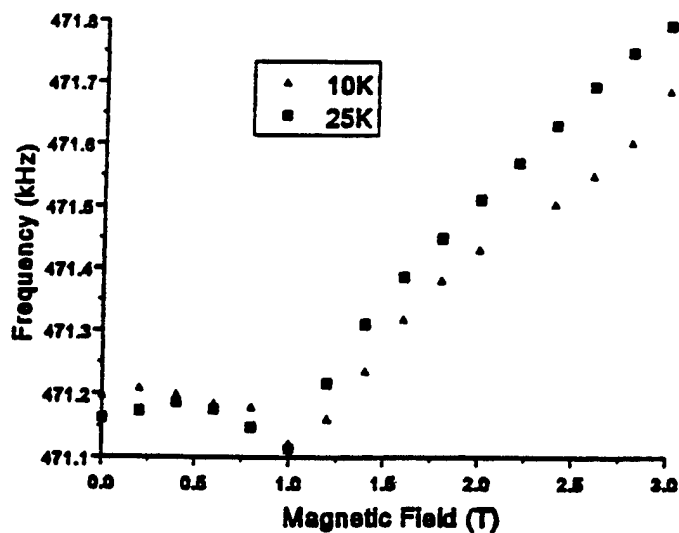
T_n essentially independent of field direction, suggesting free energy couples as M^2H^2



Effects above the Neel transition in applied field

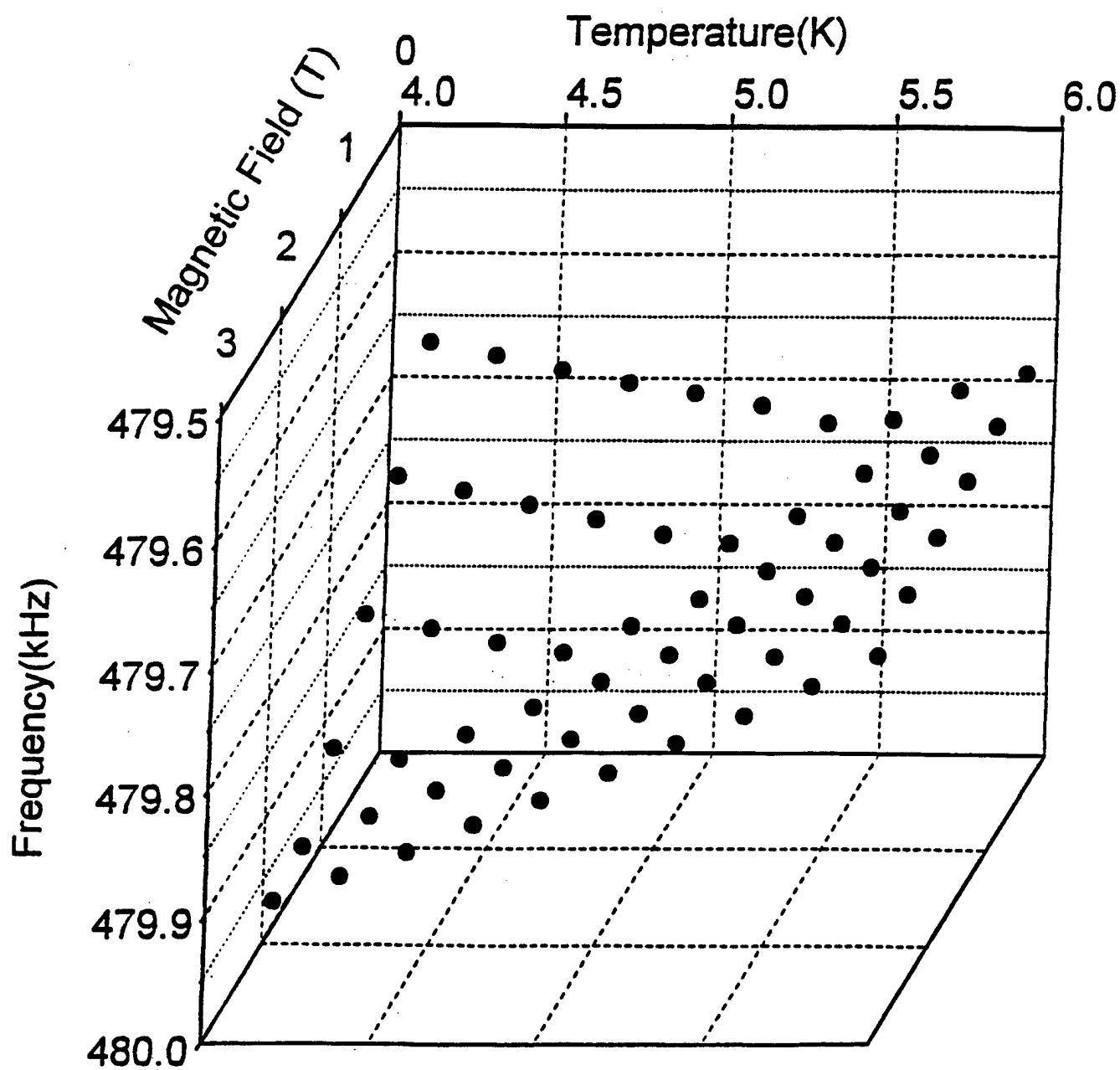


The above is indicative of a weak phase transition of unknown origin



This effect disappears above about 70K

PMSN

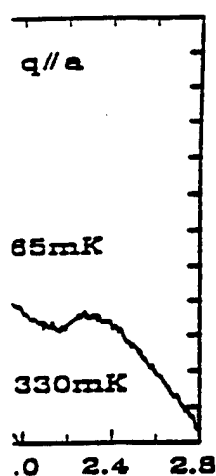
 $\sim 6 \text{ K}$ superconductor $H_{c2}(\text{T})$ 

transverse-sound

on velocity mea-
all of the known
entified as possi-
3 shows $T_{c*}(H)$
signatures, com-
ned from heat-
gnatures remain
ith of the transi-
ad to several im-

r the interpreta-
and $T_{c*}(H)$, in-
us dividing the
e transition lines
ase boundary as

our resolution,
nducting transi-
 $T_{c*}(H)$, and
, for field direc-
al plane. For H
 $T_{c2}(T)$ (Refs. 16
we see no such



: longitudinal ul-
nd H_{c2} are both

different segments of the same transition

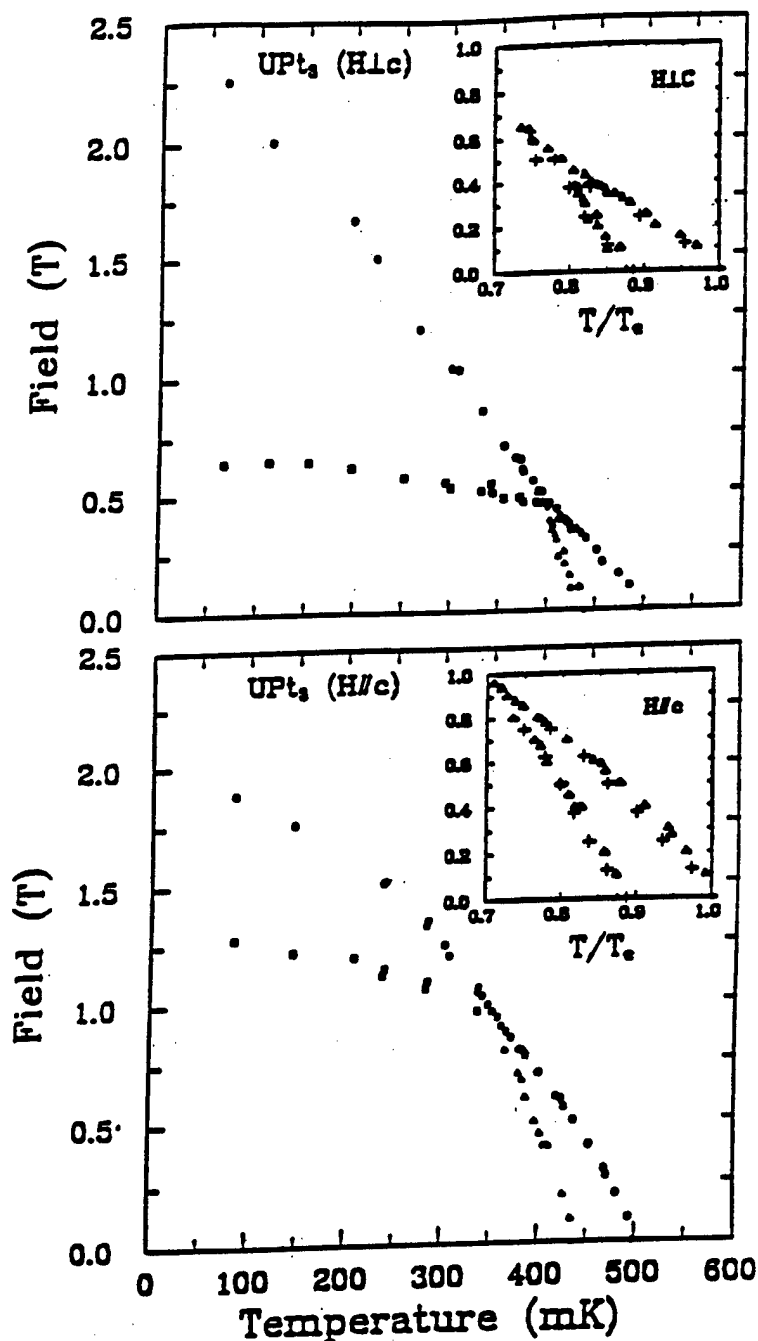


FIG. 3. Phase diagrams obtained from velocity measurements for three different orientations of the field: $H \perp c$ and $H \parallel c$. The data points for the phase boundaries are denoted as \square , H_{FL} ; \circ , H_{c2} ; and Δ , T_{c*} . The insets show our results for $T_{c*}(H)$ and $H_{c2}(T)$ from velocity measurements (Δ) in comparison with the heat-capacity data of Refs. 9 and 16 (shown as $+$). Note that we have normalized the temperature scales in the insets for the different samples.

of U
gram:
point
allow
point,
be eit
same
and K
transi
daries
relatic
The
suppo
S.A.,
suppo
Grant
suppo
the N
Grant
for pr
tion, a
Not
learne

¹D. J
and J. J
²V. N
E. Bücl

Flux lattice de-pinning $\text{La}_{2-x}\text{Sr}_x\text{CuO}_4$

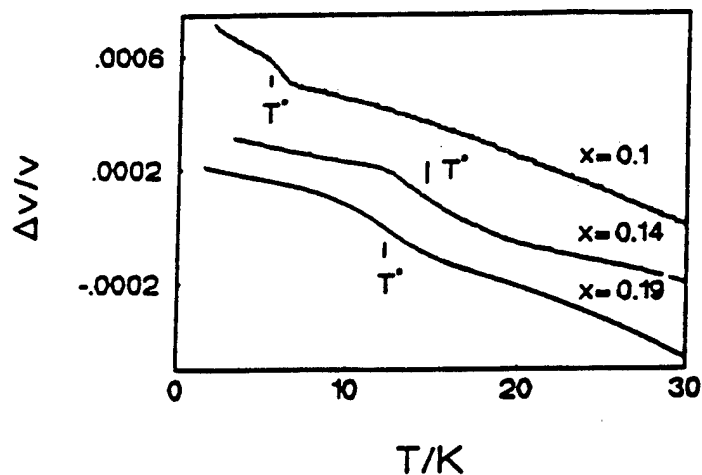


Figure 1: Change of sound velocity as a function of temperature in $B=7$ Tesla for three doping levels ($B \parallel c$, $k \parallel c$ and $k \perp u$).

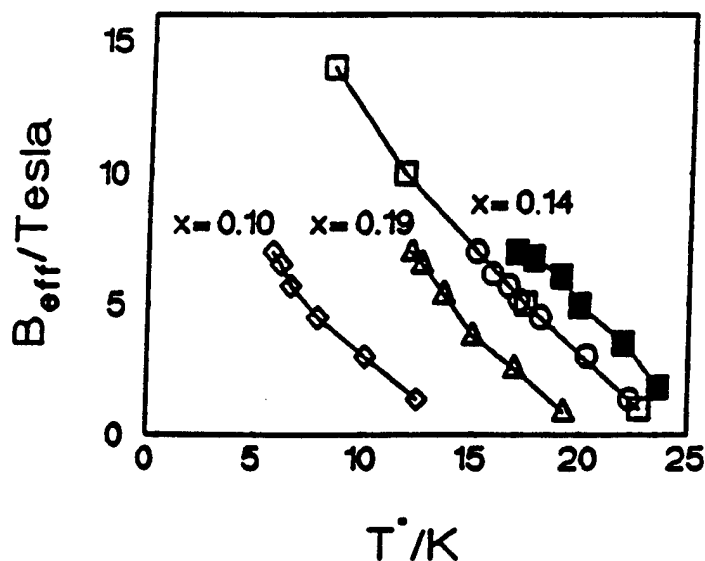


Figure 2: Phase diagram of the effective field $B_{\text{eff}}=B \cdot \cos \phi$ vs. T^* with $B \parallel c$ (\square), by rotating the field $B=7$ Tesla in the $(\bar{1}10)$ -plane (\diamond , \circ and \triangle) or in the (110) -plane (\blacksquare). Open symbols: 28 MHz, full symbols: 8.9 MHz, $\phi: \Delta(B, c)$.

P. Lemmens et al., Physica B 194 ('94) 1863

ELECTRON-PHONON INTERACTION

295

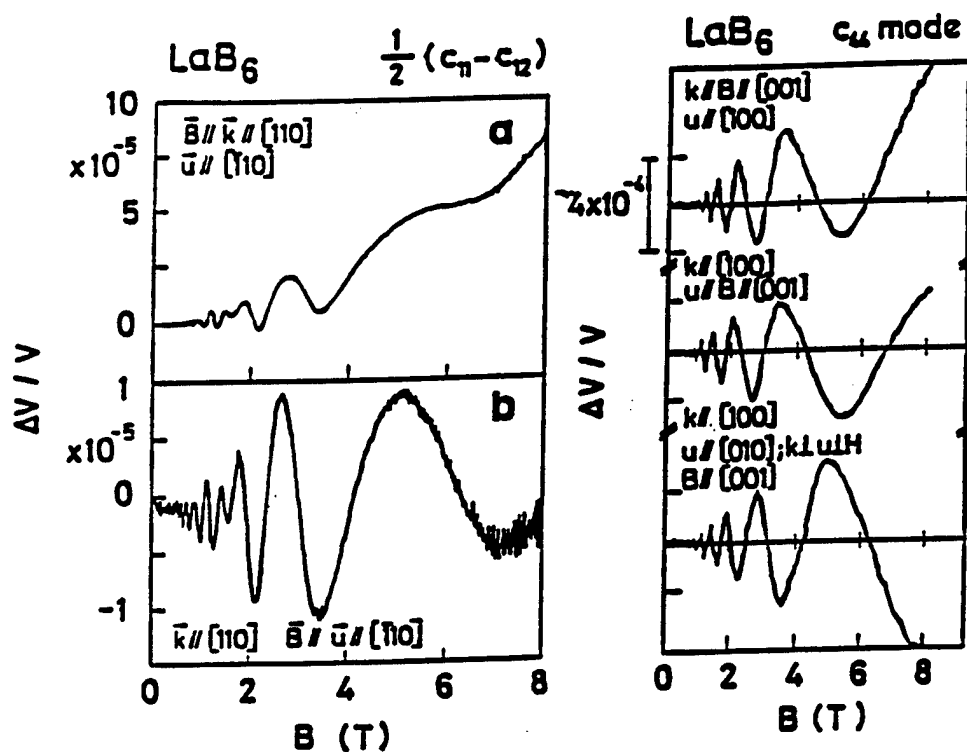


Fig. 40. Acoustic quantum oscillations in LaB_6 for the $(c_{11} - c_{12})/2$ and c_{44} modes for different geometries (Suzuki et al. 1985a).

$$L = \int_V \left[\sum_i \rho \omega^2 u_i^2 - \sum_{i,j,k,l} c_{ijkl} \frac{\partial u_i}{\partial x_j} \frac{\partial u_k}{\partial x_l} \right] dV,$$

The "standard" problem

Computational time = 1 (1)

$$L = \int_V \left[\sum_i \rho \omega^2 u_i^2 - \sum_{i,j,k,l} c_{ijkl} \frac{\partial u_i}{\partial x_j} \frac{\partial u_k}{\partial x_l} + \sum_{m,n} \overset{\substack{\text{dielectric tensor} \\ \downarrow}}{\epsilon_{mn}} \frac{\partial \phi}{\partial x_m} \frac{\partial \phi}{\partial x_n} - 2 \sum_{k,l,m} \overset{\substack{\text{piezoelectric tensor} \\ \downarrow}}{e_{mk}} \frac{\partial \phi}{\partial x_m} \frac{\partial u_k}{\partial x_l} \right] dV,$$

Electric field effects

Computational time = 16 (7.6)

solved by Ohno [Phys. Chem. Minerals 17 (1990) 371]
0.5% effects on frequencies

$$L = \int_V \left[\sum_i \rho \omega^2 u_i^2 - \sum_{i,j,k,l} c_{ijkl} \frac{\partial u_i}{\partial x_j} \frac{\partial u_k}{\partial x_l} + \sum_{m,n} \overset{\substack{\text{permeability tensor} \\ \downarrow}}{\mu_{mn}} H_m H_n - 2 \sum_{k,l,m} \overset{\substack{\text{piezomagnetic tensor} \\ \downarrow}}{m_{mk}} H_m \frac{\partial u_k}{\partial x_l} \right] dV,$$

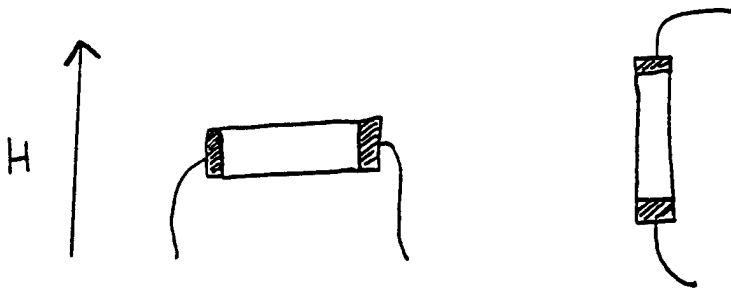
Magnetic field effects

Computational time = 64 (19)

$\sigma_{ij} \neq \sigma_{ji}$ due to torques
(so 81 elastic constants — generally ignored in pulse-echo)

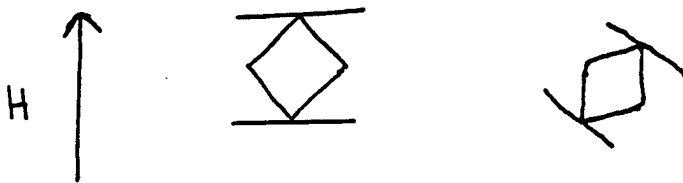
Experimental Field Alignment

- Pulse-echo

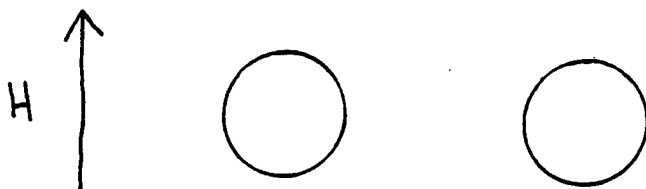


- RUS

Rotatable probe head



RST



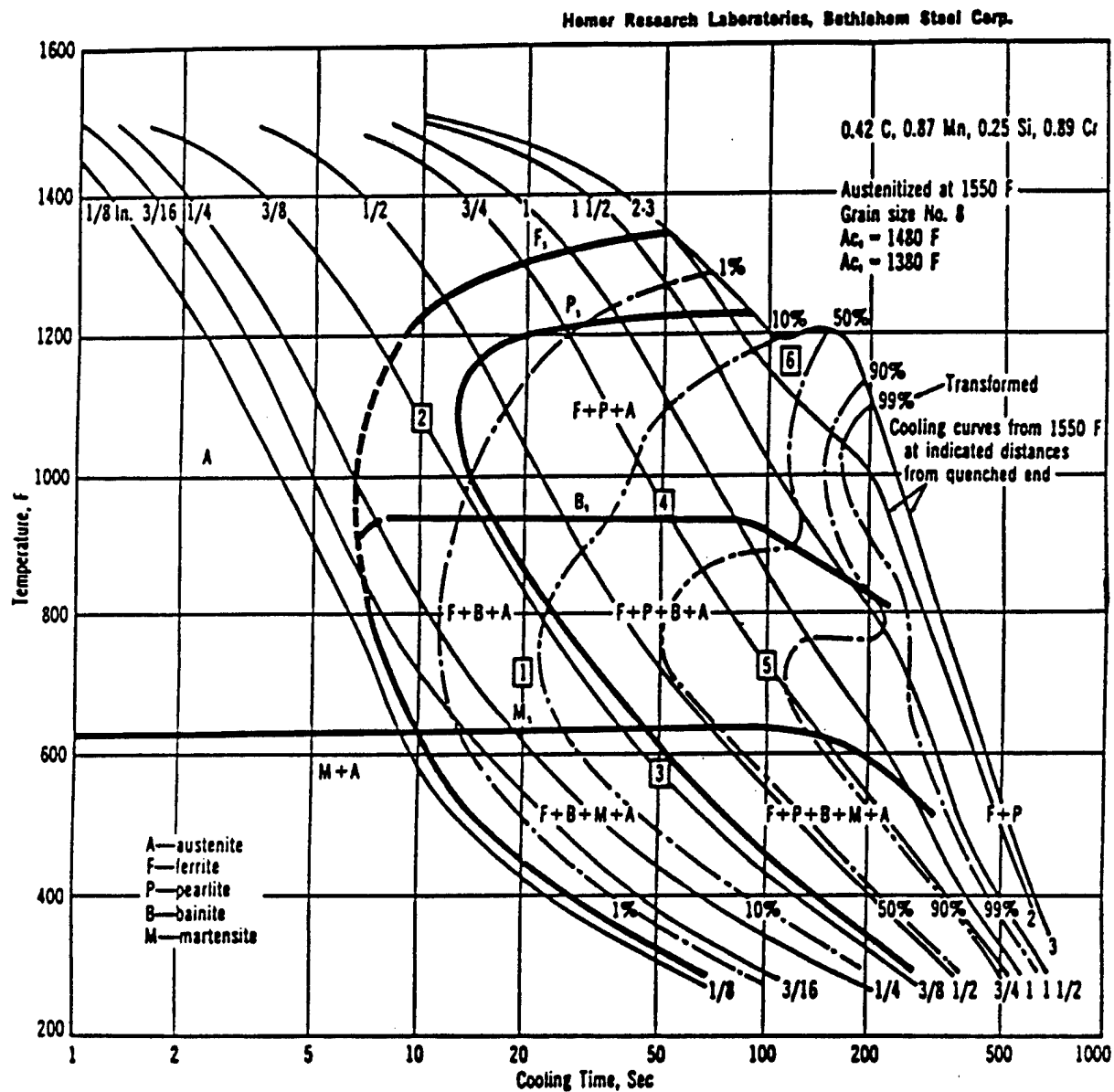
High Temperature RUS and the Elastic Constants of Steel

Tim Darling
Philip Armstrong
Albert Migliori

Raj Vaidya
Carolynn Scherer

Los Alamos National Laboratory

- ◆ RUS Application
- ◆ “Real Time” following of elastic constants during heat treatment
- ◆ Improved elastic constants for 51XX grade steels as a function of temperature
- ◇ Comparison of two resonance methods - RUS and rod resonance
- ◇ Comparison of single mode vs full fit



Diffusive transformations (slow, high temperature activated) compete with non-diffusive (Martensitic, fast, low temperature activated) transformations to produce a complex combination of phases, microstructures and strains.

Samples: 5180, 5140, 5120 steel (assume isotropic)

RUS: RPR 4.8 x 5.0 x 5.2 mm

Rod: 1/4" diameter x 4" long

Procedure:

1. heat treat and quench to get "100%" phases
2. measure resonance frequencies with temperature

- ◆ RUS: Lithium Niobate/Alumina metal bonded transducers

$T < 500\text{C}$

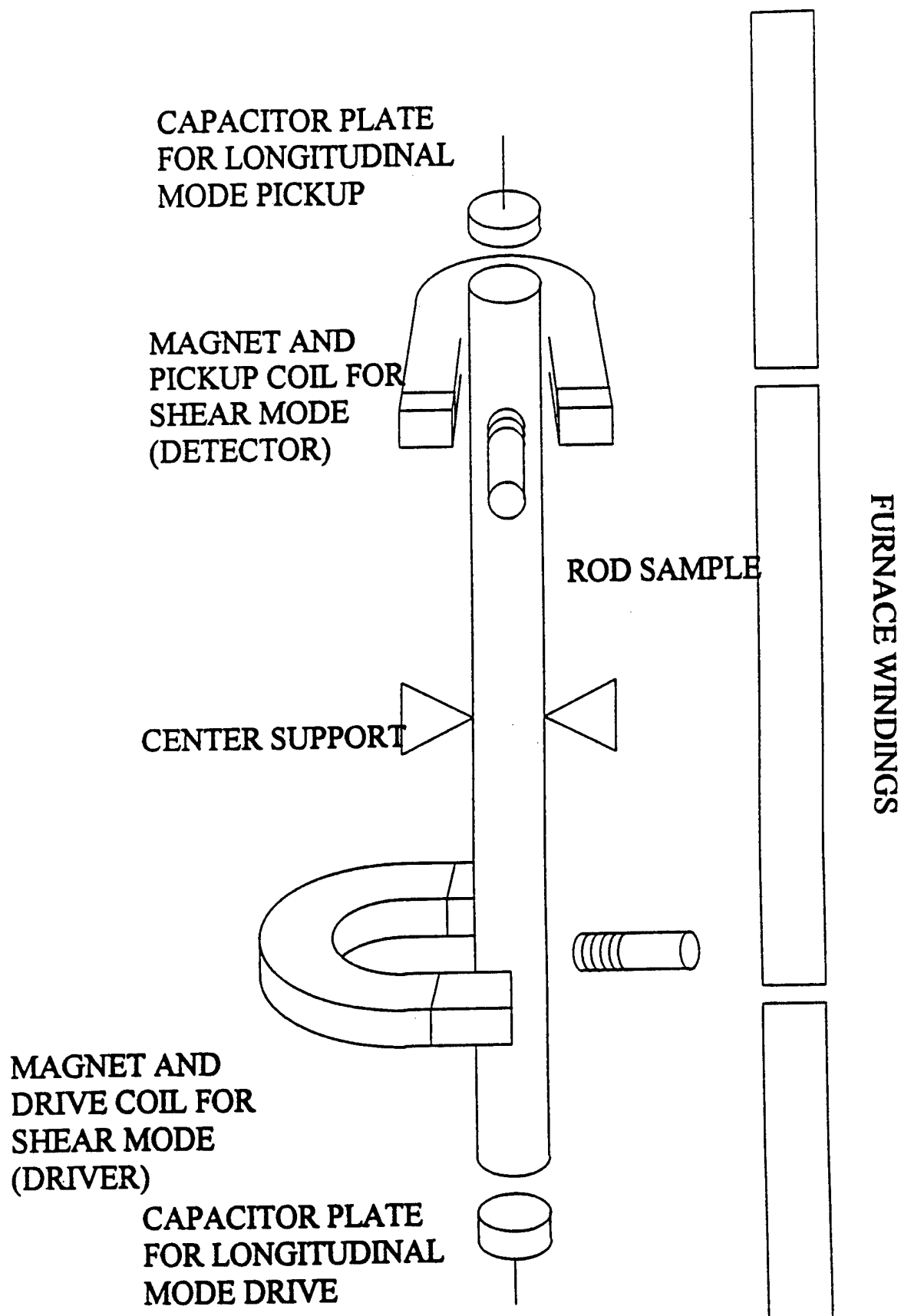
Measure and fit 40-50 lines $\rightarrow C_{11}$ and C_{44}

Sensitive to symmetry and homogeneity

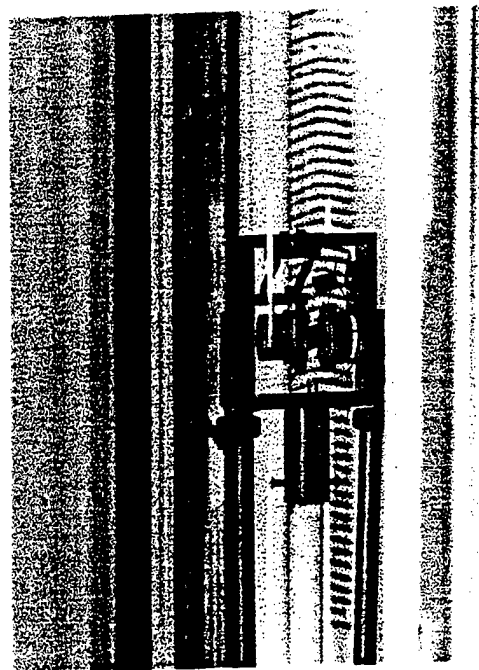
- ◆ Rod: Centre node mount, capacitive/magnetic transducers

$T < 1000\text{C}$

Measure fundamental longitudinal and shear modes $\rightarrow E$ and G (Young's and shear modulus)



Schematic of the Rod Resonance technique



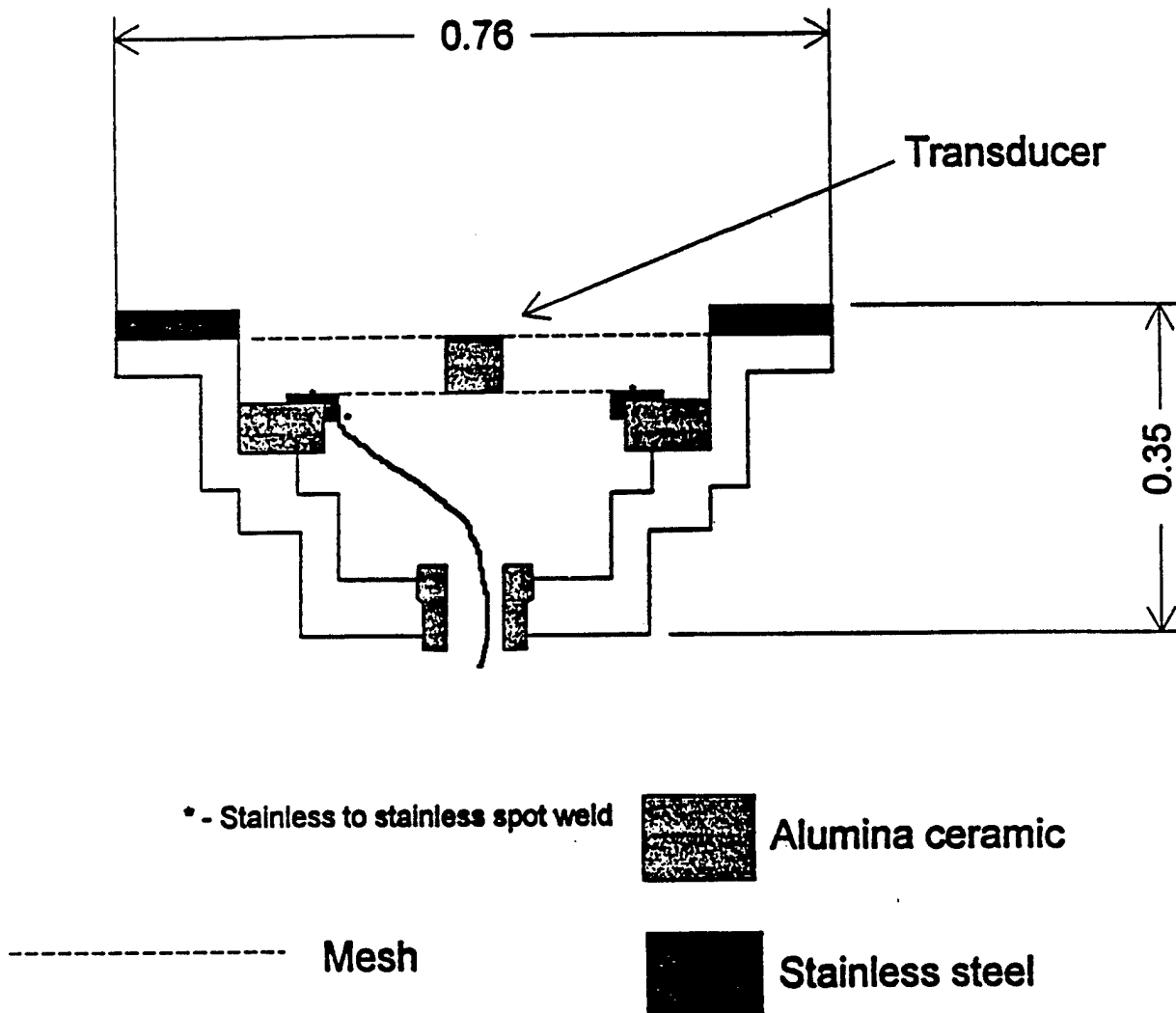


Table 4. RR measurements of Young's modulus - 5180 Pearlite (normalized)

Temperature (C)	Length/L20	Longitudinal Frequency(kHz)	Young's Modulus (GPa)
20	1.0000	25.581	211.3
77	1.0009	25.626	211.8
108	1.0014	25.362	207.4
147	1.0020	25.277	205.9
238	1.0035	24.935	200.0
343	1.0053	24.429	191.7
345	1.0053	24.423	191.6
350	1.0054	24.389	191.0
453	1.0072	23.819	181.9
523	1.0085	23.226	172.7
556	1.0091	23.113	170.9
21	1.0000	25.629	212.1
27	1.0001	25.633	212.1
104	1.0013	25.445	208.8
222	1.0032	24.992	201.0
501	1.0081	23.561	177.8
695	1.0117	20.378	132.5
694	1.0117	20.358	132.3
658	1.0110	22.108	156.1
615	1.0102	22.53	162.2
602	1.0099	22.743	165.3
549	1.0090	23.166	171.7
20	1.0000	25.656	212.5
653	1.0109	22.295	158.7
805	1.0129	19.398	119.9
803	1.0129	19.438	120.4
789	1.0124	19.638	123.0
765	1.0117	19.913	126.5
745	1.0110	20.103	129.0
725	1.0104	20.273	131.3
726	1.0104	20.283	131.4
717	1.0102	20.383	132.8
716	1.0101	20.412	133.2
716	1.0101	20.383	132.8
706	1.0098	20.453	133.7
696	1.0095	20.643	136.3
696	1.0095	20.803	138.4
695	1.0095	20.933	140.1
695	1.0095	21.013	141.2
694	1.0094	21.193	143.7
694	1.0094	21.413	146.6
691	1.0093	21.734	151.1
693	1.0094	21.777	151.7
692	1.0094	21.813	152.2
692	1.0094	21.82	152.3
676	1.0113	20.68	136.5
641	1.0107	21.659	149.9
631	1.0105	22.07	155.6

Sample ms01 5180 steel ms per TWD 250C
 mass= 0.8919 gm rho= 7.643 gm/cc

mass= 0.8919 gm rho= 7.643 gm/cc							fraction of	
n	f-expt	f-model	%err	weight	k	i	C11	C44
							d7/d(moduli)	
1	0.273840	0.272363	-0.54	1.0	4	1	0.00	1.00
2	0.303360	0.302188	-0.39	1.0	4	2	0.00	1.00
3	0.367920	0.369609	0.46	1.0	6	1	0.05	0.95
4	0.380640	0.380712	0.02	1.0	7	1	0.06	0.94
5	0.383040	0.384115	0.28	1.0	3	2	0.01	0.99
6	0.393230	0.393999	0.20	1.0	2	1	0.01	0.99
7	0.000000	0.399060	0.00	0.0	1	1	0.04	0.96
8	0.400830	0.401842	0.25	1.0	8	1	0.01	0.99
9	0.000000	0.434440	0.00	0.0	5	1	0.00	1.00
10	0.444150	0.443232	-0.21	1.0	6	2	0.32	0.68
11	0.000000	0.446697	0.00	0.0	5	2	0.00	1.00
12	0.000000	0.457719	0.00	0.0	5	3	0.00	1.00
13	0.469230	0.468069	-0.25	1.0	8	2	0.15	0.85
14	0.000000	0.468456	0.00	0.0	7	2	0.29	0.71
15	0.479870	0.479327	-0.11	1.0	2	2	0.15	0.85
16	0.000000	0.479395	0.00	0.0	1	2	0.30	0.70
17	0.498000	0.497998	0.00	1.0	3	3	0.15	0.85
18	0.000000	0.535291	0.00	0.0	8	3	0.01	0.99
19	0.544800	0.542180	-0.48	1.0	5	4	0.35	0.65
20	0.000000	0.552534	0.00	0.0	5	5	0.34	0.66
21	0.553120	0.554548	0.26	1.0	4	3	0.05	0.95
22	0.556240	0.555254	-0.18	1.0	2	3	0.01	0.99
23	0.000000	0.566521	0.00	0.0	6	3	0.10	0.90
24	0.000000	0.569224	0.00	0.0	7	3	0.09	0.91
25	0.571580	0.569744	-0.32	1.0	1	3	0.08	0.92
26	0.576260	0.574978	-0.22	1.0	3	4	0.01	0.99
27	0.000000	0.618932	0.00	0.0	7	4	0.08	0.92
28	0.000000	0.619188	0.00	0.0	1	4	0.10	0.90
29	0.000000	0.626533	0.00	0.0	6	4	0.05	0.95
30	0.648000	0.650363	0.36	1.0	1	5	0.09	0.91
31	0.658500	0.661049	0.39	1.0	7	5	0.09	0.91
32	0.661200	0.663693	0.38	1.0	6	5	0.10	0.90
33	0.703800	0.705123	0.19	1.0	5	6	0.89	0.11
34	0.706200	0.706173	0.00	1.0	6	6	0.06	0.94
35	0.000000	0.714476	0.00	0.0	3	5	0.11	0.89
36	0.000000	0.721312	0.00	0.0	2	4	0.09	0.91
37	0.730800	0.730772	0.00	1.0	7	6	0.06	0.94
38	0.000000	0.733186	0.00	0.0	8	4	0.07	0.93
39	0.000000	0.736673	0.00	0.0	4	4	0.00	1.00
40	0.738900	0.739970	0.14	1.0	3	6	0.09	0.91
41	0.000000	0.742701	0.00	0.0	2	5	0.10	0.90
42	0.000000	0.743813	0.00	0.0	5	7	0.10	0.90
43	0.747900	0.747665	-0.03	1.0	8	5	0.10	0.90
44	0.751200	0.749611	-0.21	1.0	1	6	0.06	0.94

c11 **c12** **c44**
2.5530 **1.0972** **0.7279**

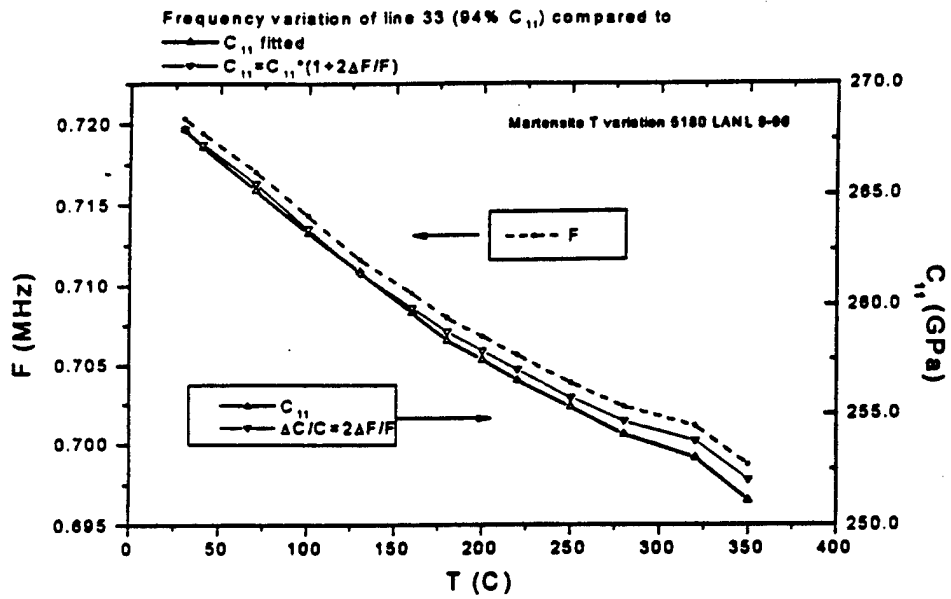
d1 **d2** **d3**
 0.51150 0.49000 0.46560

loop# 5 **rms error= 0.2799 %**

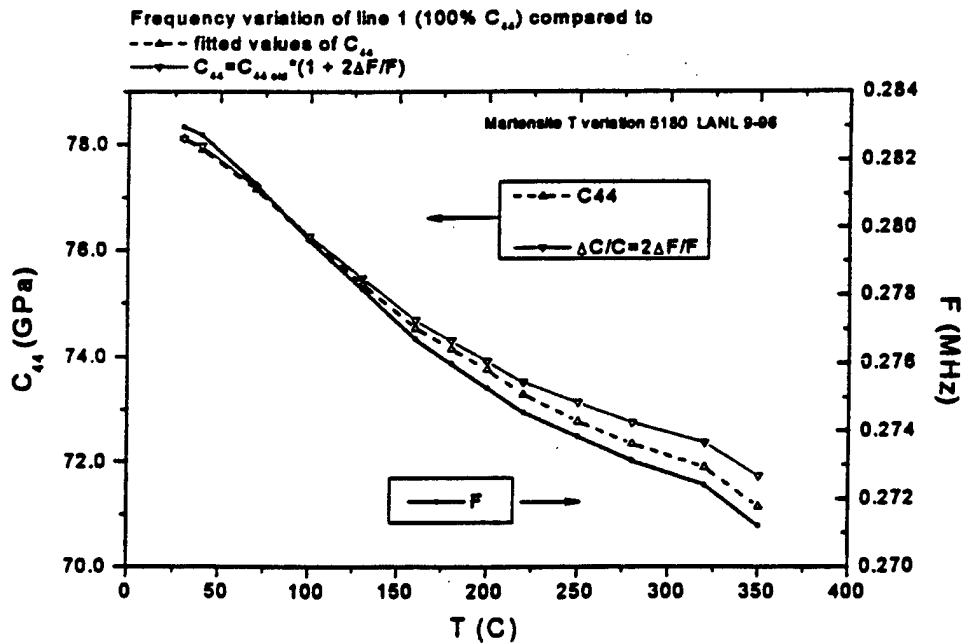
chisquare increased 2% by the following % changes in independent parameters

C₁₁ : 0.40%

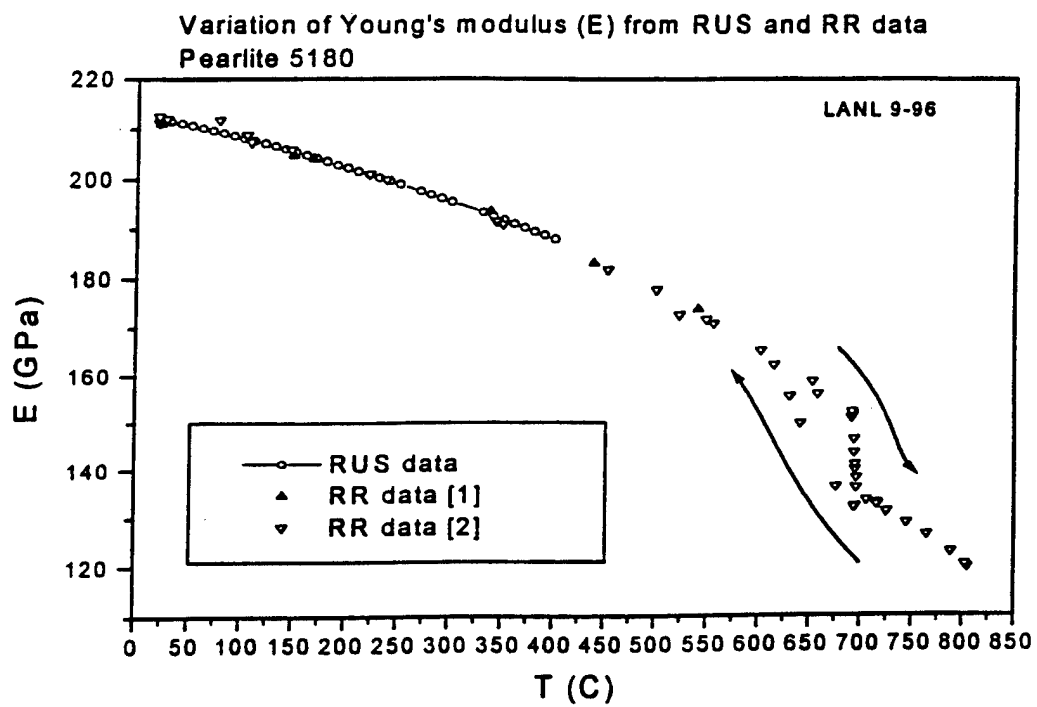
C₄₄ : 0.09%

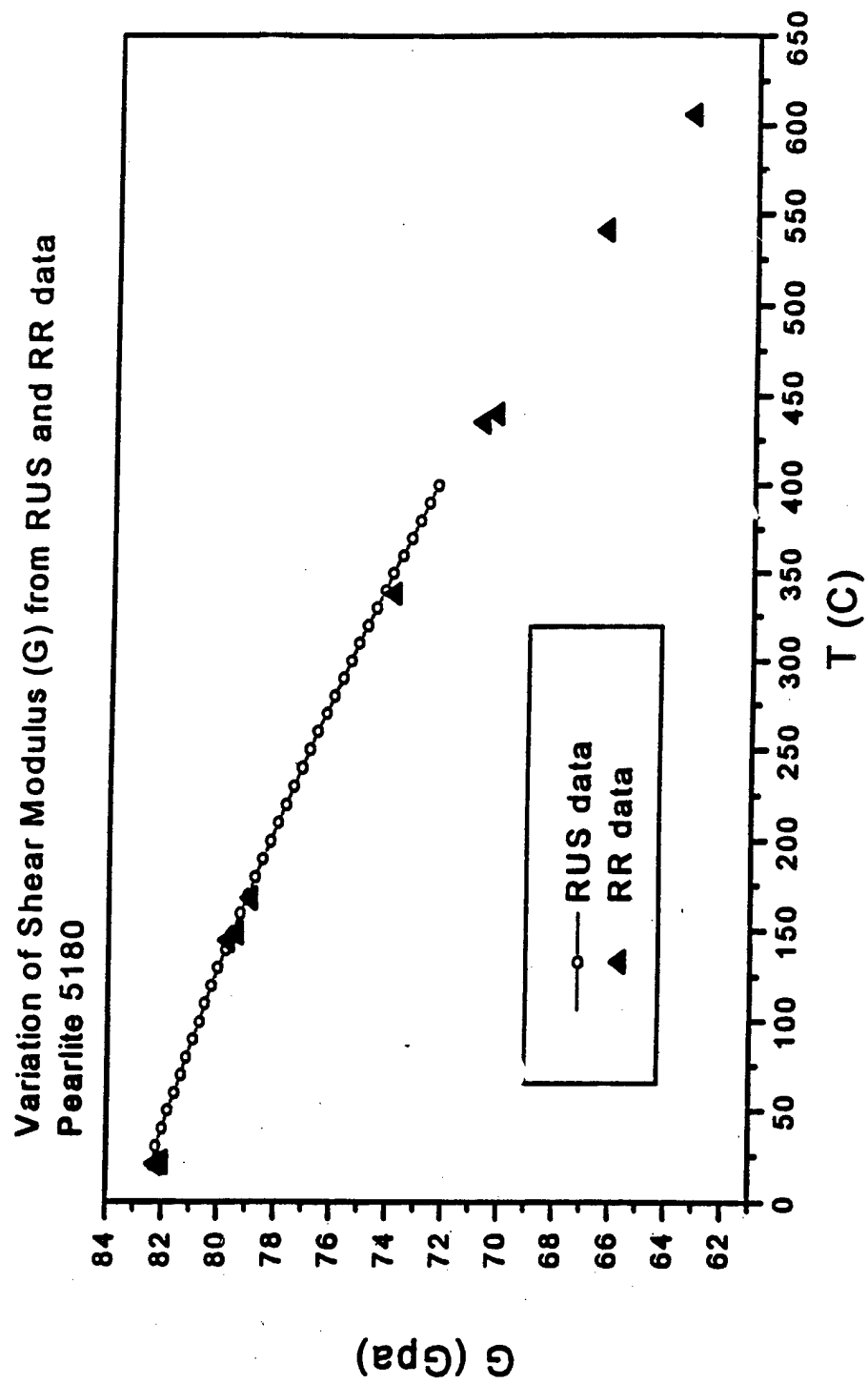


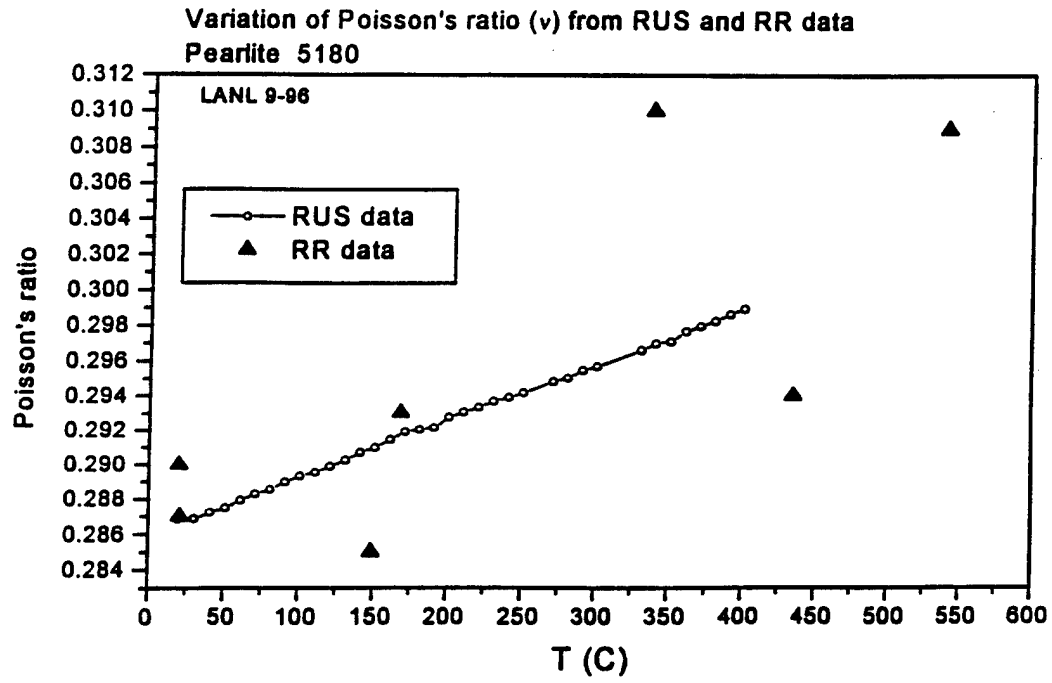
Comparison of full RUS data fit and single pure mode fit for C_{11}



Comparison of full RUS data fit and single pure mode fit for C_{44}

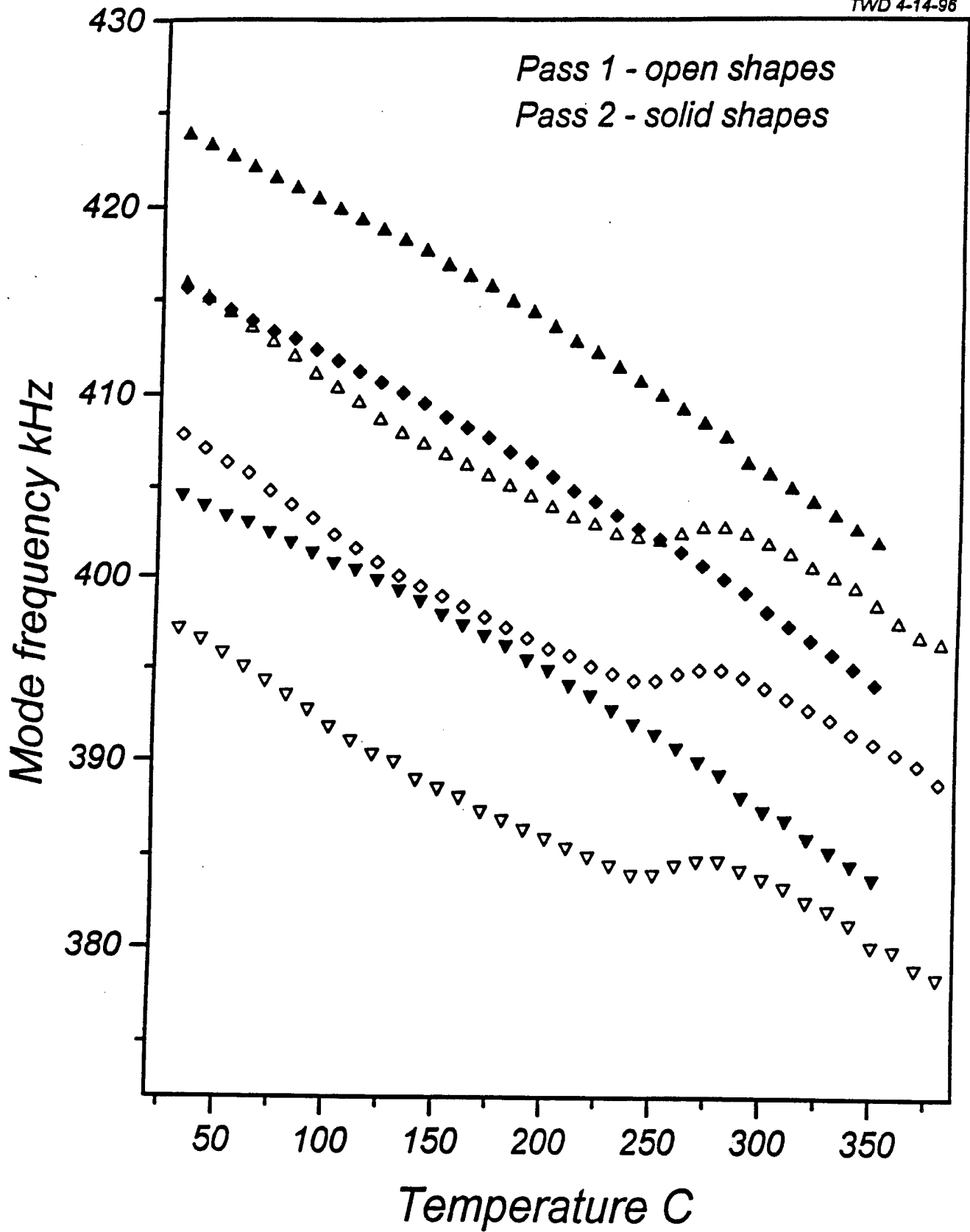






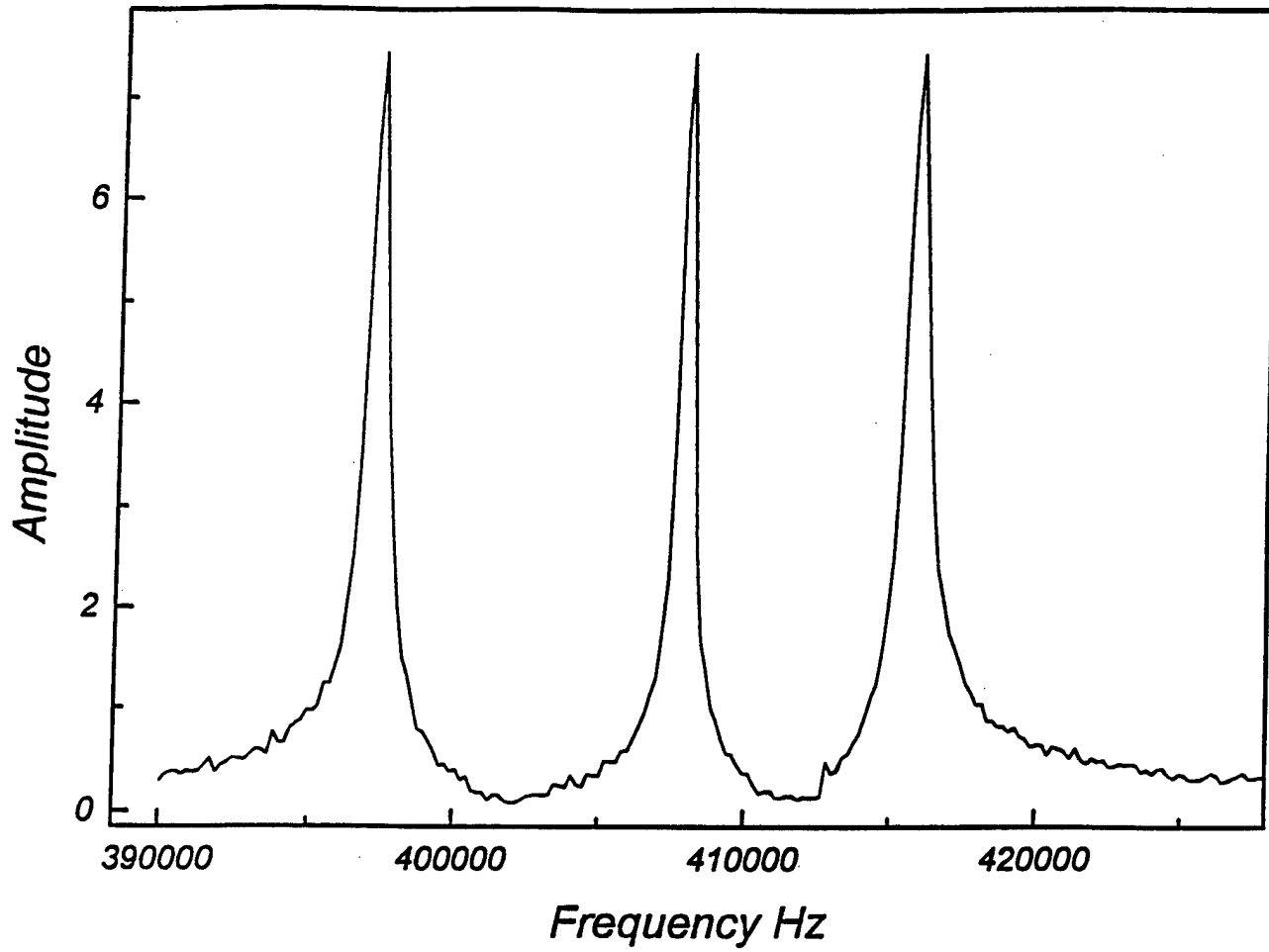
5180 steel sample A9 - resonance frequencies

TWD 4-14-98



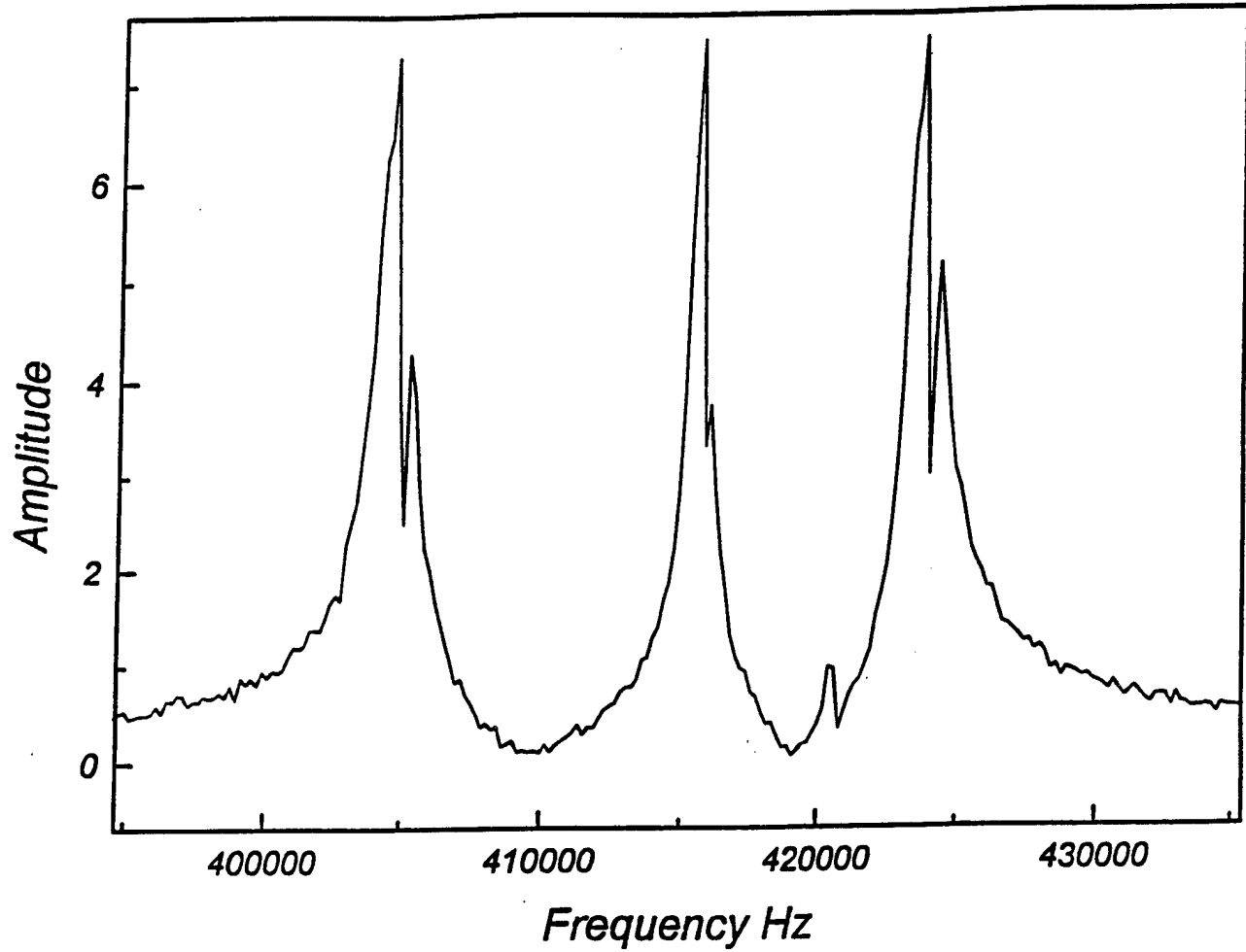
5180 steel sample A9 T=30C, First pass

TWD 4-14-98



5180 steel sample A9 T=30C, Second pass

TWD 4-14-88



- + Fulfilled the “engineering” aspect
 - $E(T)$, $G(T)$ for a number of phases

- + Happy agreement between RUS and rod method

- ? Did not look at attenuation - this may be the most important piece of ultrasound information when watching transitions in microstructured materials

- ? Connection between observed splitting and distortion of the RPR

RESONANT ULTRASOUND STUDY OF TEXTURE IN POLYCRYSTALLINE MATERIALS*

Keir Foster and Robert G. Leisure

Department of Physics
Colorado State University
Fort Collins, CO 80523

and

George Alers
NIST
Boulder, CO 80303

*Work supported by the Colorado Advanced Materials Institute

OUTLINE

I. Introduction

II. Effect of texture on elastic constants of polycrystalline materials.

III. RUS measurements on textured copper: elastic constants and orientation distribution function coefficients.

IV. Ultrasonic pole plots

V. Conclusions

INTRODUCTION

- **Texture**
 - Nonrandom orientation of crystallites (grains) in polycrystalline aggregates.
 - Arises in fabrication processes (rolling, drawing), welding, etc.
 - Has strong effects on formability, and on nondestructive testing.

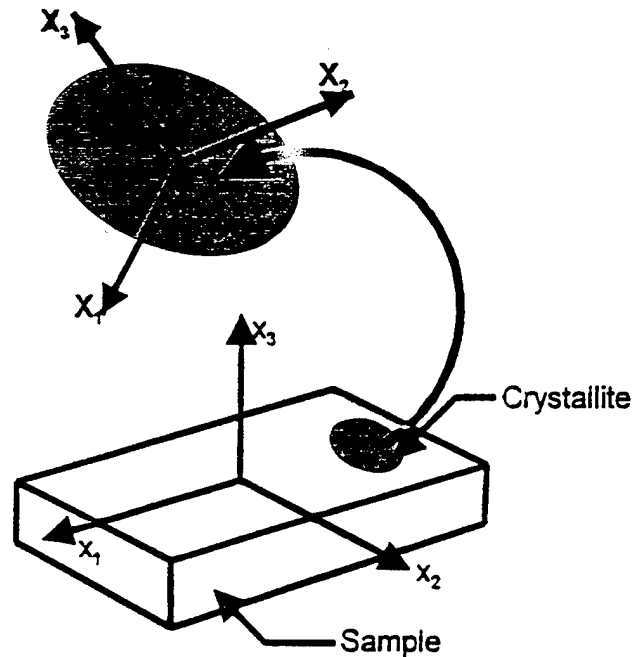
- **Methods of Investigation**
 - X-ray diffraction
 - Neutron diffraction
 - Ultrasound

- **Objectives of Present Study**

Use Resonant Ultrasound Spectroscopy to investigate the weak anisotropic elasticity due to texture.

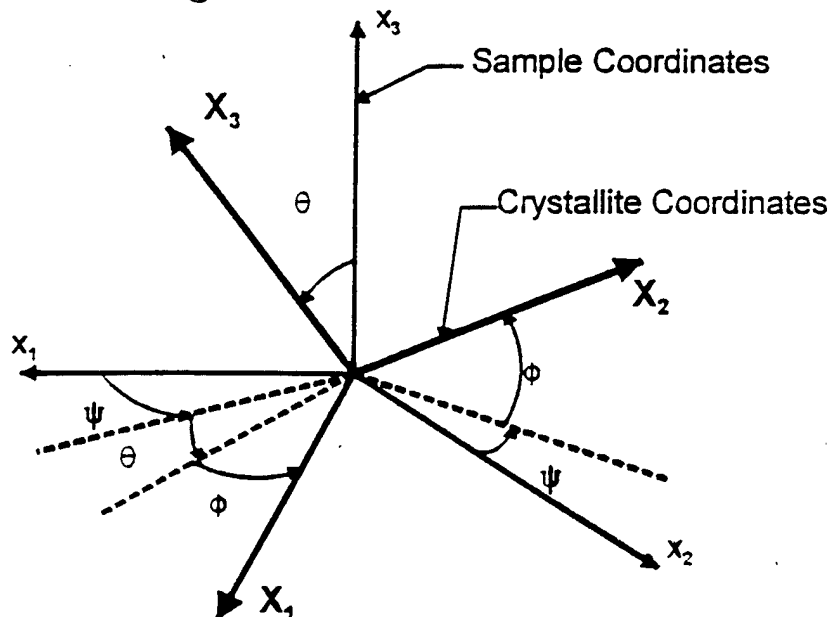
TEXTURE AND ELASTIC CONSTANTS

- **Sample and Crystallite Coordinates**



For plates, x_1 = "rolling direction", x_2 = "transverse direction", and x_3 = "normal direction".

- **Euler Angles**



- **Transformation between the crystallite and sample coordinate systems**

Vector

$$x_i = \sum_{j=1}^3 a_{ji} X_j$$

Elastic constant tensor

$$C_{ijkl}' = \sum_{p=1}^3 \sum_{q=1}^3 \sum_{r=1}^3 \sum_{s=1}^3 a_{pi} a_{qj} a_{rk} a_{sl} C_{pqrs}.$$

The transformation matrix is

$$a = \begin{pmatrix} \cos \psi \cos \theta \cos \phi - \sin \psi \sin \phi & \sin \psi \cos \theta \cos \phi + \cos \psi \sin \phi & -\sin \theta \cos \phi \\ -\cos \psi \cos \theta \sin \phi - \sin \psi \cos \phi & -\sin \psi \cos \theta \sin \phi + \cos \psi \cos \phi & \sin \theta \sin \phi \\ \cos \psi \sin \theta & \sin \psi \sin \theta & \cos \theta \end{pmatrix}$$

● **Elastic constants of *crystallite* in *sample* coordinate system**

Transform the crystallite elastic constants to the sample coordinate system.

Results for a crystallite with cubic symmetry.

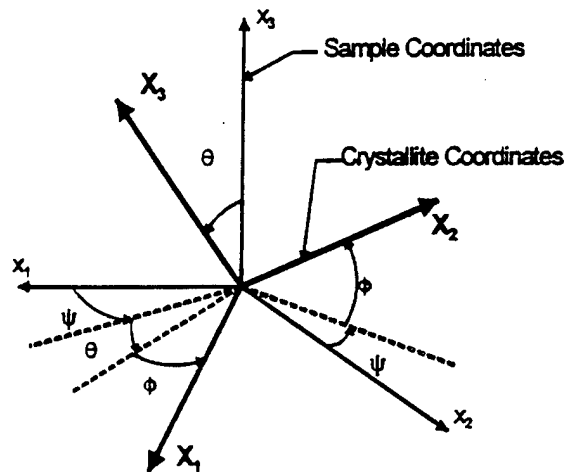
$$\begin{aligned}
 C_{11}' &= C_{11} - 2Cr_1 & r_1 &= a_{11}^2 a_{21}^2 + a_{11}^2 a_{31}^2 + a_{21}^2 a_{31}^2 \\
 C_{22}' &= C_{11} - 2Cr_2 & r_2 &= a_{12}^2 a_{22}^2 + a_{12}^2 a_{23}^2 + a_{22}^2 a_{23}^2 \\
 C_{33}' &= C_{11} - 2Cr_3 & r_3 &= a_{13}^2 a_{23}^2 + a_{13}^2 a_{33}^2 + a_{23}^2 a_{33}^2 \\
 C_{44}' &= C_{44} + Cr_4 & r_4 &= a_{12}^2 a_{13}^2 + a_{22}^2 a_{23}^2 + a_{32}^2 a_{33}^2 \\
 C_{55}' &= C_{44} + Cr_5 & r_5 &= a_{13}^2 a_{11}^2 + a_{23}^2 a_{21}^2 + a_{33}^2 a_{31}^2 \\
 C_{66}' &= C_{44} + Cr_6 & r_6 &= a_{11}^2 a_{12}^2 + a_{21}^2 a_{22}^2 + a_{31}^2 a_{32}^2 \\
 C_{23}' &= C_{12} + Cr_7 & r_7 &= a_{12}^2 a_{13}^2 + a_{22}^2 a_{23}^2 + a_{32}^2 a_{33}^2 \\
 C_{13}' &= C_{12} + Cr_8 & r_8 &= a_{11}^2 a_{13}^2 + a_{21}^2 a_{23}^2 + a_{31}^2 a_{33}^2 \\
 C_{12}' &= C_{12} + Cr_9 & r_9 &= a_{11}^2 a_{12}^2 + a_{21}^2 a_{22}^2 + a_{31}^2 a_{32}^2
 \end{aligned}$$

$$C = C_{11} - C_{12} - 2C_{44}$$

Note: Other C_{ij} are ignored because orthorhombic symmetry for the *sample* will be assumed later.

● **Orientation distribution function $w(\xi, \psi, \phi)$ ($\xi = \cos(\theta)$)**

$w(\xi, \psi, \phi) d\xi d\psi d\phi$ = probability of finding crystallites with orientations between (ψ, θ, ϕ) and $(\psi + d\psi, \theta + d\theta, \phi + d\phi)$.



It will be convenient* to expand $w(\xi, \psi, \phi)$

$$w(\xi, \psi, \phi) = \sum_{l=0}^{\infty} \sum_{m=-l}^{+l} \sum_{n=-l}^{+l} W_{lmn} Z_{lmn} e^{-im\psi} e^{-in\phi},$$

where the Z_{lmn} are generalized, associated Legendre functions. *The W_{lmn} are the Orientation Distribution Coefficients (ODC's) and are determined experimentally.*

*R.-J. Roe, J. Appl. Phys. **36**, 2069 (1966)

- The $\langle C'_{ij} \rangle$ of the sample, in the Voigt approximation, will be the average of the C'_{ij} over the orientation distribution function. These will be of the form

$$\langle C'_{11} \rangle = \langle C_{11} \rangle - 2 \langle C \rangle \langle r_1 \rangle$$

etc.

To calculate, expand the r_i

$$r_i(\xi, \psi, \phi) = \sum_{l=0}^{\infty} \sum_{m=-l}^{+l} \sum_{n=-l}^{+l} R_{lmn}^i Z_{lmn} e^{-im\psi} e^{-in\phi}$$

Calculate the averages

$$\langle r_i \rangle = \int_0^{2\pi} \int_{-1}^1 \int_0^{2\pi} r_i(\xi, \psi, \phi) w(\xi, \psi, \phi) d\psi d\xi d\phi$$

$$= 4\pi^2 \sum_{l=0}^{\infty} \sum_{m=-l}^{m=+l} \sum_{n=-l}^{n=+l} R_{lmn}^i W_{lmn}$$

● Finally!

$$\langle C_{11}' \rangle = \lambda + 2\mu + \left(\frac{12\sqrt{2} \langle C \rangle \pi^2}{35} \right) (W_{400} - \frac{2\sqrt{10}}{3} W_{420} + \frac{\sqrt{70}}{3} W_{440})$$

$$\langle C_{22}' \rangle = \lambda + 2\mu + \left(\frac{12\sqrt{2} \langle C \rangle \pi^2}{35} \right) (W_{400} + \frac{2\sqrt{10}}{3} W_{420} + \frac{\sqrt{70}}{3} W_{440})$$

$$\langle C_{33}' \rangle = \lambda + 2\mu + \left(\frac{32\sqrt{2} \langle C \rangle \pi^2}{35} \right) W_{400}$$

$$\langle C_{44}' \rangle = \mu - \left(\frac{16\sqrt{2} \langle C \rangle \pi^2}{35} \right) (W_{400} + \sqrt{\frac{5}{2}} W_{420})$$

$$\langle C_{55}' \rangle = \mu - \left(\frac{16\sqrt{2} \langle C \rangle \pi^2}{35} \right) (W_{400} - \sqrt{\frac{5}{2}} W_{420})$$

$$\langle C_{66}' \rangle = \mu + \left(\frac{4\sqrt{2} \langle C \rangle \pi^2}{35} \right) (W_{400} - \sqrt{70} W_{440})$$

$$\langle C_{23}' \rangle = \lambda - \left(\frac{16\sqrt{2} \langle C \rangle \pi^2}{35} \right) (W_{400} + \sqrt{\frac{5}{2}} W_{420})$$

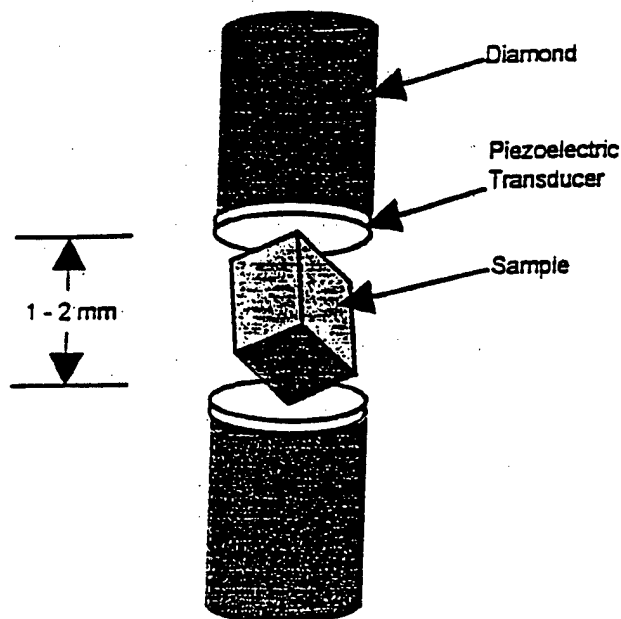
$$\langle C_{13}' \rangle = \lambda - \left(\frac{16\sqrt{2} \langle C \rangle \pi^2}{35} \right) (W_{400} - \sqrt{\frac{5}{2}} W_{420})$$

$$\langle C_{12}' \rangle = \lambda + \left(\frac{4\sqrt{2} \langle C \rangle \pi^2}{35} \right) (W_{400} - \sqrt{70} W_{440})$$

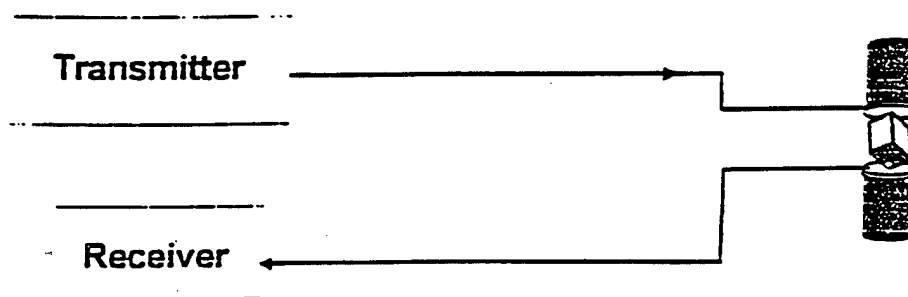
The theoretical values of the Lamé constants λ and μ , and the anisotropy constant $\langle C \rangle$, depend on the averaging methods used (Voigt, Reuss, Hill, etc.) for the texture-free material. The *sample* is assumed to have orthorhombic symmetry.

Resonant Ultrasound Spectroscopy

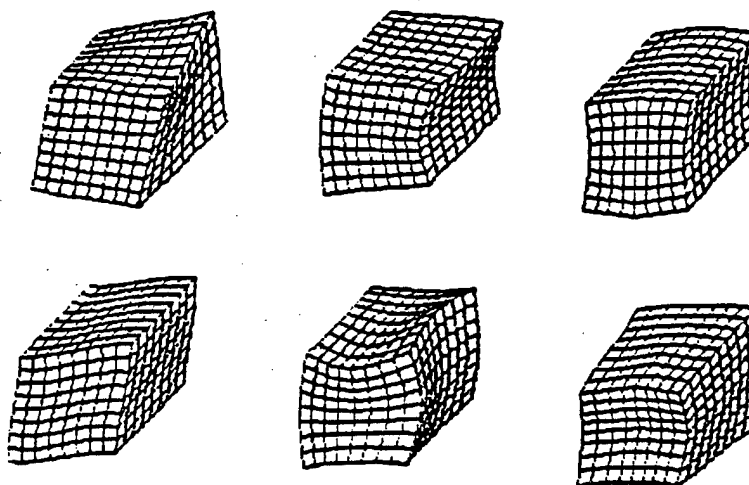
I. Sample-Transducer Arrangement



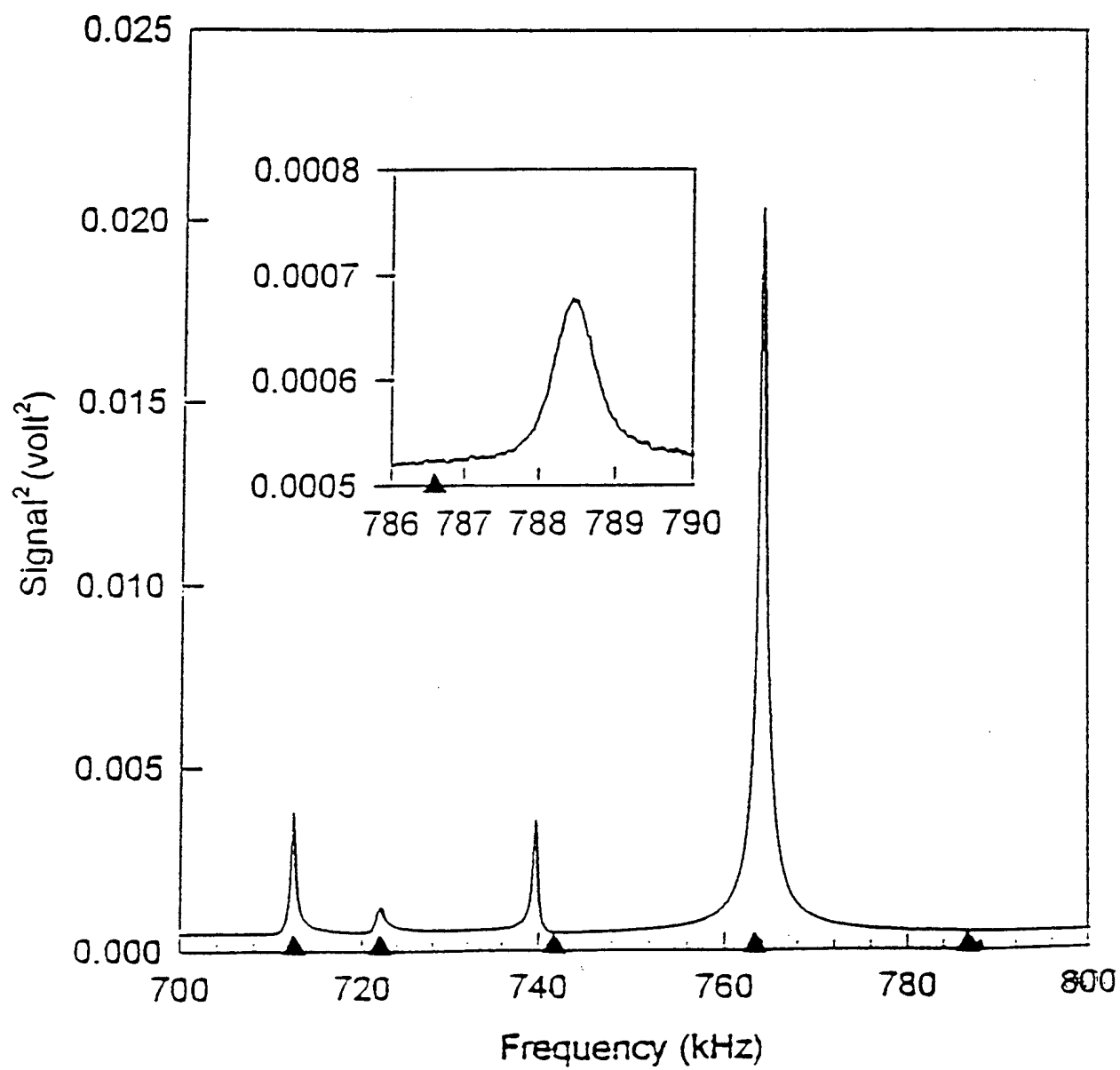
II. Spectrometer



III. Typical Modes



Olin Type C110 polycrystalline copper



EXPERIMENTAL RESULTS FOR OLIN TYPE C110 COPPER (Copper + 0.021 wt % Oxygen)

- Measurements on three, independently prepared, copper samples at room temperature.

Elastic Constant	Sample 1	Sample 2	Sample 3	Mean	% Error
C_{11} (GPa)	199.7	198.4	201.9	200.0	0.51
C_{22} (GPa)	199.9	199.1	201.0	200.0	0.28
C_{33} (GPa)	195.7	197.6	197.4	196.9	0.31
C_{44} (GPa)	44.06	45.24	45.47	44.96	1.02
C_{55} (GPa)	44.04	45.04	45.66	44.91	1.05
C_{66} (GPa)	44.59	45.79	45.41	45.26	0.78
C_{23} (GPa)	109.8	107.5	112.0	109.8	1.18
C_{13} (GPa)	109.2	106.1	109.0	108.1	0.93
C_{12} (GPa)	108.6	111.7	109.7	110.0	0.82

- A least squares fitting of the sample 1 results to the theoretical expressions, using $\langle C \rangle = -100.25$ GPa, gives,

W_{400}	-2.36×10^{-4}
W_{420}	$+4.56 \times 10^{-5}$
W_{440}	-5.11×10^{-5}
λ (GPa)	109.1
μ (GPa)	44.37

Computed values using single crystal C_{ij} for copper.

	Voigt Average	Reuss Average
λ (GPa)	101.5	111.0
μ (GPa)	54.6	40.0

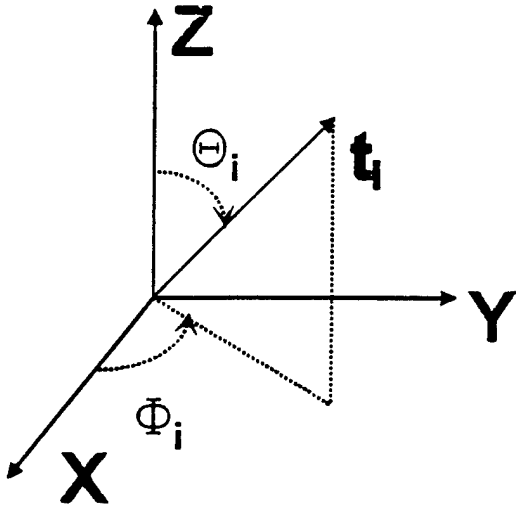
Using the values of the W 's, λ and μ we compute the C_{ij} and compare to the results for sample 1.

	Experimental	Computed
$C_{11}(\text{GPa})$	199.7	198.1
$C_{22}(\text{GPa})$	199.8	198.0
$C_{33}(\text{GPa})$	195.7	198.2
$C_{44}(\text{GPa})$	44.06	44.26
$C_{55}(\text{GPa})$	44.04	44.17
$C_{66}(\text{GPa})$	44.59	44.34
$C_{23}(\text{GPa})$	109.8	109.1
$C_{13}(\text{GPa})$	109.2	108.9
$C_{12}(\text{GPa})$	108.6	109.1

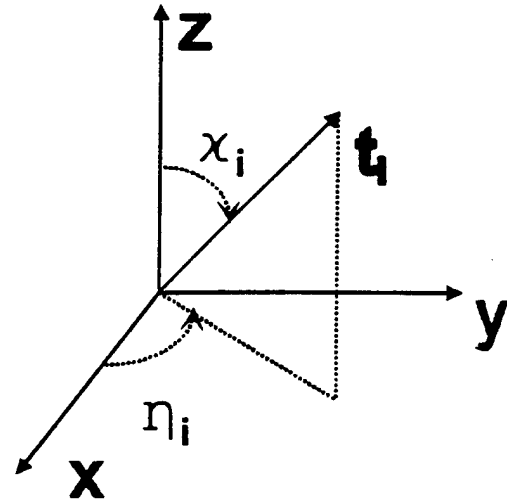
RMS Error = 0.7%

- **Reciprocal lattice vector orientation distribution function**
 $q(\zeta_i, \eta_i)$ ($\zeta_i = \cos(\chi_i)$)

Consider a reciprocal lattice vector \mathbf{t}_i



Crystallite Coordinates



Sample Coordinates

$q_i(\zeta, \eta) d\zeta d\eta$ = Probability to find vector \mathbf{t}_i between (χ, η) and $(\chi + d\chi, \eta + d\eta)$

It can be shown*

$$q_i(\zeta, \eta) = \frac{1}{4\pi} + S(\Xi_i, \Phi_i) \left[P_4^0(\zeta) W_{400} + 2P_4^2(\zeta) \cos(2\eta) W_{420} + 2P_4^4(\zeta) \cos(4\eta) W_{440} \right]$$

$$S(\Xi_i, \Phi_i) = \frac{2\sqrt{2}\pi}{3} \left[P_4^0(\Xi_i) + \frac{10}{\sqrt{70}} P_4^4(\Xi_i) \cos(4\Phi_i) \right], \quad \Xi_i = \cos(\Theta_i)$$

where $P_m^n(z)$ are the normalized, associated Legendre functions.

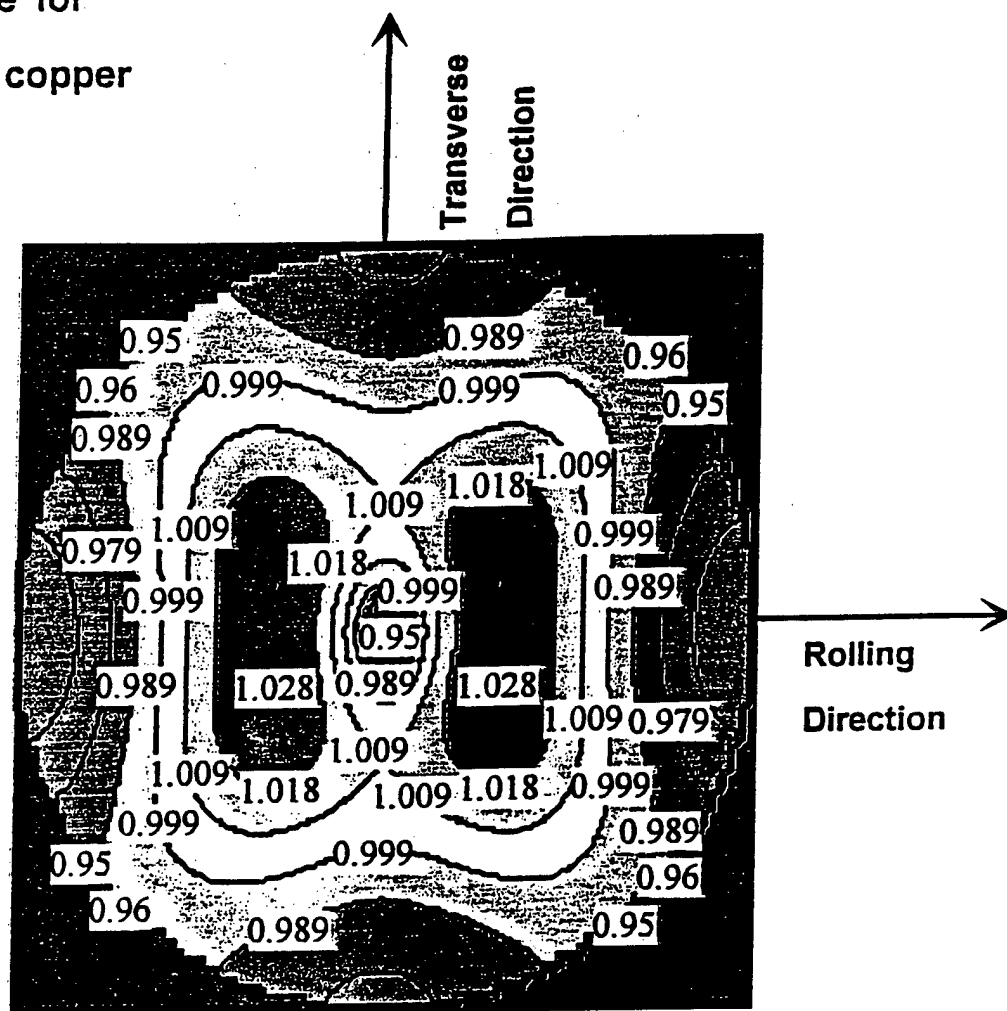
- **Ultrasonic pole plots**

Contour plots of $q_i(\zeta, \eta)$ for a particular reciprocal lattice vectors \mathbf{t}_i

*M. Hirao, K. Aoki, and H. Fukuoka, J. Acoust. Soc. Am. **81**, 1434 (1987).

[100] pole figure for
Olin type C110 copper
(Sample 1)

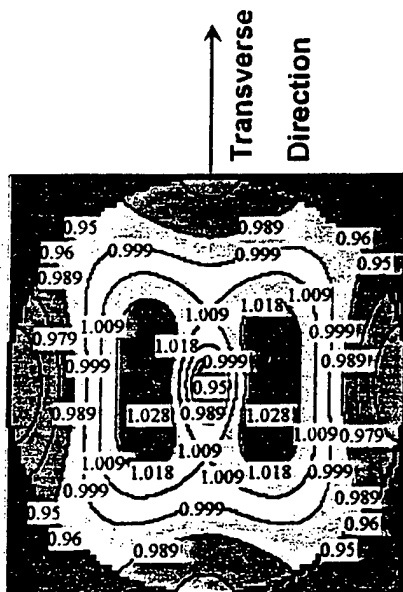
Unannealed



P

[100] pole figures for
Olin type C110 copper
(Sample 1)

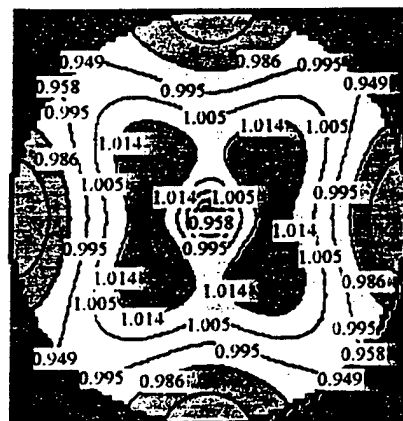
unannealed



Annealed at 250 C
for 1 hr.

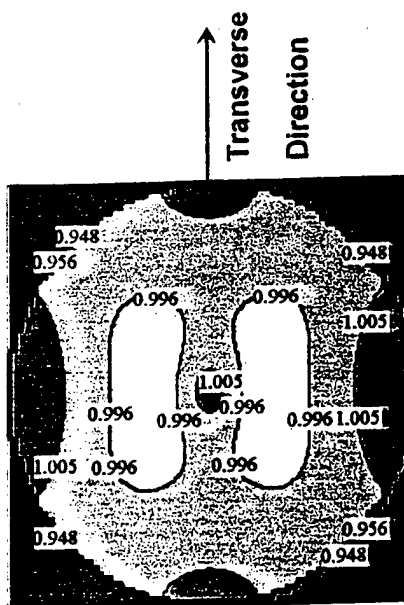


Annealed at 300 C
for 1 hr.



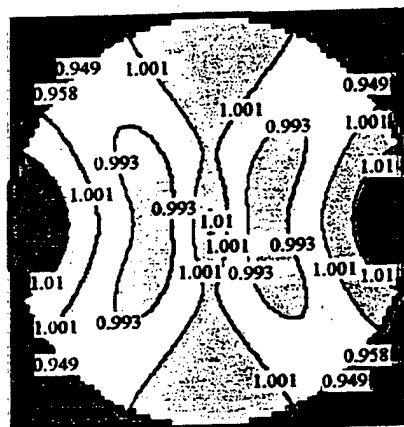
[110] pole figures for
Olin type C110 copper
(Sample 1)

Unannealed



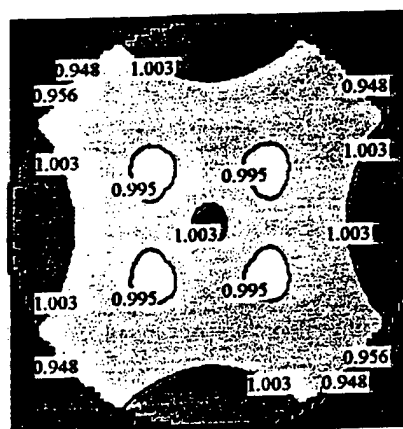
P

Annealed at 250 C
for 1 hr.



P

Annealed at 300 C
for 1 hr.



P

CONCLUSIONS

- **PRESENT RESULTS**
- RUS elastic constant measurements on Olin type C110 copper described by orthorhombic elastic constant matrix, but indicate very small anisotropy - in disagreement with sound velocity results.
- C_{33}' appears to deviate from the theoretical expressions.
- **OUTLOOK**
- Measurements on materials with stronger anisotropy needed, with a careful comparison to ultrasonic velocity measurements.
- RUS has potential to characterize texture.

COMPARISON OF RUS MEASUREMENTS
with

Conventional Methods

C.M. Fortunko & H. Ledbetter

NIST
Materials Science and Engineering Laboratory
Division 853.05
325 Broadway
Boulder, Co 80303

ph. (303) 497-3062
fax (303) 497-5030

e-mail fortunko@boulder.nist.gov

COLLABORATORS

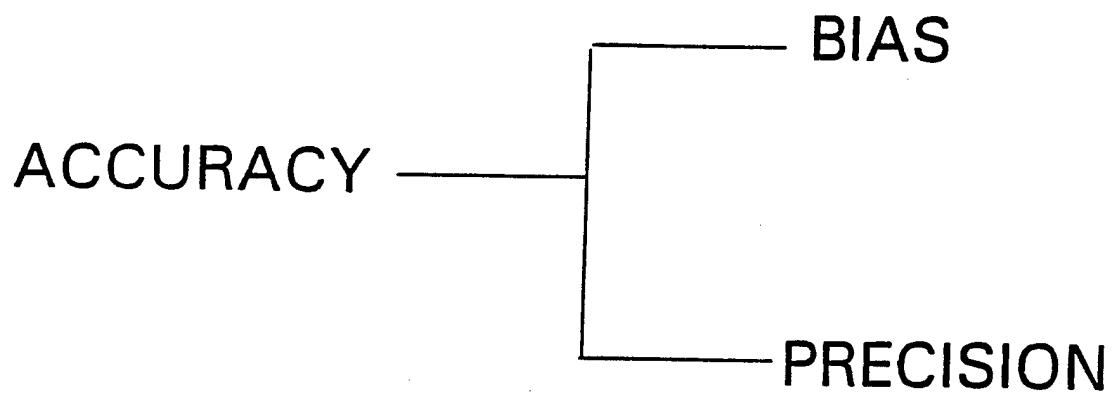
- M.C. RENKEN
- K.W. HOLLMAN
- S. KIM
- N. SIZOVA

TECHNICAL APPROACH:

- ESTABLISH "TRUE" LONGITUDINAL-WAVE VELOCITY IN A HOMOGENOUS ISOTROPIC SPECIMEN USING A NUMBER OF SHORT-PULSE EXPERIMENTAL GEOMETRIES AND SIGNAL-ANALYSIS METHODS.
- ESTABLISH LONGITUDINAL VELOCITY USING RUS ON THE SAME SPECIMEN.
- CALCULATE THE ERROR

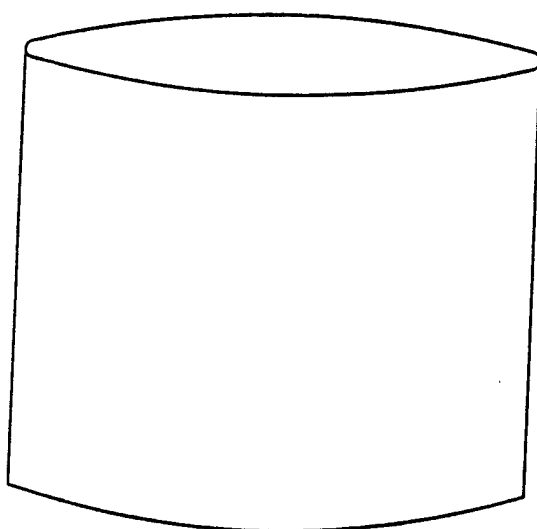
WE NOW USE RESONANT ULTRASONIC
SPECTROSCOPY FOR ROUTINE DETERMINATION OF
ELASTIC-STIFFNESS COEFFICIENTS. IT IS THEREFORE
OF INTEREST TO ESTABLISH THE ACCURACY OF THE
METHOD.

COMPONENTS OF ACCURACY



Fused-Silica Specimen

← 25.4 mm →



↑
25.634 mm
↓

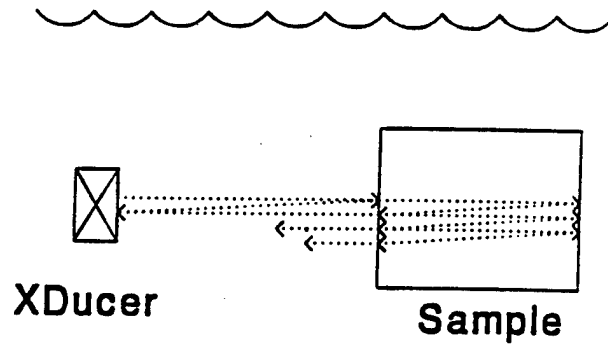
$$\rho = 2.202 \text{ g/cm}^3$$

SHORT-PULSE EXPERIMENTAL GEOMETRIES (PULSE-ECHO)

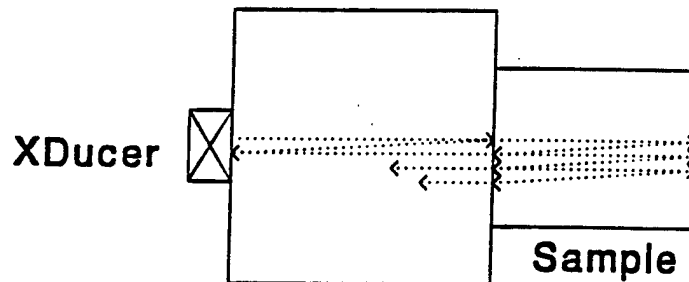
- WATER-IMMERSION
- BUFFER-ROD
- DIRECT-CONTACT

Some Physical Configurations (Pulse-Echo)

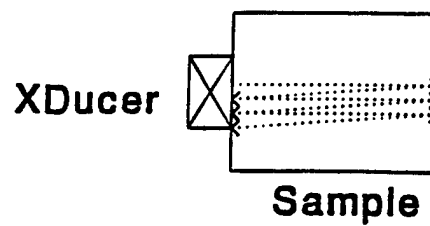
(1) Liquid Immersion



(2) Buffer-Rod

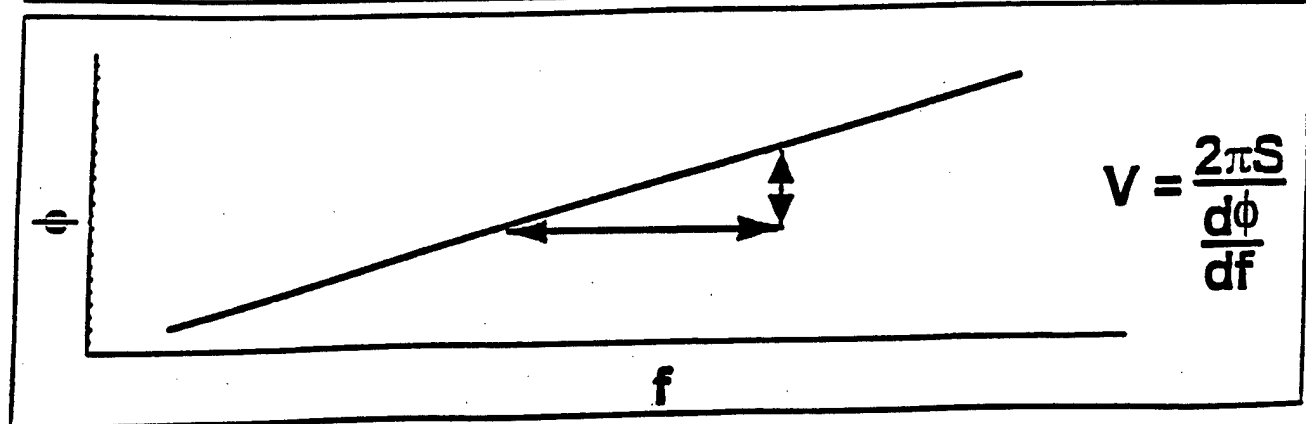
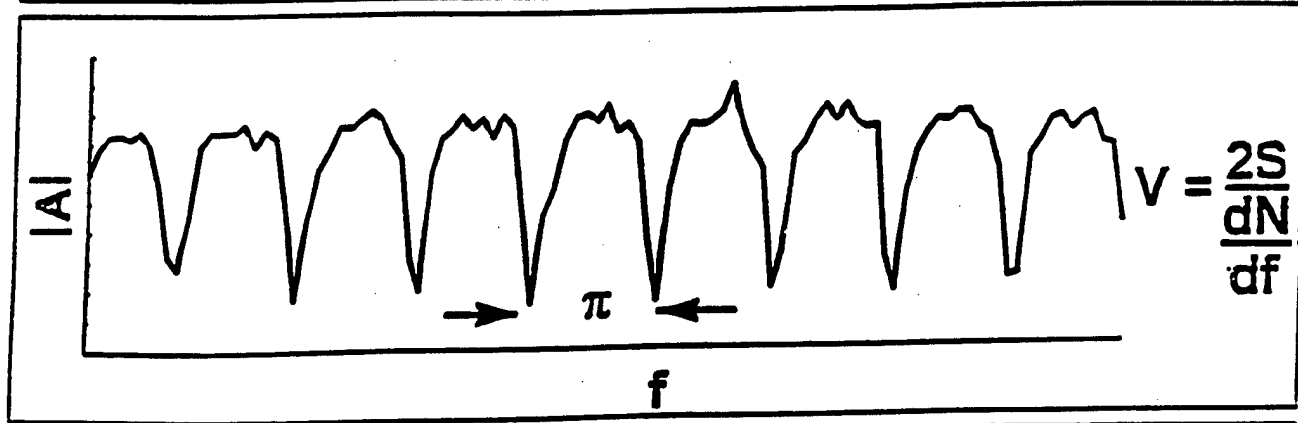
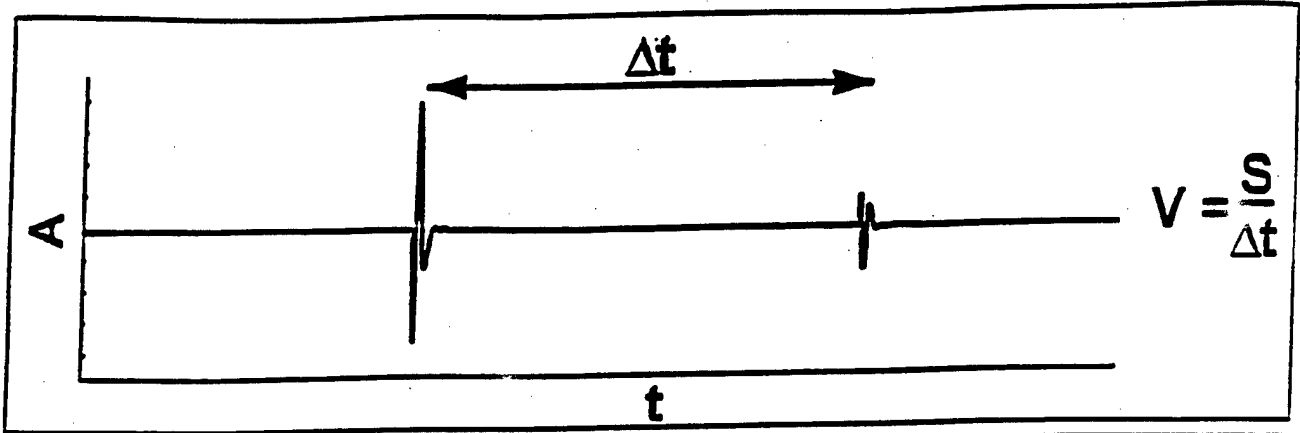


(3) Direct Contact



SHORT-PULSE SIGNAL ANALYSIS METHODS

- **PULSE-ECHO SUPERPOSITION/VISUAL OVERLAP**
- **AMPLITUDE-SPECTRUM/PI-POINT**
- **PHASE-SPECTRUM/DECONVOLUTION**
- **PULSE-ECHO CROSS-CORRELATION/AUTOMATED**
- **TIME-FREQUENCY/(UNDER DEVELOPMENT)**



RESOLUTION OF SHORT-PULSE METHODS


$$V = \frac{L}{\Delta t}$$

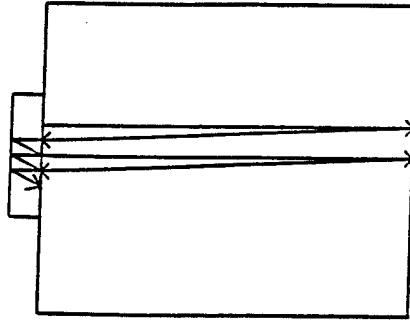
- 1) L is known to 0.008%
- 2) Δt is affected by Bandwidth, sampling rate and signal to noise (0.04%)

"As Measured" Velocities (No Corrections)

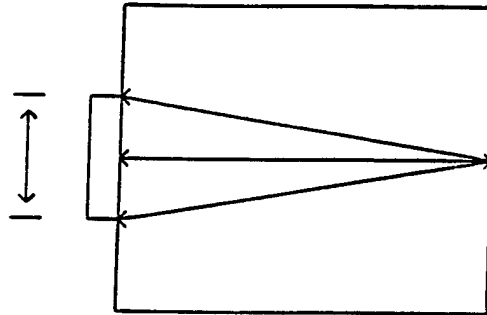
Fused Silica	Overall Chart	(mm/us)				
Ledbetter's	No Corrections					
(25.634 mm)	Signal Processing					
	Method	Pulse-Echo	Amplitude Spectrum	Phase-Spectrum	Pulse-Echo	Time/Frequency
Physical		Superposition	Pi-Point	Deconvolution	Cross-Correlation	Analysis
Configuration	Immersion Tank					
	Pulse-Echo Config.	5.9309354	5.927888889	5.9247602	5.935156707	5.929244444
	Dry Contact PZT					
	Pulse-Echo Config.	5.827608667	5.874125	5.9144	5.870609784	
	Dry Contact Quartz					
	Pulse-Echo Config.	5.928316667	5.838533333	5.809666667	5.846210537	
	Dry Buffer Rod					
	Pulse-Echo Config.	5.93035		5.9221	5.933796296	

Physical Sources of Error (Short-Pulse Methods)

(1)  Transducer has finite thickness



(2) Transducer has finite diameter



(3) Temperature Differences

(4) Pulse-Shape / Bandwidth Effects

Velocities (with Corrections)

Fused Silica	Overall Chart	(mm/us)				
Ledbetter's	With Corrections					
(25.634 mm)	Signal Processing					
	Method	Pulse-Echo	Amplitude Spectrum	Phase-Spectrum	Pulse-Echo	Time/Frequency
Physical		Superposition	Pi-Point	Deconvolution	Cross-Correlation	Analysis
Configuration	Immersion Tank*					
	Pulse-Echo Config.	5.9309354	5.927888889	5.9247602	5.935156707	5.929244444
	Dry Contact PZT					
	Pulse-Echo Config.	5.842104123	5.87992341	5.920362489	5.885337594	
	Dry Contact Quartz					
	Pulse-Echo Config.	5.93256504	5.914261234	5.885182892	5.932682948	
	Dry Buffer Rod*					
	Pulse-Echo Config.	5.93035		5.9221	5.933796296	

* Without Diffraction Correction (estimated to be less than 0.1%)

Coefficient of thermal expansion is $5.5e-7$. Temperature Range = 2.7 C
 Temperature correction is less than 0.01%

**"TRUE" Value for Velocity = 5931.0 m/s
(as calculated from below)**

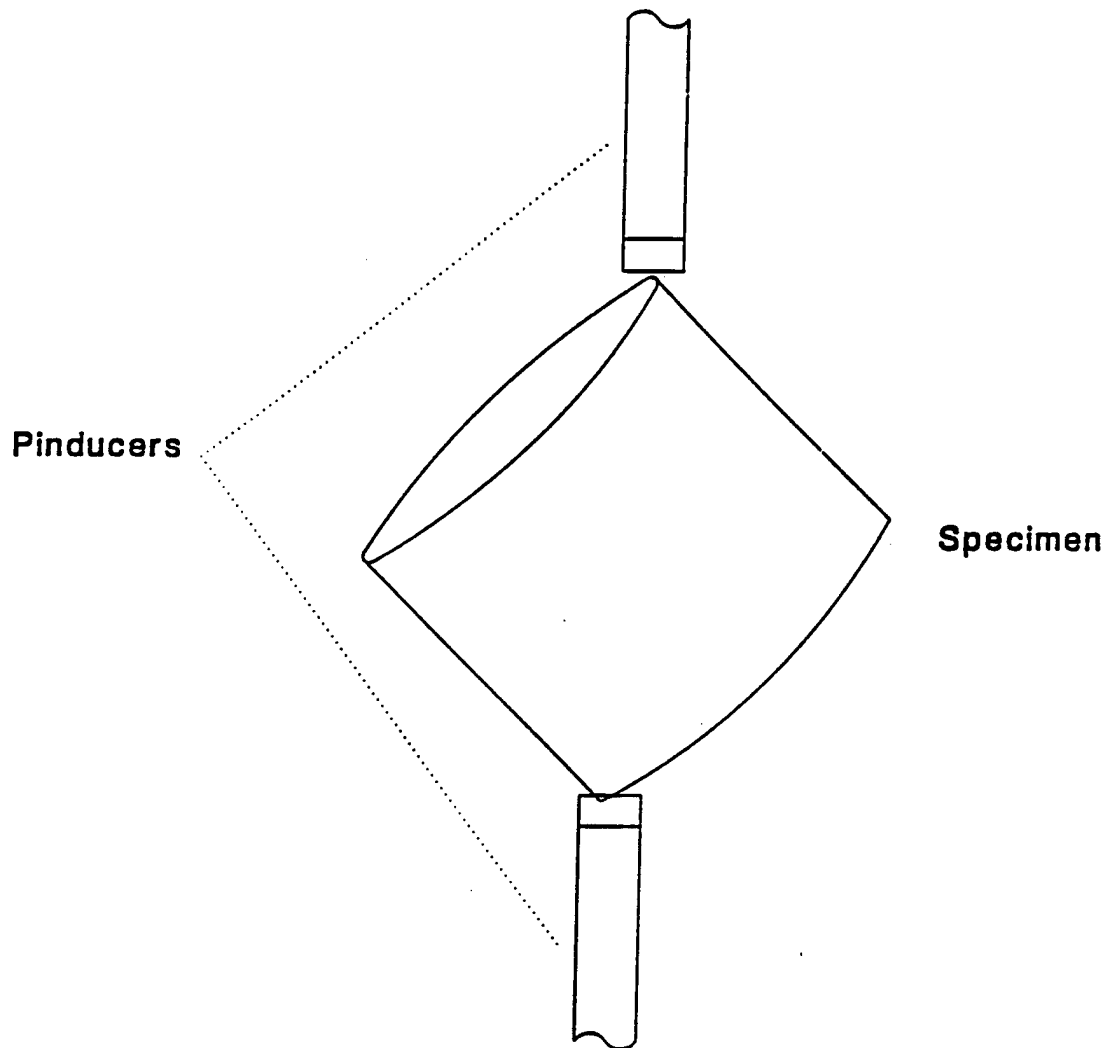
Average Velocity without outliers
with corrections
(mm/us)
5.931016935
Standard Deviation without outliers
0.00336829

With Error of +/- 0.11% using a 95% confidence interval

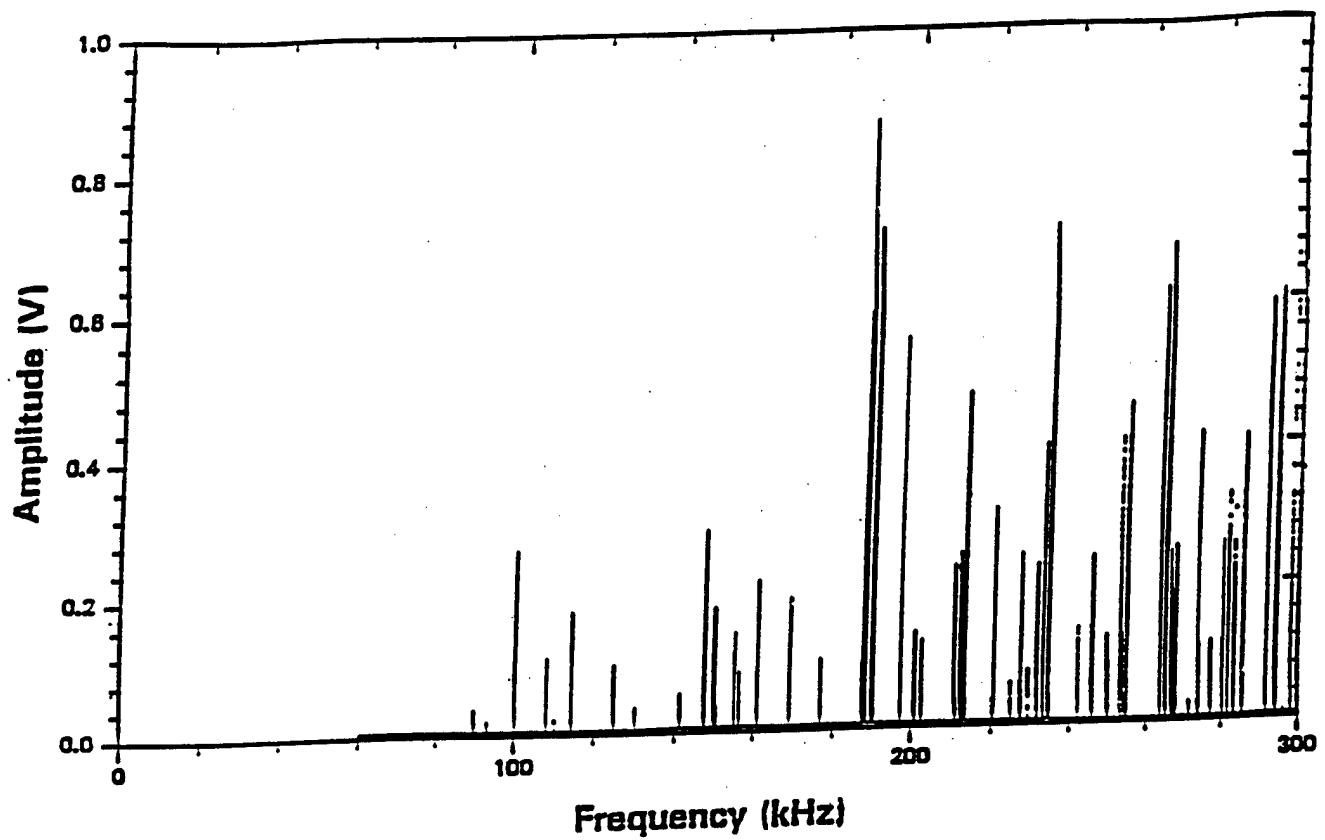
Short-Pulse Velocity Comparison

	Velocity (mm/us)	Residual %		Velocity (mm/us)	Residual %
Immersion Tank			Dry Contact PZT		
Pulse-Echo Config.	5.930935	0.001375	Pulse-Echo Config.	5.842104	1.499116
Pulse-Echo Superposition			Pulse-Echo Superposition		
Immersion Tank			Dry Contact PZT		
Pulse-Echo Config.	5.927889	0.05274	Pulse-Echo Config.	5.879923	0.861463
Amplitude Spectrum			Amplitude Spectrum		
Pi-Point			Pi-Point		
Immersion Tank			Dry Contact PZT		
Pulse-Echo Config.	5.92476	0.105492	Pulse-Echo Config.	5.920362	0.179639
Phase Spectrum			Phase Spectrum		
Immersion Tank			Dry Contact PZT		
Pulse-Echo Config.	5.935157	0.069799	Pulse-Echo Config.	5.885338	0.770177
Cross-Correlation			Cross-Correlation		
Immersion Tank			Dry Contact Quartz		
Pulse-Echo Config.	5.929244	0.029885	Pulse-Echo Config.	5.932565	0.026102
Time/Frequency			Pulse-Echo Superposition		
Al Buffer Rod (Dry, PZT)			Dry Contact Quartz		
Pulse-Echo Config.	5.93035	0.011245	Pulse-Echo Config.	5.914261	0.28251
Pulse-Echo Superposition			Amplitude Spectrum		
			Pi-Point		
Al Buffer Rod (Dry, PZT)					
Pulse-Echo Config.	5.9221	0.150344	Dry Contact Quartz		
Phase Spectrum			Pulse-Echo Config.	5.885183	0.772786
			Phase Spectrum		
Al Buffer Rod (Dry, PZT)					
Pulse-Echo Config.	5.933796	0.046861	Dry Contact Quartz		
Cross-Correlation			Pulse-Echo Config.	5.932683	0.02809
			Cross-Correlation		

RUS Experimental Geometry



RUS SIGNAL ANALYSIS WE USE METHODS DEVELOPED BY P. HEYLIGER (COLORADO STATE UNIVERSITY) CALCULATES ELASTIC-STIFFNESS MODULI FROM OBSERVED RESONANT-FREQUENCY SPECTRUM. THE METHOD CAN HANDLE A VARIETY OF SHAPES AND CRYSTAL SYMMETRIES, INCLUDING TRIGONAL.

**Fused silica**

Sample position: cylinder diagonal
T = 23.2 C
File: silica.srs

Input voltage: 7 V
Frequency sweep: 60-300 kHz
Couplant: none
28 JAN 1997

Gain: 5000

ERRORS IN RUS METHOD

$$V = \sqrt{\frac{C}{\rho}}$$

VALUE OF C IS IMPACTED BY TRANSDUCER
CLAMPING AND SPECIMEN GEOMETRY (0.08%)

ρ IS KNOWN TO 0.004%

COMPARISON OF VELOCITIES

SHORT-PULSE: $5931.2 \text{ m/s} \pm 6.7 \text{ m/s}$

which is 0.11% with a 95% Confidence Interval

RUS: 5939.8 m/s

ERROR is 0.15%

ANISOTROPIC MATERIALS

**COMPARE RUS ELASTIC STIFFNESS
CONSTANTS FOR HIGH-QUALITY SILICON
SPHERE WITH THOSE OBTAINED BY
MCSKIMIN (0.1%) 4 DECADES AGO.**

Silicon's Voigt stiffnesses (GPa)

	<u>present</u>	<u>literature</u>	<u>ratio</u>
C₁₁	165.61 ± 0.03	165.78	0.9990
C₁₂	63.84 ± 0.03	63.91	0.9989
C₄₄	79.55 ± 0.01	79.61	0.9992

C'	50.89	50.94	0.9990
B	97.76	97.87	0.9989

NEED FOR ACCURATE VELOCITY MEASUREMENTS

Internal Strain	0.1%	0.01%
Pressure Effects	0.1%	0.01%
Texture	1 %	0.1%
Phase Mixtures		0.1%
Hardness		0.1%
Defects	0.1%	0.1%

**Sampled CW investigation of
vortex viscosity and phase
transitions in $\text{YBa}_2\text{Cu}_3\text{O}_{7-\delta}$ single
crystals.**

**D. Dasgupta, J. R. Feller, C. Hucho*,
Bimal K. Sarma and M. Levy**

Department of Physics



University of Wisconsin-Milwaukee

Work sponsored by Office of the Naval Research

* Present address : FB Physik, Germany

OUTLINE

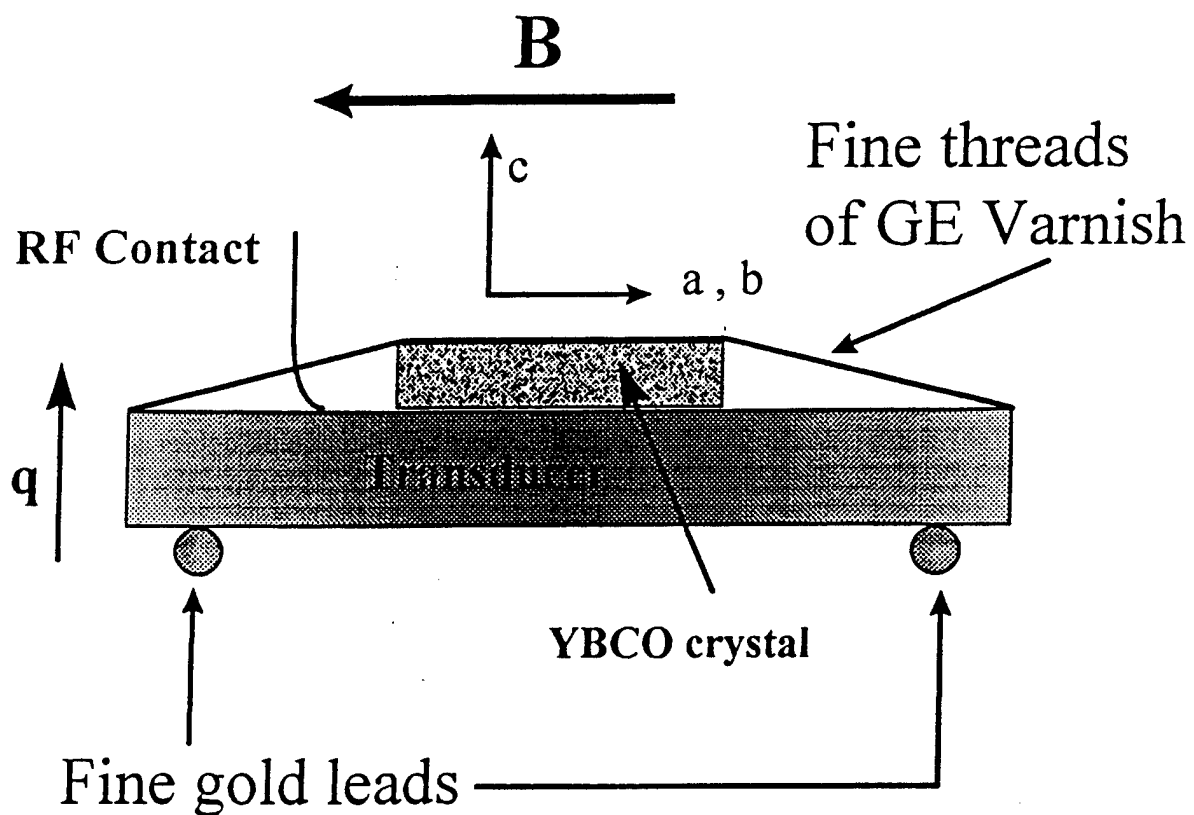
- **Sampled CW technique**
- **Attenuation vs Magnetic Field**
 - **At low magnetic fields ($< 0.5\text{T}$)**
 - **At high fields upto 1.6T**
- **Attenuation vs Temperature in different constant fields**

What we do ..

Ultrasonic studies on high temperature superconducting single crystals.

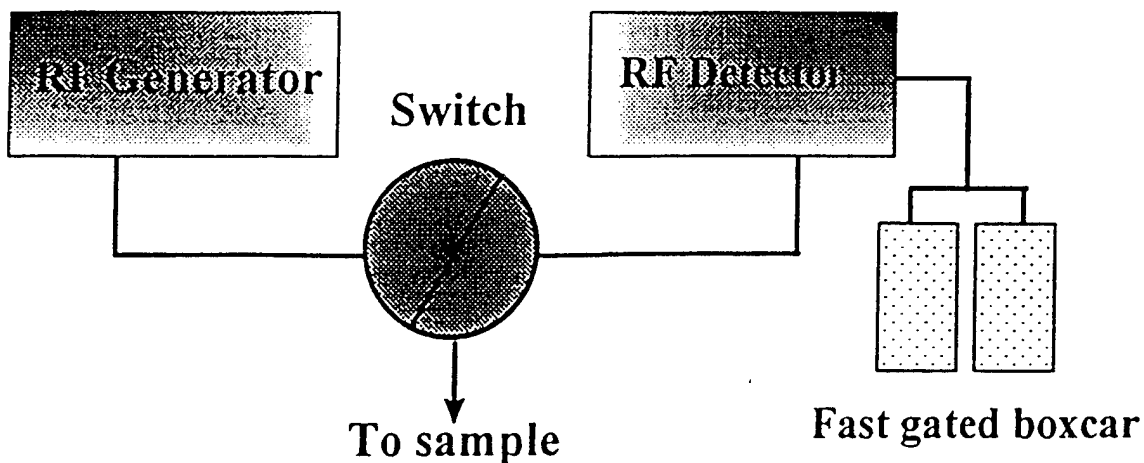
Sampled CW technique.

Setup schematic :





How we do it ...



Excitation frequency : 5 MHz

Longitudinal velocity ~ 5000 m/s $\lambda \sim 1$ mm

Typical crystal thickness : $50 \mu\text{m}$

- * long wavelength limit
- * bulk measurement

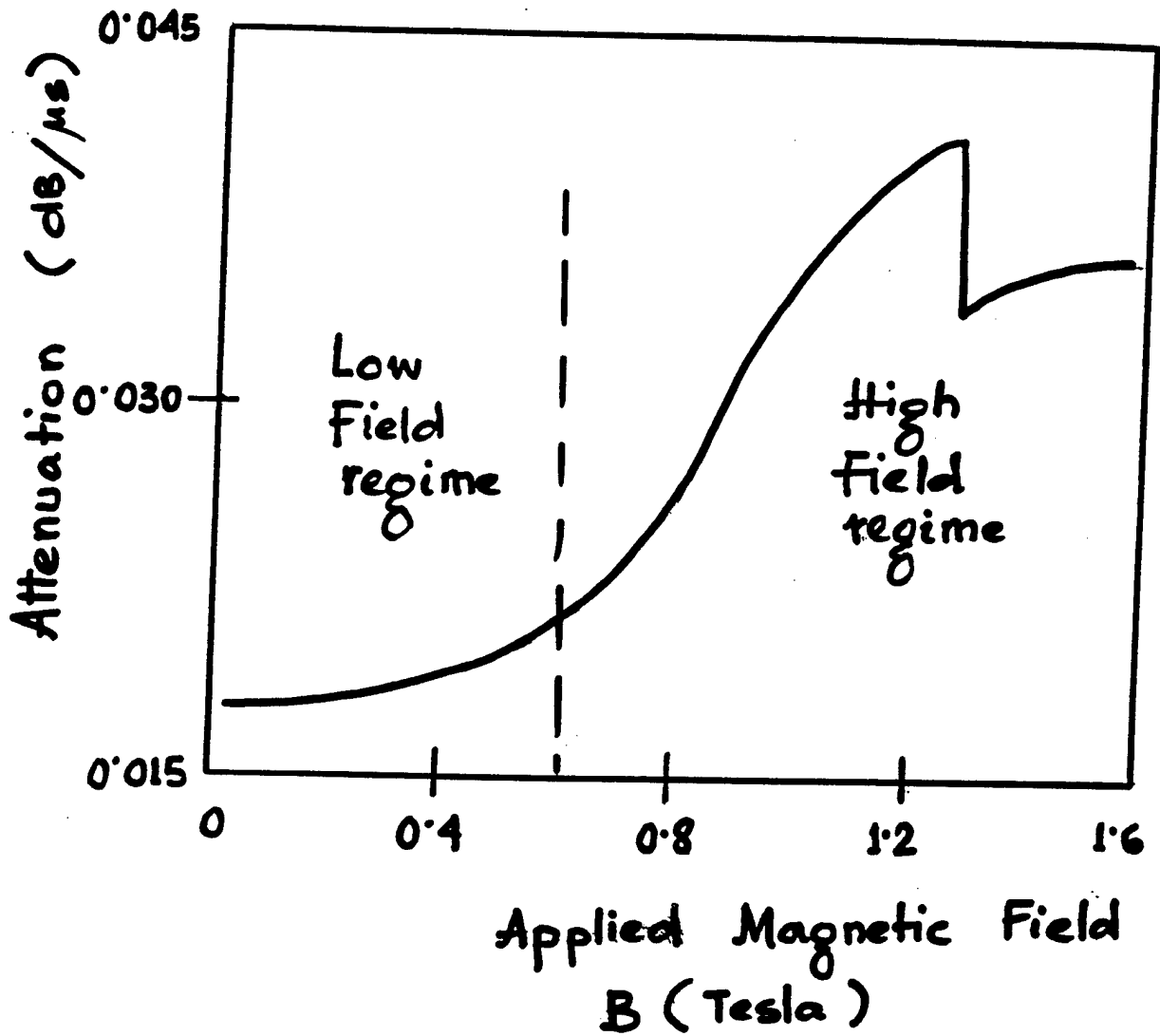
Current densities :

Sampled CW method	$\sim 10^{-5} \text{ A/cm}^2$
Transport measurement	$\sim 0.5 \text{ A/cm}^2$

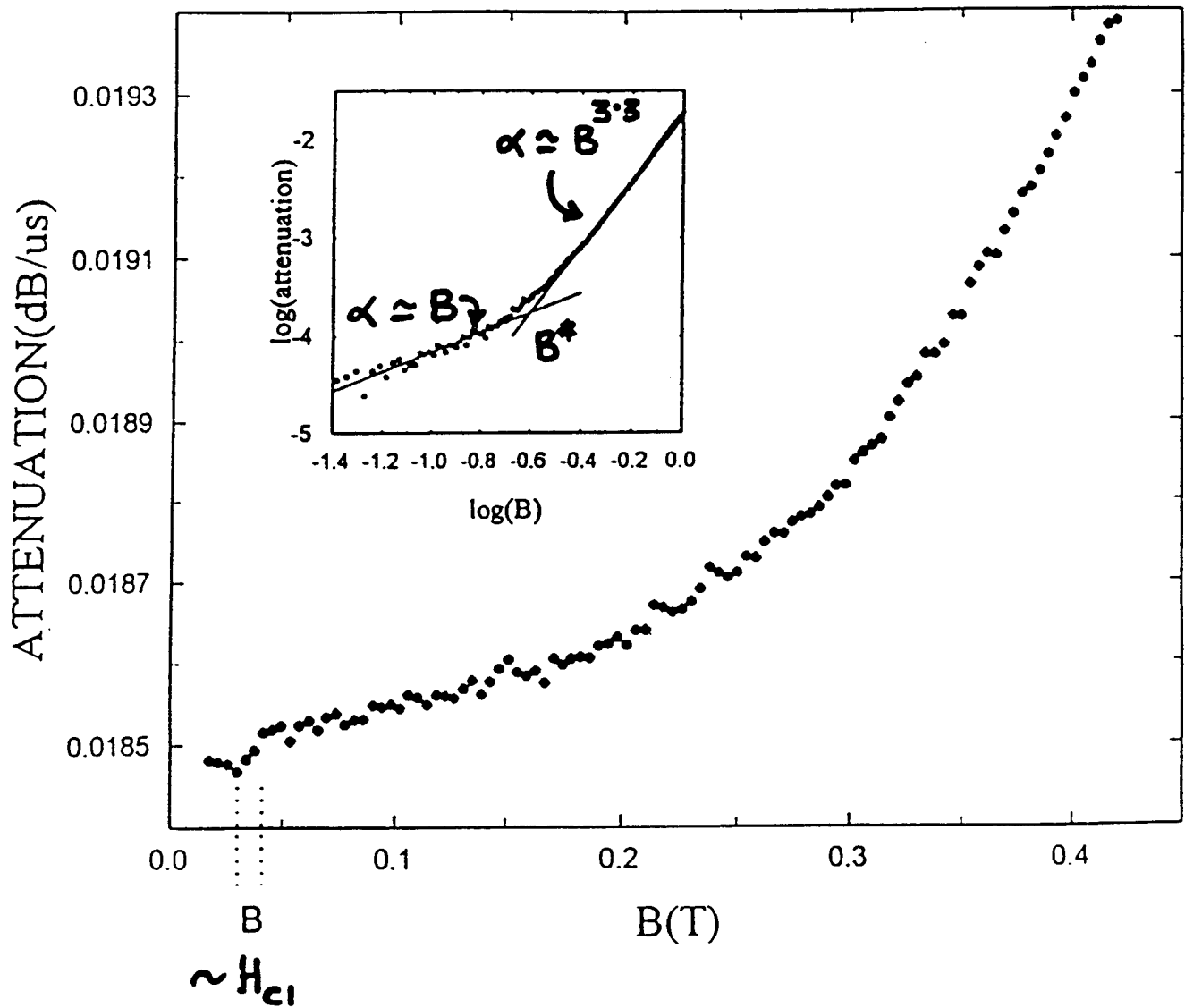
Attenuation units : $1 \text{ dB}/\mu\text{s}$ or 2 dB/cm

Sensitivity : $10^{-4} \text{ dB}/\mu\text{s}$

General Profile



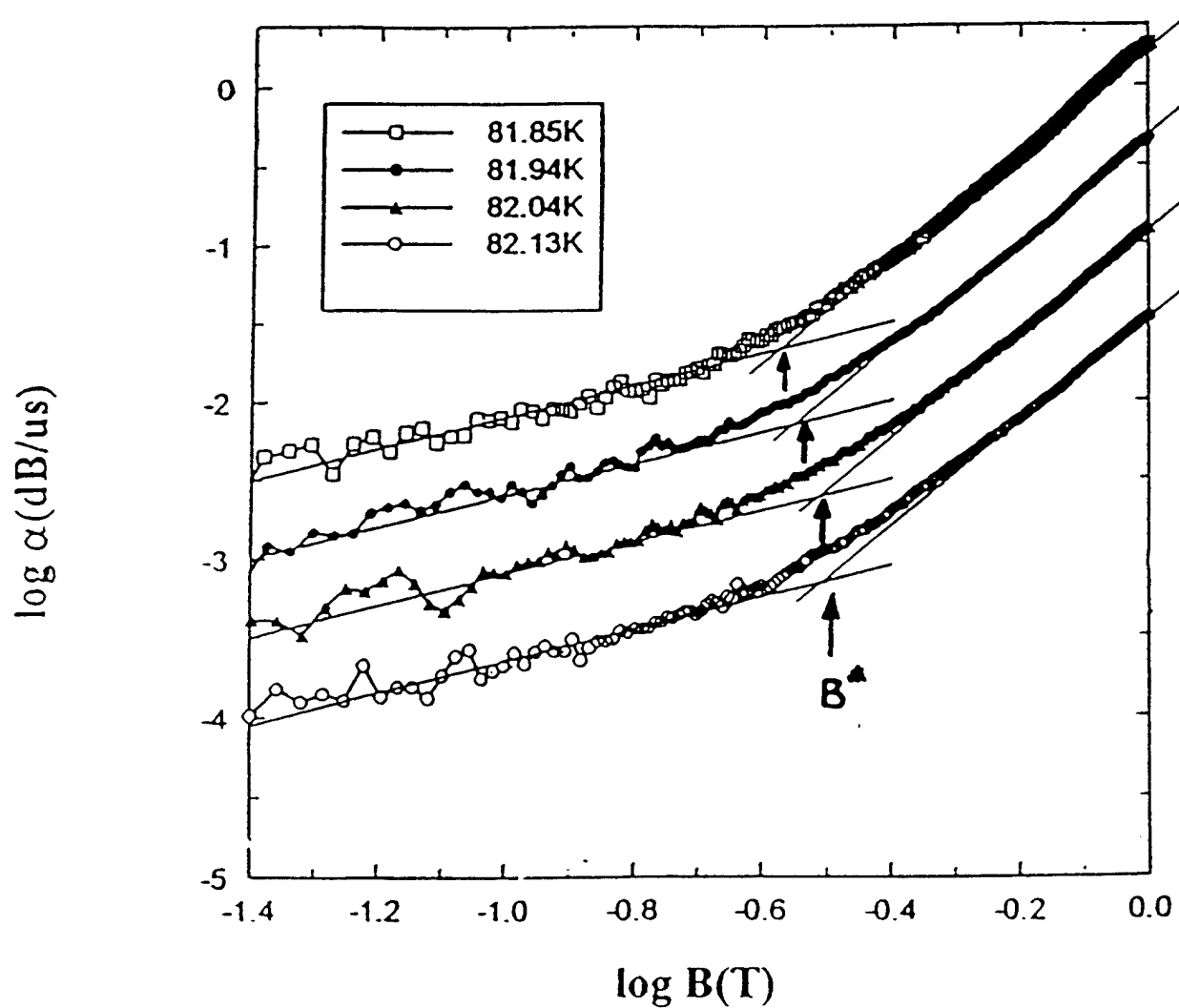
Attenuation vs. applied magnetic field
($H \parallel a$ - b plane ; $T = 81.85$ K)



$\alpha \approx B \Rightarrow$ soft lattice

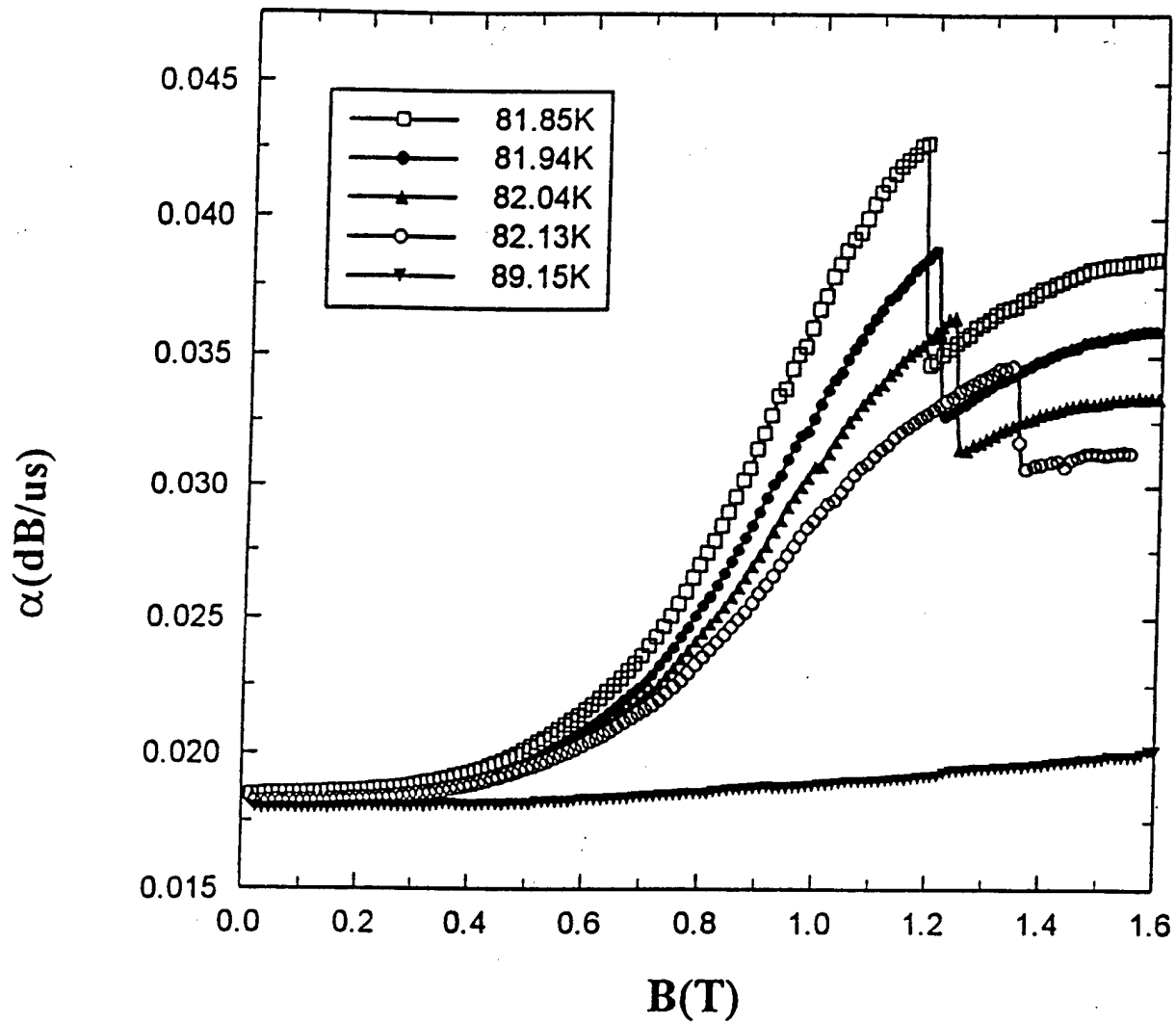
$\alpha \approx B^{3.3} \Rightarrow$ rigid lattice \leftarrow
 vortex - vortex interaction

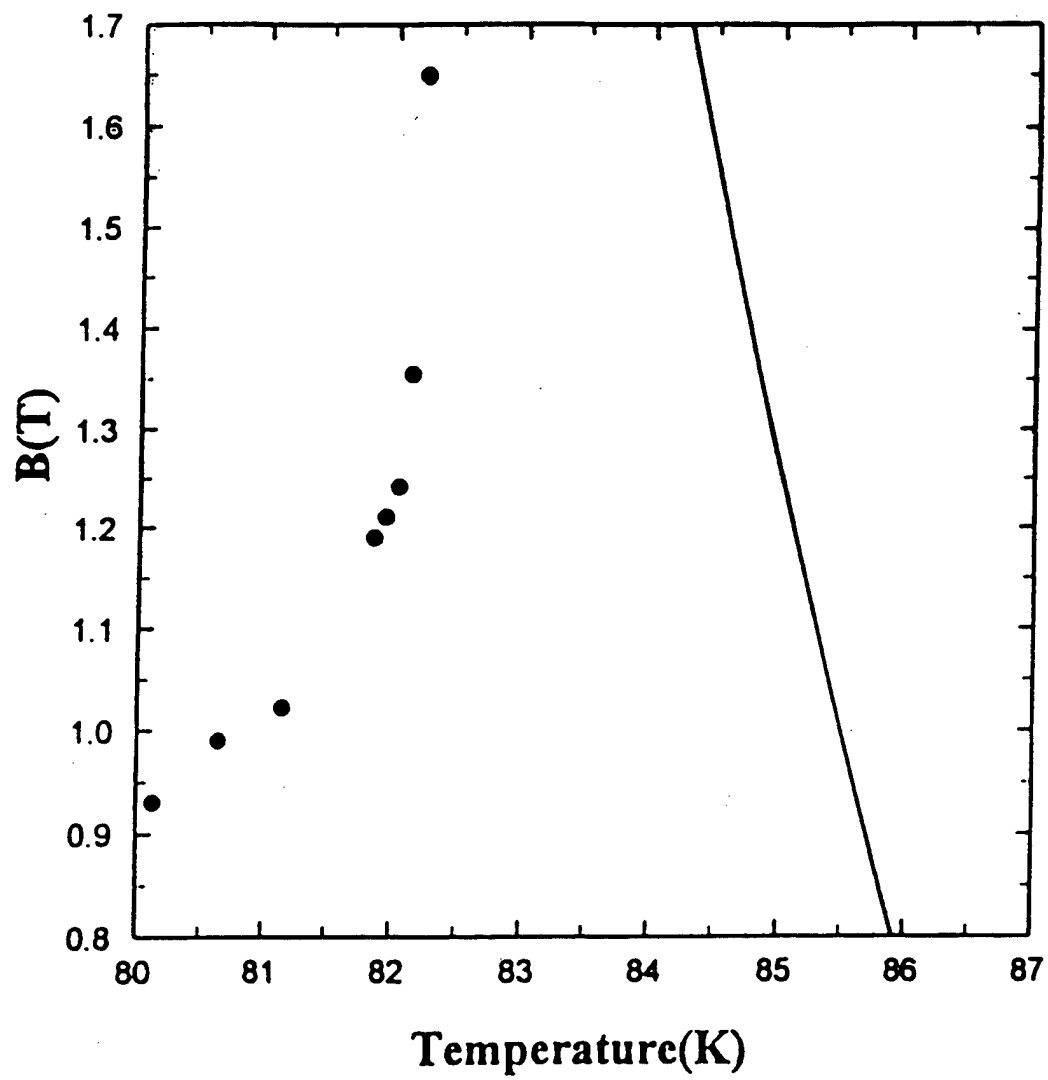
Log α vs. log B at different const. T

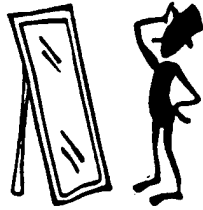


B^* increases with increasing T

Attenuation vs applied magnetic field
at different const. T







Summary

- Vortex pinsite interaction is dominant at low fields
($B_{app} < 0.3T$)
- Intervortex interaction is dominant at higher fields
($B_{app} > 0.3T$)
- Low frequency ultrasound measurement shows transition in vortex system :
 - At low fields flux lattice is soft
 - At high fields flux line lattice is rigid

Sampled Continuous Wave Investigation
of the Vortex State in $\text{YBa}_2\text{Cu}_3\text{O}_{7-\delta}$ Single Crystals:
Measurement Considerations

University of Wisconsin-Milwaukee

J. R. Feller, D. Dasgupta, M. Levy

Work supported by Office of Naval Research

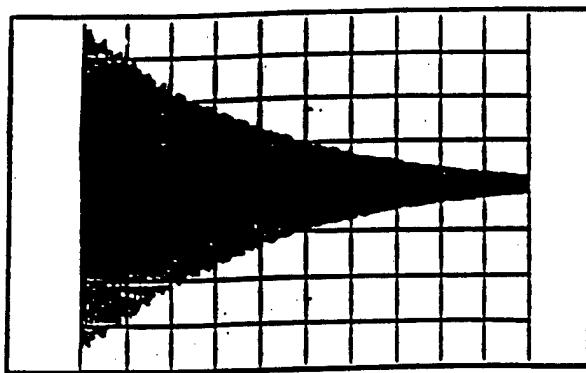
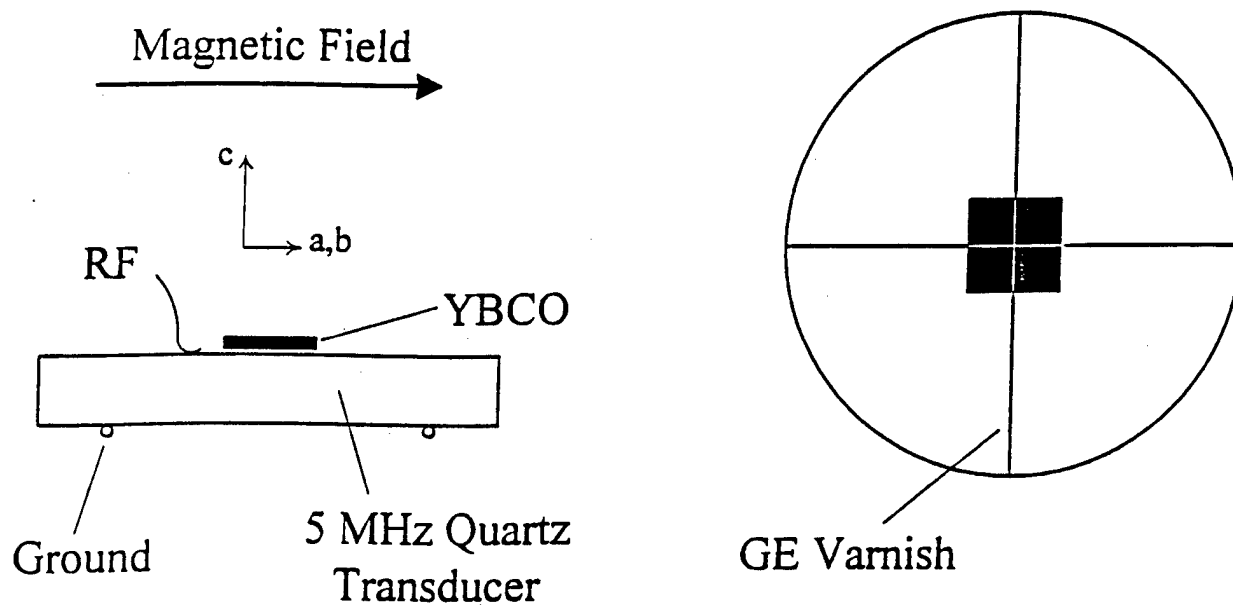
Possible Reasons for High Sensitivity

- Low current density ($J < 10^{-4} \text{ A/cm}^2$)

$J \sim 1 \text{ A/cm}^2$ for transport (dc resistivity) measurements

- Long acoustic wavelength ($\lambda \sim 1 \text{ mm}$) compared with sample thickness ($\sim 50 \text{ }\mu\text{m}$)
- Low amplitude
- Weak acoustic coupling

Sampled Continuous Wave Measurement of YBCO Single Crystals



Resolution $\sim 5 \times 10^{-5} \text{ dB}/\mu\text{s}$

Weak Coupling and Sensitivity

Define a coupling parameter: $0 \leq a \leq 1$

Effective bond area: $A_{\text{bond}} = aA_{\text{sample}} \quad 0 \leq A_{\text{bond}} \leq A_{\text{sample}}$

Assume

$$\alpha_m = \alpha_t + a\alpha_s$$

α_m : measured attenuation
 α_t : transducer attenuation coefficient
 α_s : sample attenuation coefficient

$$Q_m = \frac{\omega}{2(\alpha_t + a\alpha_s)}$$

Define the *sensitivity* as

$$S_\alpha \equiv \frac{\partial Q_m}{\partial \alpha_s} = -\frac{\omega}{2} \frac{a}{(\alpha_t + a\alpha_s)^2}$$

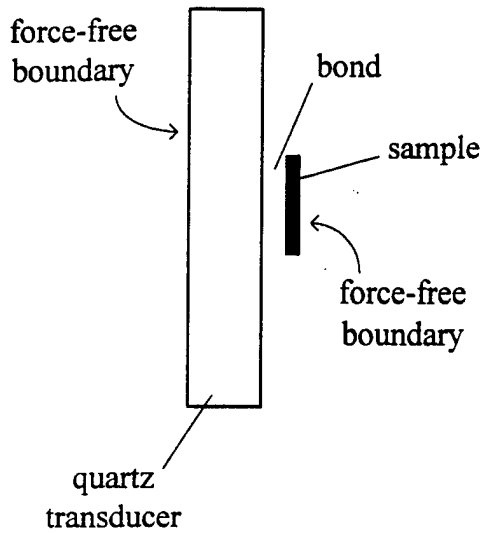
$|S_\alpha|$ is maximized by varying a :

$$\frac{\partial S_\alpha}{\partial a} = 0 \Rightarrow \alpha_t = a\alpha_s \Rightarrow \alpha_m = 2\alpha_t \quad \text{or} \quad Q_m = \frac{1}{2}Q_t$$

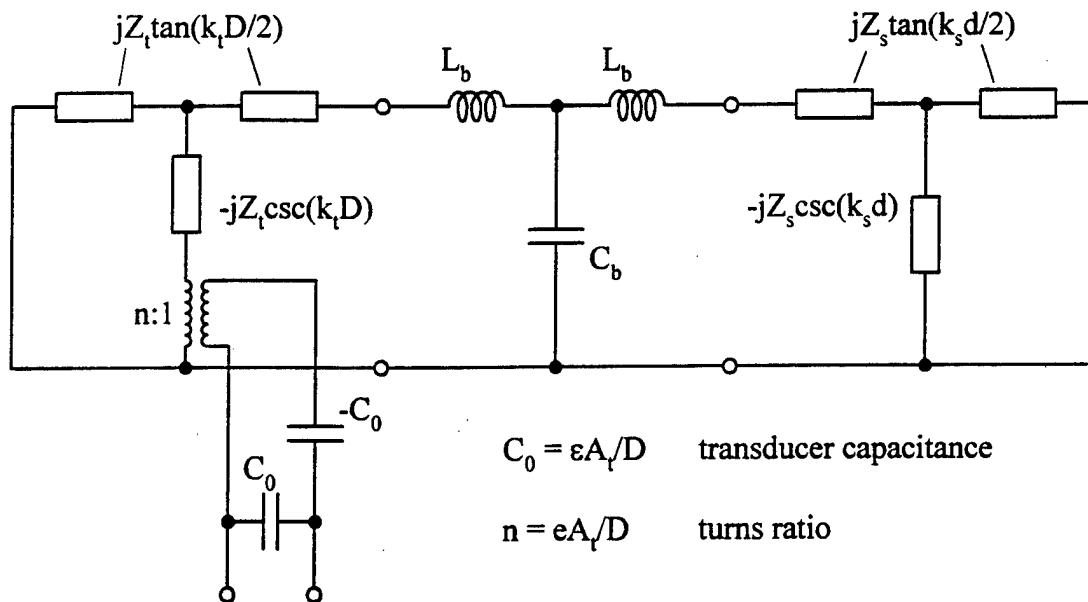
For $Q_t = 10,000$ and $Q_s = 300$, the maximum in sensitivity occurs when

$$a = 0.03 \text{ and } Q_m = 5000.$$

Weakly-coupled system



A_t Area of transducer
 A_s Area of sample
 $A_b = aA_s$ Effective area of bond
 a Coupling parameter
 $0 < a < 1$



Acoustic impedance: $Z = A\rho\omega/k$

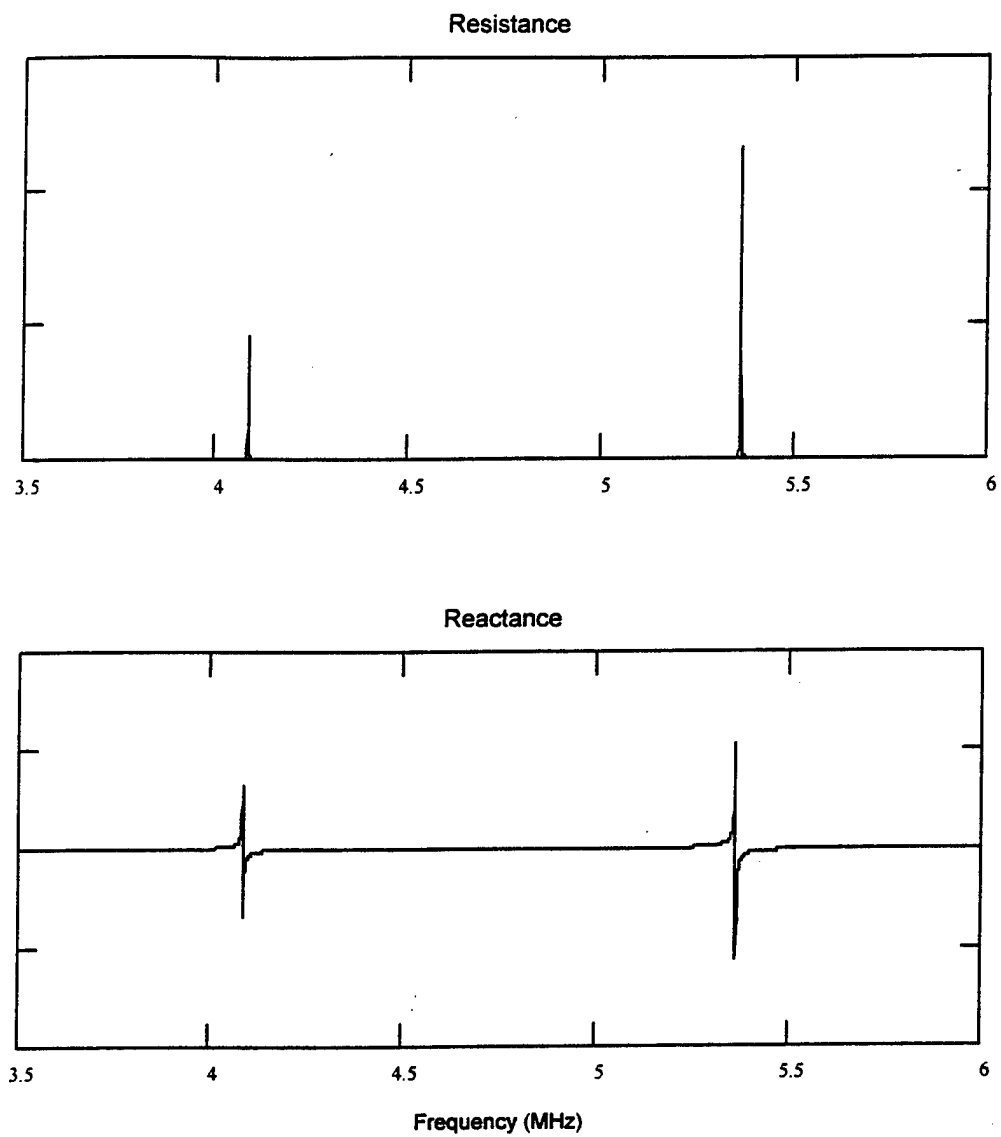
Wave number: $k = \omega/v - j\alpha/2$

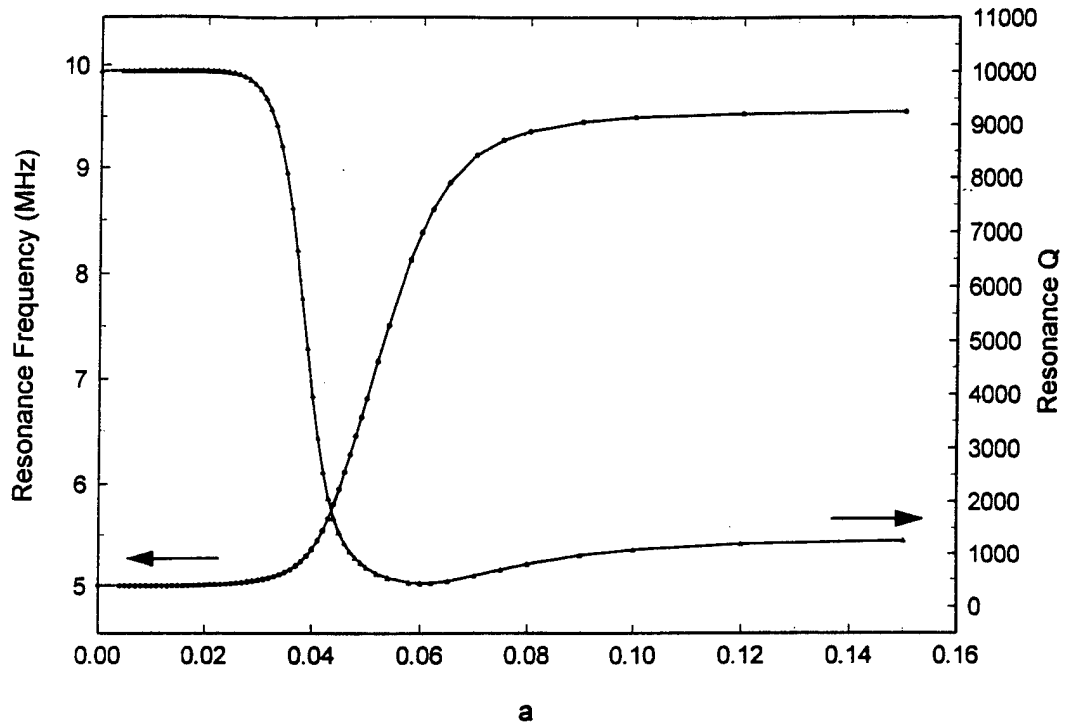
The bond:

Effective area: $A_b = aA_s$
 Effective density: $a\rho_b$
 Effective sound speed: av_b
 Effective impedance: $(aA_s)(a\rho_b)(av_b) = a^3Z_b$

$$L_b(a) \propto a^2 \quad C_b(a) \propto a^{-4}$$

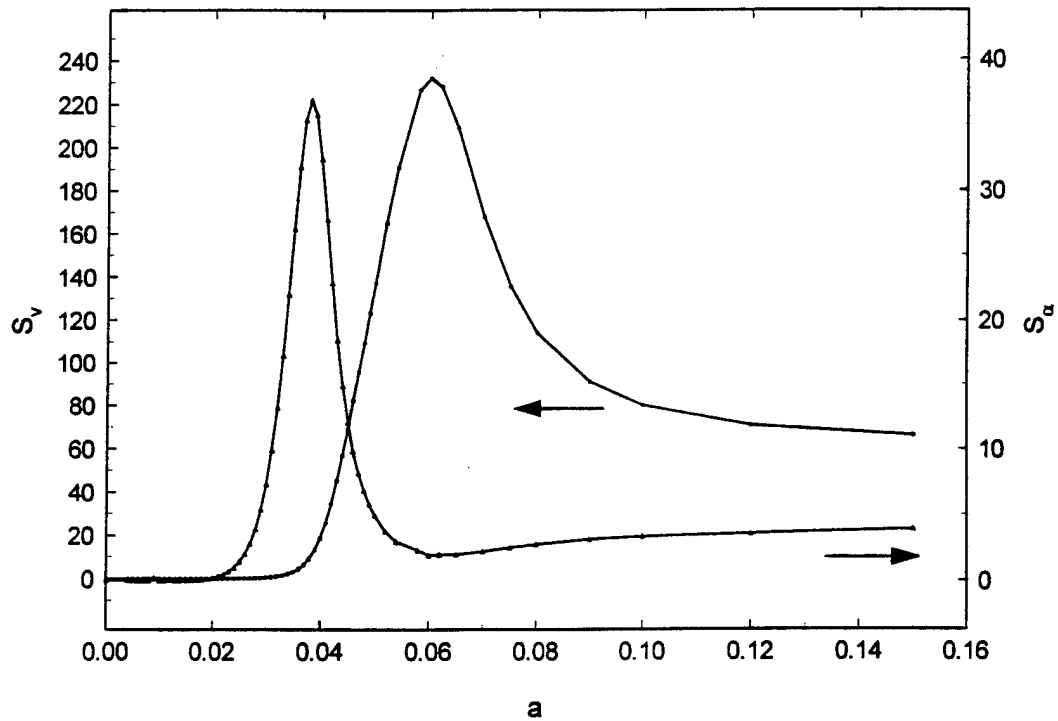
As $a \rightarrow 0$, $L_b \rightarrow 0$, $C_b \rightarrow \infty$



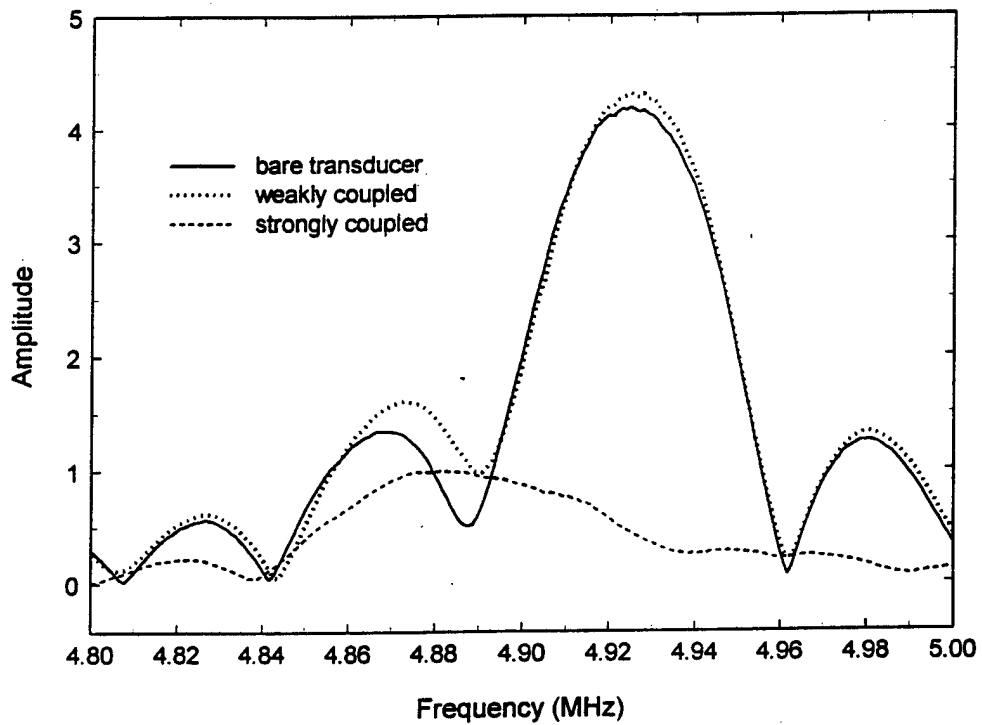
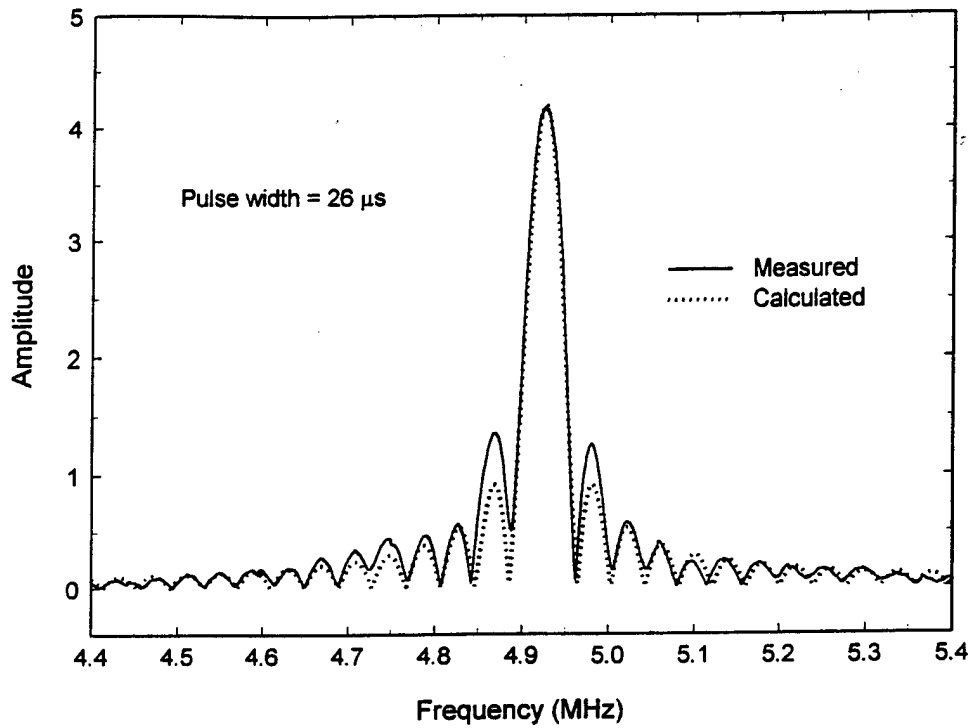


Sensitivity to v : $S_v \equiv \frac{\partial f_{\text{resonance}}}{\partial v_{\text{sample}}}$

Sensitivity to α : $S_\alpha \equiv \frac{\partial Q_{\text{resonance}}}{\partial \alpha_{\text{sample}}}$



Sampled Continuous Wave Measurements



Conclusions

- Sampled continuous wave technique demonstrated to be highly sensitive to vortex state transitions in YBCO platelets
- Factors contributing to high sensitivity: Low current density, long acoustic wavelength, low amplitude, weak acoustic coupling between transducer and sample
- Sensitivity ($\partial Q_{\text{resonance}} / \partial \alpha_{\text{sample}}$) found to exhibit a maximum in the weakly-coupled regime
- Agreement with preliminary frequency-swept measurements

Thin Film Characterization Using Resonant Ultrasound Spectroscopy

Jason White and J. D. Maynard, Department of Physics and the Acoustics
Program, The Pennsylvania State University, University Park, PA 16802

- Survey of thin film characterization techniques
- Theory of RUS on thin films
- Numerical calculations
- Experimental methods
- Conclusion

Thin Film Characterization Techniques

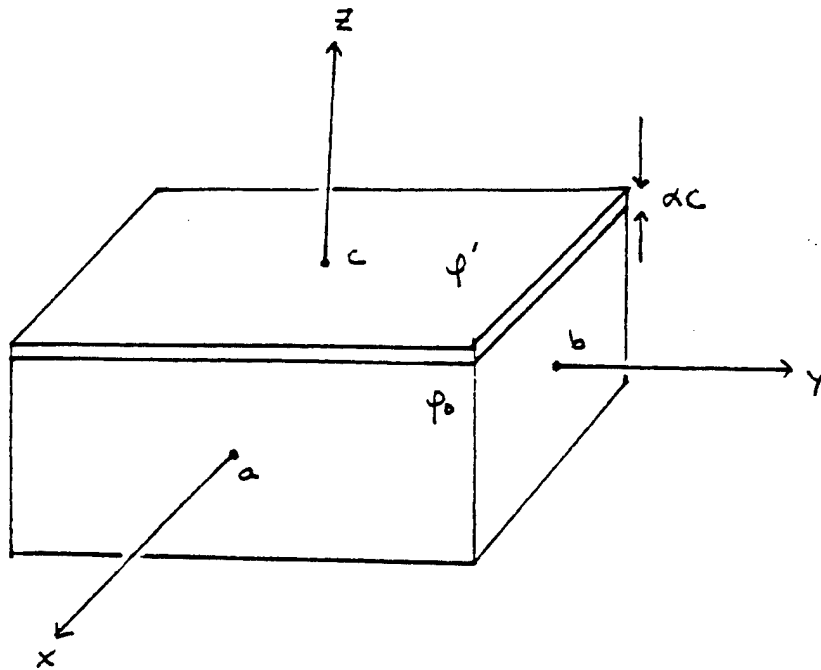
I. Direct measurement of deflection in response to an applied force

- a. Bulge test
- b. uniaxial tension test
- c. nanoindentation

II. Ultrasound methods

- a. Free-standing films
- b. Film and substrate
 - 1. SAW techniques
 - 2. Resonance method ←

III. Brillouin Scattering



Basis function:

$$\Phi_p = \left(\frac{x}{a}\right)^l \left(\frac{y}{b}\right)^m \left(\frac{z}{c}\right)^n$$

Matrix Eigenvalue Equation:

$$\omega^2 \mathbf{E} \mathbf{a} = \Gamma \mathbf{a}$$

$$\omega^2 \underset{\uparrow}{E} \underset{\uparrow}{a} = \Gamma a$$

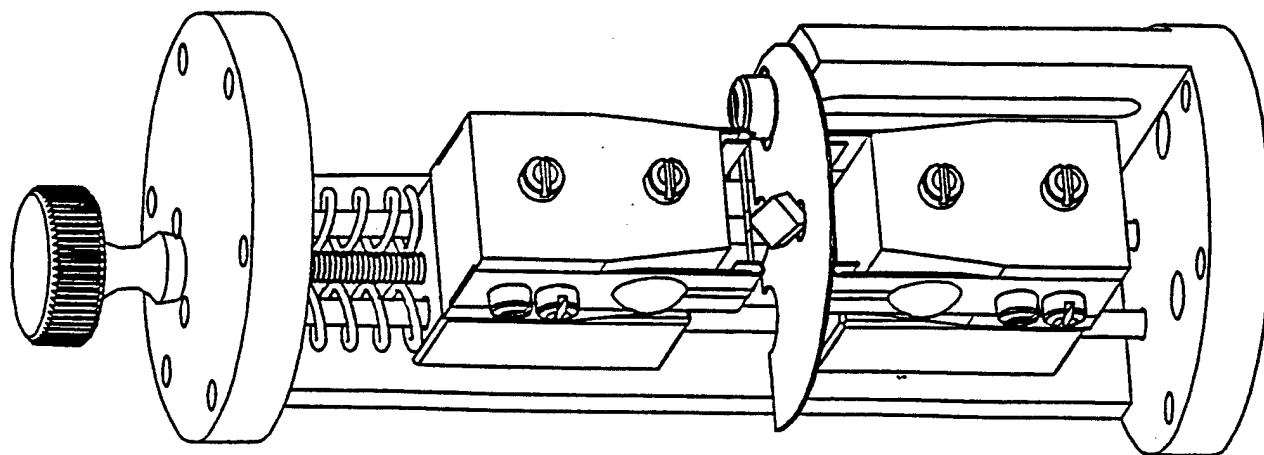
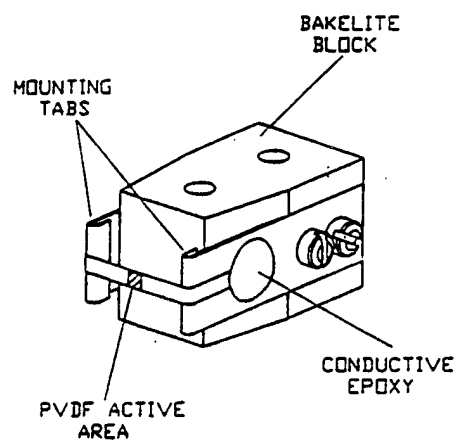
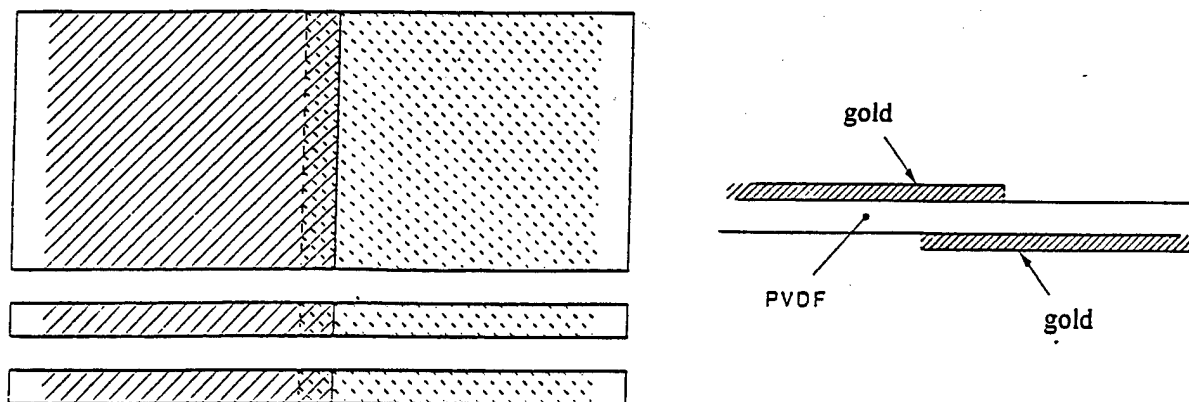
$$\begin{aligned} E_{piqj} &= \delta_{ij} \int_{-1}^1 \int_{-1}^1 \int_{-1}^1 \rho \Phi_p \Phi_q dV \\ &= \delta_{ij} \left[\rho_0 \int_{-1}^1 \int_{-1}^1 \int_{-1}^1 \Phi_p \Phi_q dV + (\rho' - \rho_0) \int_{-1}^1 \int_{-1}^1 \int_{(1-\alpha)}^1 \Phi_p \Phi_q dV \right] \end{aligned}$$

$$\begin{aligned} \Gamma_{piqj} &= \int_{-a}^a \int_{-b}^b \int_{-c}^c c_{ijkl} \frac{\partial \Phi_p}{\partial x_k} \frac{\partial \Phi_q}{\partial x_l} dV \\ &= c_{ijkl}^0 \int_{-a}^a \int_{-b}^b \int_{-c}^c \frac{\partial \Phi_p}{\partial x_k} \frac{\partial \Phi_q}{\partial x_l} dV + \delta_{ijkl} \int_{-a}^a \int_{-b}^b \int_{(c-\alpha c)}^c \frac{\partial \Phi_p}{\partial x_k} \frac{\partial \Phi_q}{\partial x_l} dV \end{aligned}$$

Si specimen $500 \times 400 \times 100 \mu\text{m}$
Al film on 500×400 face from 10 to $0.01 \mu\text{m}$ thick

no film (Mhz)	$10 \mu\text{m}$ film ($\% \Delta f$)	$1 \mu\text{m}$ film ($\% \Delta f$)	$0.1 \mu\text{m}$ film ($\% \Delta f$)	$0.01 \mu\text{m}$ film ($\% \Delta f$)
2.5791	9.571	1.031	.1037	.0104
2.7515	7.329	.8026	.0851	.0081
4.2864	6.823	.7433	.0740	.0074
5.3460	8.584	.9233	.0928	.0093
5.8465	8.106	.8757	.0881	.0088
6.0633	3.459	.3371	.0335	.0033
6.9605	6.489	.7060	.0706	.0071
7.1318	3.346	.3353	.0335	.0033
8.0462	4.291	.4204	.0420	.0042
8.3537	3.388	.3301	.0328	.0033
8.5105	3.367	.3224	.0320	.0032
8.7763	7.568	.8196	.0824	.0082
9.7565	6.496	.7075	.0709	.0071
11.0223	6.742	.7281	.0731	.0073

Experimental Setup



System Identification Alternatives to Swept Sine and Curve Fitting

Ralph Muehleisen
ASEE Fellow
Department of Physics
Naval Postgraduate School
muehleis@physics.nps.navy.mil

Purpose

- Provide some alternative approaches to Swept Sines and Curve fitting for RUS
- Why? Why not?

While the traditional approach works, there might be another approach which is better for some circumstances

Traditional Approach: Advantages/Disadvantages

- Advantages
 - It works and works well
 - Not difficult to implement
- Disadvantages
 - Not particularly fast
 - Requires some specialized equipment (e.g. lock-in amp)
 - Not “real time” or even close
 - Not especially suitable for production line testing

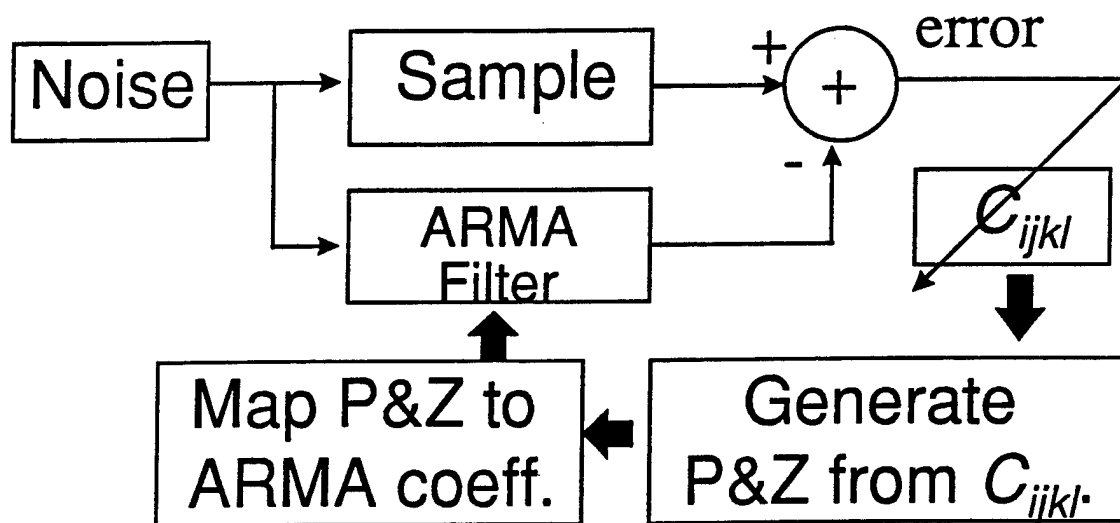
Step 1: Replace Swept Sine with Sampled Noise

- Wideband noise excites sample
- Instead of $H(\omega)$, ARMA System ID methods are used to find impulse response $h[n]$ and hence the discrete time poles and zeros of the system
- Resonance freq. and damping are extracted directly from $h[n]$ and the standard inversion process is used to find C_{ijkl}

- Advantages:
 - A standard high speed data acq. card can be used
 - No lock-in amplifier is required
 - Should be faster than Swept Sine but avoids FFT problems
 - Technique has worked well for structural modal analysis problems. and and in other systems with well separated poles.
 - Literature is replete with papers on ARMA system and spectral estimation.

Step 2: Replace Curve Fit with Adaptive Filter system

- Instead of finding resonances and doing a non-linear curve fit, use an adaptive filter technique for online identification of the elastic constants



- Operation
 - The filter is adjusted until the error goal is reached.
 - There are many algorithms for adjusting C_{ijkl} (LMS, RLS, etc.) most of which are forms of a non-linear least squares curve fit.
- Advantages:
 - True online measures of C_{ijkl} are obtainable (great for production testing)
 - Adaptive algorithms are usually faster than their standard least squares counterparts because they use efficient routines for updating the error gradient estimate

The Step Beyond: Directly Determine C_{ijkl}

- Reformulate the problem entirely - do not solve the variational based eigenvalue problem
- Instead convert the bounded elastic wave equation to a discrete time equivalent (maybe a state space system?)
 - Why? This might yield an exact ARMA filter with coefficients proportional to the C_{ijkl}
 - Determination of the ARMA model would then determine the C_{ijkl} . This might be done in real time.

Summary

- Use ARMA system ID methods to replace the Swept Sine
 - Faster determination of resonances
 - Requires only a fast data acq. board
- Use Adaptive Filters to replace the Curve Fitting
 - Faster determination of C_{ijkl}
 - True online operation
- Use alternate form of problem
 - C_{ijkl} might be found directly and in real time.
- Techniques useful for real time production line testing of samples

Resonant Ultrasound Spectroscopy Measurements for Spheres Under Pressure With Different Gases

D.G. Isaak, J.D. Carnes, O.L. Anderson
UCLA

H. Oda
Okayama University, Japan

Goals

- Use RUS to measure 3rd order elastic moduli.
- Pressure dependence of elastic moduli from RUS.
- Effects of gas loading on frequency shifts?
- Test dC_{ij}/dP from pulse-echo experiments.

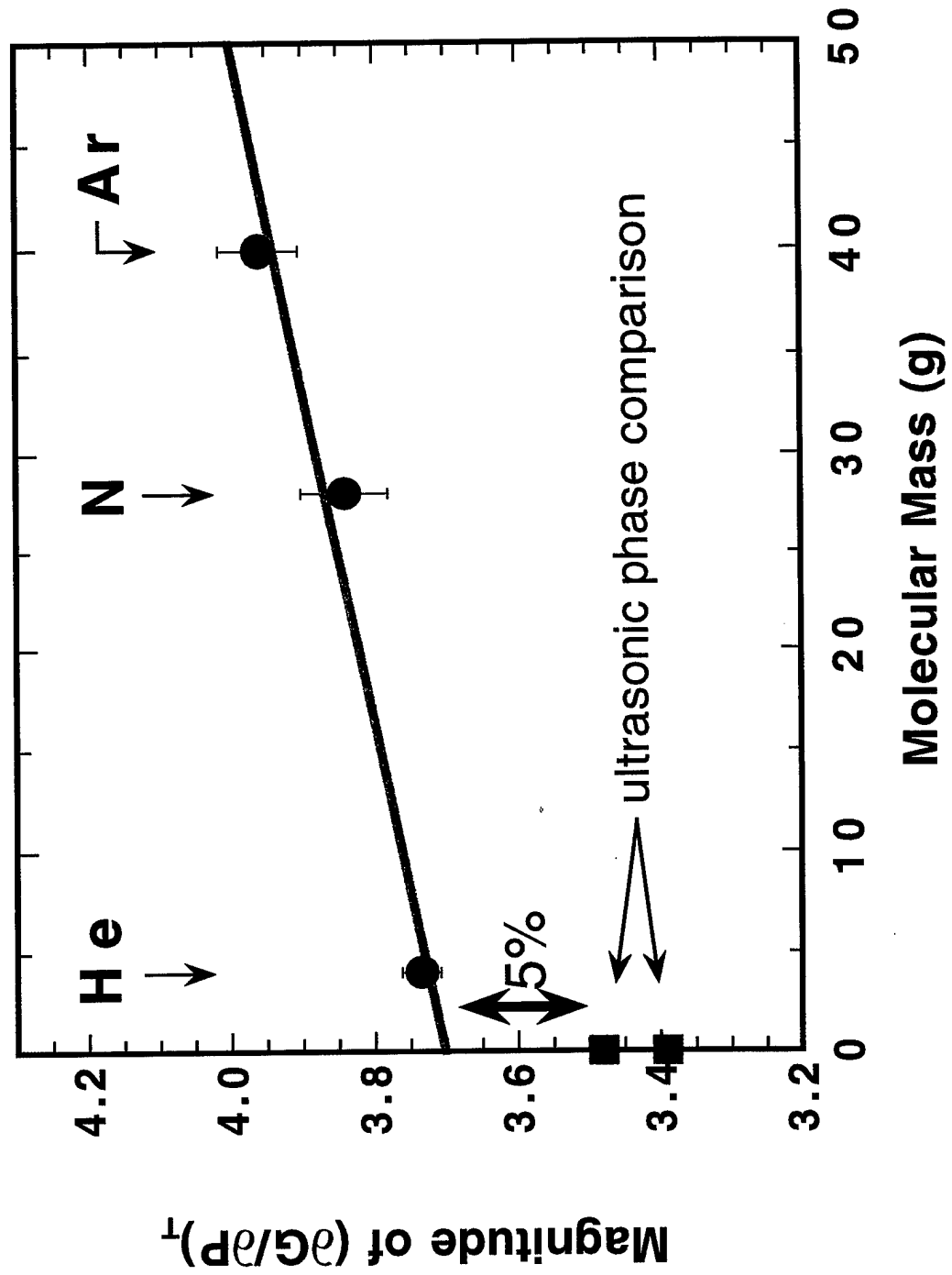
“The effect of the bond has been one of the most abominable problems plaguing high precision ultrasonic measurements. There has been a long history in studying bond effects . . . Conclusive results on the nature and the effect of the bond are still lacking.”

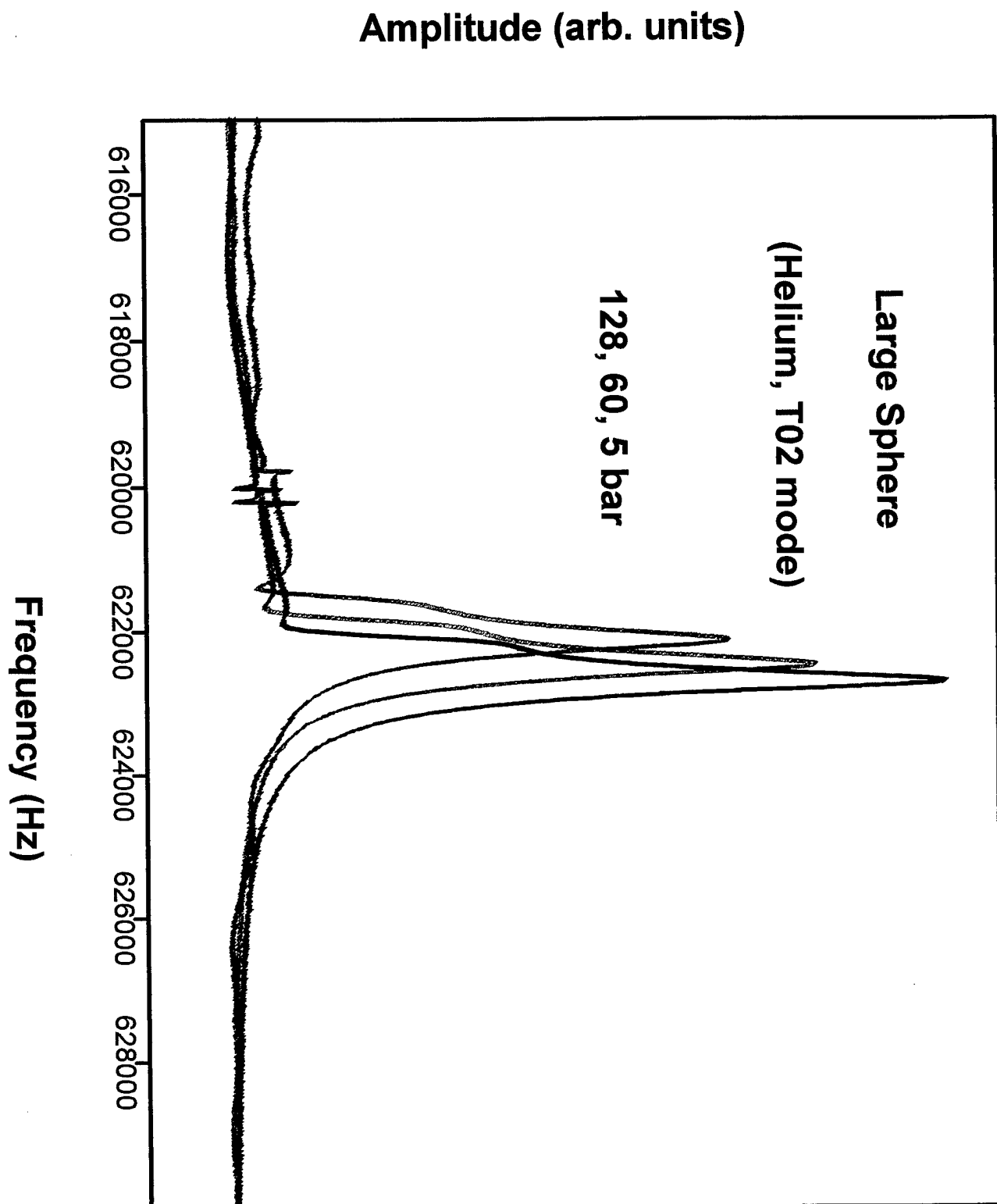
Spetzler, Chen, Whitehead, and Getting, *Pure and Applied Geophysics*, **141**, 341-377, 1993

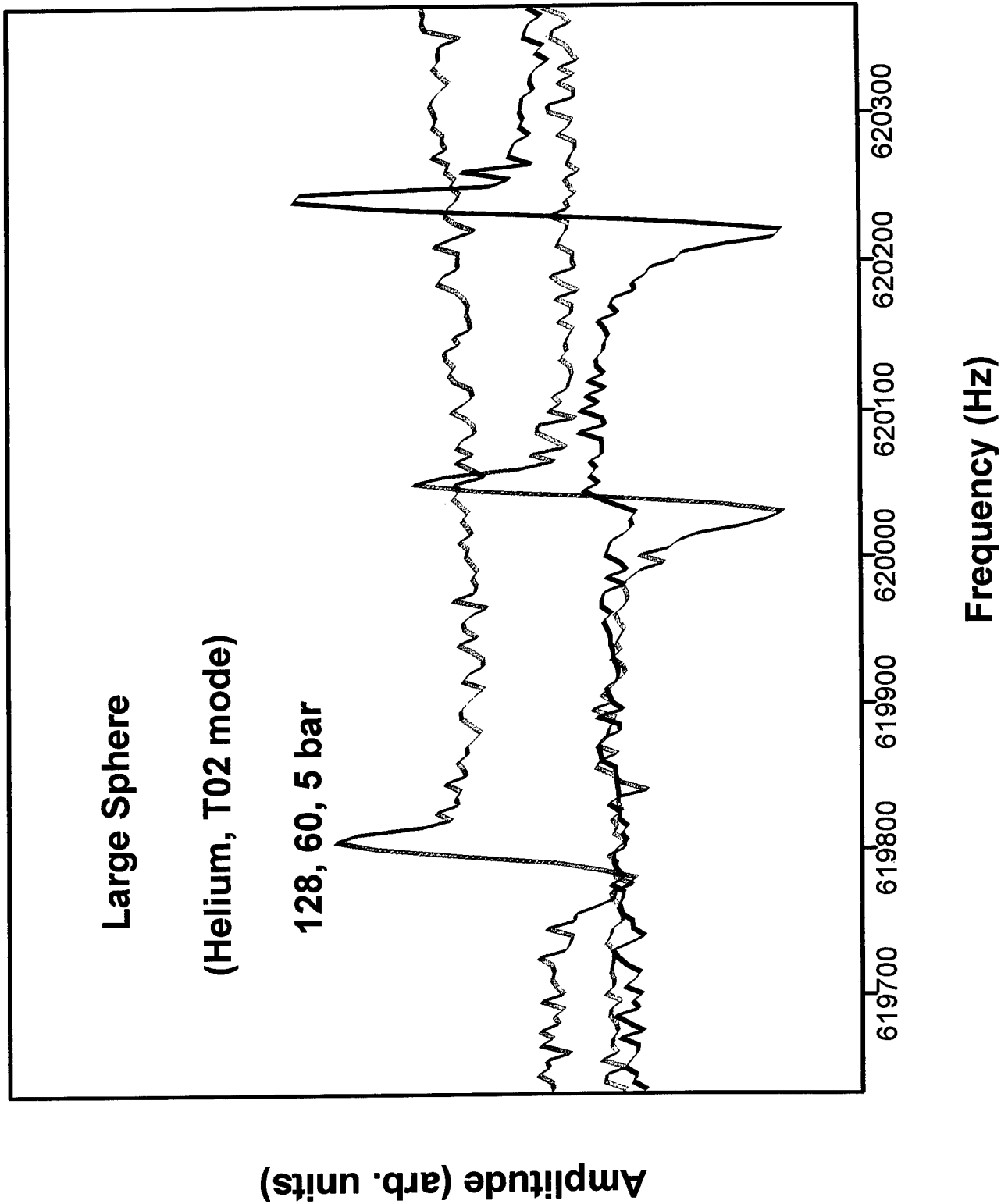
Report on Fused Silica

- Two spherical specimens ($r=2.4154, 1.945$ mm)
- Three gases (helium, nitrogen, argon)
- Two specimen-holding configurations
- Two torsional modes, T_{02} and T_{03}

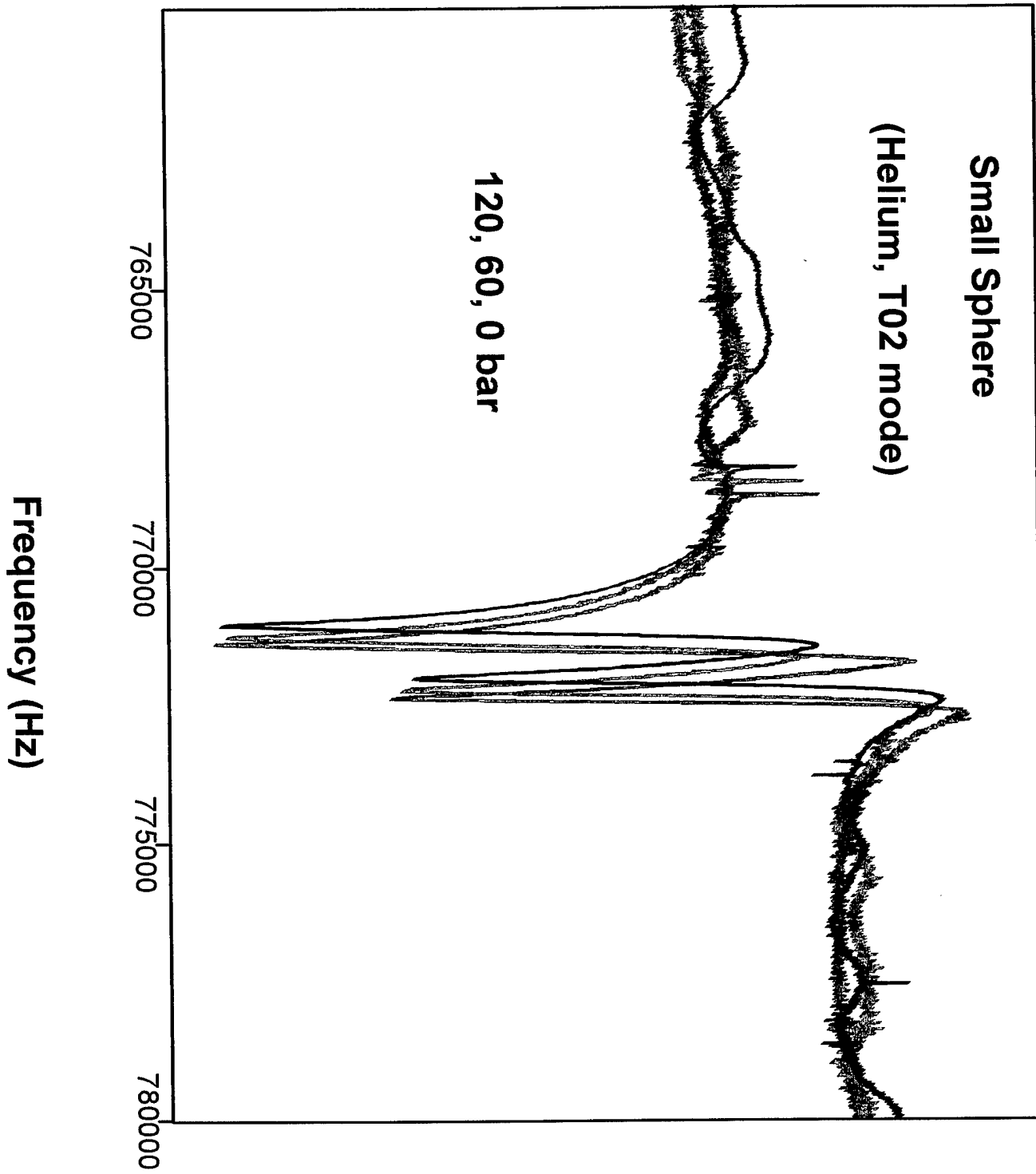
Dependence of $(\partial G / \partial P)_T$ on Molecular Mass of Gas
 - Helium, Nitrogen, Argon -

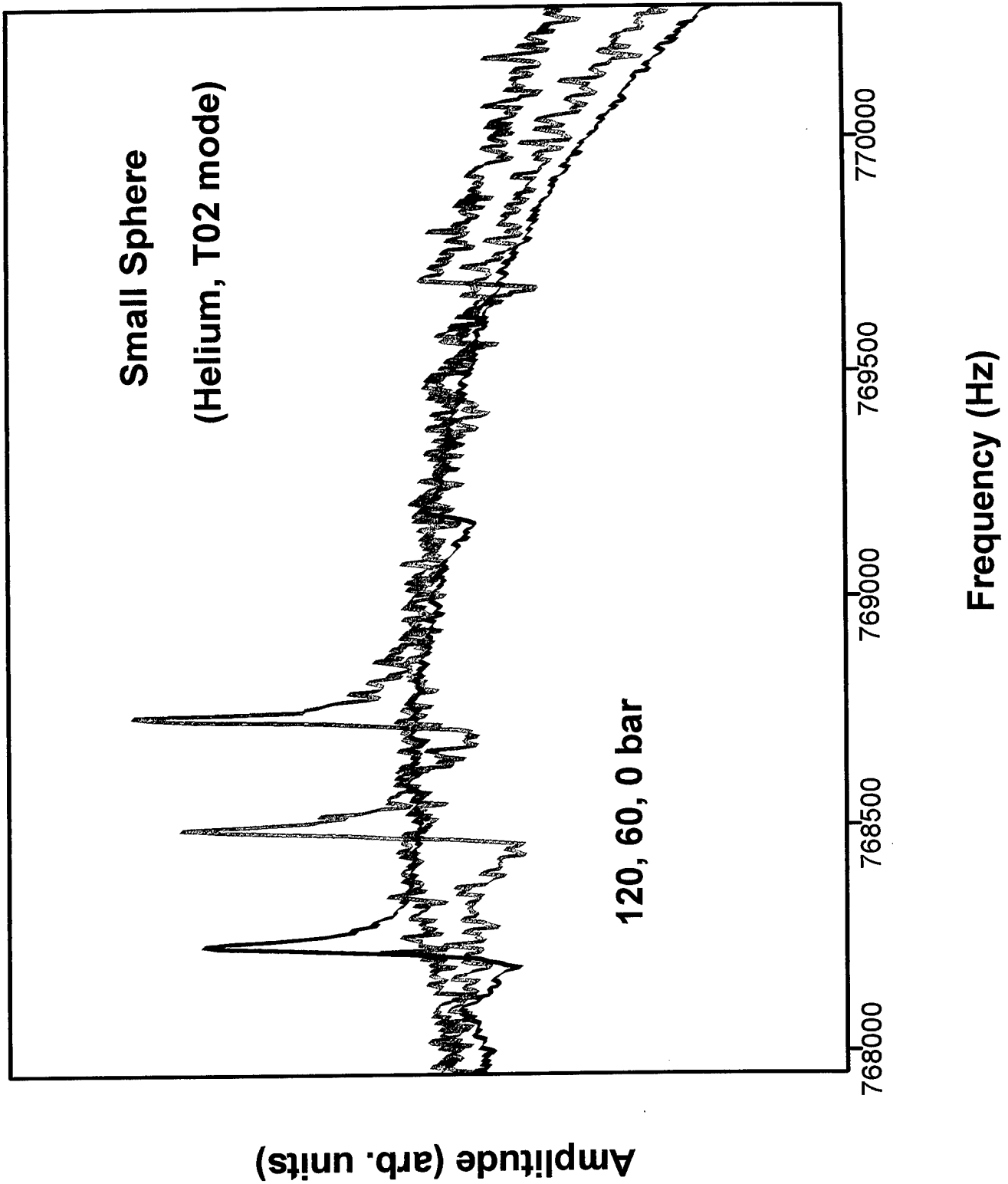


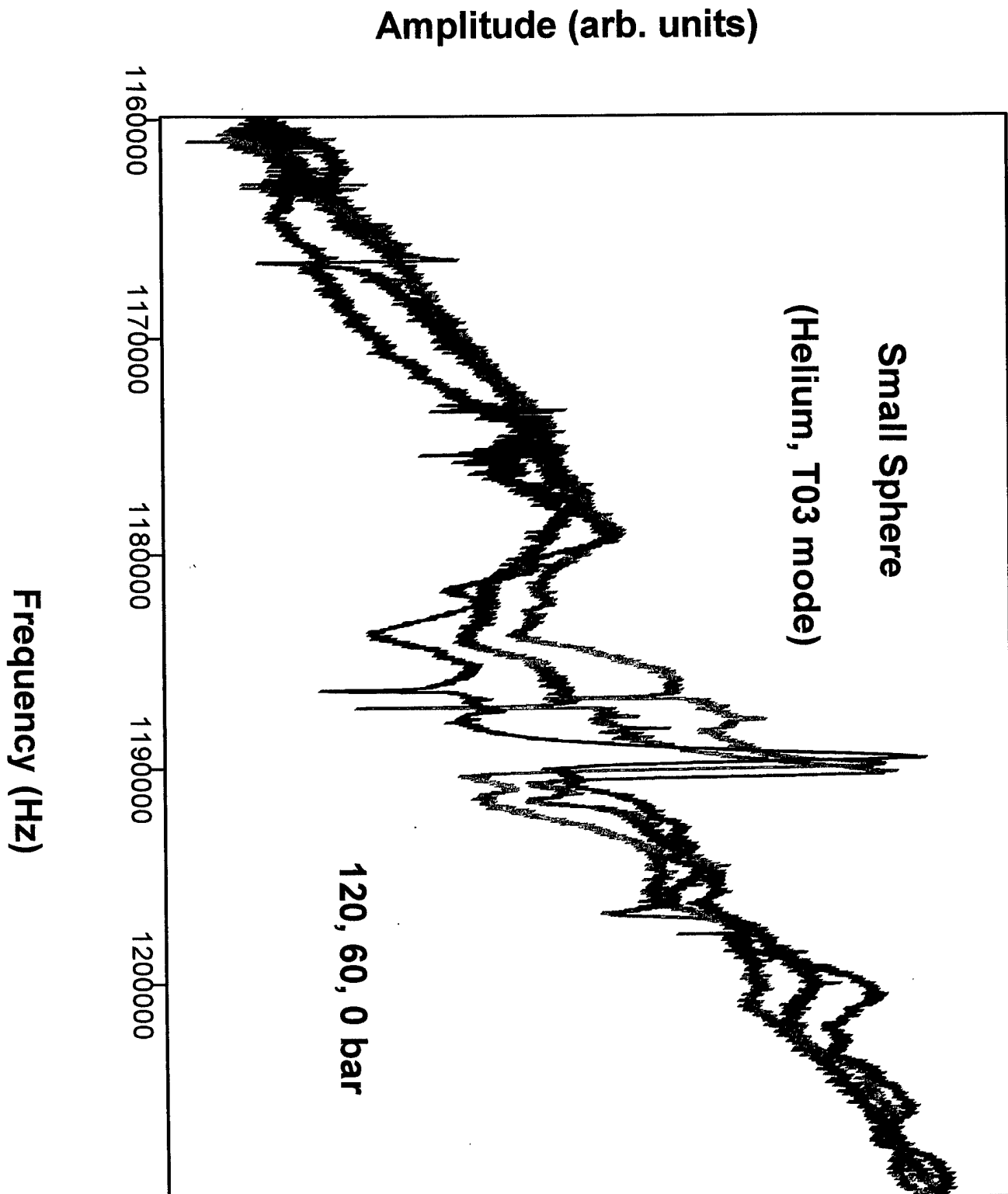


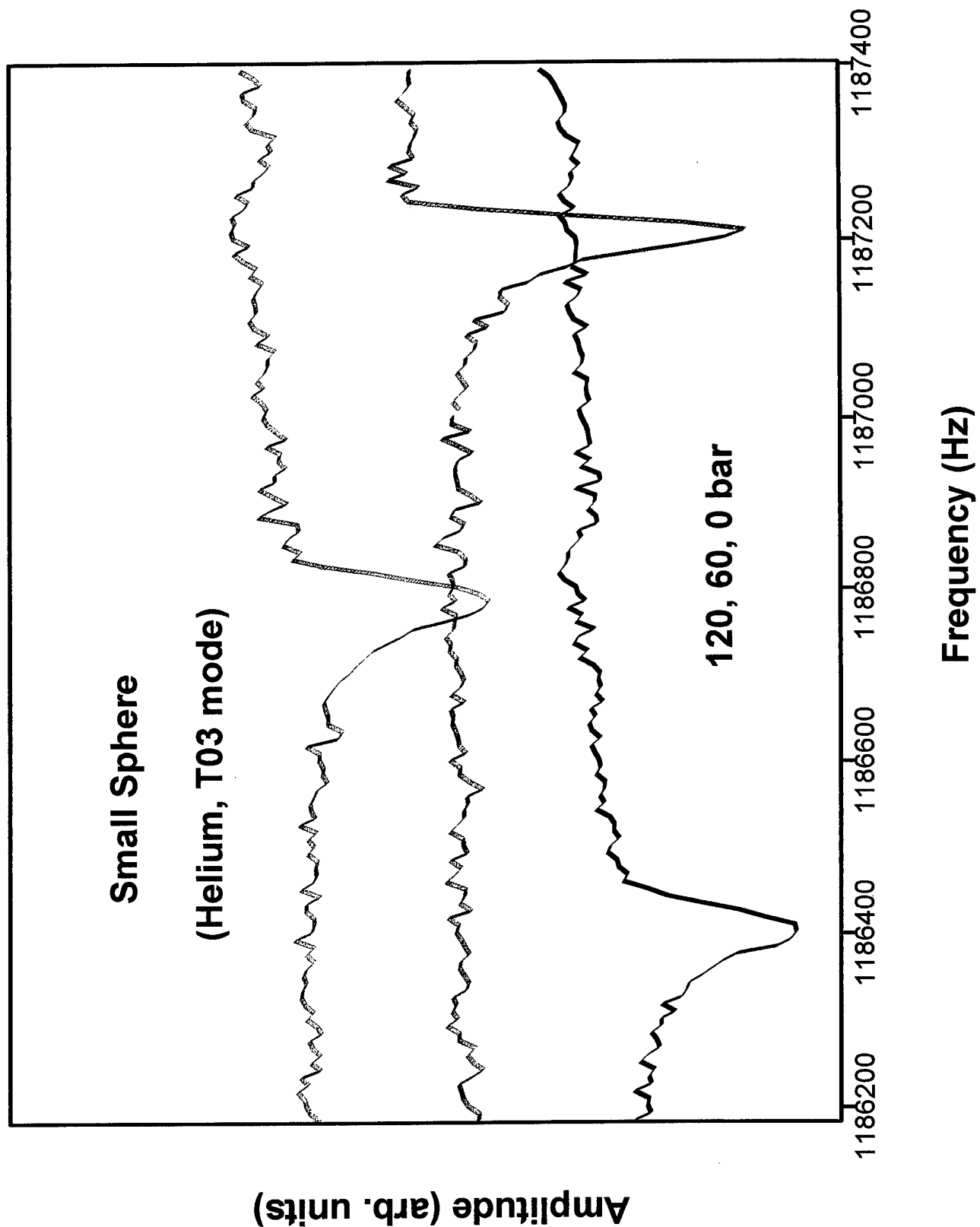


Amplitude (arb. units)

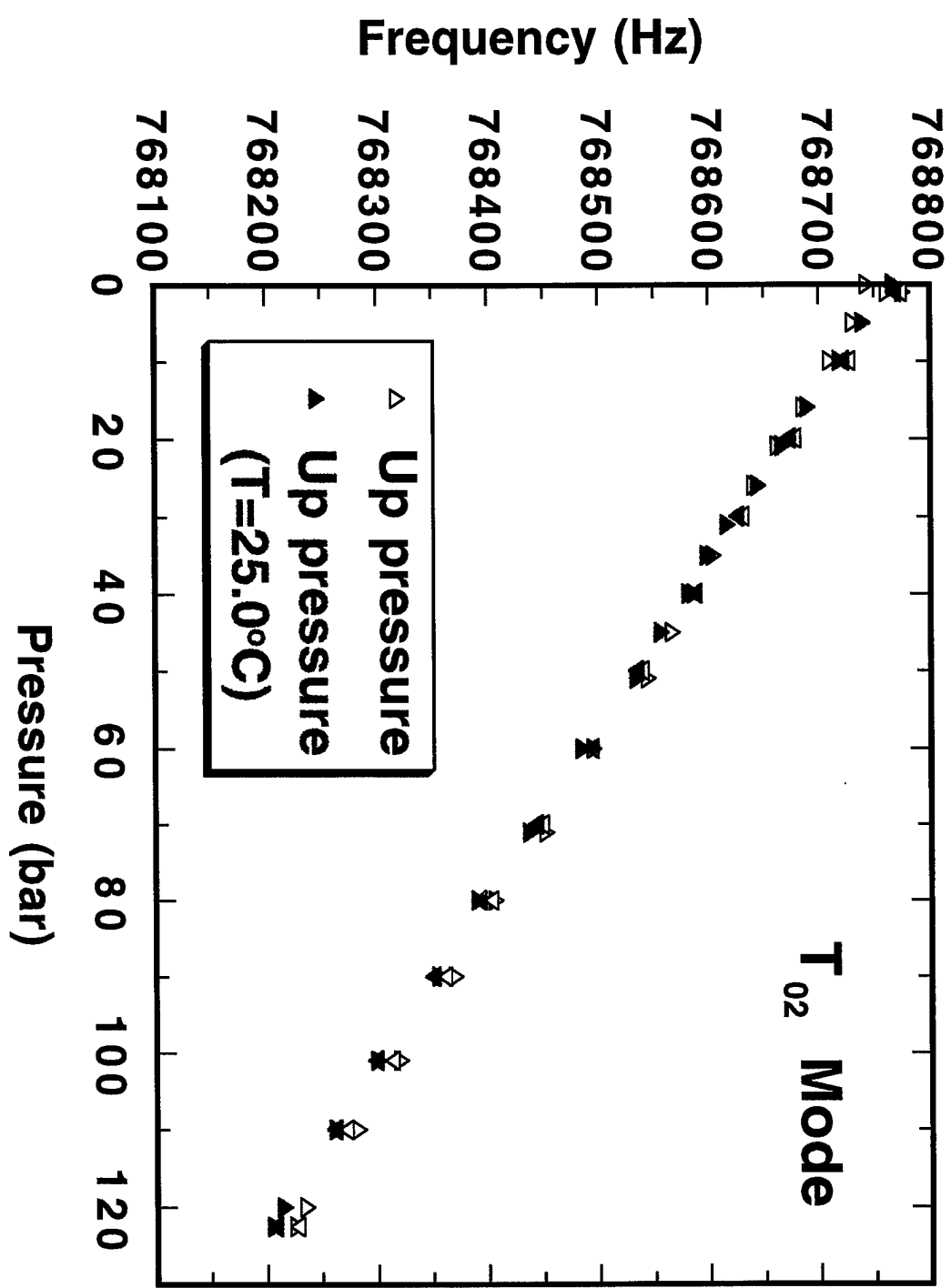


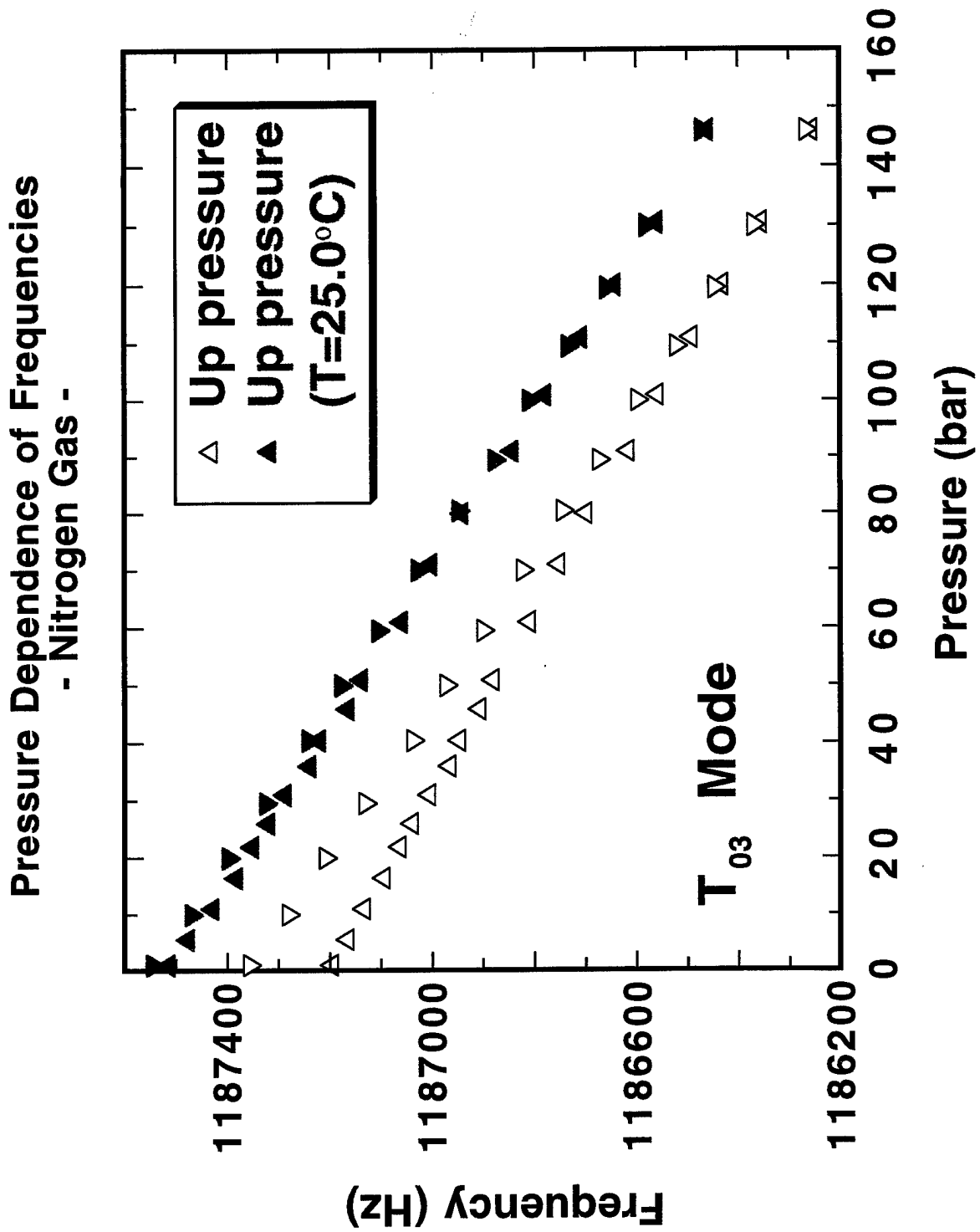




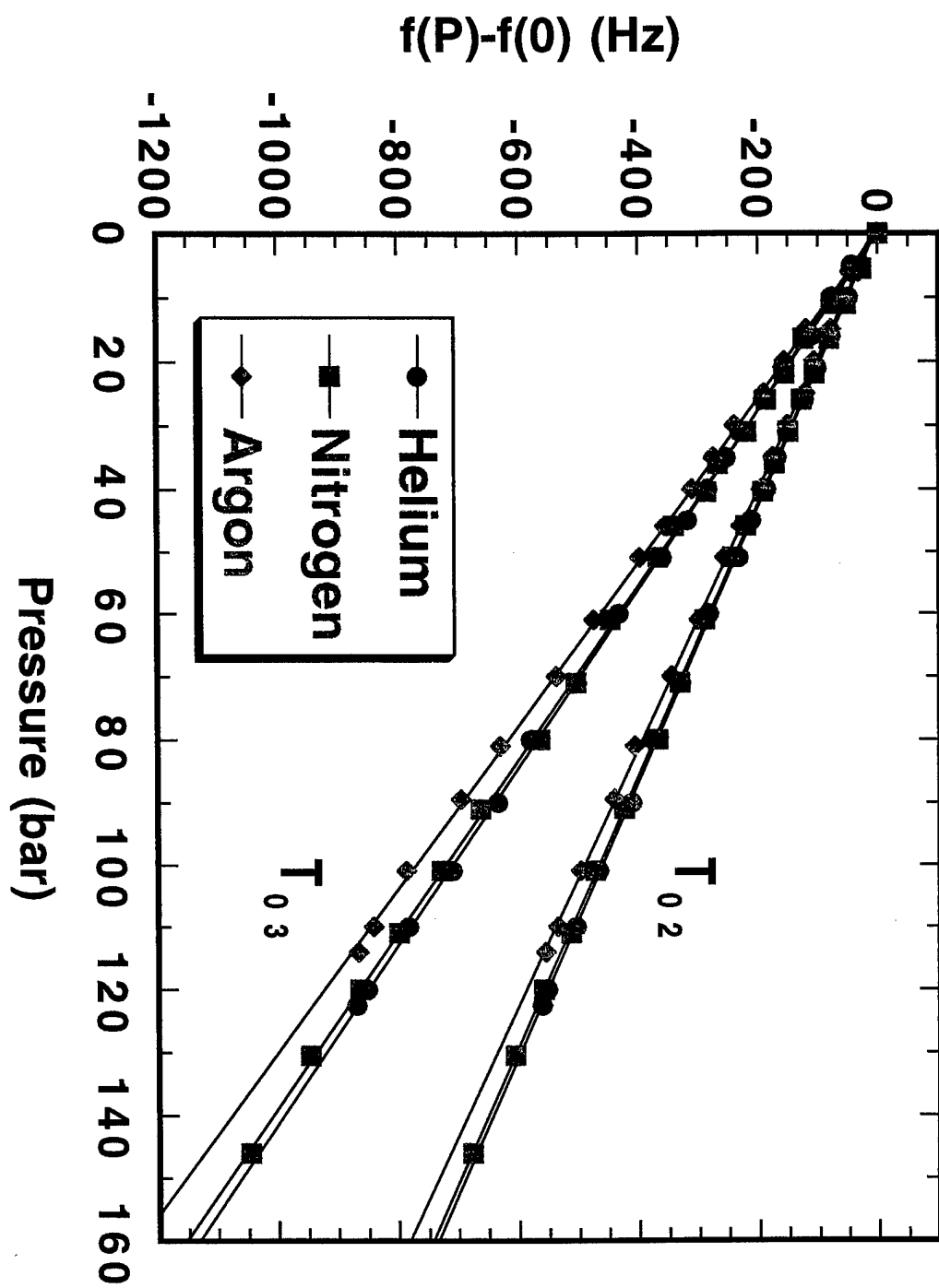


Pressure Dependence of Frequencies
- Helium Gas -





Dependence of Frequencies on Pressure and Gas

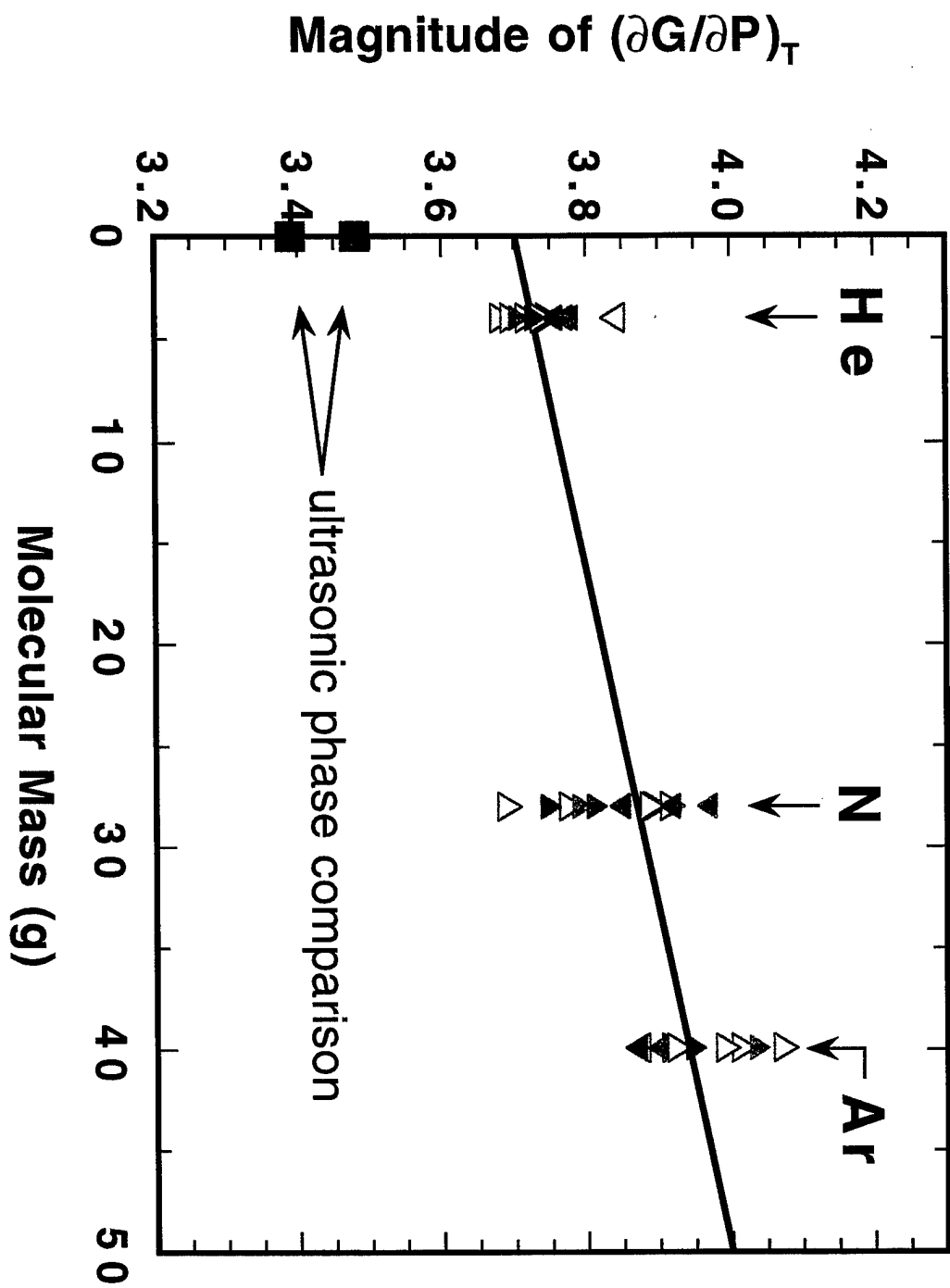


Obtaining G' from $f(P)$:
$$\left(\frac{\partial G}{\partial P}\right)_T = \left(\frac{dG}{df}\right)\left(\frac{\partial f}{\partial P}\right)_T$$

Temperature corrections:
$$\left(\frac{\partial f}{\partial T}\right)_P \Delta T = \left(\frac{df}{dG}\right)\left(\frac{\partial G}{\partial T}\right)_P \Delta T$$

	f (Hz)	df/dG (Hz/bar)	(df/dT) _P (Hz/°C)
Large Sphere			
T ₀₂	620577	0.99134	39.6
T ₀₃	958903	1.53179	61.3
Small Sphere			
T ₀₂	770217	1.23038	49.2
T ₀₃	1190124	1.90116	76.1

Dependence of $(\partial G/\partial P)_T$ on Molecular Mass of Gas
 - Helium, Nitrogen, Argon -



Conclusions on Fused Silica

- Small, measurable effect of pressurizing gas on dG/dP .
($dG'/dm = 6 \times 10^{-3} \text{ g}^{-1}$, $m \sim$ mole. mass of gas)
- Magnitude of dG/dP is 3.70 (for $m=0$), 8% higher than for pulse-echo.
- Evidence of bond effects in pulse-echo?

Gas Pressure Dependence of Radiation Impedance of a Resonating Sphere

University of Wisconsin-Milwaukee
J. R. Feller, R. Sorbello, D. Beck, M. Levy

University of California, Los Angeles
Institute of Geophysics and Planetary Physics
D. Isaak

Work at UW-M supported by Office of Naval Research

Outline

Part I.

- Discussion of Isaak's RUS data on the silica sphere.
- Pressure dependence of Q and resonant frequency of the T02, S11, S00 modes.

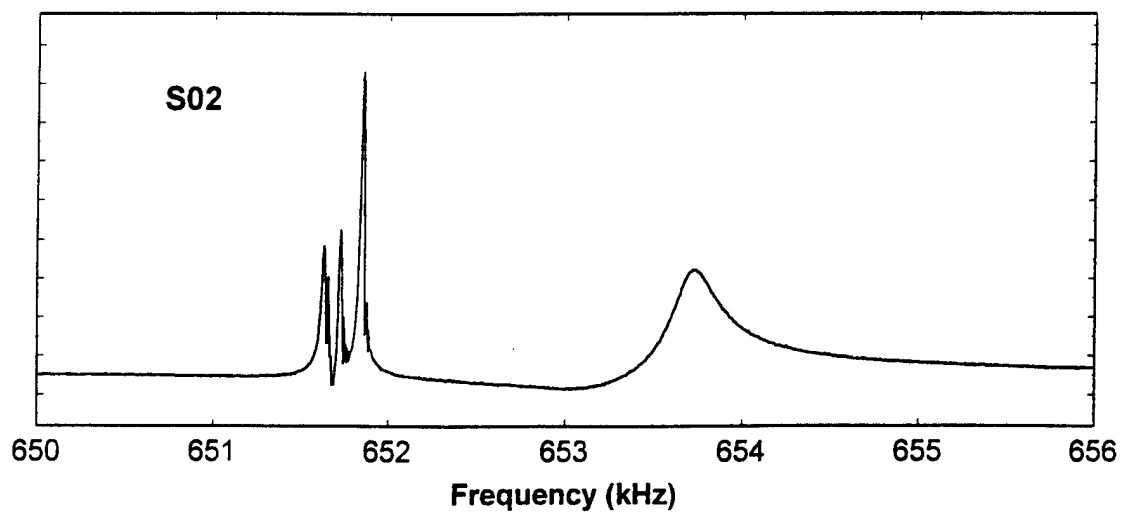
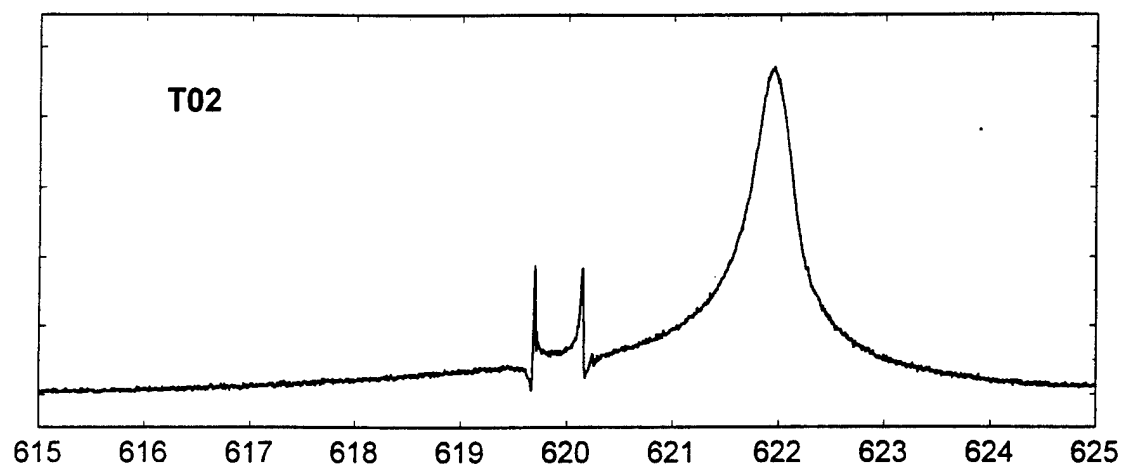
Part II.

- Theoretical examination of the radiation impedance.
- Dependence of resonance Q on pressure and molecular weight.
- Expected frequency shift due to mass loading.
- Comparison with experimental results.

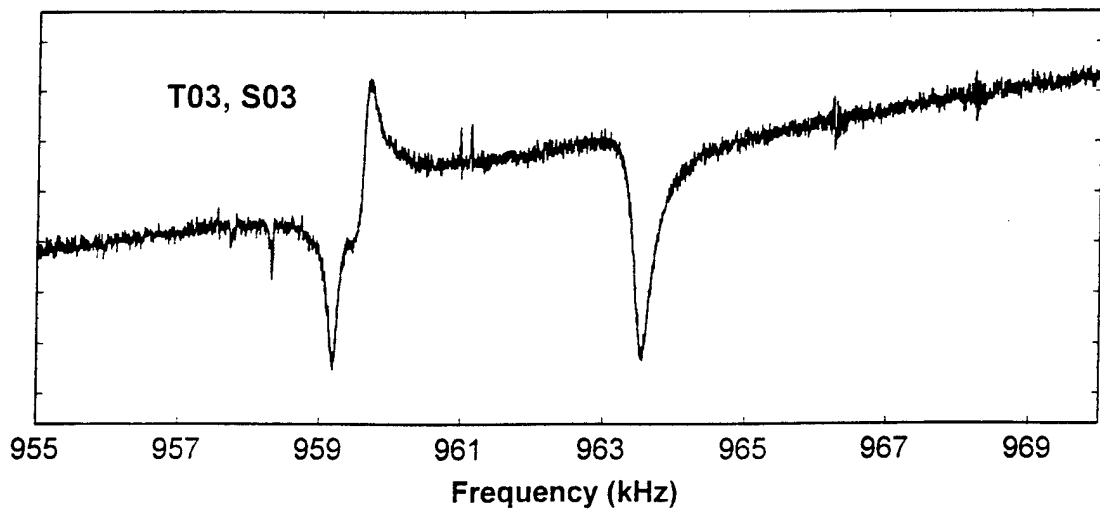
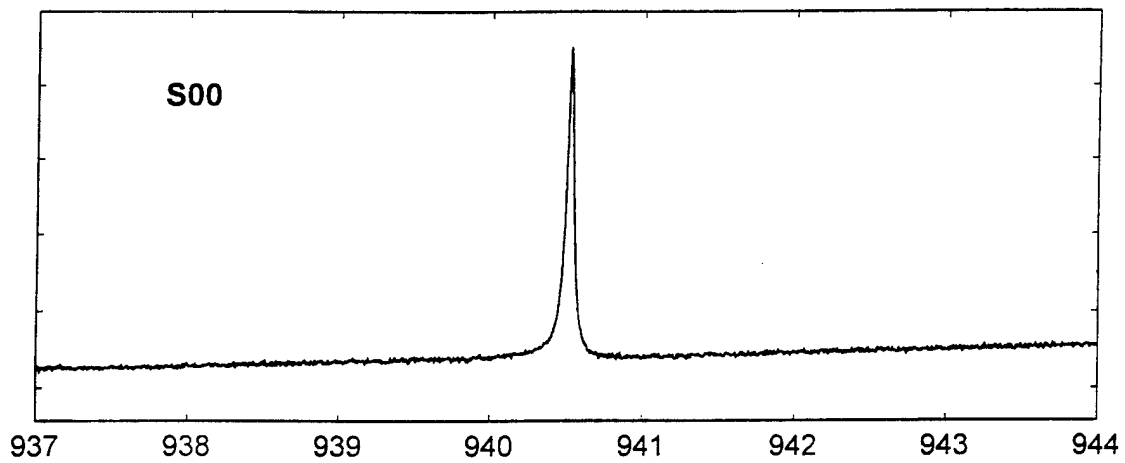
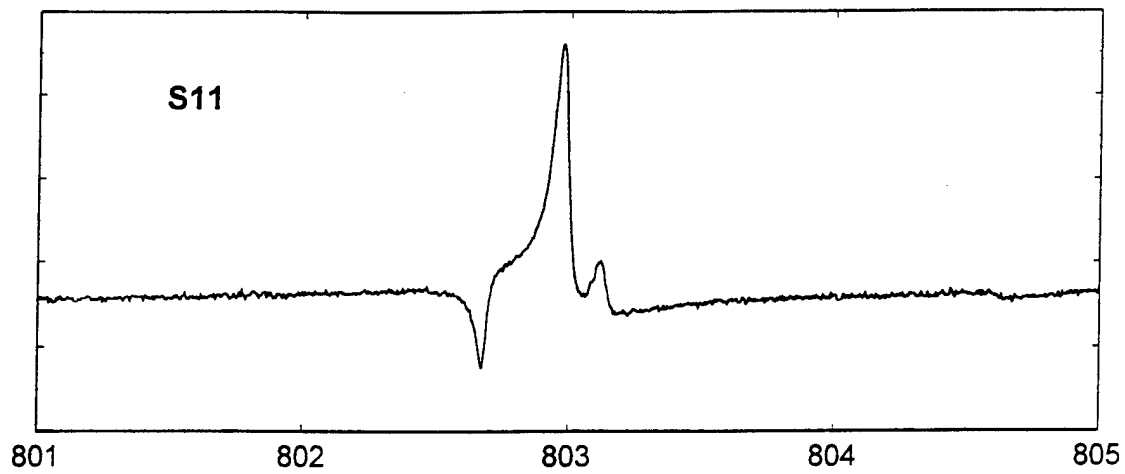
Fused Silica Sphere (Radius 2.414 mm)

	N	L	Freq. (kHz)
T	0	2	620.57691
S	0	2	652.04321
S	1	1	804.52548
S	0	0	944.70449
T	0	3	958.90296
S	0	3	961.98376

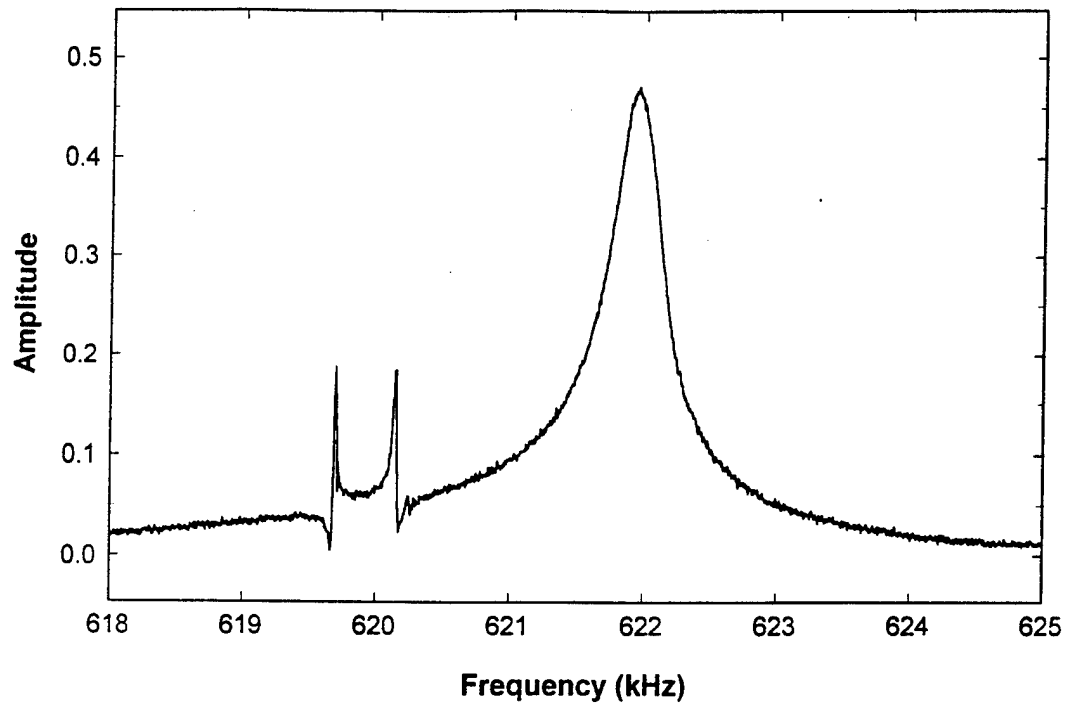
Measurements of D. Isaak, UCLA:



Fused Silica Sphere (Radius 2.414 mm)



Fused Silica Sphere (Radius 2.414 mm) T02 Mode



Degenerate modes: $n = 0$, $l = 2$, $m = 0, \pm 1, \pm 2$

$m = 0$:

$$u_{\theta} = 0$$

$$u_{\phi} = A \sin 2\theta \cos \omega t$$

$m = \pm 1$:

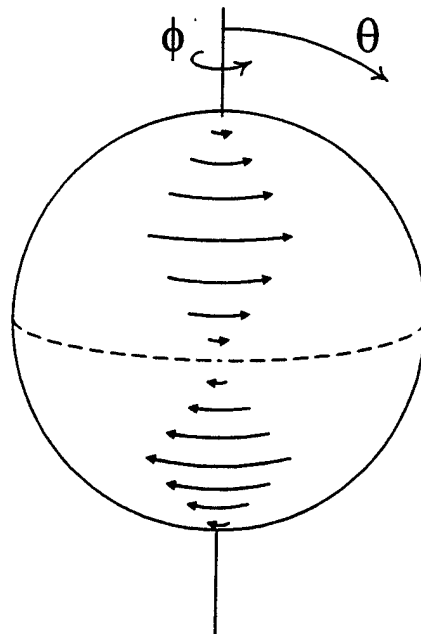
$$u_{\theta} = A \cos \theta \cos(\omega t \pm \phi)$$

$$u_{\phi} = A \cos 2\theta \cos(\omega t \pm \phi)$$

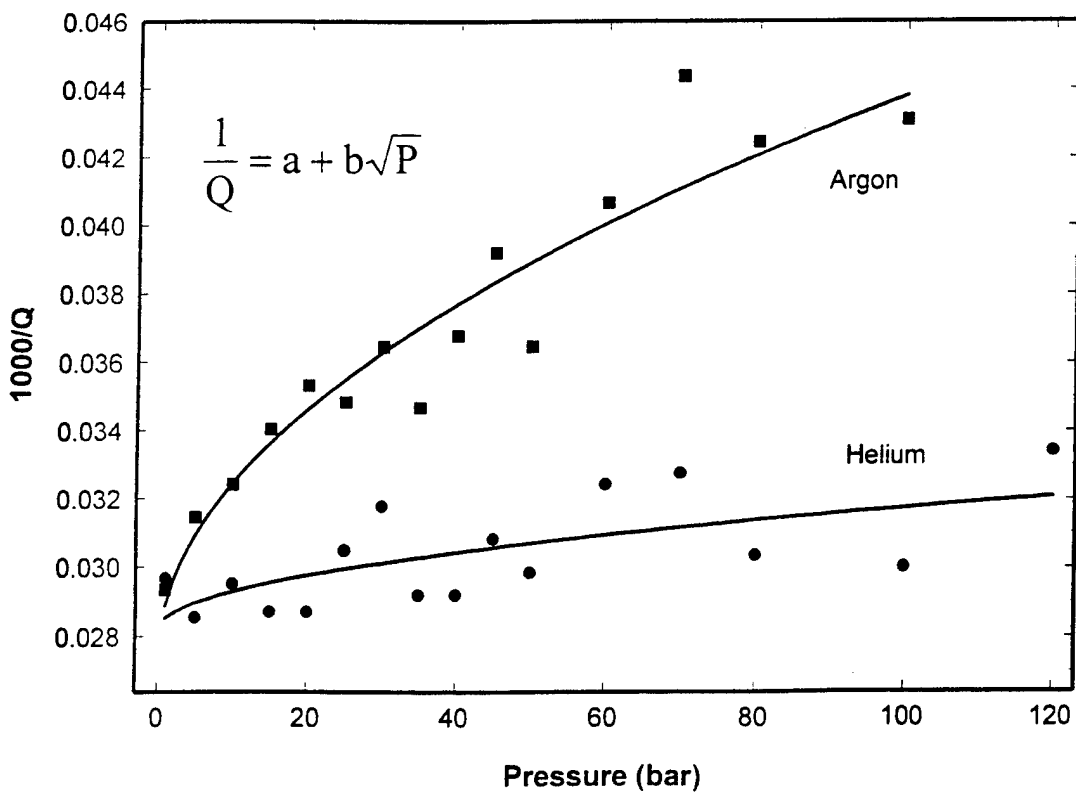
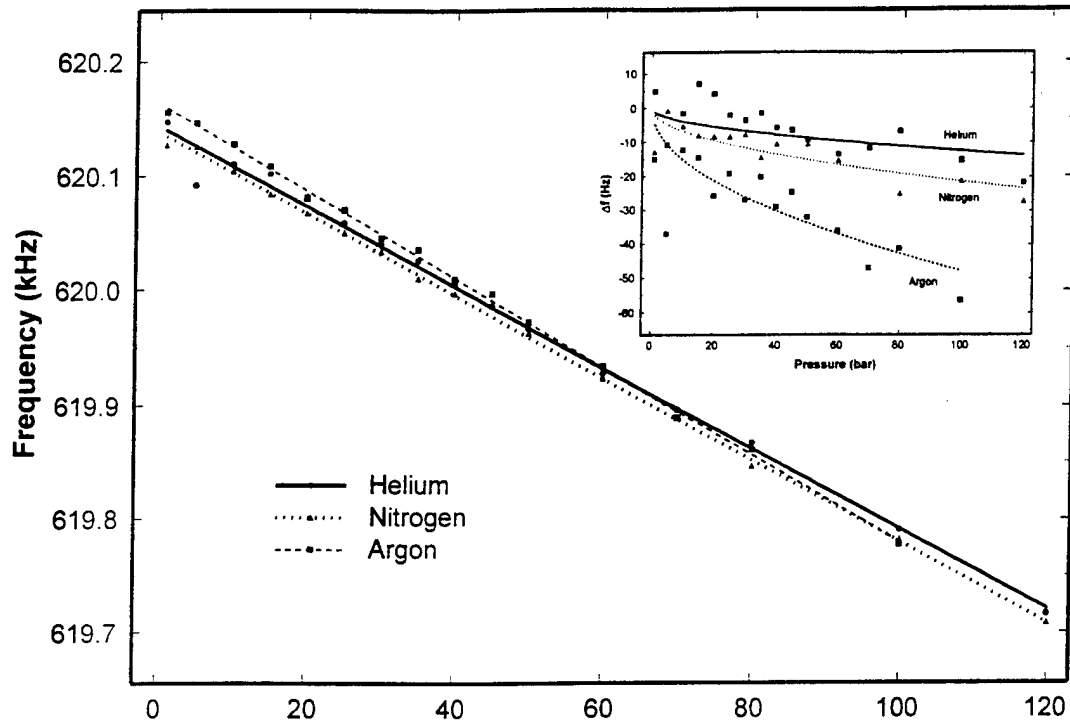
$m = \pm 2$:

$$u_{\theta} = A \sin \theta \cos(\omega t \pm 2\phi)$$

$$u_{\phi} = \frac{1}{2} A \sin 2\theta \cos(\omega t \pm 2\phi)$$



Fused Silica Sphere (Radius 2.414 mm) T02 Mode



$$\alpha_{\text{measured}} = \alpha_0 + \alpha_R \qquad \frac{1}{Q_{\text{measured}}} = \frac{1}{Q_0} + \frac{1}{Q_R}$$

Residual loss:

$$\frac{1}{Q_0} = \text{constant} \approx 10^{-5}$$

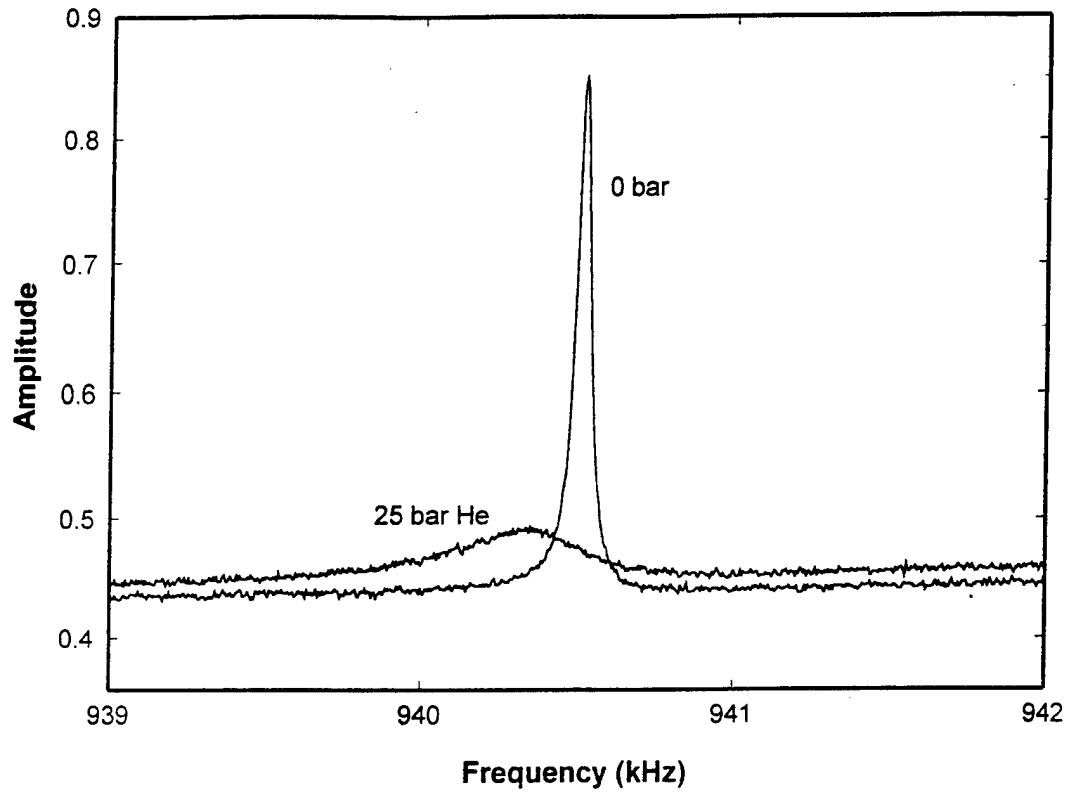
Radiation loss:

$$\frac{1}{Q_R} \propto \begin{cases} \sqrt{P} & \text{T02} \\ P & \text{S00, S11} \end{cases}$$

$$f_{\text{measured}} = f_0 + \Delta f$$

$$\Delta f \propto \begin{cases} -\sqrt{P} & \text{T02} \\ -P & \text{S00, S11} \end{cases}$$

Fused Silica Sphere (Radius 2.414 mm) S00 Mode



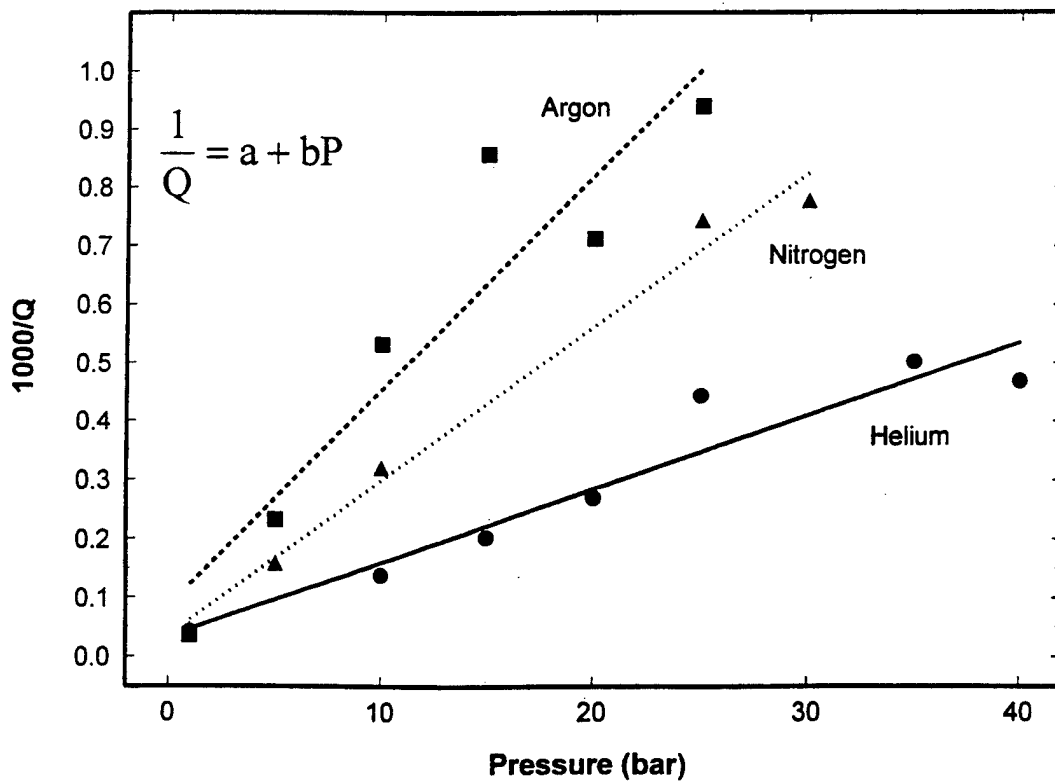
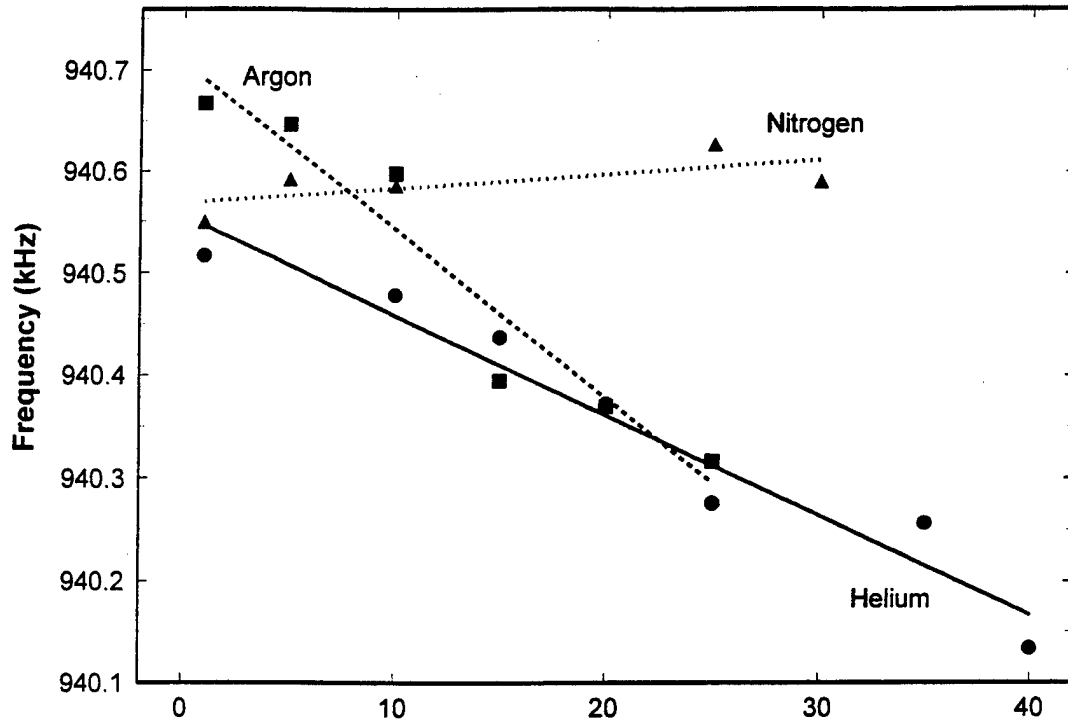
$$n = 0, \quad l = 0, \quad m = 0$$

$$u_r = A \cos \omega t$$

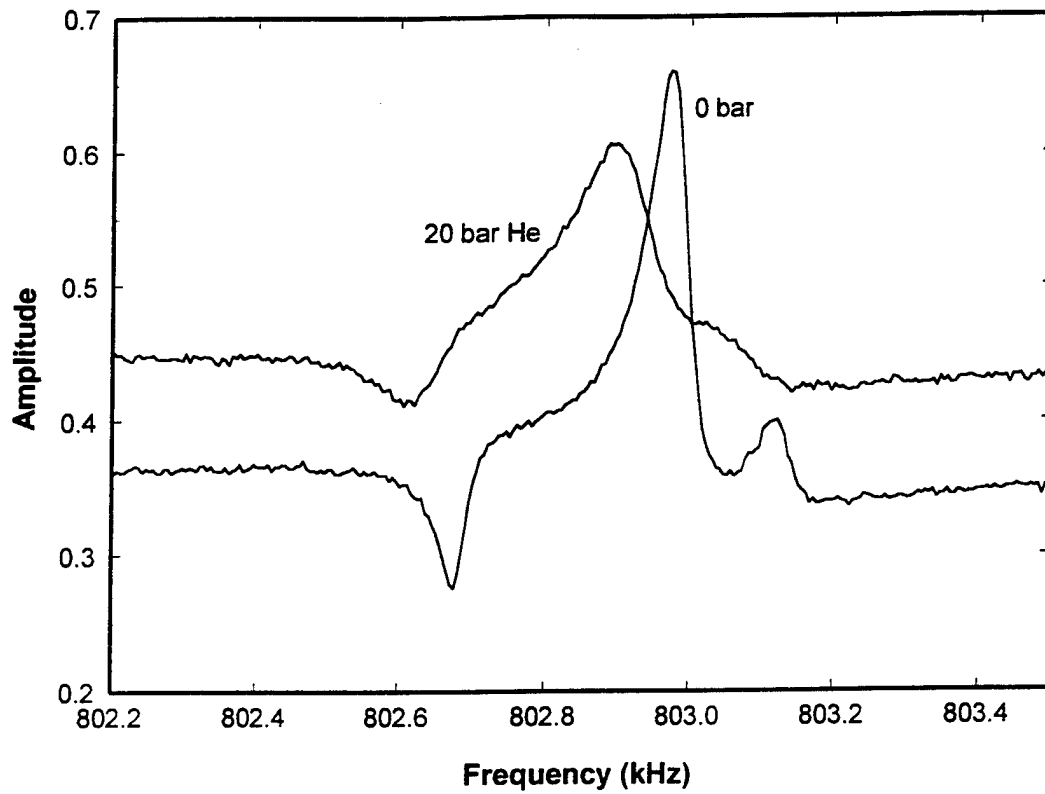
$$u_\theta = u_\phi = 0$$

(Pure radial breathing mode)

Fused Silica Sphere (Radius 2.414 mm) S00 Mode



Fused Silica Sphere (Radius 2.414 mm) S11 Mode



Degenerate modes: $n = 1$, $l = 1$, $m = 0, \pm 1$

$m = 0$:

$$u_r = A \cos \theta \cos \omega t$$

$$u_\theta = B \sin \theta \cos \omega t$$

$$u_\phi = 0$$

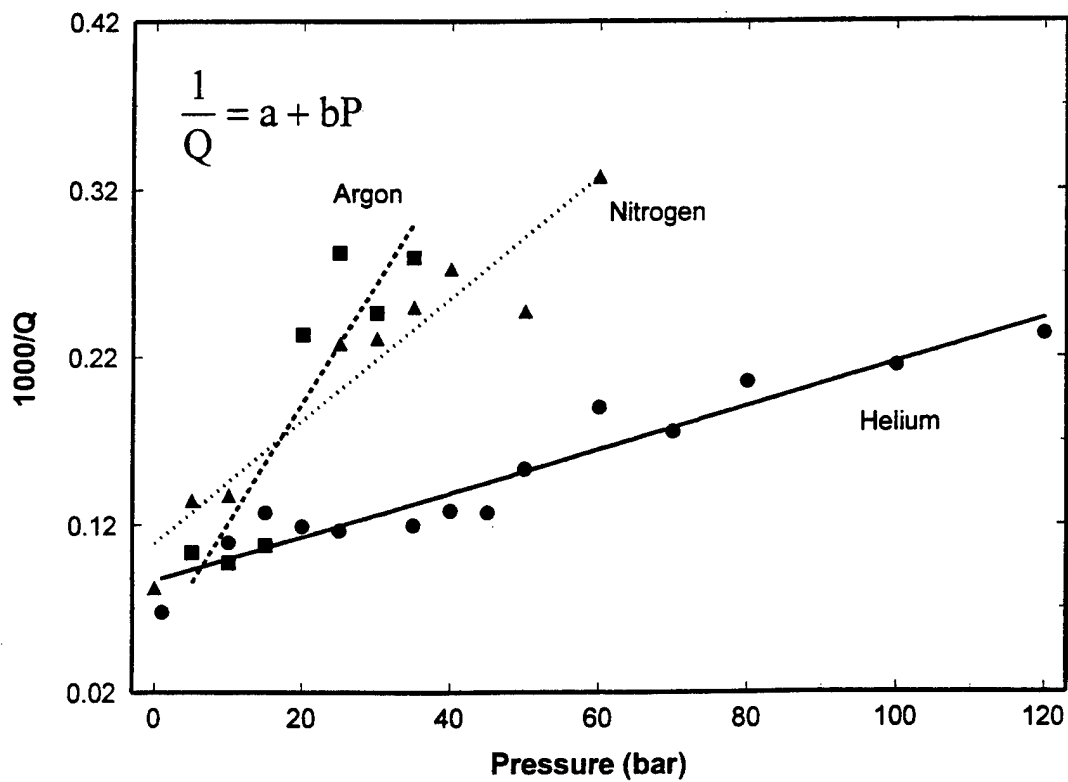
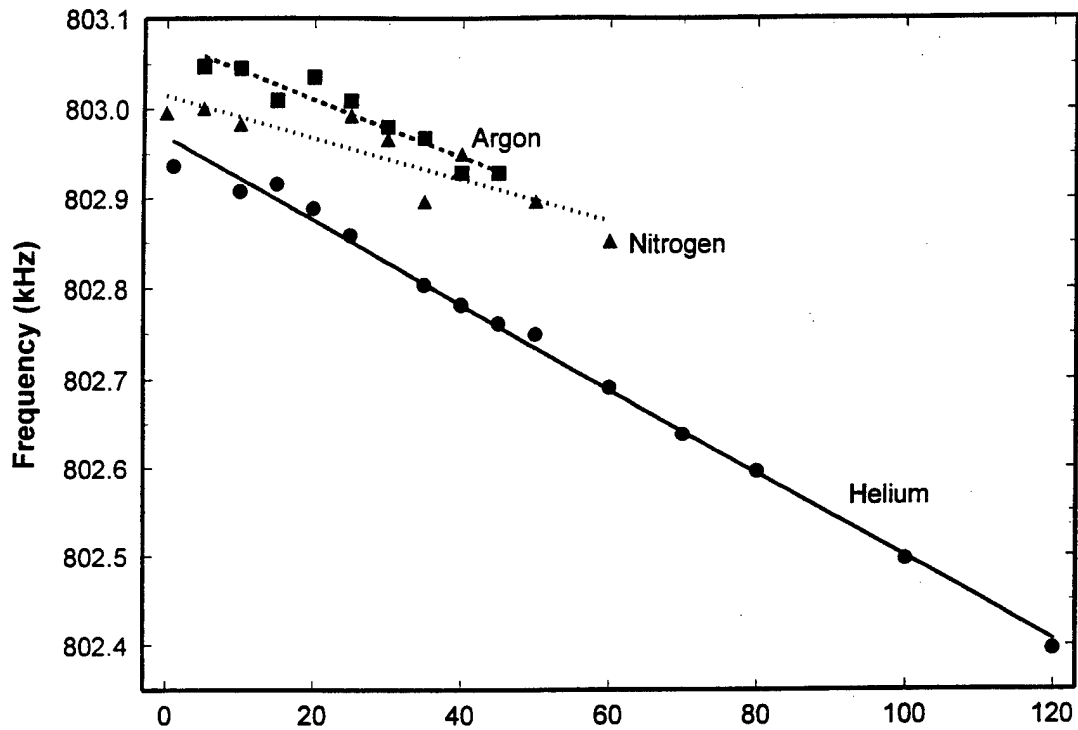
$m = \pm 1$:

$$u_r = A \sin \theta \cos(\omega t \pm \phi)$$

$$u_\theta = B \cos \theta \cos(\omega t \pm \phi)$$

$$u_\phi = B \cos(\omega t \pm (\phi + \frac{\pi}{2}))$$

Fused Silica Sphere (Radius 2.414 mm) S11 Mode



THEORY

WAVE EQ:
$$\rho \frac{\partial^2 u_i}{\partial t^2} = \frac{\partial T_{ij}}{\partial x_j}$$

u_i = i -th component of displacement \mathbf{u}

$$T_{ij} = \lambda \nabla \cdot \mathbf{u} \delta_{ij} + \mu \left(\frac{\partial u_i}{\partial x_j} + \frac{\partial u_j}{\partial x_i} \right) = \text{stress tensor}$$

SOLUTIONS (See, e.g., Lapwood & Usami, 1981):

I. IRROTATIONAL:
$$\mathbf{u}_I = \nabla \Phi e^{i\omega t}$$

$$\nabla^2 \Phi + h^2 \Phi = 0 \quad h = \omega/c_L = \omega/\sqrt{(\lambda+2\mu)/\rho}$$

$$\Phi = j_l(hr) Y_{lm}(\theta, \phi)$$

II. EQUIVOLUMINAL with $u_r = 0$:
$$\mathbf{u}_{II} = \nabla \times \mathbf{r} \psi e^{i\omega t}$$

$$\nabla^2 \psi + k^2 \psi = 0 \quad k = \omega/c_T = \omega/\sqrt{\mu/\rho}$$

$$\psi = j_l(kr) Y_{lm}(\theta, \phi)$$

III. EQUIVOLUMINAL:
$$\mathbf{u}_{III} = (1/k) \nabla \times \nabla \times \mathbf{r} \chi e^{i\omega t}$$

$$\nabla^2 \chi + k^2 \chi = 0 \quad \chi = j_l(kr) Y_{lm}(\theta, \phi)$$

SPHEROIDAL MODES:
$$\mathbf{u} = A \mathbf{u}_I + B \mathbf{u}_{III}$$

TOROIDAL MODES:
$$\mathbf{u} = \mathbf{u}_{II}$$

EIGENFREQUENCIES & RADIATION IMPEDANCE

FREE SURFACE B.C.: $T_{rr} = T_{\theta r} = T_{\phi r} = 0$

Determines resonance frequency ω_0 for unloaded sphere.

LOADED SURFACE B.C.:

Gas exerts force \mathbf{F} on surface of sphere ($r = a$),

$$\therefore T_{rr} = \frac{F_r}{A} = -p$$

and

$$T_{\theta r} = T_{\phi r} = 0 \quad (\text{neglecting viscosity of gas}).$$

RADIATION IMPEDANCE:

$$Z \equiv \frac{p}{v_{\text{gas}}} \quad (\text{evaluated at } r=a)$$

$$= \frac{p}{i \omega u_r} \quad (\text{evaluated at } r=a)$$

Outgoing radiation:

$$p = p_0 h_l^{(2)}(k_g r) Y_{lm}(\theta, \phi) e^{i\omega t}$$

where $k_g = \omega/c_g$, together with eq. of motion $-\nabla p = \rho_g \frac{\partial \mathbf{v}_{\text{gas}}}{\partial t}$ gives:

$$Z = -i \rho_g c_g h_l^{(2)}(k_g a) / h_l^{(2)'}(k_g a)$$

COMPLEX FREQUENCY SHIFT:

BC at $r=a$: $T_{rr} = -i \omega u_r Z$

or $F(\omega) = -i \omega Z$, where $F(\omega) \equiv T_{rr} / u_r$.

Solution gives complex eigenfrequency $\omega = \omega_0 + \Delta\omega$.
Small-loading expansion:

$$F(\omega_0) + F'(\omega_0) \Delta\omega = -i \omega_0 Z(\omega_0)$$

$$\therefore \Delta\omega = -i \omega_0 Z(\omega_0) / F'(\omega_0)$$

All information about surrounding gas is contained in $Z(\omega_0)$.

Further, since $F'(\omega_0)$ is real,

$$\text{Re } \Delta\omega / \omega_0 = \text{Im } Z(\omega_0) / F'(\omega_0)$$

and

$$\text{Im } \Delta\omega / \omega_0 = \text{Re } Z(\omega_0) / F'(\omega_0)$$

The Quality factor $Q = \omega_0 / (2 \text{Im } \omega)$ can then be obtained from

$$\frac{1}{Q} = 2 \text{Re } Z(\omega_0) / F'(\omega_0)$$

S00-MODE ($l = 0$):

$$u_r = A j_0'(\omega r/c_L) \cos \omega t \quad (u_\theta = u_\phi = 0)$$

$$T_{rr} = \lambda (du_r/dr + 2 u_r/r) + 2 \mu du_r/dr ; \quad F(\omega) = T_{rr} / u_r$$

$$\text{Transcendental equation as before:} \quad F(\omega) = -i \omega Z$$

$$\text{where} \quad Z = -i \rho_g c_g h_l^{(2)}(k_g a) / h_l^{(2)'}(k_g a)$$

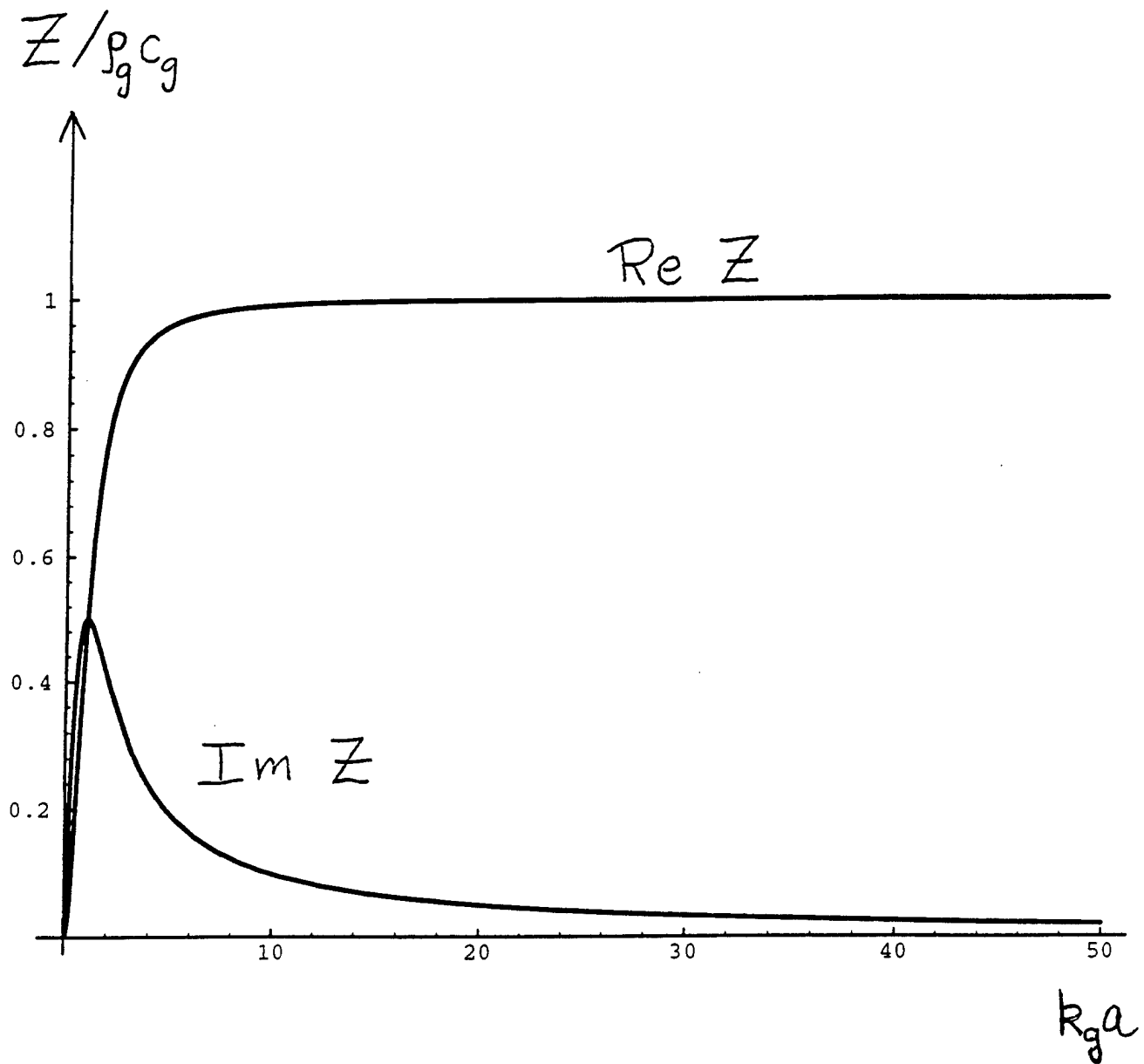
$$= \rho_g c_g \left[\frac{1 + i (k_g a)^{-1}}{1 + (k_g a)^{-2}} \right]$$

For reported expts , $k_g a = 16$ for He and 49 for Ar. So dependence on molecular mass M of gas and static pressure p of gas can be obtained by taking $k_g a \gg 1$ limit for Z :

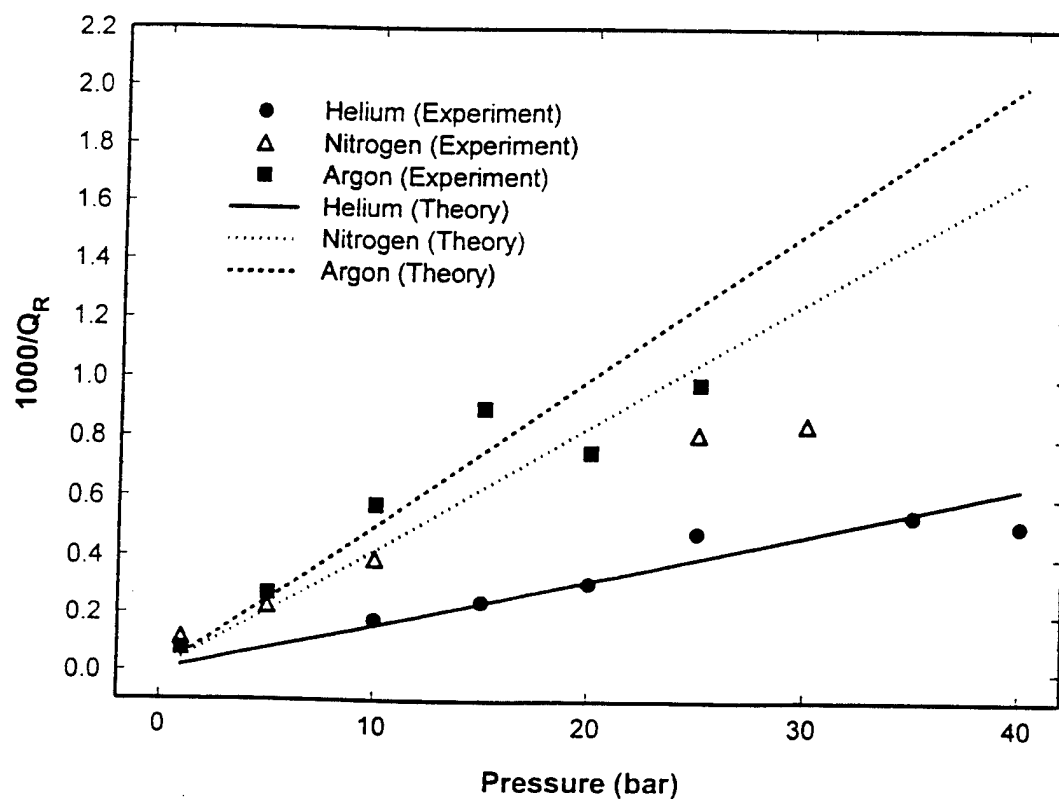
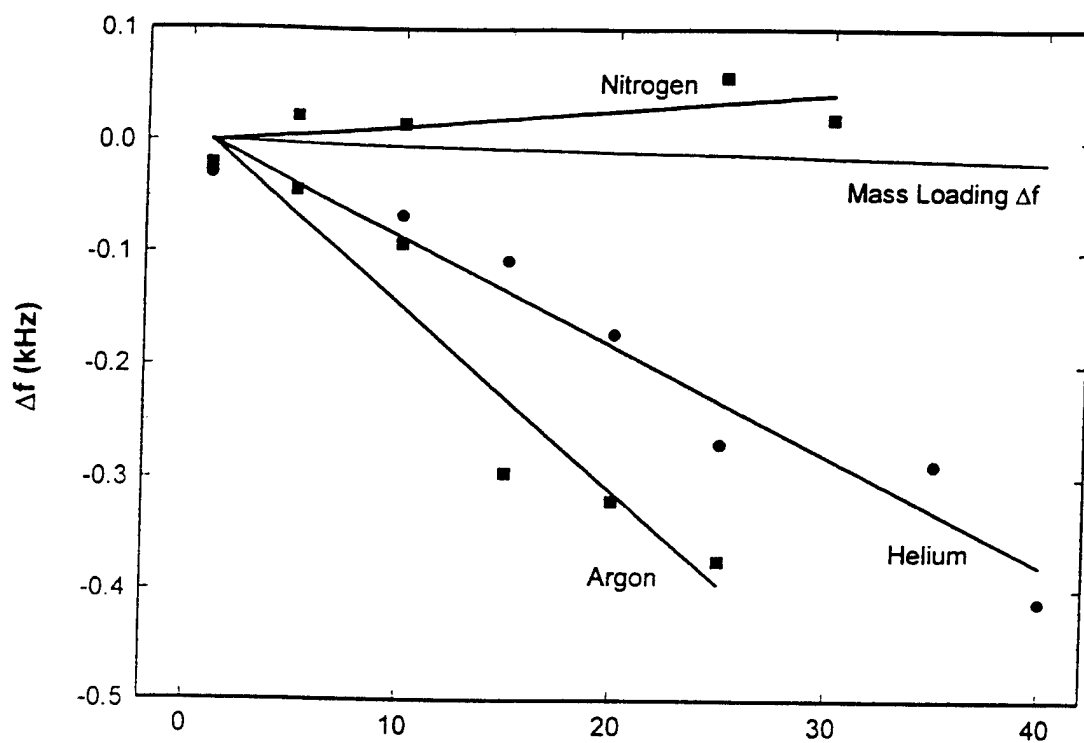
$$\frac{1}{Q} \propto \text{Re } Z \approx \rho_g c_g \propto p M M^{-1/2} = p M^{1/2}$$

$$\Delta f \propto \text{Im } Z \approx \rho_g c_g / (k_g a) = \rho_g c_g^2 / (\omega a) \propto p M M^{-1} = p M^0$$

Theoretical results reported here for $1/Q$ and Δf are obtained using full expressions for Z and $F'(\omega_0)$.

Z for SOO-mode

Fused Silica Sphere (Radius 2.414 mm) S00 Mode



S11-MODE ($l = 1, m = 0 \pm 1$):

$$\mathbf{u} = A \mathbf{u}_I + B \mathbf{u}_{III}$$

$$\text{At } r=a: \quad T_{rr} = (\alpha A + \beta B) Y_{lm}(\theta, \phi)$$

$$T_{\theta r} = (\gamma A + \delta B) \partial Y_{lm}(\theta, \phi) / \partial \theta$$

$$T_{\phi r} = (\gamma A + \delta B) \text{im } Y_{lm}(\theta, \phi) / \sin \theta$$

$$\alpha = -(\lambda + 2\mu)h^2 j_1(ha) - (4\mu h/a)j_1'(ha) + (4\mu/a^2)j_1(ha)$$

$$\beta = (4\mu/k)(k j_1'(ka)/a - j_1(ka)/a^2)$$

$$\gamma = 2\mu(h j_1'(ha)/a - j_1(ha)/a^2)$$

$$\delta = \mu k j_1''(ka) \quad (h \equiv \omega/c_L ; k \equiv \omega/c_T)$$

UNLOADED SPHERE:

$$\text{B.C. at } r=a: \quad T_{rr} = T_{\theta r} = T_{\phi r} = 0$$

$$\therefore (\alpha A + \beta B) = 0 \quad \text{and} \quad (\gamma A + \delta B) = 0.$$

Consistency requires determinant = 0. $\therefore \alpha\delta - \beta\gamma = 0$ gives ω_0 .

LOADED SPHERE:

$$\text{B.C. at } r=a: \quad 1) \quad T_{rr} / u_r = -i \omega Z$$

$$2) \quad T_{\theta r} = T_{\phi r} = 0$$

Using u_r , T_{rr} and $T_{\theta r}$ in these equations, get usual form:

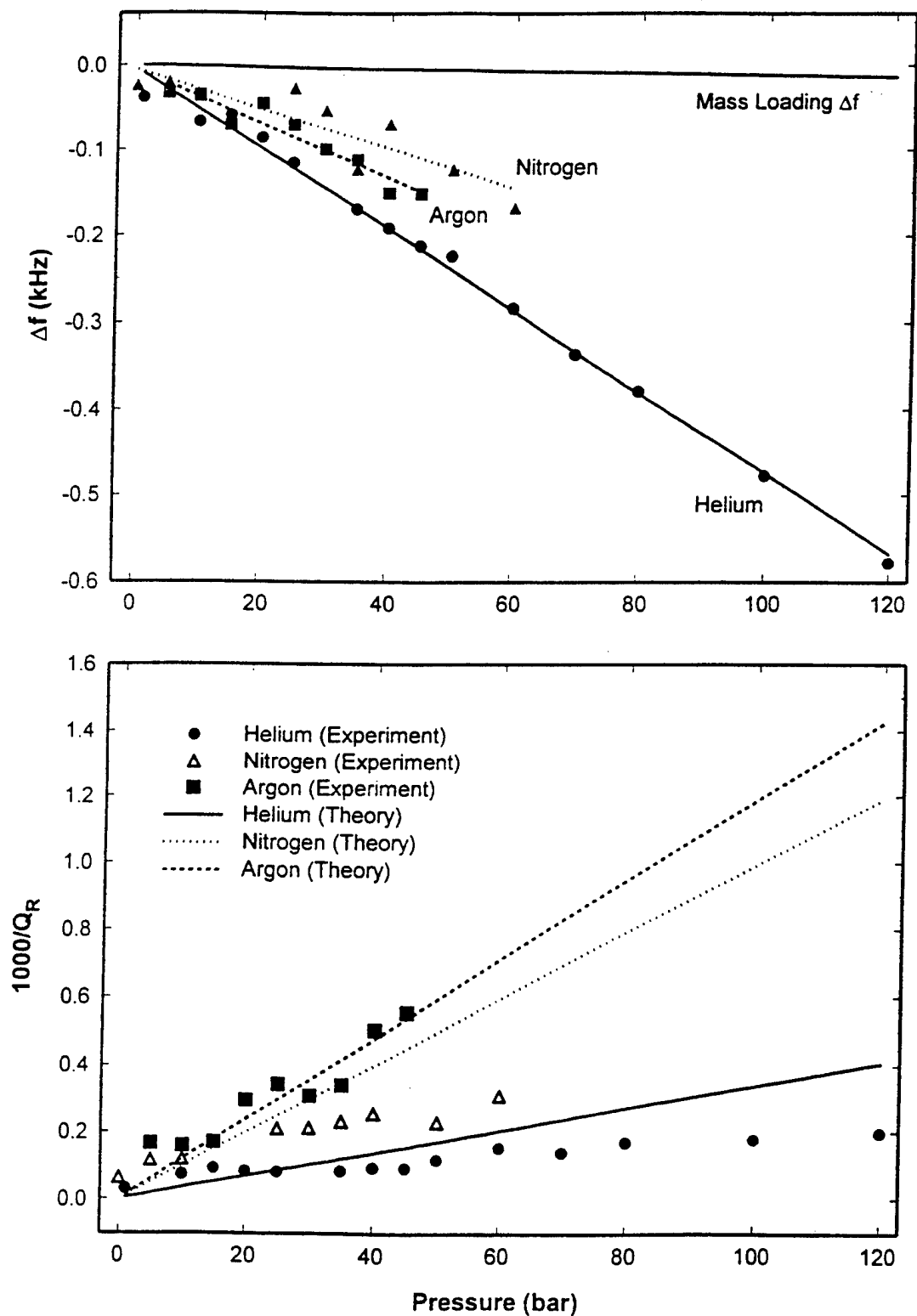
$$F(\omega) = -i \omega Z$$

where

$$F(\omega) = \frac{\alpha\delta - \beta\gamma}{h j_1'(ha)/a - (2\gamma/ka) j_1(ka)/a^2}$$

Numerical results for Δf and $1/Q$ shown in figure.

Fused Silica Sphere (Radius 2.414 mm) S11 Mode



TOROIDAL MODES

$u_r = 0 \Rightarrow$ no coupling to a non-viscous gas. ($\therefore 1/Q = 0$ and $\Delta f = 0$.)

\therefore Need to include viscous coupling.

Consider toroidal modes with $m=0$:

$$u_r = u_\theta = 0 \Rightarrow T_{rr} = T_{\theta r} = 0$$

$$u_\phi = j_l(kr) \partial P_l(\theta) / \partial \theta$$

$$T_{\phi r} = \mu(k j_l''(kr) - j_l(kr)/r) \partial P_l(\theta) / \partial \theta$$

UNLOADED SPHERE BC at $r=a$: $T_{\phi r} = 0$ gives ω_o .

LOADED SPHERE BC at $r=a$:

$$T_{\phi r} = T^{\text{viscous}} = -\mu_g \frac{\partial v_{\text{gas}} \phi}{\partial r} \quad \text{where } \mu_g = \text{viscosity coeff. of gas.}$$

Assuming viscous length $\delta \ll a$:

$$v_{\text{gas}} \phi \propto e^{-k'r} \quad \text{with } k' = \frac{1+i}{\delta} \quad \text{and } \delta^{-1} = \sqrt{\rho_g \omega / 2\mu_g}$$

$$\therefore T^{\text{viscous}} = \mu_g k' v_{\text{gas}} \phi$$

Defining $Z = T^{\text{viscous}} / v_{\text{gas}}$, the BC at $r=a$ has usual form

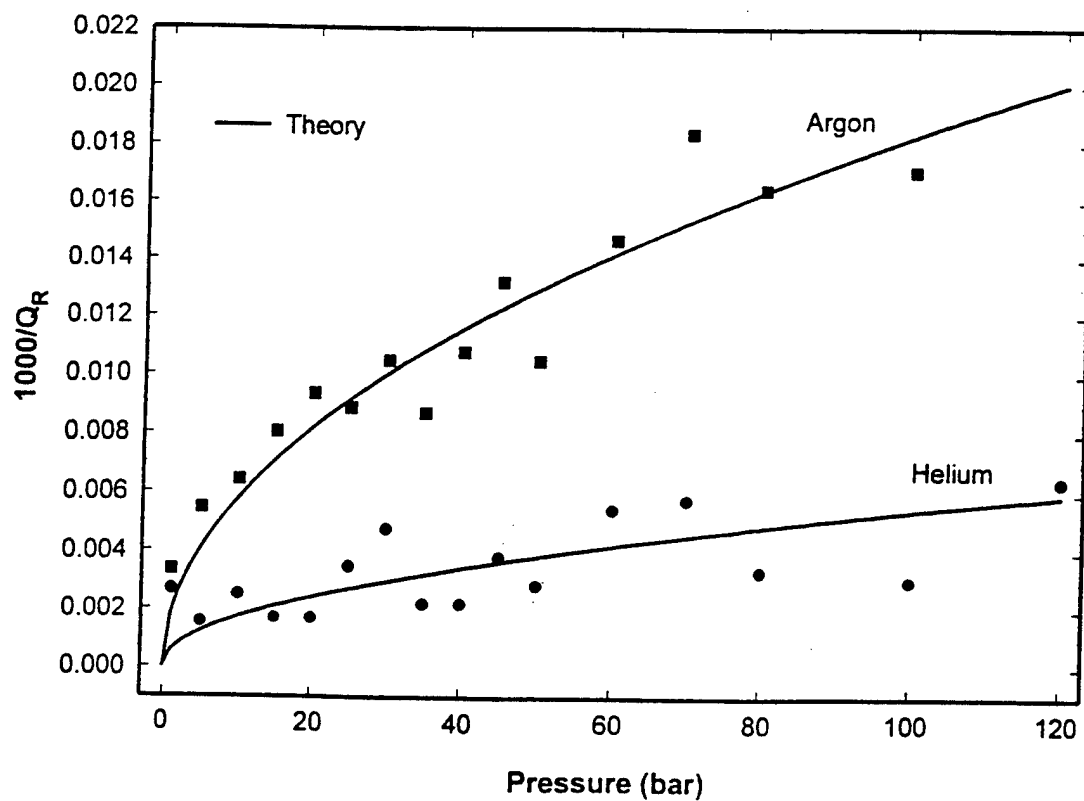
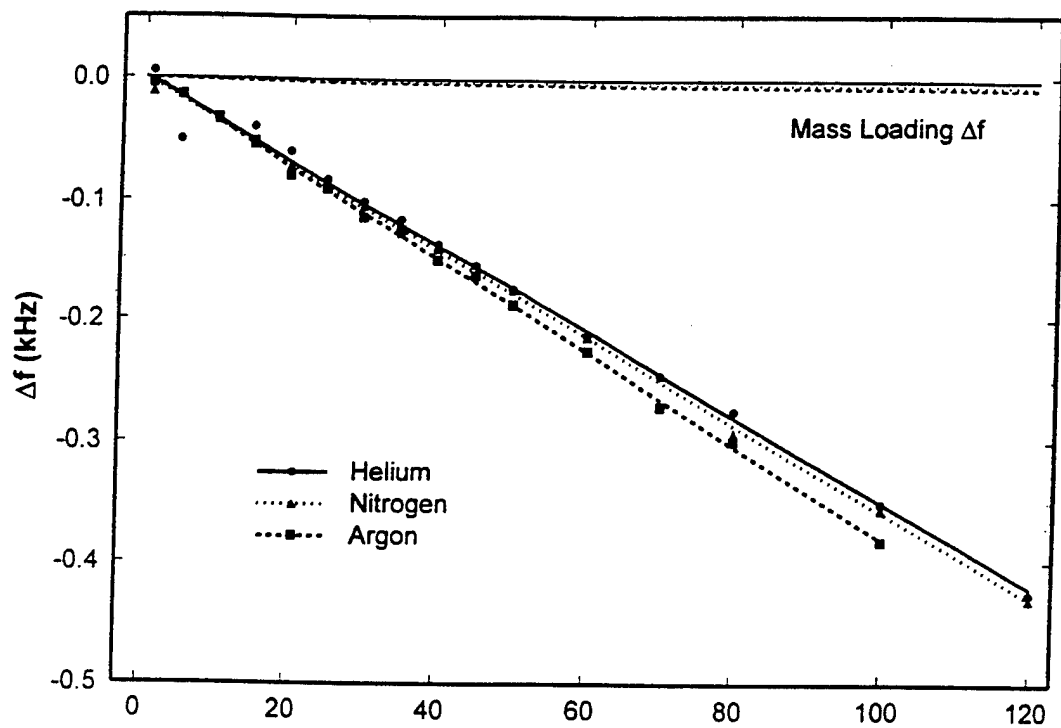
$$F(\omega) = -i \omega Z$$

where $F(\omega) = T_{\phi r}(u_\phi) / u_\phi = \mu(k j_l''(ka) - j_l(ka)/a) / j_l(ka)$, and

$$Z = \frac{\mu_g}{\delta} (1+i)$$

Note $Z \propto p^{1/2}$ since μ_g is independent of p .

Fused Silica Sphere (Radius 2.414 mm) T02 Mode



CONCLUSION

- Our radiation impedance analysis gives results in rather good agreement with measured Q values. Our frequency shifts Δf are much smaller than the measured values, which implies that the measured Δf are not due to mass loading by the surrounding gas. This is consistent with the data on the T02 mode, where there is very little dependence of Δf on gas species. However, the measured Δf for the S11 and S00 modes show large contributions to Δf that depend on gas species, and this is perplexing.
- All effects of gas loading are contained in Z, from which we can obtain

$$\Delta f/f = \text{Im } Z(\omega_0) / F'(\omega_0)$$

$$1/Q = 2 \text{ Re } Z(\omega_0) / F'(\omega_0)$$

where all relevant details of the elastic medium for the unloaded case are contained $F'(\omega_0)$.

- The last two relations give the very general result

$$\frac{\Delta f/f}{1/Q} = \frac{\text{Im } Z(\omega_0)}{2 \text{ Re } Z(\omega_0)}$$

which can be applied to samples of more general shape, provided that the appropriate Z is calculated for such samples.

Helmholtz Radiation from a Parallelepiped with sides a, b and c centered at the origin.

Assume a rigid structure vibrating with surface velocities given by

$$u_z^o(x, y), \quad u_x^o(y, z), \quad u_y^o(z, x).$$

Ansatz: The pressure outside the piped can be expressed as

$$p(\vec{r}) = -i k \rho c \iint d\sigma \frac{e^{i k R}}{2 \pi R} \hat{n} \cdot \vec{u}(\vec{r}_0)$$

where $R = \sqrt{(x-x_0)^2 + (y-y_0)^2 + (z-z_0)^2}$
and the integration is over the surface of the parallelepiped.

B.C. at
 $\vec{r} = \infty$
okay

Consider the face at $z = c/2$.

This face contributes a term

$$-i k \rho c u_z(x, y)$$

to

$$\hat{n} \cdot \vec{\nabla} p \Big|_{z=c/2} = -i k \rho c u_z^o(x, y) = -\frac{\partial}{\partial z} p.$$

There are also contributions to $-\frac{\partial}{\partial z} p$

from the other faces of the parallelepiped,

$$u_z^o(x, y) = u_z(x, y) - \frac{\partial}{\partial z} \iint_{\{ \neq c/2 \}} d\sigma \frac{e^{i k R}}{2 \pi R} \hat{n} \cdot \vec{u} \Big|_{z=c/2}$$

where the integration is over all of the faces except the one at $z = c/2$.

Computational Scheme:

Make initial guesses for u_x, u_y, u_z ,
and use

$$u_z^{(j+1)}(x, y) = u_z^0(x, y) + \frac{\partial}{\partial z} \iint_{\{x=\frac{a}{2}\}} d\sigma_0 \frac{e^{ikR}}{2\pi R} \hat{n} \cdot \vec{u}^{(j)} \Big|_{z=\frac{c}{2}}$$

$$u_x^{(j+1)}(y, z) = u_x^0(y, z) + \frac{\partial}{\partial x} \dots, \text{ etc.}$$

to iterate to self-consistent solutions
of these equations.

Difficulties: The integrals over the
faces adjacent to the $z = c/2$ face
have logarithmic singularities at
the edges; $z = c/2 + x = a/2$, $z = c/2 + y = b/2$, etc.

Consider

$$\begin{aligned} & - \frac{\partial}{\partial z} \int_{-b/2}^{b/2} dy_0 \int_{-c/2}^{c/2} dz_0 \frac{e^{ikR}}{2\pi R} u_x(y_0, z_0) \Big|_{x=a/2} \\ &= \int_{-b/2}^{b/2} dy_0 \int_{-c/2}^{c/2} dz_0 \left(\frac{\partial}{\partial z_0} \frac{e^{ikR}}{2\pi R} \right) u_x(y_0, z_0) \\ &= \int_{-b/2}^{b/2} dy_0 \frac{e^{ikR}}{2\pi R} u_x(y_0, z_0) \Big|_{z_0=c/2} + (\dots) \end{aligned}$$

Solution: Compute for $z = c/2 + h$
where h is a small positive length.
Set $h = 0$ for the calculation of

Determining the Radiation Impedance for Arbitrarily Shaped Surfaces

J. D. Maynard and Jason White
The Pennsylvania State University

Technology Issue

Calculate the sound radiation (acoustic impedance) for a vibrating surface.

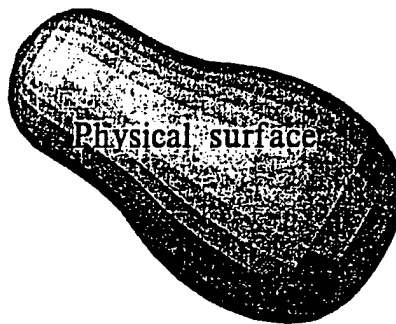
Applications

- Noise control
- Improving sound radiation from hi-fi speakers, musical instruments, etc.
- Fluid loading (Resonant Ultrasound Spectroscopy for samples under pressure)

Objective

Develop a method for calculating the acoustic impedance for a vibrating surface with an arbitrary shape.

Acoustic impedance for a vibrating surface



Physical surface with surface normal velocity $v(\vec{r}_S) e^{-i\omega t} = \hat{n} \cdot \vec{v}(\vec{r}_S) e^{-i\omega t}$

Wave Eqn. $\nabla^2 P - 1/c^2 \partial^2 P / \partial t^2 = 0 \rightarrow$ Helmholtz Eqn. $\nabla^2 P + k^2 P = 0$, $k = \omega/c$.

Boundary value problem: $v(\vec{r}_S)$ determines unique solution $P(\vec{r})$

Evaluate $P(\vec{r})$ at $\vec{r} = \vec{r}_S$. Acoustic impedance is $Z(\vec{r}_S) = P(\vec{r}_S) / v(\vec{r}_S)$.

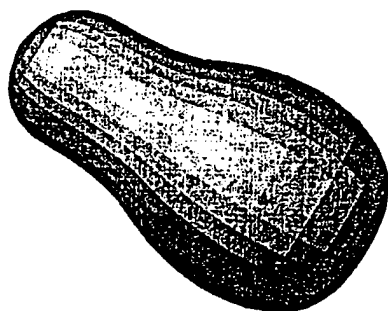
In RUS, $\text{Im}\{P(\vec{r}_S)\} = \text{Im}\{Z(\vec{r}_S)\} v(\vec{r}_S)$ gives stress boundary condition, shifts frequencies.

$1/2 \text{Re}\{P(\vec{r}_S)\} v(\vec{r}_S)$ gives dE/dt , the acoustic energy radiated to infinity. In RUS, quality factor $Q = \omega E / (dE/dt)$.

The Green's Function for the Boundary value Problem

Green's function $G(\vec{r})$ satisfies:

$$\nabla^2 G + k^2 G = -4\pi\delta(\vec{r})$$



AND $G(\vec{r}_S) = 0$ or $\hat{n} \cdot \vec{\nabla} G(\vec{r}_S) = 0$
on the boundary \vec{r}_S .

Solution: $P(\vec{r}) = \int \int v(\vec{r}_S) G(\vec{r} - \vec{r}_S) d\vec{r}_S$. NOTE: $G(\vec{r} - \vec{r}_S) \neq \frac{e^{ikR}}{R}$!

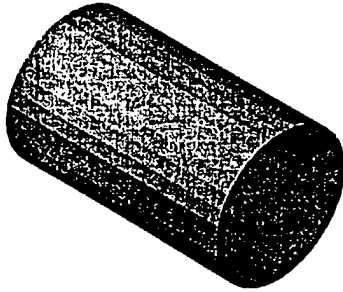
The Green's function may be found if the boundary surface corresponds to the level surface of a separable coordinate system.

The Helmholtz eqn. has **Eleven separable coordinate systems**



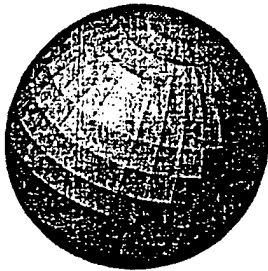
Cartesian coordinates x, y, z

$$e^{i(k_x x + k_y y + k_z z)}$$



Cylindrical coordinates ρ, ϕ, z

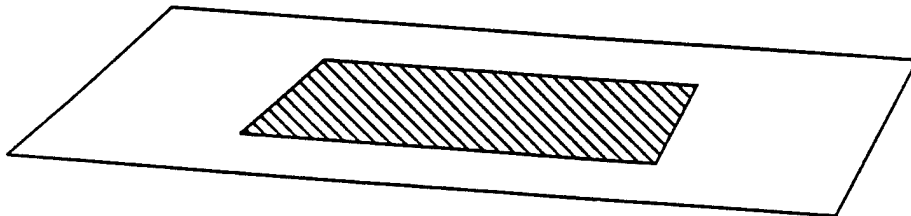
$$H_m(k_\rho \rho) e^{im\phi} e^{ik_z z}$$



Spherical coordinates r, θ, ϕ

$$h_m(kr) e^{im\phi} P_l^m(\cos \theta)$$

Cartesian coordinates x, y, z



General soln.
$$P(x, y, z) = \frac{1}{4\pi^2} \int \int A(k_x, k_y) e^{i(k_x x + k_y y + k_z z)} dk_x dk_y$$

Surface velocity
$$v(x, y) = \frac{1}{i\rho c k} \frac{\partial P}{\partial z} (z = 0)$$

$$= \frac{1}{4\pi^2} \int \int \left[A(k_x, k_y) \left(\frac{k_z}{\rho c k} \right) \right] e^{i(k_x x + k_y y)} dk_x dk_y$$

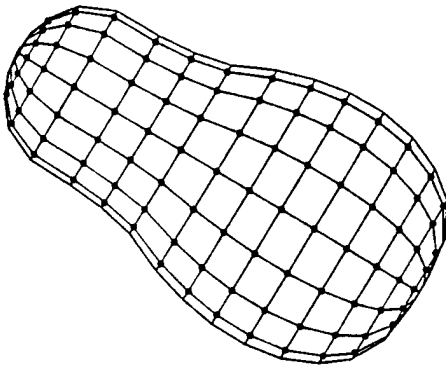
Fourier Transform
$$\hat{v}(k_x, k_y) = \int \int v(x, y) e^{-i(k_x x + k_y y)} dx dy$$

Solution
$$P(x, y) = \frac{1}{4\pi^2} \int \int \left[\rho c \hat{v}(k_x, k_y) \left(\frac{k}{k_z} \right) \right] e^{i(k_x x + k_y y)} dk_x dk_y$$

Arbitrarily Shaped Sources

NOT level surface of a sep. coord. sys.

Must find the Green's function numerically



Use discrete points

OR

Use isoparametric boundary elements

Green's Thm.
$$P(\vec{r}) = \int \int \left[P(\vec{r}_S') \hat{n} \cdot \vec{\nabla} G(\vec{r} - \vec{r}_S') - i v(\vec{r}_S') G(\vec{r} - \vec{r}_S') \right] d r_S'$$

where $G(R) = e^{ikR}/R$ with $R = |\vec{r} - \vec{r}_S|$.

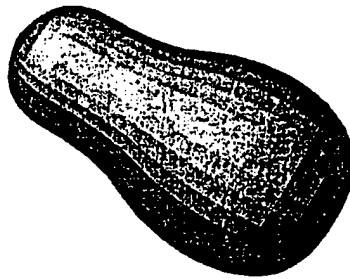
Evaluate at $\vec{r} = \vec{r}_S \rightarrow$ Surface Helmholtz Integral Equation (SHIE)

$$P(\vec{r}_S) = \int \int \left[P(\vec{r}_S') \hat{n} \cdot \vec{\nabla} G(\vec{r}_S - \vec{r}_S') - i v(\vec{r}_S') G(\vec{r}_S - \vec{r}_S') \right] d r_S'$$

Integral eqn for $P(\vec{r}_S)$. Discretization \rightarrow matrix eqn. Invert to find $P(\vec{r}_S)$.

Problems with the Surface Helmholtz Integral Equation

- e^{ikR}/R is singular when $\vec{r}_S' = \vec{r}_S$
- At certain frequencies, there are **interior resonances** corresponding to eigenfunctions which are zero on the surface.



There is no unique solution to the SHIE; the matrices are singular and cannot be inverted!

There are methods for avoiding the interior resonances; e.g. the Combined Helmholtz Integral Eqn. Formulation (CHIEF), where the field at selected points in the interior are required to be zero. All such methods are messy, because they require user intervention to select interior points, etc., and the computer codes are long and complicated.

Solution to the Arbitrarily Shaped Surface Problem

With accessible high-speed computers, there is an **Easy Solution**

Index surface points with 'j'. Let $P_j = P(\vec{r}_{Sj})$.

Any solution to the Helmholtz eqn. may be expanded as series of eigenfunctions, e.g. spherical wavefunctions:

$$P(\vec{r}) = \sum_l \sum_m A_{lm} h_l(kr) e^{im\phi} P_l^m(\cos\theta)$$

Let the index ν represent (l, m) . Let $M_{j\nu} = h_l(kr_j) e^{im\phi_j} P_l^m(\cos\theta_j)$. Then

$$P_j = M_{j\nu} A_\nu$$

Invert matrix to find $A_\nu = [M_{j\nu}]^{-1} P_j$. FINISHED!

Added Benefit! By using eigenfunctions which only radiate outward, the problem of interior resonances is entirely avoided!

Why not before? If not level surface, then many evaluations of h_l , etc., and no FFT's. Not viable for on-site noise-control engineers.

Determining the change of Q in RUS due to fluid loading

$$\frac{1}{Q} = \frac{1}{\omega E} \frac{dE}{dt}$$

$$E = \frac{1}{2} abc \sum_{\mu} \sum_{\nu} [\rho \omega^2 E_{\mu\nu} + \Gamma_{\mu\nu}] a_{\mu} a_{\nu}$$

$$\frac{dE}{dt} = \frac{1}{2} \int \int P(r_S) v(r_S) d^2r$$

$$= \frac{1}{2} \sum_i P_i v_i A_i$$

$$= \frac{1}{2} \sum_i \left[\rho c \sum_j M_{ij} v_j \right] v_i A_i$$

$$= \frac{1}{2} \rho c \omega^2 \sum_i \sum_j M_{ij} \psi_i \psi_j A_i$$

Determining the change of Q in RUS due to fluid loading

$$\begin{aligned}\frac{1}{Q} &= \frac{1}{\omega E} \frac{1}{2} \rho c \omega^2 \sum_i \sum_j M_{ij} \psi_i \psi_j A_i \\ &= \frac{\rho c}{\rho_{SCS}} \sum_i \sum_j M_{ij} \left[\sqrt{\frac{\rho_{SCS} \omega A}{2E}} \psi_i \right] \left[\sqrt{\frac{\rho_{SCS} \omega A}{2E}} \psi_j \right] \left(\frac{A_i}{A} \right)\end{aligned}$$

In RUS: $\psi_i = \sum_{\mu} a_{\mu} \Phi_{\mu}(\vec{r}_i)$

Normalize a_{μ} with $\sqrt{\frac{\rho_{SCS} \omega A}{2E}}$

Solving Boundary Value Problems with Spherical Wavefunctions

J. D. Maynard, The Pennsylvania State University

Assume a time dependence $\exp(-i\omega t)$ and a complex sound pressure field $P(\vec{r}) = \text{Re}\{P(\vec{r})\} + i\text{Im}\{P(\vec{r})\}$ satisfying the Helmholtz equation with wavevector $k = \omega/c$. The complex particle velocity field is

$$\vec{v}(\vec{r}) = \frac{1}{i\rho ck} \vec{\nabla} P(\vec{r}) \quad (1)$$

Using separation of variables, we find a complete set of complex linearly independent functions which radiate out to infinity (an important boundary condition). With three space variables, there must be two independent constants of separation and two mode labels. Thus we can write for these basis functions:

$$\nabla^2 \Phi_{lm}(\vec{r}) + k^2 \Phi_{lm}(\vec{r}) = 0 \quad (2)$$

Any solution to a radiation problem may be written as a linear combination of these functions:

$$P(\vec{r}) = \sum_l \sum_m A_{lm} \Phi_{lm}(\vec{r}) \quad (3)$$

Let $A_{lm} = a_{lm} + ib_{lm}$ and $\Phi_{lm}(\vec{r}) = R_{lm}(\vec{r}) + iS_{lm}(\vec{r})$, where the new constants and fields are purely real. Now

$$P(\vec{r}) = \sum_l \sum_m [(a_{lm} R_{lm}(\vec{r}) - b_{lm} S_{lm}(\vec{r})) + i(a_{lm} S_{lm}(\vec{r}) + b_{lm} R_{lm}(\vec{r}))] \quad (4)$$

The known boundary condition is the normal component of the particle velocity at a surface given by points \vec{r}_s . Note that the known surface velocity is purely real. We let the known data be given by the real function defined by

$$f(\vec{r}_s) = \rho c \hat{n}(\vec{r}_s) \cdot \vec{v}(\vec{r}_s) \quad (5)$$

where $\hat{n}(\vec{r}_s)$ is the unit normal at the surface point \vec{r}_s . Combining Eqs. 1, 4, and 5, we have

$$f(\vec{r}_s) = \sum_l \sum_m \left[a_{lm} \left(\frac{1}{k} \hat{n}(\vec{r}_s) \cdot \vec{\nabla} S_{lm}(\vec{r}_s) \right) + b_{lm} \left(\frac{1}{k} \hat{n}(\vec{r}_s) \cdot \vec{\nabla} R_{lm}(\vec{r}_s) \right) \right]$$

$$\begin{aligned}
& -i \sum_l \sum_m \left[a_{lm} \left(\frac{1}{k} \hat{n}(\vec{r}_s) \cdot \vec{\nabla} R_{lm}(\vec{r}_s) \right) - b_{lm} \left(\frac{1}{k} \hat{n}(\vec{r}_s) \cdot \vec{\nabla} S_{lm}(\vec{r}_s) \right) \right] \\
& = \sum_l \sum_m [(a_{lm} S'_{lm}(\vec{r}_s) + b_{lm} R'_{lm}(\vec{r}_s)) - i(a_{lm} R'_{lm}(\vec{r}_s) - b_{lm} S'_{lm}(\vec{r}_s))] \quad (6)
\end{aligned}$$

where $R'_{lm}(\vec{r}_s) = (1/k) \hat{n}(\vec{r}_s) \cdot \vec{\nabla} R_{lm}(\vec{r}_s)$ and $S'_{lm}(\vec{r}_s) = (1/k) \hat{n}(\vec{r}_s) \cdot \vec{\nabla} S_{lm}(\vec{r}_s)$.

Since $f(\vec{r}_s)$ is purely real, the imaginary part of the left hand side of Eq. 6 must vanish, and we have

$$\sum_l \sum_m a_{lm} R'_{lm}(\vec{r}_s) = \sum_l \sum_m b_{lm} S'_{lm}(\vec{r}_s) \quad (7)$$

Now assume that the normal component of the particle velocity field is known at a finite set of discrete points \vec{r}_s with $s = 1, 2, 3, \dots, N$. We simplify notation by writing $f(\vec{r}_s) = f_s$, and similarly for other functions of \vec{r}_s . We use the symbol u as an index similar to s . We also simplify notation by letting the one integer μ index the two subscripts l and m : $\mu = [l(\mu), m(\mu)]$. We truncate to a finite number of basis functions, so that $\mu = 1, 2, 3, \dots, L$. Let ν be an index similar to μ . Finally, we use the convention that an index repeated in a term indicates a sum over that index. Now we can rewrite Eqs. 6 and 7 as

$$f_s = S'_{s\mu} a_\mu + R'_{s\mu} b_\mu \quad (8)$$

$$R'_{s\mu} a_\mu = S'_{s\mu} b_\mu \quad (9)$$

Now f_s is a vector of length N , a_μ and b_μ are vectors of length L , and $R'_{s\mu}$ and $S'_{s\mu}$ are N by L matrices. We shall have $N > L$, so that the matrices are not square. The method of Singular Value Decomposition (SVD) allows one to find the inverse of such matrices. Let $T_{\nu u}$ be the inverse of $S'_{s\mu}$. Multiplying Eq. 9 by $T_{\nu u}$ solves for the vector b in terms of the vector a :

$$b_\nu = T_{\nu u} R'_{u\mu} a_\mu \quad (10)$$

Substituting Eq. 10 into Eq. 8 yields

$$f_s = (S'_{s\mu} + R'_{s\nu} T_{\nu u} R'_{u\mu}) a_\mu \quad (11)$$

Use SVD a second time to find the inverse of the matrix in parentheses in Eq. 11. Indicating this inverse with $Q_{\mu s}$, we now have

$$a_\mu = Q_{\mu s} f_s \quad (12)$$

This is equivalent¹ to adjusting the coefficients a_μ to least-squares fit the boundary data f_s . With Eq. 10 we also have b_μ . From Eq. 4 we have

$$\operatorname{Re}\{P(\vec{r}_s)\} = R_{s\mu}a_\mu - S_{s\mu}b_\mu \quad (13)$$

$$\operatorname{Im}\{P(\vec{r}_s)\} = S_{s\mu}a_\mu + R_{s\mu}b_\mu \quad (14)$$

With $P(\vec{r}_s)$ and $f(\vec{r}_s) = \rho c \hat{n}(\vec{r}_s) \cdot \vec{v}(\vec{r}_s)$, all other acoustic quantities may be calculated using closed-form expressions.

We shall separate variables in spherical coordinates (r, θ, ϕ) but \vec{r}_s and $\hat{n}(\vec{r}_s)$ will be given in cartesian coordinates (x, y, z) . We shall make all lengths non-dimensional by multiplying by the wavenumber $k = \omega/c$. We simplify notation by letting $kx \rightarrow x$, $ky \rightarrow y$, $kz \rightarrow z$, $kr \rightarrow r$, and $(1/k)\vec{\nabla} \rightarrow \vec{\nabla}$. We also define $\zeta = \cos \theta$. We have

$$r = \sqrt{x^2 + y^2 + z^2} \quad \phi = \tan^{-1}(y/x) \quad \zeta = z/r \quad (15)$$

$$\begin{aligned} \frac{\partial r}{\partial x} &= \frac{x}{r} & \frac{\partial r}{\partial y} &= \frac{y}{r} & \frac{\partial r}{\partial z} &= \frac{z}{r} \\ \frac{\partial \phi}{\partial x} &= \frac{-y}{x^2 + y^2} & \frac{\partial \phi}{\partial y} &= \frac{x}{x^2 + y^2} & \frac{\partial \phi}{\partial z} &= 0 \\ \frac{\partial \zeta}{\partial x} &= \frac{-xz}{r^3} & \frac{\partial \zeta}{\partial y} &= \frac{-yz}{r^3} & \frac{\partial \zeta}{\partial z} &= \frac{x^2 + y^2}{r^3} \end{aligned} \quad (16)$$

With $\hat{n}(\vec{r}) = (n_x, n_y, n_z)$, we make the following definitions:

$$h_r(x, y, z) = n_x \frac{\partial r}{\partial x} + n_y \frac{\partial r}{\partial y} + n_z \frac{\partial r}{\partial z} \quad (17)$$

$$h_\phi(x, y, z) = n_x \frac{\partial \phi}{\partial x} + n_y \frac{\partial \phi}{\partial y} + n_z \frac{\partial \phi}{\partial z} \quad (18)$$

$$h_\zeta(x, y, z) = n_x \frac{\partial \zeta}{\partial x} + n_y \frac{\partial \zeta}{\partial y} + n_z \frac{\partial \zeta}{\partial z} \quad (19)$$

We now have

$$\hat{n} \cdot \vec{\nabla} = h_r \frac{\partial}{\partial r} + h_\phi \frac{\partial}{\partial \phi} + h_\zeta \frac{\partial}{\partial \zeta} \quad (20)$$

Separating variables in spherical coordinates yields the spherical wave functions:

$$\Phi_{lm}(r, \theta, \phi) = (j_l(r) + iy_l(r))(\cos m\phi + i \sin m\phi) Y_{lm}(\cos \theta) \quad (21)$$

where

$$Y_{lm}(\zeta) = \sqrt{\frac{2l+1}{4\pi} \frac{(l-m)!}{(l+m)!}} P_l^m(\zeta) \quad (22)$$

The j_l and y_l are the spherical Bessel functions, and the P_l^m are the associated Legendre polynomials. The Y_{lm} are similar to the spherical harmonics, but with the ϕ dependence removed; the ϕ dependence is included explicitly in Eq. 21.

Note that $-l \leq m \leq l$. Eq. 22 is for $m \geq 0$ only; for $m < 0$, we use the Condon and Shortley phase: $Y_{l,-m}(\zeta) = (-1)^m Y_{lm}(\zeta)$.

We truncate the number of basis functions by letting L_{\max} be the highest order for the spherical Bessel functions. The the total number of basis functions is

$$L = \sum_{l=0}^{L_{\max}} (2l+1) = (L_{\max} + 1)^2 \quad (23)$$

The real and imaginary parts of Φ_{lm} are

$$R_{lm}(r, \phi, \zeta) = (j_l(r) \cos m\phi - y_l(r) \sin m\phi) Y_{lm}(\zeta) \quad (24)$$

$$S_{lm}(r, \phi, \zeta) = (j_l(r) \sin m\phi + y_l(r) \cos m\phi) Y_{lm}(\zeta) \quad (25)$$

We now have

$$\frac{\partial R_{lm}}{\partial r} = (j'_l(r) \cos m\phi - y'_l(r) \sin m\phi) Y_{lm}(\zeta) \quad (26)$$

$$\frac{\partial R_{lm}}{\partial \phi} = -m (j_l(r) \sin m\phi + y_l(r) \cos m\phi) Y_{lm}(\zeta) \quad (27)$$

$$\frac{\partial R_{lm}}{\partial \zeta} = (j_l(r) \cos m\phi - y_l(r) \sin m\phi) Y'_{lm}(\zeta) \quad (28)$$

$$R'_{lm}(r, \phi, \zeta) = h_r \frac{\partial R_{lm}}{\partial r} + h_\phi \frac{\partial R_{lm}}{\partial \phi} + h_\zeta \frac{\partial R_{lm}}{\partial \zeta} \quad (29)$$

and similar expressions for S_{lm} and S'_{lm} .

It should be noted that h_ϕ is singular when $x = y = 0$. Also, $Y'_{l,\pm 1}(\zeta)$ is singular when $\zeta = \pm 1$ (i.e. when $x = y = 0$). When these singularities occur, Y_{lm} is zero and h_ζ is zero. The zeros dominate except when $m = \pm 1$. After some algebra, we find that when $x = y = 0$ ($\zeta = \pm 1$ and ϕ is undefined) and $m = \pm 1$, then

$$\begin{aligned}
R'_{lm}(r, \zeta) &= -\frac{1}{z} (j_l(r) n_x - y_l(r) m n_y) \left(\sqrt{1 - \zeta^2} Y'_{lm}(\zeta) \right) \\
&= -\frac{1}{z} (j_l(r) n_x - y_l(r) m n_y) \left(\frac{m}{2} l(l+1) \zeta^l \right)
\end{aligned} \tag{30}$$

$$\begin{aligned}
S'_{lm}(r, \zeta) &= -\frac{1}{z} (j_l(r) m n_y + y_l(r) n_x) \left(\sqrt{1 - \zeta^2} Y'_{lm}(\zeta) \right) \\
&= -\frac{1}{z} (j_l(r) m n_y + y_l(r) n_x) \left(\frac{m}{2} l(l+1) \zeta^l \right)
\end{aligned} \tag{31}$$

The spherical Bessel functions and the associated Legendre functions may be calculated by computer using the upward and downward recursion relations as in Ref. 1. The derivatives of the functions may also be found by computer using the following relations:

$$j'_l(r) = j_{l-1}(r) - (l+1) j_l(r) / r$$

and when $\zeta \neq \pm 1$ and $0 \leq m \leq l$,

$$Y'_{lm}(\zeta) = \frac{1}{1 - \zeta^2} ((l+m) Y_{l-1,m}(\zeta) - l \zeta Y_{lm}(\zeta))$$

Note that if $|m| > l$, then $Y_{lm}(\zeta) = 0$. In a computer program which calculates the associated Legendre functions care must be taken when $\zeta = \pm 1$. In particular, the limiting value indicated in Eqs. 30 and 31 should be used rather than the singularity.

1. W. H. Press, S. A. Teukolsky, W. T. Vetterling, and B. P. Flannery, *Numerical Recipes* (Cambridge University Press, Cambridge, 1992).

**Temperature dependency of elastic moduli of
spinel MgAl_2O_4 by the resonant sphere
technique, RST**

1997.5.12.

Resonance Meeting, Pacific Grove, California, May 11-15

Isao Suzuki, Ichiro Ohno* and Orson L. Anderson**

Department of Earth Sciences, Faculty of Science,
Okayama University, 1 - 1 Tsushima-naka-3, Okayama, 700 Japan

*Department of Earth Sciences, Faculty of Science,
Ehime University, Bunkyou-cho 2-5 , Matsuyama, 790-77 Japan

**Institute of Geophysics and Planetary Physics,
University of California, Los Angeles, California 90095-1567,
U.S.A.

ABSTRACT:

The resonant sphere technique, RST, was applied to measure elastic moduli of spinel single crystal sphere with 3.6675 mm in diameter. Resonance frequency of 23 modes were measured between 293 and 1200 K. As similar to previous measurement for a rectangular prism specimen (Suzuki and Anderson, 1982), resonance frequencies of all modes decrease with temperature, and some of them show discontinuous change of slopes near 904 K, whereas some other modes do not show the change clearly.

Inversion of the frequency data provide us a set of independent elastic moduli of K_s , C_s and C_{44} (or another set of C_{11} , C_{12} and C_{44}) as a function of temperature. The standard error of observed frequency after iterative calculation is $\sigma = 0.16\text{kHz}$ (ca. 0.012%). Therefore, estimated probable errors of these moduli are very small as compared with those in previous measurements with RST.

Elastic moduli of the spinel specimen with density $\rho = 3.5846\text{ g/cm}^3$ at 293K (20 °C) and their probable errors are:

$$C_{11} = 281.31 \pm 0.01$$

$$C_{12} = 155.43 \pm 0.01$$

$$C_{44} = 154.588 \pm 0.007$$

and $C_s = 62.936 \pm 0.003$ in GPa. The anisotropy factor is $A = C_{44}/C_s = 2.4561$, which is much larger than that of MgO ($A = 1.55$) and CaO ($A = 0.98$). Isotropic properties are

$$K_s = 197.39 \pm 0.01,$$

and $\mu = 107.81$ (Hill average).

Combining with thermal expansion data, we can evaluate anharmonic parameters. For example:

	Gruneisen parameter	Anderson-Gruneisen parameter	
	$\gamma =$	$\delta_s =$	$\delta_T =$
at 300K	1.16	2.98	4.72
1,200K	1.17	4.46	6.37

One of shear moduli, C_{44} , do not have clear discontinuity in the slope against temperature, whereas another shear modulus $C_s (= (C_{11} - C_{12})/2)$ has distinctive bend at 904 K, and bulk modulus $K_s (= (C_{11} + 2C_{12})/3)$ has intermediate between those, because of opposite change of slopes in C_{11} and C_{12} above 904 K.

Deviation at 904 K from assumed linear tendency is about 2 % for C_s and less for the other moduli. The abrupt change of the Gruneisen parameter at 904K is $\Delta\gamma = 0.1$, mostly due to lambda transition in thermal expansion coefficient.

Preliminary MD calculation shows that the second order transition may be caused by the site preference of magnesium ions to octahedral sites at high temperature.

KEY WORDS:

resonant sphere technique, RST, anisotropy, elasticity, spinel, thermal expansion

Introduction

Elasticity and its pressure and temperature dependency of minerals is greatly important in study for constituents and their state in the Earth interior. For the measurement of elasticity, we take notice of a resonance method adopting a sphere shape for specimens, no matter which they are isotropic or anisotropic. This method may be called the resonant sphere technique, or RST and is advanced in these years for anisotropic materials. The sphere shape of specimens in the resonance method brings many advantages in measurement of elasticity and anelasticity (Suzuki et al., 1991, 1992).

In the Earth's mantle, one of major constituents of orthosilicate, olivine, changes its structure having high density, as demonstrated by many high pressure experiments. The phase is called as the gamma-phase and has been greatly taken notice of (e.g., Suzuki et al., 1979-a). Its crystal structure is the same as spinel MgAl_2O_4 . The gamma-phase is not stable at ambient pressure, and much attention has been focused on spinel, MgAl_2O_4 as its analogue

Spinel MgAl_2O_4 is also one of important minerals for practical uses, and many physical properties have been measured. A clear inflection point is found at 933 K in the linear expansion curve of spinel (Suzuki and Kumazawa, 1982), and such inflection was also found in electrical conductivity near the temperature (Weeks and Sonder, 1980). Crystal structure was studied extensively (e.g., Yamanaka and Takeuchi, 1982) and they suggested an order-disorder phase change due to preferred site occupation of cations.

Temperature change of elasticity was once measured for the rectangular prism specimen, and the similar change was confirmed in elasticity change (Suzuki and Anderson, 1982), though some systematic deviation of frequency had brought in some ambiguity. In the present measurements, we used a synthetic specimen of

spinel shaped into an accurate sphere. Frequency changes of it were traced up to 1,167 K well above the transition temperature.

Data Reduction

In order to deduce elastic moduli C_{ij} from resonant frequencies, it is necessary to compute accurately enough the eigenfrequencies of the specimen, since the deduction is made by comparing the measured resonant frequencies with reference eigenfrequencies given by the elastic moduli assumed on the specimen. Theoretical evaluation of eigenfrequencies for anisotropic materials is described elsewhere (Michizuki, 1988; Isoda et al., 1990)

In order to obtain elastic moduli from n 's observed resonance frequencies, the residual equations are defined as:

$$\Delta f_k = \sum_{ij} \left(\frac{\partial f_k}{\partial C_{ij}} \right) \Delta C_{ij} + \delta_k$$

$$(k = 1, 2, 3 \dots n)$$

where $\Delta f_k = f_k - f_k^o$ is difference of observed frequency f_k and computed reference frequency f_k^o for the k - th mode, $\Delta C_{ij} = C_{ij} - C_{ij}^o$ is difference of specimen's elastic moduli C_{ij} and assumed values of reference elastic moduli C_{ij}^o (e.g., Chang and Barsch, 1973), δ_k is residual of the k - th mode. Summation is made for possible numbers of i and j satisfying a relation $i \leq j$. The f_k^o and $\partial f_k / \partial C_{ij}$ are computed by using the reference elastic moduli C_{ij}^o , dimension and mass of the specimen. The ΔC_{ij} are the unknowns to be determined by minimizing the squared sum of residuals, $\sum \delta_k^2$. The elastic moduli of the specimen are finally obtained by $C_{ij} = \Delta C_{ij} + C_{ij}^o$.

Experimental

Apparatus and specimen

The block diagram of the RST measurement system is shown in Figure 1. This system is basically not different from those shown in Fig.4 in Ohno (1976) or Figs. 1 and 2 in Sumino et al.(1976), when continuous wave (CW) method is applied for data acquisition. Recently further developments were made to realize the FT-method (Inouye, 1993; Fujio, 1995) and high pressure measurement (Ohno et al., 1993).

A synthetic boule of spinel was cut and shaped into a sphere with the so-called two-pipe method (Fraser and LeCraw, 1964). For accurate determination of elasticity, we try to make the relative error of diameter less than a few micro-meters.

Measurements

Resonance frequency under no external forces was obtained by measurements changing applied force to zero (Table 1). At higher temperature, frequency was measured under constant supporting force, of which effect was corrected with the frequency of zero-force at room temperature.

Temperature was measured with chromel-alumel thermocouples set very near to the specimen. Measurements of frequency were made for 23 modes between room temperature 293 K and 1173 K (Figure 2). Temperature intervals were about 30 K around the transition temperature and some tens Kelvin otherwise. Reproducibility was confirmed by measurements at several temperatures of the cooling run made at the close temperatures of the heating run. They do not show much difference from the heating run. Hysteresis is quite small, if possible.

Figure 3-a and -b compare the temperature dependency of frequency near the temperature of 904 K. Some of modes change clearly their slopes in both sides of the transition temperature.

Results

Elasticity

Elasticity of the spinel specimen is obtained by the least squares calculation mentioned above and listed in Table 2. Aggregate isotropic properties are obtained by the Voigt-Reuss-Hill averaging scheme (Kumazawa, 1964) and also listed. The iterative calculation was made, and this could reduced the standard error very much as shown in Table 2.

Temperature dependency of elastic moduli are shown in Figures 4 and 5. In the cubic symmetry, three of elastic moduli are independent. Least squares calculations using the modes with clear change of slopes and without those show that results are very close each other within errors, and this confirms the consistency of observed frequency data.

Anisotropy factor

Anisotropy factor of cubic symmetry is defined by the ratio of two shear moduli as

$$A = C_{44}/C_s$$

where C_s is a shear modulus defined by $C_s = (C_{11} - C_{12})/2$. The A of spinel is about 2.5. For isotropic materials, A is unity, and MgO and CaO have 1.11 and 1.22 respectively. Elastic properties of spinel is said to be quite anisotropic. Also, the A shows clear inflection at 904 K as shown in Figure 6.

Thermal expansion

Thermal expansion data of spinel is reproduced in Figure 7. Smoothed values of expansion coefficients are obtained applying the Gruneisen's theory of thermal expansion (Suzuki et al., 1979-b). Expansion coefficients just below the transition are expressed by a quadratic equation as shown in Figure 7. Inflection temperatures from thermal expansion measurement and frequency measurement are a little different, probably due to differences in

measurement system and specimen. In the calculation using thermal expansion data, this small discrepancy is adjusted by assignment of $\alpha(T_r) = 28.6 \times 10^{-6}/K$ and $\alpha(T_0) = 25.6 \times 10^{-6}/K$, where T_r is the transition temperature, $T_0 = 800$ K, and a function $\alpha(T - T_0)^2 + b(T - T_0) + \alpha_0$ is assumed between T_0 and T_r . The Grüneisen parameter is evaluated combining bulk modulus, thermal expansion and heat content data (Robie et al., 1978), and shown in Figure 8.

Discussion

In the present measurements, we can obtain accurate values of elastic moduli of spinel, and also we can trace temperature dependency of them precisely. Much of these are due to the sphere shape of the specimen. The xyz algorithm (Visscher et al., 1991) is useful for iterative calculation, when combined with the variational method for evaluation of $\partial f / \partial C_{ij}$ (Oda et al. 1993). This reduced the standard error very much as shown in Table 2. This magnitude of error is much smaller than those in previous reports by the resonance methods.

Two shear moduli of spinel, C_{44} and C_s are quite different in magnitude as shown in Figure 5 (b) and (d) and in Figure 6, and this causes large elastic anisotropy as compared with other cubic crystal, such as MgO and CaO. The C_s is less than a half of C_{44} , which means the structure is very compliant to shear stress parallel to [110] direction and this may be also the reason of large temperature effect on C_s and the phase transition.

Preliminary calculation with the MD method shows that magnesium ion in tetrahedral sites is easy to move to octahedral sites at high temperature (personal communication, Matsui 1997). This may be the reason of the transition at about 900 K.

Both of observed thermal expansion coefficient α and isothermal bulk modulus have discontinuities at the transition

temperature under ambient pressure. The boundary of the low and high temperature phases can be estimated: difference of isothermal bulk modulus at the transition temperature is 1 GPa or smaller, the boundary is about 100 GPa or higher at room temperature.

Acknowledgement: The authors are grateful to Dr. H. Oda and Mr. K. Yamada for the computation, and Messrs. S. Sawane and K. Ohno for their help in high temperature measurements. Discussion with Dr. A. Yoneda helps improve the contents.

References

- Chang Z. P. and Barsch, G. R., Pressure dependence of single crystal elastic constants and anharmonic properties of spinel, J. Geophys. Res., **78**, 2418-2433, 1973
- Fraser, D. B. and LeCraw, R. C., Novel method of measuring elastic and anelastic properties of solids, Rev. Sci. Instr., **35**, 1113-1115, 1964
- Fujio, T., FT-RST, Fourier Transform - Resonant Sphere Technique, (in Japanese), Mr. thesis, Okayama University, 1995
- Inouye, Y., "Development and application of the resonant sphere technique, Mr. thesis, Okayama University, pp.75, 1993
- Isoda, S., Oda, H., Suzuki, I. and Seya, K. Displacement distribution of a freely oscillating rutile sphere, " Tohoku Geophys. J. (Sci. Rep. Tohoku Univ., Ser.5) **32**, (3, & 4), 55-76, 1990
- Kumazawa, M., The elastic constants of rocks in terms of elastic constants of constituent mineral grains, petrofabric and interface structures, J. Earth Science, Nagoya University, **12**, 147-176, 1964
- Matsui, M., personal communication, 1997
- Mochizuki, E., Sphere resonance method to determine elastic constants of crystal, J. Appl. Phys., **63**, 5668-5673, 1988
- Oda, H., I. Suzuki and I. Ohno, Partial derivatives of eigenfrequencies of a rectangular parallelepiped and a sphere of elastically anisotropic solid, J. Phys. Earth, **41**, 271-289, 1993
- Ohno, I., Free vibration of a rectangular parallelepiped crystal and its application to determination of elastic constants of orthorhombic crystals, J. Phys. Earth, **24**, 355-379, 1976
- Ohno, I., Y. Hanayama, M. Kimura, I. Suzuki, H. Oda, and M. Kumazawa, "Pressure derivatives of elastic constants of iron by cavity resonance method," in High Pressure Science and

- Technology -1993, Part 1, pp.931-934, AIP Press, 1994
- Robie, R. A., Hemingway, B. S. and Fisher, J. R., Thermodynamic properties of minerals and related substances at 298.15K and 1 bar (10^5 pascals) pressure and at high temperature, U.S. Geol. Surv. Bull., 1452, pp.456, 1978
- Sumino, Y., I. Ohno, T. Goto and M. Kumazawa, "Measurement of elastic constants and internal friction of single-crystal MgO by rectangular parallelepiped resonance," J. Phys. Earth, 24, 263-273, 1976
- Suzuki, I., Ohtani, E. and Kumazawa, M., Thermal expansion of γ - Mg_2SiO_4 , J. Phys. Earth, 27, 53-61, 1979-a
- Suzuki, I., Okajima, S. and Seya, K., Thermal expansion of single-crystal manganosite, J. Phys. Earth, 27, 63-69, 1979-b
- Suzuki, I. and Kumazawa, M., Anomalous thermal expansion in spinel MgAl_2O_4 , Phys. Chem. Min., 5, 279-284, 1980
- Suzuki, I. and Anderson, O. L., abstract, Eos, Trans. Am. Geophys. Union, 1982
- Suzuki, I., Oda, H., Ohno, I. and Kumazawa, M., Resonant sphere technique determining anisotropic elastic moduli of single-crystal in wide range of physical conditions, The 28th Annual Technical Meeting of the Society of Engineering Science, Gainesville, Florida, ESP28.91021, p.1-10, 1991
- Suzuki, I., Inouye, Y., Hirao, J., Oda, H., Saito, T. and Seya, K., The resonant sphere technique for measurements of elasticity and anelasticity of a small mineral specimen: An application to olivine, Zisin (J. Seism. Soc. Japan), 45, 213-228, 1992
- Visscher, W. M., A. Migliori, T. M. Bell and R. B. Reinert, On the normal modes of free vibration of inhomogeneous and anisotropic elastic objects," J. Acoust. Soc. Am., 90, 2154-2162, 1991
- Weeks, R. A. and Sonder, E., Electrical conductivity of pure and Fe-doped magnesium-aluminum spinel, Am. Ceramic Soc., 63, 92-95, 1980
- Yamanaka, T. and Takeuchi, Y., Thermal atomic displacement in the structure of MgAl_2O_4 and silicate spinels, p.61-72, in The Japan. Assoc. Mining Petrol. Economic Geology, special issue ed. by I. Sunagawa and K. Aoki, Sendai, Japan, 1982

Table 1. Observed frequency of the spinel specimen
with diameter 3.6675mm.

no.	mode	f ^o /kHz
1	Eg -1	977.25
2	T2u-1	1003.16
3	Eu -1	1390.13
4	T1u-1	1414.93
5	A2g-1	1432.84
6	T2g-1	1465.34
7	T2g-2	1748.48
8	T1g-1	1834.20
9	T1u-2	1919.90
10	Eg -2	1933.64
11	T2u-2	1987.20 *
12	T2u-3	2096.48
13	A1g-1	2107.10
14	A2u-1	2202.08
15	T1g-2	2238.40
16	Eu -2	2280.10 =
17	A1g-2	2280.10 =
18	T1u-3	2400.88
19	Eg -3	2435.85
20	T2g-3	2507.80
21	T2u-4	2546.30
22	T1g-3	2608.55
23	T2g-4	2652.35
24	Eg -4	2691.70
25	Alu-1	2708.00

*: not observed at high temperatures

=: cannot be distinguished

Table 2. Elasticity of single crystal spinel MgAl_2O_4
with density $\rho=3584.6 \text{ Mg/m}^3$,
and its aggregate properties, at 293K.

Single crystal elastic properties in GPa

K_s	197.395	± 0.013
C_s	62.936	± 0.003
C_{44}	154.587	± 0.007
C_{11}	281.310	± 0.014
C_{12}	155.437	± 0.013

standard deviation in the least squares
calculation $\sigma=0.16/\text{kHz}$

Isotropic properties of the Hill average

bulk modulus	$K_s=197.39$	GPa
rigidity modulus	$\mu=107.806$	GPa
Young's modulus	$E=273.61$	GPa
Poisson's ratio	$\nu=0.26898$	
elastic wave velocity	$V_p=9.755$	km/s
	$V_s=5.484$	km/s

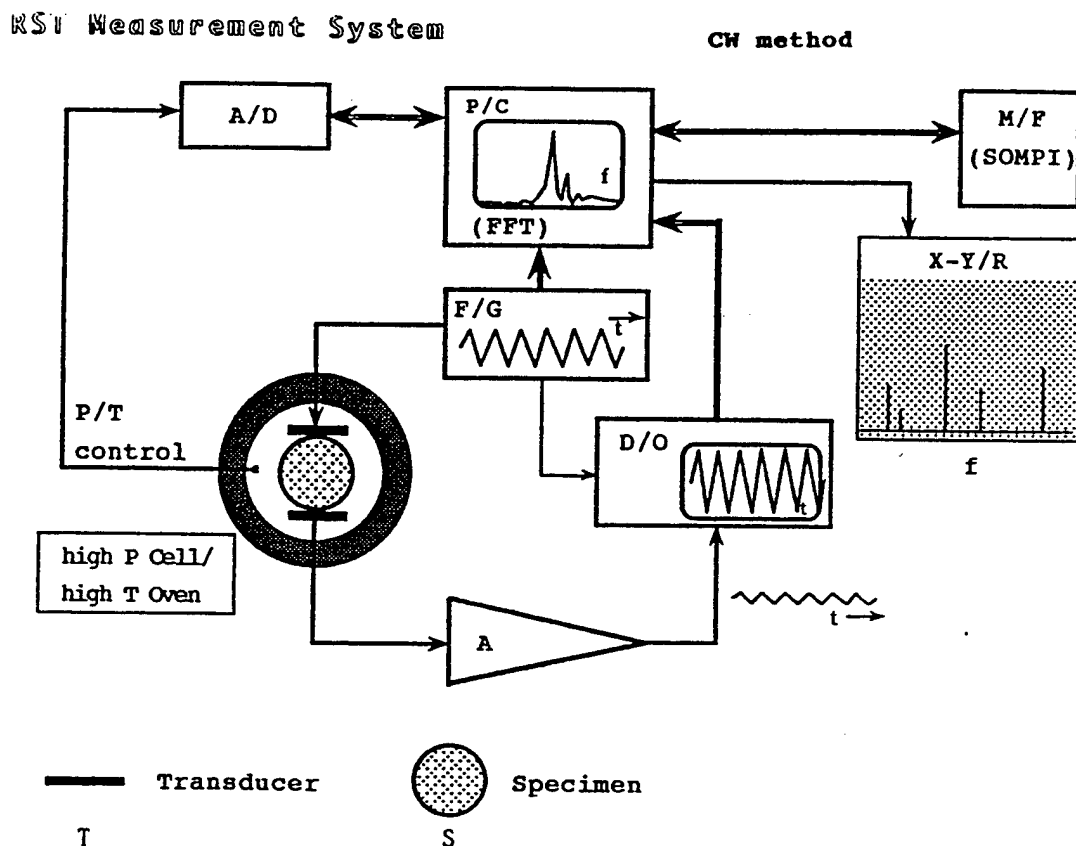


Figure 1. Computer-controlled system for data acquisition in the Resonant Sphere Technique. Thick arrows show computer control of the devices and data acquisition through the GP-IB. Thin arrows show transmission of analogue signal. A/D: Analogue-digital converter, P/C: Personal computer, P/T: Pressure and/or temperature sensor, O/P: Oven and/or pressure vessel. S: Specimen, T: Transducer, X-Y/R: x-y recorder, M/F: Main Frame for the least squares calculation.

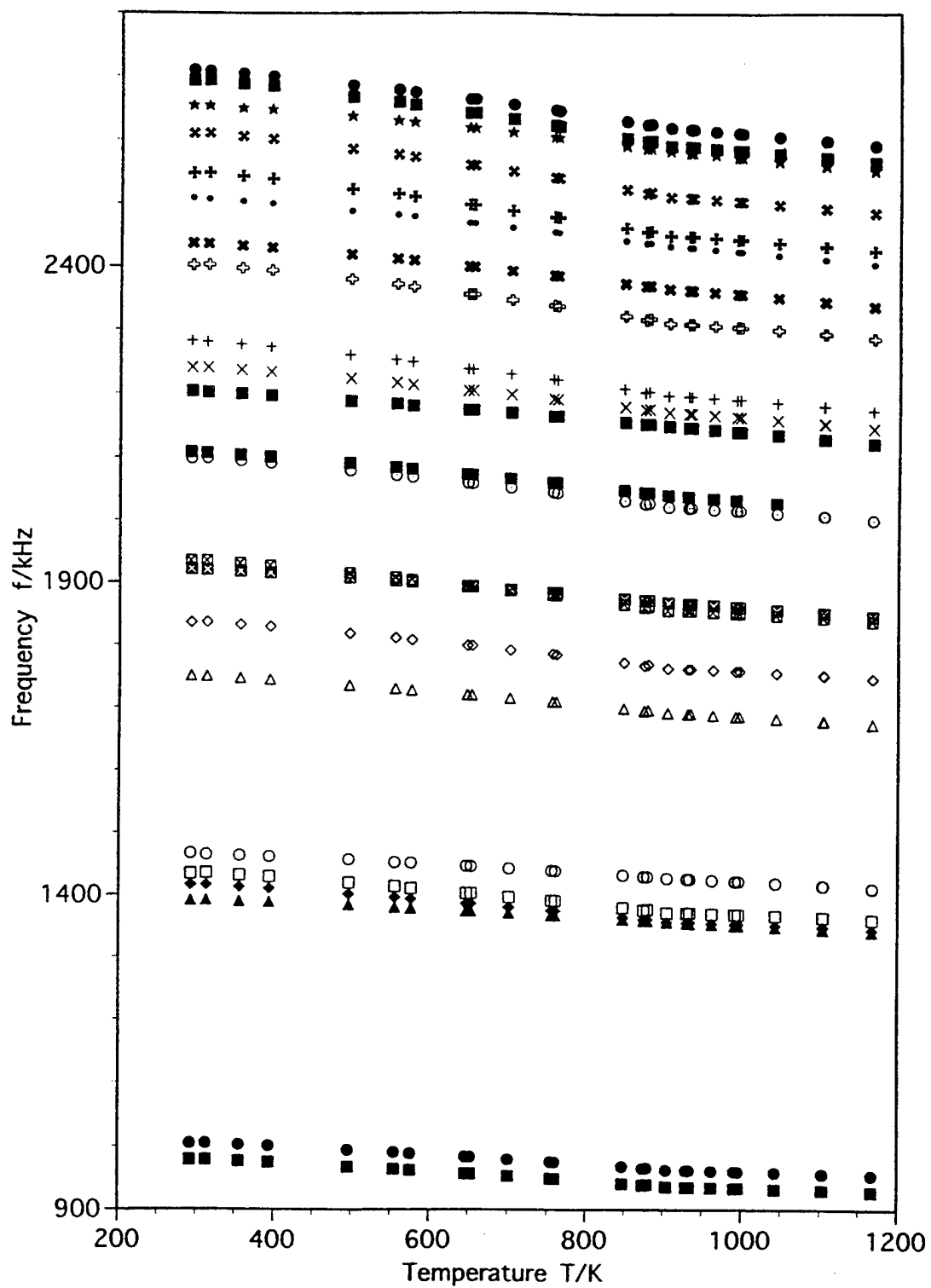


Figure 2. Observed frequencies of 23 modes between 293 and 1167 K

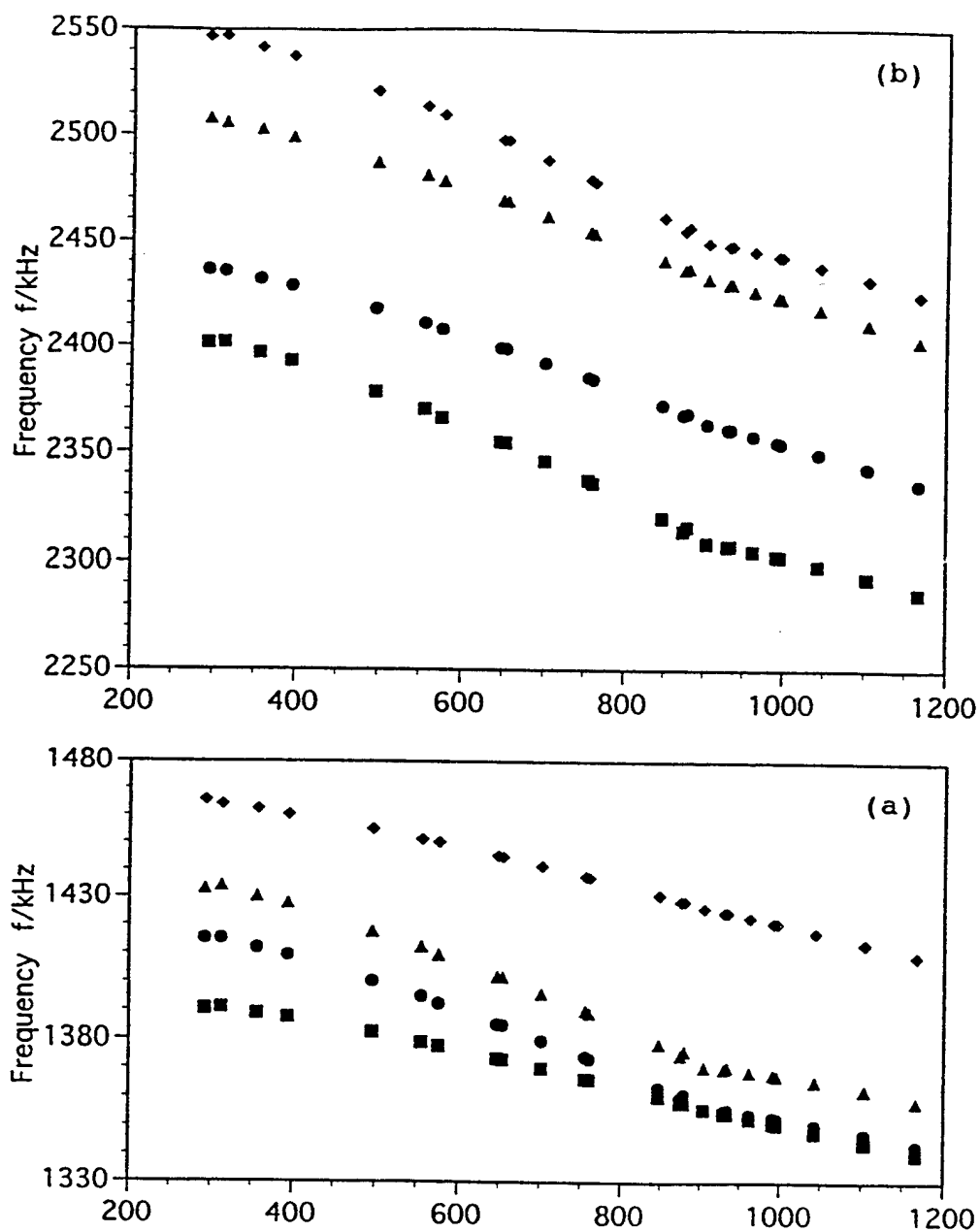


Figure 3 . Magnified illustration of Figure 2 around 1,400 and 2,500 kHz. (a) From lower to higher frequency: Eu-1, Tlu-1, A2g-1 and T2g-1 modes. Two modes Tlu-1 and A2g-1 show clear inflection at 904 K, and the others are almost linear with convex curvature. (b) From lower to higher frequency: Tlu-3, Eg-3, T2g-3 and T2u-4 modes. The modes Tlu-3 and T2u-4 show clear inflection at 904 K.

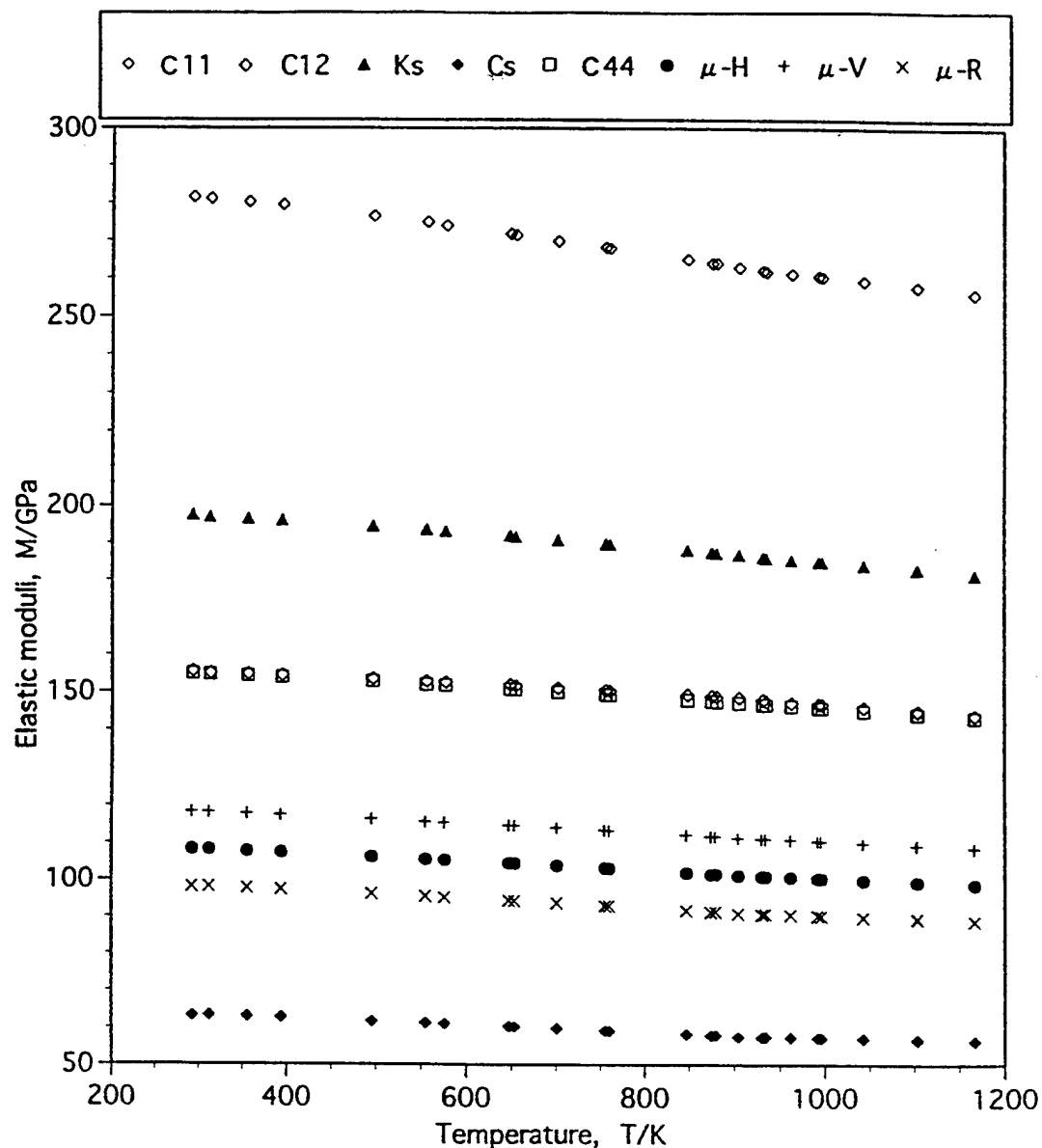


Figure 4. Elastic moduli of spinel in the temperature range between 293 and 1167 K. Three of those are independent. Adiabatic and isothermal bulk moduli are $K_s = (C_{11} + 2C_{12})/3$ and $K_T = K_s / (1 + \alpha \gamma T)$, respectively. Shear modulus is $C_s = (C_{11} - C_{12})/2$. Rigidity modulus μ are obtained by the Voigt-Reuss-Hill averaging schemes.

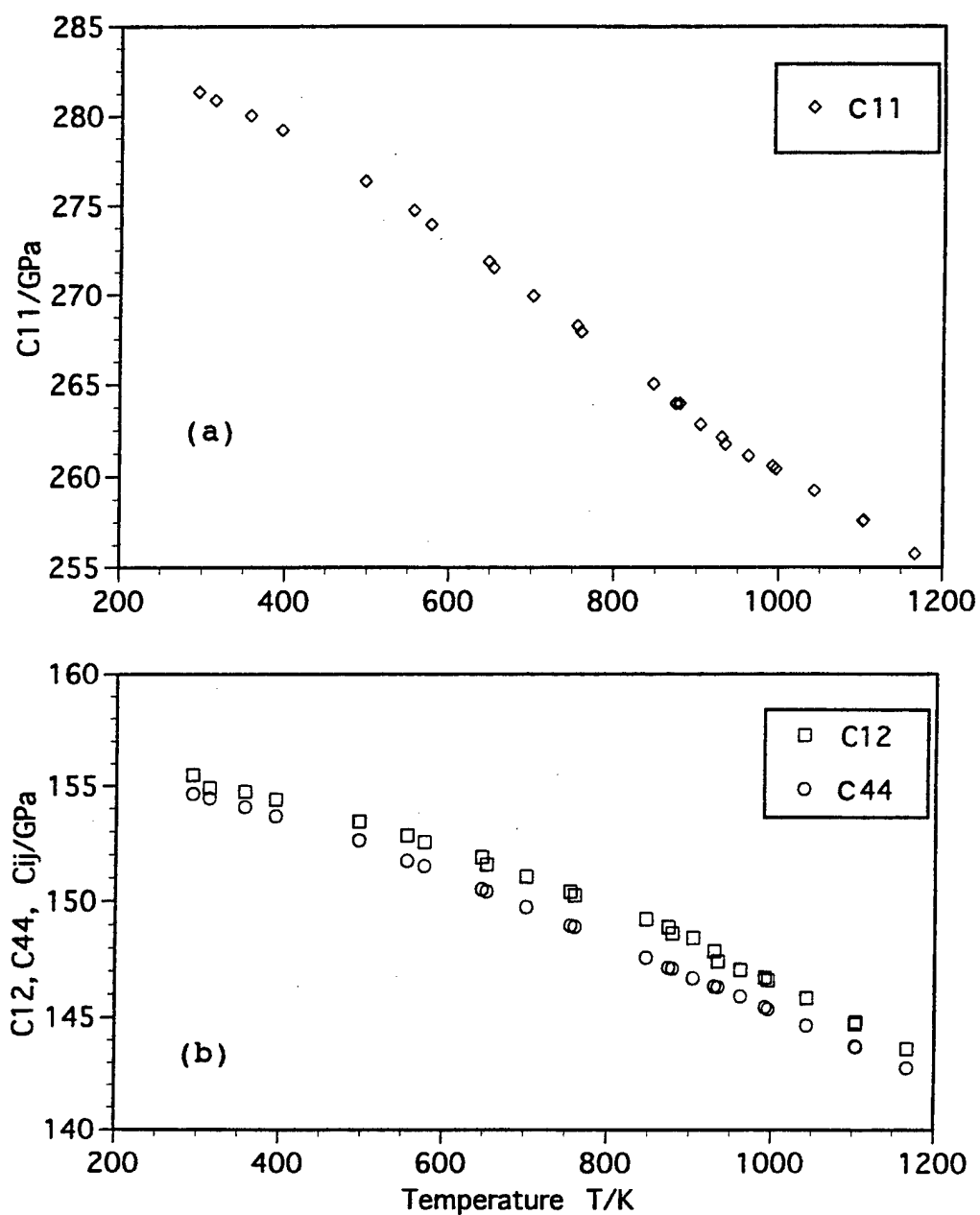
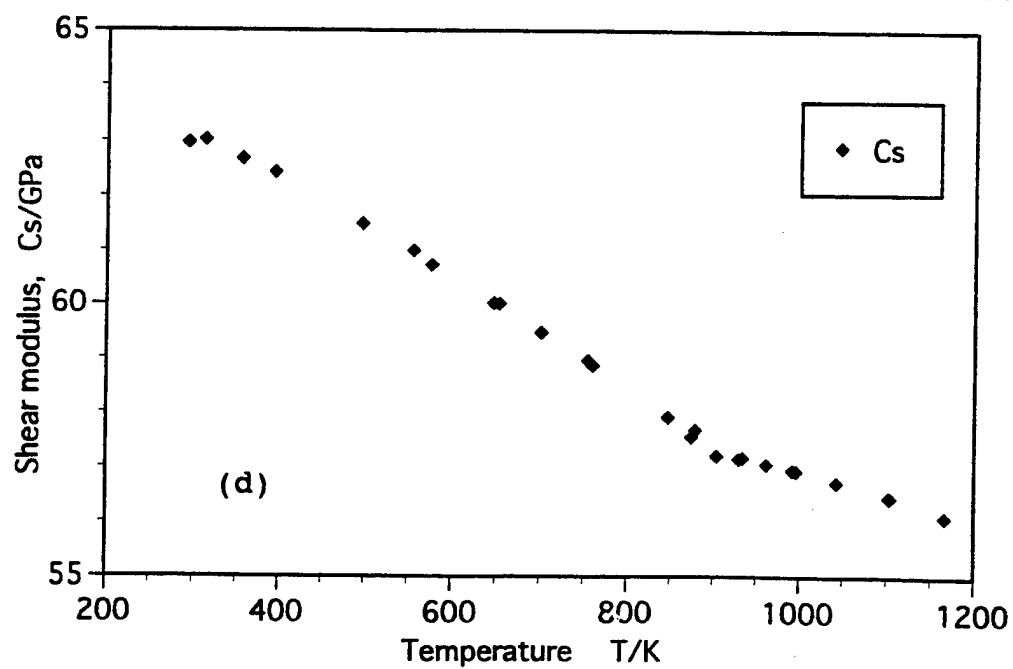
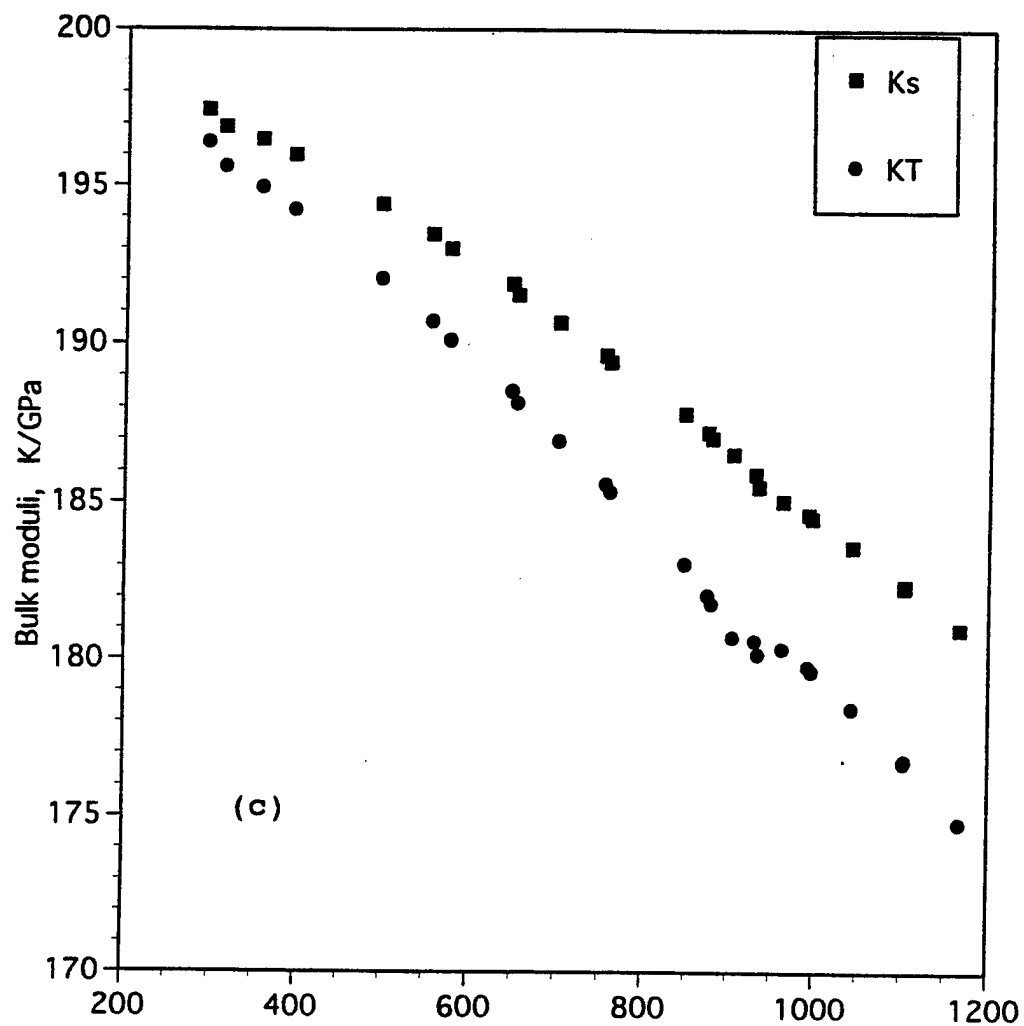


Figure 5. Magnified illustration of Figure 4.

Thermal expansion data and the Gruneisen parameter are used to evaluate isothermal bulk modulus in the panel (c). (a) C_{11} , (b) C_{12} and C_{44} , (c) bulk moduli, K_s and K_T , (d) shear modulus C_s , and (e) rigidity modulus μ .



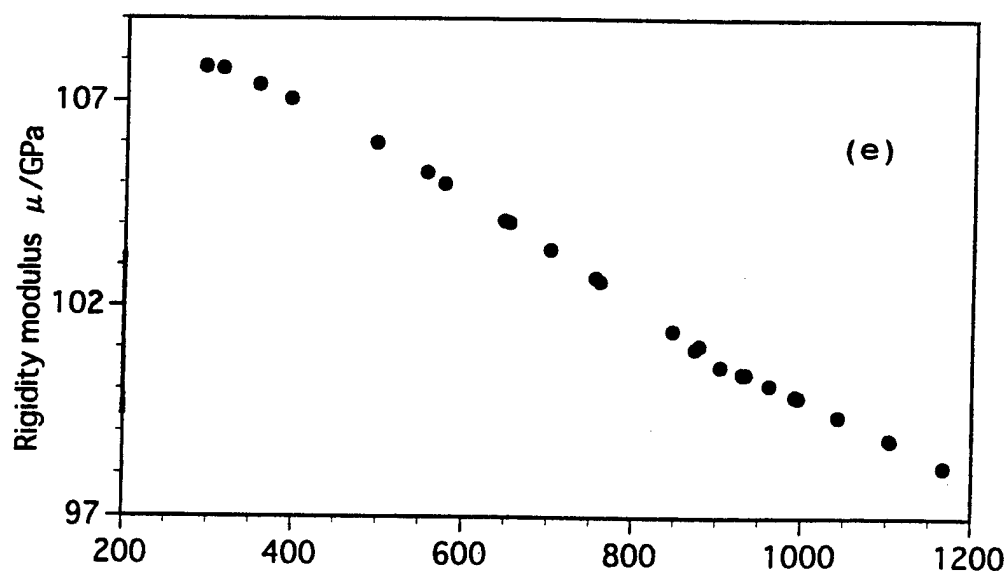


Figure 5 (e)

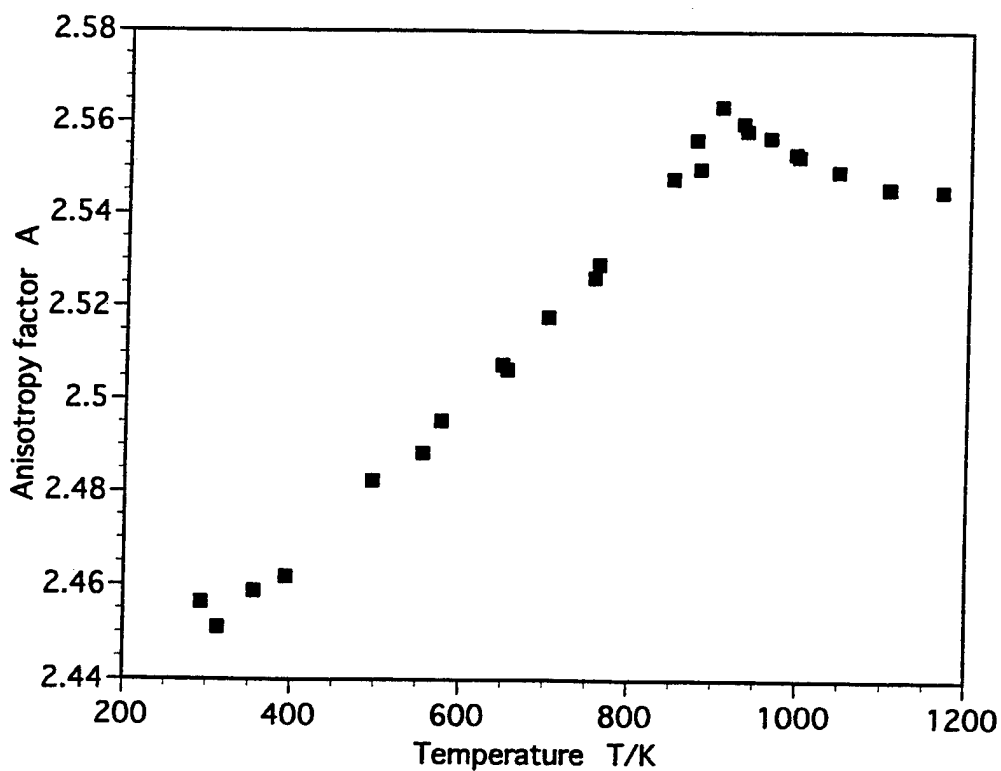


Figure 6. Anisotropy factor A changes its slope clearly at 904 K. The A is defined as $A = C_{44}/C_s$.

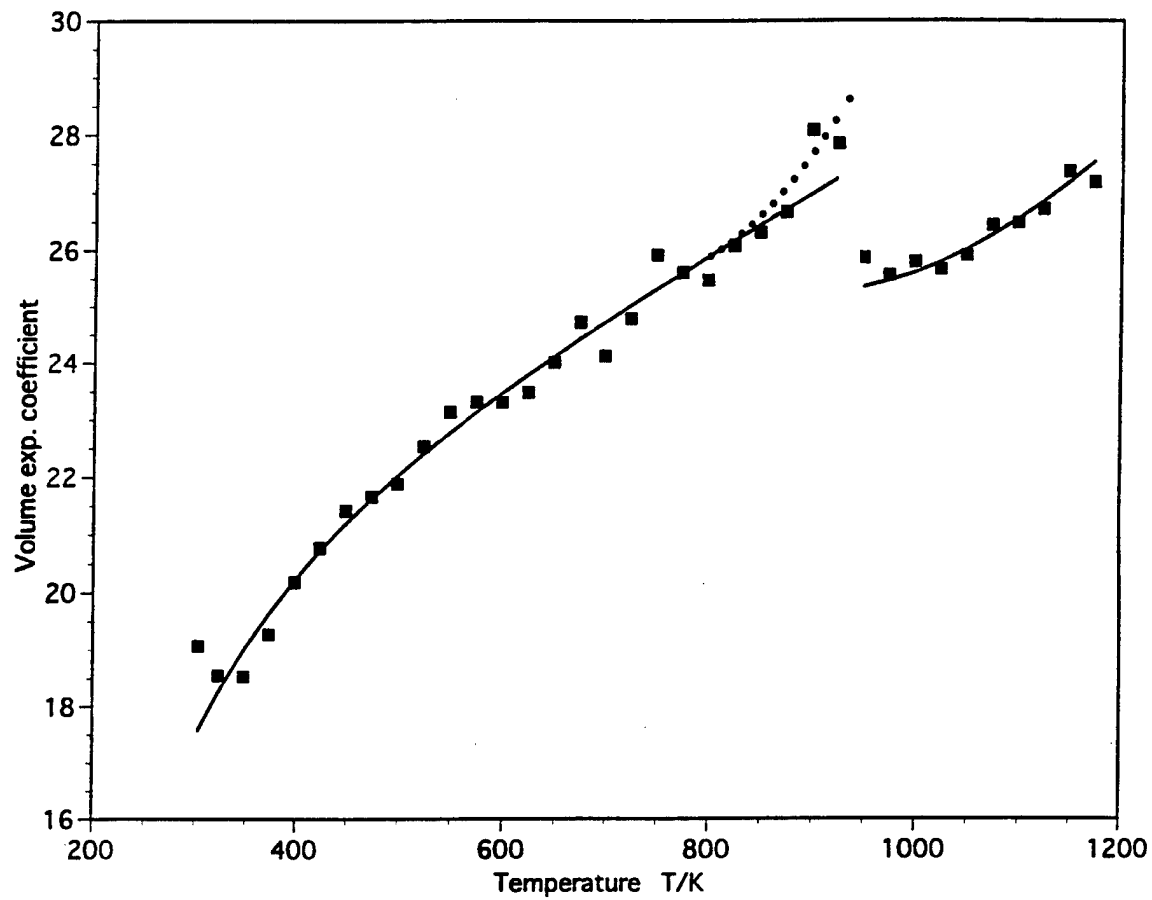


Figure 7. Thermal expansion coefficient of spinel in $10^{-6}/K$.
 square: obtained by numerical differentiation of observed expansion
 data; smooth curve: by least squares fit of the Gruneisen equation;
 dot: by a quadratic equation just before the transition.

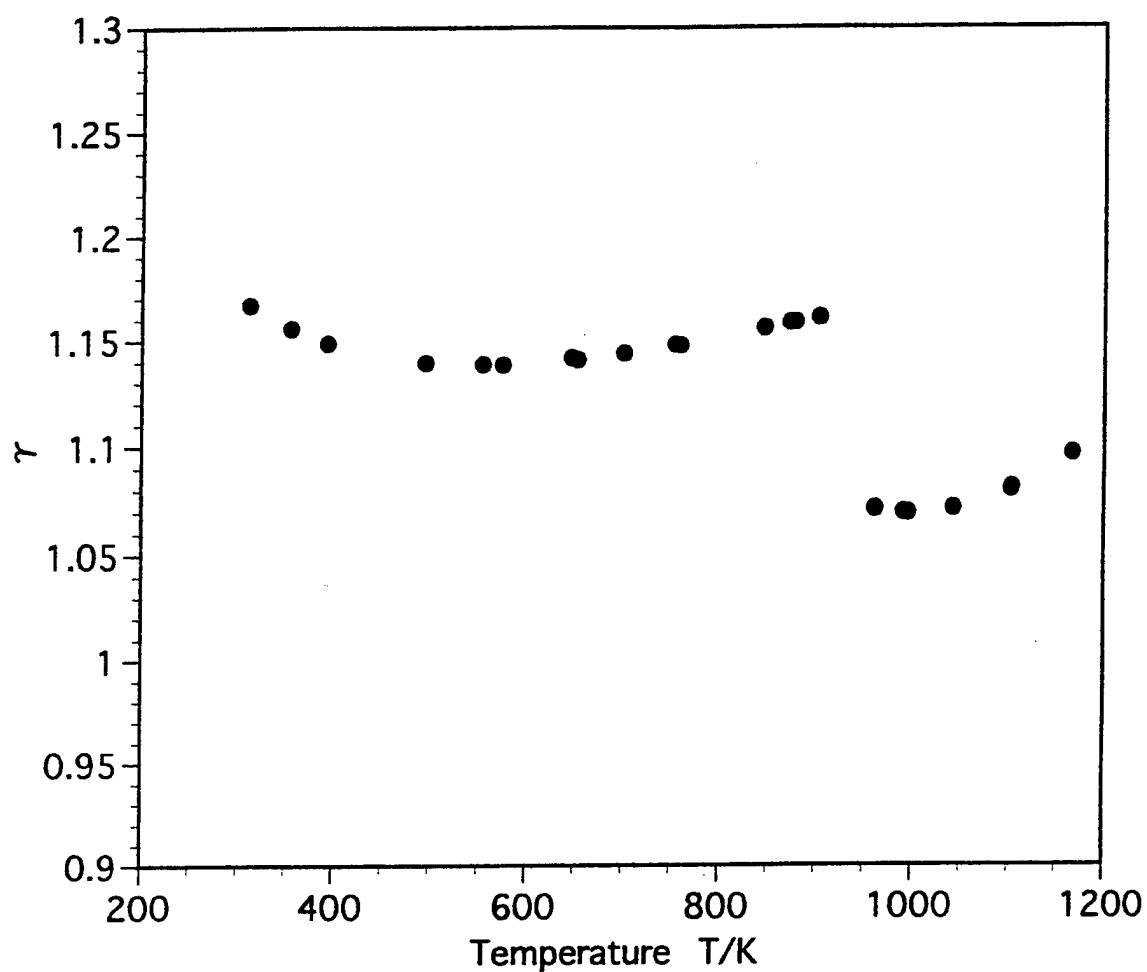


Figure 8. Gruneisen parameter of spinel with discontinuity at 904 K.

Resonant frequency of an elastic sphere at high pressures

Hitoshi Oda, Kouichi Yamada, and Isao Suzuki

Department of Earth Sciences, Okayama University, Okayama 700, Japan

1. Introduction

In order to extend pressure range for application of the resonant sphere technique (RST), the cavity resonance method has been developed by Ohno et al. (1993). In this method, a spherical specimen is placed in the center of a spherical container which is filled by high pressure gas, and resonant frequencies of the spherical specimen are measured under the confining pressure. Since the elastic constants are determined by minimizing, in a least squares sense, the differences between measured and computed resonant frequencies of the specimen, the free vibration frequencies have to be computed for three layered sphere which is composed of the inner spherical specimen, high pressure gas layer and outer solid layer. However the free vibration of a radially heterogeneous sphere having a gas layer has not been known in detail so far. In the present study, we investigate how the resonance spectrum of the inner spherical specimen is affected by the gas layer, solving a problem of free vibration of the three layered sphere.

The spherical shell structure composed of three layers is shown in Figure 1. The outer layer is a solid container of tungsten carbide, WC, and helium gas, He, fills the middle layer as pressure medium to compress an inner spherical sample. This model is called "cavity model". The problem of free vibration was solved for two cavity models, where the inner spherical specimen is elastically isotropic (model A) and anisotropic (model B). The elastic constants, density and radius of both models are given in Table 1. The computer program coded by Saito (1988) was used for computing the frequencies and eigenfunctions of normal modes of the three layered sphere with isotropic elasticity.

2. Free Vibration for cavity model with an isotropic specimen

Resonance modes for model A are described by torsional ${}_nT_l$ and spheroidal ${}_nS_l$ modes, where n and l are the radial and angular order numbers, respectively. These normal modes are characterized on the basis of the distribution of strain energy excited in the three layered sphere. The strain energy of torsional modes is confined only in the inner sample or the outer solid layer because of no excitation of the torsional displacements in the gas layer. However the energy of spheroidal modes is generally excited over the entire space of the three layered sphere. Figure 2 depicts the strain energy distribution of spheroidal modes. The strain energy is localized in the inner sample, gas or outer layer because of a large difference in acoustic impedance between the gas and solid layers. We call such a mode "sample", "gas" or "container" mode, whose nomenclature derives from the layer where the strain energy is localized. In these modes, the frequencies of sample modes provide information regarding the elastic constants of the inner spherical specimen.

The resonant frequencies of the three layered sphere were computed as a function of pressure in gas layer. The changes in elastic constants and density due to pressure and the volume change of the sample and container were taken into account for the computation of resonant frequency. The pressure derivatives of elastic constants are listed in Table 1. In Figure 3, the pressure dependence of the computed frequencies of the ${}_nS_2$ modes for model A is shown for the sample, gas and container modes. The number of gas modes is largest in the three kinds of resonance modes. The gas mode shows the largest slope in the pressure change of resonant frequency, and its pressure curve often intersects those of sample and container modes. For a careful

examination of the intersections of the pressure curves, a small rectangular part in Figure 3, where the pressure curves of sample and gas modes appear to cross at the pressure of 22.3 MPa, is enlarged in Figure 4. The curve of $_{10}S_2$ mode approaches that of $_{11}S_2$ mode as the confining pressure increases up to the intersection pressure, and both modes gradually separate with further increase in pressure. Figure 5 depicts the change of strain energy distribution of the $_{10}S_2$ and $_{11}S_2$ modes. As the pressure increases, the $_{10}S_2$ changes from gas mode to sample mode and the $_{11}S_2$ changes from sample mode to gas mode.

When our attention is focused on the sample or gas mode, the intersection is regarded as an interchange from $_{11}S_2$ to $_{10}S_2$ for the sample mode and from $_{10}S_2$ to $_{11}S_2$ for the gas mode. Such an interchange occurs only between the spheroidal modes of $_nS_l$ and $_{n'}S_{l'}$ satisfying the conditions of $l=l'$ and $n-n'=\pm 1$.

3. Free Vibration for cavity model with an anisotropic specimen

In the case of model B in which the inner spherical specimen is elastically anisotropic, the free oscillation of three layered sphere can be computed by the Rayleigh-Ritz (variational) method, where the normal mode displacements of spherical shell structure with an isotropic specimen are used as the basis functions. Figure 6 shows the frequency spectrum computed for the cavity model with a spherical periclase specimen. The resonance modes, as well as those for model A, are classified into sample, gas and container modes on the basis of the strain energy distribution. It is found that most of resonance modes are gas modes. For a comparison, the frequency spectrum computed for the cavity model with an isotropic specimen is also shown in Figure 6. The elastic constants of the isotropic specimen were obtained by the Voigt averaging scheme of the elastic constants of the periclase. A larger number of sample modes are identified in a given frequency interval, in comparison with free vibration for the cavity model with the isotropic specimen. This increase in sample modes is attributed to split of degenerate modes due to the elastic anisotropy of the inner specimen. The pressure dependence of resonant frequencies for model B is shown for mode groups peculiar to the cubic crystal symmetry to which the periclase specimen belongs (see Figure 7). The interchange between the gas mode and sample or container modes occurs only in the resonance modes belonging to the same mode group. The resonant frequencies of sample and container modes increase only by about 1kHz as the confining pressure increases up to 60MPa, while the increase in frequency of gas mode is about 200kHz for the same pressure increase. The large frequency increase of gas mode may be attributed to larger change rate in bulk modulus of gas layer.

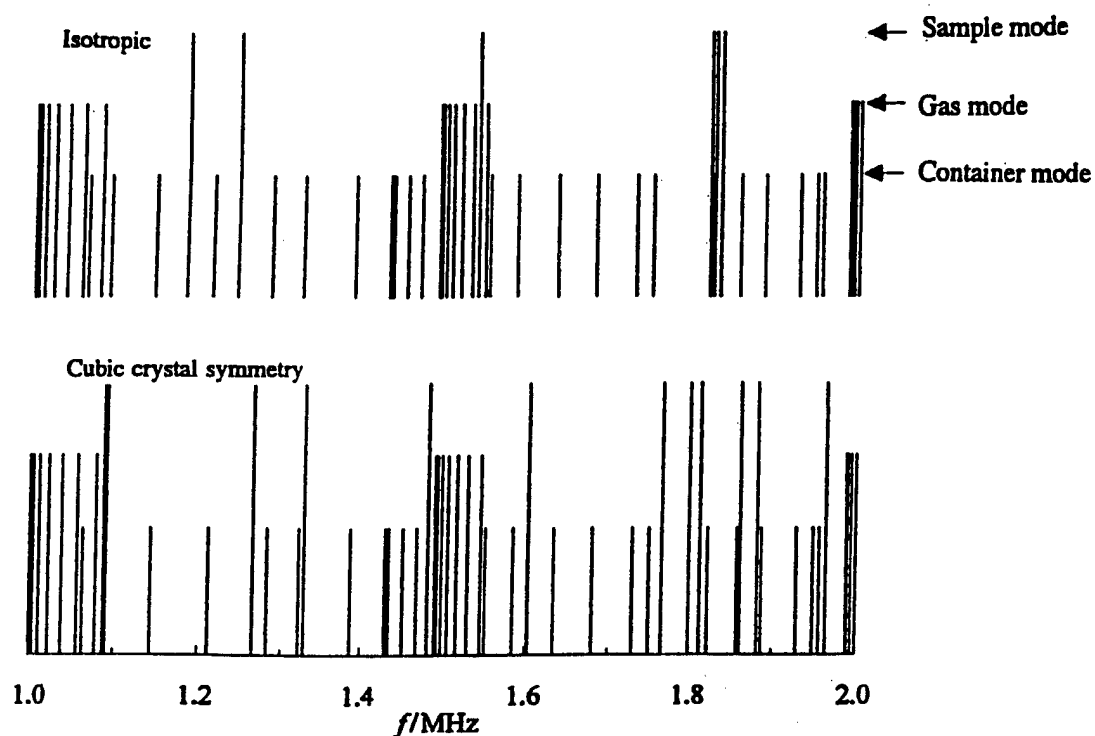


Figure 6. Resonance spectrum (bottom figure) for model B, where a periclase specimen is used as the inner spherical specimen of three layered model. For a comparison, frequency spectrum computed for the cavity model with an isotropic specimen is shown in the top figure. The elastic constants of the isotropic specimen were obtained by the Voigt averaging scheme of the elastic constants of the periclase. The long, middle and short bars represent the resonant frequencies of sample, gas and container modes, respectively. A larger number of sample modes are found in a given frequency interval, in comparison with the free oscillation for the cavity model with the isotropic specimen. This increase in the number of sample modes is attributed to split of degenerate modes due to the elastic anisotropy of the inner sample.

4. Discussion

As seen in Figures 3, 4 and 7, the intersection between the pressure curves makes the mode identification difficult because there are two or more resonance modes in the vicinity of the intersection. In order to avoid such a trouble in the mode identification, it is necessary to make a vibration system that the number of gas modes is as small as possible in a given frequency interval because the intersection occurs between gas mode and sample or container mode. Figure 8 shows the effect of thickness of gas layer on the number of gas modes. The frequency difference between adjacent gas modes is larger as the thickness of gas layer is thinner. This result implies that the possibility of intersections between gas and sample modes may be lower for the model of three layered sphere with thinner gas layer.

The resonant frequencies were measured for a spherical periclase specimen by the cavity resonance method. The measured frequencies are compared with the computed frequencies in Figure 9. Agreement between measured and computed frequencies are good. This result indicates the justification of our computation for free vibration of an elastically anisotropic sphere under high pressure. Therefore the RST is applicable to elasticity measurements of anisotropic materials under high pressure.

5. Conclusion

In order to make it possible to employ the RST for the elasticity measurements under high pressure, we computed free vibration for cavity models of spherical shell structure composed of three layers of solid sample, gas and solid container. The results obtained are summarized as follows.

- 1) It is possible to compute the free vibration of the three layered sphere. A good agreement is obtained between computed and measured resonant frequencies.
- 2) The resonance modes for the cavity model are divided into sample, gas and container modes, whose strain energy distributions are localized into sample, gas and container layers, respectively.
- 3) Interchange takes place between adjacent resonance modes belonging to the same mode group, and it makes the mode identification difficult.
- 4) To avoid such an interchange between resonance modes, it may be a better way to make the thickness of gas layer as thin as possible.

References

- Ohno, I., Y. Hanayama, M. Kimura, I. Suzuki, H. Oda and M. Kumazawa, Pressure derivatives of elastic constants of iron by cavity resonance method, *Proceedings of High Pressure Science and Technology*, 931-934, 1993.
- Saito, M., Disper 80: A subroutine package for the calculation of seismic normal mode solutions, *Seismological Algorithms* edited by D. J. Doornbos, Academic Press, 293-319, 1988.

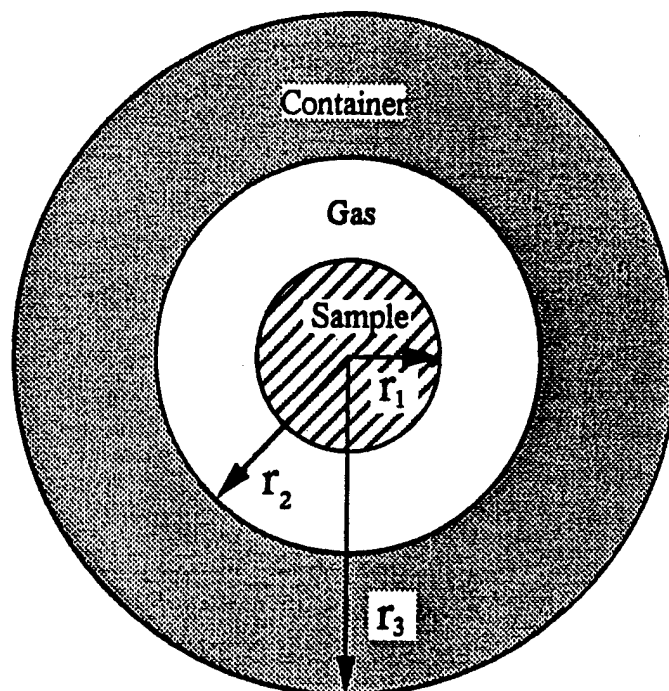


Figure 1. Model of spherical shell structure that is composed of sample, gas and container layers. Radii of sample, gas and container layers are denoted by r_1 , r_2 and r_3 , respectively. The elastic constants and density of each layer are given in Table 1. We consider two cases where the inner spherical sample is elastically isotropic (model A) and anisotropic (model B). In model B, the inner specimen is a single-crystal periclase.

Tabel 1. Paramater values of model B

		Density (g/cm ³)	Radius (mm)	Elastic Constants (GPa)				
				K	μ	C ₁₁	C ₁₂	C ₄₄
Sample	MgO	3.589	2.057	162.83	133.69	296.15	95.35	155.89
Gas	He	2.5E-04	3.057	2.4E-04	-	-	-	-
Container	WC	15.1	7.057	391.00	219.00	-	-	-
				∂K/∂P	∂ μ /∂P	∂ C ₁₁ /∂P	∂ C ₁₁ /∂P	∂ C ₁₁ /∂P
Sample	MgO			4.22	2.08	8.98	2.84	2.09
Gas	He			(α=0.99239+5.4467P-24.270P ² +80.028 P ³)				
Container	WC			6.0	2.5	-	-	-

α : Sound velocity in km/s.

The elastic constants of MgO, K and μ , were obtained by the Voigt averaging scheme of C_{ij}.

Table 1. Paramater values of model A

Table 1. Parameters								
		Density (g/cm ³)	Radius (mm)	Elastic Constants (GPa)				
				K	μ	C ₁₁	C ₁₂	C ₄₄
Sample	Steel	7.789	2.384	165.0	79.5	-	-	-
Gas	He	2.5E-04	5.0	2.4E-04	-	-	-	-
Container	WC	15.1	8.5	391.0	219.0	-	-	-
				$\partial K/\partial P$	$\partial \mu/\partial P$	$\partial C_{11}/\partial P$	$\partial C_{11}/\partial P$	$\partial C_{11}/\partial P$
Sample	Steel			5.0	1.9	-	-	-
Gas	He			$(\alpha=0.99239+5.4467P-24.270P^2+80.028 P^3)$				
Container	WC			6.0	2.5	-	-	-

α : Sound velocity in km/s.

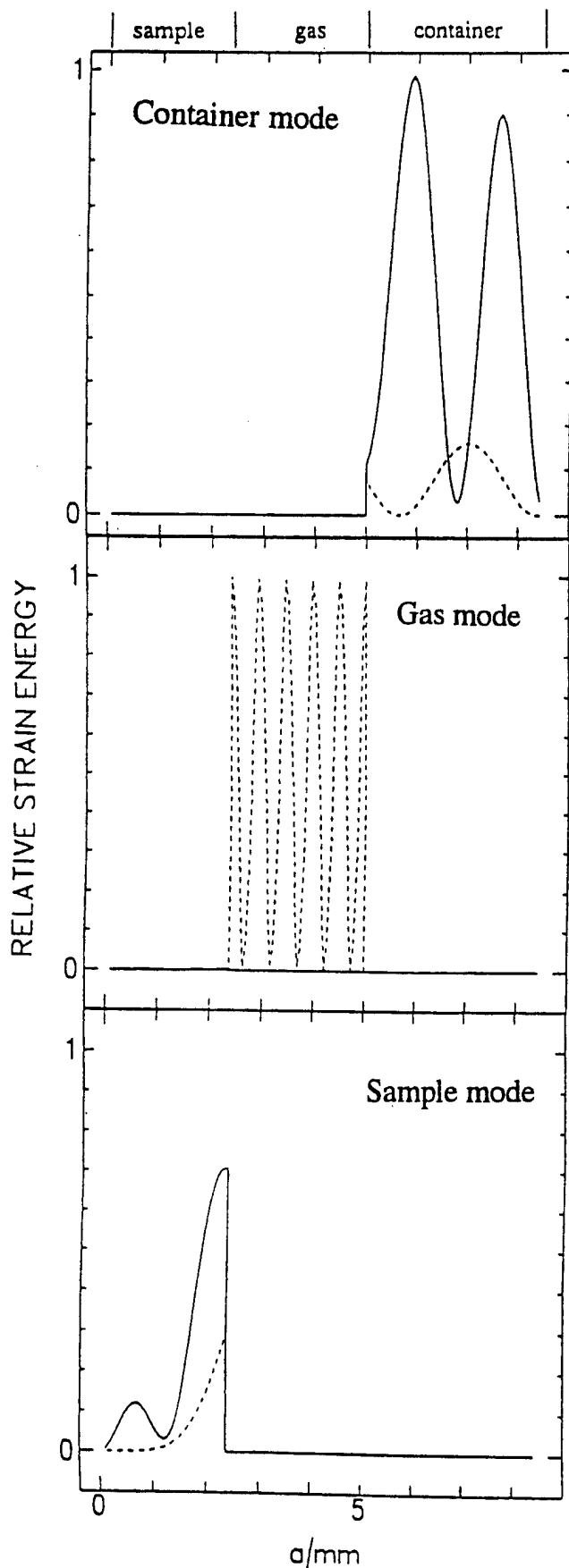


Figure 2. Distribution of strain energy excited in the three layered sphere with an isotropic specimen (model A). The strain energy distributions for rigidity and bulk moduli are represented by the solid and dashed lines, respectively. The strain energy is localized in the inner sample, gas or outer layer because of a large difference in acoustic impedance between the gas and solid layers. Such a mode is called "sample", "gas" or "container" mode, whose nomenclature derives from the layer where the strain energy is localized. In these modes, the frequencies of sample modes provide information regarding the elastic constants of the inner sample.

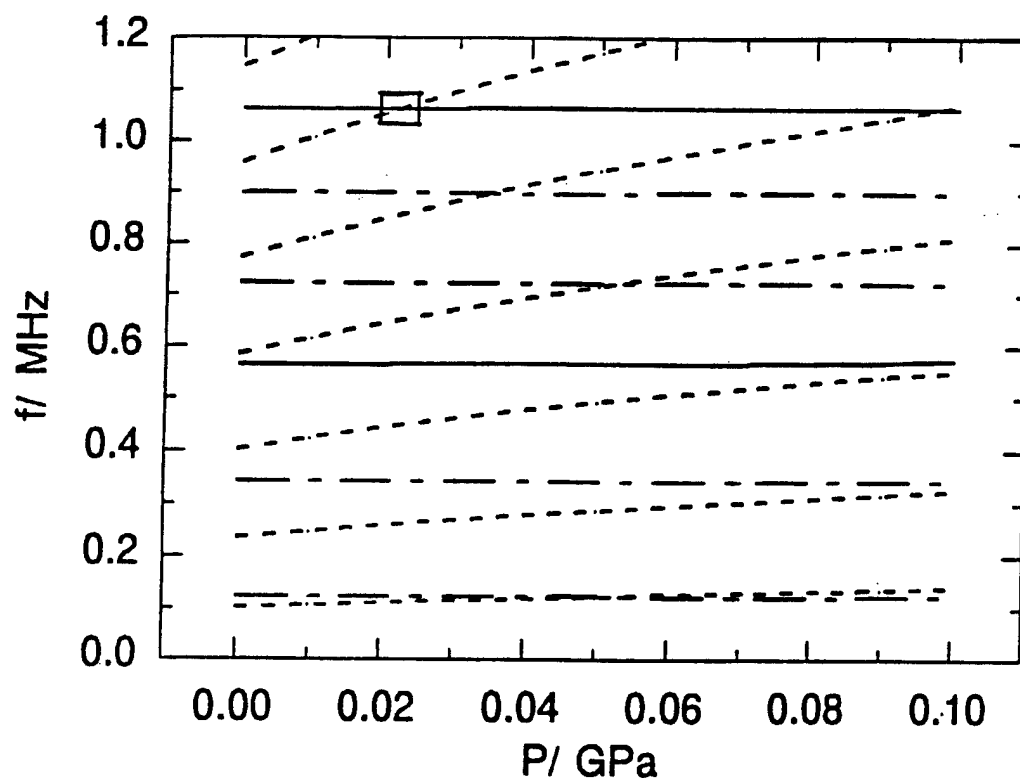


Figure 3. Pressure dependence of resonant frequencies of sample (solid line), gas (dashed line) and container (dotted and dashed line) modes, which are equivalent to the nS_2 modes of model A. The number of gas modes is largest in the three kinds of resonance modes. The gas mode shows the largest change in the pressure dependence of the resonant frequencies and its pressure curve often intersects those of sample and container modes. A small rectangular area is enlarged in Figure 4.

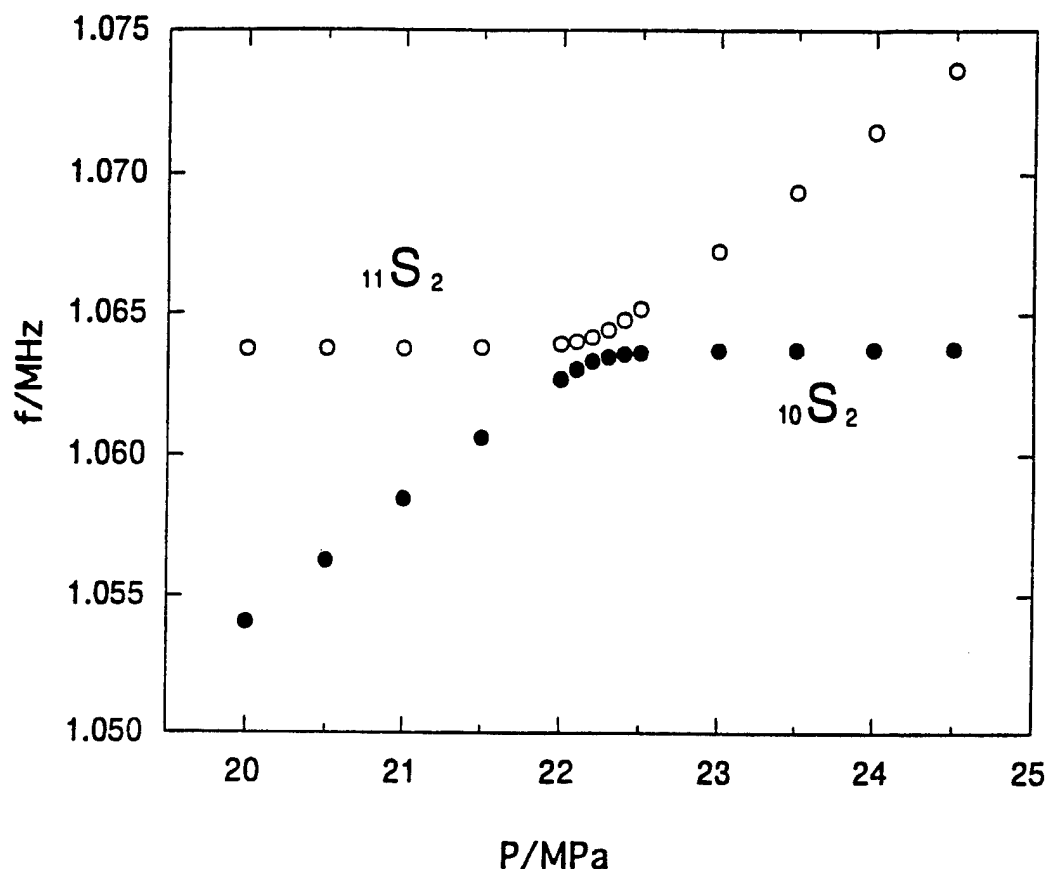


Figure 4. Pressure dependence of the frequencies of $_{10}S_2$ (solid circles) and $_{11}S_2$ (open circles) modes in the pressure interval from 20 to 25 MPa. The pressure curve of $_{10}S_2$ mode approaches that of $_{11}S_2$ mode as the confining pressure increases up to about 22.3 MPa, and then both curves gradually separate with further increase in pressure. When our attention is focused on the sample or gas mode, the intersection seen in the small rectangular area of Figure 3 is regarded as an interchange from $_{11}S_2$ to $_{10}S_2$ for the sample mode and from $_{10}S_2$ to $_{11}S_2$ for the gas mode. Such an interchange occurs only between the spheroidal modes of $_nS_l$ and $_nS_{l'}$ satisfying the conditions of $l=l'$ and $n-n'=\pm 1$, where n and n' are the radial order numbers of the spheroidal oscillation, and l and l' are the angular order numbers.

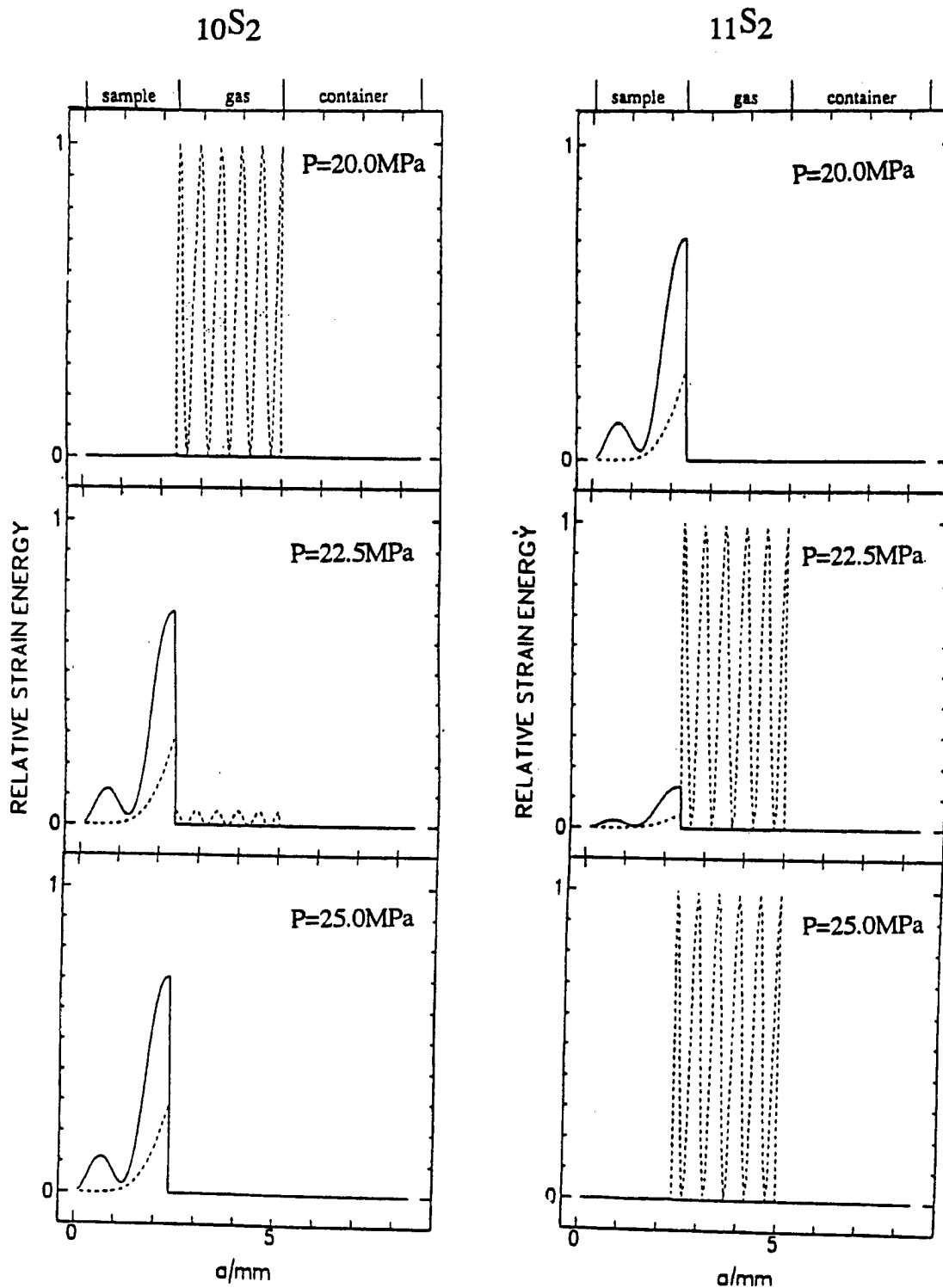


Figure 5. Change of the strain energy distribution of $_{10}S_2$ and $_{11}S_2$ modes against confining pressure. The resonant frequencies of both modes are nearly equal at about 22.3 MPa. As the pressure increases, the $_{10}S_2$ changes from gas mode to sample mode and the $_{11}S_2$ changes from sample mode to gas mode.

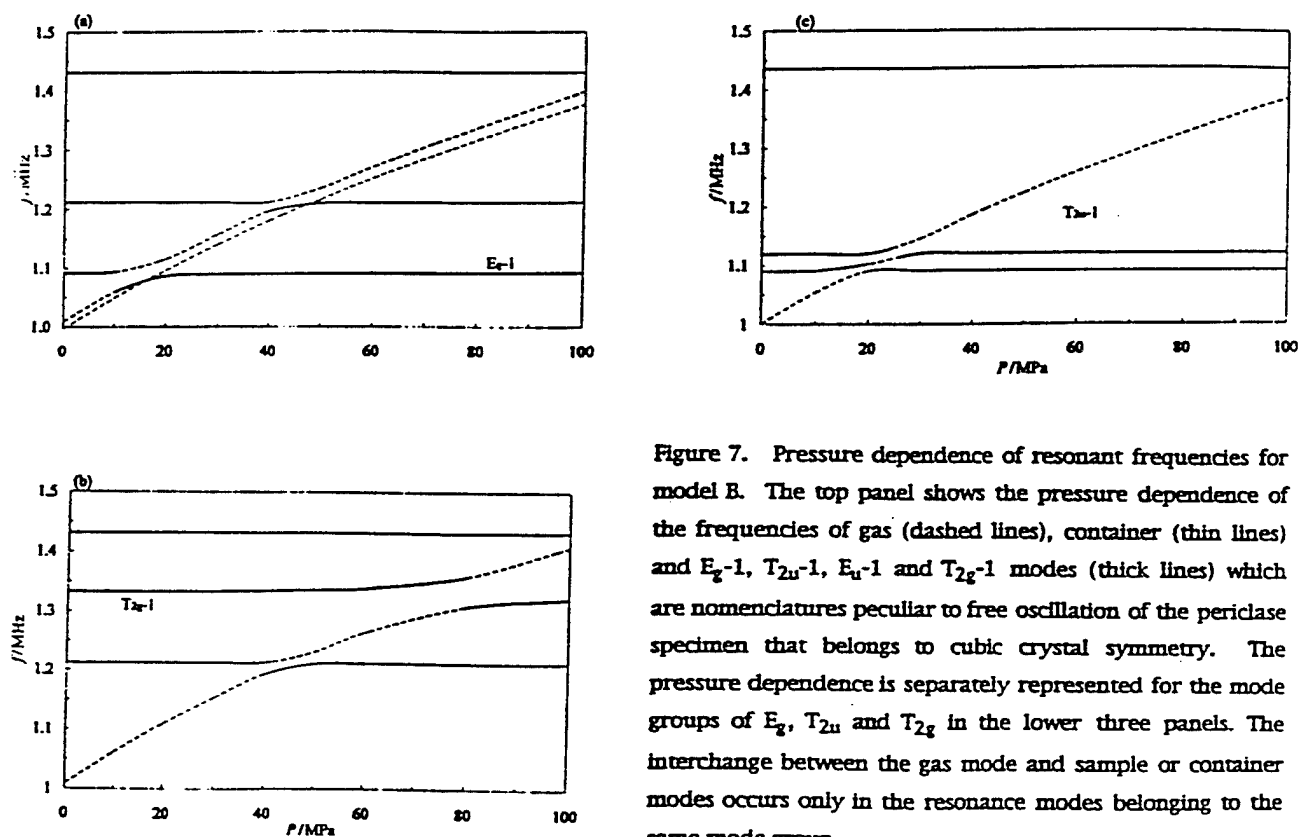
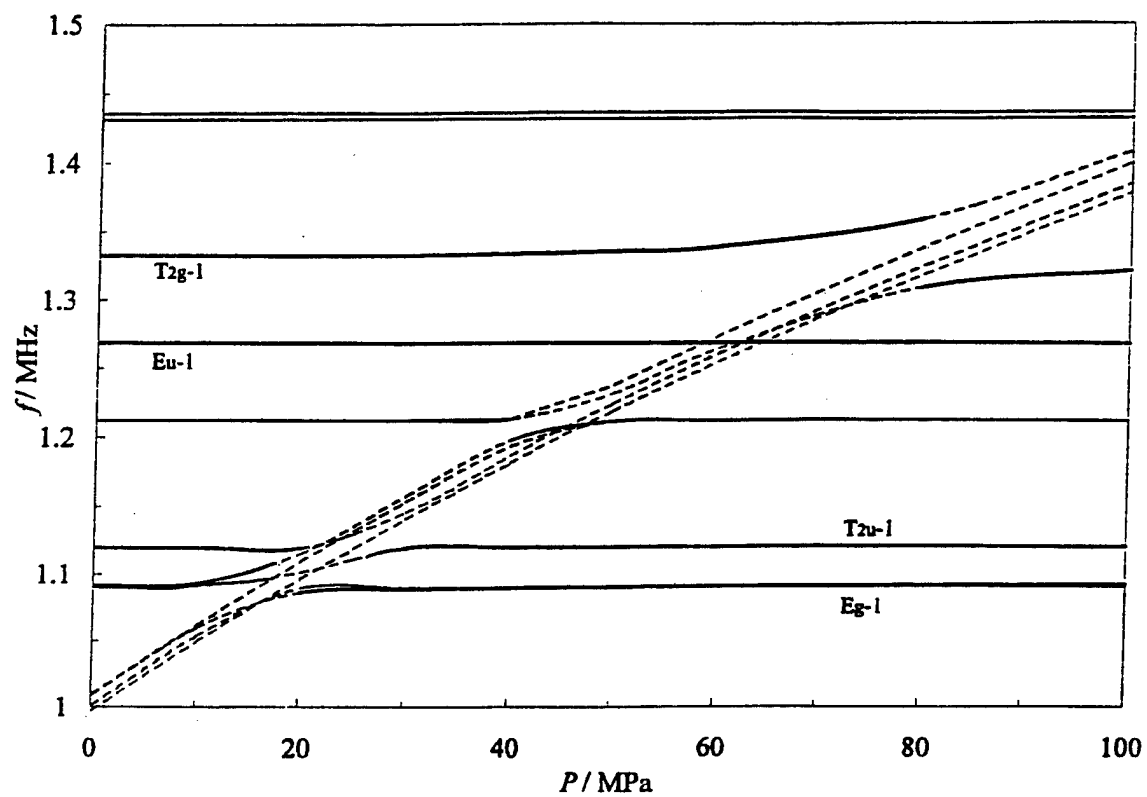


Figure 7. Pressure dependence of resonant frequencies for model B. The top panel shows the pressure dependence of the frequencies of gas (dashed lines), container (thin lines) and E_g-1 , $T_{2u}-1$, E_u-1 and $T_{2g}-1$ modes (thick lines) which are nomenclatures peculiar to free oscillation of the periclase specimen that belongs to cubic crystal symmetry. The pressure dependence is separately represented for the mode groups of E_g , T_{2u} and T_{2g} in the lower three panels. The interchange between the gas mode and sample or container modes occurs only in the resonance modes belonging to the same mode group.



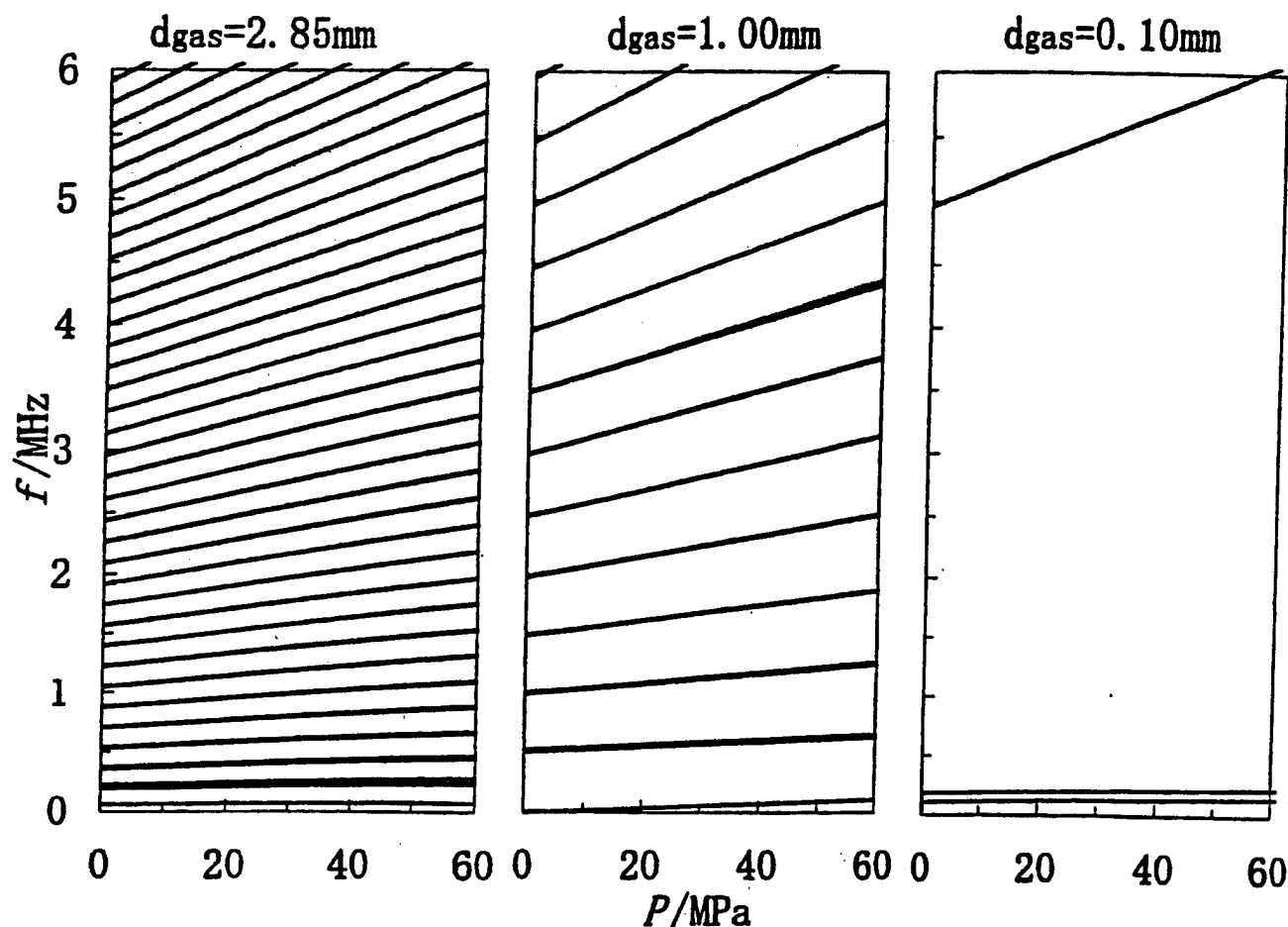


Figure 8 The effect of the gas layer's thickness on the frequency of gas mode. Pressure dependence of the frequency is shown for different thickness of the gas layer, d_{gas} . The left, middle and right panels correspond to the cases of $d_{\text{gas}}=2.85$, $=1.0$ and $=0.1\text{mm}$, respectively. As the thickness of gas layer is thinner, the frequency difference between adjacent gas modes is larger and the number of gas modes decreases in a given frequency interval. This result implies that the possibility of intersections between gas and sample modes may be lower for a model of three layered sphere with thinner gas layer.

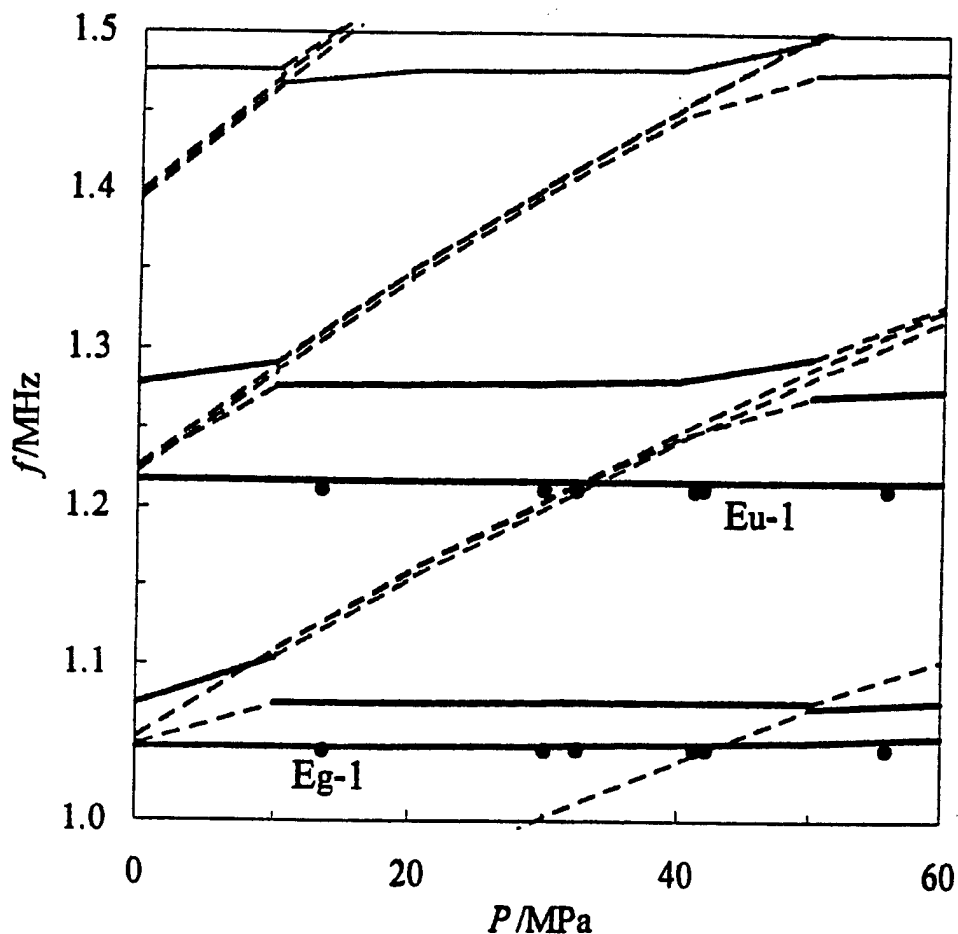


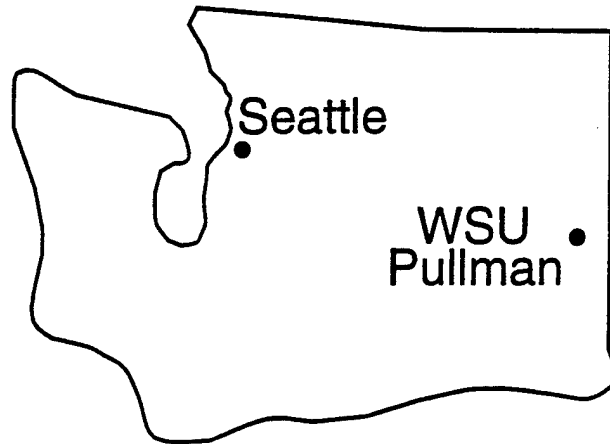
Figure 9 Comparison of calculated frequencies with resonant frequencies measured for a spherical periclase specimen. The thick, thin, and dashed lines represent the pressure dependence of the resonant frequencies of sample, container and gas modes, respectively. The measured frequencies of E_u-1 and E_g-1 modes are shown by circles. The relative difference between both frequencies is about 0.4%. Frequency increase of the sample mode due to pressure changing from 0 to 60 MPa is about 1 kHz, while the increase in frequency of gas mode is about 200kHz for the same pressure increase. If the frequency increases are measured for a number of resonance modes, the pressure derivatives of the specimen's elastic constants are estimated.

Acoustical resonator frequency shift due to the migration of suspended particles

Chris Kwiatkowski*

Department of Physics
Washington State
University

Pullman, WA 99164-2814



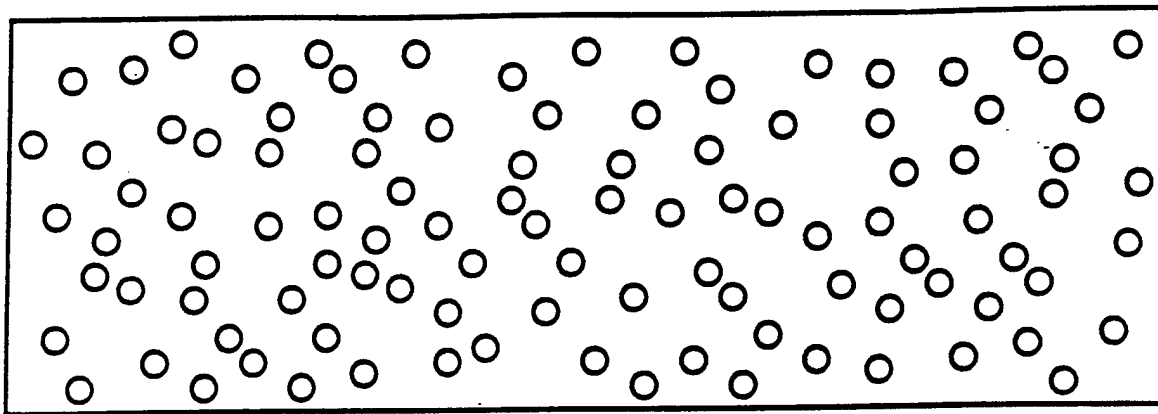
*Present address: WSU and
Sentel Technologies, Pullman, WA

Work supported by the Office of Naval Research.

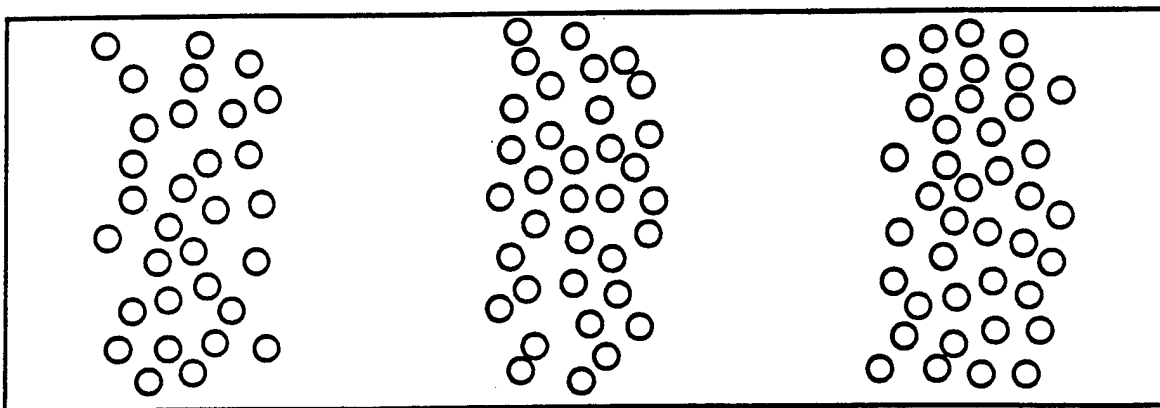
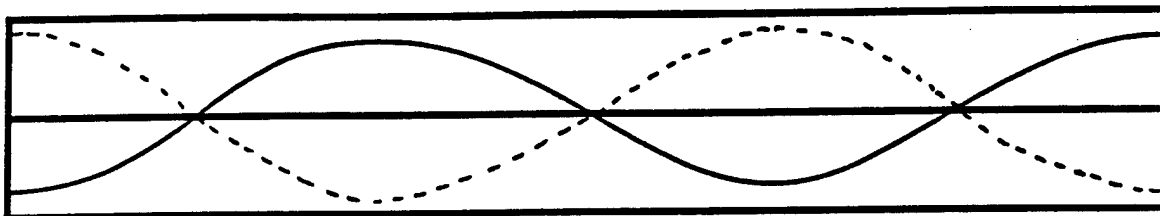
References

1. Chris Kwiatkowski, "Ultrasonic probes of aqueous particle suspensions: collinear four-wave mixing and resonator detuning," Ph.D. Thesis WSU (1996).
2. Harry J. Simpson and Philip L. Marston, "Ultrasonic four-wave mixing mediated by an aqueous suspension of microspheres: Theoretical steady-state properties," J. Acoust. Soc. Am. **98**, 1731-1741 (1994).

Particle Migration:



Pressure

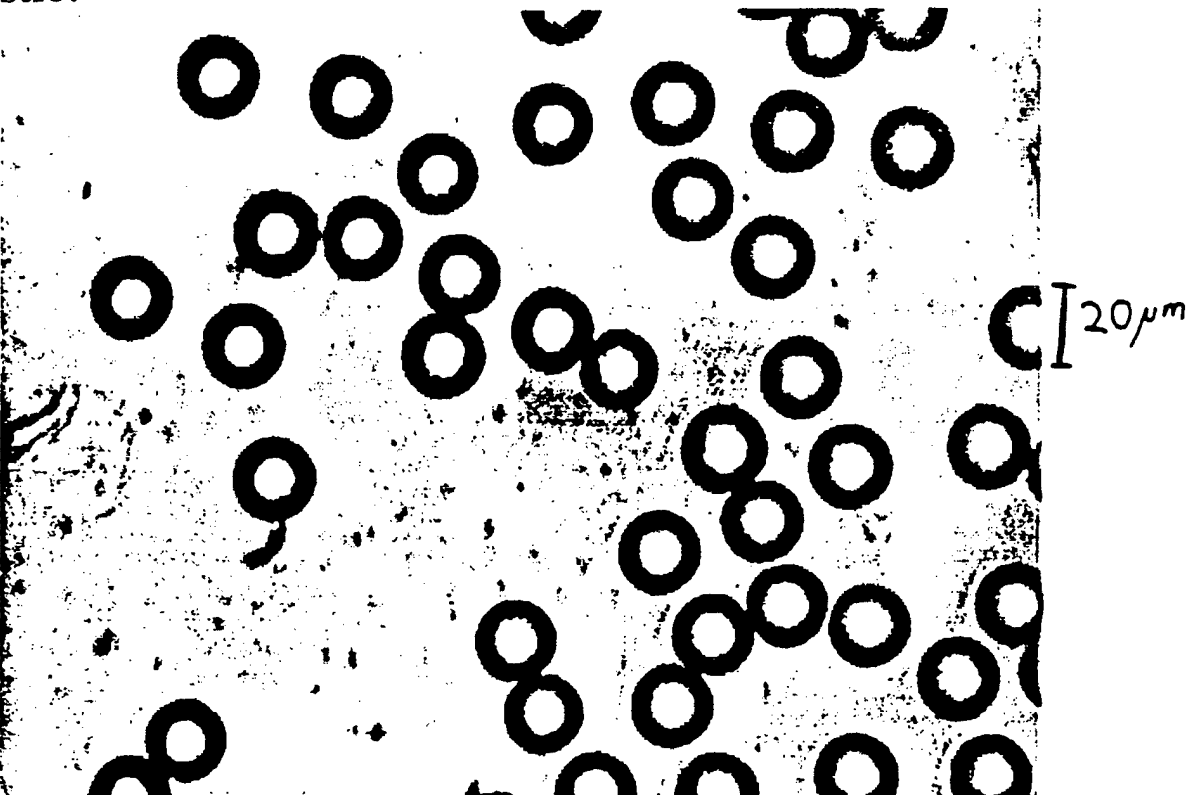


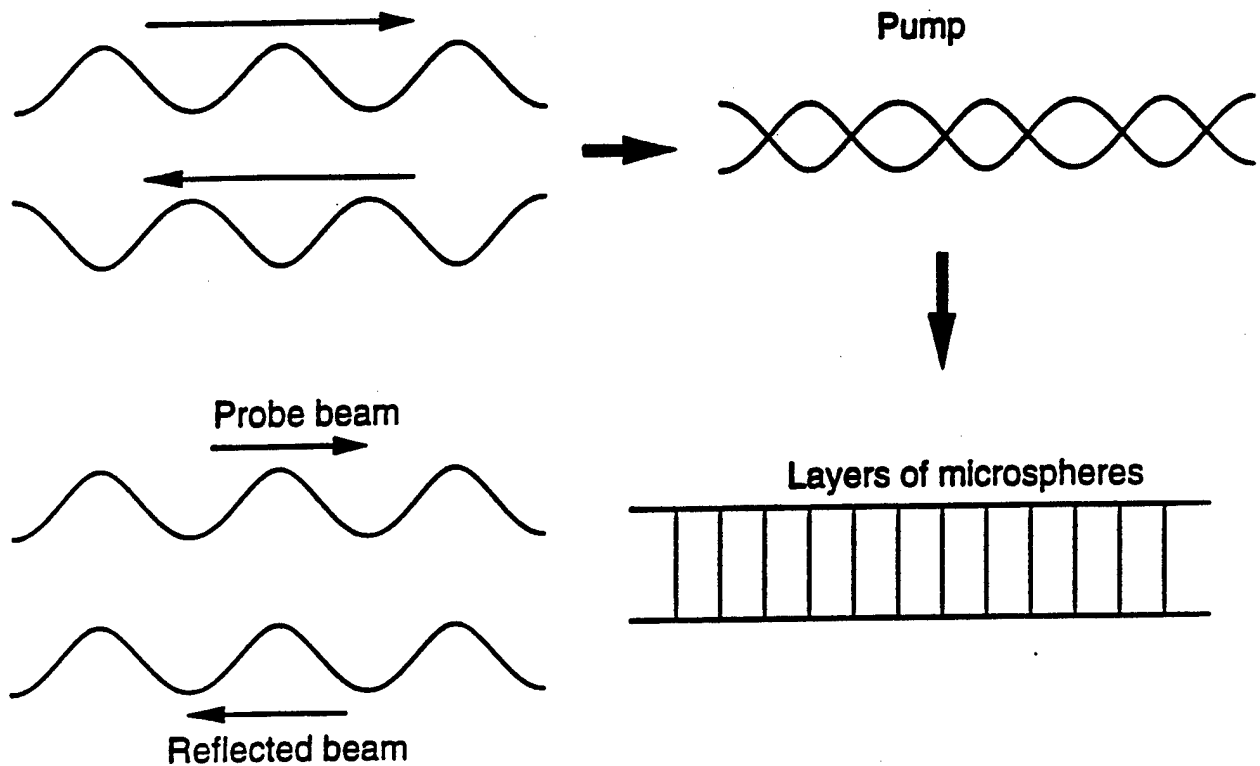
$\lambda/2$

Microsphere CCD Photographs:
Glass:



Plastic:





Collinear Four-Wave Mixing:

- At the Bragg condition layered particles scatter sound with the same phase [modulo (2π)].
- Equilibrium volume fractions as small as 0.0005 can cause appreciable reflectivities (or frequency shifts) once the particles migrate to nodes or antinodes.
- At the Bragg condition both the pump and probe waves are in the "stop band" of the spatially periodic medium caused by the particle migration.

Number density:

$$\frac{\partial}{\partial t} n_p(z, t) = D \frac{\partial^2}{\partial z^2} n_p(z, t) - \frac{2ka^2 \bar{E} F}{3\mu} \frac{\partial}{\partial z} (n_p(z, t) \sin(2kz))$$

Diffusion

Radiation Pressure

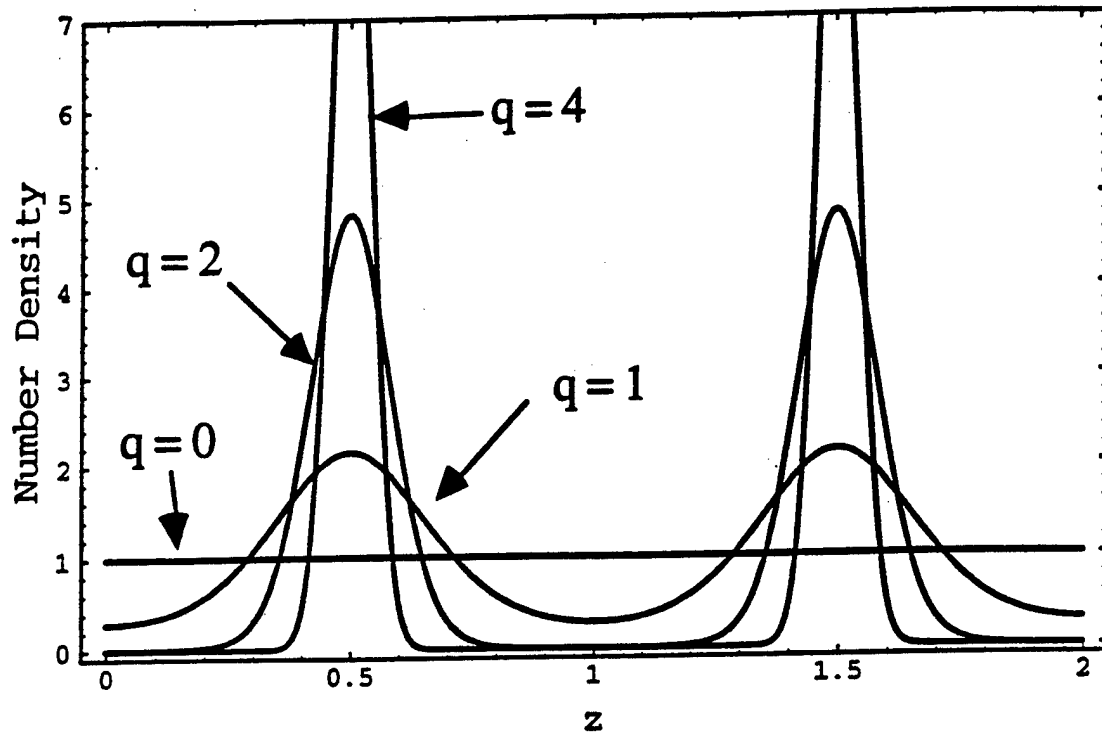
Steady state solution:

$$n_p(z) = \frac{k n_0 \exp[-q \cos(2kz)]}{\pi I_0(q)}$$

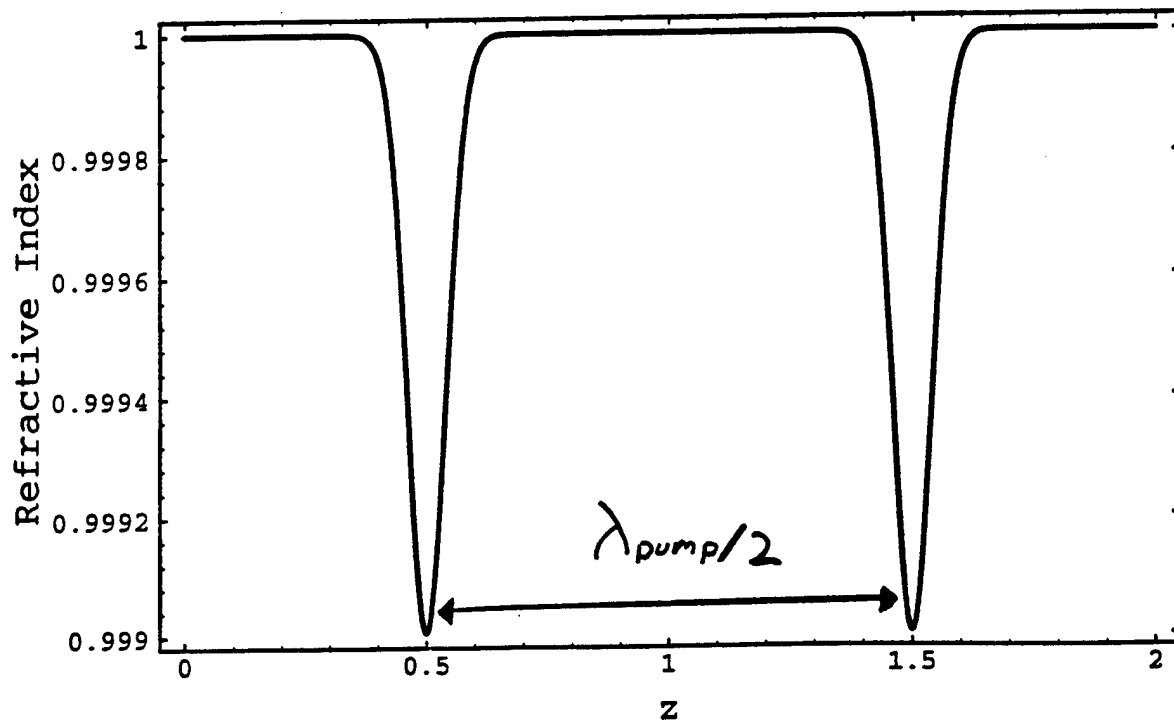
$$q = \frac{V_p \beta_0 p_0^2}{8k_B T} \left(1 - \frac{\beta_p}{\beta_0} \right) = \frac{\text{Acoustic Energy}}{k_B T}$$

a	Particle Radius	β_0	Solvent Compressibility	←
k	Pump Wavenumber	β_p	Particle Compressibility	←
$n_p(z, t)$	# Particles/Volume	μ	Solvent Viscosity	
n_0	Mean # of Particles/Area	k_B	Boltzmann's Constant	
T	Temperature	p_0	Pump Pressure Amplitude	
V_p	Particle Volume	D	Particle Diffusivity	
\bar{E}	Standing Wave Energy Density	F	Compressibility Factor	

Number Density:



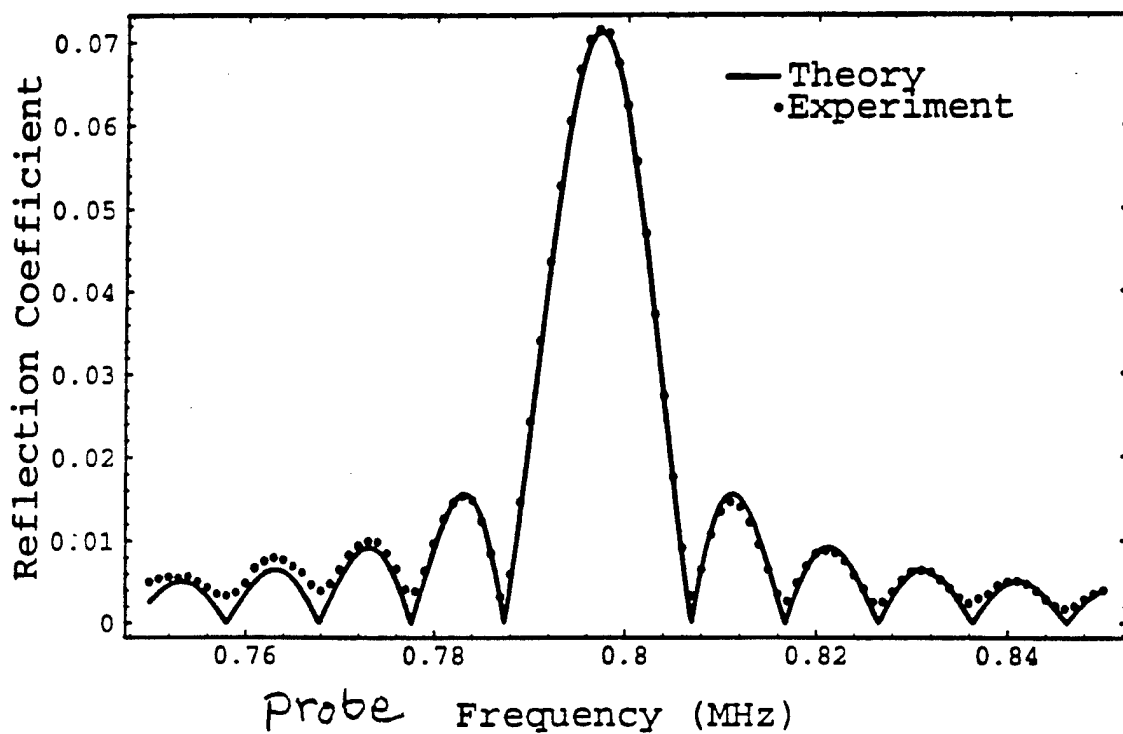
Refractive Index:



Reflection coefficient for N layers:

Born approximation \rightarrow Incident wave is not depleted

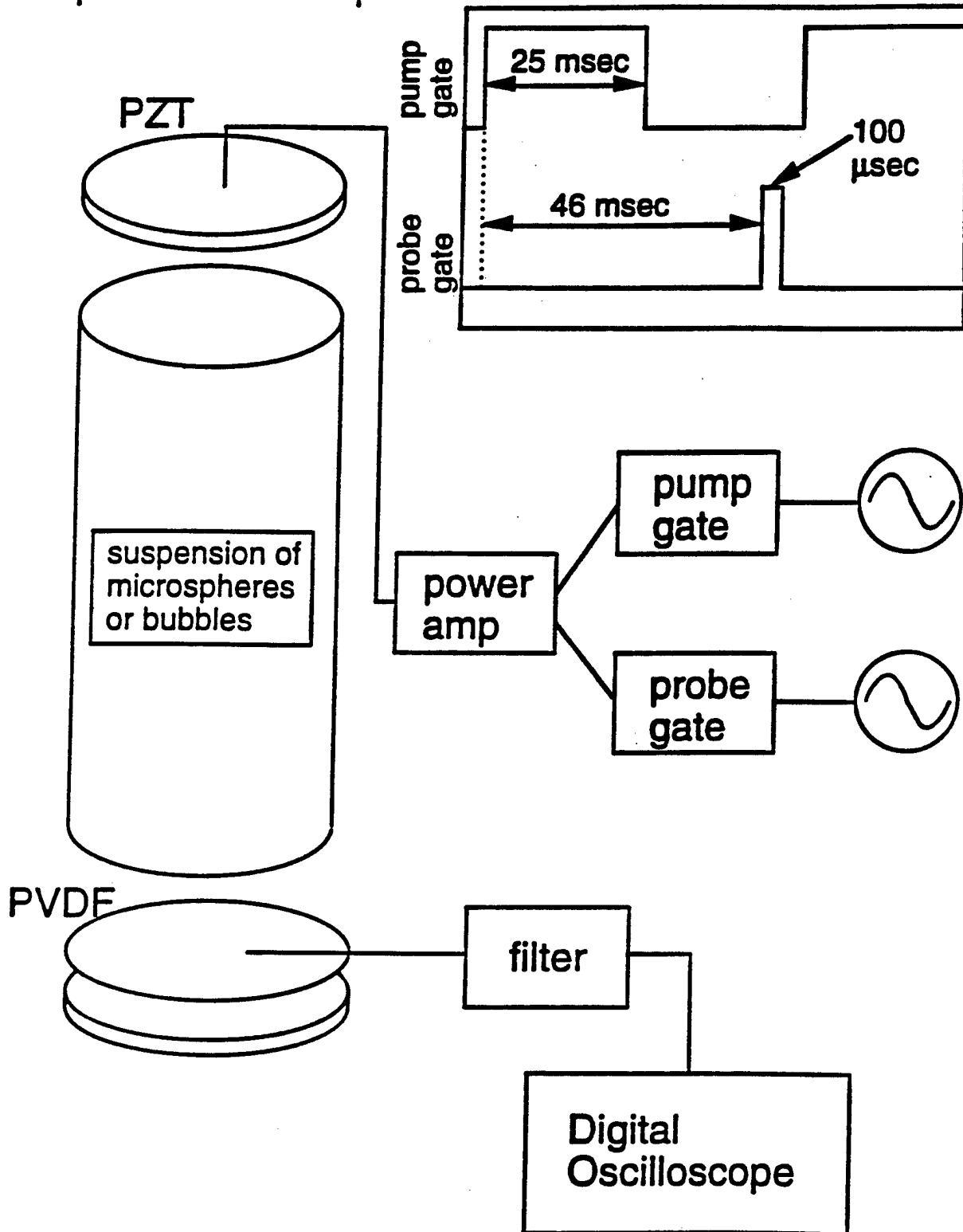
$$R_N = R_1 \frac{\sin[N k d]}{\sin[k d]}$$



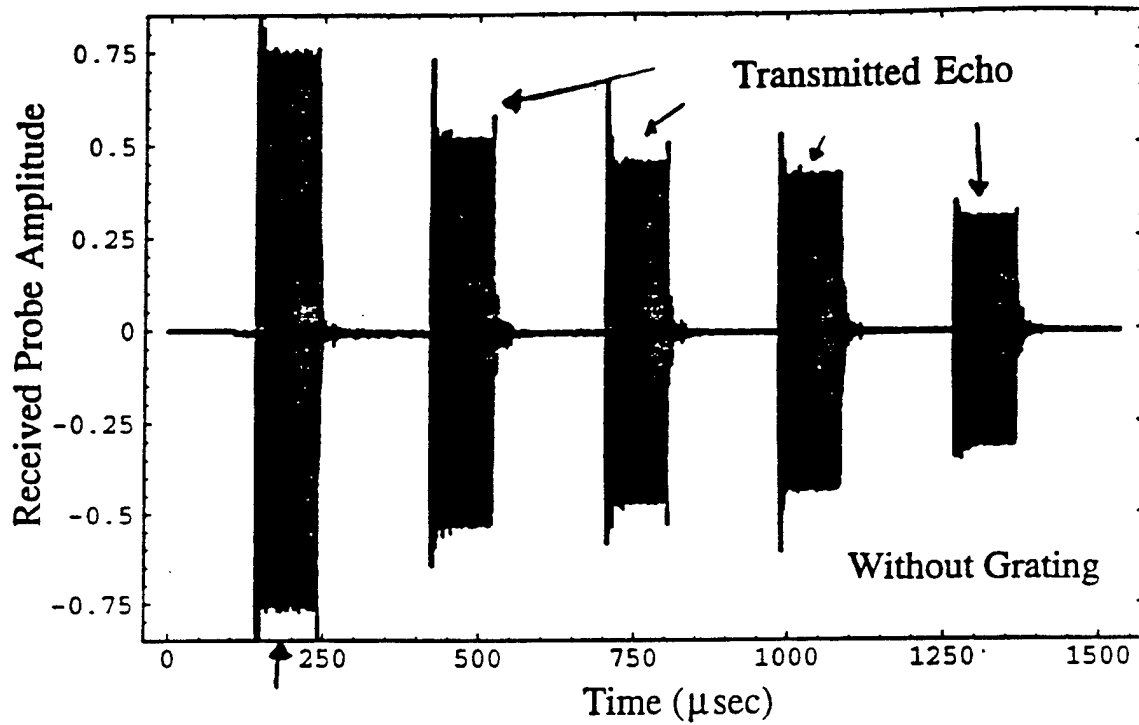
~80 layers
glass microspheres

pump frequency ≈ 800 kHz

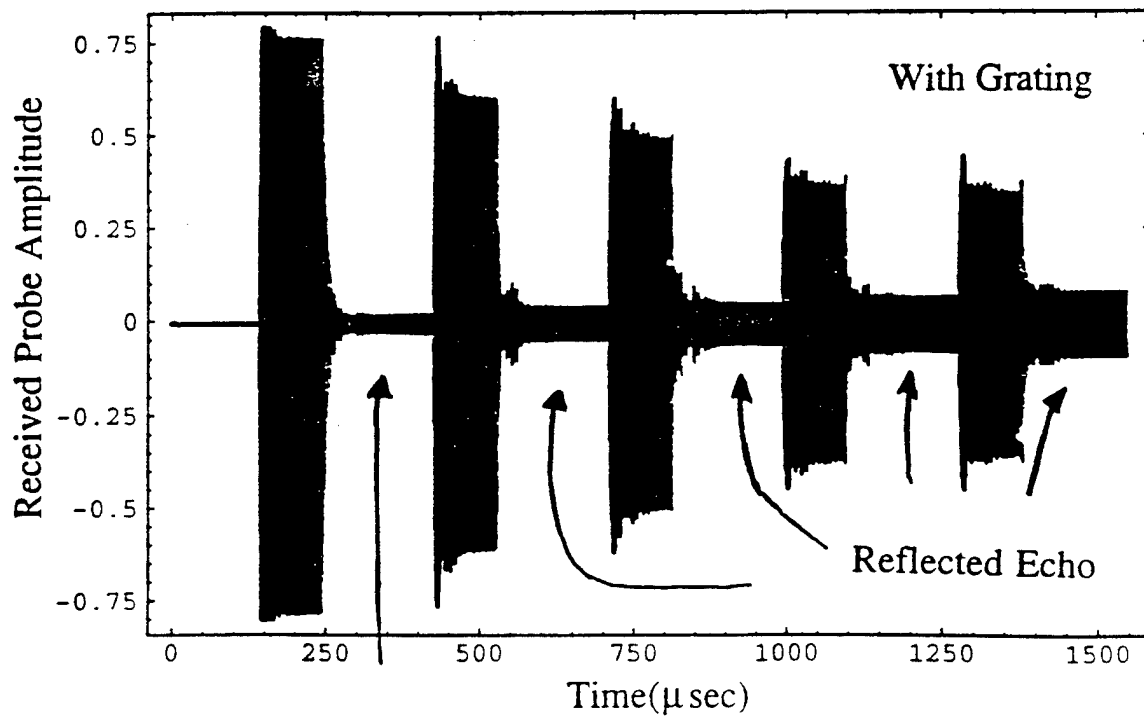
Experimental Setup



Received Probe Wave Signals:

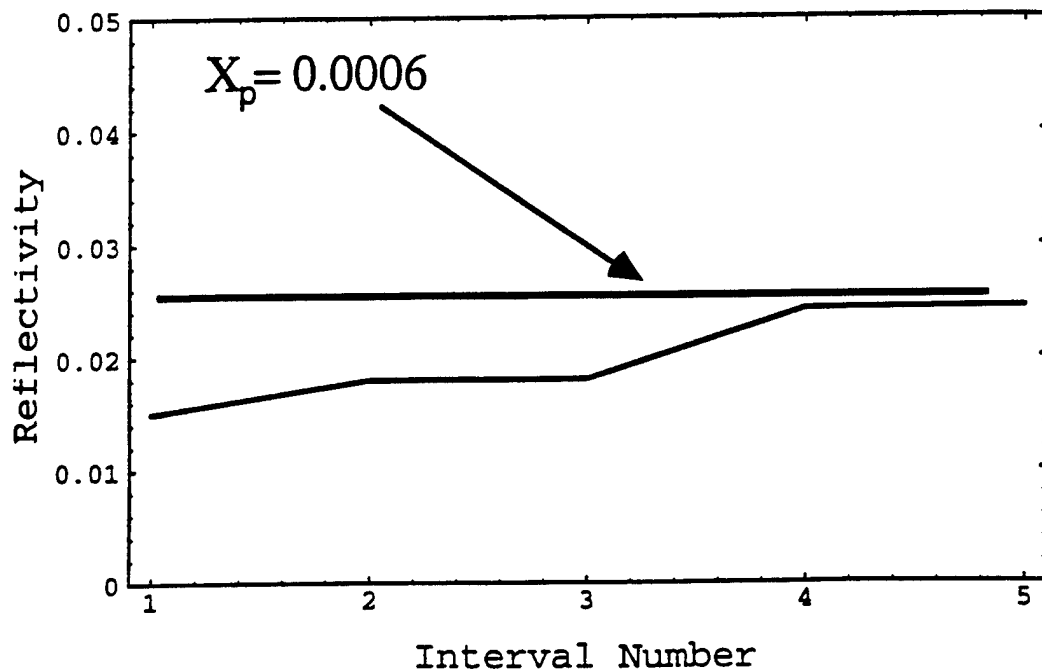
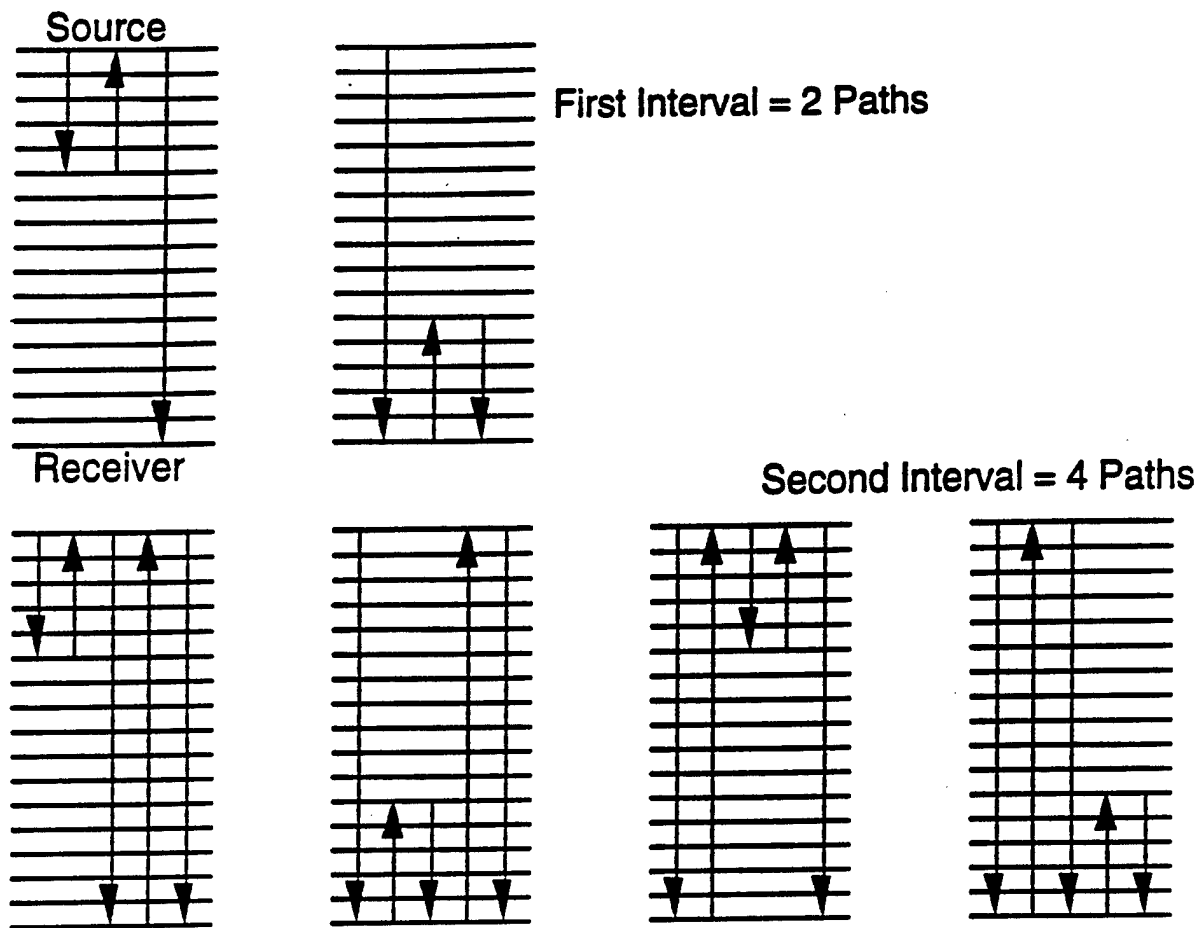


Directly Transmitted
From Source

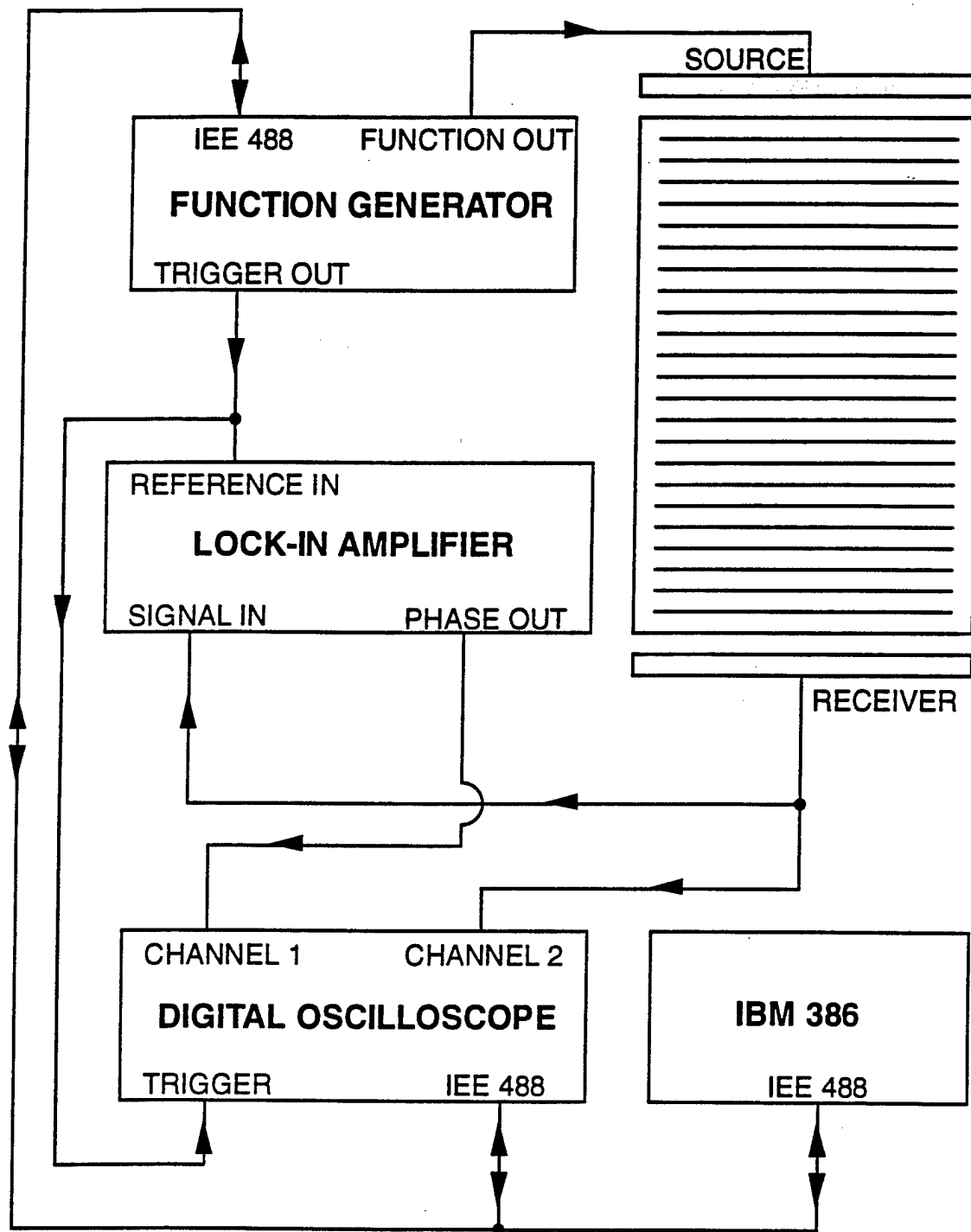


Reflected From Grating

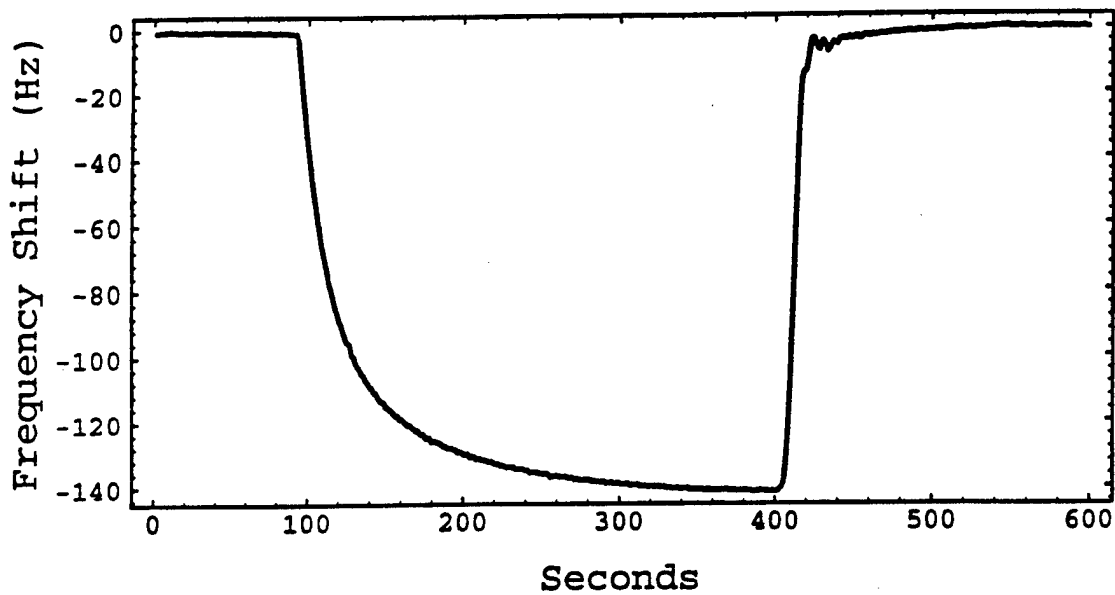
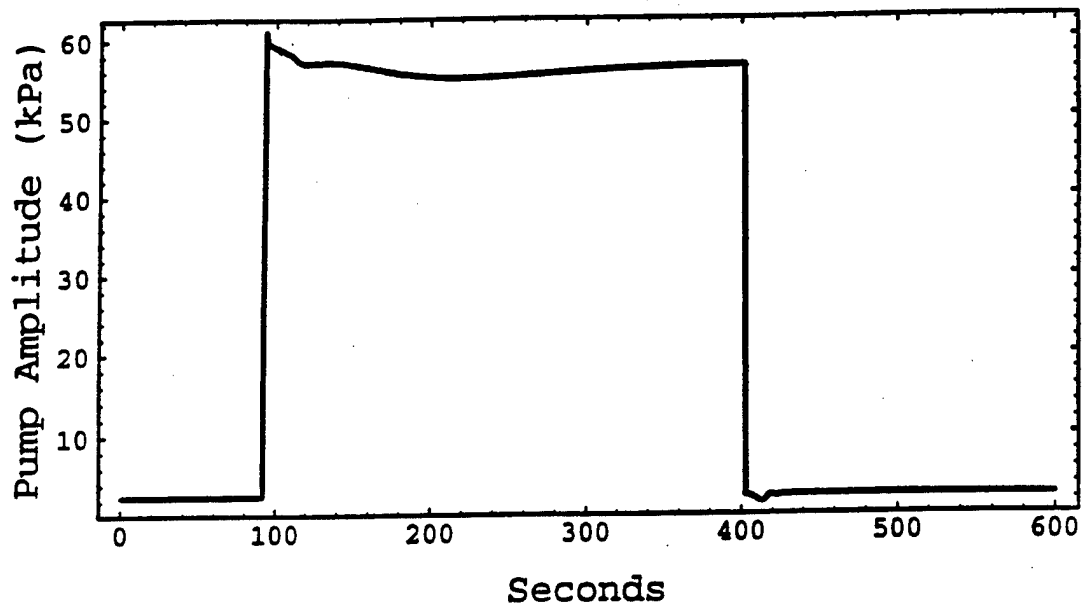
Normalization of the Received Probe Wave:



Frequency Shift Experimental Setup

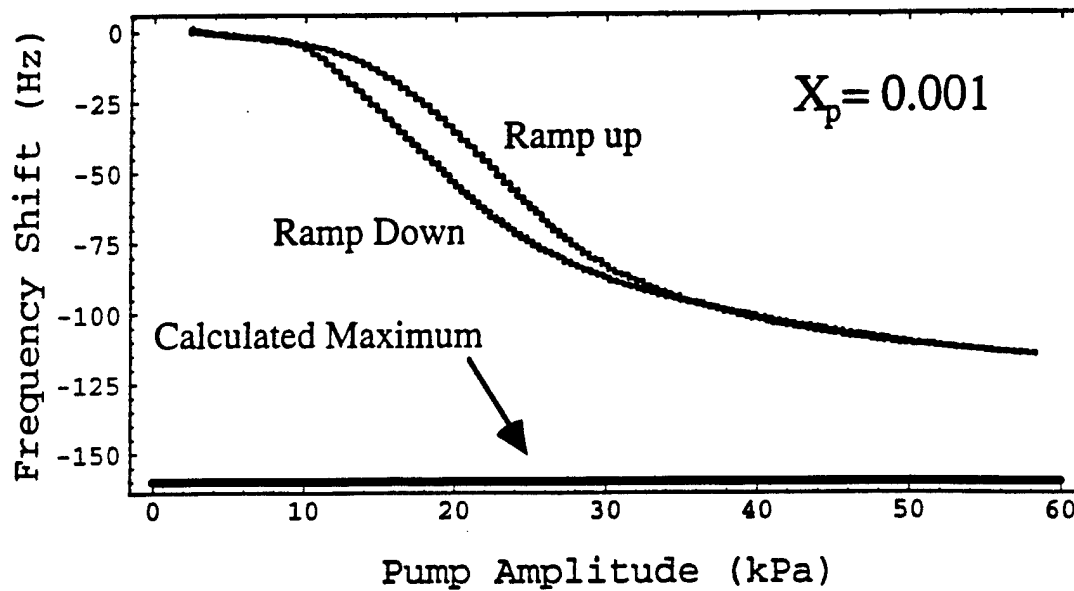
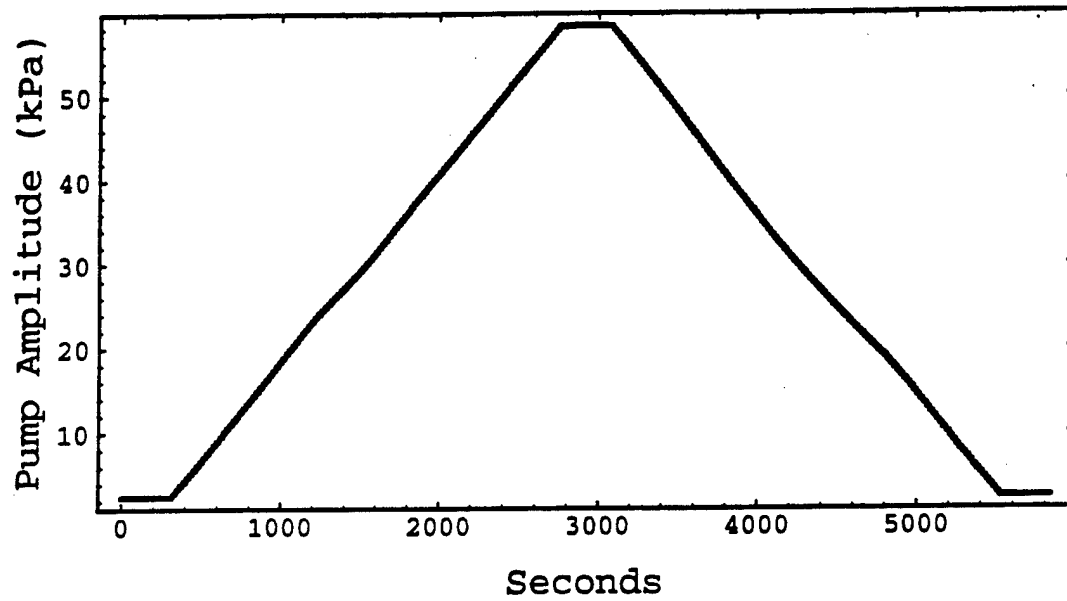


Gated pump amplitude frequency shift:



plastic microspheres
1.05 gm/cc sugar solution
volume fraction = 0.001

Ramped pump amplitude frequency shift:

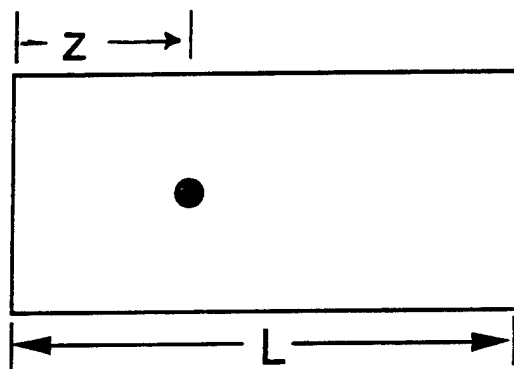


plastic microspheres
1.05 gm/cc salt solution
volume fraction = 0.001

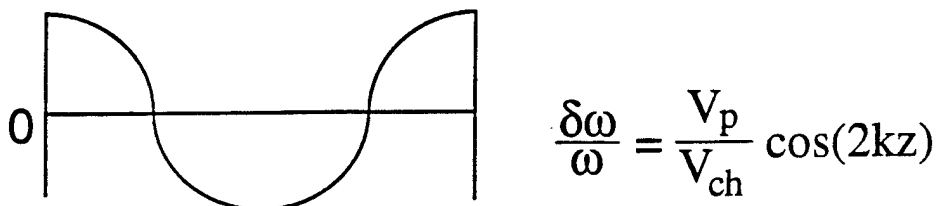
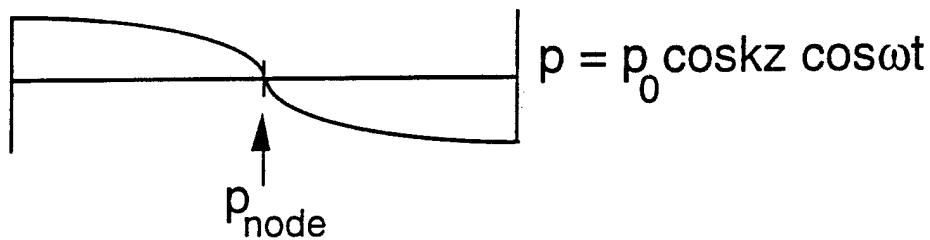
Shift in Frequency from Excluded Volume

$$\frac{\text{Maximum Kinetic Energy}}{\text{Maximum Potential Energy}} = 1 \Rightarrow$$

$$k^2 = \int |\nabla \phi|^2 dV / \int |\phi|^2 dV = \left(\frac{\omega}{c} \right)^2$$



Rigid particle
of volume V_p
Chamber volume = V_{ch}



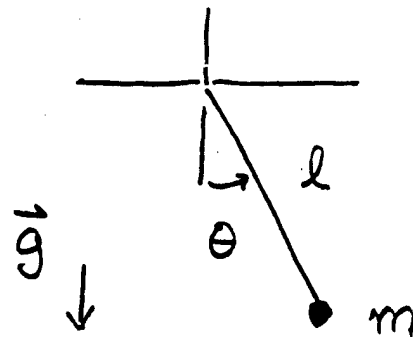
Scattering correction: T. Wang et al. JASA (1982).

Adiabatic invariance/radiation pressure: Putterman (1989).

Frequency Shift:

Adiabatic invariance:

$$dE = \frac{E_0}{\omega_0} d\omega$$



Pendulum
Analogy

Change in frequency for a single particle:

$$(\omega_0 - \omega_1) = \frac{\omega_0}{E_0} [U(z_0) - U(z_1)]$$

Potential energy felt by particle: Gor'kov (1962)

$$U(z) = \frac{E_0}{2} \frac{V_p}{V_{ch}} \left(1 - \frac{\beta_p}{\beta_0} \right) \cos(2kz)$$

$$\frac{\Delta v}{v_0} = -\frac{1}{2} \frac{V_p}{V_{ch}} \left(1 - \frac{\beta_p}{\beta_0} \right) [\cos(2kz_0) - \cos(2kz_1)]$$

Change in frequency for a distribution of particles:

$$\frac{\Delta v}{v_0} = -\frac{1}{2} \frac{V_p}{L} \left(1 - \frac{\beta_p}{\beta_0} \right) \int_{-L/2}^{L/2} n_p(z) \cos\left(2\pi \frac{z}{L}\right) dz$$

E_0	System energy	V_{ch}	Resonator volume
V_p	Particle volume	ω_0	Unperturbed frequency
L	Grating spacing		

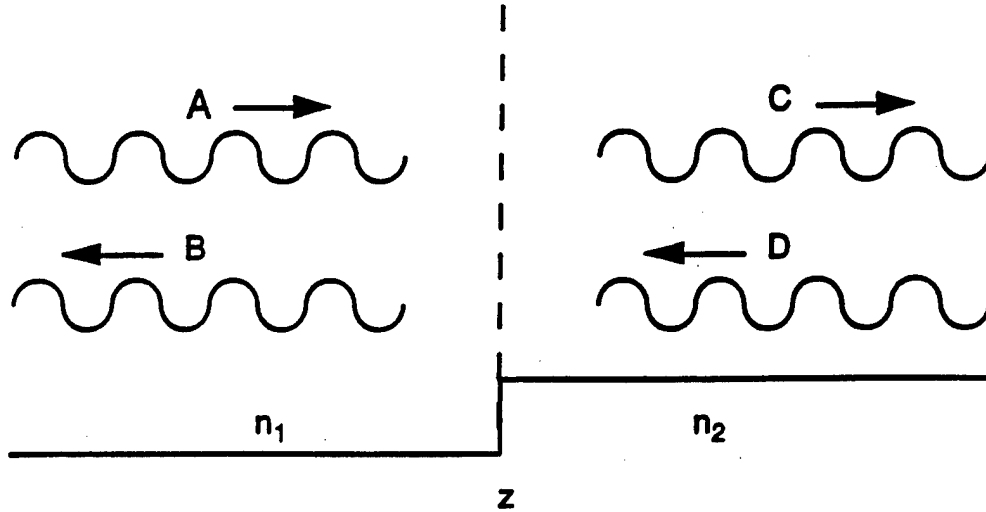
Maximum frequency shift:

$$n_p(z) \Rightarrow \sum_n \delta(z - z_n)$$

$$\Delta v_{\max} = -\frac{1}{2} \left(1 - \frac{\beta_p}{\beta_0} \right) X_p v_0$$

$$\phi_1(z) = A \exp(ik_1 z) + B \exp(-ik_1 z)$$

$$\phi_2(z) = C \exp(ik_2 z) + D \exp(-ik_2 z)$$



Continuity of pressure and velocity at boundary:

$$-i\omega\rho_1\phi_1(0) = -i\omega\rho_2\phi_2(0)$$

$$-\frac{\partial}{\partial z}\phi_1(z)\Big|_{z=0} = -\frac{\partial}{\partial z}\phi_2(z)\Big|_{z=0}$$

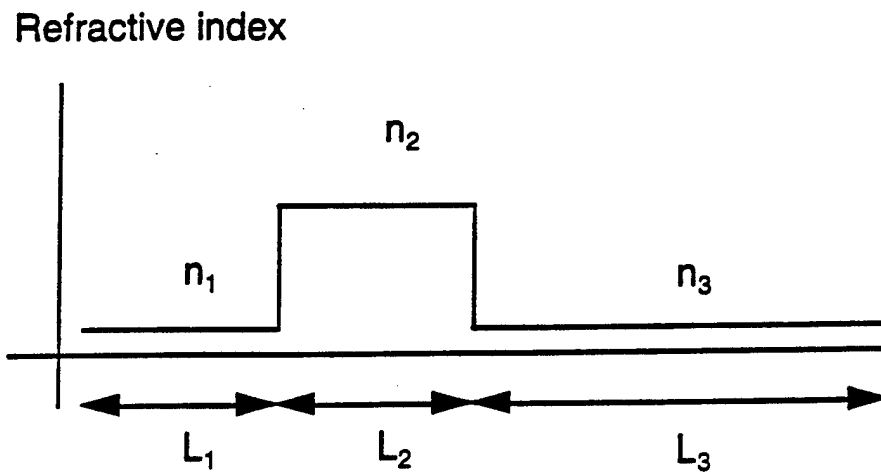
$$\begin{pmatrix} \frac{\rho_2}{i\omega n_2} & -\frac{\rho_2}{i\omega n_2} \\ \frac{\rho_2}{c_0} & -\frac{\rho_2}{c_0} \end{pmatrix} \begin{pmatrix} C \\ D \end{pmatrix} = \begin{pmatrix} \frac{\rho_1}{i\omega n_1} & -\frac{\rho_1}{i\omega n_1} \\ \frac{\rho_1}{c_0} & -\frac{\rho_1}{c_0} \end{pmatrix} \begin{pmatrix} A \\ B \end{pmatrix}$$

Definition of discontinuity matrix:

$$\begin{pmatrix} C \\ D \end{pmatrix} = \frac{1}{2} \begin{pmatrix} \frac{\rho_1}{\rho_2} + \frac{n_1}{n_2} & \frac{\rho_1}{\rho_2} - \frac{n_1}{n_2} \\ \frac{\rho_1}{\rho_2} - \frac{n_1}{n_2} & \frac{\rho_1}{\rho_2} + \frac{n_1}{n_2} \end{pmatrix} \begin{pmatrix} A \\ B \end{pmatrix}$$

$$\begin{pmatrix} C \\ D \end{pmatrix} = d_{12} \begin{pmatrix} A \\ B \end{pmatrix}$$

Transfer matrix approach for frequency shift:



$$t(\omega) = p_3 \cdot d_{23} \cdot p_2 \cdot d_{12} \cdot p_1$$

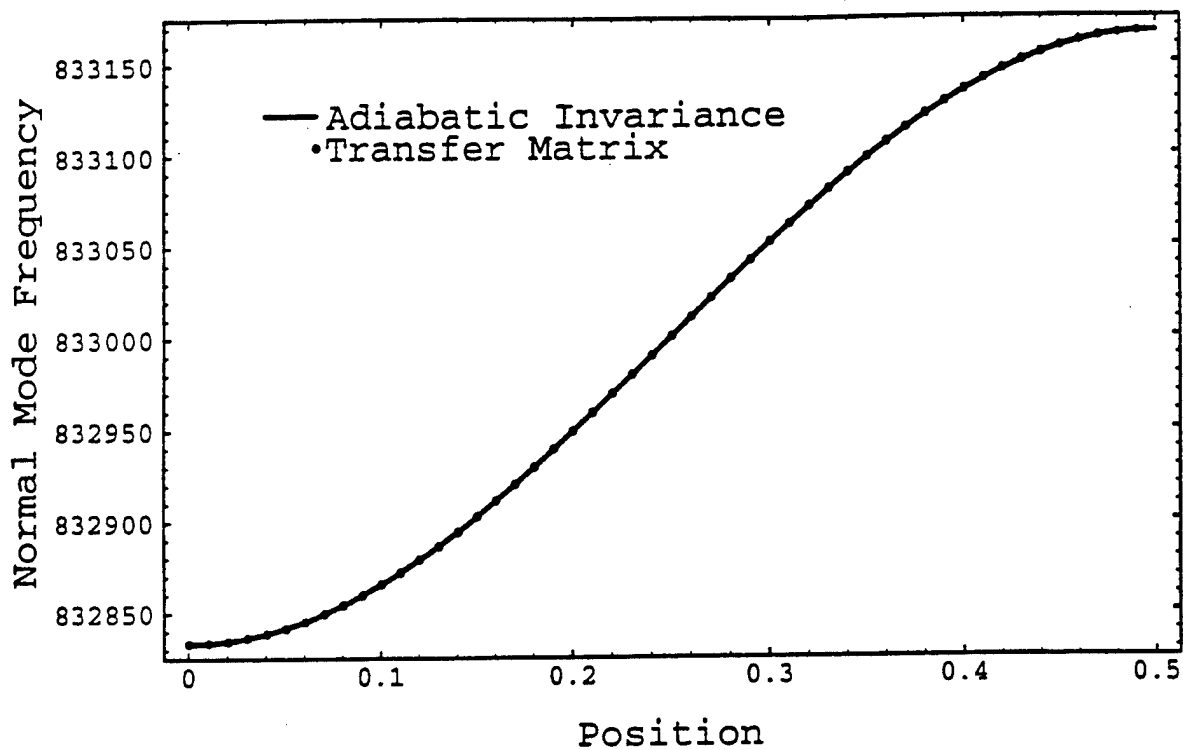
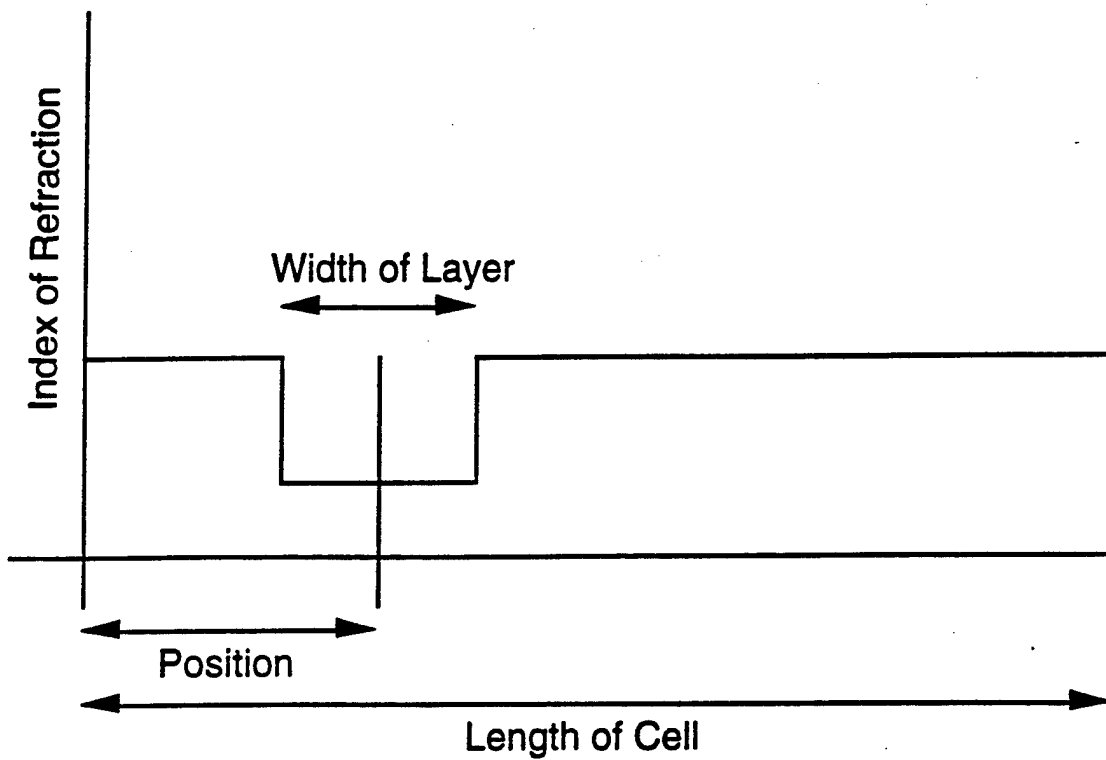
Pressure release boundaries

$$\begin{pmatrix} 1 & 1 \end{pmatrix} t(\omega) \begin{pmatrix} 1 \\ -1 \end{pmatrix} = t_{11}(\omega) - t_{12}(\omega) + t_{21}(\omega) - t_{22}(\omega) \\ = 0$$

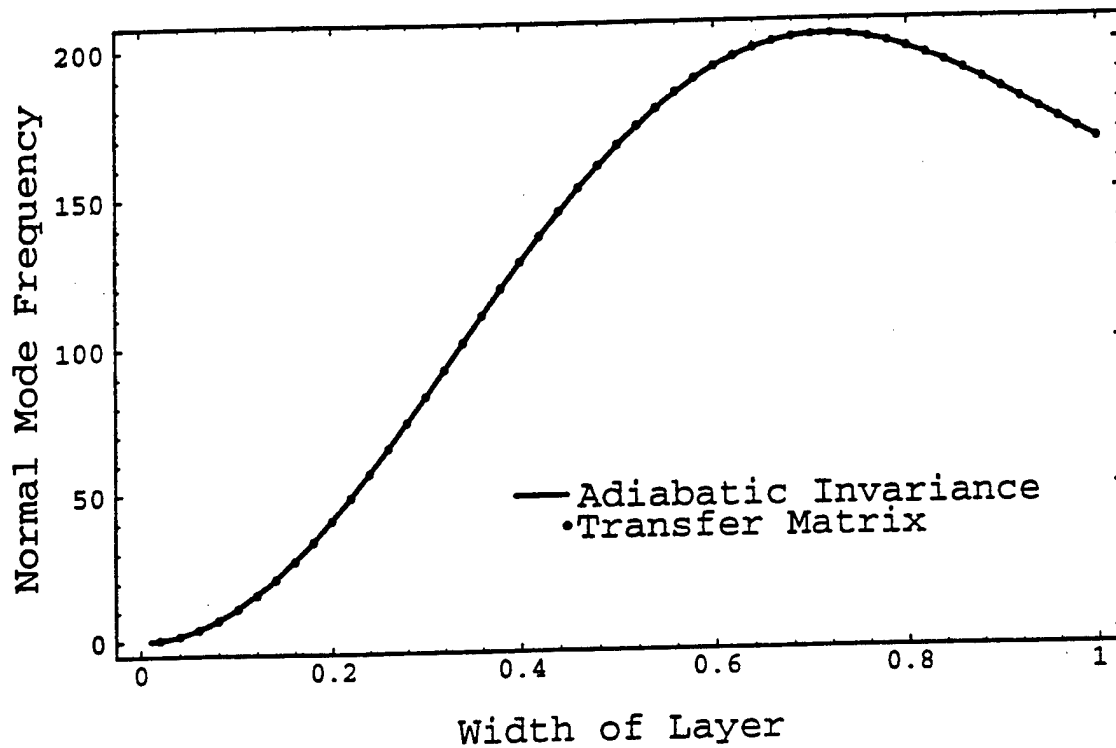
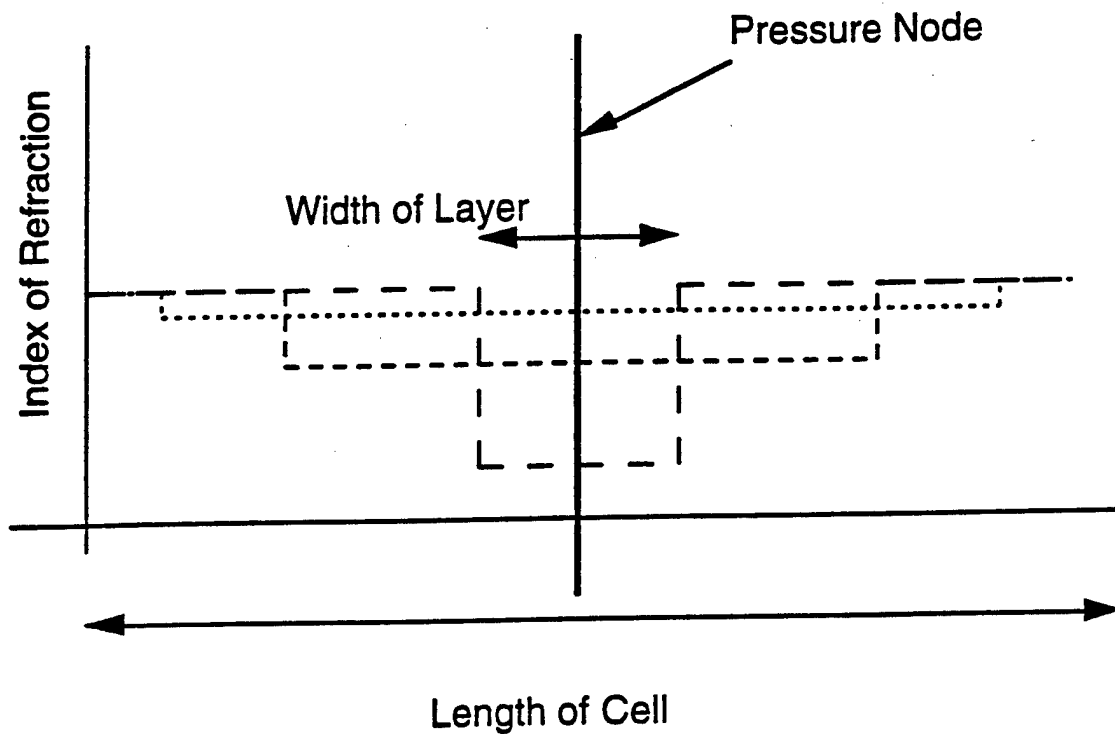
Rigid boundaries

$$\begin{pmatrix} 1 & -1 \end{pmatrix} t(\omega) \begin{pmatrix} 1 \\ 1 \end{pmatrix} = t_{11}(\omega) + t_{12}(\omega) - t_{21}(\omega) - t_{22}(\omega) \\ = 0$$

$$\frac{\Delta v}{v} = -\frac{1}{2} \frac{V_p}{L} \left(1 - \frac{\beta_p}{\beta_0} \right) \int_{-L/2}^{L/2} n_p(z) \cos\left(2\pi \frac{z}{L} \right) dz$$



$$\frac{\Delta v}{v} = -\frac{1}{2} \frac{V_p}{L} \left(1 - \frac{\beta_p}{\beta_0}\right) \int_{-L/2}^{L/2} n_p(z) \cos\left(2\pi \frac{z}{L}\right) dz$$



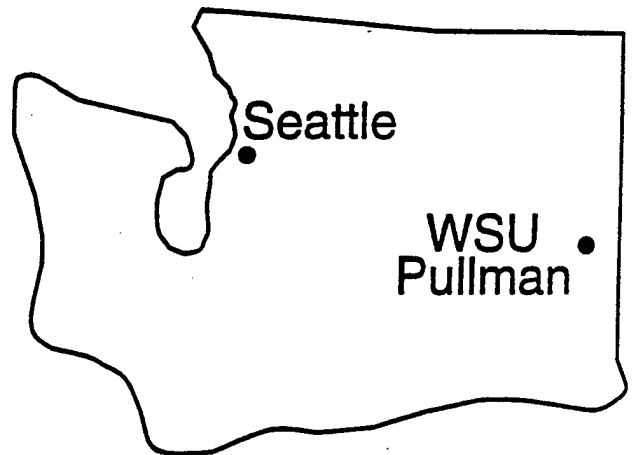
Conclusions on Frequency Shifts:

- Even for volume fractions as small as 0.001, radiation pressure induced particle migration introduces frequency shifts Δf as large as 200 ppm.
- Adiabatic invariance model based on Gorkov radiation potential well yields the general magnitude of the final Δf .
- The approach to equilibrium Δf following pump wave turn-on has been modeled with moderate success.
- Frequency shift of a simulated resonator-layer system computed exactly from the transfer matrix agrees well with adiabatic invariance model for low simulated volume fractions.

Resonances and other mechanisms for elastic contributions to the scattering of sound by objects in water

Philip L. Marston
Scot F. Morse
Karen Gipson

Department of Physics
Washington State University
Pullman, WA 99164-2814



Work supported by the Office of Naval Research

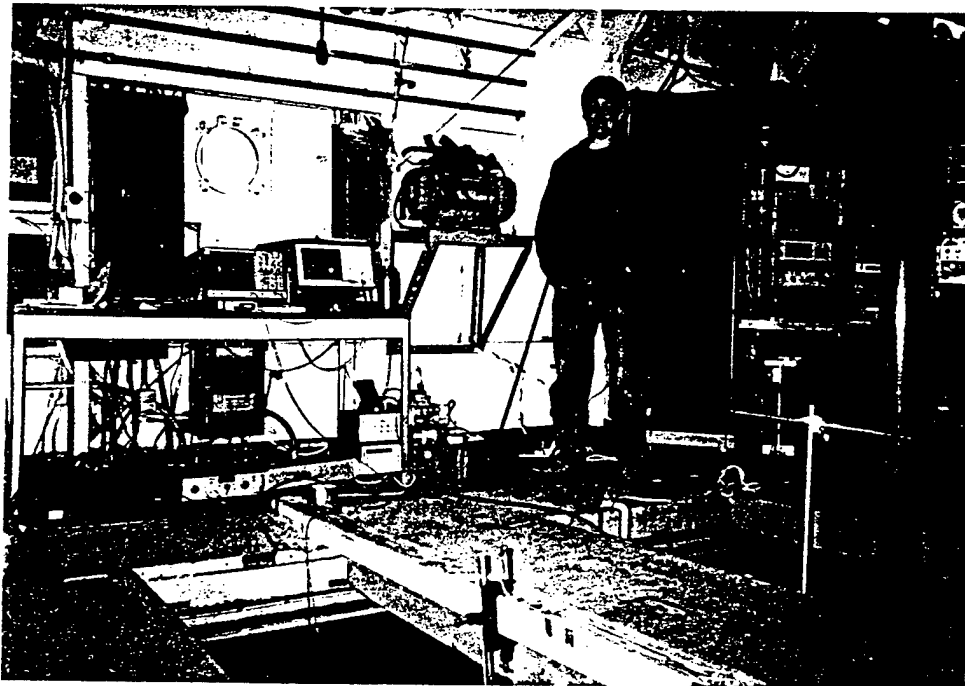
Assistance in measurement for large shell:

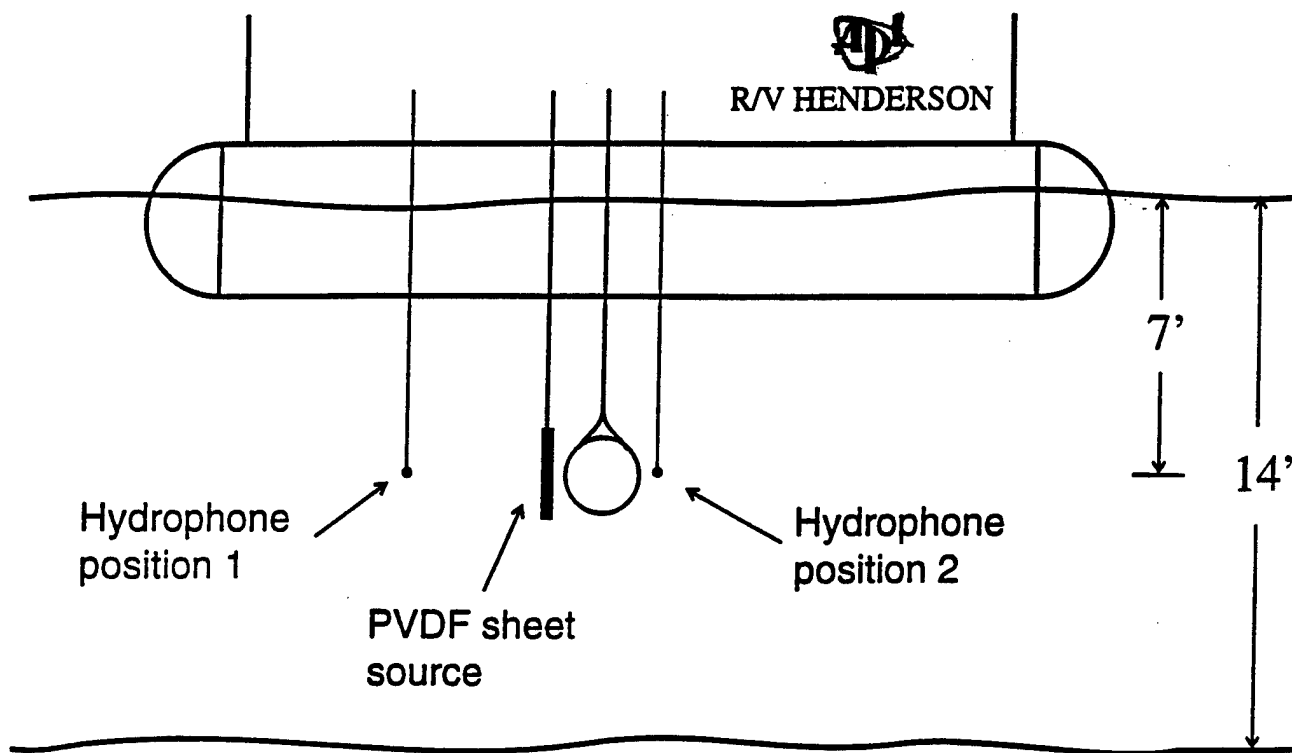
B. T. Hefner (WSU)

K. L. Williams (Applied Physics Laboratory, University of Washington)

Outline

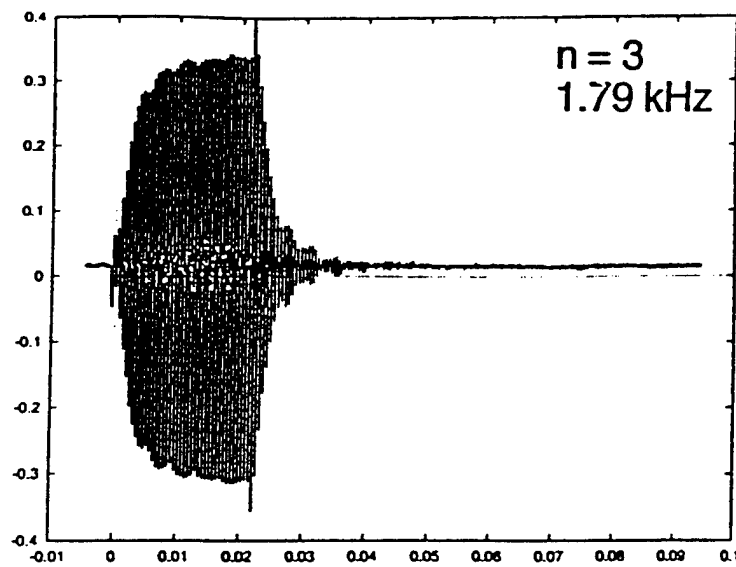
1. Experiments on resonances of a large spherical shell in Lake Union.
2. Normal mode description of resonances:
Resonance Scattering Theory and fluid loading effects for perfectly elastic spheres.
3. Ray descriptions of resonances
 - Leaky or supersonic waves
 - Subsonic waves
 - Anomalies for shells
4. Scattering amplitude for high Q resonances of spheres
5. Noncanonical *shapes* [REDACTED]: High frequency meridional ray backscattering enhancements for high frequency sonar (not a resonance).



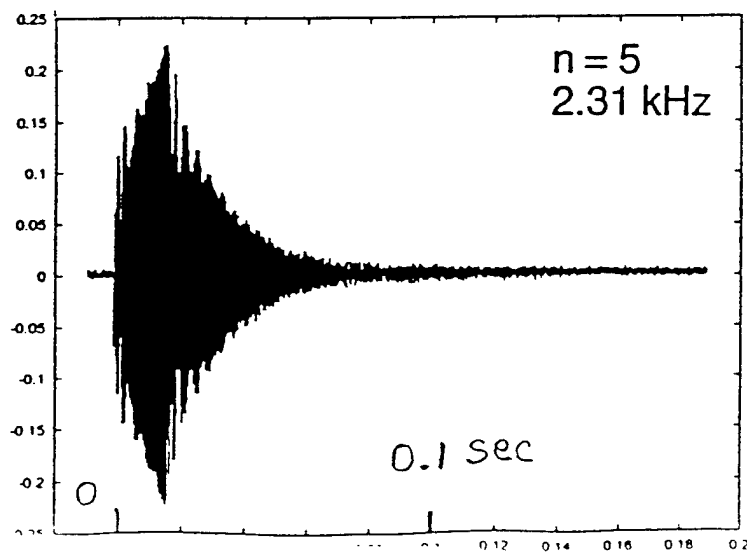
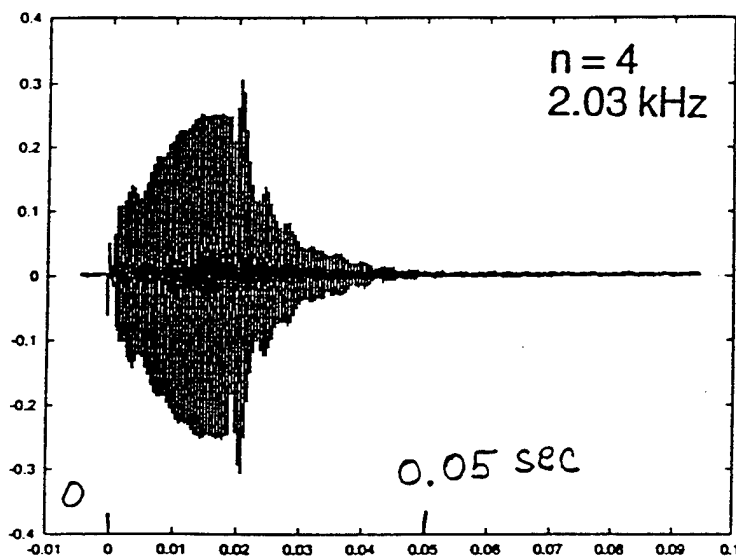


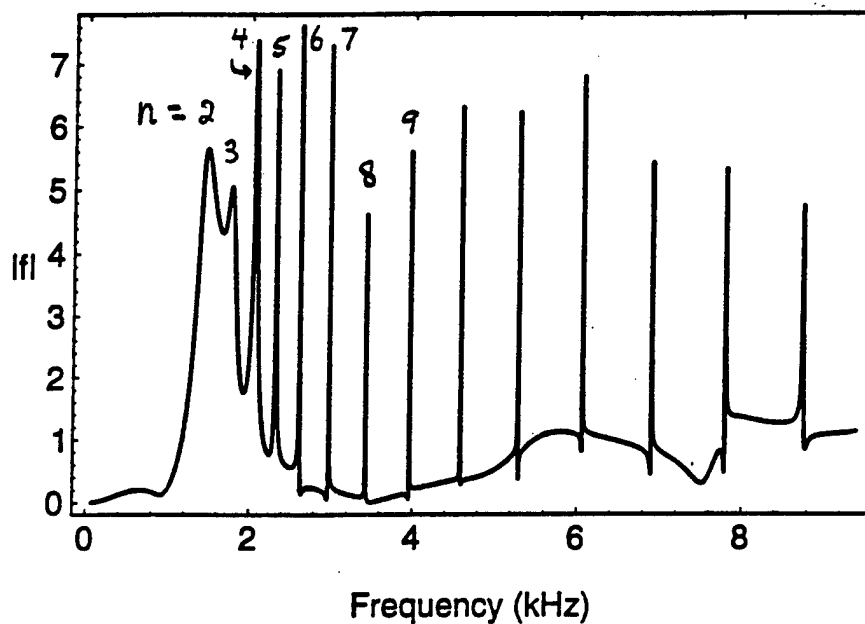
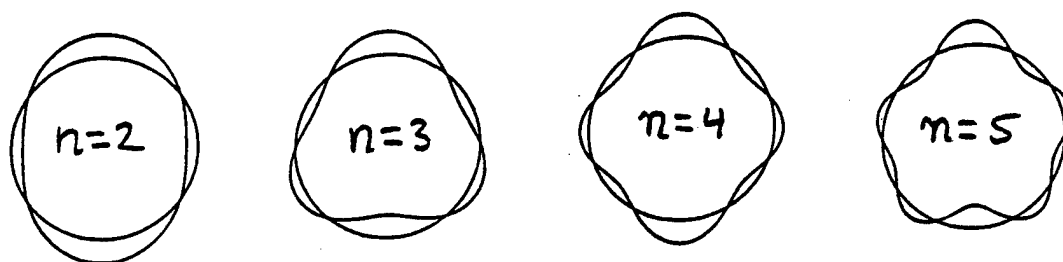
Sphere: stainless steel 316

outside radius	$a = 29.85 \text{ cm}$
thickness	$h = 1.52 \text{ cm}$
	$h/a = 5.1\%$
dry weight	130 kg
density	$r = 7.98 \text{ g/cm}^3$
longitudinal sound speed	$c_L = 5770 \text{ m/s}$
shear sound speed	$c_S = 3110 \text{ m/s}$



Forward
scattering
measurements
on n th
mode
resonance

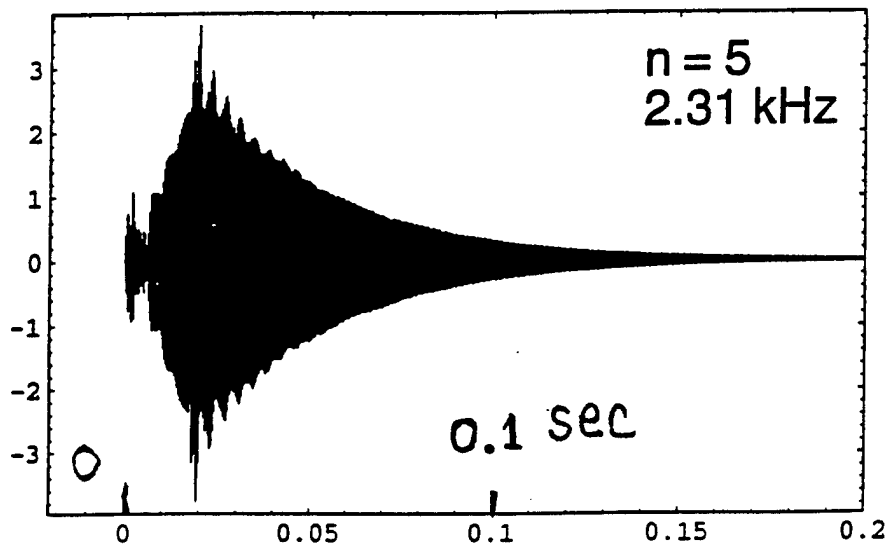
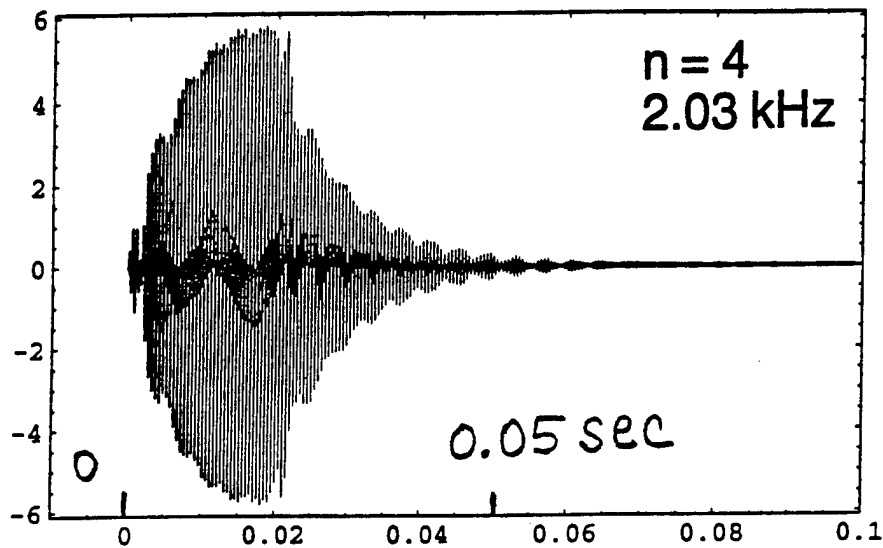
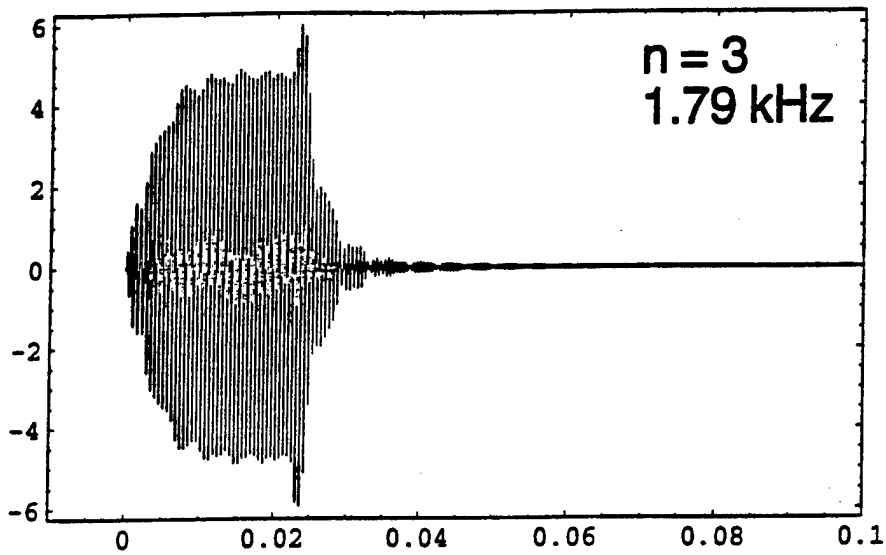




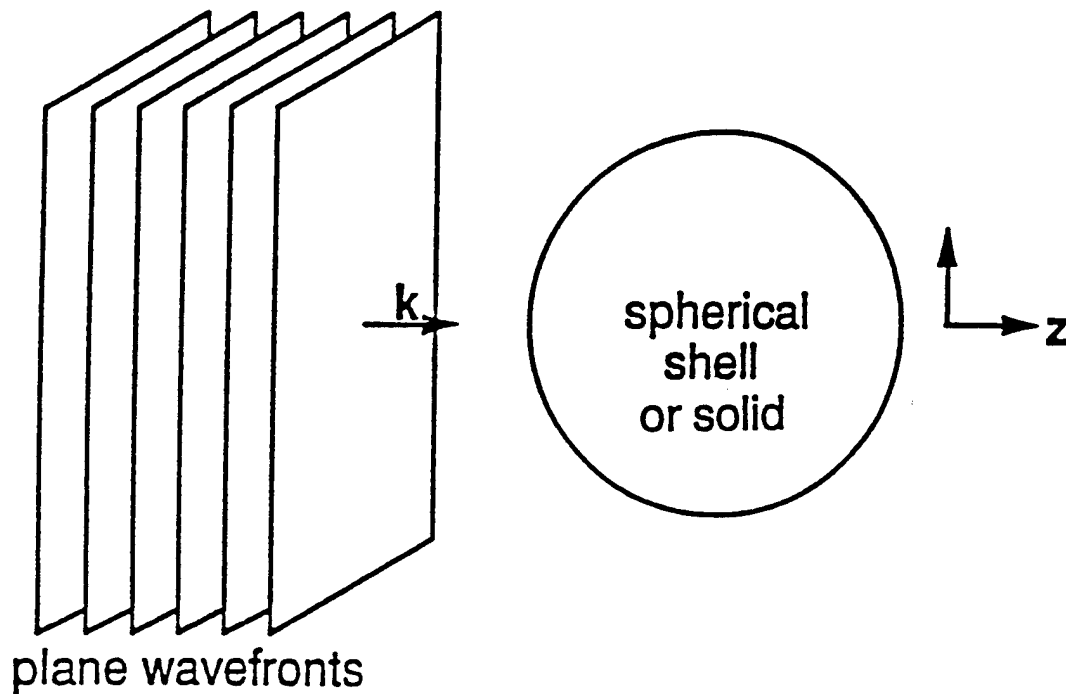
“flexural” resonances

n	Frequency	
	calculated (kHz)	measured (kHz)
2	1.46	1.50
3	1.76	1.79
4	2.05	2.03
5	2.31	2.31
6	2.60	2.60
7	2.96	2.96
8	3.40	3.39
9	3.93	3.93

Synthesized
far field
backscatter
40 cycle burst



BACKSCATTERING BY ISOTROPIC SPHERES



Total far-field pressure

$$r \gg ka^2$$

$$p = e^{ikz} + (a e^{ikr} / 2r) f$$

$f = \text{form function}$

Backscattering

$$f_{\text{PWS}} = (2/i(ka)) \sum (-1)^n (2n + 1) B_n(ka) / D_n(ka)$$

B_n and D_n are 5×5 determinants
(empty shells)

[or 3×3 determinants (solid spheres)]

containing spherical Bessel, Neumann, and Hankel functions.

RST analysis of monostatic and bistatic acoustic echoes from an elastic sphere

G. C. Gaunard and H. Überall^{a)}

Naval Surface Weapons Center, R43 White Oak, Silver Spring, Maryland 20910

J. Acoust. Soc. Am. 73 (1), January 1983

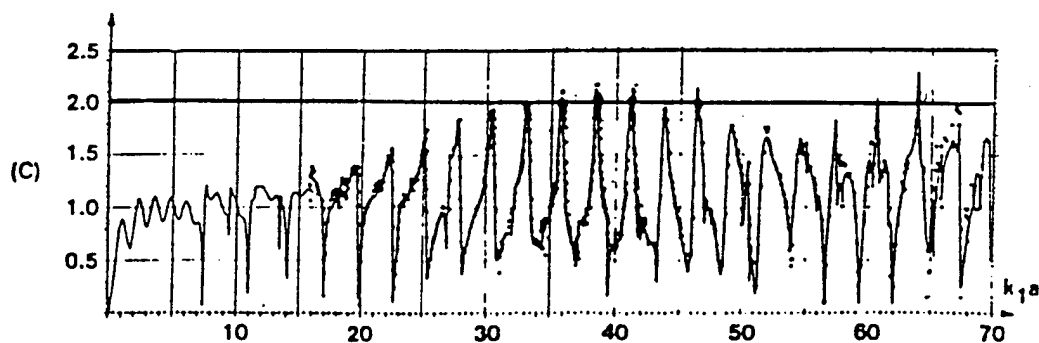
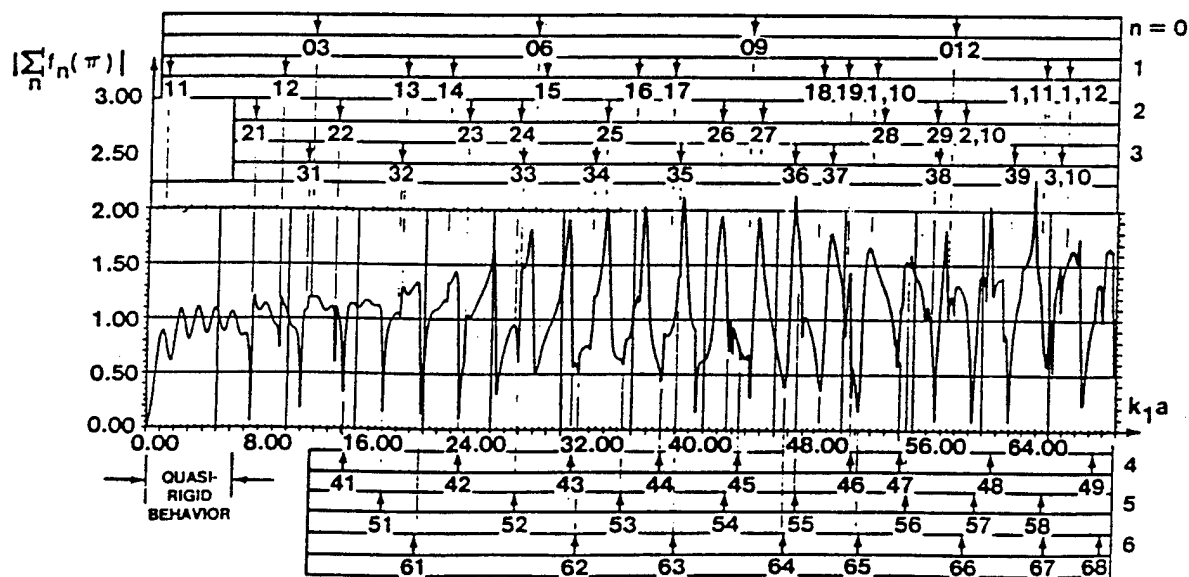


FIG. 2. Form-function versus $k_1 a$ for the tungsten carbide sphere. (A) Measurements (from Ref. 13), (B) classical theory, (C) comparison.



Resonance Scattering Theory: Flax et al.. JASA 63, 723(1978).

Flax, Gaunaurd, and Überall, *Physical Acoustics*, Vol. 15(1981).

Product Expansion of the S function:

Marston, Kargl, and Sun, in *Acoustic Resonance Scattering*, edited by H. Überall (Gordon and Breach, 1992) pp. 305-333.

$$f(x) = \sum_{n=0}^{\infty} f_n(x), \quad f_n = i^{-1} g_n B_n / D_n, \quad x = ka, \quad D_n(x_{nl}) = 0$$

complex \nearrow

(+) = Sphere, (-) = Infinite Cylinder

$$[g_n(x)]^{(+)} = 2(-1)^n (2n+1)/x, \quad [g_n(x)]^{(-)} = 2(-1)^n [i\epsilon_n / (i\pi x)^{1/2}],$$

$$f_n(x) = (2i)^{-1} [S_n(x) - 1] g_n, \quad S_n = S \text{ function with } |S_n| = 1$$

$$S_n = S_n^{(b)} S_n^{(e)}, \quad S_n^{(e)} = \prod_l \frac{(x_{nl}^* - x)(x_{nl} + x)}{(x_{nl}^* + x)(x_{nl} - x)}, \quad n \neq 0$$

$$x_{nl} = X_{nl} - i\Gamma_{nl}/2$$

cancel for weak damping

$$f_n^{(b)} = \left[(S_n^{(b)} - 1)/2i \right] g_n, \quad f_n^{(e)} = \left[(S_n^{(e)} - 1)/2i \right] g_n S_n^{(b)},$$

$$f_n = f_n^{(b)} + f_n^{(e)}, \quad f_{nl} = (1/2) S_n^{(b)} g_n \Gamma_{nl} [X_{nl} - x - (i/2)\Gamma_{nl}]^{-1}$$

background RST weak damping contribution to $f_n^{(e)}$

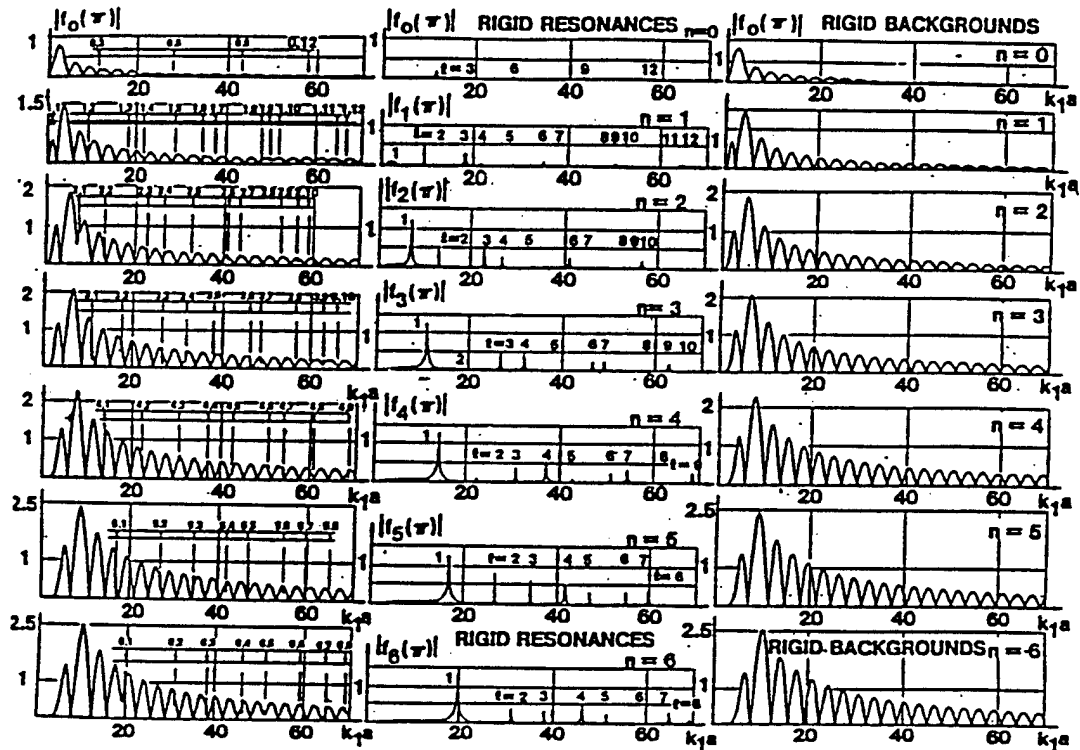
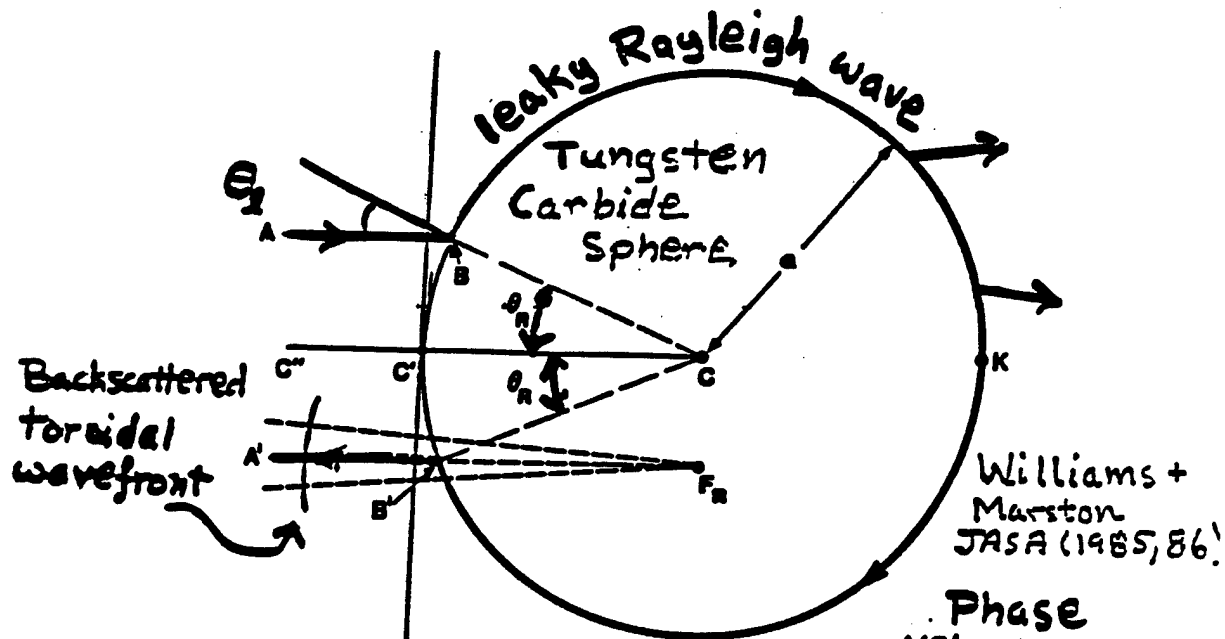


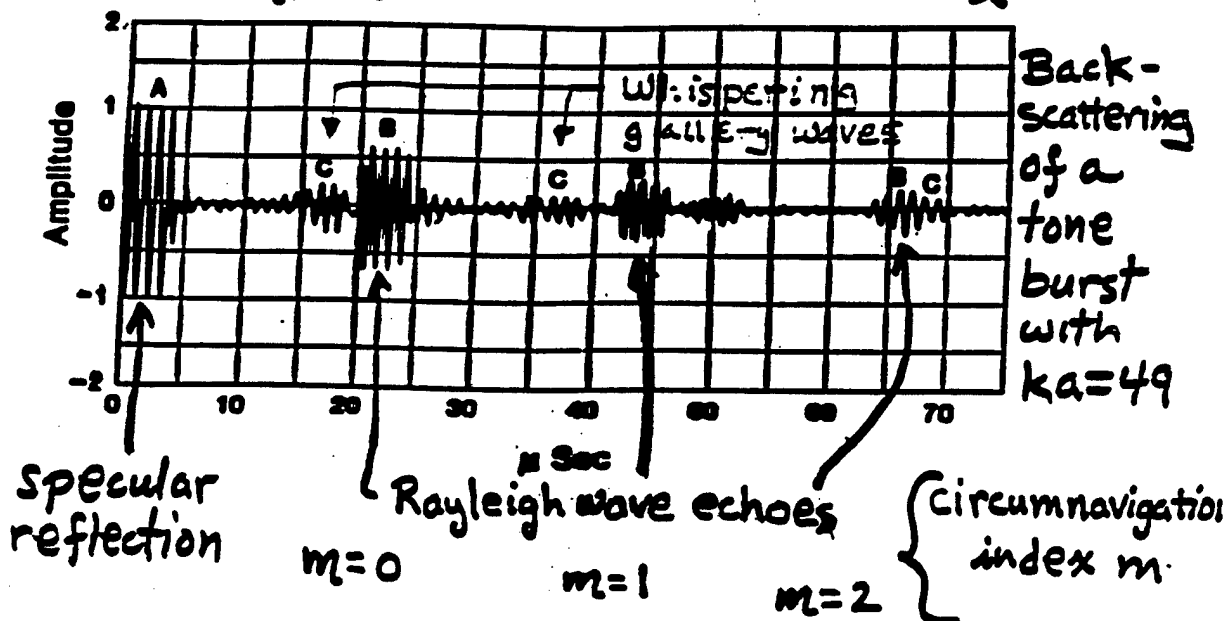
FIG. 3. Separation of the first seven partial waves (left) into resonances (center) and rigid backgrounds (right). Resonances are labeled by an index l with node n . Arrows show resonance features (or dips) in the modes.



Angle of incidence for coupling to leaky wave of type 2

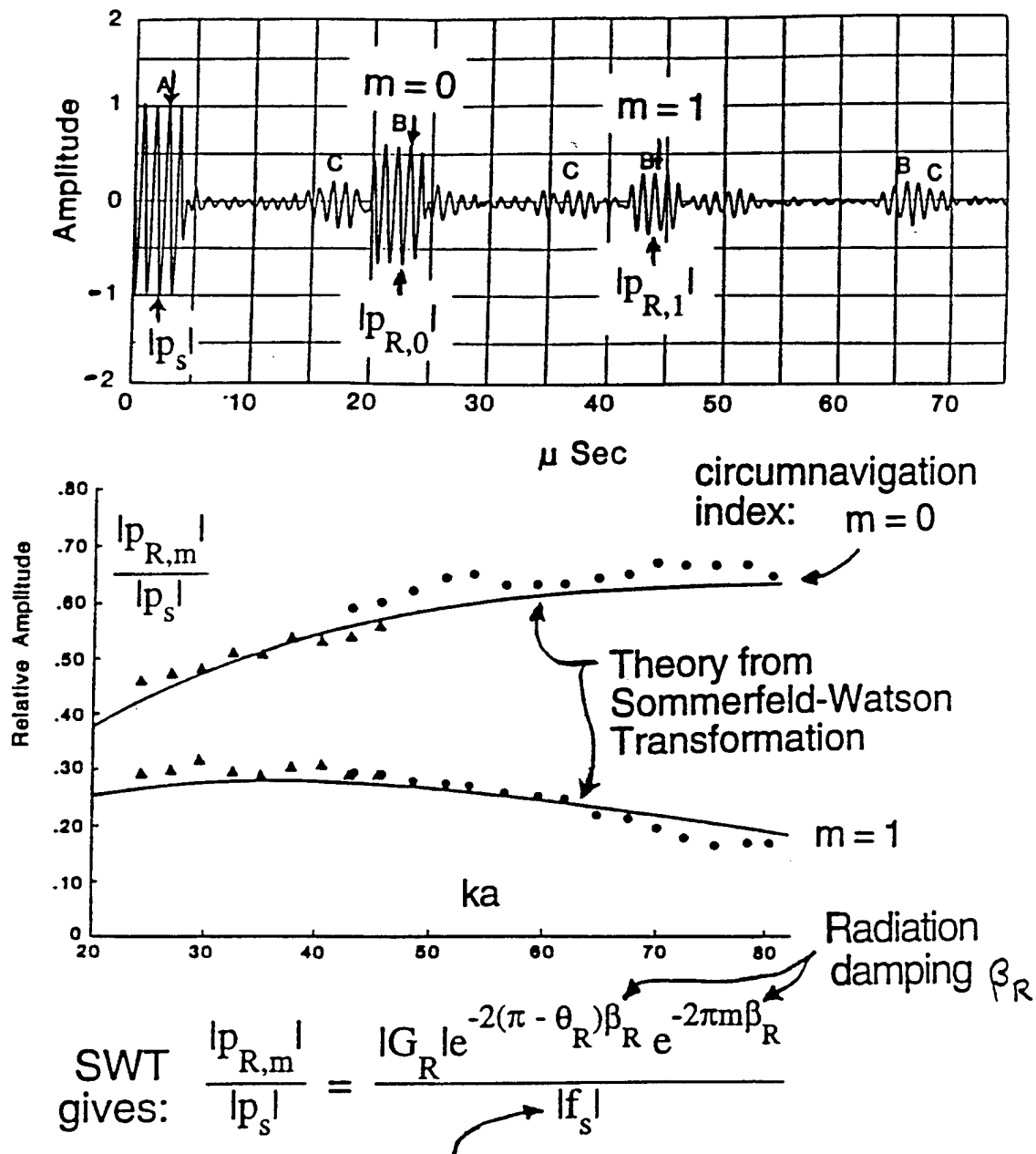
$$\theta_2 = \sin\left(\frac{c}{c_2}\right)$$

Phase velocity of surface wave $c_2 > c$



$$ka = \left(\frac{2\pi}{\lambda \text{ in Water}}\right) (\text{sphere radius}) = \left(\frac{\omega_{\text{burst}}}{c}\right) a$$

Backscattering amplitudes from a tungsten carbide sphere

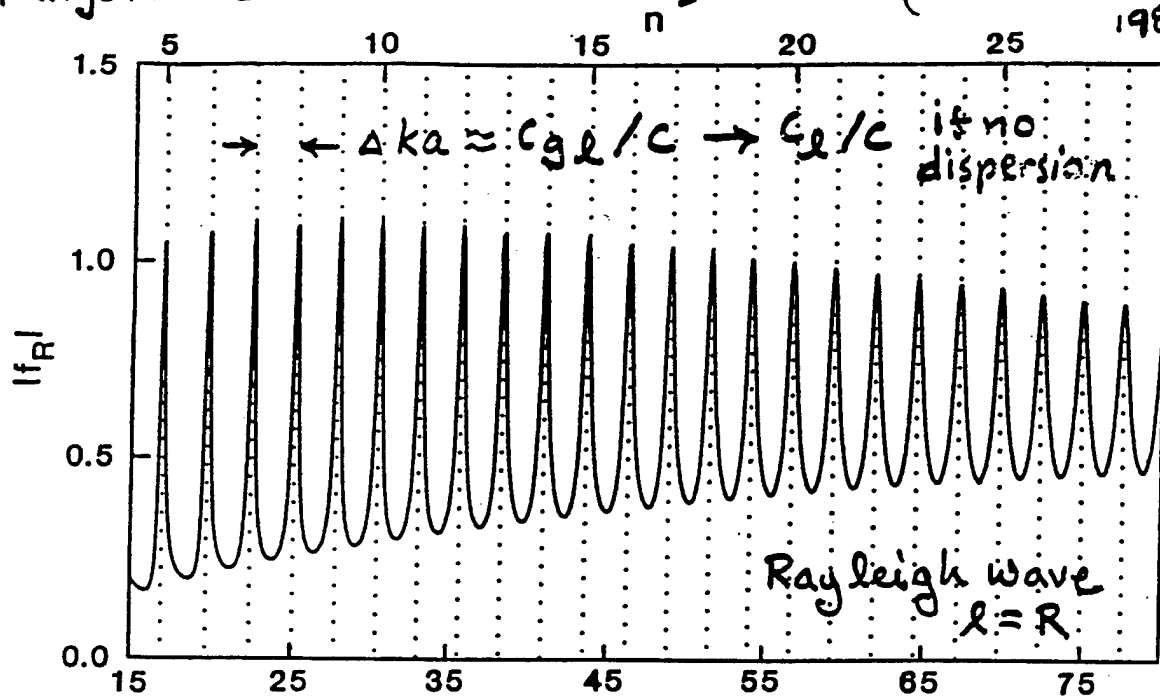


specular form function $|f_s| = (\rho_{EC_L} - \rho_{WC}) / (\rho_{EC_L} + \rho_{WC})$

G_R is a coupling coefficient which accounts for:
 (1) interaction for the acoustic field with the Rayleigh wave and (2) axial caustic for sphere.

tungsten carbide in water

(Williams Thesis, 1985)



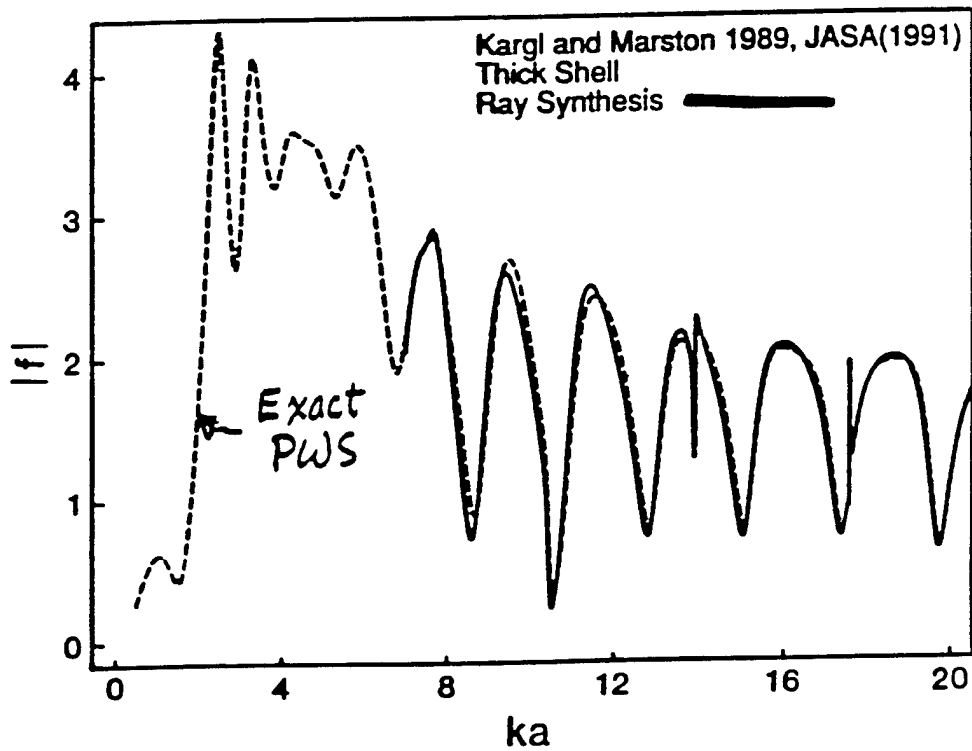
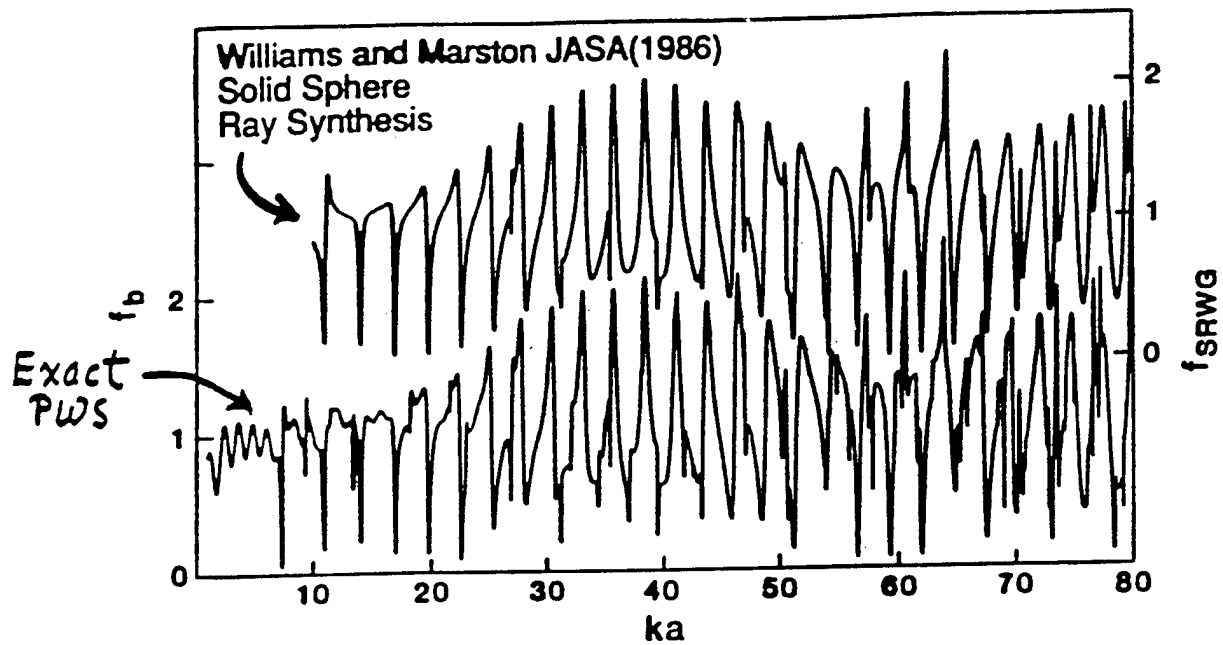
Fabry-Perot form for the l th surface wave

$$f_l = \frac{-G_l e^{-2(\pi - \theta_l)\beta_l} e^{i\eta_l}}{[1 + \exp(-2\pi\beta_l + i2\pi xc/c_l)]}, \quad x \equiv ka$$

1. Works both "on" and "off" resonance.
2. The damping β_l need not be small.
3. Resonances need not be isolated.

GTD for backscattering from elastic spheres and cylinders in water and the coupling of surface elastic waves with the acoustic field Philip L. Marston JASA (January, 1988)

$$|f_l(x \approx x_{nl})| \approx |f_{nl}(x)| \begin{cases} \text{RST} \\ \text{Breit-Wigner} \end{cases}$$



$\beta_l, \epsilon_l/c$ from roots of $D_l(ka)=0$
complex \nearrow \nwarrow real

G_l from comparison with RST

Ray theory near a resonance reduces to:

$$f_l(x) \approx \left(-G_l e^{i\eta_l/4\pi i\beta_{nl}} \right) \left\{ \gamma_{nl} \left[\bar{X}_{nl} - x - (i/2)\gamma_{nl} \right]^{-1} \right\},$$

where $x = \bar{X}_{nl}$ denotes the resonance conditions

Require that complex frequency plane residue match the RST residue in

$$f_{nl} = (1/2) S_n^{(b)} g_n \Gamma_{nl} \left[X_{nl} - x - (i/2)\Gamma_{nl} \right]^{-1}$$

$$\text{sphere: } n^{(+)} = (xc/c_l) - (1/2); \quad \text{cylinder: } n^{(-)} = xc/c_l,$$

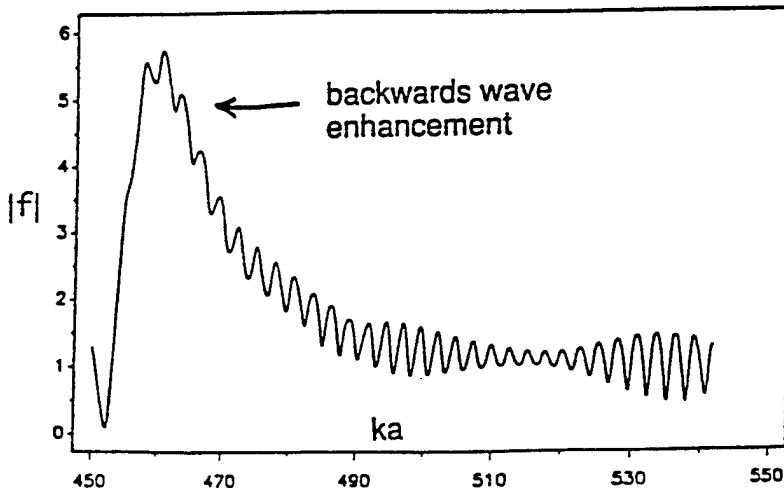
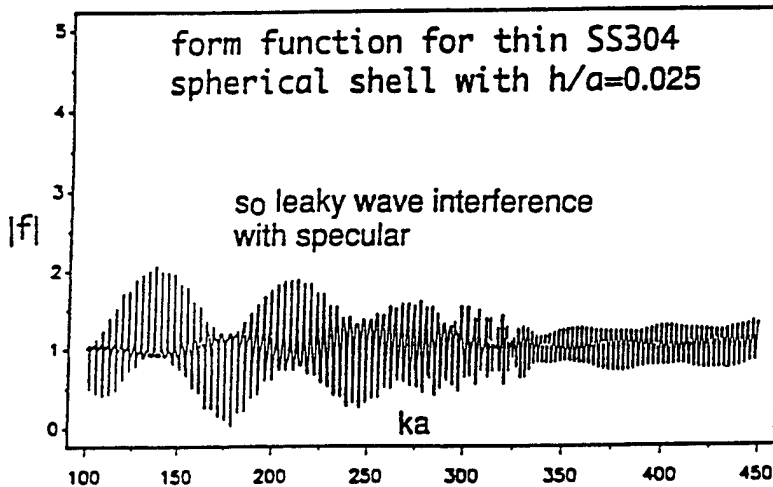
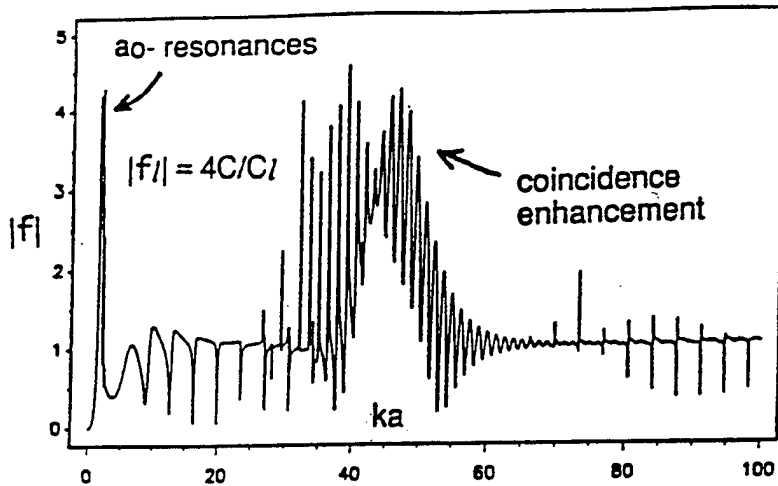
$$\text{gives } G_l \approx -2\pi i \beta_l g_n S_n^{(b)} e^{-i\eta_l} \quad \text{and since } |S_n^{(b)}| = 1$$

$$\left| G_l^{(+)}(x) \right| \approx 8\pi \beta_l c/c_l, \quad \left| G_l^{(-)}(x) \right| \approx 8\pi \beta_l / (\pi x)^{1/2}.$$

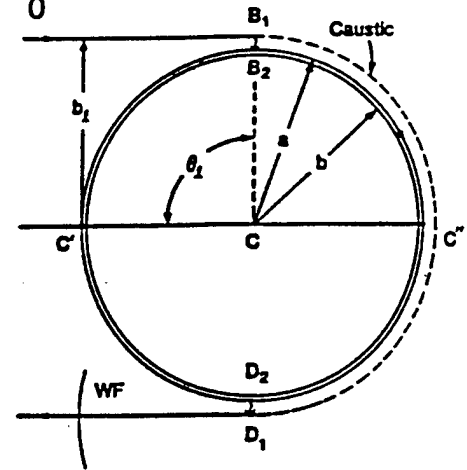
Marston JASA (1987, 1988). For rigid background:

$$\text{As } ka \rightarrow \infty, \quad \arg \left[G_l^{(-)} \right] \rightarrow \pi/4, \quad \arg \left[G_l^{(+)} \right] \rightarrow 0$$

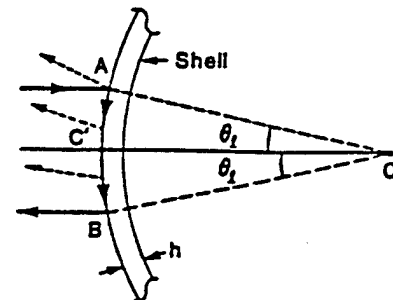
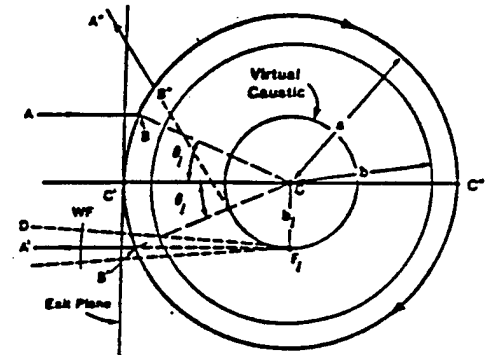
General background: Marston, Wave Motion (1995)

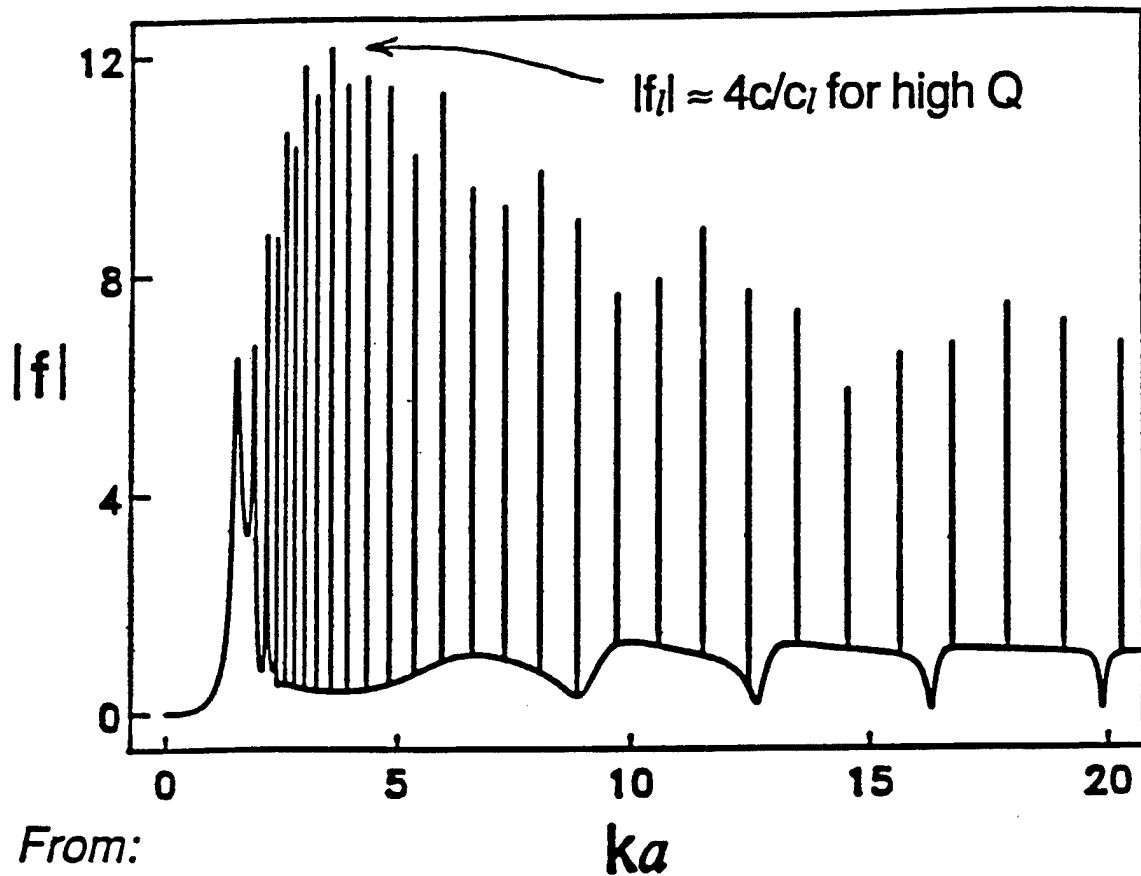


a_0^- wave

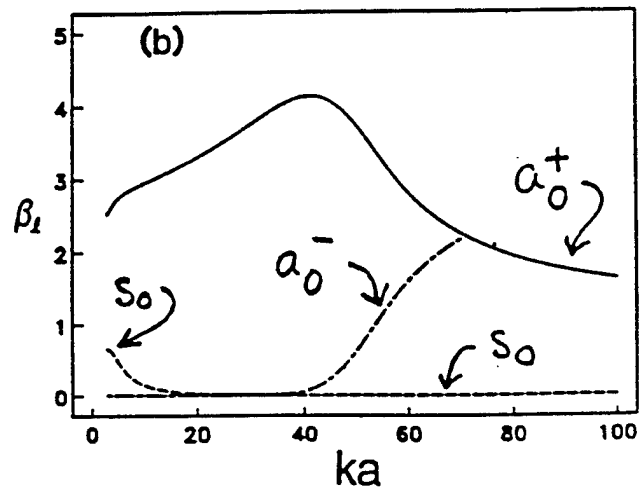
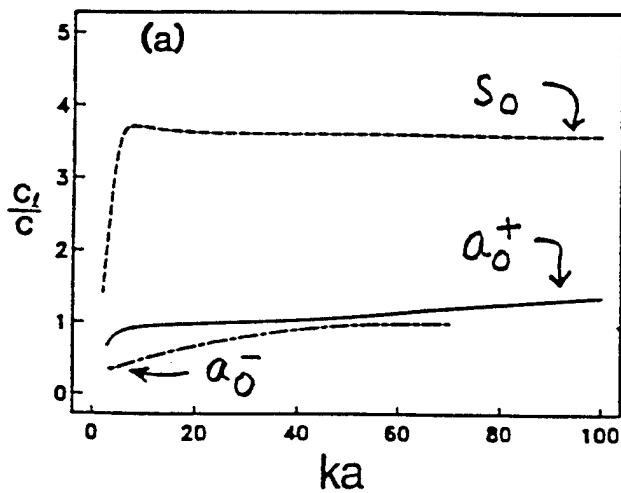


s_0 wave



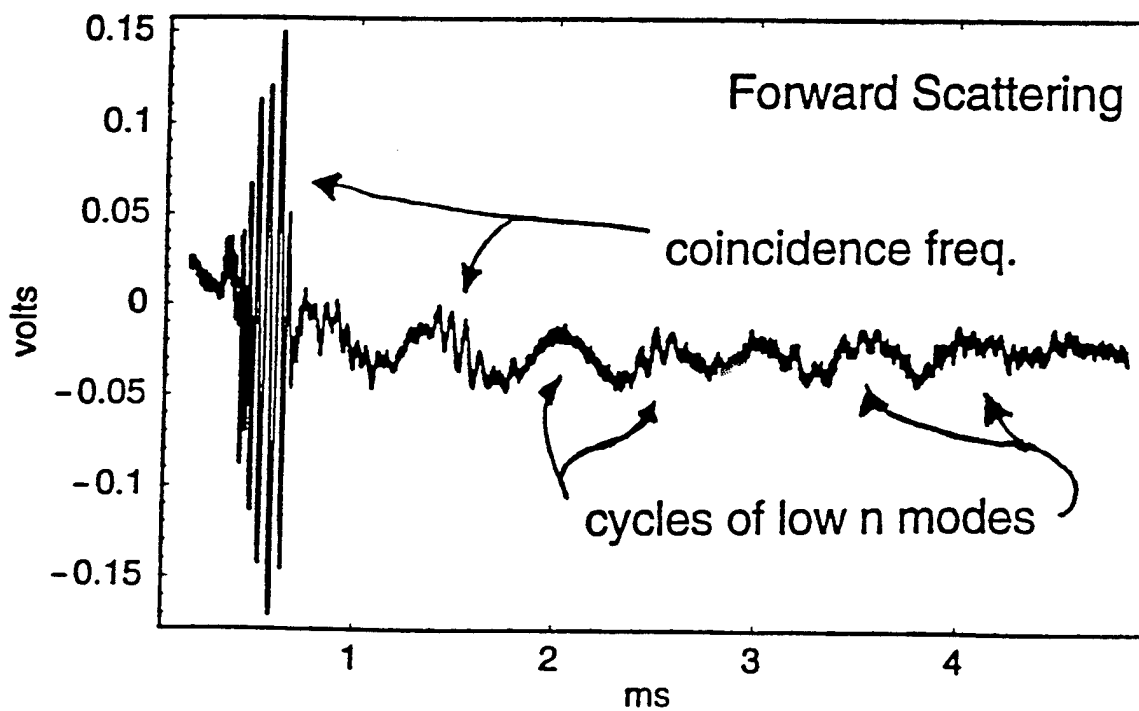
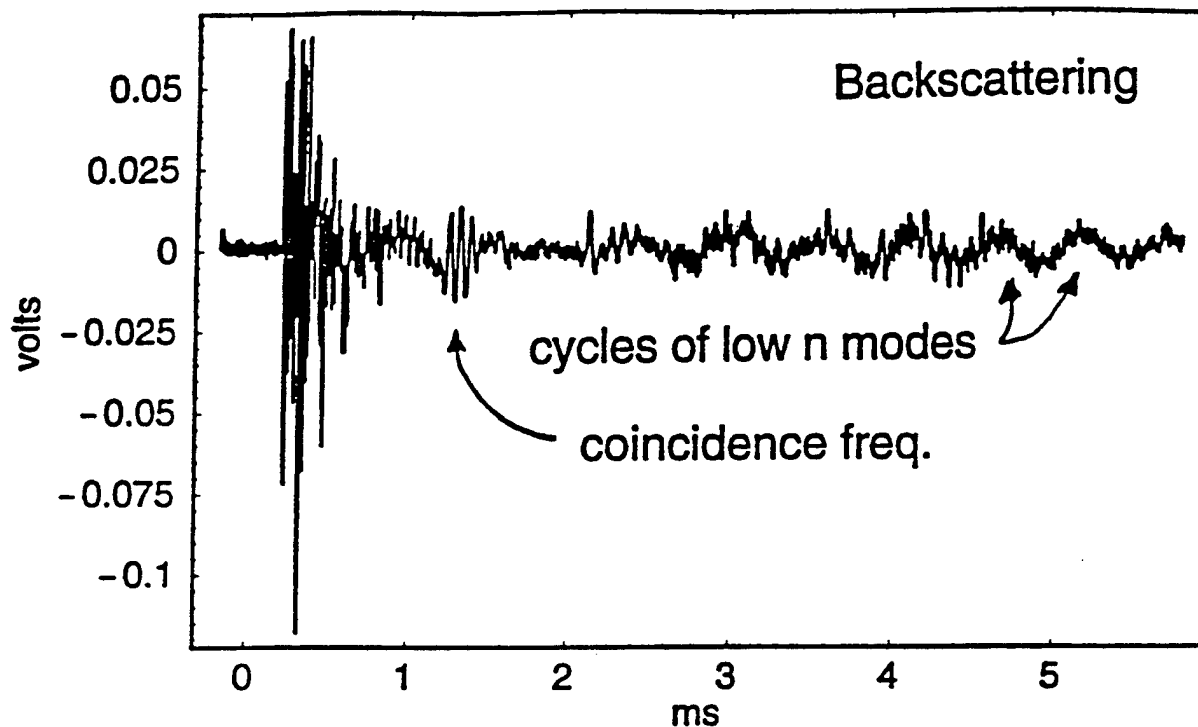


Marston and Sun, "Resonance and interference scattering near the coincidence frequency of a thin spherical shell: An approximate ray synthesis," JASA 92, 3315-3319 (1992)



← coincidence freq. →

Experiment at APL Barge



High frequency back scattering enhancement for general shapes

Experiments

1. G. Kaduchak et al., "Elastic wave contributions in high-resolution acoustic images of fluid-filled, finite cylindrical shells in water," JASA **100**, 64-71 (1996).
2. S. F. Morse et al., "High frequency backscattering enhancements by thick finite cylindrical shells in water at oblique incidence: experiments, interpretation and calculations," (submitted JASA).
3. K. Gipson, Experiments in progress.

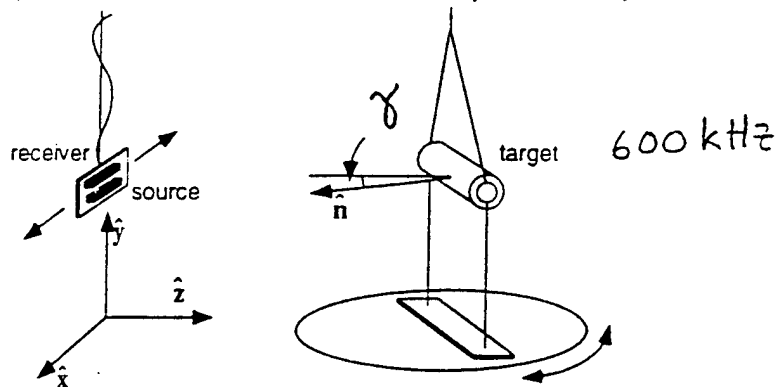
Theory

1. P. L. Marston, "Leaky waves on weakly curved scatterers. II. Convolution formulation for two-dimensional high-frequency scattering," JASA **97**, 34-41 (1995).
2. Marston, "Approximate meridional leaky ray amplitudes for tilted cylinders: end-backscattering enhancements and comparisons with exact theory for infinite solid cylinders" (accepted in JASA).

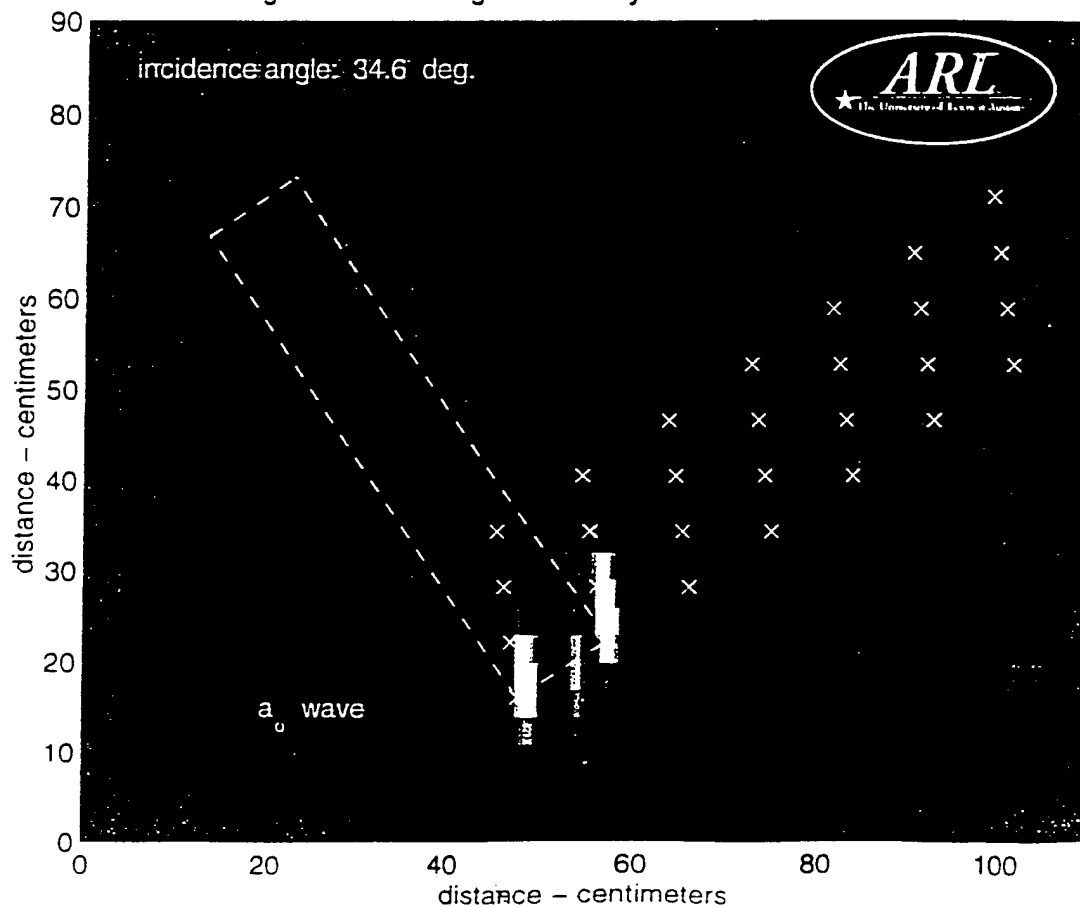
Applied Research Laboratory
The University of Texas at Austin

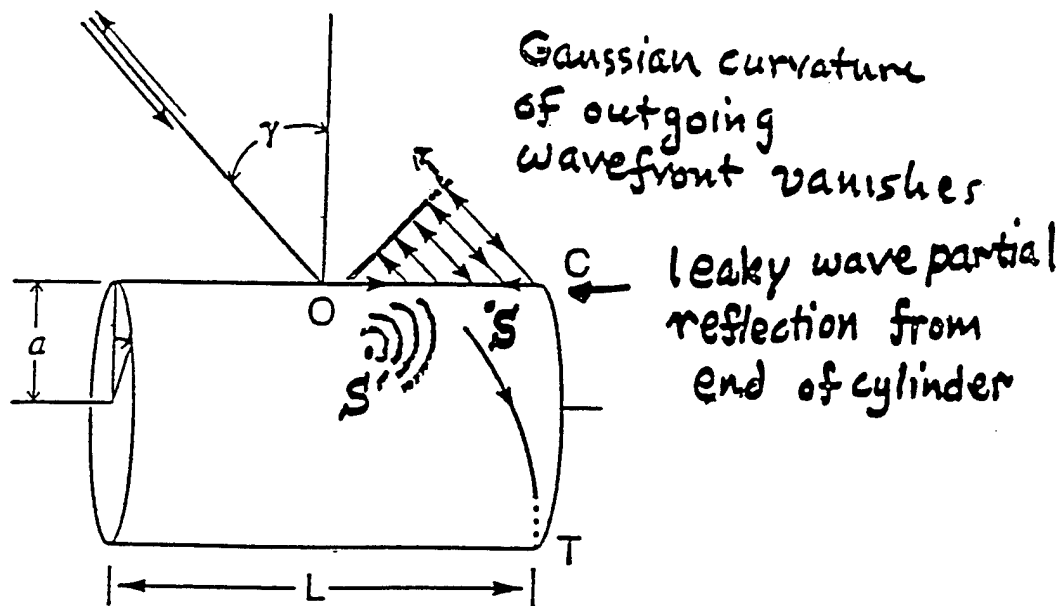


G. Kaduchak and C. M. Loeffler, "Elastic wave contributions in high resolution acoustic images of fluid-filled, finite cylindrical shells in water," to appear in JASA June 1996. 100, 64 (1996).



High resolution image of finite cylindrical shell: $b/a=0.9449$



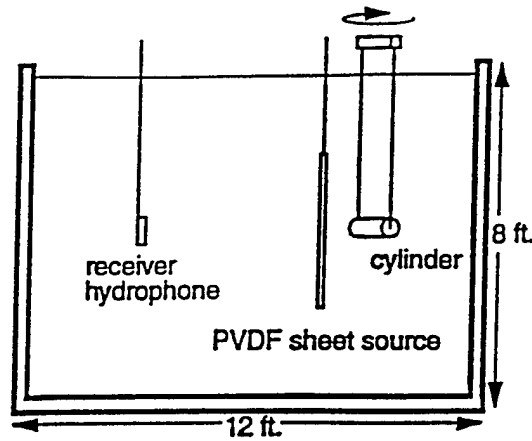


Spatial surface convolution approximation of leaky wave contributions to three-dimensional scattering

- gives spatial dependence of surface wave amplitude directly (for image interpretation)
- not limited to thin-shell mechanics
- avoids singularities of "pure ray theory"
- meridional ray example is for an especially large contribution and gives expected flat surface limit as radius a diverges.

P.L. Marston, Geometrical and catastrophe optics methods in scattering, *Physical Acoustics* 21, 1-234 (1992)

PVDF sheet source: Kaduchak, Kwiatkowski, Marston JASA (1995)



Submitted to JASA
WSU experiments

(a)

S. Morse
impulse response
spectra as a
function of tilt.

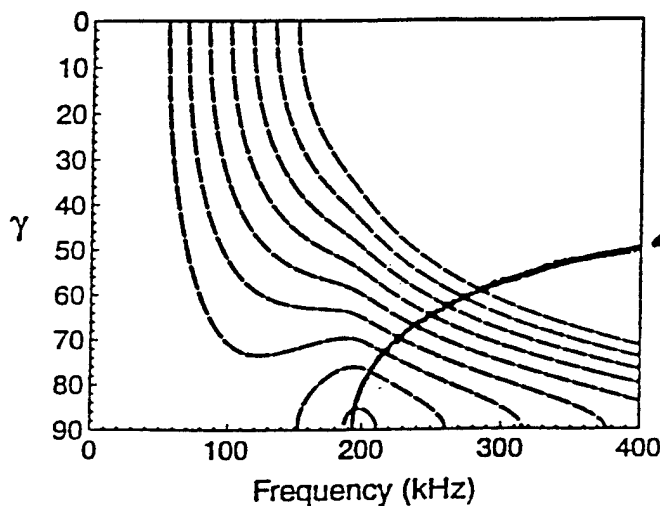
7.5% thick
shell

tilt
angle
(deg)



(b)

tilt
angle
(deg)

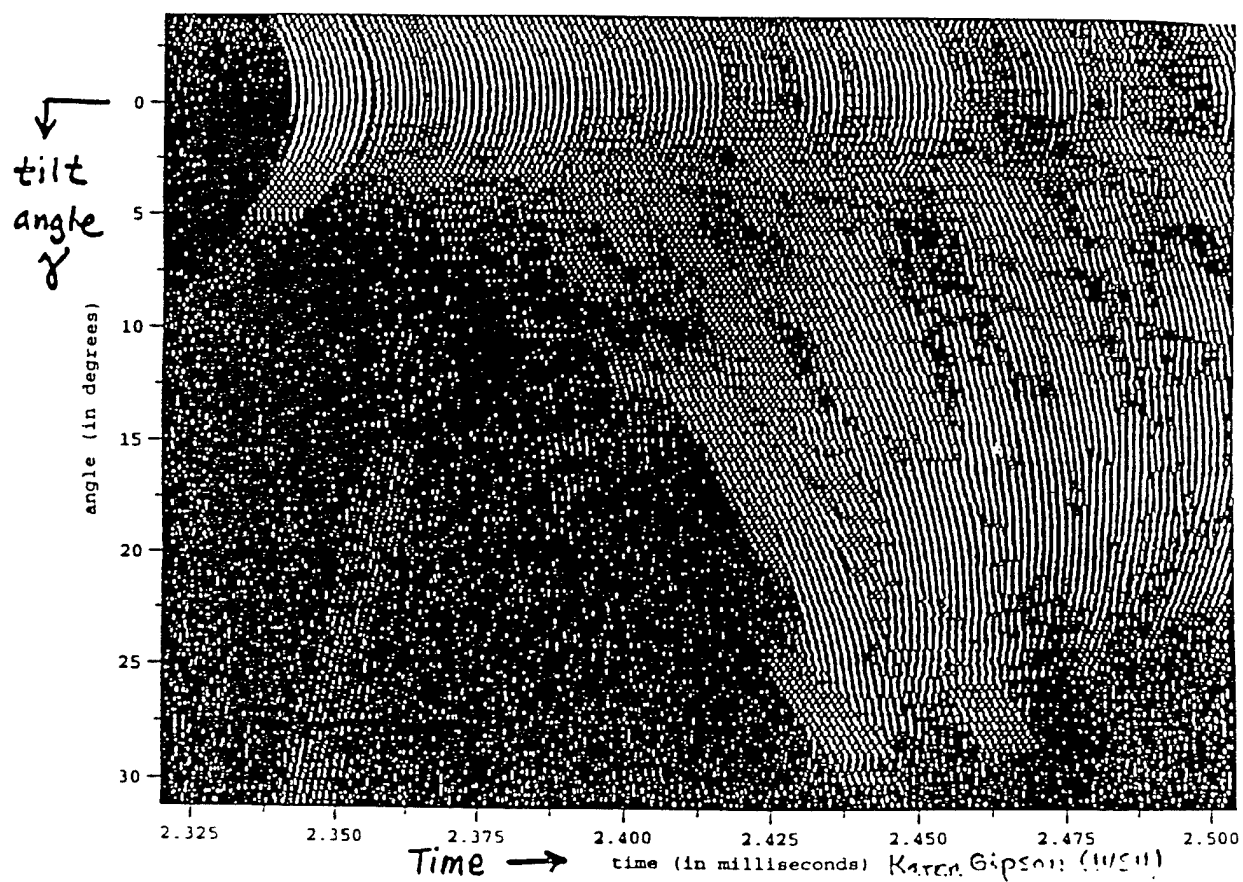


$$\theta_2 = \sin^{-1}(c/c_2)$$

for a_0^+

(c)

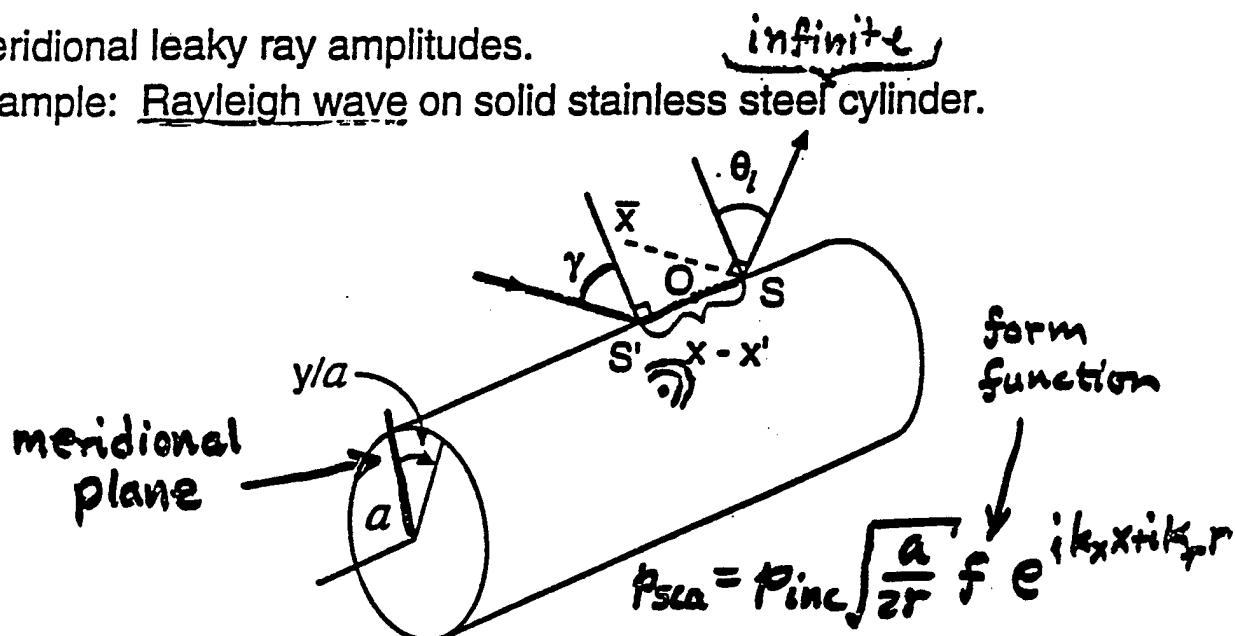
leaky Lamb
wave



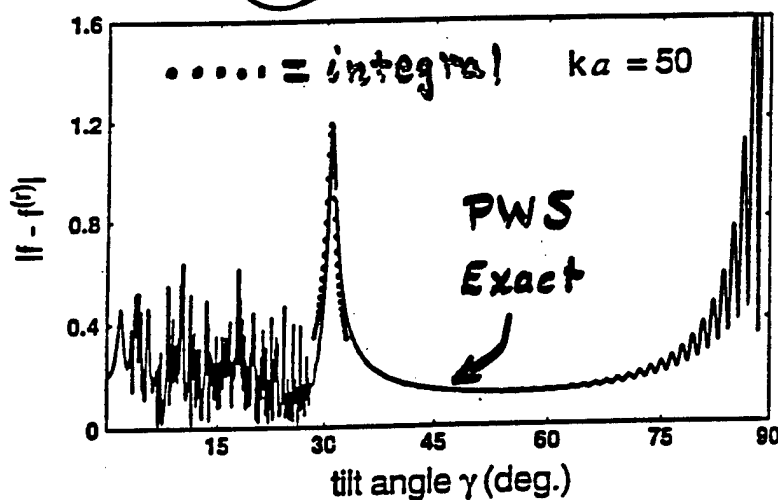
Backscattering due to Rayleigh waves on stainless steel cylinder
(800 kHz tone bursts)

Meridional leaky ray amplitudes.

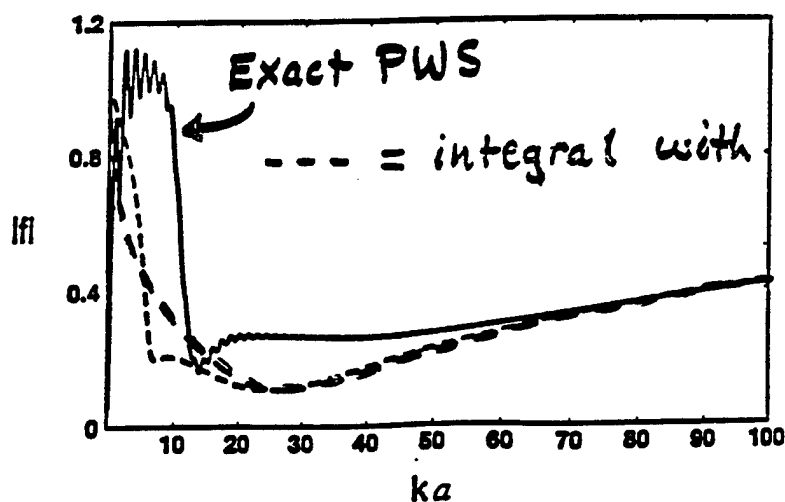
Example: Rayleigh wave on solid stainless steel cylinder.



$|f - f_{rigid}|$
subtracted
form
function

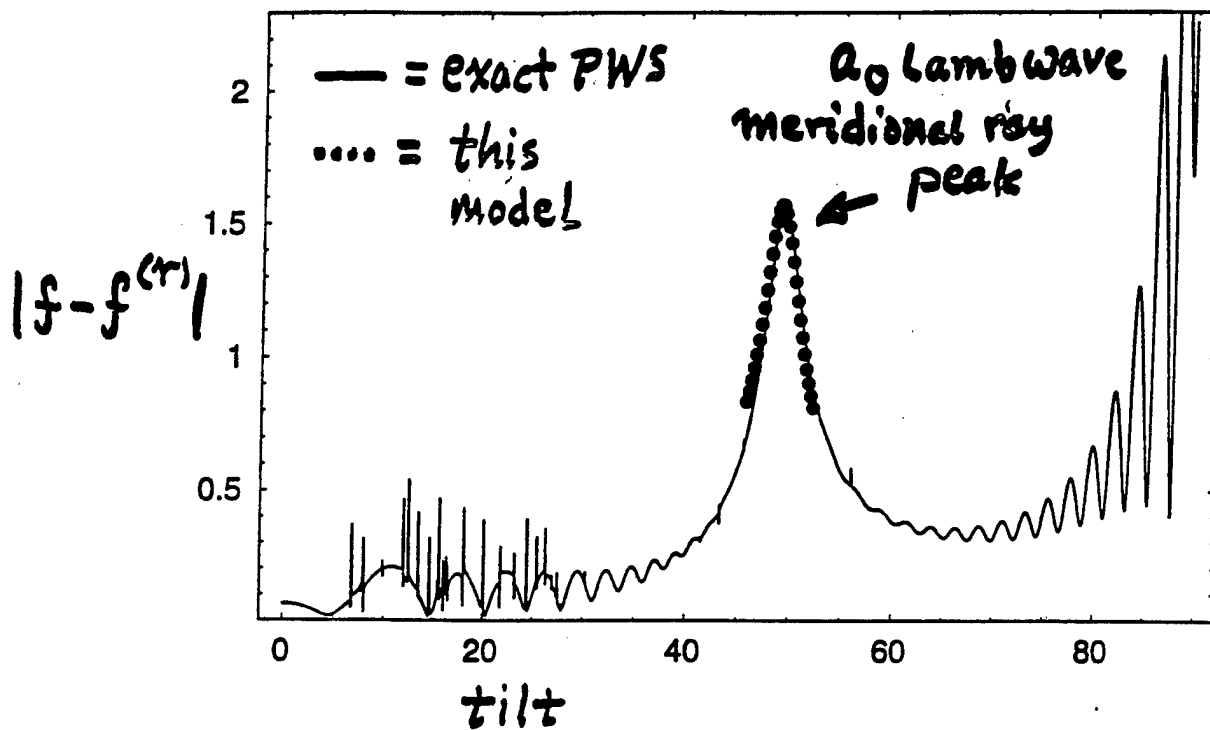


$|f|$
form
function
(total)



flat surface
 k_z and α

Empty infinite SS304 cylindrical shell in water

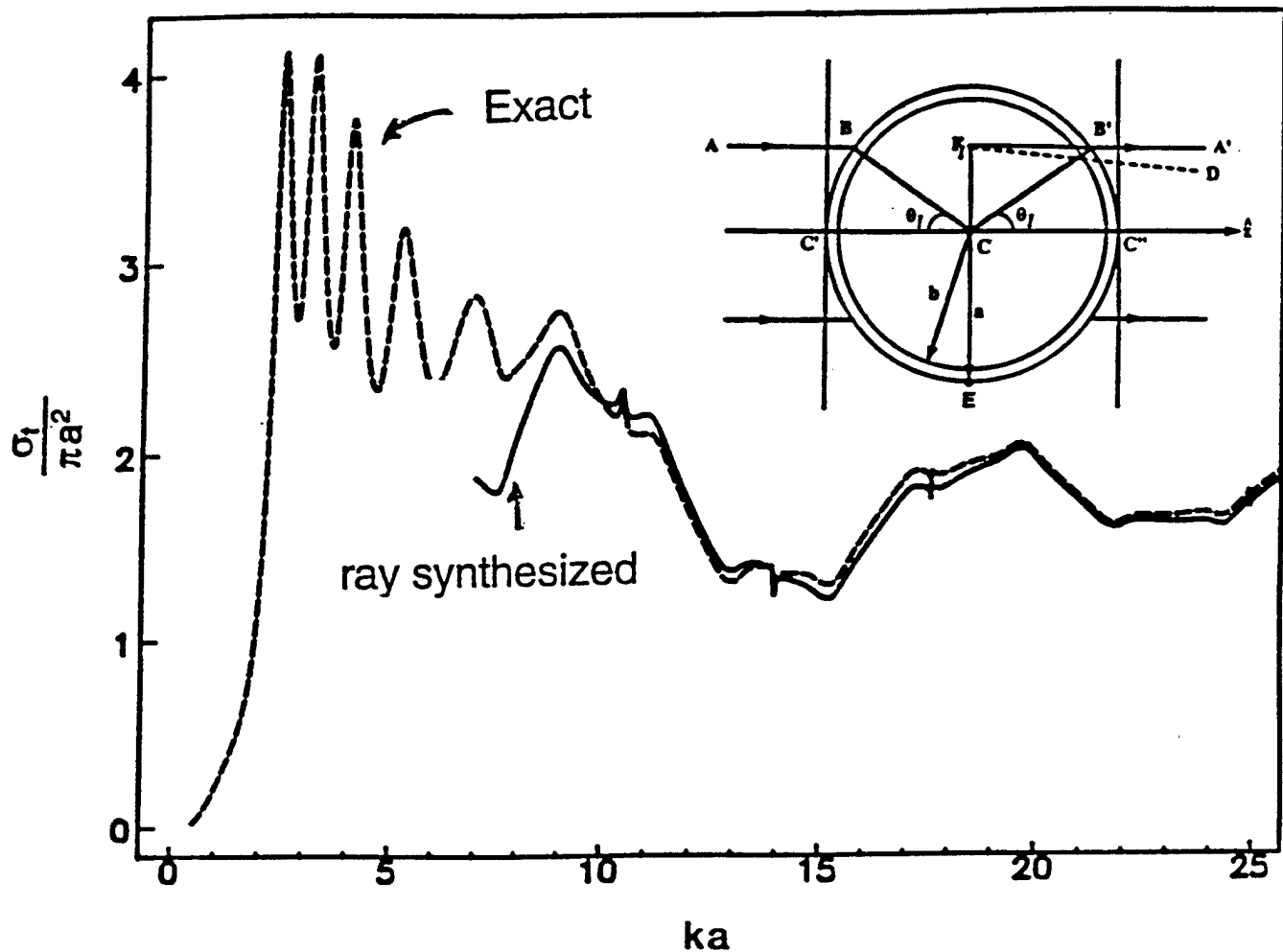


$$b/a = 0.924 \quad h/a = 0.076 \quad ka = 32.7$$

$$f = 400 \text{ kHz} \quad (\text{S. Morse W/SU})$$

No adjustable parameters in model

Exact and ray synthesized total scattering cross section of a thick spherical shell in water. Kargl and Marston JASA (1990).

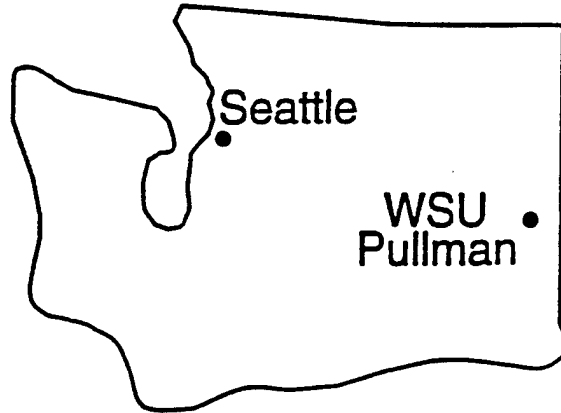


Note: (1) There are no acoustically active high Q low frequency modes; (2) The torsional modes of the shell are not acoustically active (e.g. T_2 is at 60 kHz or ka of 4.9 and T_3 is at 94 kHz or ka of 7.6).

Magnetic excitation and acoustic detection of spherical shell modes in air and in water

Brian T. Hefner
Philip L. Marston

Department of Physics
Washington State University
Pullman, WA 99164-2814



Work supported by the Office of Naval Research

Ultrasonic spectroscopy of metallic spheres using electromagnetic-acoustic transduction

Ward L. Johnson, Stephen J. Norton, Felix Bendec,^{a)} and Robert Pless
Metallurgy Division, National Institute of Standards and Technology, Gaithersburg, Maryland 20899

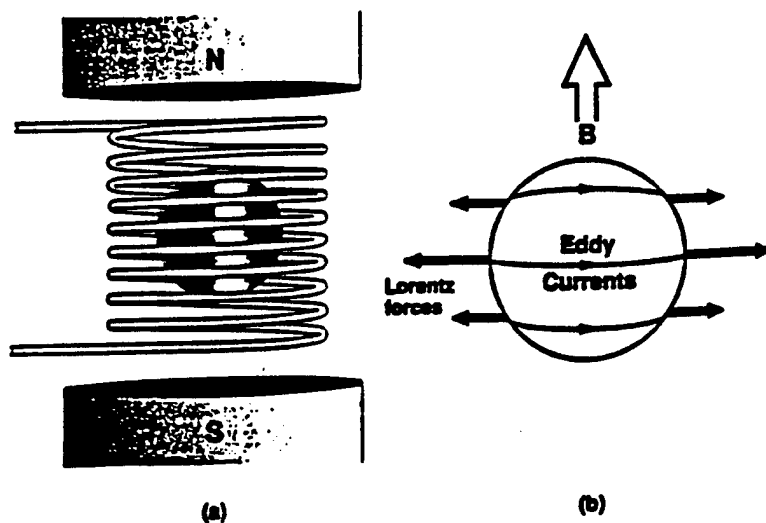


FIG. 1. (a) Sample/transducer configuration. The spherical metallic sample is supported between the poles of two permanent magnets and surrounded by a coil with its axis parallel to the magnetic field. The pedestal supporting the sample and insulating tube supporting the coil are not shown. (b) Schematic of transduction physics.

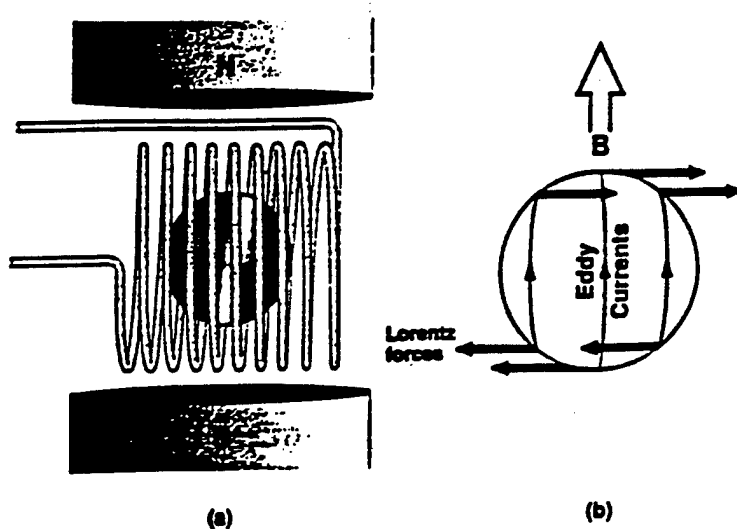
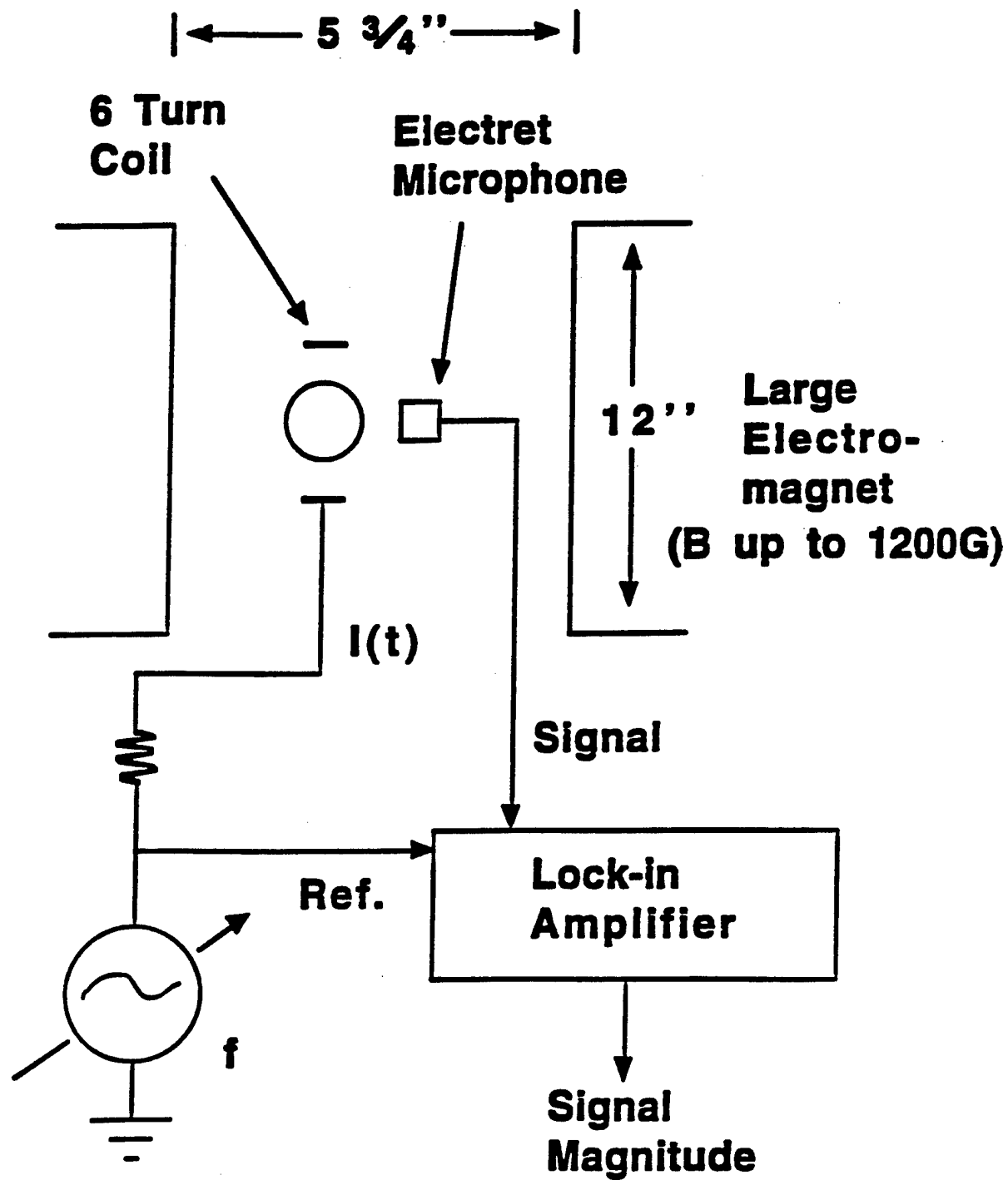
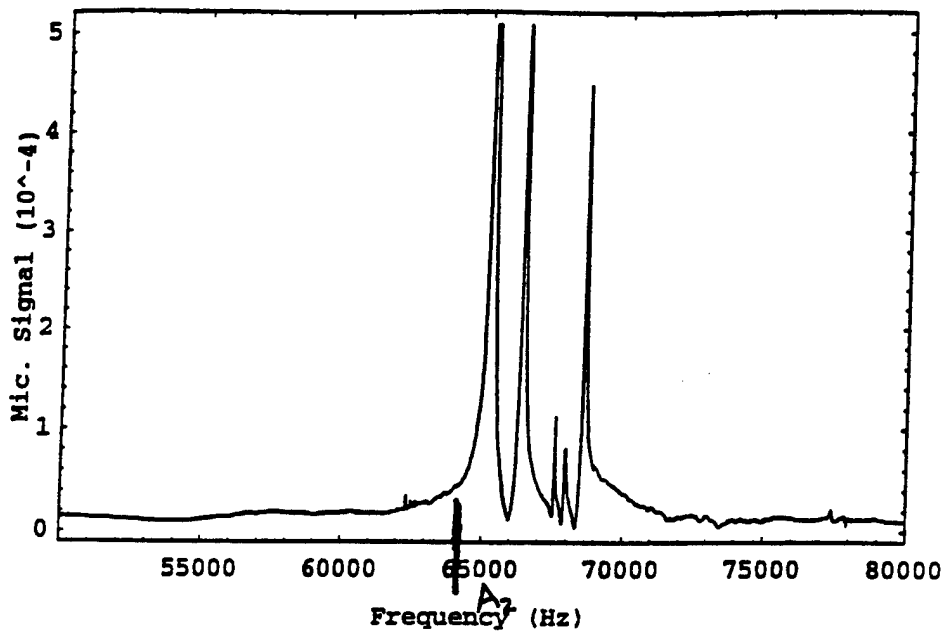


FIG. 2. Same as Fig. 1, except the coil axis is perpendicular to the magnetic field.



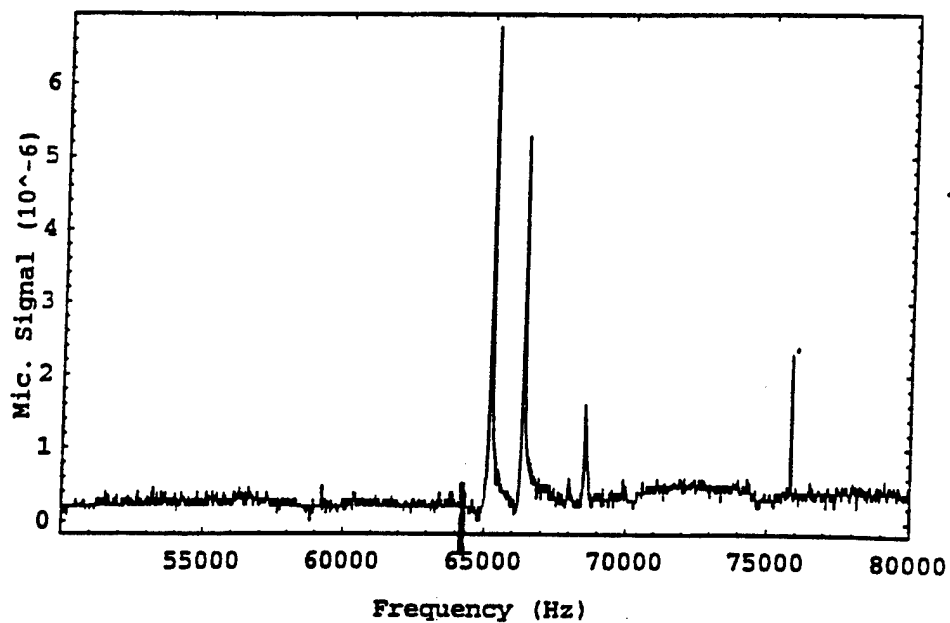
Reference Frequency = f or $2f$

Aluminum Shell with Bias Field



$$f_{ref} = f$$

Aluminum Shell w/o Bias Field



$$f_{ref} = f$$

Properties:

Radius: $a = 9.27 \text{ mm}$

Thickness: $h = 0.51 \text{ mm}$

$$h/a = 0.055$$

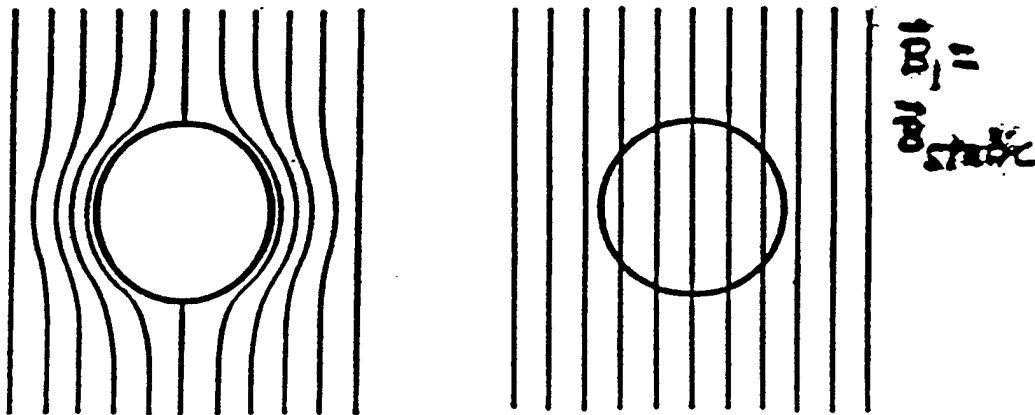
Total field $\vec{B}(\vec{r}, t) = \vec{B}_1 + \vec{B}_2(\vec{r}, t)$ where $\vec{B}_1 = B_1 \hat{z}$ is a uniform static field. What is the distribution of Maxwell stresses on the shell in a B field with an oscillating component?

Note: At typical excitation frequency of 64 kHz the skin depth δ for aluminum is less than the shell thickness $h = 0.5$ mm.

1. The oscillating B field obey approximately the diffusion equation and only weakly penetrates the interior of the sphere

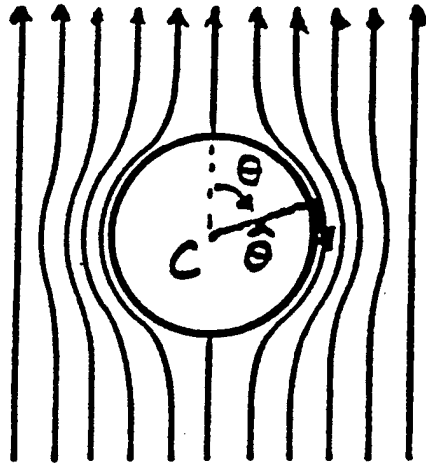
$$\nabla^2 \vec{B} = \mu_0 \sigma \frac{\partial \vec{B}}{\partial t}, \quad \sigma = \text{conductivity}$$

2. As a first approximation the shell may be treated as a perfect electrical conductor (PEC) so that $\vec{B}_2(\vec{r}, t)$ is completely excluded from the shell. ↘



3. The $B_2(\vec{r}, t)$ field pattern is roughly that of a static B-field for a perfectly diamagnetic sphere ($\mu_{\text{inside}} = 0$). For a uniform applied field $\vec{B}_0 \sin \omega t$ with $\vec{B}_0 = B_0 \hat{z}$, at the sphere's surface.

$$\vec{B}_2(r = a, t) = -\hat{\theta} B_0 (\sin \omega t) (3/2) \sin \theta$$



$$\text{Total } \vec{B} = \hat{z} B_1 - \hat{\theta} B_3 \sin \theta$$

$$B_3 = B_0 (3/2) \sin \omega t$$

Local Maxwell Stress on the surface

$$\vec{T} = \frac{1}{\mu_0} \left[\vec{B}\vec{B} - \frac{1}{2} |\vec{B}|^2 \vec{I} \right]$$

Normal (or radial) stress component

$$F_{Mr} = \hat{r} \cdot \left(\vec{T}_{out} - \vec{T}_{in} \right) \cdot \hat{r}$$

$$\hat{r} \cdot \vec{T}_{out} \cdot \hat{r} = \frac{1}{\mu_0} \left[B_1^2 \cos^2 \theta - \frac{(B_\theta^2 + B_r^2)}{2} \right]$$

$$\text{where } B_\theta^2 = (B_1 + B_3)^2 \sin^2 \theta$$

$$B_r^2 = B_1^2 \cos^2 \theta$$

$$F_{Mr} = -\frac{3}{2\mu_0} B_0 B_1 (\sin\theta)^2 (\sin\omega t) \quad (\text{Term 1})$$

$$-\frac{9}{8\mu_0} B_0^2 (\sin\theta)^2 (\sin\omega t)^2 \quad (\text{Term 2})$$

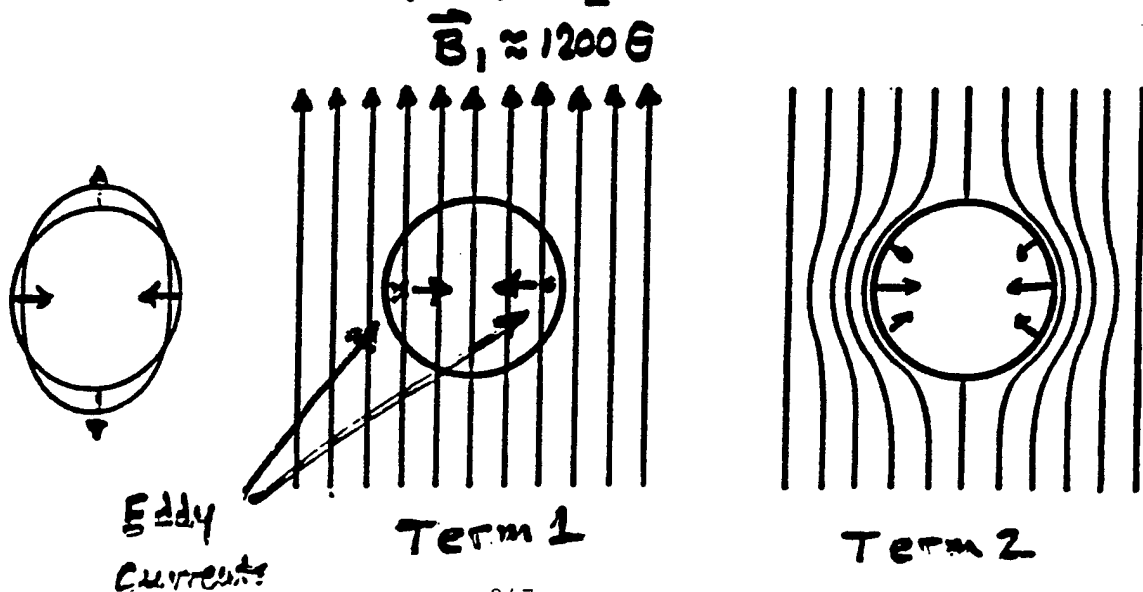
Term 1 describes Lorentz force of static field on the eddy current. It oscillates at ω .

Term 2 describes the radial Maxwell stress of the oscillating term alone. It has an oscillating component at 2ω since $(\sin\omega t)^2 = \frac{1}{2} (1 - \cos 2\omega t)$.

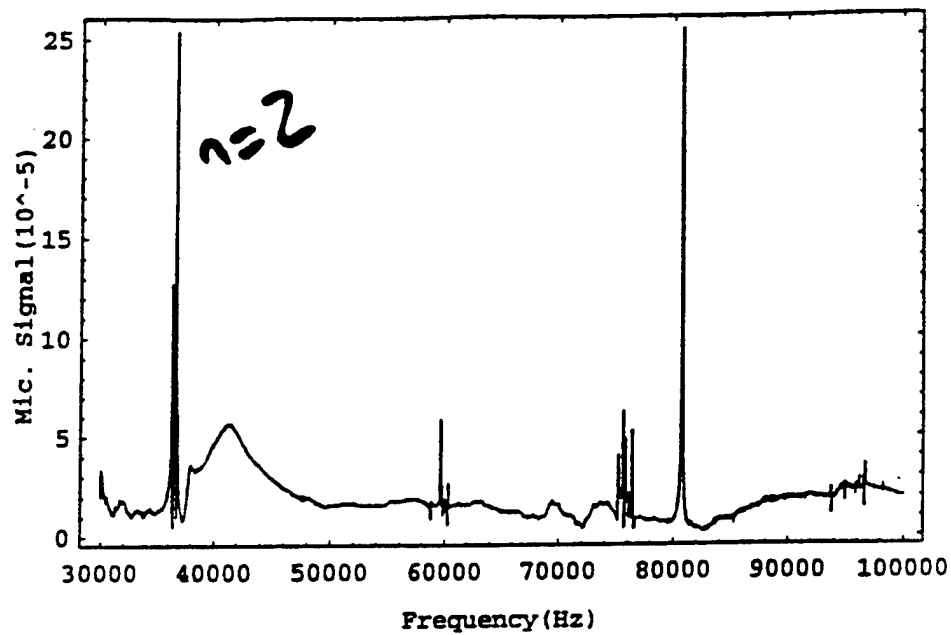
Both Terms 1 and 2 couple to the $n = 2$ shell mode:

since $P_2(\cos\theta) = (3\cos^2\theta - 1)/2$,

$\sin^2\theta = 1 - \cos^2\theta = - (2/3) [P_2(\cos\theta) - 1]$

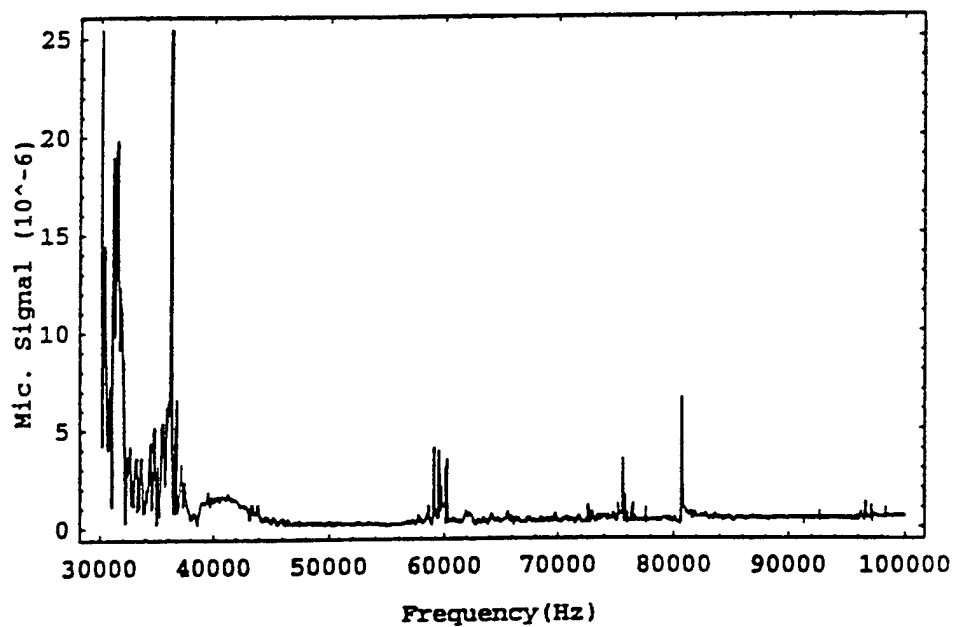


Steel Shell w/ Bias Field

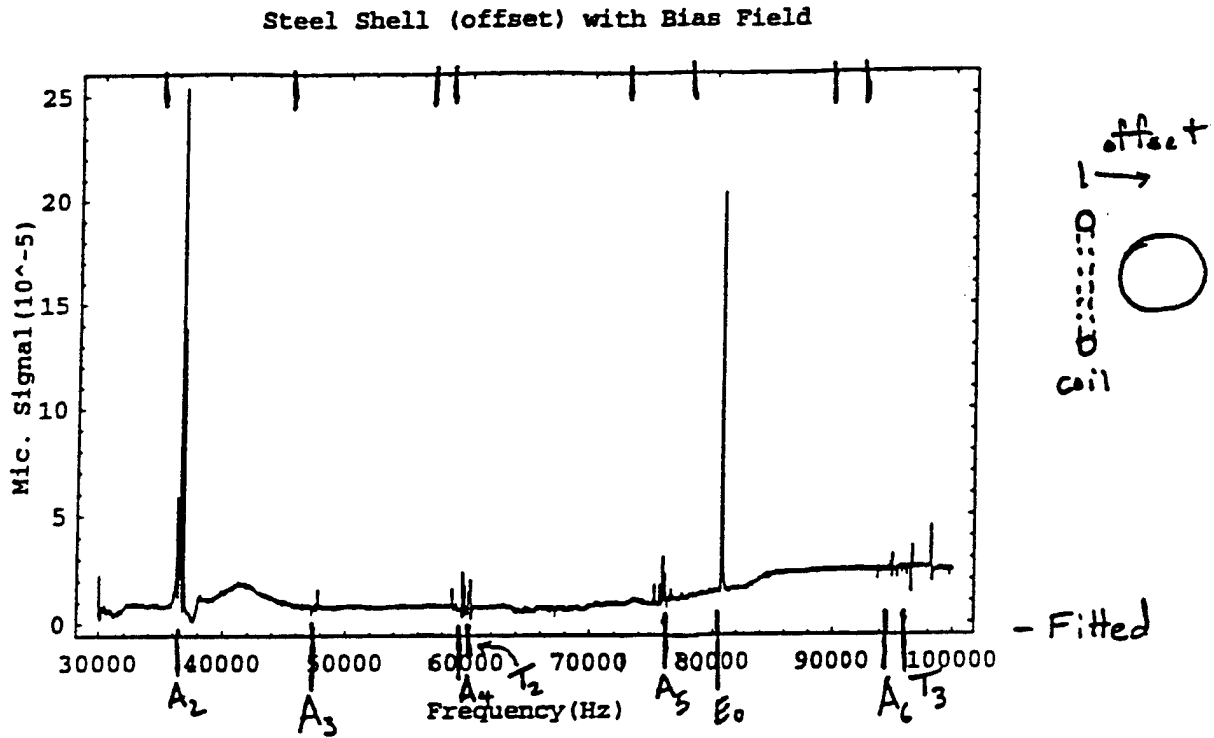


$$f_{ref} = f$$

Steel Shell w/o Bias Field



$$f_{ref} = 2f$$

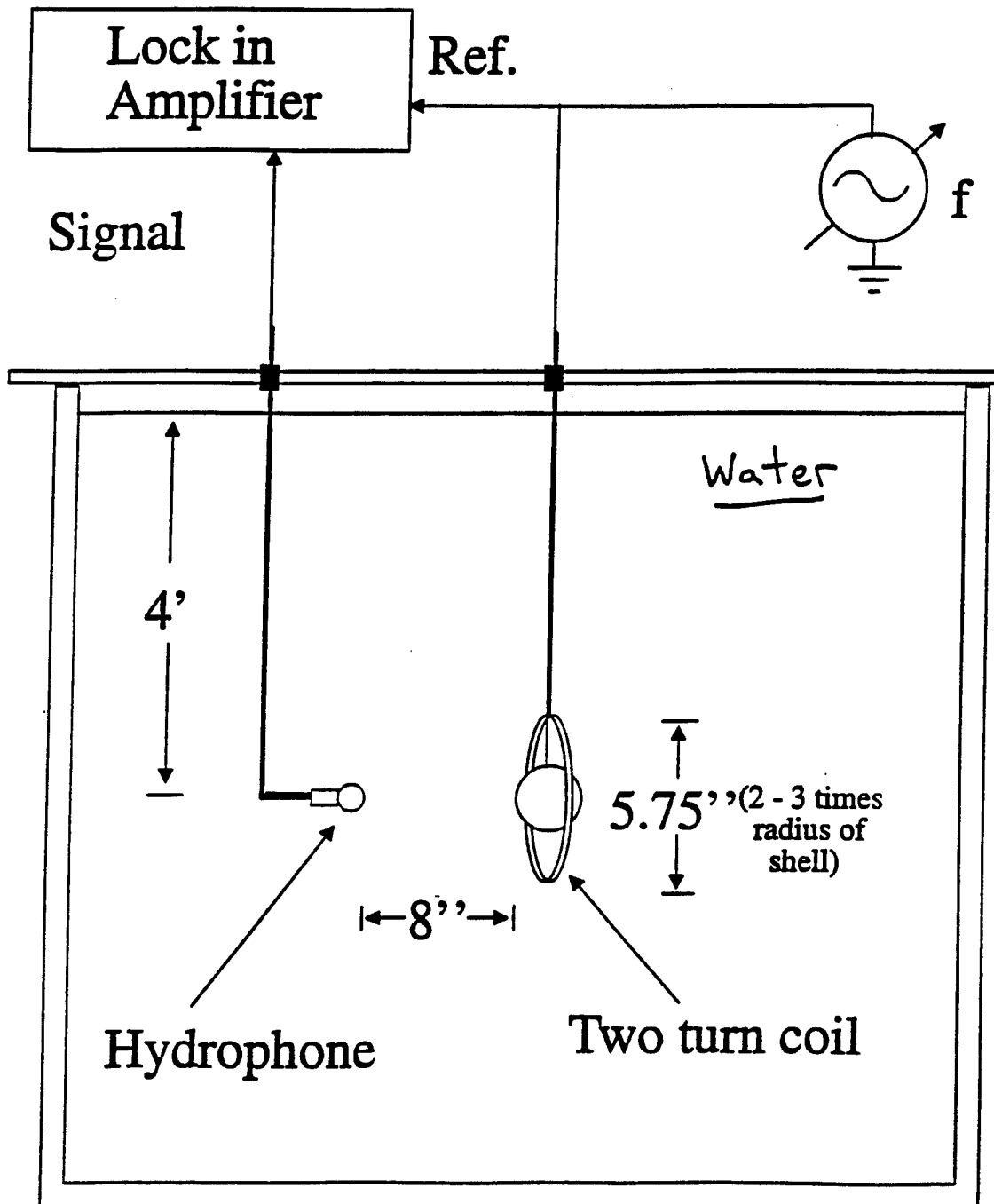


Wave velocities for stainless steel shell

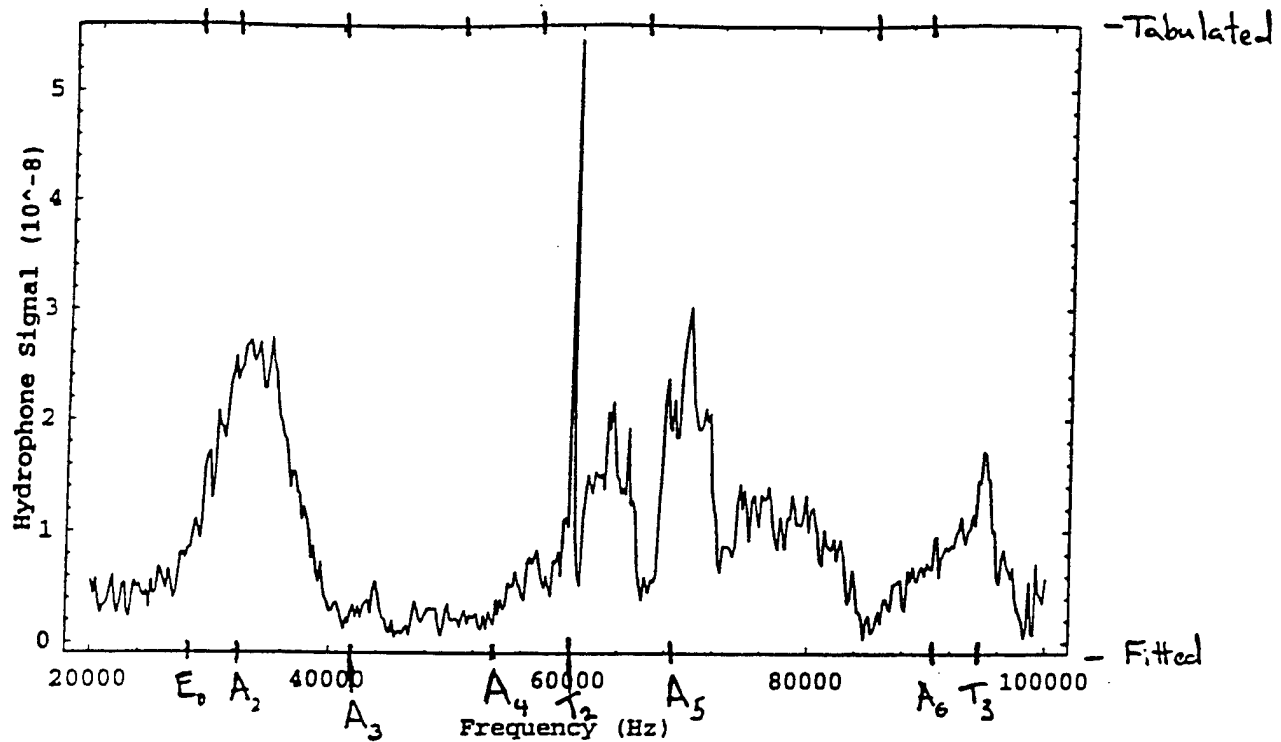
	Tabulated 440c (m/s)	Fitted (m/s)
c_L	5854	5960
c_S	3150	3321

Mode	Calculated (kHz)		Measured (kHz)
	fitted c_L, c_S	tabulated 440c c_L, c_S	
A_2	36.60	34.83	36.60
A_3	47.52	45.36	47.74
T_2	60.00	56.91	
A_4	59.81	57.19	59.60
A_5	76.01	72.81	75.64
E_0	80.30	77.99	80.76
T_3	94.87	89.97	
A_6	96.04	92.06	96.72

Fluid Loading Experiment



Fluid Loaded Shell (response at 2f)

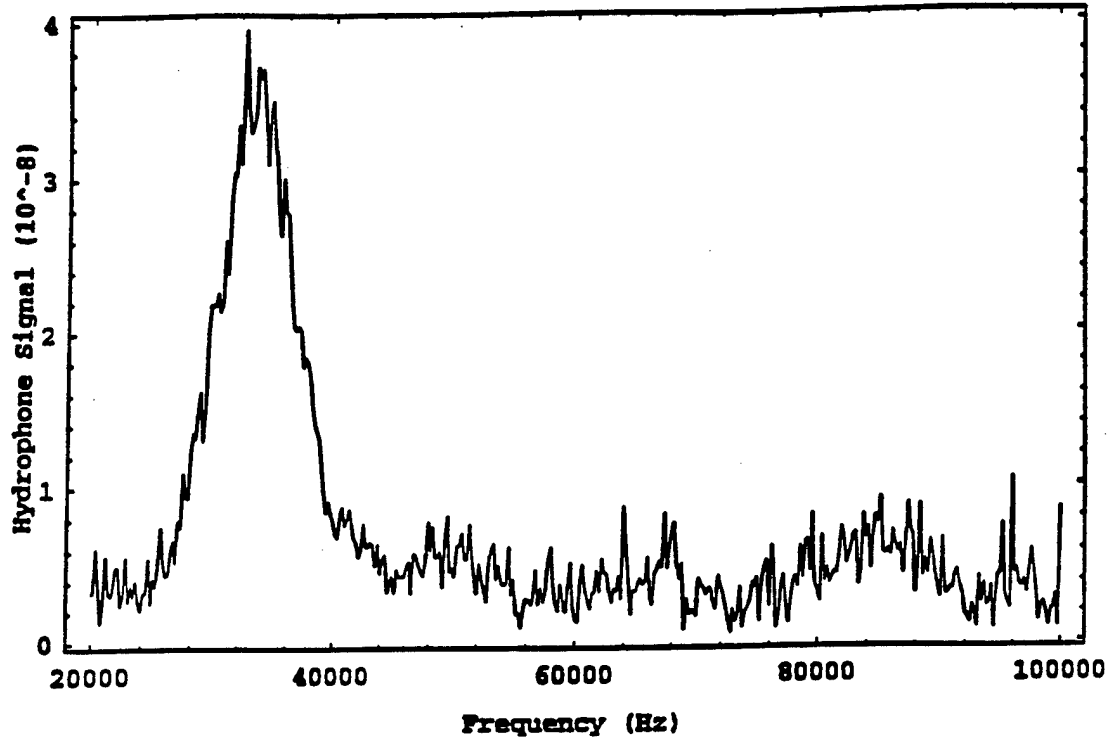


Wave velocities for stainless steel shell

	Tabulated 440c (m/s)	Fitted (m/s)
c_L	5854	5960
c_s	3150	3321

Mode	Calculated Fluid Loading Frequencies (kHz)		Measured (kHz)
	fitted c_L, c_s	tabulated 440c c_L, c_s	
A_2	32.54	31.89	31.60
A_3	41.93	40.05	
A_4	53.19	50.07	
T_2	60.00	56.91	60.00
A_5	68.84	65.70	
E_0	28.16	28.16	
A_6	90.74	85.1	94.2
T_3	94.87	89.97	

Non-magnetic Fluid Loaded Shell (2f-response)

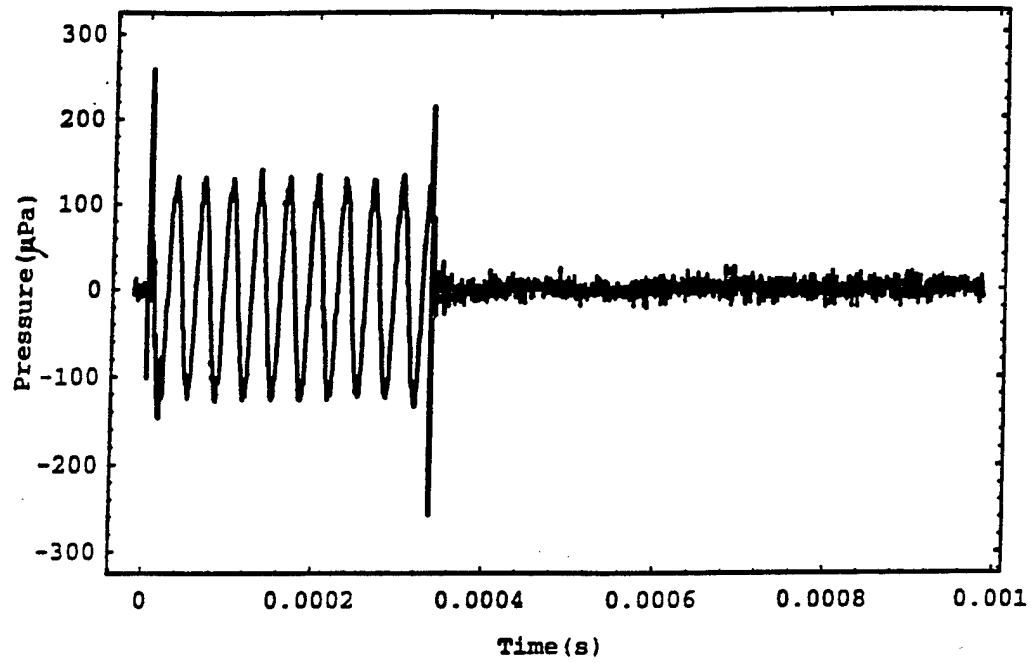
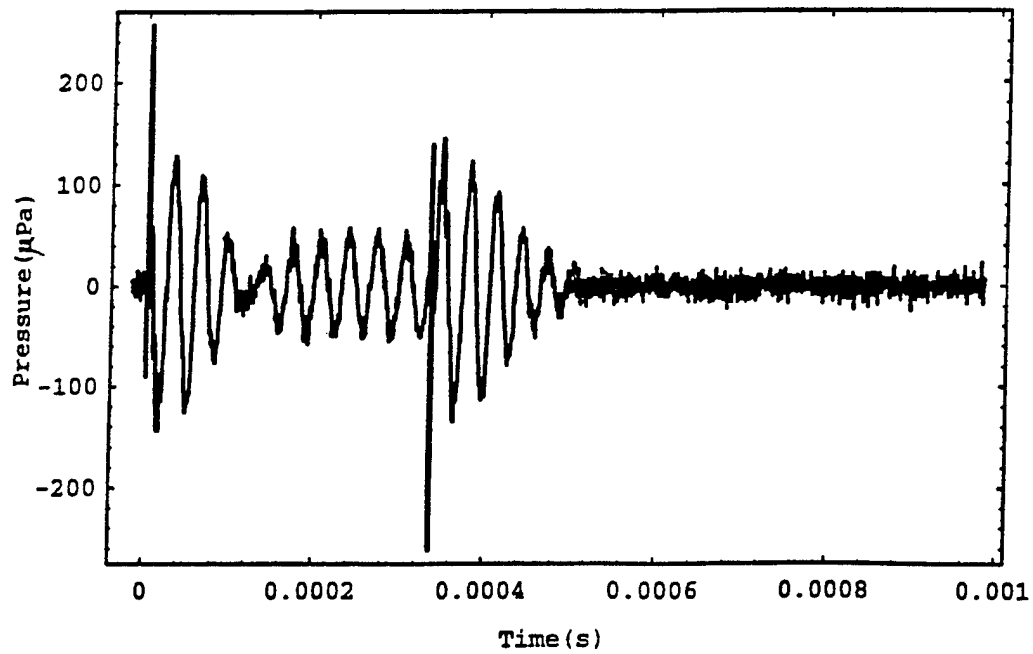


Non-magnetic shell:

- No response at f .
- No resonances excited other than A_2 . Most notable is the absence of the sharp resonances present with the magnetized shell.

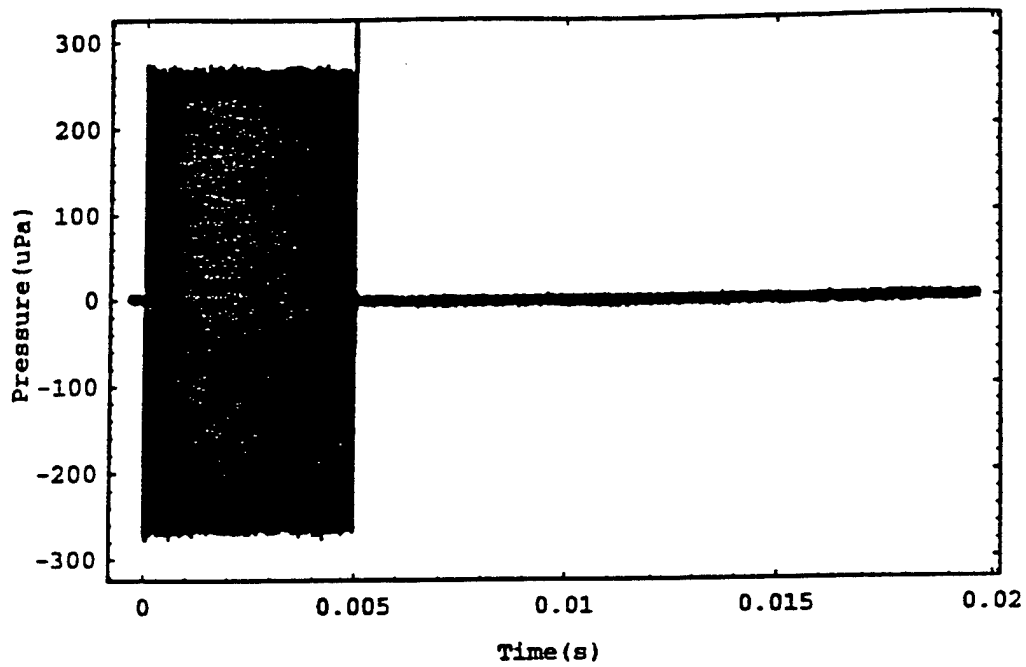
response at f

10-cycle 30 kHz burst w/o shell

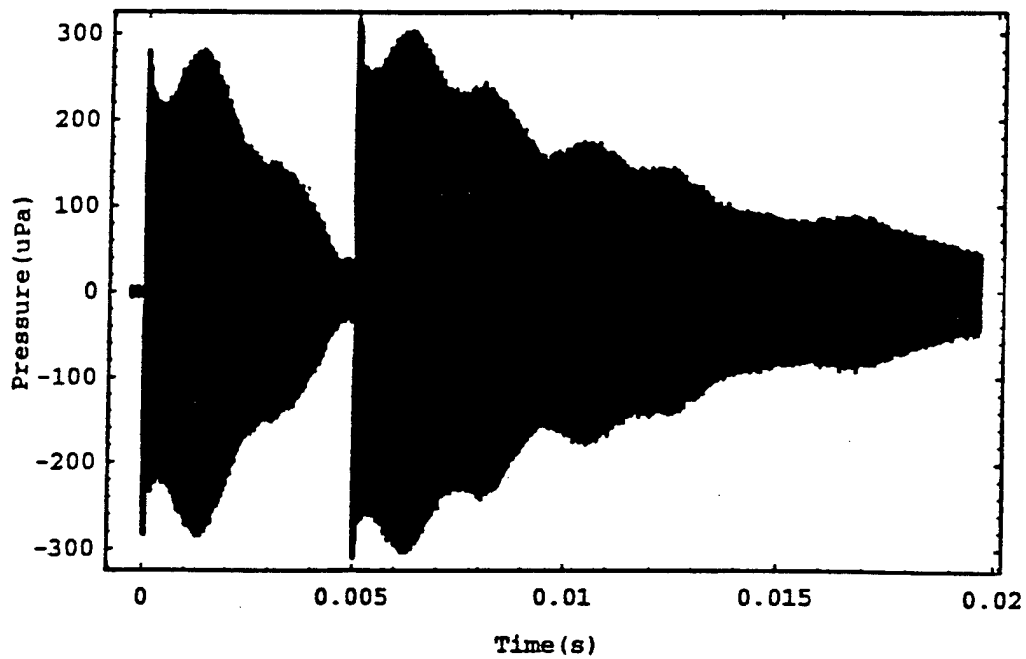
10-cycle 30 kHz burst with shell (A_z mode)

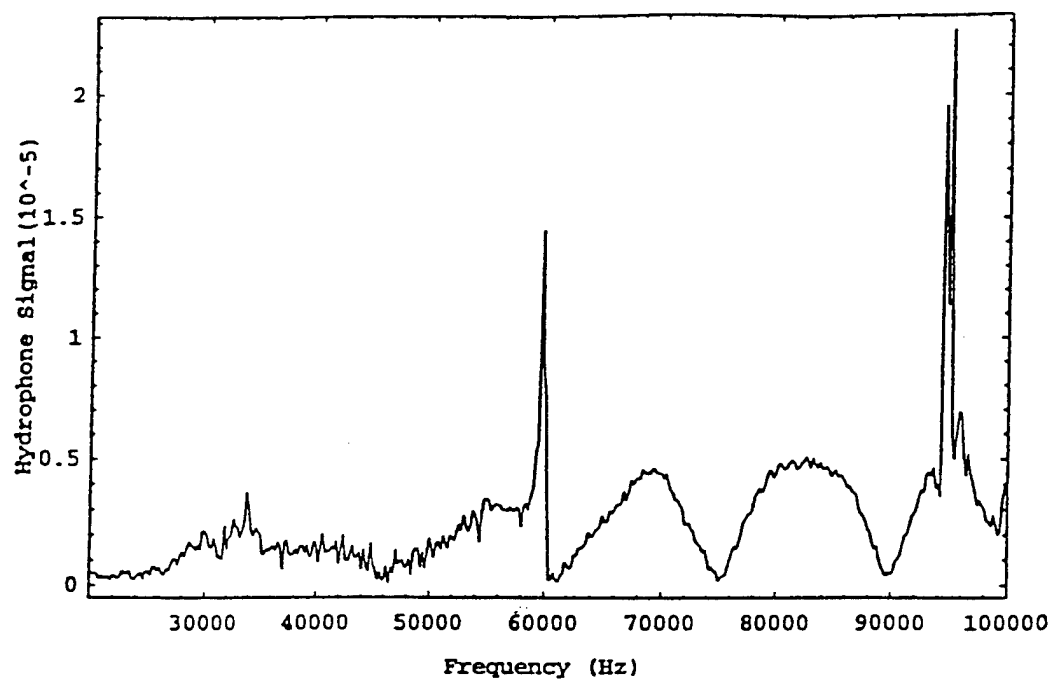
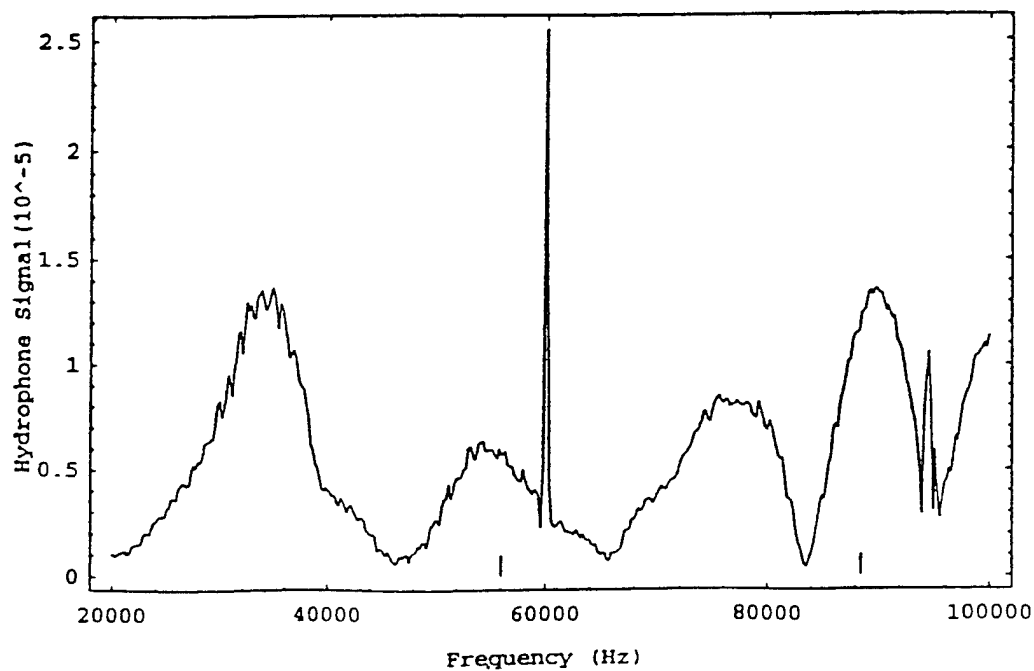
response at -

300-cycle 60 kHz burst w/o shell



300-cycle 60 kHz burst with shell

 $Q \sim 1500$

Fluid Loaded Shell w/ m perpendicular to the axis of the coilFluid Loaded Shell w/ m parallel to the axis of the coil

Possible torsional excitation mechanisms:

1 Eddy currents and “self field”.

Recall Johnson et. al.

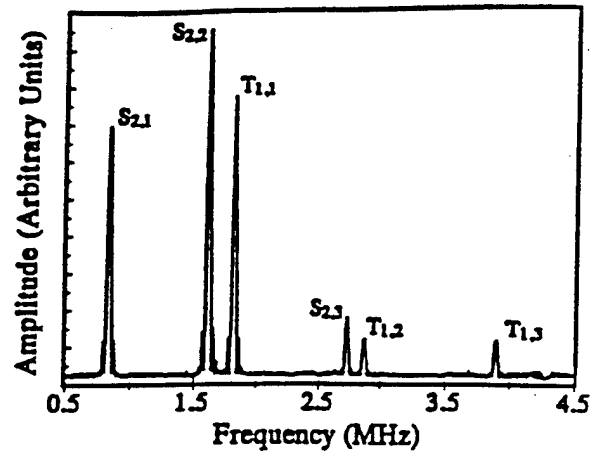
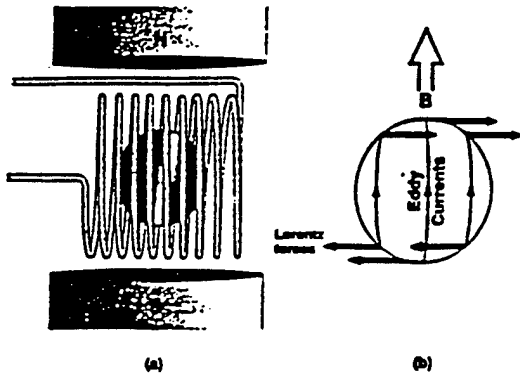
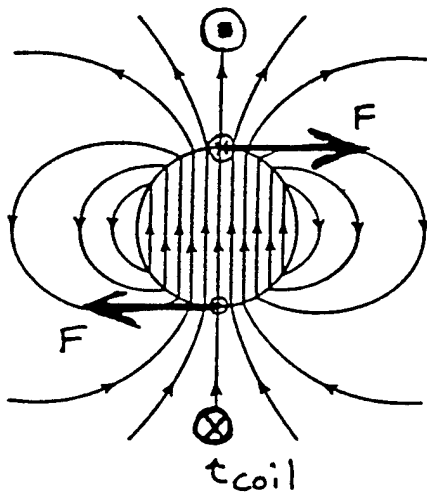


FIG. 6. Vibrational spectrum of the 3.145-mm 2024 aluminum sphere with the coil configured as in Fig. 2(a).



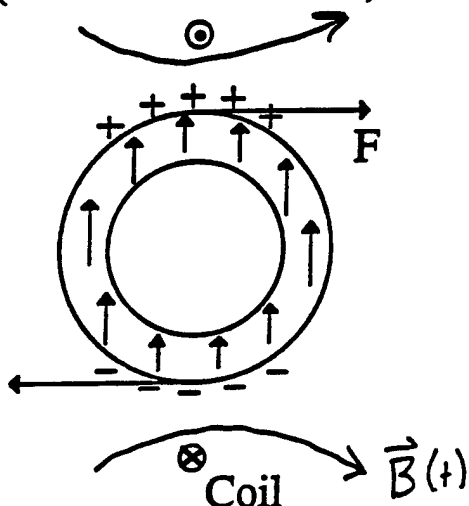
“Self field” of the shell is aligned perpendicular to the field of the coil.

- Drives T_3 mode

2. Torque on distributed magnetic moment by oscillating fields.

(a) does not rely on eddy currents

(b) for uniform magnetization M may be modeled by force on surface magnetization charge density (source of static H)



- Uniform M drives T_3 mode

Asymmetries in either the magnetization or the position of the shell in the coil could drive the T_2 mode.

3. **M aligned with coil axis:** Microscopic domain wall motion or domain rotation and the conservation of angular momentum. (Einstein-de Haas effect and/or torsional magnetostriction)

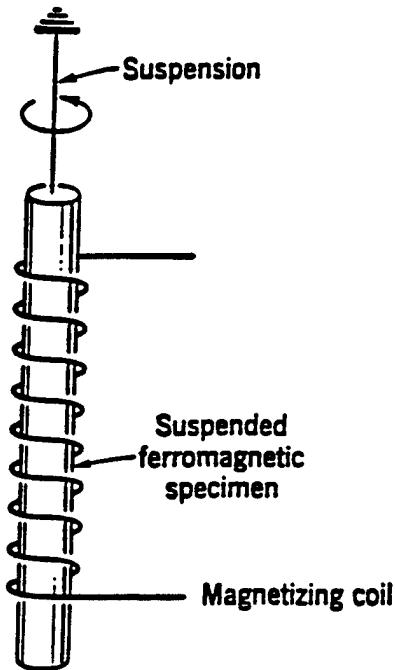
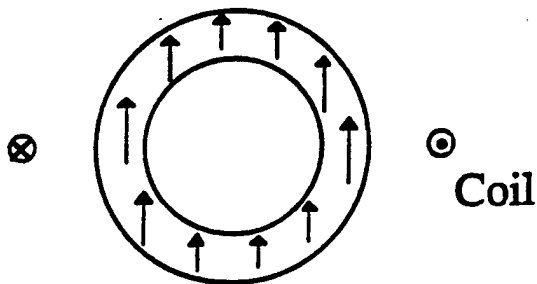
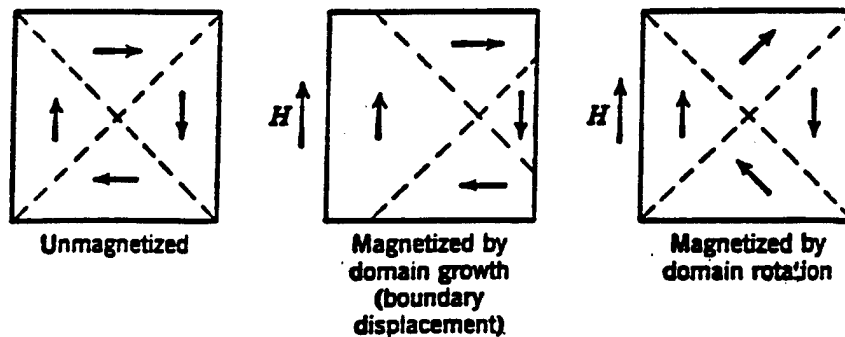


Fig. 15.4. Einstein-de Haas gyromagnetic experiment. When the current in the magnetizing coil is reversed, the magnetization in the specimen is reversed and the specimen rotates.

Kittel (2nd ed.)

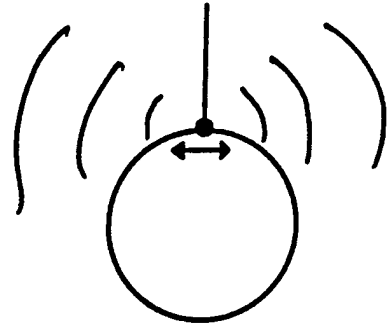


Couple to T_3 or (if offset) T_2

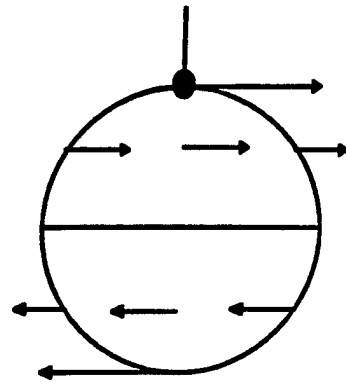
How can the torsional modes be radiating sound?

Two possible mechanisms:

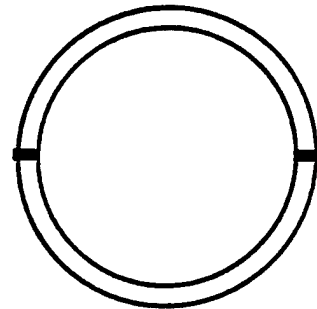
1. The sphere is attached to fishing line by a small bit of epoxy. This could be moving with the shell surface and radiating sound.



For example, the $T_{2,2}$ mode will cause the epoxy and string to move parallel to the axis of the coil and hence radiate sound.



2. The shell is composed of two separate halves which are bonded together. These halves may not be sufficiently identical for the torsional modes to be purely rotational.



Conclusions:

- Demonstrated that the modes of a spherical metallic shell could be driven magnetically and the acoustic signal could be used to measure the response in both air and water.
- A static bias field is not needed if the acoustic detection is carried out at twice the driving frequency.
- For magnetized spherical shells in water the low lying torsional modes could be excited and detected and these modes have very large Q .

MATERIAL PROPERTY MEASUREMENTS VIA DIGITAL GHz INTERFEROMETRY

Hartmut Spetzler

Geological Sciences/CIRES
University of Colorado

Procedure for CT-EOS

at $P=0$ $l_0, \rho_0, C_P(T), \alpha(T)$

at P and T $t_p(T,P), t_s(T,P)$

$$v_i = \frac{l}{t_i}, \quad K_S = \rho(v_P^2 - \frac{3}{4}v_S^2), \quad \gamma(T, 0) = \frac{\alpha K_S}{\rho C_P}$$

$$K_T(T, 0) = \frac{K_S}{1 + \alpha \gamma T}$$

at $P=\Delta P$

$$\rho(T, \Delta P) = \rho(T, 0) \left(1 + \frac{\Delta P}{K_T(T, 0)} \right), \quad \frac{l}{l_0} = \left(\frac{\rho_0}{\rho} \right)^{1/3}$$

$$v_i, \quad K_S, \quad \alpha(T, \Delta P) = -\frac{1}{\rho} \left(\frac{\partial \rho(T, \Delta P)}{\partial T} \right)_P$$

$$\left(\frac{\partial C_P(T, \Delta P)}{\partial P} \right)_T = -\frac{T}{\rho} \left\{ \alpha^2 + \left(\frac{\partial \alpha}{\partial T} \right)_P \right\}$$

FIGURE 2

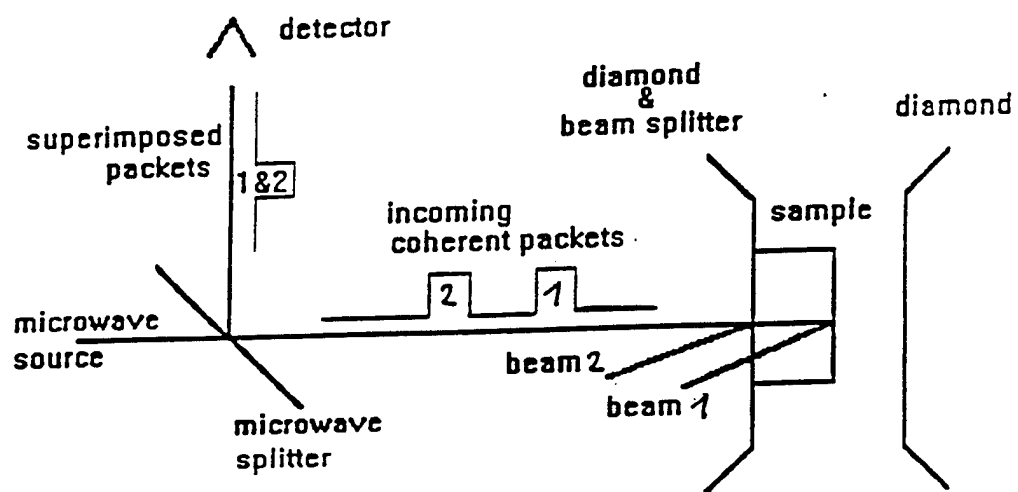


FIGURE 3

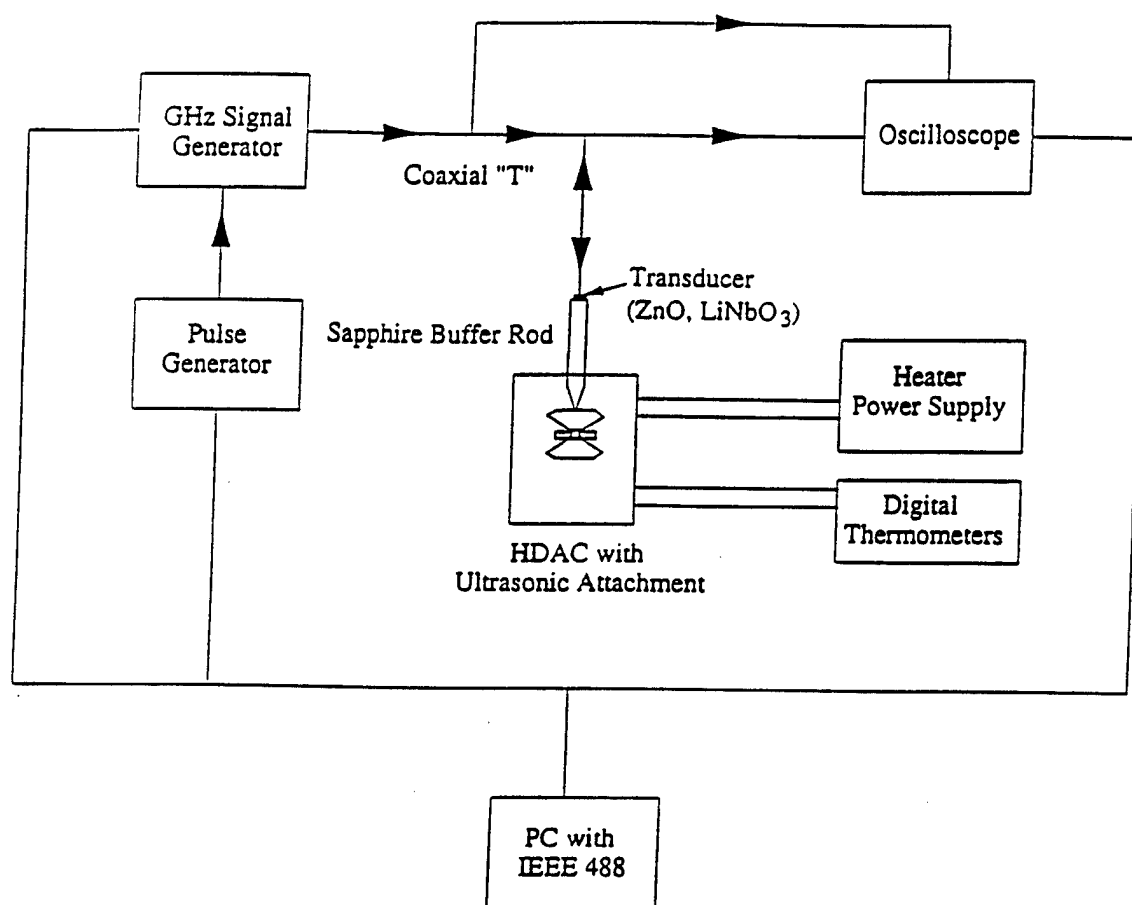


FIGURE 4

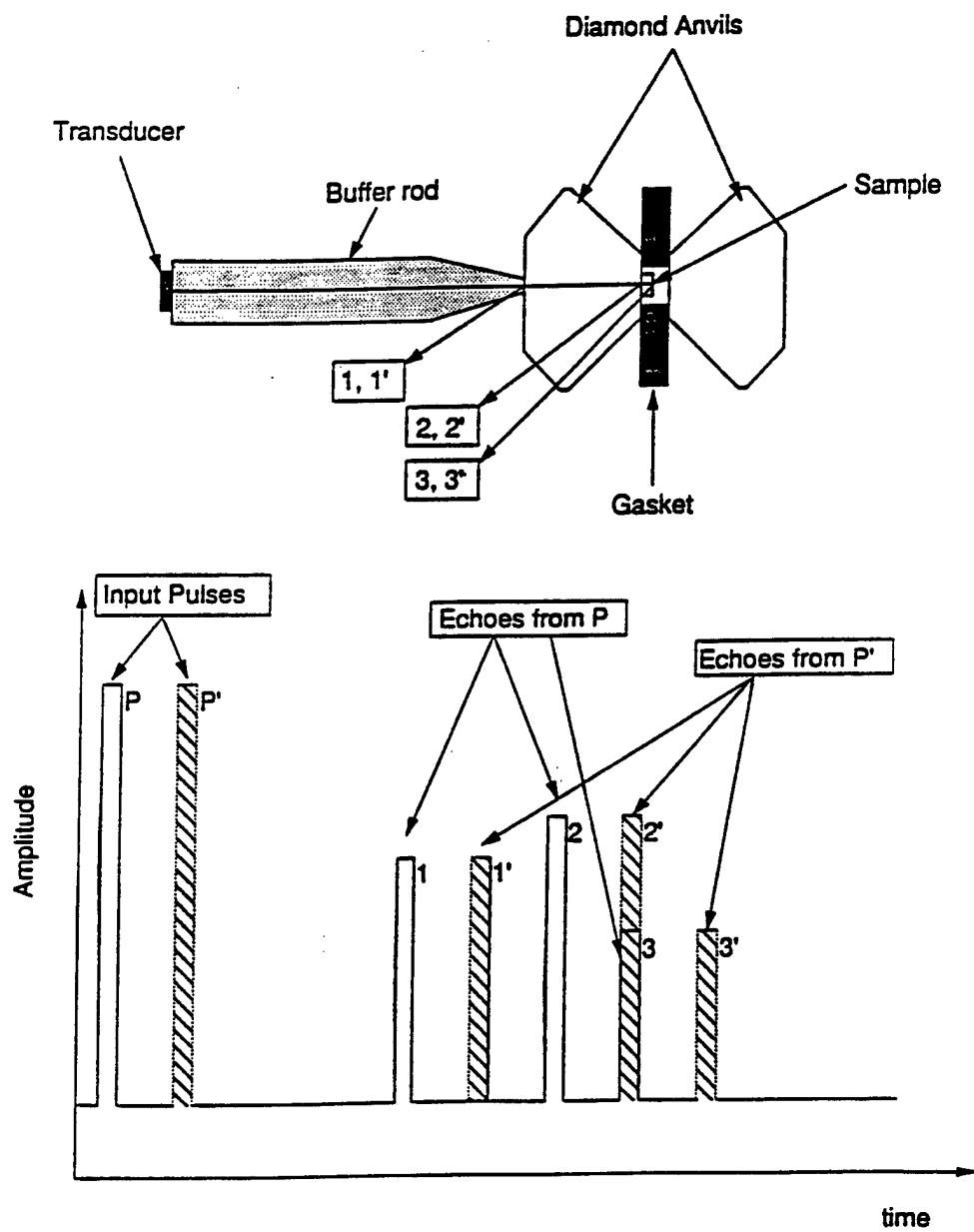


FIGURE 5

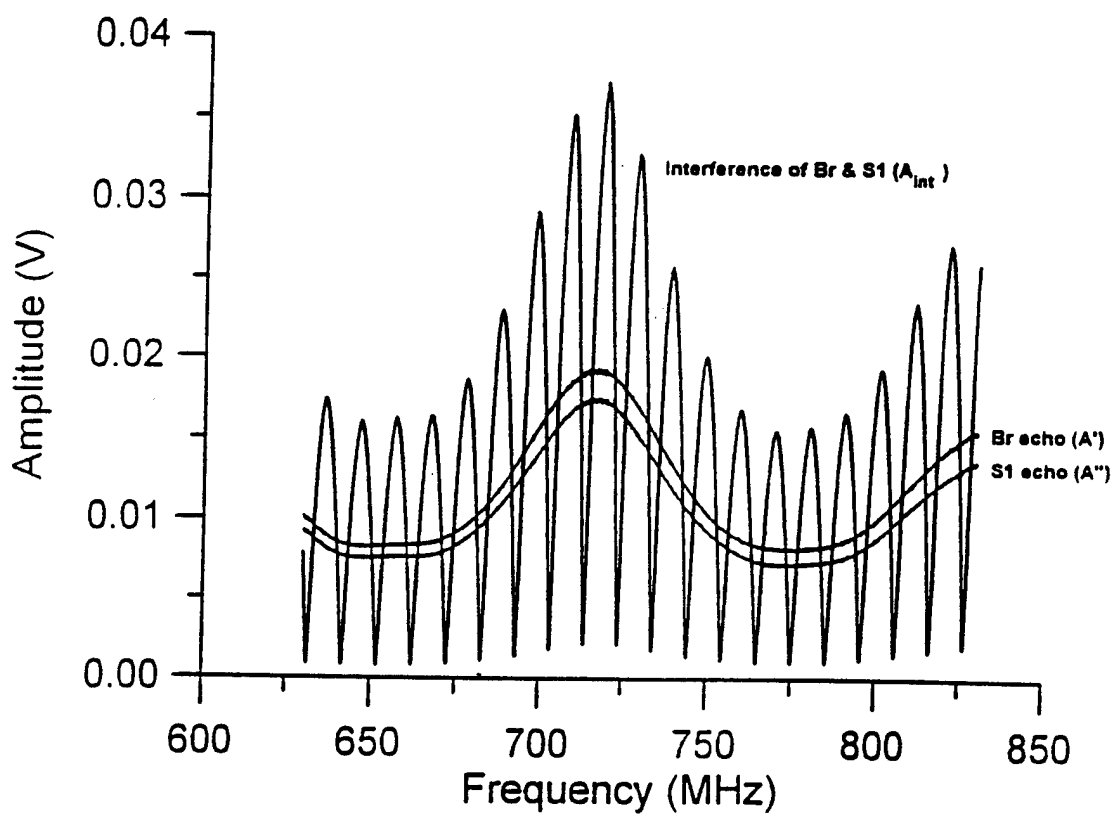


FIGURE 6

Travel Time from Raw Interference Amplitude Data

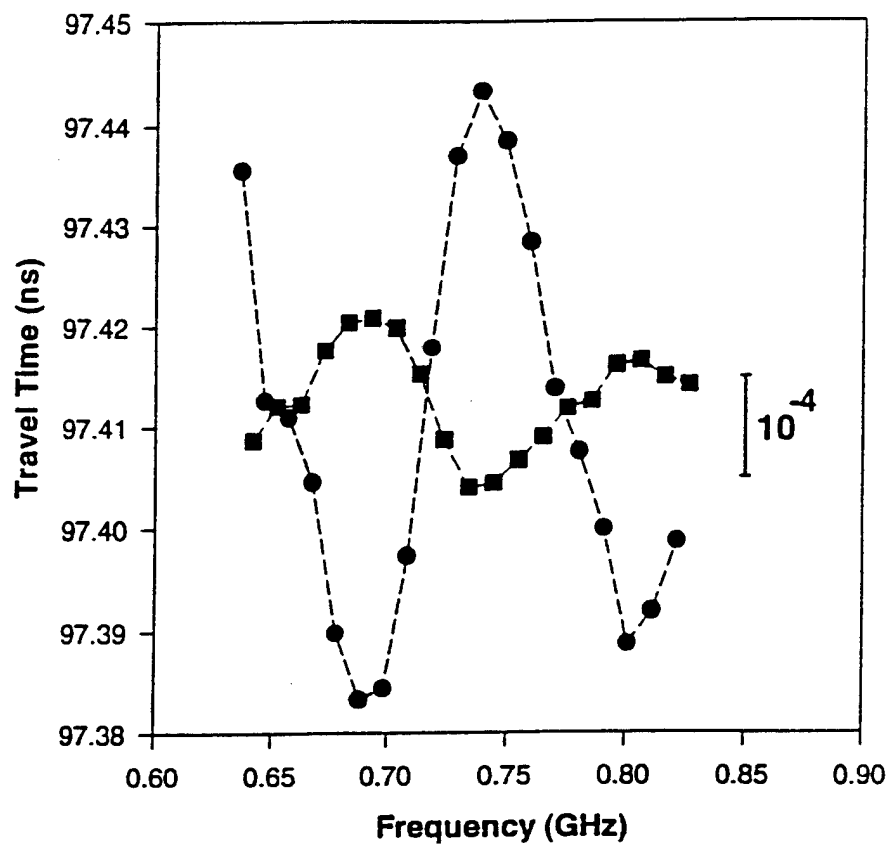


FIGURE 7

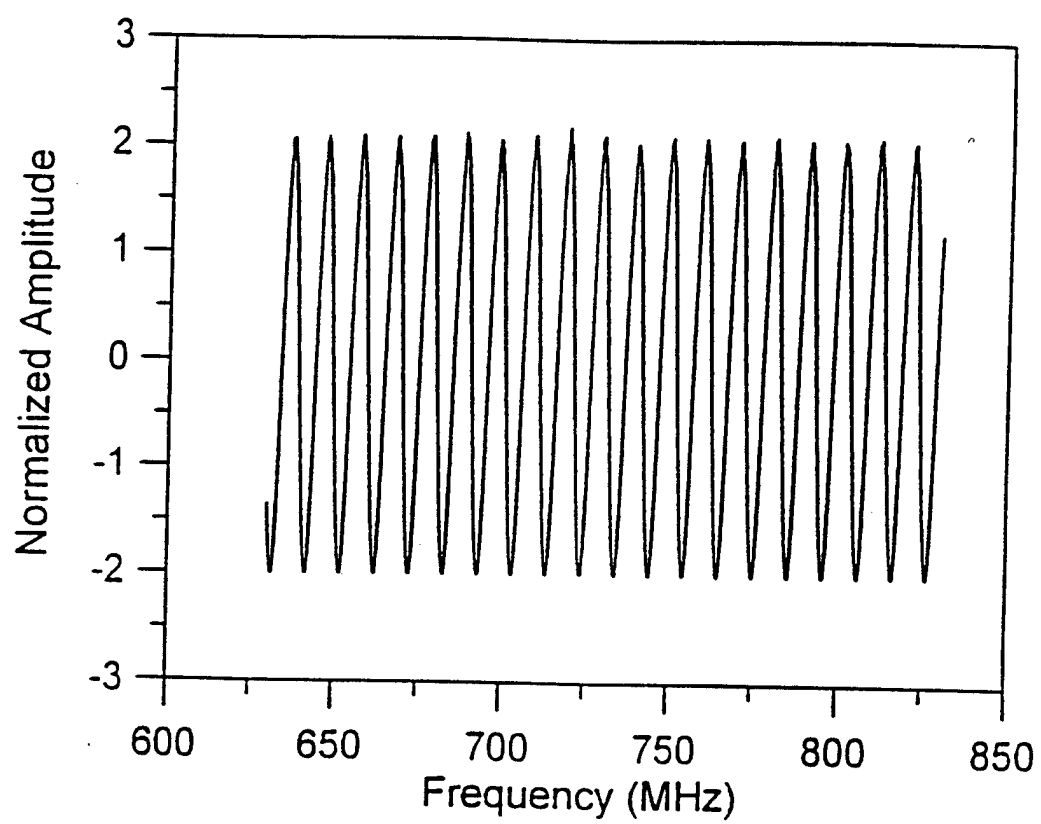


FIGURE 8

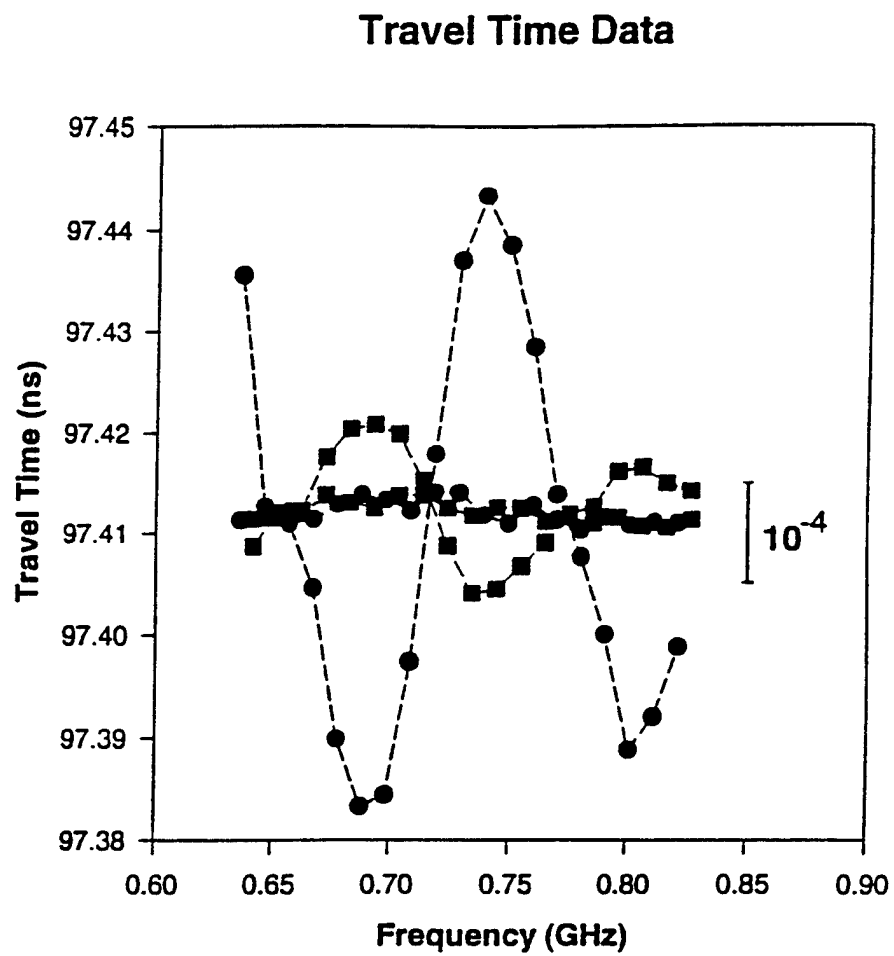


FIGURE 9

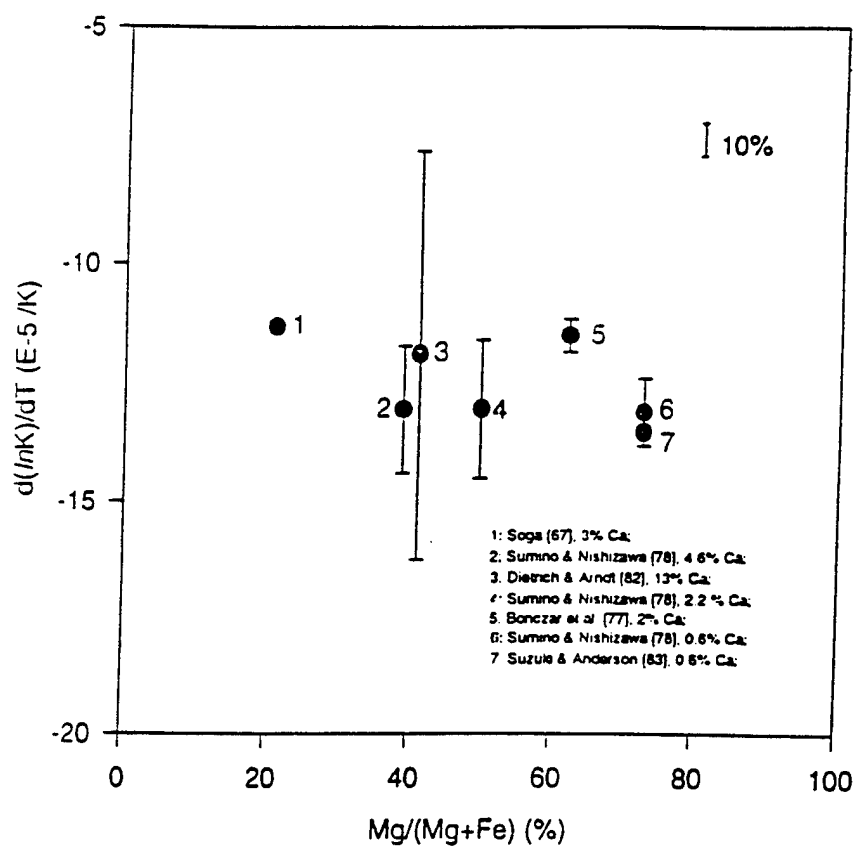


FIGURE 10

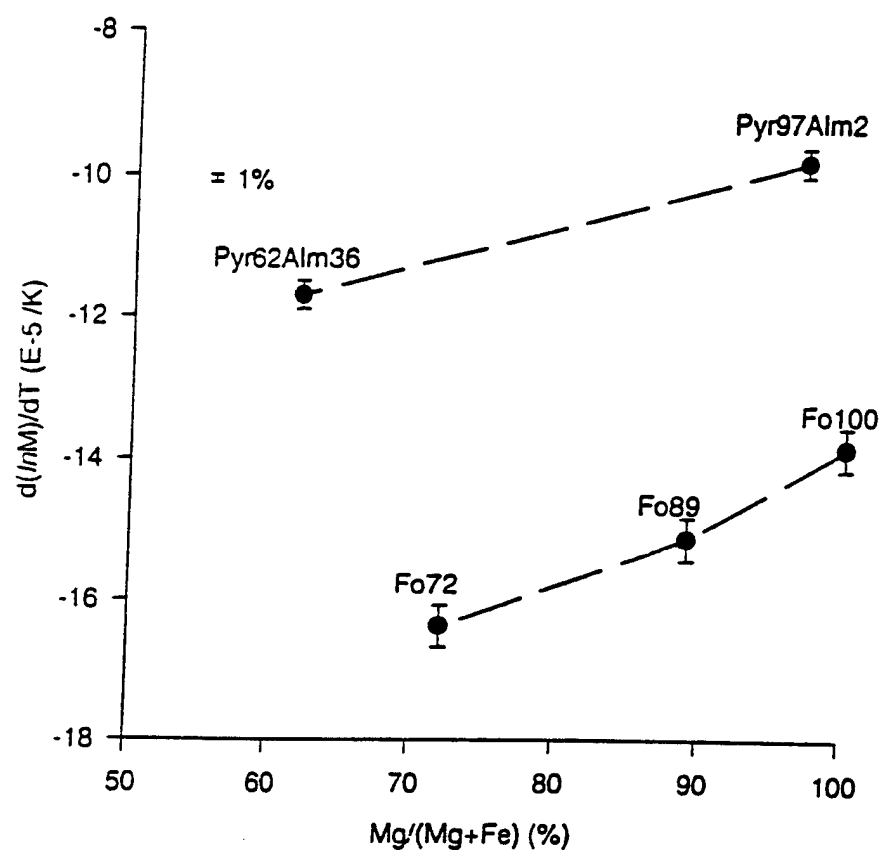


FIGURE 11

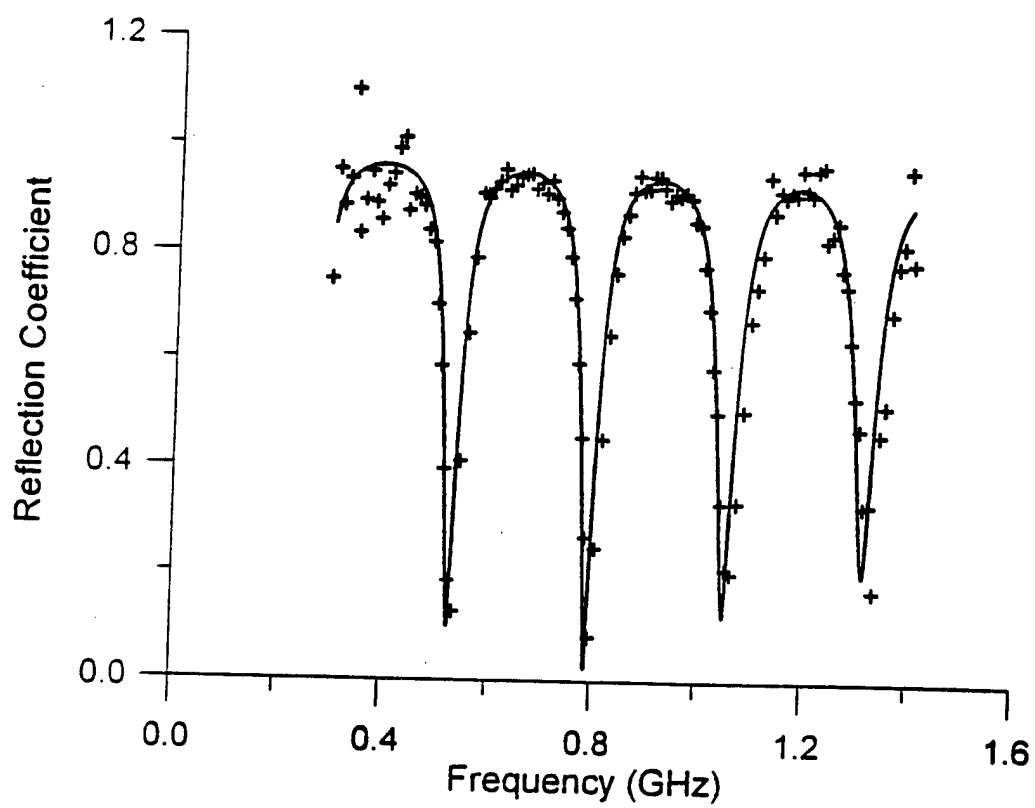


FIGURE 12

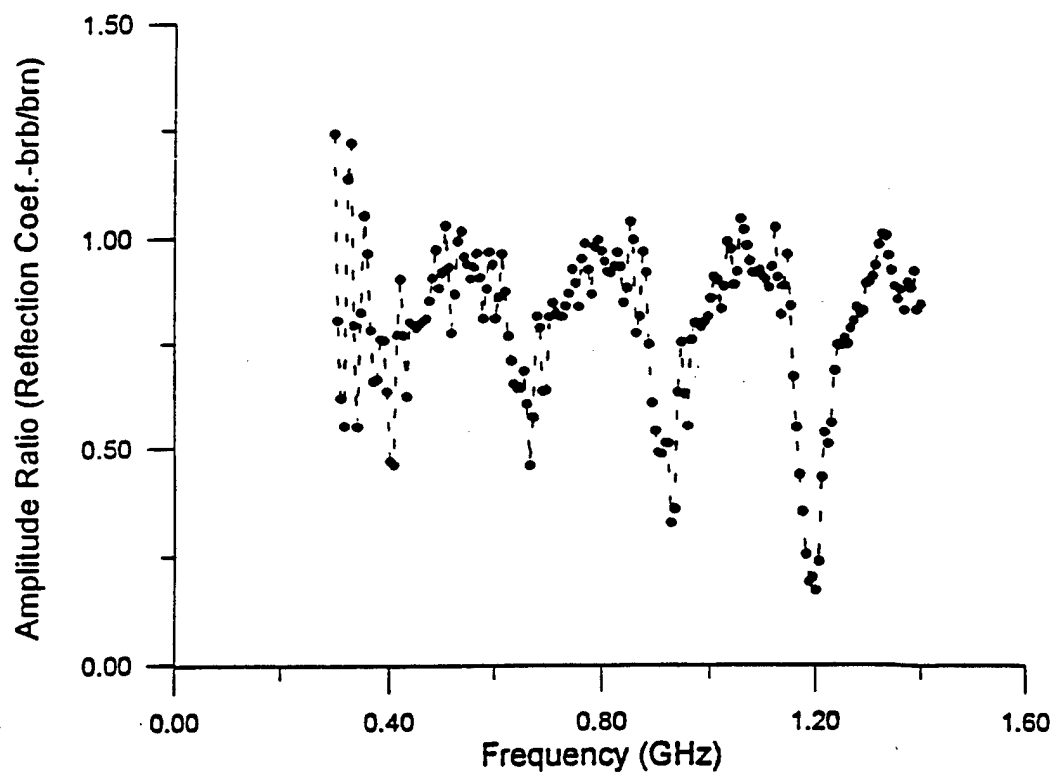
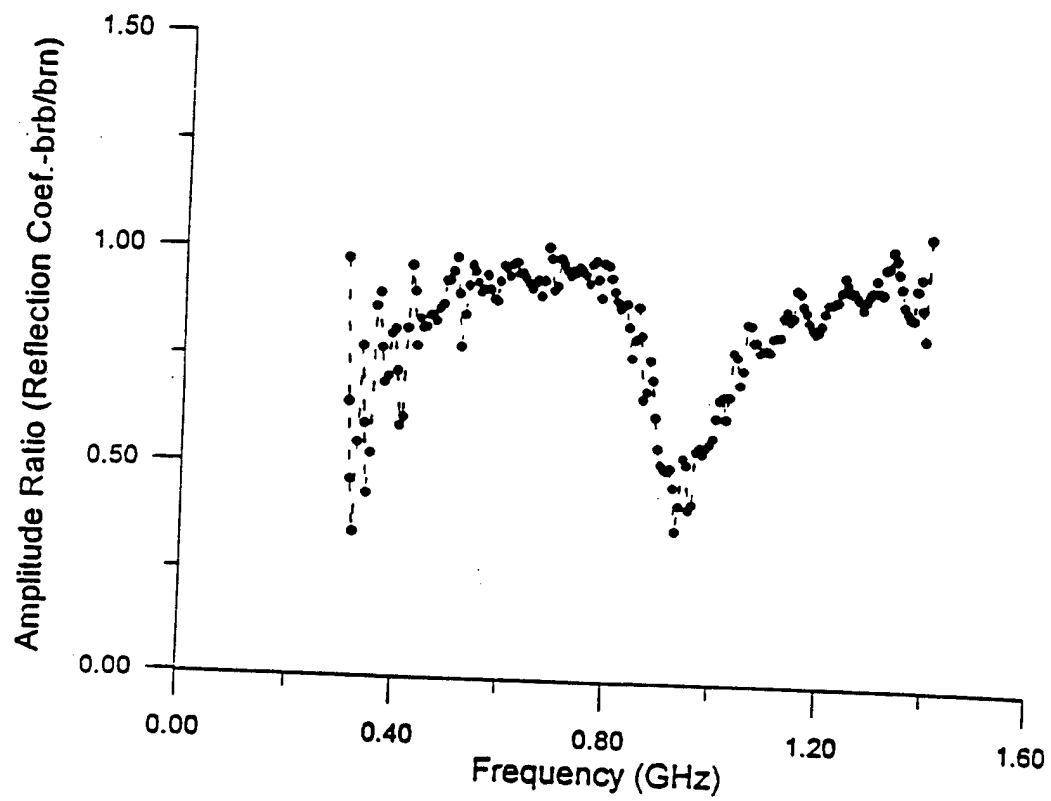


FIGURE 13



GHz Interferometry in a Diamond Anvil Cell

(under development, CU and Bayreuth)

- a.) Complete Equation of State over P (10 GPa) and T(1200 K) simultaneously.
- b.) Small samples (50 microns), thus solid solution series and high pressure phases possible.
- c.) Simultaneous measurements with X-rays yield new absolute pressure scale.

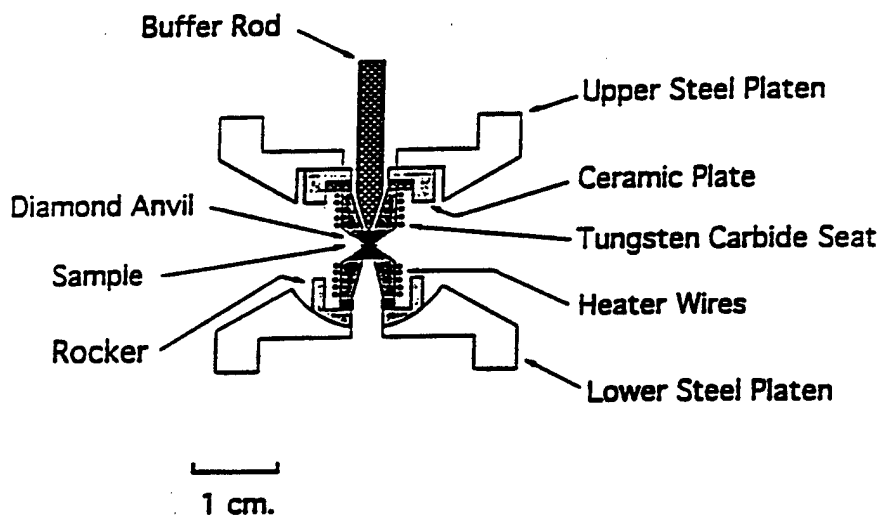
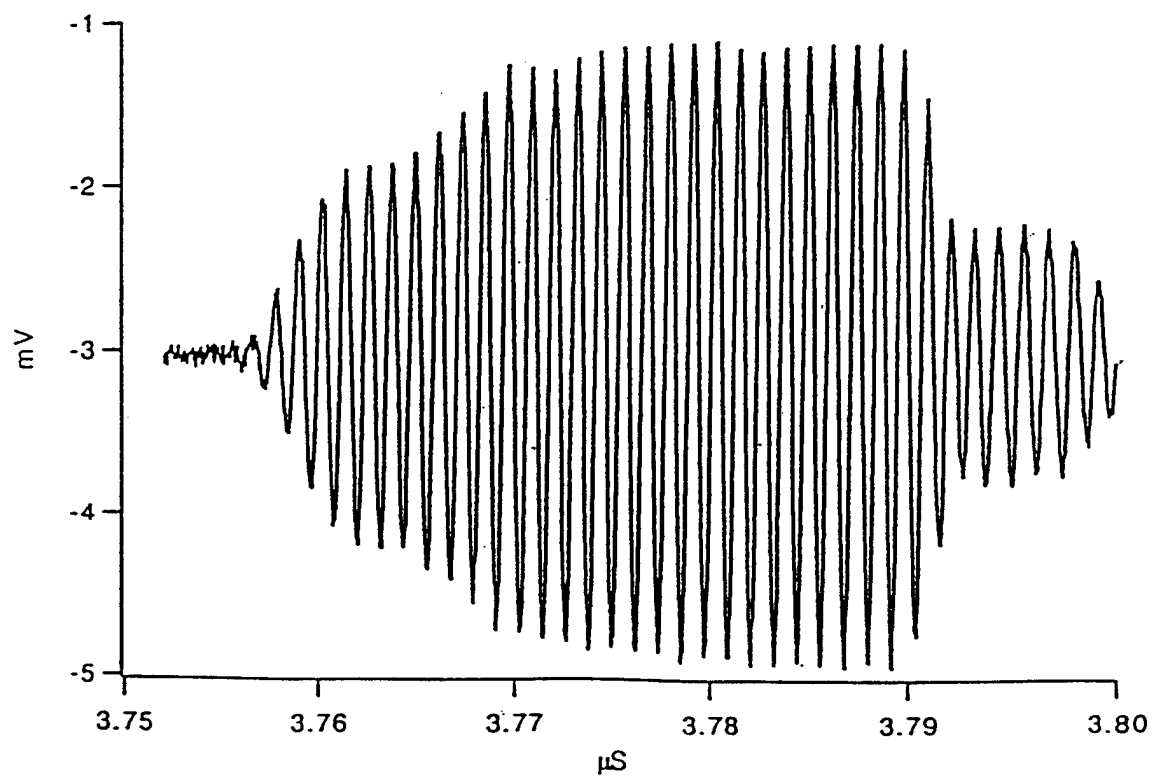
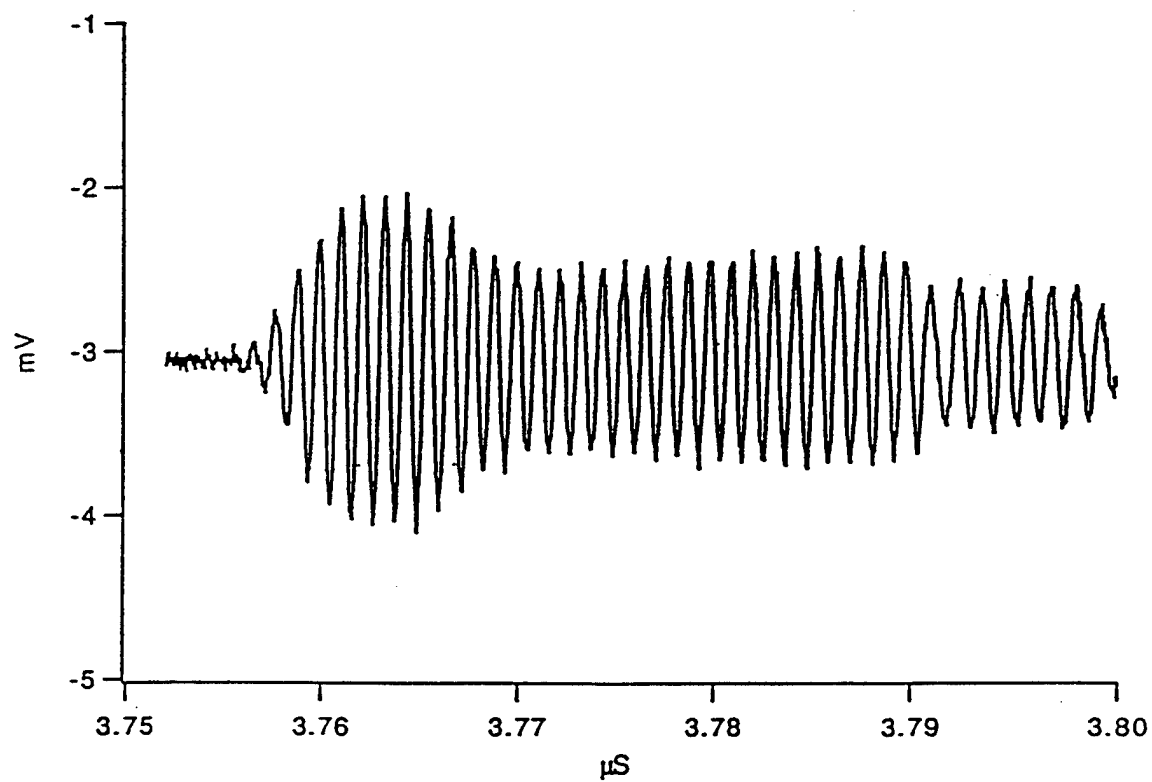


FIGURE 15



Raw data showing the minimum and maximum of interference

FIGURE 16

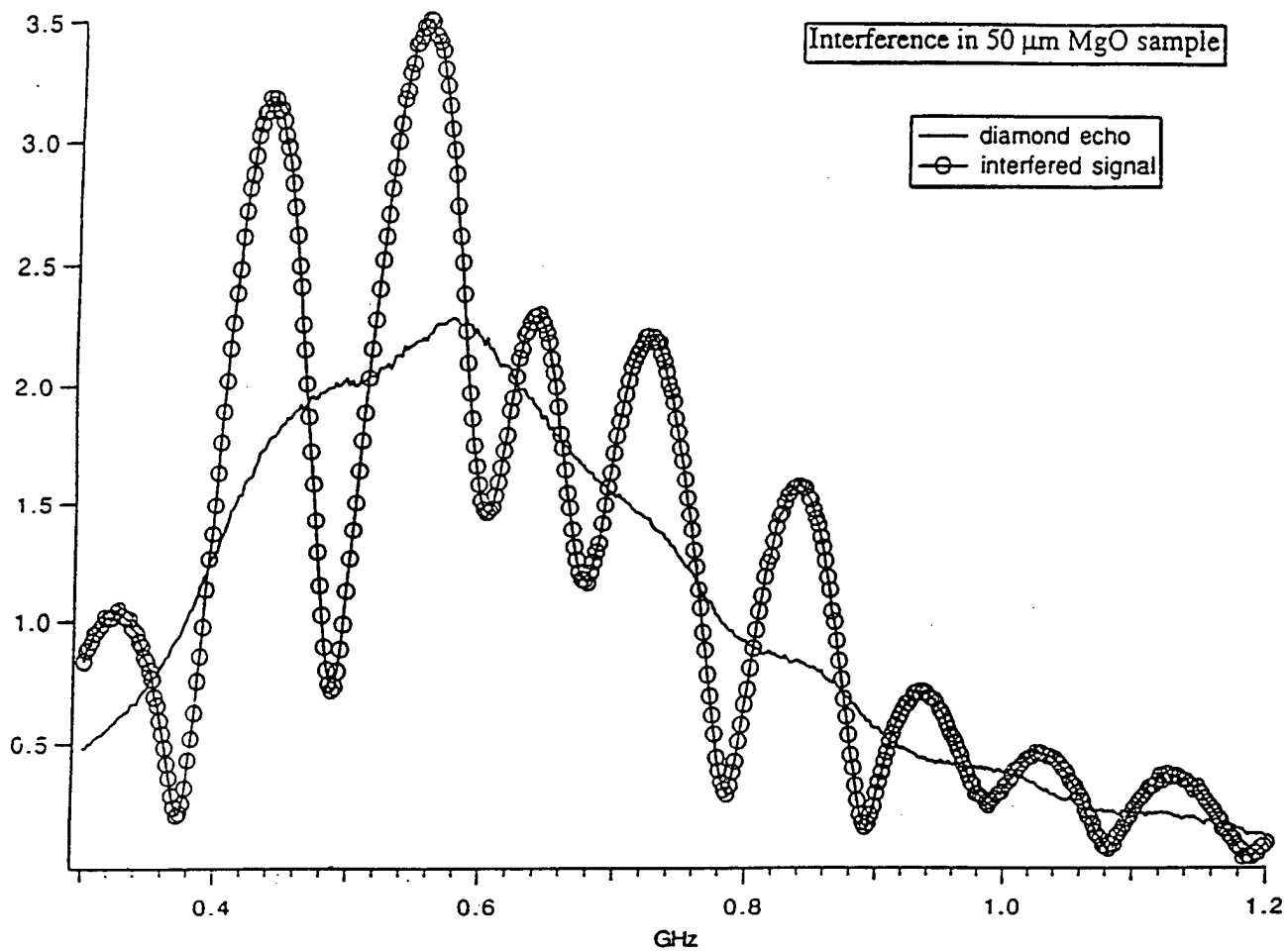


FIGURE 17

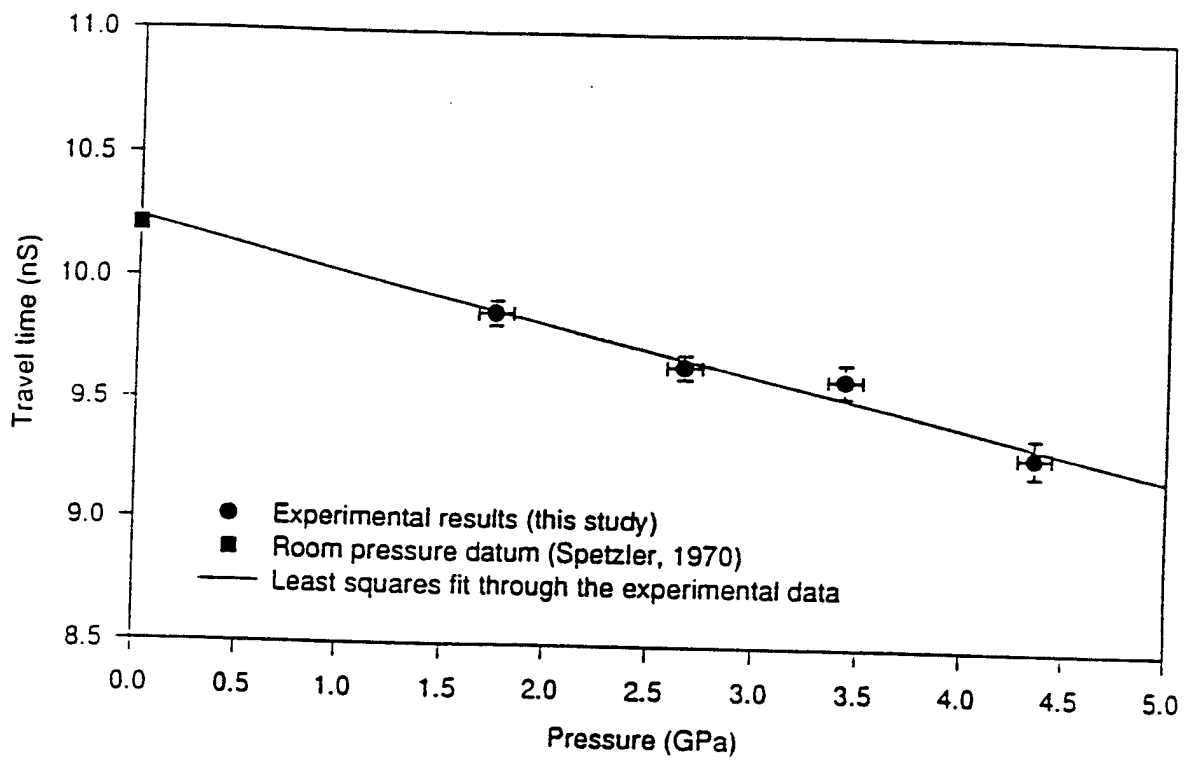
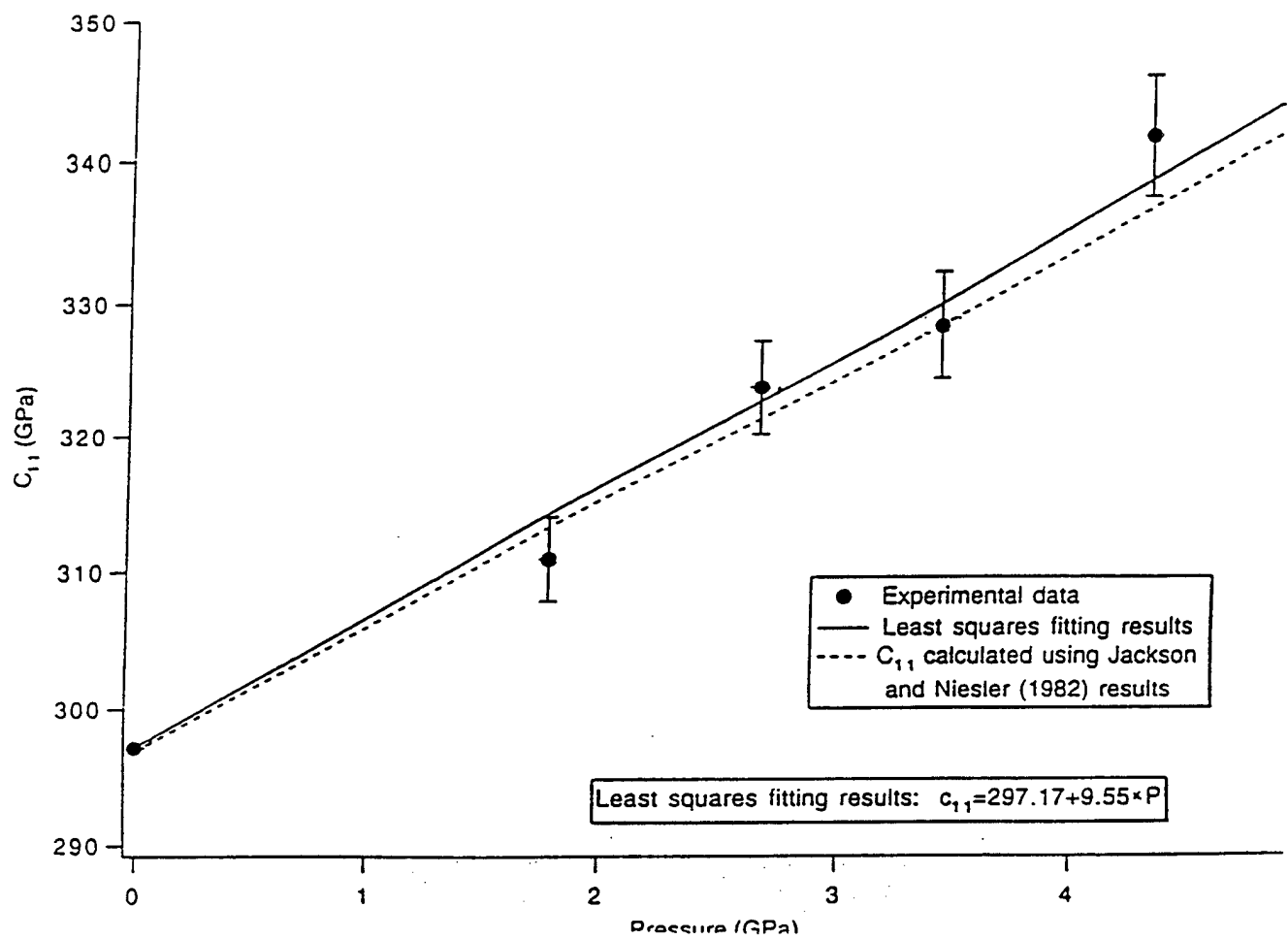


FIGURE 18



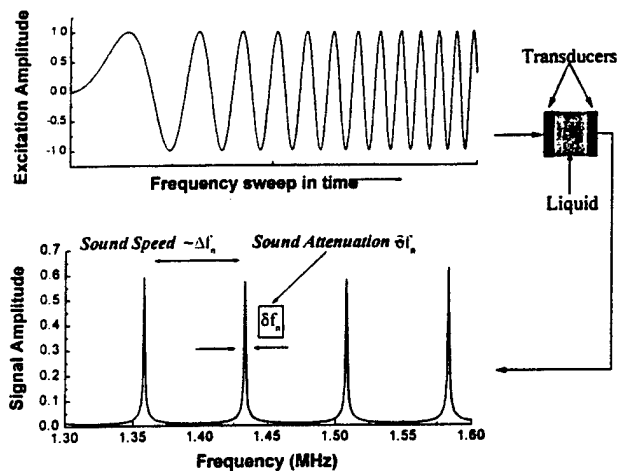
APPLICATIONS OF ULTRASONIC INTERFEROMETRY

Dipen N. Sinha, Kendall Springer, Wei Han, and
David Lizon

Los Alamos National Laboratory

Sponsors: Office of the Assistant to the Secretary of Defense,
Counterproliferation Program
Defense Special Weapons Agency

Determination of Sound Speed and Attenuation from Ultrasonic Interferometry



$$c_l = 2d\Delta f; \text{ sound speed}$$

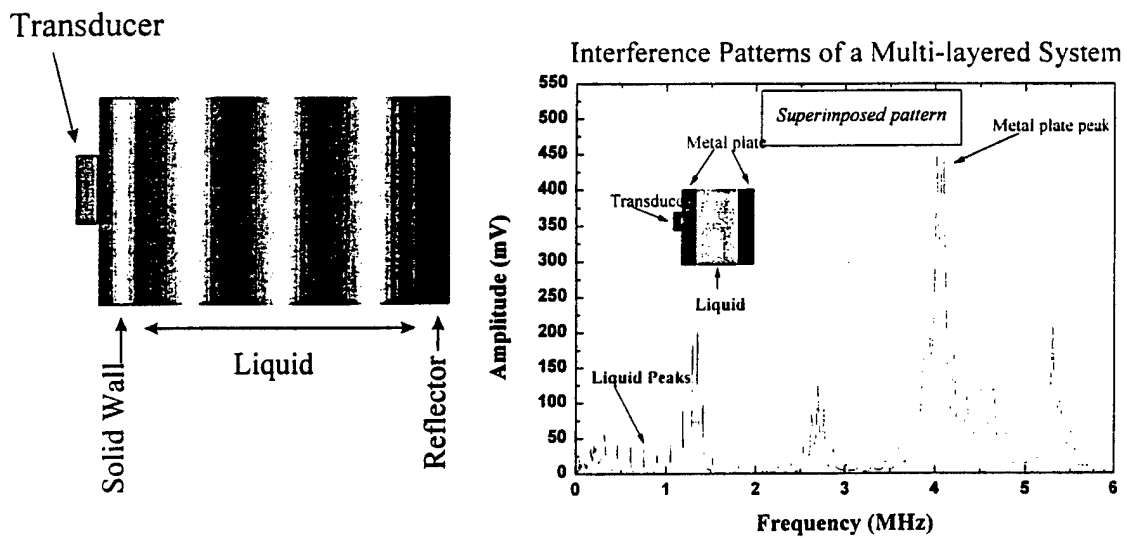
$$\delta f = \frac{2c_l}{\pi\sigma d} + \frac{c_l\alpha_l(f)}{\pi}$$

$$\left[\frac{1}{(T_{\min}/T_{\max})} - 1 \right]^{-\frac{1}{2}} = \frac{2}{\sigma} + \alpha_l(f)d$$

$$\sigma = \frac{z_w}{z_l} + \frac{z_l}{z_w} \quad \begin{array}{l} \text{impedance ratio} \\ l = \text{liquid} \\ w = \text{wall} \end{array}$$

d = path length; T = transmission amplitude; α = sound attenuation; f = frequency

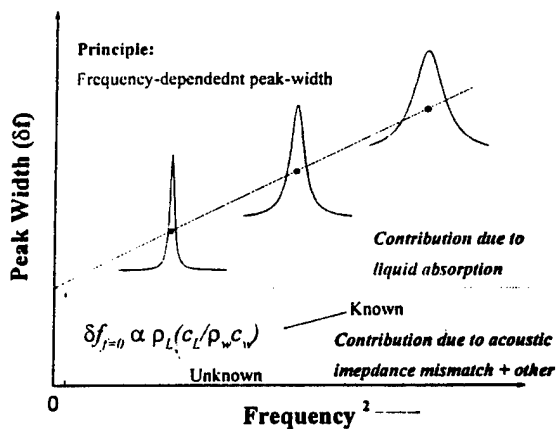
Ultrasonic Interferometry in Multi-Layered Systems



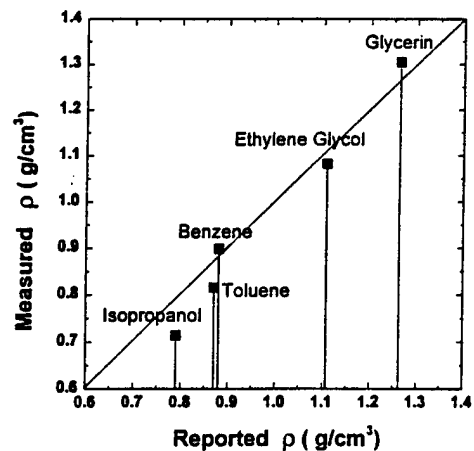
- Detected signal is a superimposition of interference in both wall and liquid
- Peak-width includes effect of impedance mismatch at the wall-liquid interface

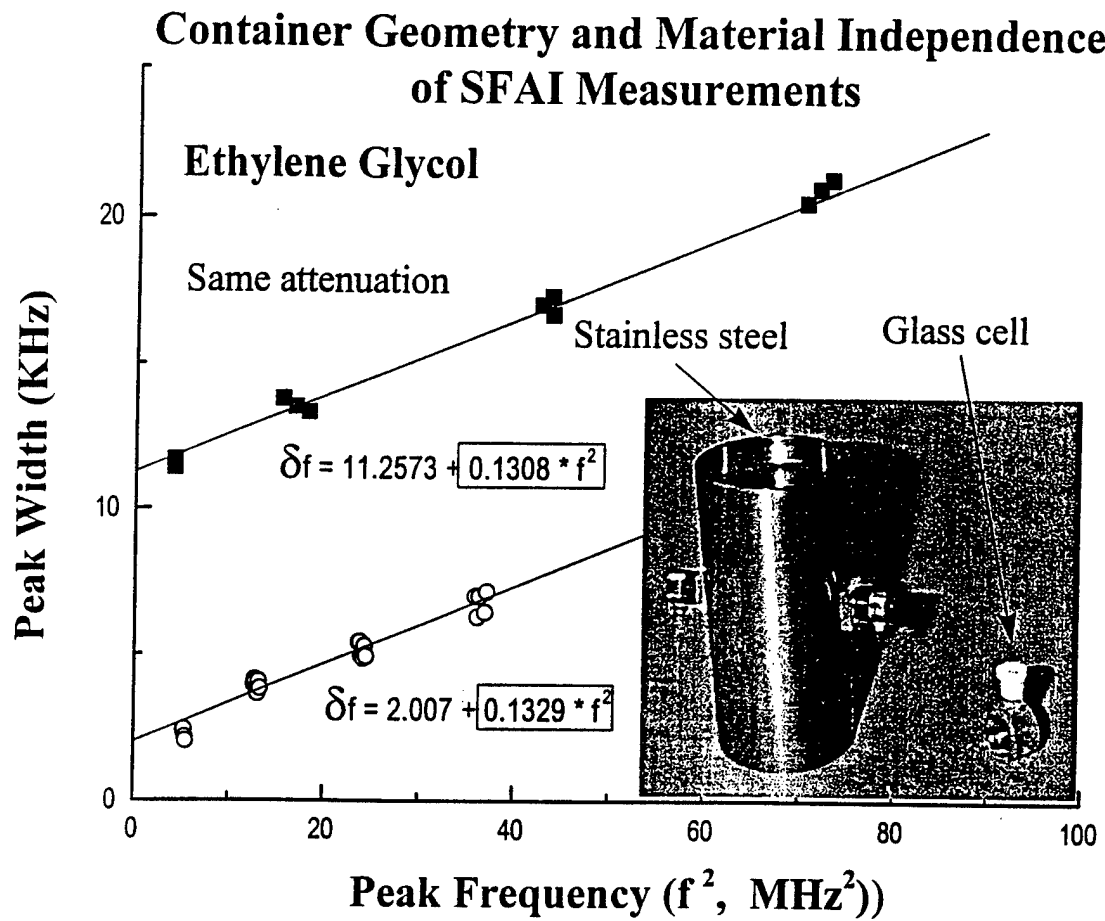
Non-Invasive Liquid Density Determination Using Ultrasonic Interferometry

Liquid Density Determination

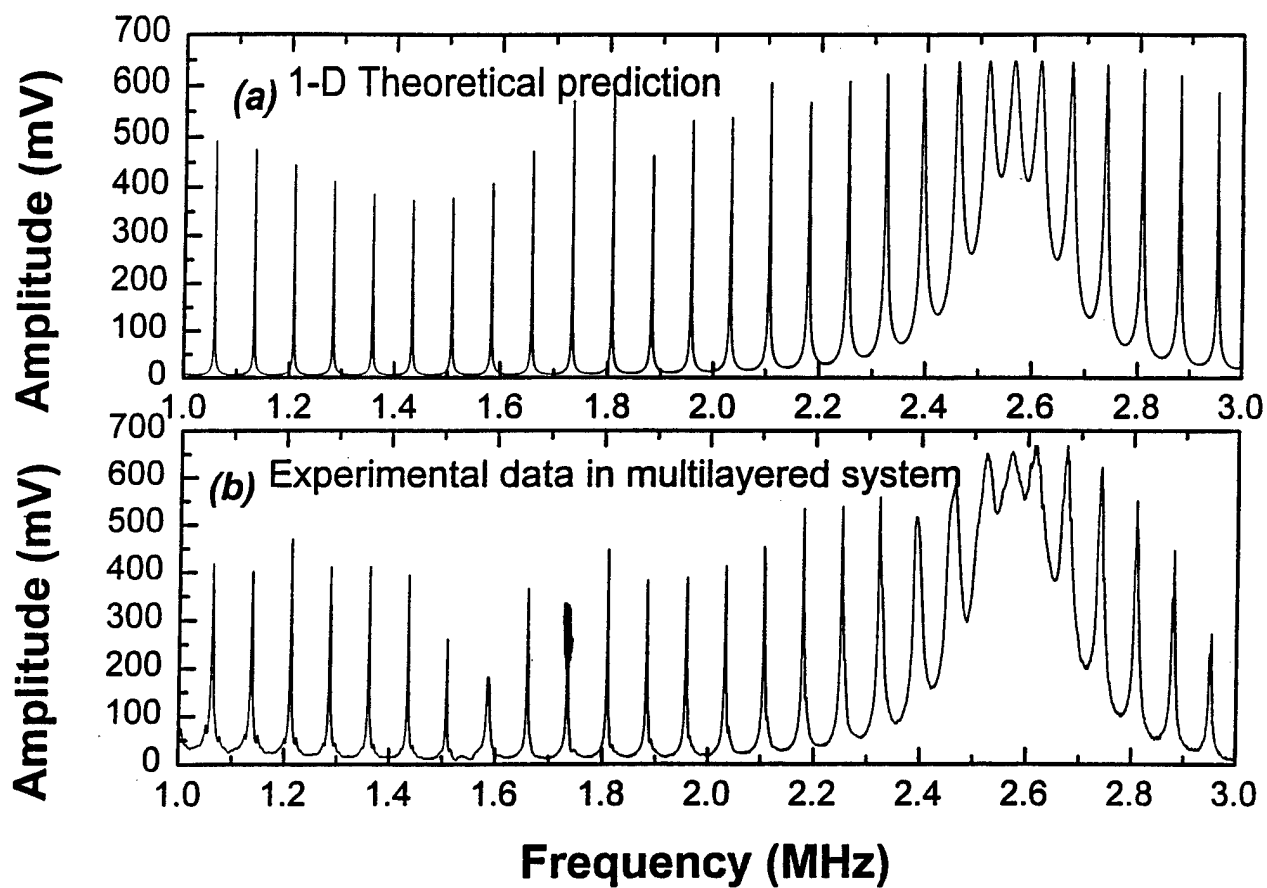


Non-invasive Liquid Density Determination



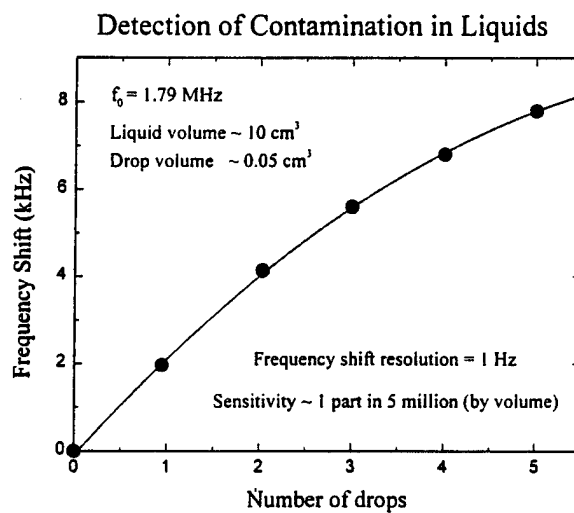
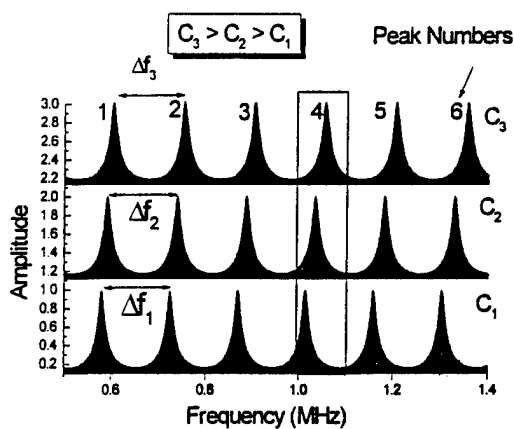


Comparison with Theory

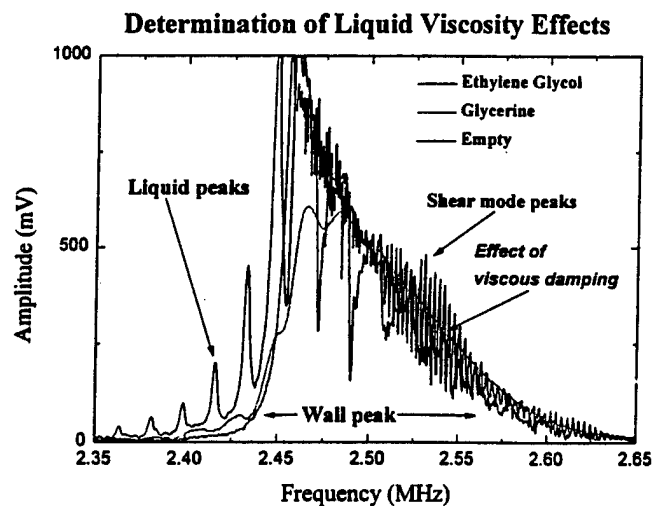
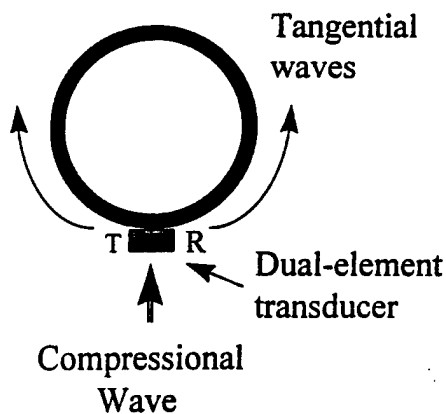


Sensitivity of Ultrasonic Interferometry Technique

Single Peak Tracking



Ultrasonic Interferometry in Cylindrical Containers

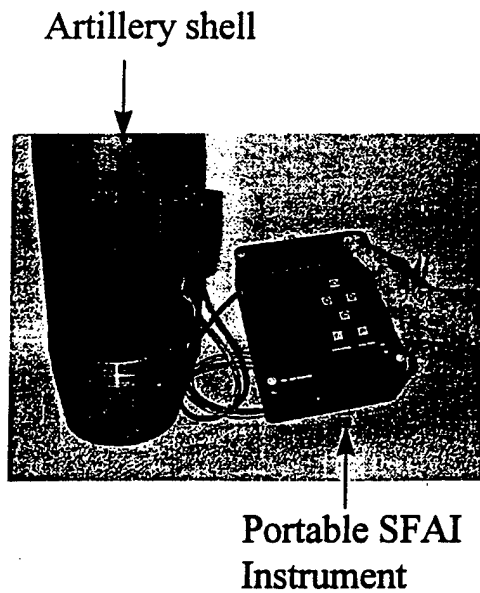


Liquid viscosity can be determined from the interaction between tangential waves and the liquid inside. The asymmetry in the container wall thickness mode resonance peak is due to the contribution of tangential modes.

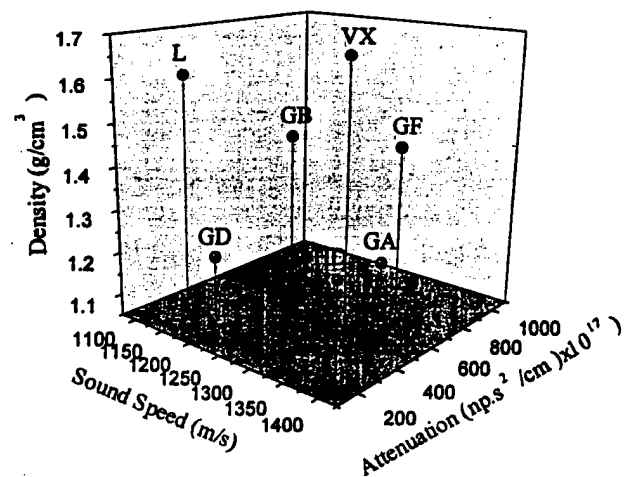
AREAS OF APPLICATION OF ULTRASONIC INTERFEROMETRY

- **Chemical Weapons Verification**
- **Basic Research**
- **Industrial Process Monitoring**
- **Biomedical**
- **Food and Beverage**
- **Environmental Sensors**
- **Materials Diagnostics**
- **Customs and Drug Interdiction**
- **Geological studies**
- **Ultrasonic Tomography**

Non-Invasive Identification of CW Agents



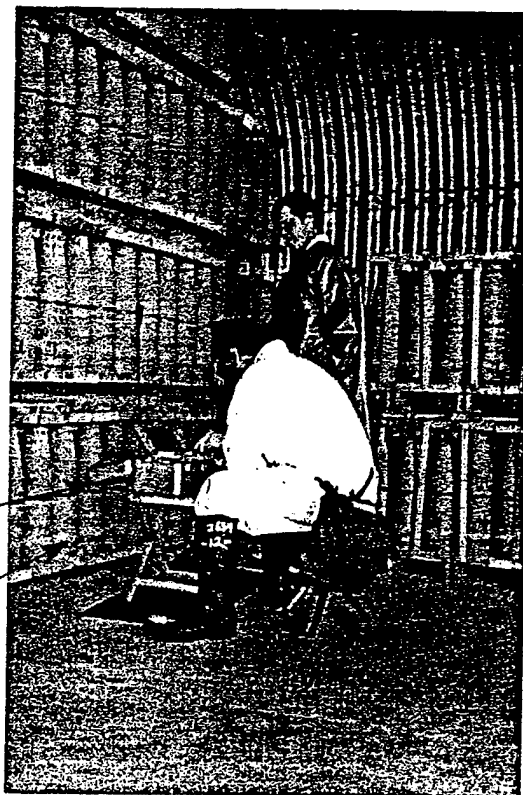
SFAI measurements of CW agent physical properties



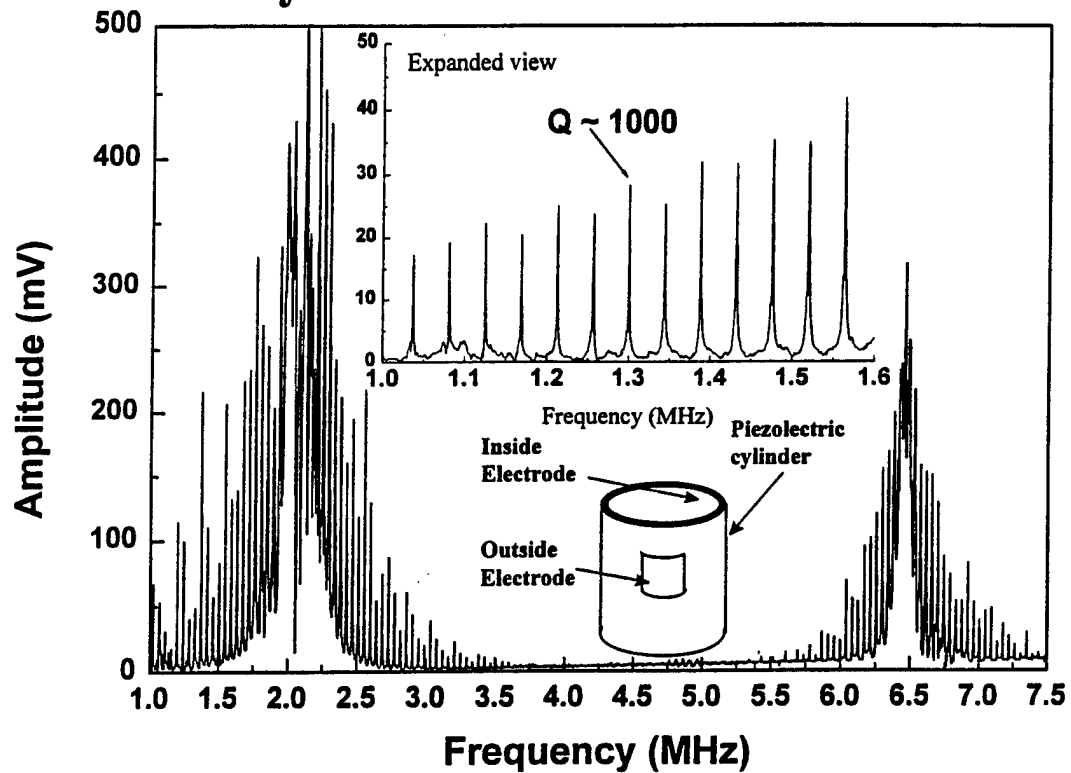
**Use of Ultrasonic
Interferometry in
Non-Invasive
Identification of
Chemical Warfare
Compounds in
Sealed Munitions**

Portable Instrument

Chemical Munitions



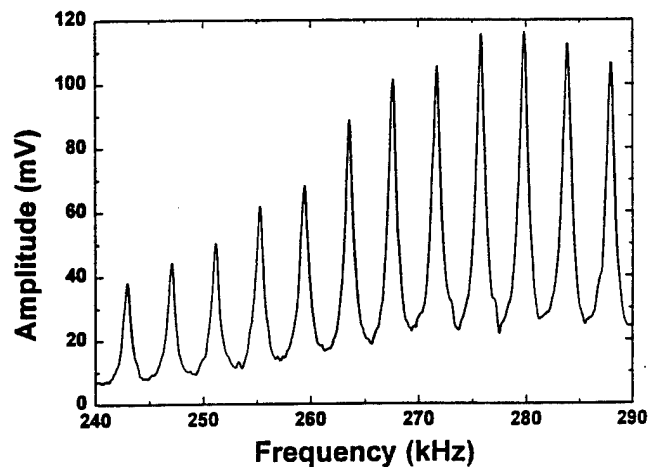
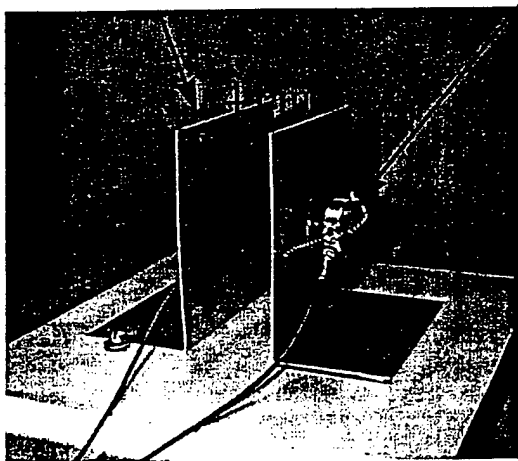
Cylindrical Piezoelectric Resonator



Ultrasonic Interferometry in Air

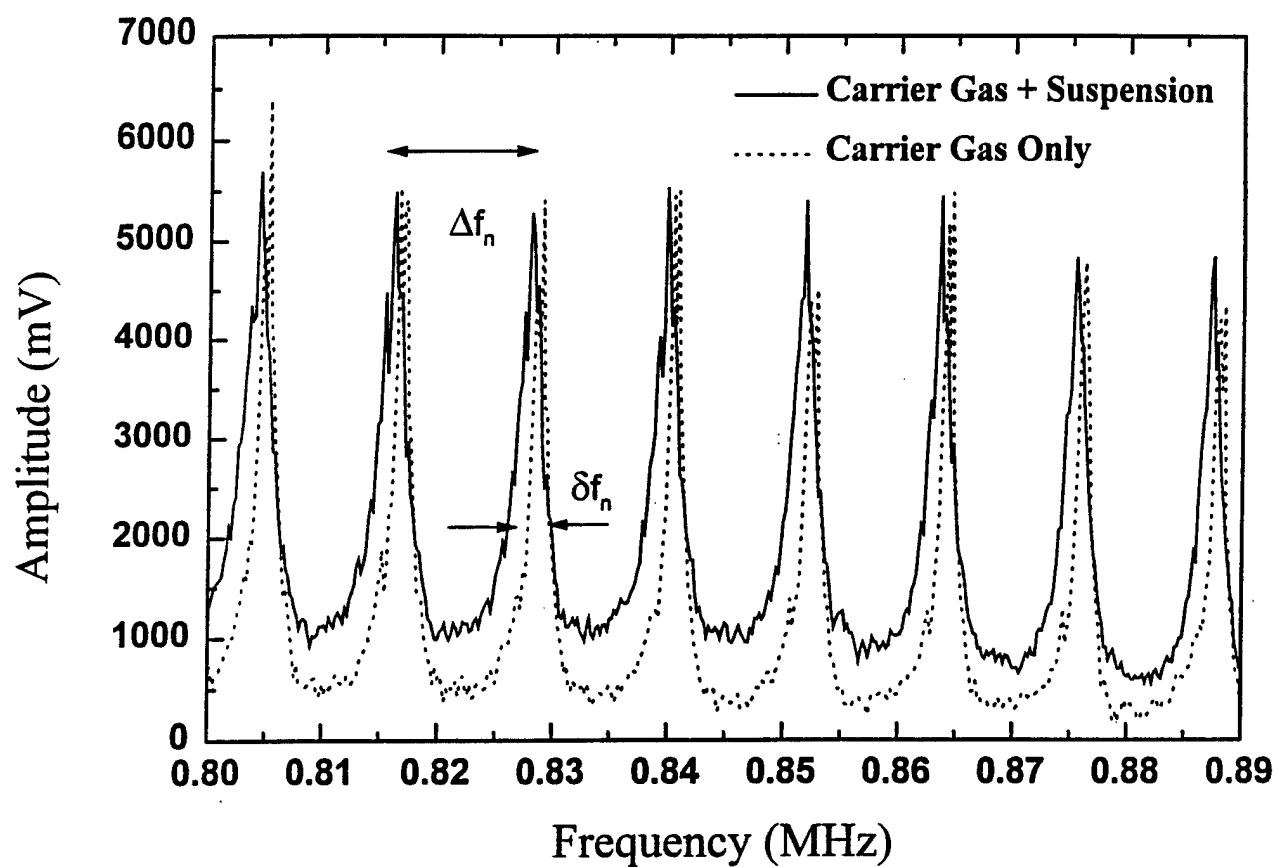
Aluminum Plate

Transducer

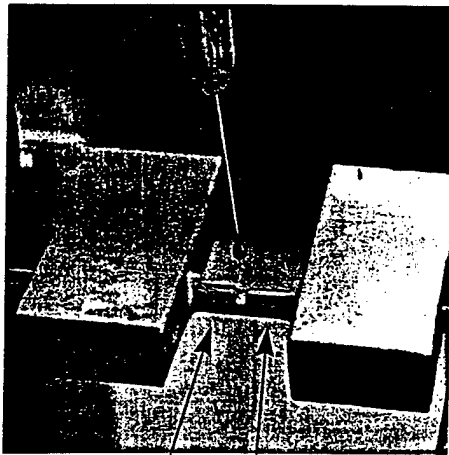


Usage: *Gas flow, humidity, detection of suspended particulates*

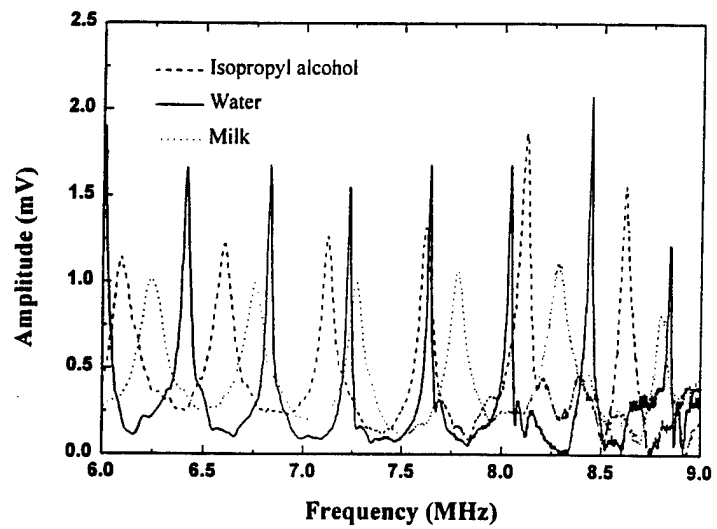
Noninvasive Detection of Aerosol in Sealed Metal Container



Ultrasonic Interferometric Characterization of a Single Drop of Liquid

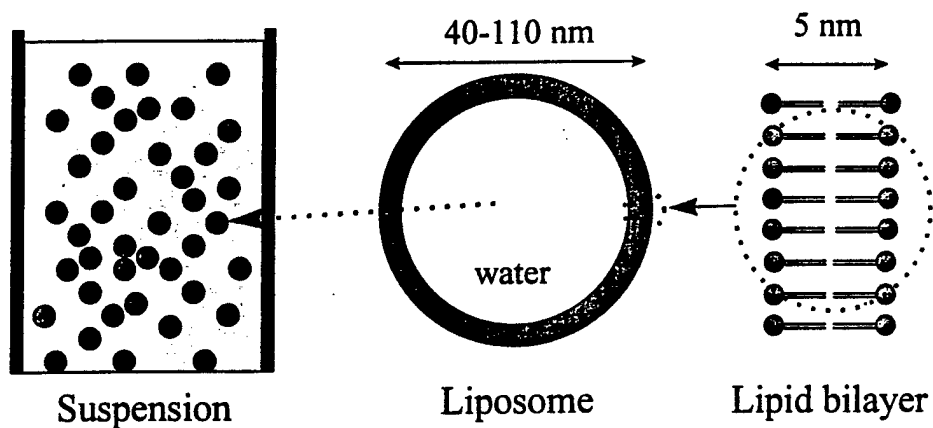


Miniature transducers

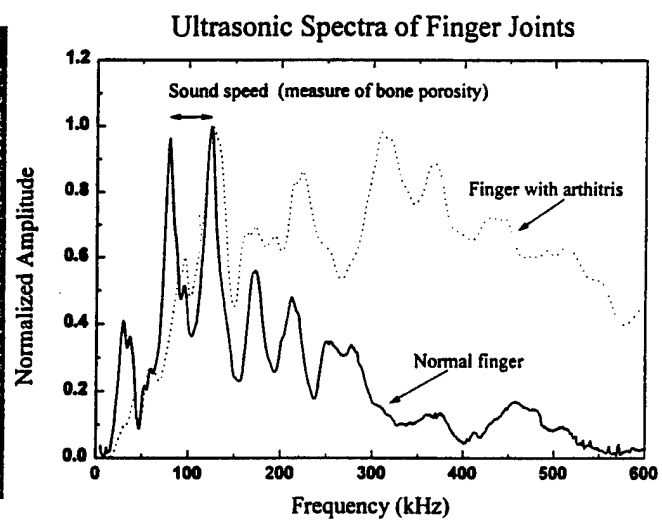
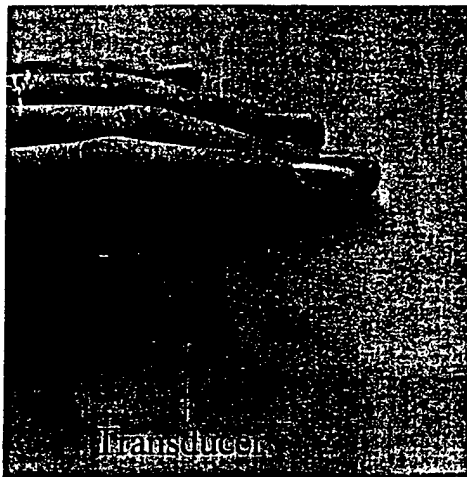


Broad-Spectrum Toxicity Sensor for Monitoring Water Pollutants

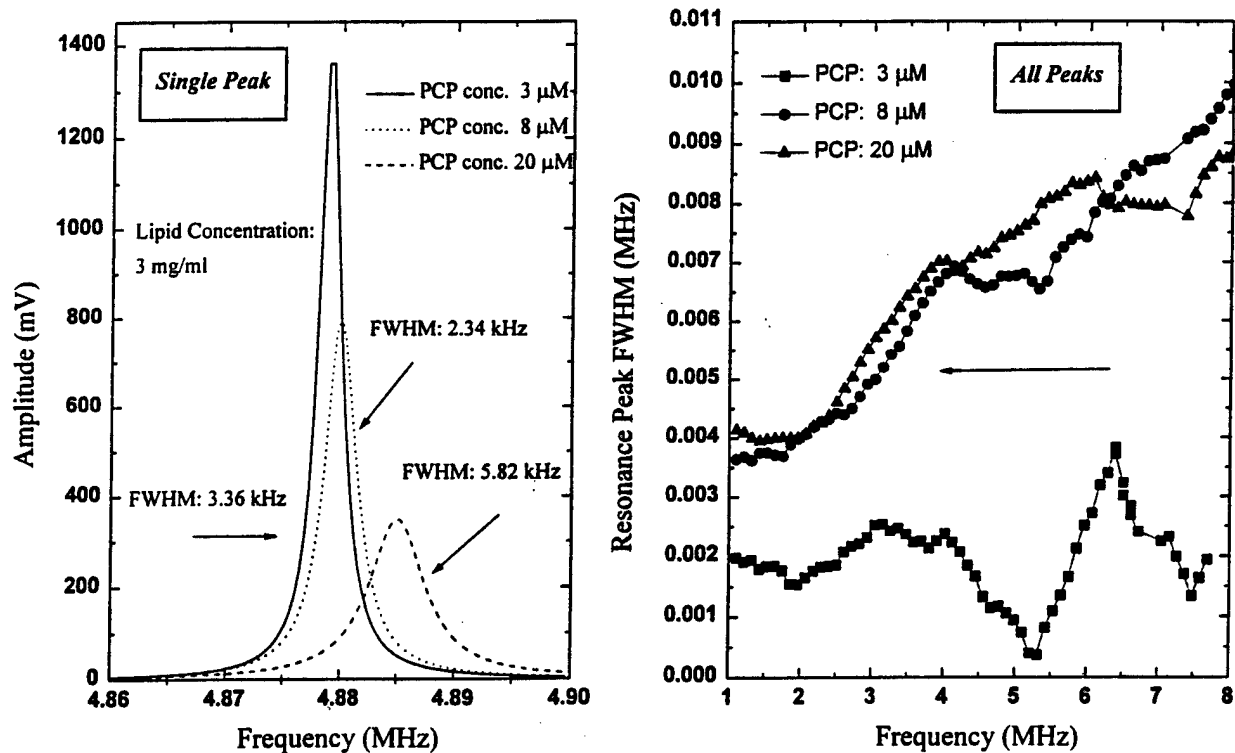
Effect on liposomes is monitored using ultrasonic interferometry



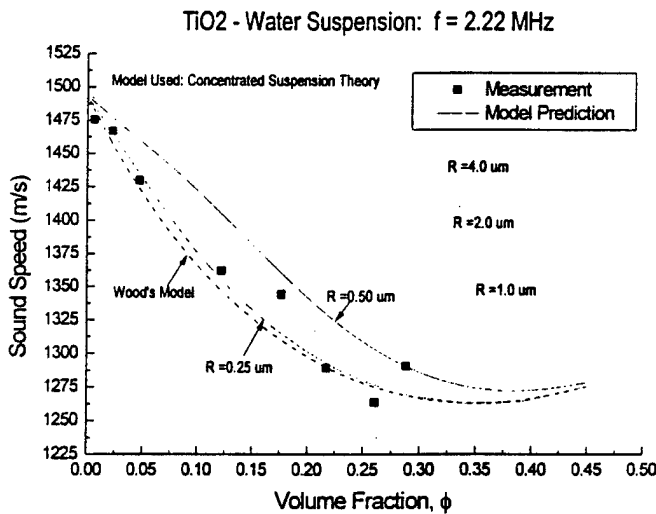
Ultrasonic Interferometric Characterization of Bones and Joints



Effect of PCP on Liposome Suspension Sound Attenuation

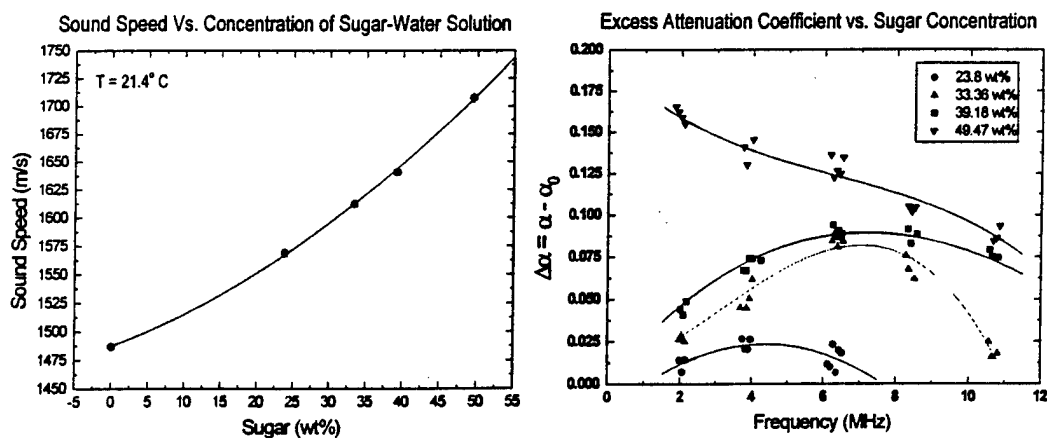


Particle Size and Volume Fraction Determination in Liquid Suspensions



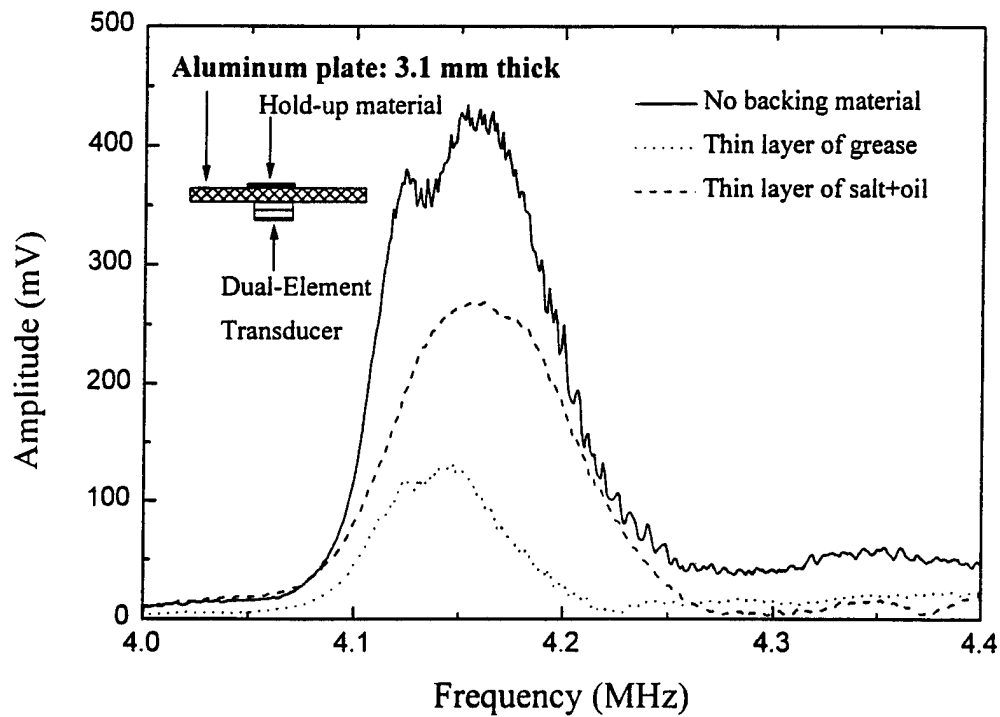
Both sound speed and attenuation in a suspension depend on the particle size. Sound speed measurements are shown as a function of volume fraction. The particle size can be determined by curve-fitting the measured data with theory.

Measurement of Concentration of Chemicals using Ultrasonic Interferometry

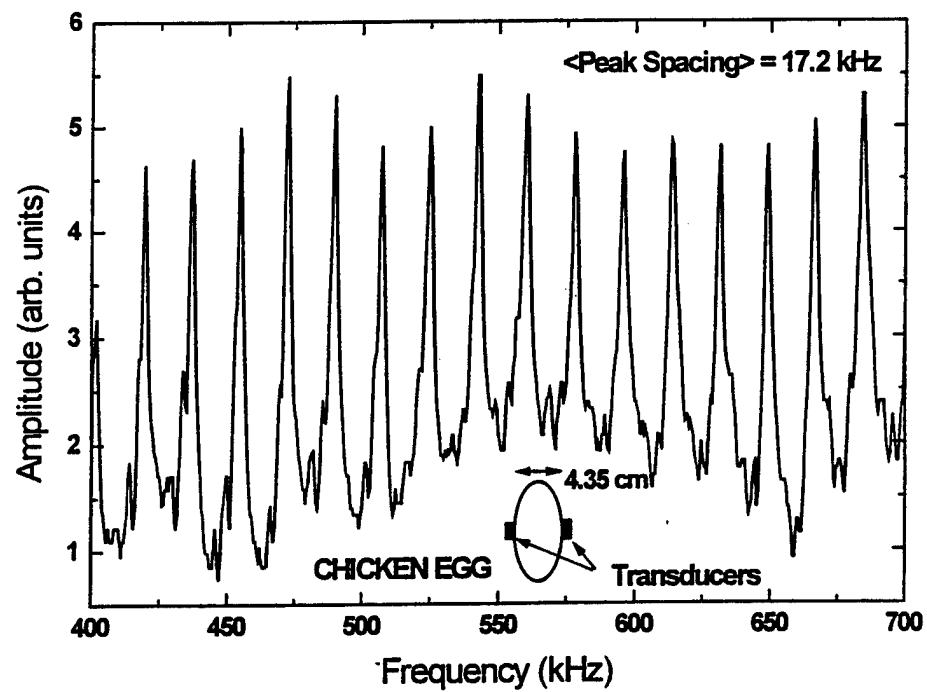


Sound speed and sound attenuation as a function of frequency can be noninvasively monitored.

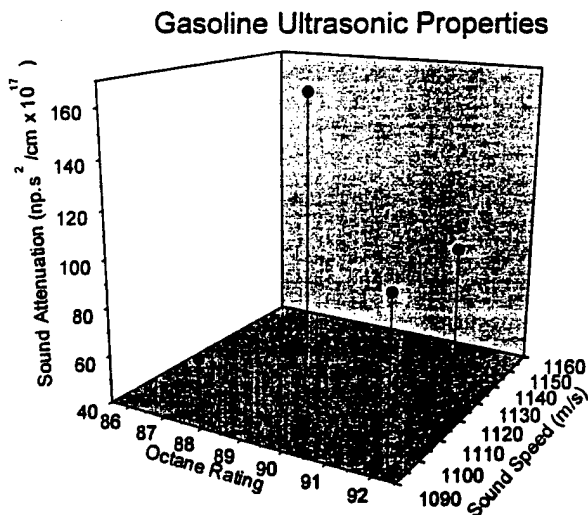
Detection of Material Deposition Using Ultrasonic Interferometry



Noninvasive Characterization of Eggs using Ultrasonic Interferometry



Non-Invasive Monitoring of Petroleum Products



Chemical composition,
of petroleum products and
other chemicals can be non-
invasively monitored
using ultrasonic interfero-
metry

RUS use in chemical weapons convention and resonant photoacoustic spectroscopy of aerosols

by

**W. Patrick Arnott
Desert Research Institute, DRI
Reno NV 89506**

pat@sage.dri.edu

RUS use in chemical weapons...

- 1. Manufacture the Los Alamos system for use in the verification portion of the Chemical Weapons Convention (CWC).**
 - a. Technology transfer supported by the Defense Special Weapons Agency and DRI cost share.**
 - b. Can operate within DRI, can transfer to Desert Research Corporation.**
- 2. DRI team includes...**
 - a. Rick Purcell, M.S. Mechanical Engineering.**
 - b. Morien Roberts, Ph.D. Computer Engineering.**
 - c. Dan Wermers, M.S. Electrical Engineering.**
 - d. W. Patrick Arnott, Ph.D. Physics,**

The PTS - Preparatory Commission - OPCW Home Page

The Chemical Weapons Disarmament Website

[Info](#) | [Documents](#) | [A Guided Tour of the CWC](#) | [Contact Address](#)

THIS PAGE LOOKS NICER IF YOU LET IT'S ORIGINAL COLOUR SCHEME SHOW!

Media! NGOs!

All information on the First Conference of the
States Parties (May 1997)

Documentation on
a common transmission file
structure is now available.

A list of interesting jobs
at OPCW

Do not forget to check the
Billboard!
Most recent update 4 April 1997.

The forms for industrial
declarations are now
available

At this website the Provisional Technical Secretariat of the Preparatory Commission for the Organisation for the Prohibition of Chemical Weapons (what a name! just call us the Secretariat) provides information on the Chemical Weapons Convention but also on other issues relating to toxic chemicals and chemical protection.



The Chemical Weapons Convention

(the complete text of the Chemical Weapons Convention)



The PrepCom and its members

(includes lists of points of contact in most Member States)



What's happening at the PrepCom

(be prepared through the PrepCom Calendarium)



The National Authority Adviser

(almost everything a new or well established National Authority needs to know)



Fact-finding files

(plenty on chemical weapons and other toxic chemicals, protection, relevant publications, etc.)

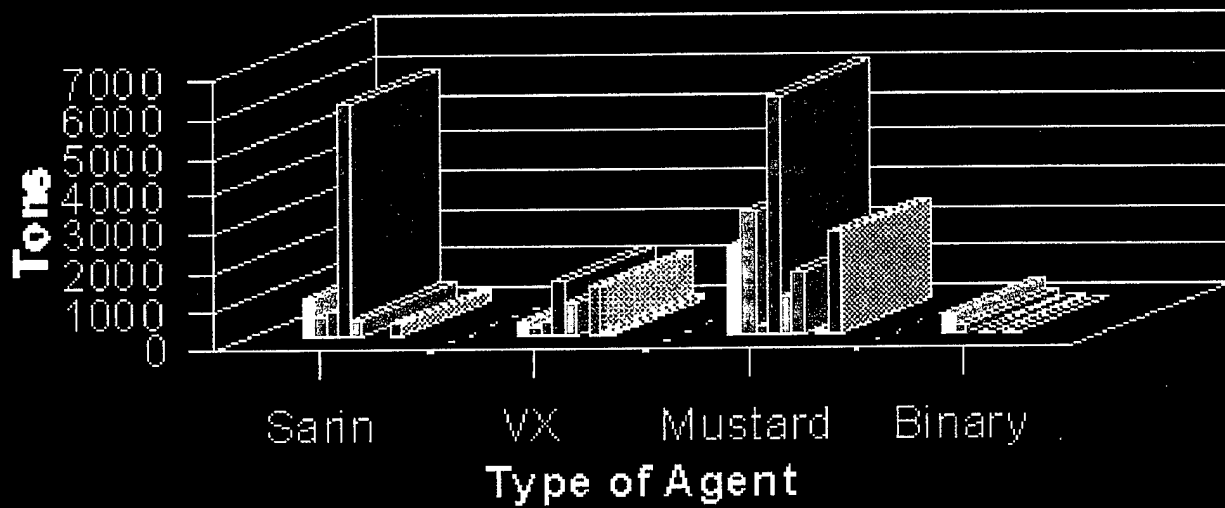










Links to other Internet sources

(the hottest links on the Web for anyone interested in CW matters)

<http://www.opcw.nl/>



Chemical Weapons Stored in the US



	Umatilla, OR		Pine Bluff, AR
	Johnston Atoll		Tooele, UT
	Anniston, AL		Aberdeen, MD
	Newport, IN		Lexington, KY
	Pueblo, CO		

<http://www.stimson.org/pub/stimson/cwc/vstypes.gif>









Table 1

 Toxicity of Chemical and Biological Agents <i>Estimated Lethal Dose</i> <i>in mg/person*</i> 	
Chemical Agents	1000 mg
	100 mg
	10 mg
	1 mg
	.1 mg
Biological Agents	.01 mg
	.001 mg
	.0001 mg
	.00001 mg
	.000001 mg
	.0000001 mg
	.00000001 mg
Toxin Agents	

** One paperclip weighs approximately 500 mg.*

Source: Office of Technology Assessment, *Technologies Underlying Weapons of Mass Destruction* (Washington, D.C.: U.S. Government Printing Office, December 1993), p. 77.

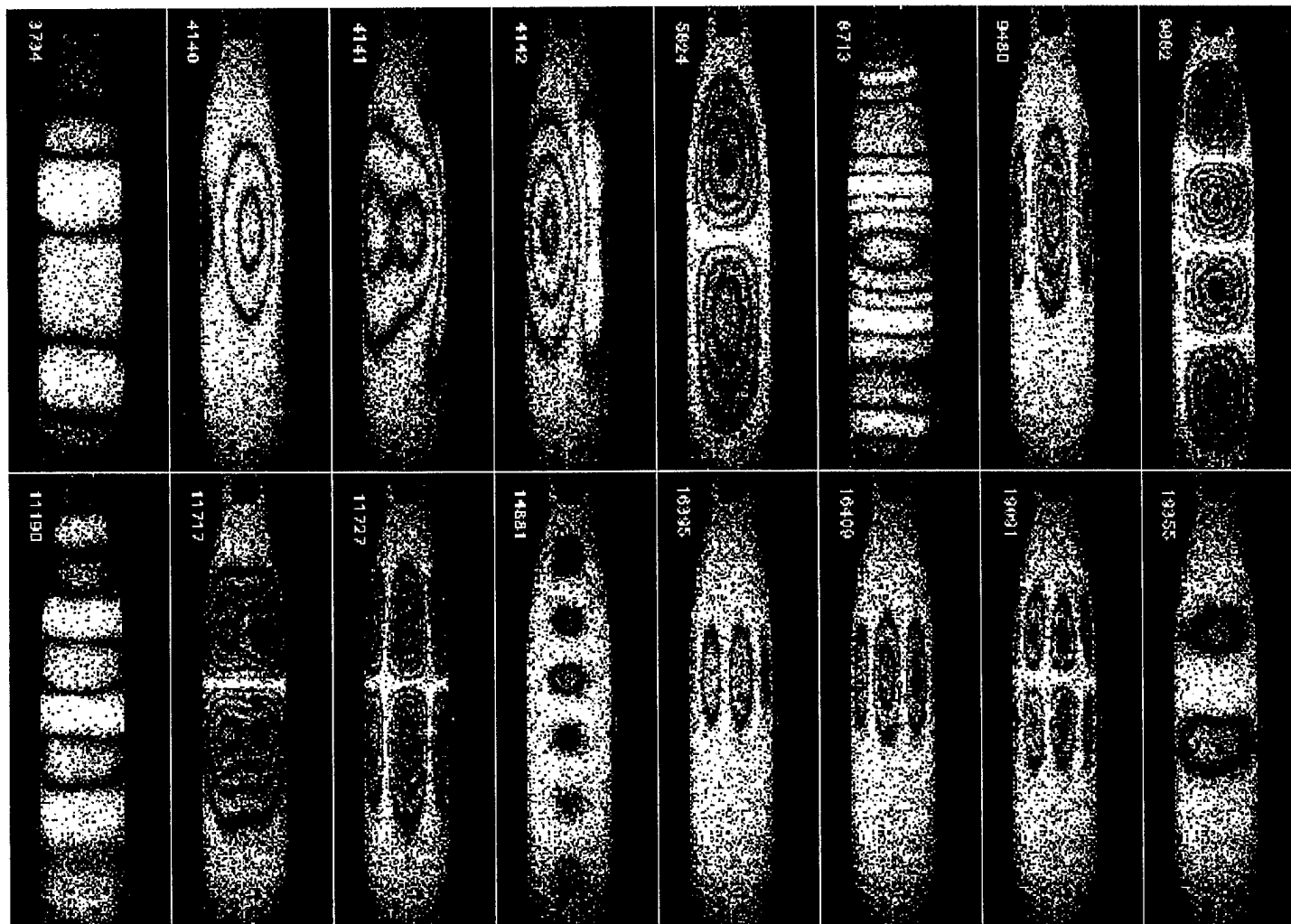
ARS Papers

-  (Paper: 124K),  (Presentation: 1.5M) R. Roberts, P. Lewis, and O. Vela. **A pattern recognition algorithm for the blind discrimination of liquid and solid filled munitions.** (LAUR-95-3789) To appear in *Proc. 29th Asilomar Conf. on Signals, Systems, and Computers*, IEEE, Pacific Grove, CA, Nov. 1995. ([Abstract](#))
-  (Paper: 30K) O. Vela, P. Lewis, R. Roberts, J. Chen, and D. Sinha. **Acoustic classification of chemical weapon munitions.** (LAUR-95-1073) In *Proc. ONSITE 3rd Int. Conf. On-Site Analysis*, Houston, TX, Jan. 1995. ([Abstract](#))
-  (Paper: 154K),  (Presentation: 242K) R. Roberts, P. Lewis, J. Chen, and O. Vela. **Techniques for classifying acoustic resonant spectra.** (LAUR-94-3977) In *Proc. 28th Asilomar Conf. on Signals, Systems, and Computers*, pp 1195-1199, IEEE, Pacific Grove, CA, Nov. 1994. ([Abstract](#))
-  (Paper: 169K) R. Roberts, J. Chen, O. Vela, and P. Lewis. **Munitions classification using an acoustic resonance spectroscopic technique.** (LAUR-93-4108) In *Proc. 27th Asilomar Conf. on Signals, Systems, and Computers*, pp 991-995, IEEE, Pacific Grove, CA, Nov. 1993. ([Abstract](#))
-  (Presentation: 591K) P. Lewis. **Acoustic Resonance Spectroscopy (ARS) for Chemical Weapon Munition Identification.** (LAUR-93-2115) Briefing presented in Moscow, Russia, November 1993.
-  (Paper: 531K) D. Sinha. **Acoustic resonance spectroscopy.** *IEEE Potentials*, 11(2):10-13, April 1992.

This Page: <http://www.esa.lanl.gov/ars/papers/ars-papers.html> - Last Update: 8 Nov 95
 Paul Lewis - Los Alamos National Laboratory - Group ESA-MT
 Email: roberts@lanl.gov -

ARS HOLOGRAPHY

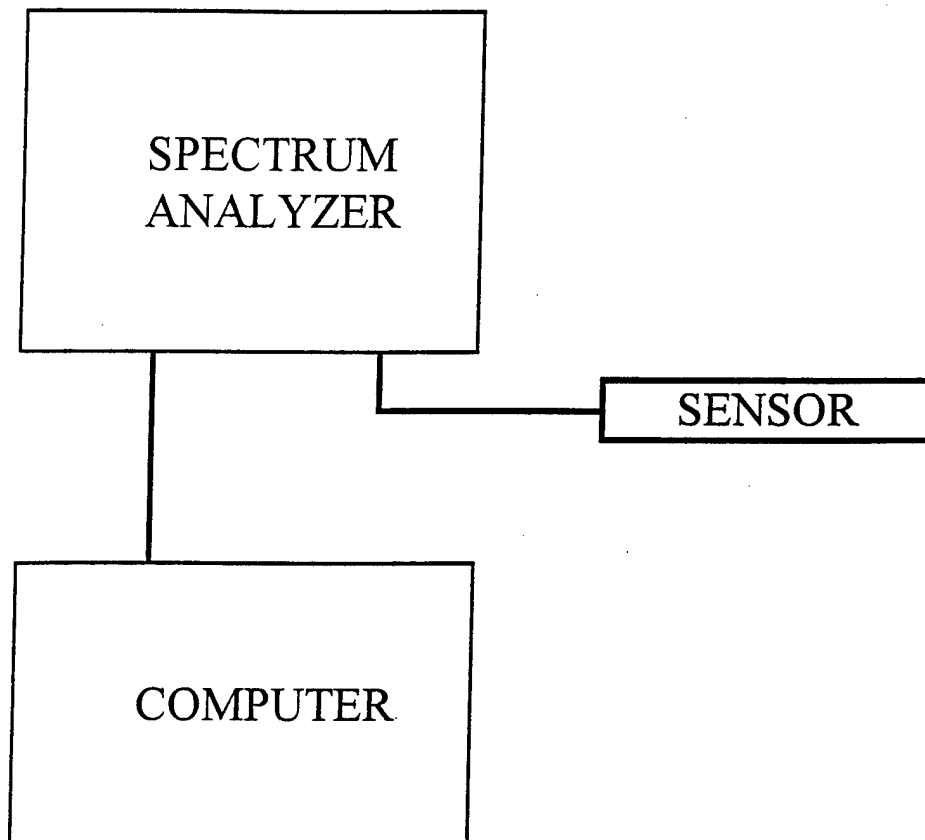
Video holograms showing some of the vibrational resonance modes of a 105mm munition. Each "contour" corresponds to 1/2 micron.



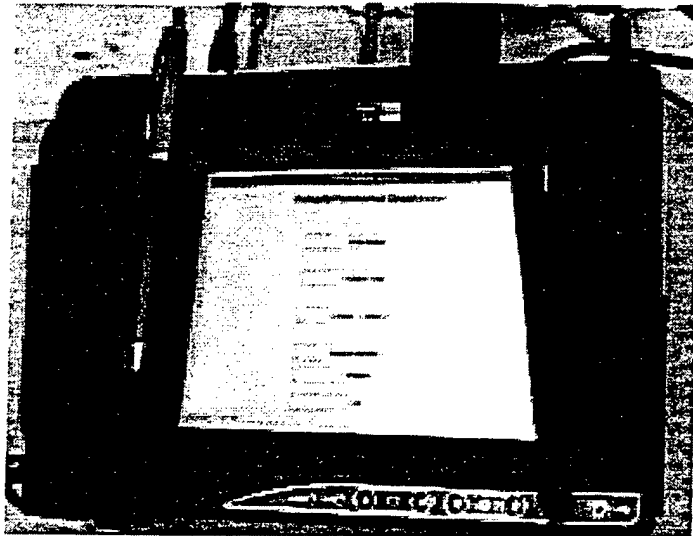
This Page: <http://www.esa.lanl.gov/ars/ars-home.html> - Last Update: 18 Oct 95
Randy Roberts - Los Alamos National Laboratory - Group ESA-MT
Email: roberts@lanl.gov

SIMPLE BLOCK DIAGRAM

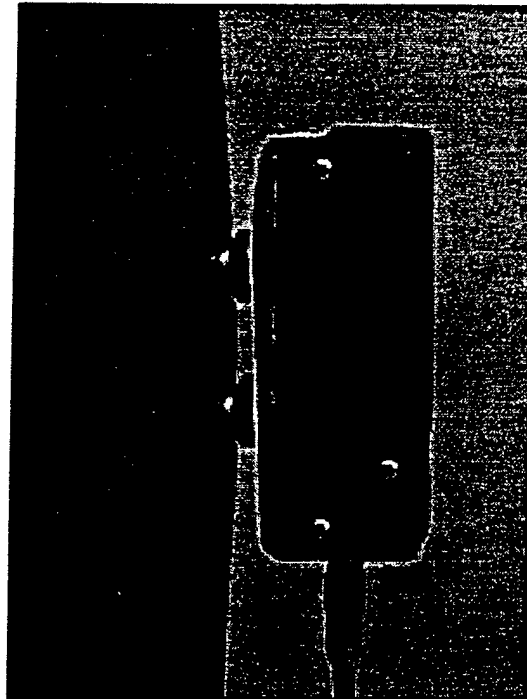
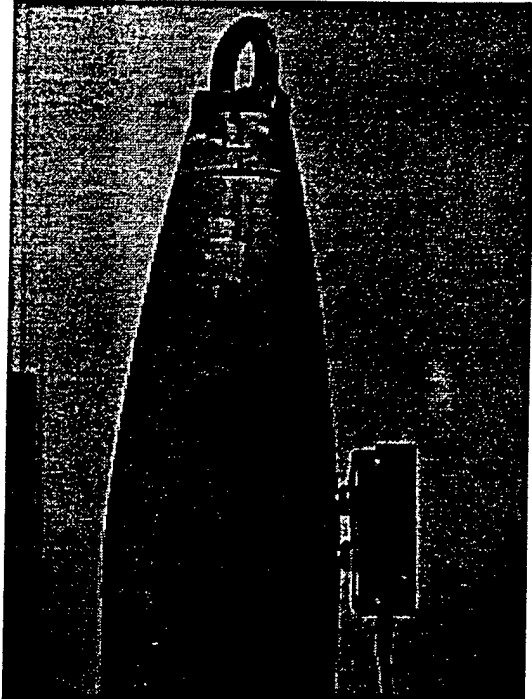
1. Digital Signal Analyzer (DSA).
2. Acoustic Resonance Spectroscopy Software (ARS).
3. Piezoelectric source and receiver attached to shell by magnets.



**ARS IS PORTABLE
(PC BASED PEN COMPUTER, WINDOW 3.1)**



SENSOR ATTACHMENT TO MUNITION



1. Set up the computer for your particular site and expected munitions.

Acoustic Resonance Spectroscopy

Site Setup

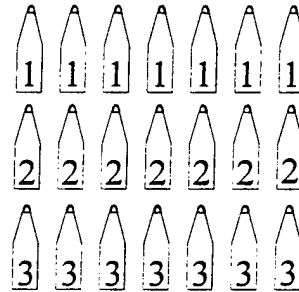
Collect Data

Create Template

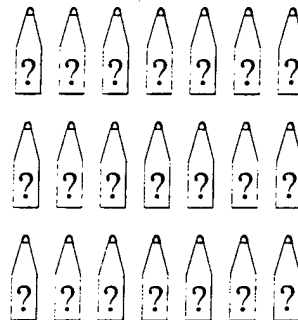
View & Analyze

Exit

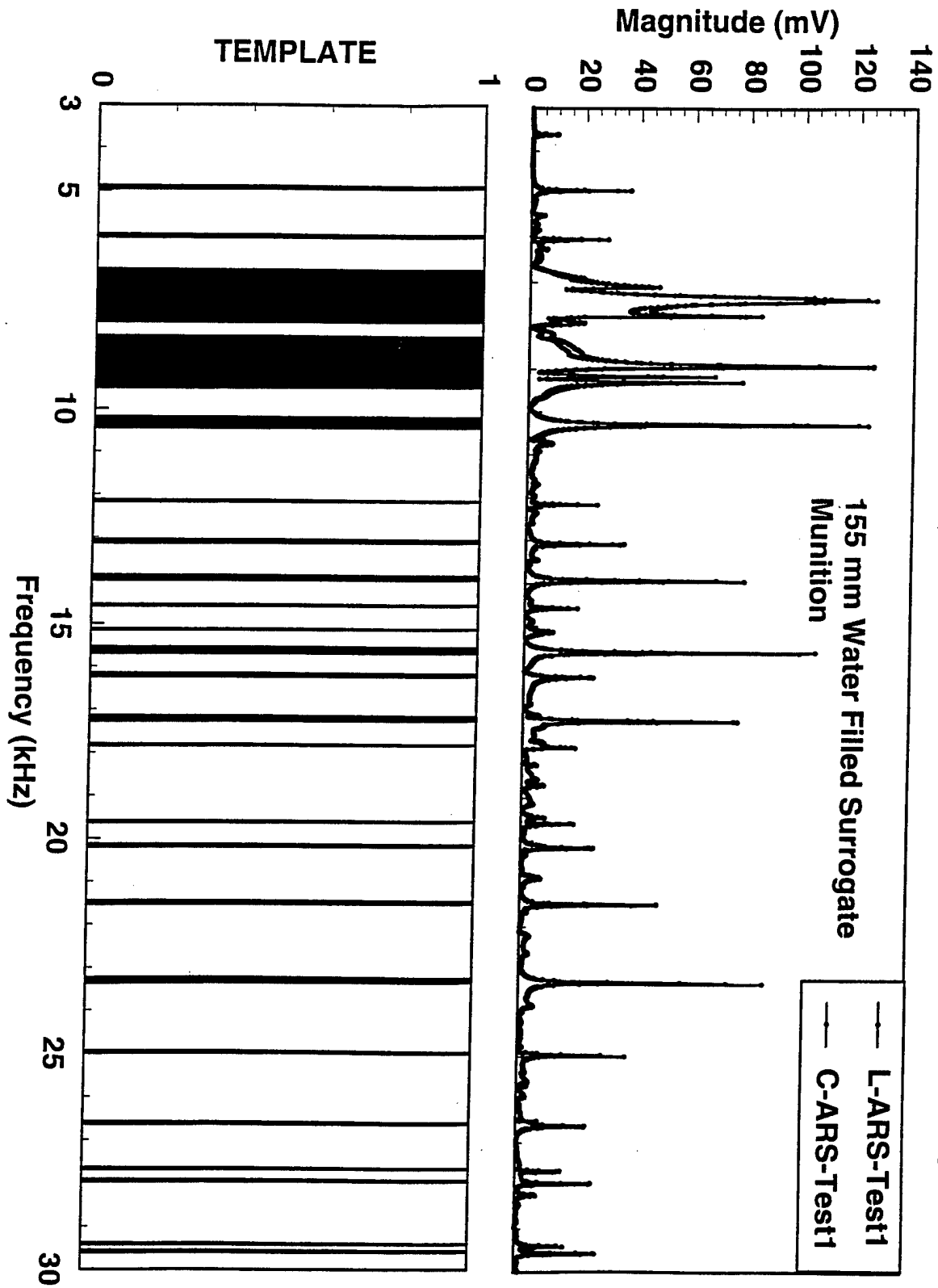
2. Make templates using munitions with known chemical fills. ARS uses these templates (one for each fill agent) to estimate the chemical fill in other munitions of the same size.



3. Use ARS to estimate the type of fill contents in other munitions.



EXAMPLE FREQUENCY SPECTRA AND QUALITATIVE TEMPLATE IDEA

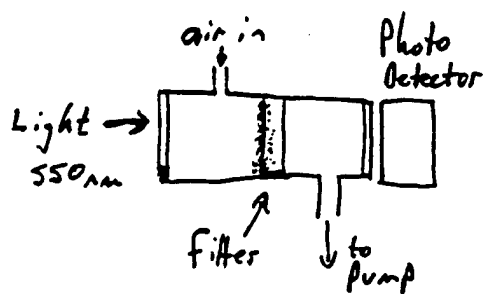


- Light Absorption - Visibility
- Health

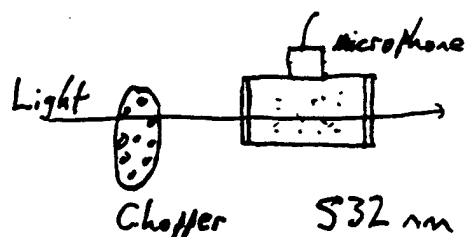
Table 3. Emission factors for different sources of elemental (black) carbon (from Ogren and Charlson, 1984)

Source	Elemental carbon (g)	
	Fuel (kg)	
Vehicles, diesel engine	2	
Fireplace, softwood	1.3	
Jet engine	1	
Fireplace, hardwood	0.39	
Vehicles, gasoline engine	0.02	
Solid fossil fuel	0.001	Lignite, Briquets
Natural gas	0.0003	

Reproduced by permission of Munskaard International.



Aethalometer



532 nm
685 nm

Photoacoustic

Hornth, 93

**PRELIMINARY EVALUATION OF THE DRI PHOTOACOUSTIC
SPECTROMETER**

**Comparison with aethalometer data from the Brighton site during NFRAQS
Dec 96 thru Jan 97**

by

**W. Patrick Arnott, Hans Moosmüller, C. Fred Rogers
Desert Research Institute**

**Assistance in the field by
John Walker, Pueblo CO
Mitch Walker, ARS, Fort Collins CO**

**532 nm laser provided by
Professor Jin, Professor Bruch
Physics Department, University of Nevada Reno**

**Photoacoustic spectrometer development supported by
Environmental Protection Agency Office of Exploratory Research**

**Field operation supported by
Desert Research Institute, IPA grant**

OUTLINE

- 1. The North Front Range Air Quality Study.**
- 2. The photoacoustic spectrometer.**
- 3. Comparison of photoacoustic spectrometer and aethalometer results..**

The North Front Range Air Quality Study.

The Northern Front Range Air Quality Study (NFRAQS) is a major effort

- to determine the sources of existing air pollution in the Denver urban region, attributing to each source or source category an estimate of its emissions.
- to collect data necessary to support informed decisions leading to attainment of state visibility goals and federal air quality standards.

DRI is the main contractor for NFRAQ

OUR FIELD SITE LOCATION:

BRIGHTON COLORADO

(DEC 96, JAN-FEB 97)

X
BOULDER, CO

X BRIGHTON, CO

X
DENVER, CO

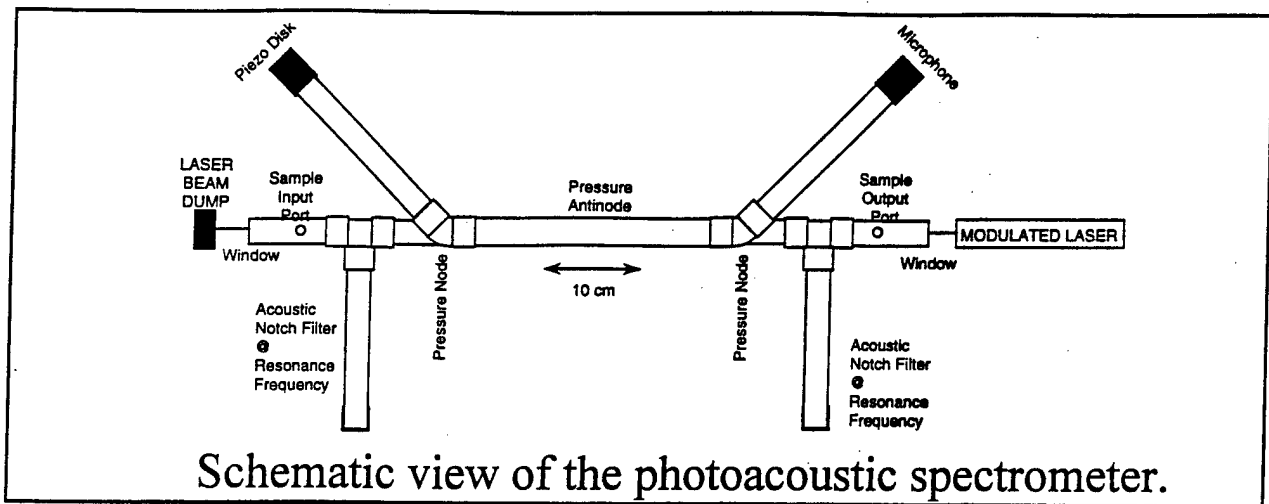
— **~ 20**
MILES —



Looking
Southwest
from
the
Brighton
Site



Looking
West..



Light Absorption in Dimensions of Inverse Distance = B_{abs}

$$B_{abs} = \frac{P_m}{P_L} \frac{A_{res}}{\gamma - 1} \frac{\pi^2 f_0}{Q},$$

f_0 = Resonance Frequency.

Q = Resonator Quality Factor.

P_m = Peak Acoustic Pressure at f_0 .

γ = Ratio of Isobaric and Isochoric Specific Heats For Air.

P_L = Peak Laser Beam Power at f_0 .

Q = resonator quality factor.

A_{res} = Resonator Cross Sectional Area.

TYPICAL VALUES:

P_L = 50 mW to 105 mW (depending on the laser used),

$A_{res} = 5.07 \text{ cm}^2$,

$f_0 = 500 \text{ Hz}$,

$Q = 80$,

Bandwidth of spectrometer $\approx f_0/Q = 6.25 \text{ Hz}$,

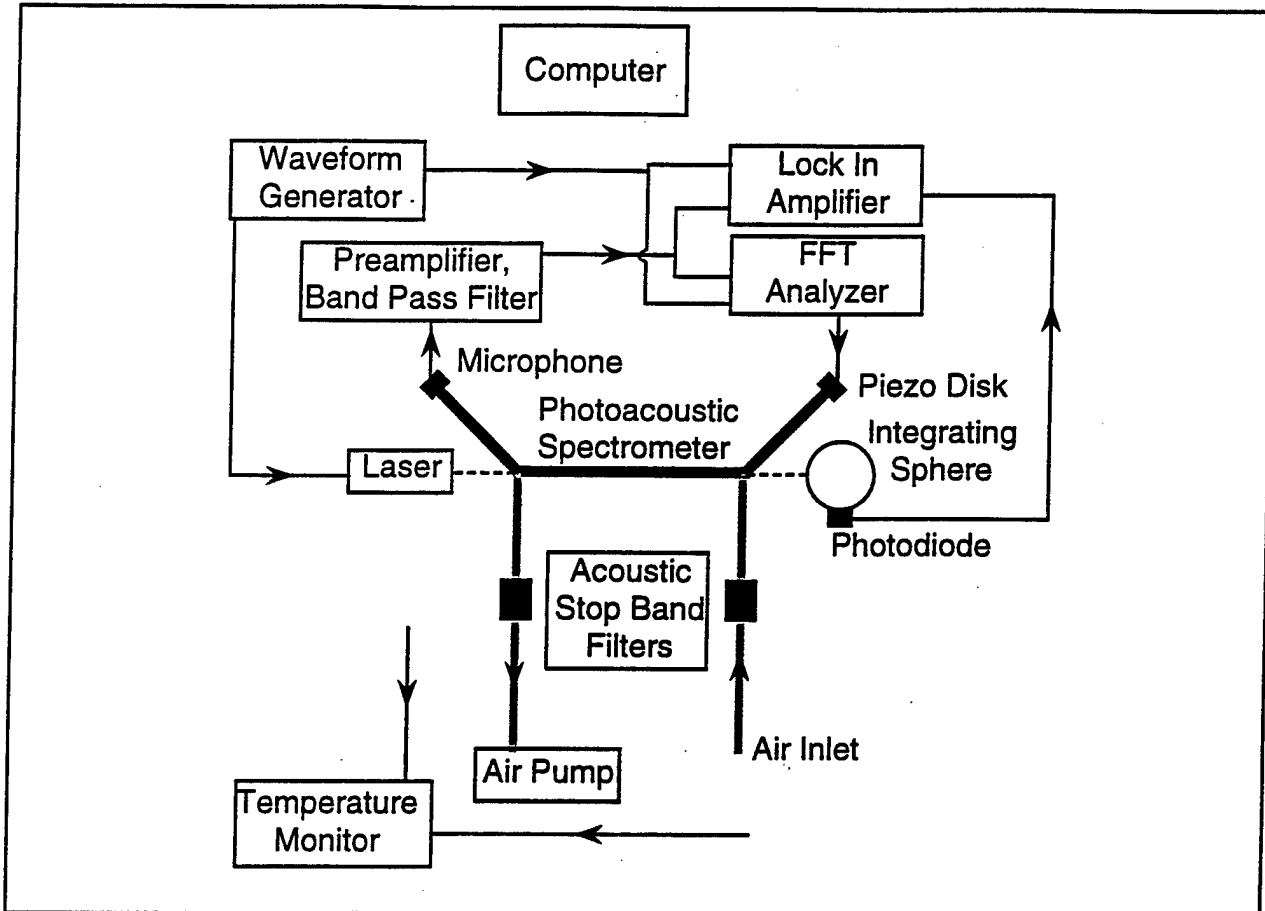
$P_m = 6 \text{ } \mu\text{Pa}$ ($P_m = -10.5 \text{ dB Rel. } 20 \text{ } \mu\text{Pa}$),

$$B_{abs} = 7.5 \text{ Mm}^{-1}.$$

Broadband noise background equivalent to $B_{abs} = 0.5 \text{ Mm}^{-1}$

ENBW of Phase Sensitive Detection $\approx 7.5 \text{ mHz}$.

Block Diagram of the Photoacoustic Spectrometer and Detection Electronics

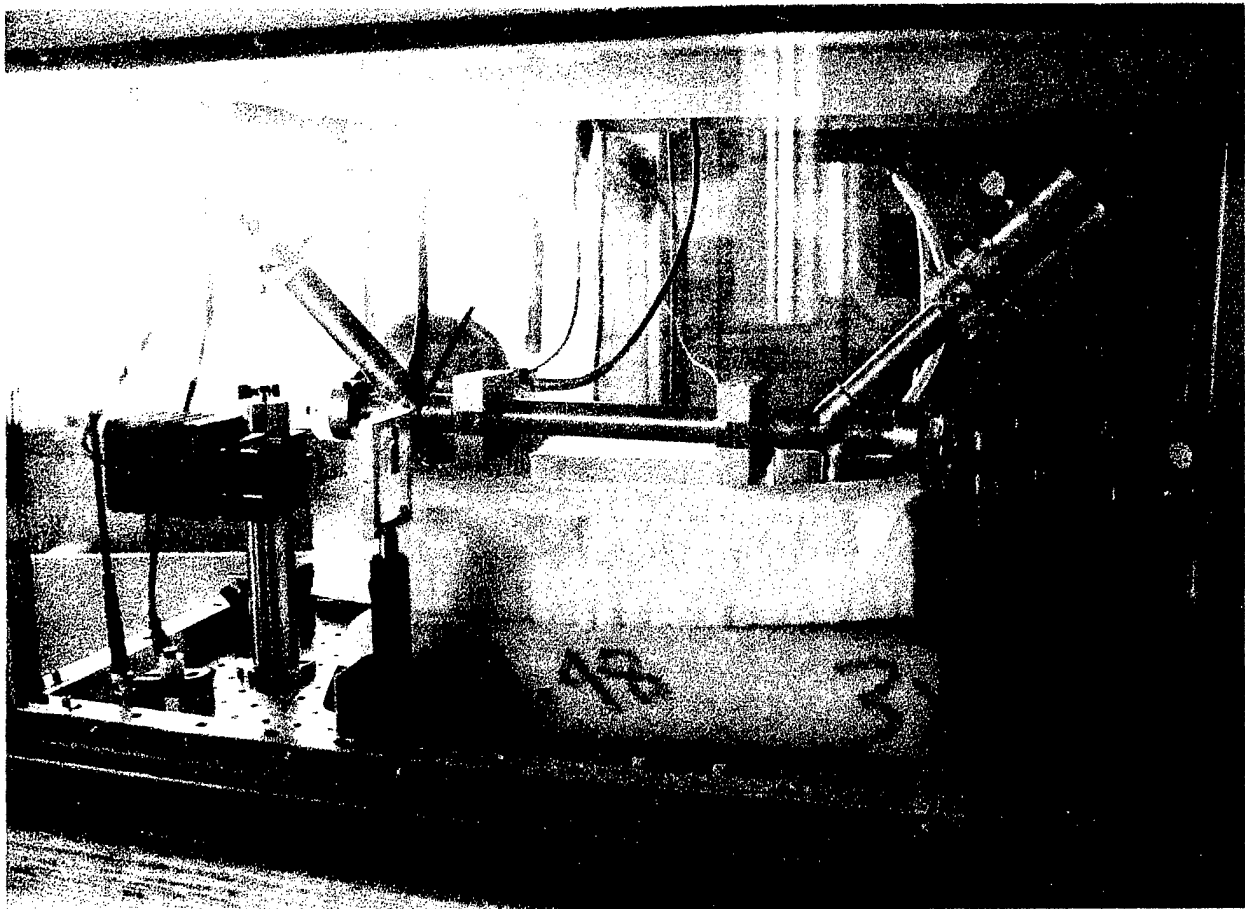


Lasers used were both very compact and efficient:

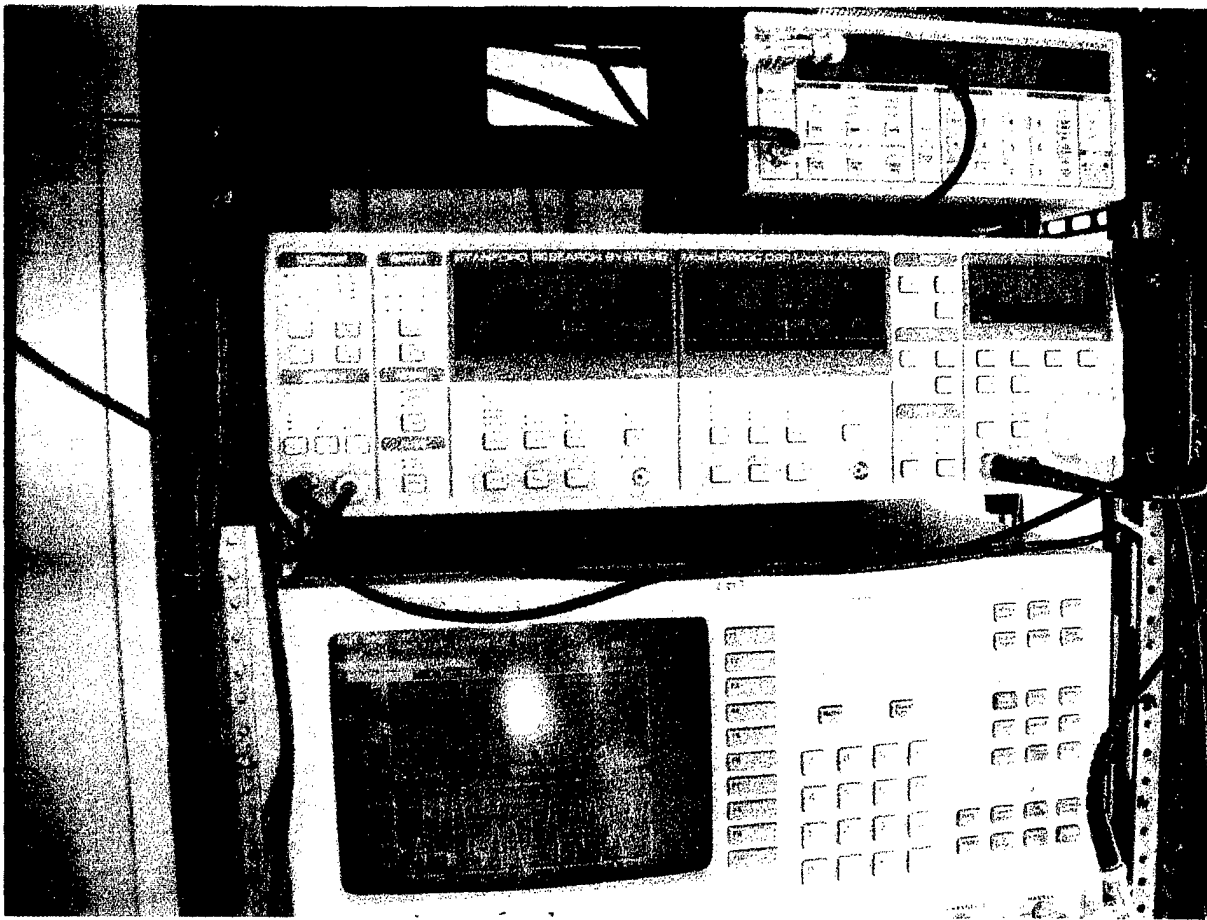
- 532 nm frequency doubled NdYAG laser diode pumped laser, ≈ 60 mW modulated power.
- 685 nm laser diode, ≈ 102 mW modulated power.

532 nm laser was only available for 2 days.

The 685 nm laser diode was confined to pass cleanly through the spectrometer only with the use of an initial collimating objective very near the diode followed by a cylindrical lens to reduce astigmatism in the beam, and finally followed by a converging lens to reduce the beam width.



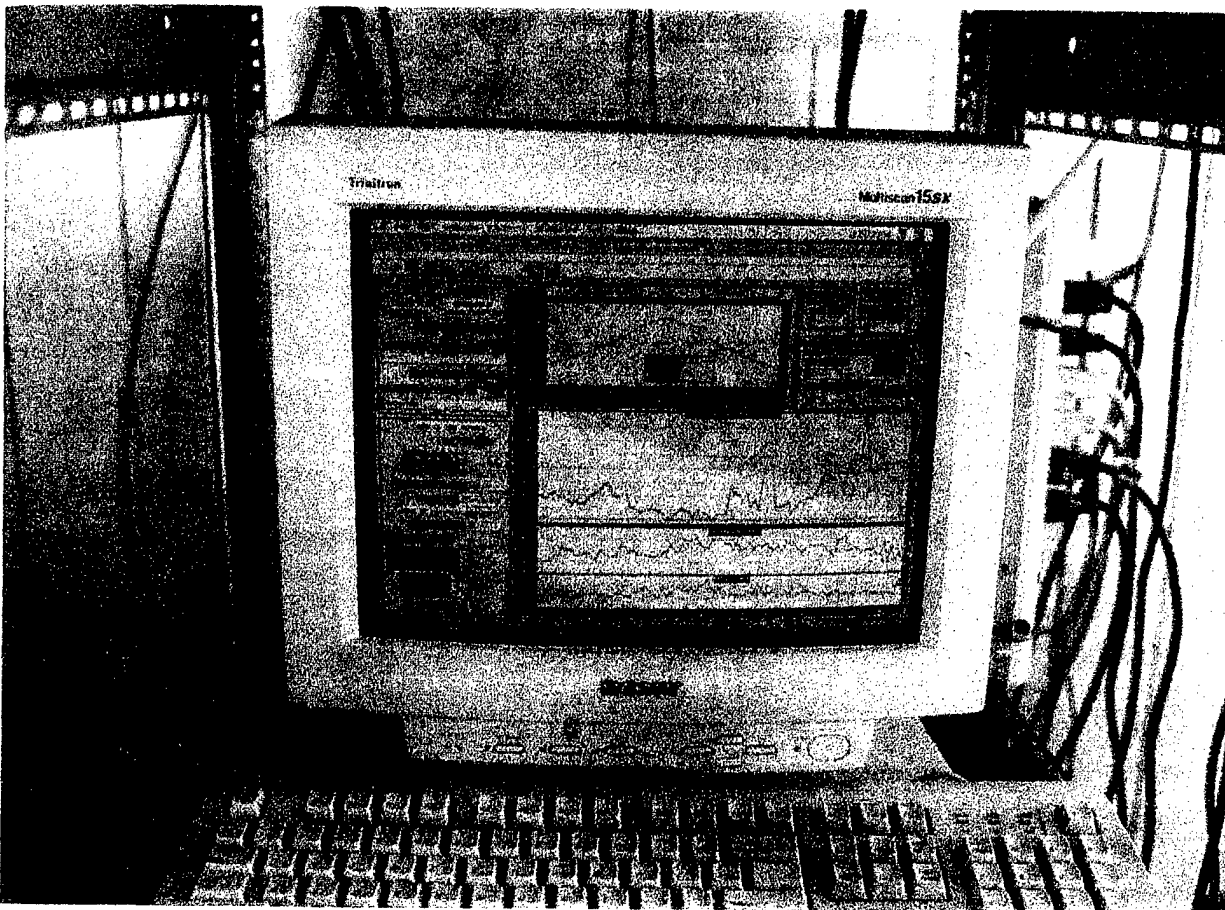
Photoacoustic spectrometer at
the Brighton CO Site during
NFRAQS (96 Dec, 97 Jan-Feb).



Function
Generator

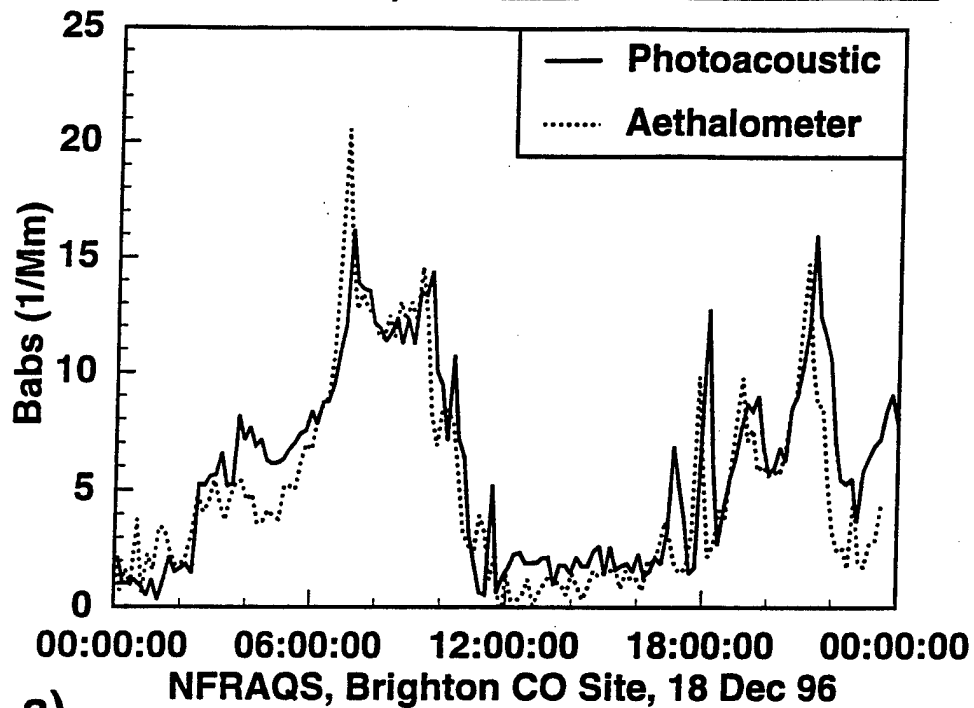
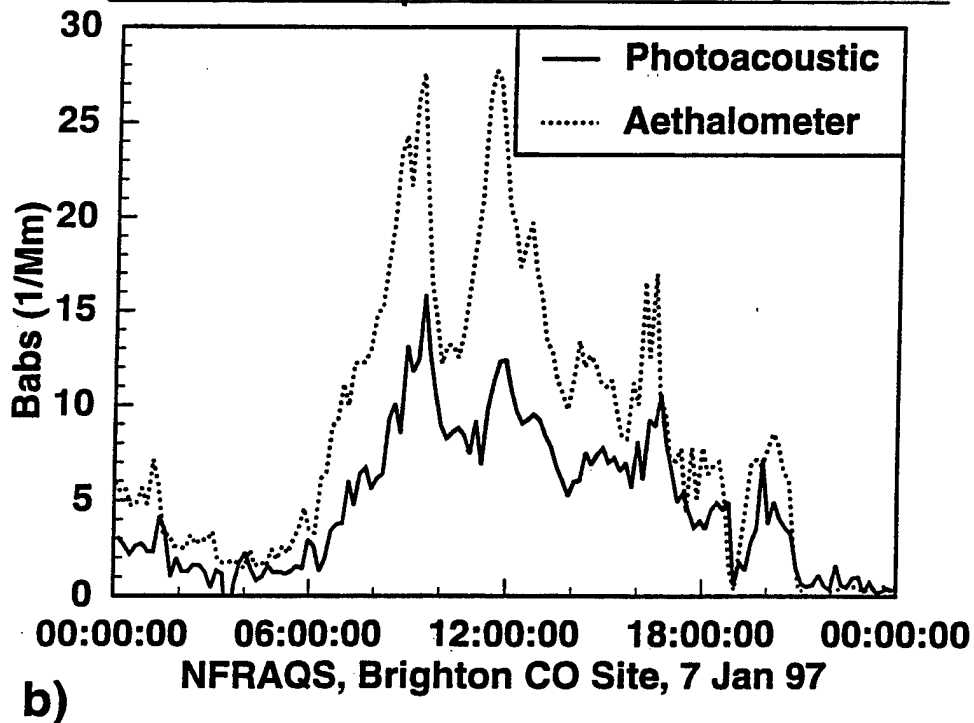
Lock-In
Amplifier

FFT
Analyzer



Meas.
automated
w/
LabView.

← Bobs

Photoacoustic Spectrometer with 532 nm Laser**Photoacoustic Spectrometer with 685 nm Laser**

Typical comparison of aethalometer and photoacoustic spectrometer determinations of light absorption by aerosols during NFRAQS. In a), the 532 nm laser was used for the photoacoustic spectrometer, though the 685 nm laser was used in b).

Crude Theoretical Investigation.

Light absorbing aerosols are not likely simple spherical particles.

Rayleigh Scattering Limit of Mie Theory for Spheres:

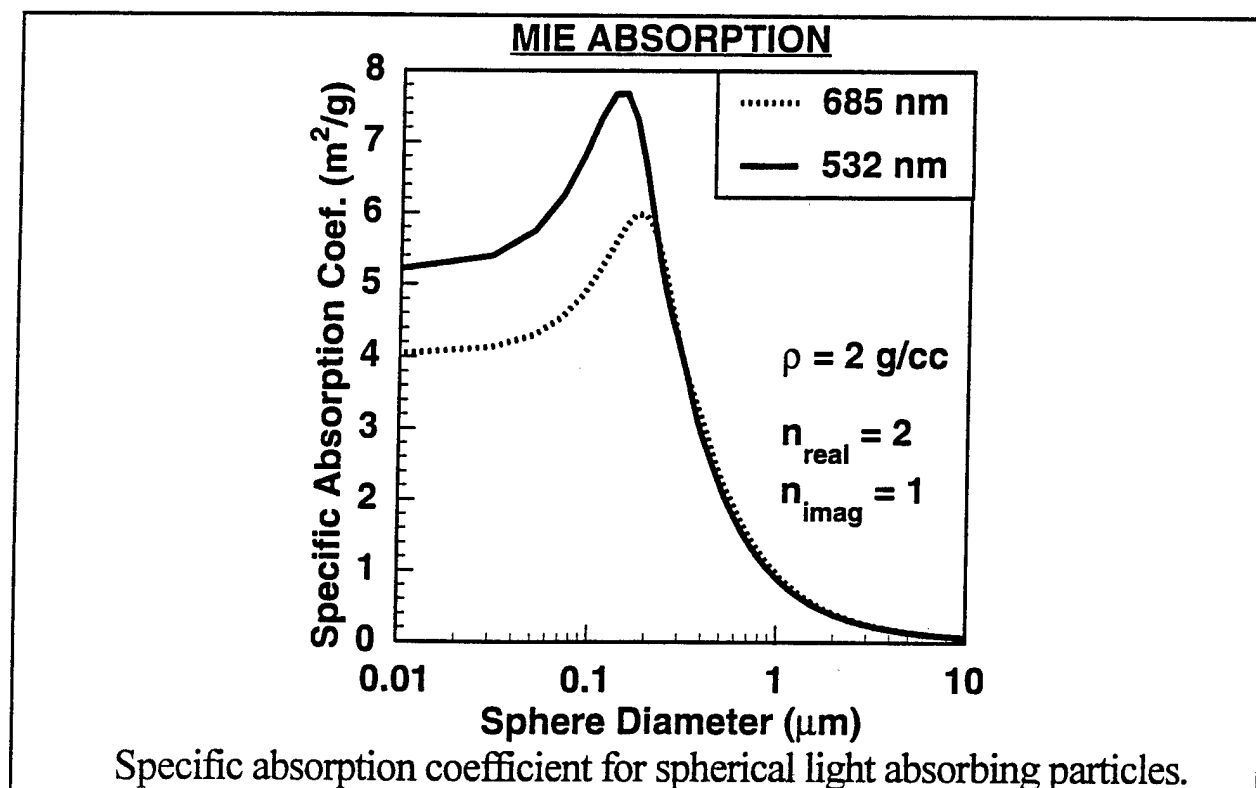
Specific Absorption Coefficient k_a (m^2/g):

$$k_a = \frac{6\pi}{\rho_p \lambda} \frac{6n_r n_i}{(n_r^2 - n_i^2 + 2)^2 + (2n_r n_i)^2},$$

where:

ρ_p is the particle density, λ is the wavelength, and n_r and n_i are the wavelength dependent real and imaginary parts of the particle refractive index.

- Small particle limit, k_a is independent of particle diameter, and is dependent on wavelength, both explicitly and through the complex refractive index.



VARIOUS EFFORTS WITH 'CYLINDRICAL' RESONATORS

DRI

Plane wave mode, $f_0 = 500$ Hz, $Q = 80$.

(Laser power, integration time limited)

532 nm and 685 nm Semiconductor, Solid State Lasers 50 mW to 100 mW

Detection Limit $B_{abs} = 0.4 \text{ Mm}^{-1}$

OTHERS

ADAMS:

Best result with azimuthal mode, $f_0 = 3970$ Hz, $Q = 220$.

(Window absorption limited)

514.5 nm Argon Ion laser 1 W (horrible efficiency).

Detection Limit $B_{abs} = 4.7 \text{ Mm}^{-1}$

EUROPEAN EFFORT (Petzold and Niessner, 1996)

Azimuthal mode, $f_0 = 6670$ Hz, $Q = 300$.

(Somewhat window absorption limited, flow noise problematic, higher Q resonator made for lower integration time)

802 nm laser diode, 450 mW

Detection Limit $B_{abs} = 1.5 \text{ Mm}^{-1}$

References.

Adams, K. M., L. I. Davis, Jr., S. M. Japar, and W. R. Pierson (1989).

"Real-Time, *In Situ* Measurement of Atmospheric Optical Absorption in the Visible via Photoacoustic Spectroscopy - II. Validation for Atmospheric Elemental Carbon Aerosol." *Atmos. Environ.* **23**, 693-700.

Petzold, A. and R. Niessner (1996). "Photoacoustic Soot Sensor for *in-Situ* Black Carbon Monitoring." *Appl. Phys. B* **63**, 191-197.

Roessler, D. M. (1984). "Photoacoustic Insights on Diesel Exhaust Particles." *Appl. Opt.* **23**, 1148-1155.

Resonant Photoacoustic Spectroscopy of Optical Materials

J. D. Maynard, Chang Yu, and Wei-li Lin
The Pennsylvania State University

Technology Issue

Develop and characterize optical materials which are highly transparent

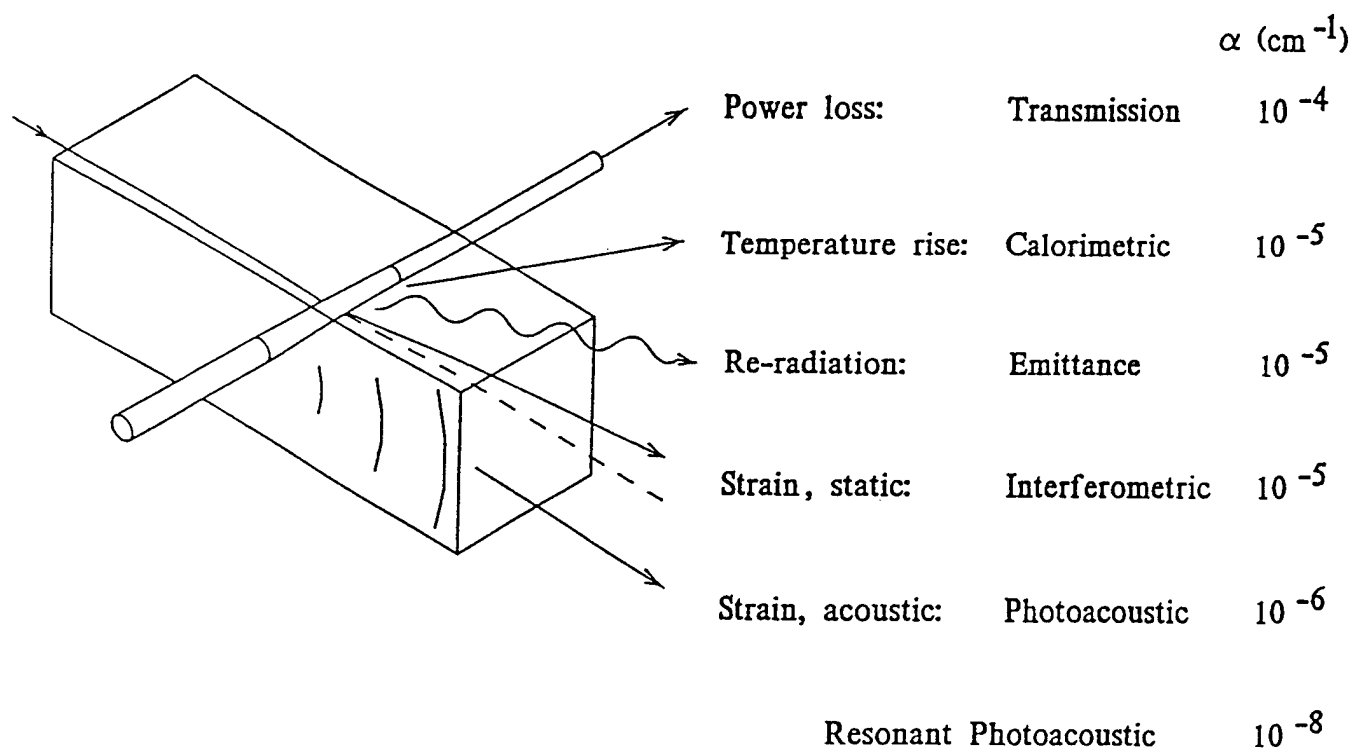
Applications

- Optical fibers in long distance communications systems
- Lenses and windows in high power laser systems
- Electro-optic, magneto-optic, and acousto-optic components

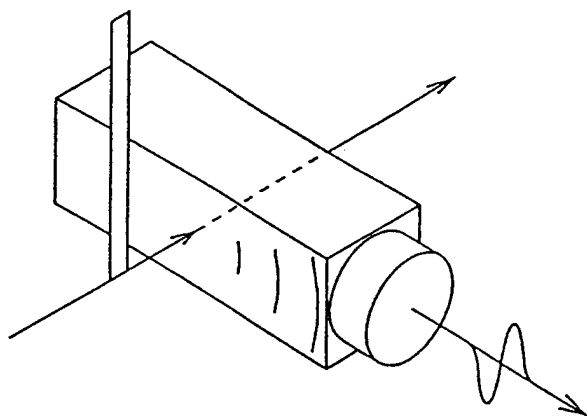
Objective

Develop a fast and sensitive method for measuring very small optical absorption coefficients

Measurement of Small Optical Absorption



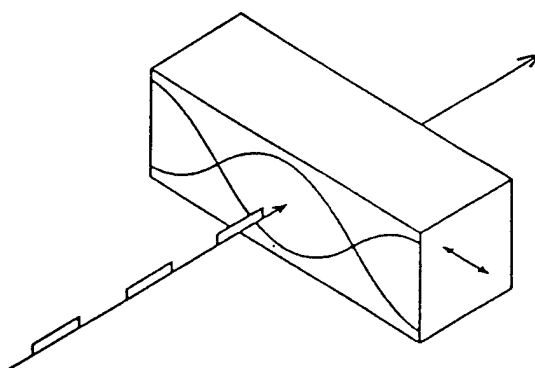
Pulse photoacoustic



Laser energy per pulse 10^{-1} J

Limited by: Noise in transducer
 Light scattered to attached transducer
 Rep rate $< 10^3$ Hz

Resonant photoacoustic

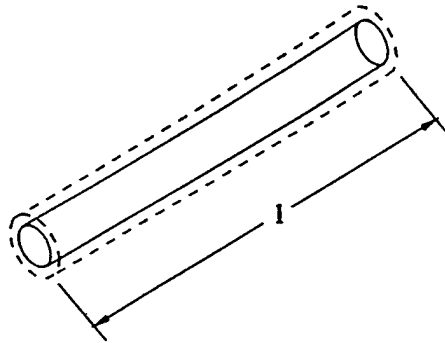


CW laser, modulated @ 10^5 Hz 10^{-4} J

Modulate at acoustic resonance of sample

Gain = Quality factor (Q) = $10^4 - 10^6$

Non-contact transducers: no scattered light, higher Q

Theory**Laser Beam as an Acoustic Line Source**

Energy absorbed

$$E = W\tau\alpha l$$

Temperature increase

$$\Delta T = \frac{W\tau\alpha l}{C_P\rho V}$$

Thermal expansion

$$\Delta V = V\beta_P\Delta T$$

Geometry

$$\Delta V = \pi(R + \Delta R)^2 l - \pi R^2 l = 2\pi R\Delta R l$$

Peak-to-peak displacement

$$\Delta R = \frac{W\tau\alpha\beta_P}{2\pi R\rho C_P}$$

Particle velocity amplitude

$$A = \omega\Delta R/2 = \frac{W\beta_P\alpha}{2\pi R\rho C_P}$$

Pressure radiated by pulsating cylinder

$$P(r) = \left[\frac{i\rho c A}{H'_0(kR)} \right] H_0(kr)$$

Green's function for line source

$$G(r) = i\pi H_0(kr)$$

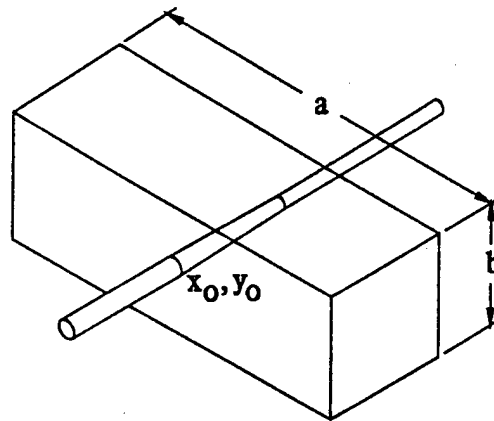
Equivalent source strength, small kR

$$S_P = \left[\frac{\rho c A}{\pi H'_0(kR)} \right] \simeq \frac{1}{2} kR \rho c A$$

Displacement source strength

$$\begin{aligned} S &= \frac{S_P}{\rho c \omega} \\ &= \frac{kR}{2\omega} A \\ &= \frac{kR}{2\omega} \frac{W \beta_P \alpha}{2\pi R \rho C_P} \\ &= \frac{kW \beta_P \alpha}{4\pi \omega \rho C_P} \end{aligned}$$

Green's function for a finite rectangle



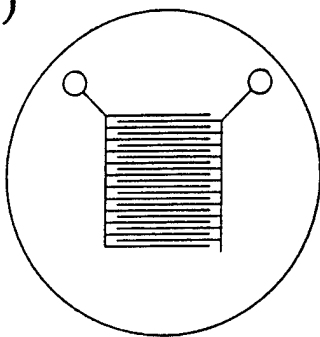
$$G(x, y, x_0, y_0) = \frac{16}{\pi ab} \sum_m \sum_n \frac{\cos\left(\frac{m\pi x}{a}\right) \cos\left(\frac{n\pi y}{b}\right) \cos\left(\frac{m\pi x_0}{a}\right) \cos\left(\frac{n\pi y_0}{b}\right)}{(m/a)^2 + (n/b)^2 - (k/\pi)^2 (1 + i/Q)}$$

Add source strength S , evaluate with $\cos = 1$, $ka = m\pi$, $n = 0$

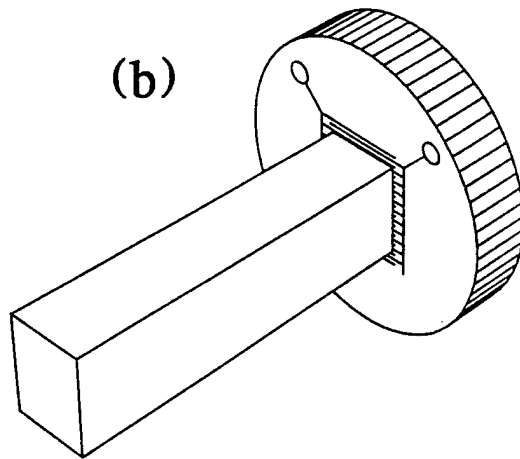
Displacement amplitude $\psi = \left(\frac{kW\beta_P\alpha}{4\pi\omega\rho C_P} \right) \frac{16}{\pi ab} \frac{Q}{(k/\pi)^2}$

Optical absorption coefficient $\alpha = \left(\frac{m^2\pi}{2} \right) \left(\frac{\rho c C_P}{\beta_P} \right) \left(\frac{1}{W} \right) \left(\frac{1}{Q} \right) \left(\frac{b}{a} \right) \psi$

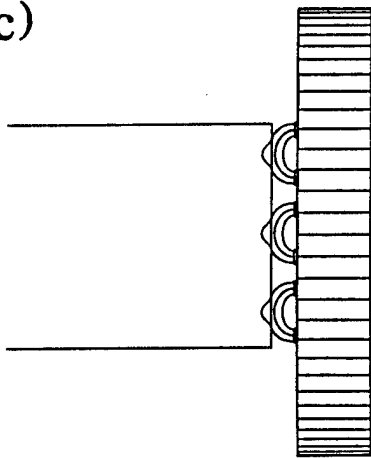
(a)



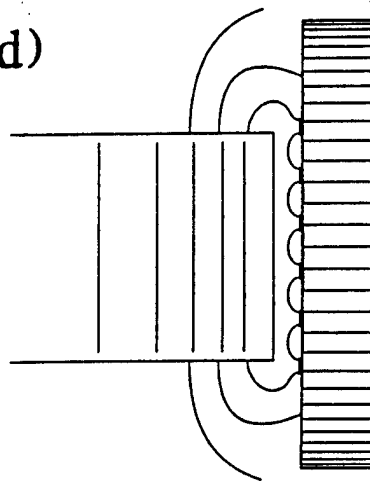
(b)

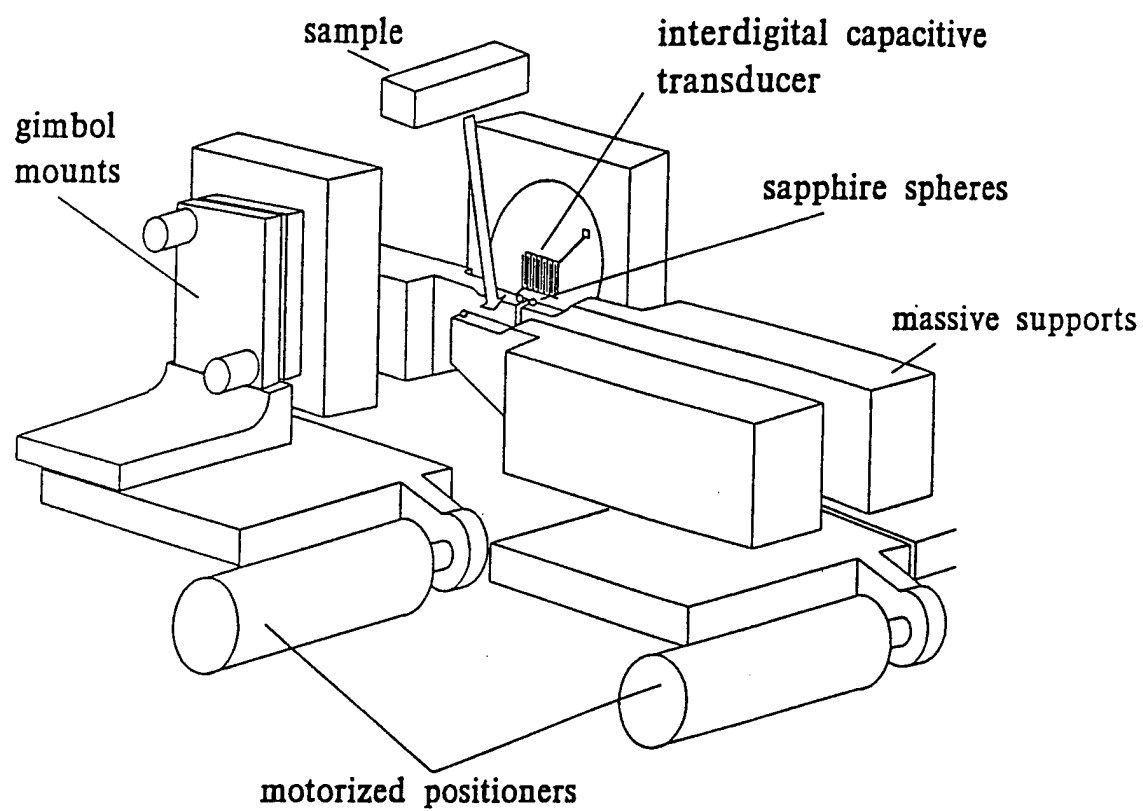


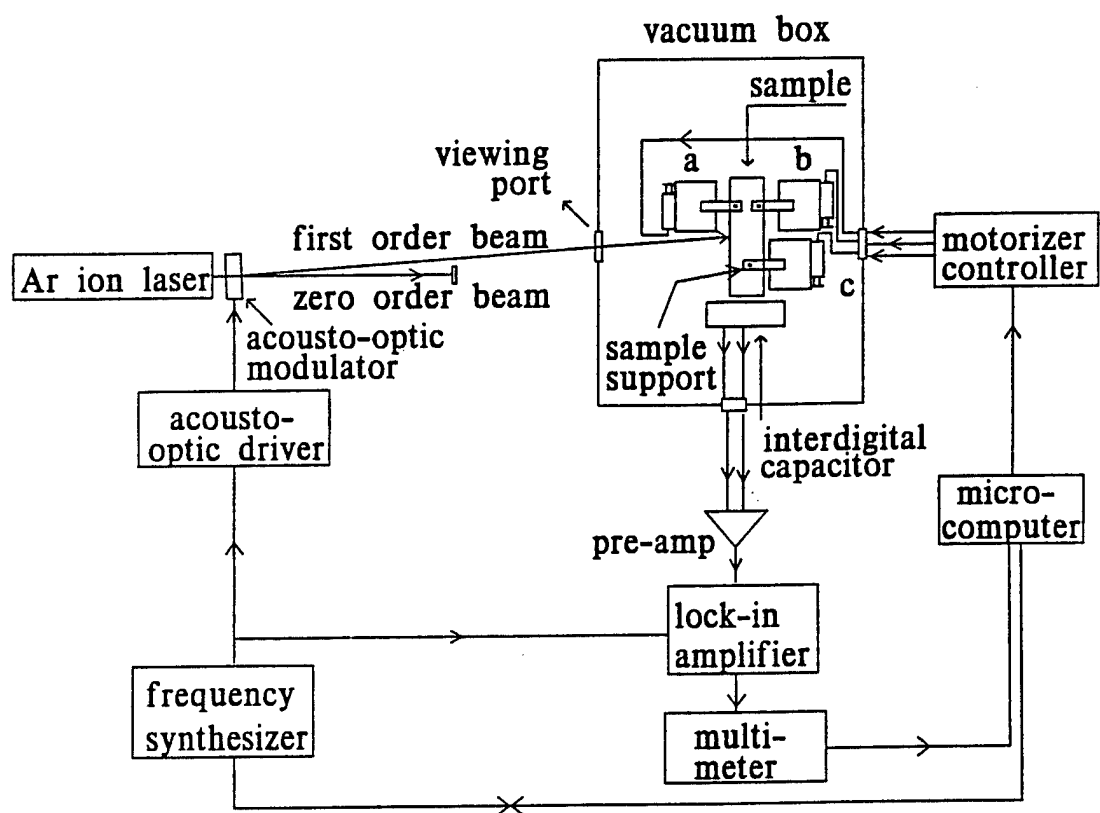
(c)

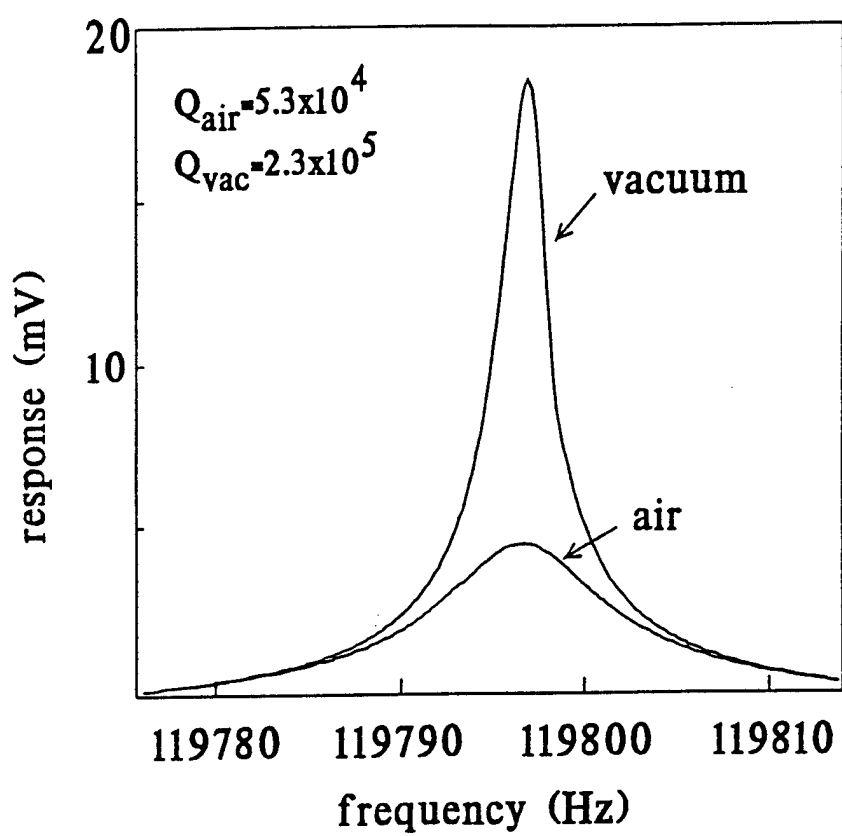


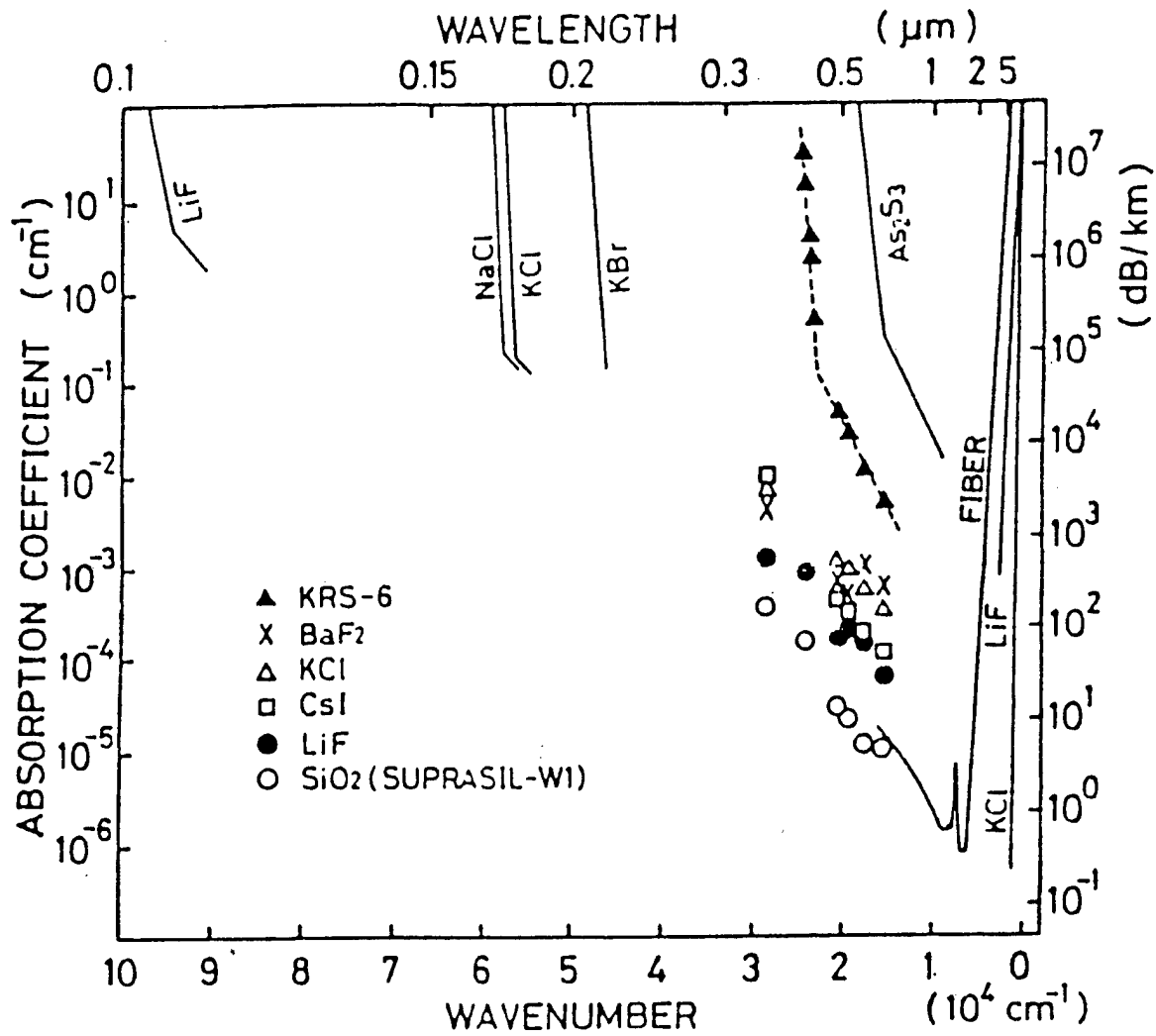
(d)

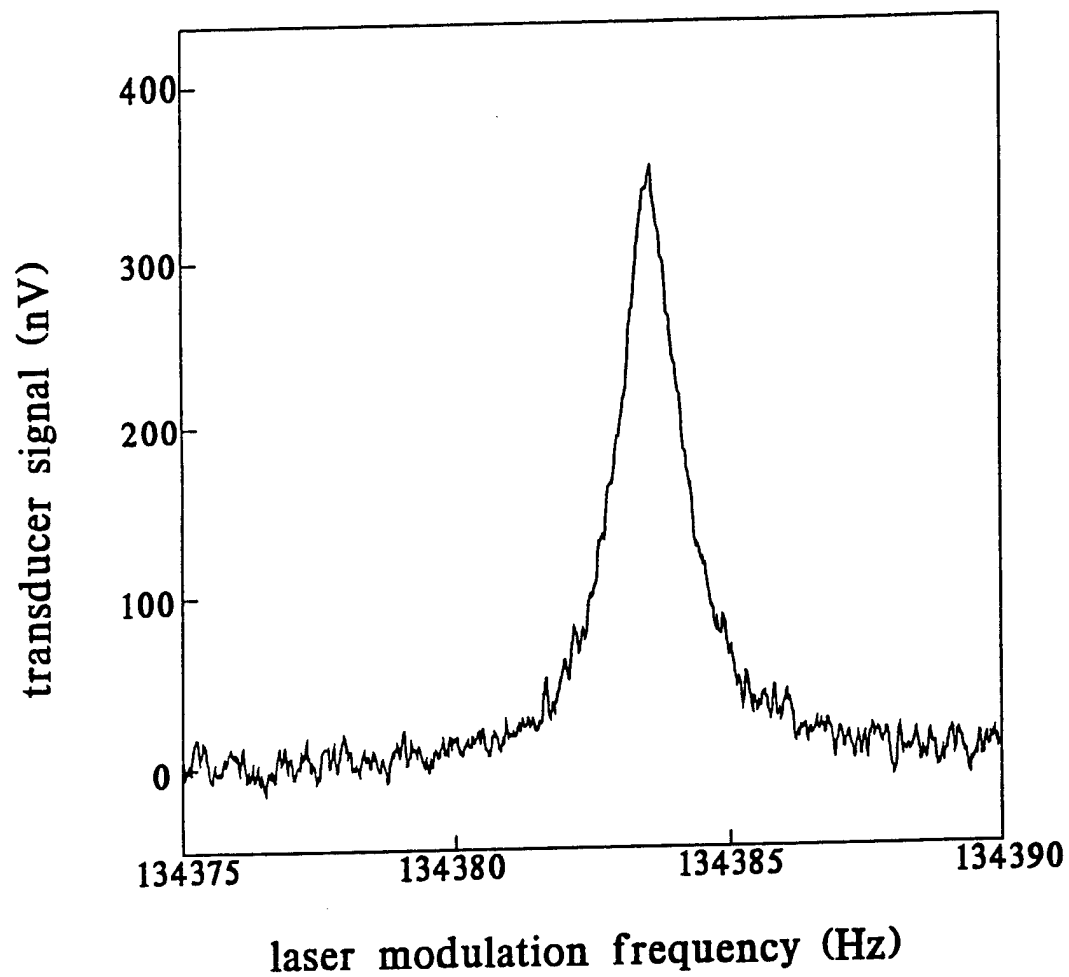












University of Massachusetts
Dartmouth

Resonant Bar Acoustic Spectroscopy:

Characterization of viscoelastic materials using the resonant modes of a free-free bar

David A. Brown¹ and Qiushuang Guo²

¹Assistant Professor Department of Electrical Engineering and
Center for Marine Science and Technology
and Adjunct Professor of Physics
University of Massachusetts Dartmouth
N.Dartmouth, Massachusetts

and Staff Research Engineer Code 213
Transducer Development
Naval Undersea Warfare Center, Newport, RI

²Qiushuang Guo is a Ph.D. graduate student in
Electrical Engineering and Physics and UMass Dartmouth and
former Assistant Professor of Physics at Tsinghua University, Beijing, PRC

Acknowledgements:

Portions of Research conducted while previously at the
Naval Postgraduate with research collaborators:

Prof. Steven L. Garrett (now at Penn State)
Prof. Don Danielson (NPS)

and graduate students:
Lt. John Miesel
Mr. David Bartlett
Mr. Beng Hock Tan

**University of Massachusetts
Dartmouth**

Outline Resonant Bar Acoustic Spectroscopy

0. Introduction and Motivation
1. Excitation and Detection of Modes in a Free-Free Bar
Resonance in bars
and determination of elastic moduli
2. Damping
3. Instrumentation
Transfer Function Techniques
Phase Locked Loop Techniques
4. Some More Data
(temperature and frequency dependence of elastic moduli)
5. Correction Factors
Warping Functions
Finite Bar length
Transducer Mass and Stiffness
Including Dissipation in the Wave Equations

Resonant acoustic determination of elastic moduli

Steven L. Garrett

Physics Department, Code 61 Gx, Naval Postgraduate School, Monterey, California 93943

(Received 11 December 1989; accepted for publication 23 February 1990)

A long rod of circular or elliptical cross section can be selectively excited in the torsional, longitudinal, and flexural resonant modes using a single pair of electrodynamic transducers consisting of coils glued to each end of the bar and placed in the field of a magnet. The elastic moduli of the material can be simply determined to high accuracy by measuring the resonance frequencies of these modes and the mass and physical dimensions of the rod. Since the longitudinal and flexural modes both yield values for the Young's modulus, the system has a built-in redundancy that makes the interpretation of the data more robust. The large signal amplitudes make automated measurement of the temperature dependence of the moduli simple through the use of a phase-locked loop to track the change in the resonance frequency with temperature.

PACS numbers: 43.40.Cw, 43.20.Ye, 62.20.Dc, 07.10 + i

INTRODUCTION

The accurate measurement of the elastic constants of materials and their dependence on temperature, static pressure, and other ambient parameters is important in many fields of science and engineering research, as well as in product design and quality control. This is particularly true for hydrophones, since most transduction schemes involve the measurement of the deformation of some solid material in response to a change in pressure. The elastic modulus relates these strains to the applied stresses, so its value and its temperature dependence are important design parameters. Interest in the measurement of these moduli in the acoustical transduction community, particularly for castable polymers, has increased recently due to the development of interferometric fiber-optic hydrophones,¹⁻² which measure the strain in the optical fiber induced by pressure changes in the fluid. Castable polymers are attractive for several hydrophone designs that use shell structures³⁻⁷ or encapsulation⁸⁻¹¹ for strain enhancement, since the optical fibers can be cast directly into those materials as well as for more conventional piezoelectric hydrophones.^{12,13}

Manufacturer's specifications for elastic constants of castable polymers are not particularly useful for the hydrophone designer since they are usually determined by static techniques, rarely contain more than one modulus (two are the minimum required to uniquely specify the elastic response of an isotropic material¹⁴), vary widely depending upon sample preparation (e.g., catalyst) and cure temperature, and never contain information about the temperature dependence of the moduli. It is also important in hydrophone design to measure the elastic moduli at the frequencies of intended operation, since it is well known that the static and dynamic moduli of plastics can differ substantially¹⁵ due to the existence of relaxation time effects that can make the modulus measured by conventional quasi-static stress-strain curves significantly lower than the dynamic modulus. Since it is the dynamic modulus that determines the acoustic sensitivity, and the static modulus that determines the deformation due to increased operating depth, it is important that both are known to the hydrophone designer.

A recent series of measurements on 31 elastomeric sam-

ples by Lagakos *et al.*^{16,17} illustrate how the assumption of a simple form for the frequency dependence of the Young's modulus can lead to unacceptable disagreement between the measured moduli and the predicted value. For the case of Uralite 3130, a polyurethane used in a prototype fiber-optic planar flexible hydrophone design,⁹ the variation between the model and measured modulus was in excess of 750%. One must question the validity of their temperature coefficient of the modulus measured at 1 MHz when extrapolated to operating frequencies of less than a kilohertz.

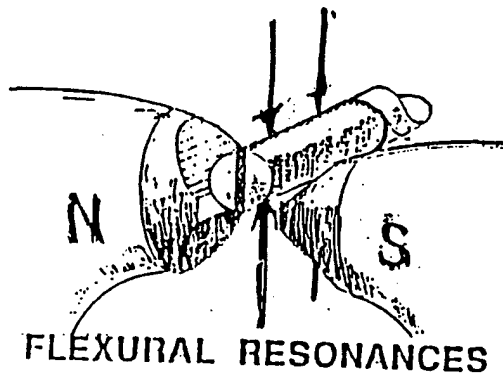
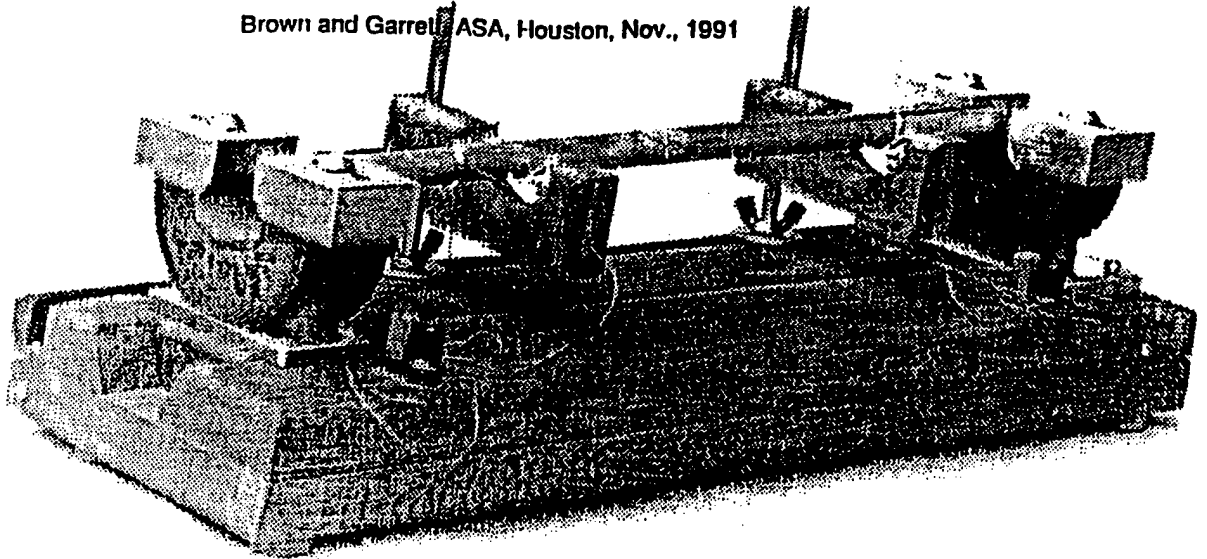
Because of the number of variations in the preparation that are available to the experimentalist (cure, catalyst, filling fraction for composites, etc.), it is important to have a convenient technique for measuring at least two moduli for reasonably small samples. Since the derivation of a third modulus from the measurement of two others can be very sensitive to the values of those moduli (particularly for samples with Poisson's ratio close to 0.5), it is important that the measurement technique have very high precision. In the following sections, a technique is described that is convenient, accurate, precise, and economical, that depends upon the measurement of the frequencies of the longitudinal, flexural, and torsional resonant modes of a single rod-shaped sample of circular cross section using the same two transducers to excite and detect all three modes.

The fact that the technique is resonant insures high signal-to-noise ratio while the fundamental measurement being a frequency means that one can obtain extremely high precision with an inexpensive instrument (i.e., a frequency counter). The technique can be used with both insulating or conducting samples that are not ferromagnetic. An additional attractive feature of this technique is the fact that Young's modulus can be determined independently in two ways by the measuring the frequencies of the longitudinal and flexural modes. This provides the experimentalist with immediate feedback on the self-consistency of his/her data and analysis. (A man with one watch thinks he knows the time; a man with two is never sure!)

The technique for measurement of the torsional mode is a refinement of one developed first by Barone and Giacomini¹⁸ to study the modes of vibration of bars having vari-

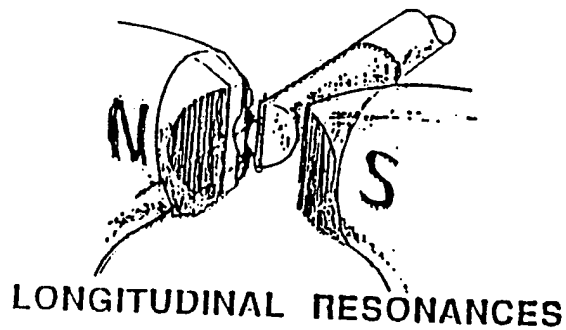
Measurement of the viscoelastic properties of materials using the resonant modes of a "free-free" bar,

Brown and Garrett, ASA, Houston, Nov., 1991



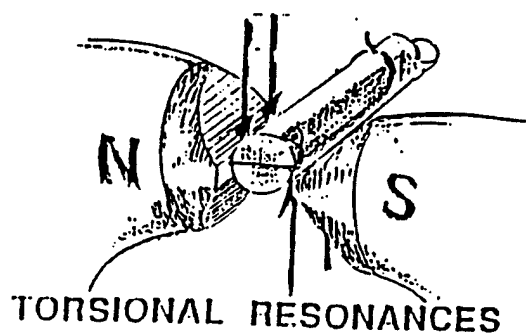
$$\frac{f_{n,T}}{n^2} = \frac{\pi}{\sqrt{1024}} \frac{d}{L^2} \sqrt{\frac{E}{\rho}}$$

$n = 3, 5, 7 \dots$



$$\frac{f_{n,L}}{n} = \frac{1}{2L} \sqrt{\frac{E}{\rho}}$$

$n = 1, 2, 3 \dots$



$$\frac{f_{n,T}}{n} = \frac{1}{2L} \sqrt{\frac{G}{\rho}}$$

$n = 1, 2, 3 \dots$

Selected References

Barome, A. and A. Giacomini, "Proc. First International Commission on Acoustics Congress on Electroacoustics, W.D. Meinema Ltd., Delft, (1953).

Barome, A. and A. Giacomini, "Experiments on some electrodynamic ultrasonic vibrators," *Acoustica*, 4, 182-184 (1954).

(Barome introduced conducting strips to electrodynamically excite resonances in free-free bars

Rudnick, I., at UCLA introduced coils of wire so that the same transducers could be used to drive all three modes.

ASTM C623-71, 1971, "Standard Test Method for Young's Modulus, Shear Modulus, and Poisson's Ratio for Glass and Glass-ceramics by Resonance," Dec. 1971.

Garrett, S.L., "Resonant acoustic determination of elastic moduli," *J. Acoust. Soc. Am.* 88(1), 210-221 (July 1990)

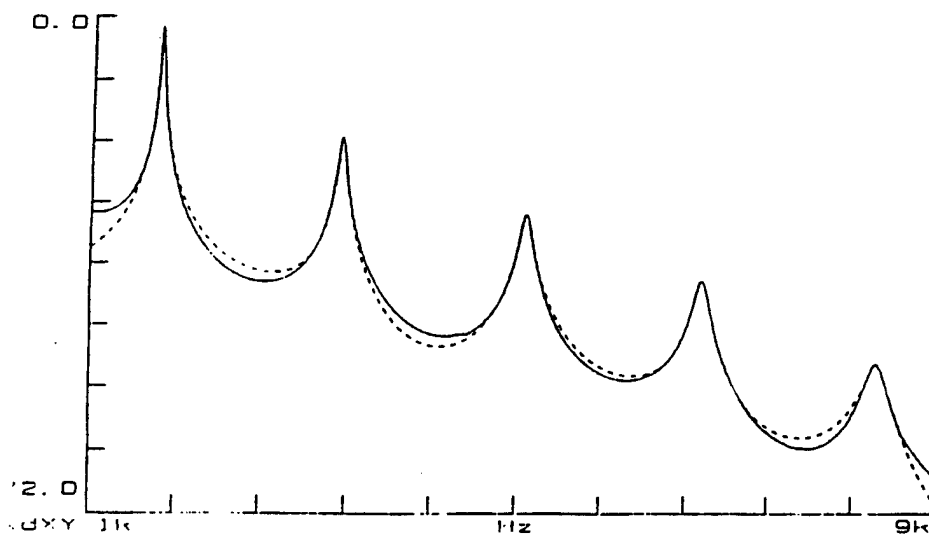
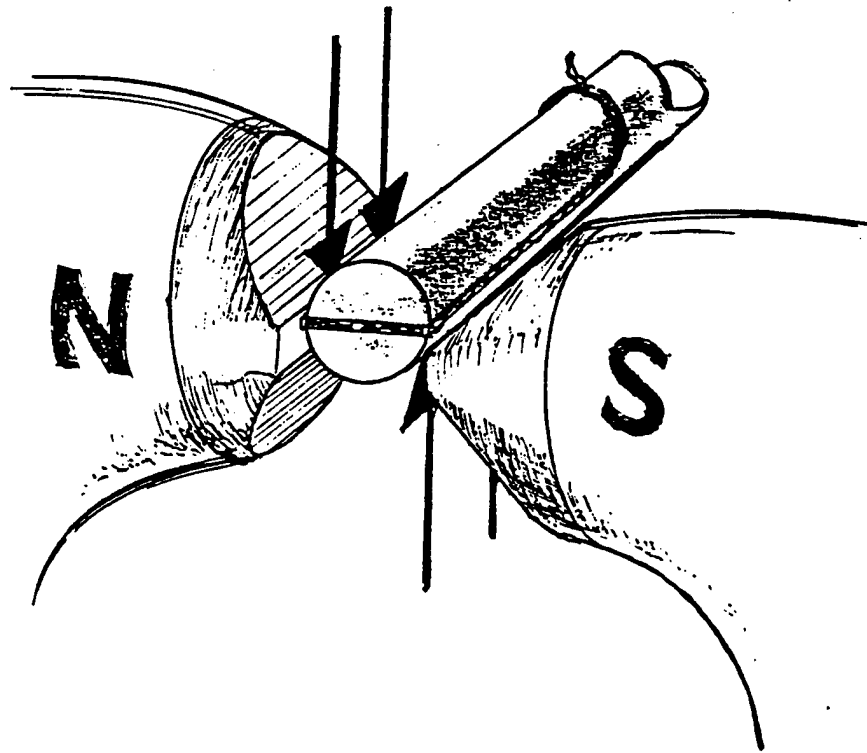
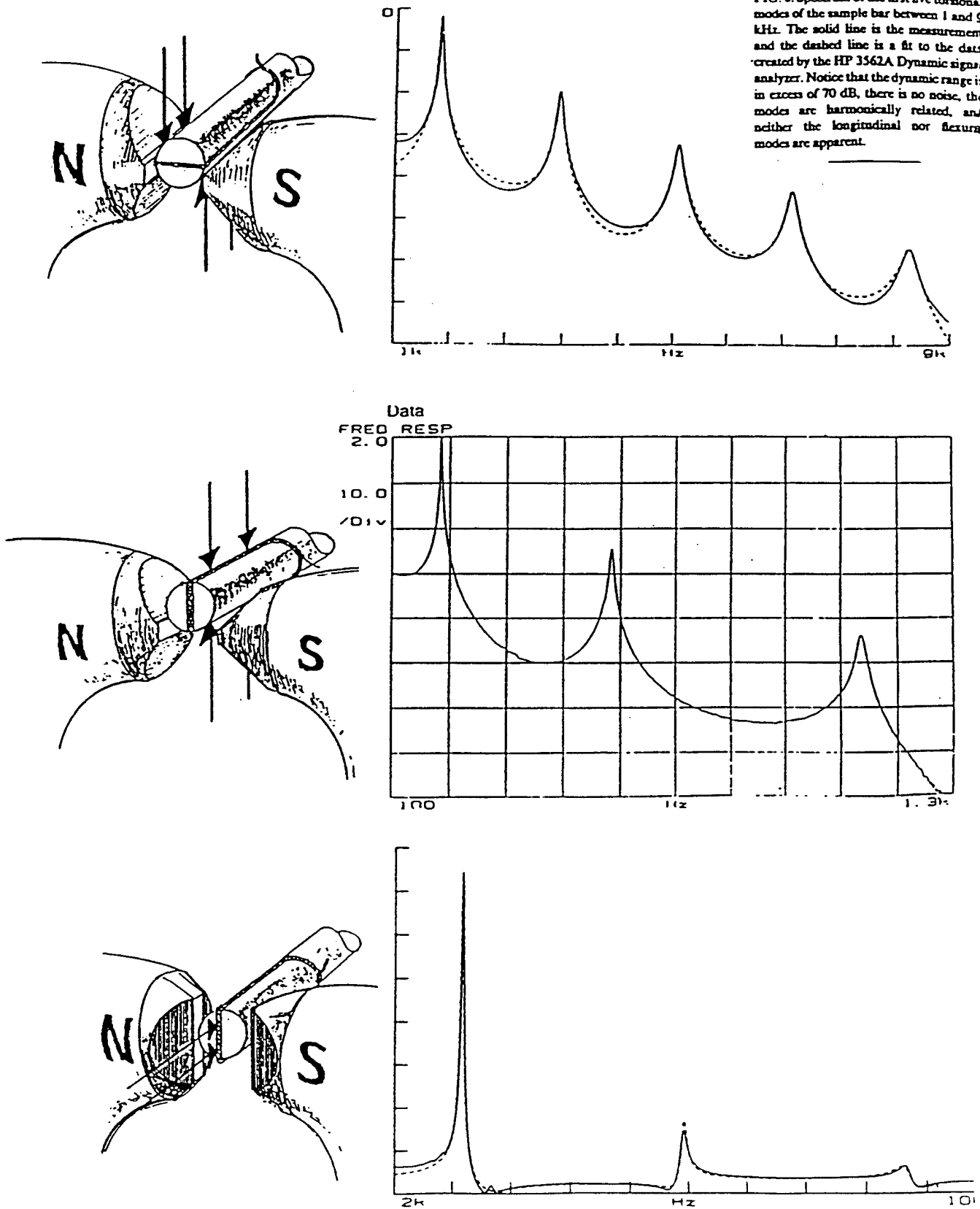


FIG. 8. Spectrum of the first five torsional modes of the sample bar between 1 and 9 kHz. The solid line is the measurement and the dashed line is a fit to the data created by the HP 3562A Dynamic signal analyzer. Notice that the dynamic range is in excess of 70 dB, there is no noise, the modes are harmonically related, and neither the longitudinal nor flexural modes are apparent.



Resonant frequencies of free-free bar

If the damping in the bar is not considered, the solution can be expressed as the linear combination of the "mode", plane harmonic wave solutions whose frequencies are the integer multiple of a basic frequency for nondispersive modes (i.e. longitudinal and torsional modes) and nearly integer multiple of a basic frequency for dispersive mode (flexural).

Under the condition of free-free ends, for nondispersive modes,

$$f_n^L = nc_L / 2L; \quad n = 1, 2, 3, \dots$$

$$f_n^T = nc_T / 2L; \quad n = 1, 2, 3, \dots$$

where $c_L = \sqrt{E / \rho}, \quad c_T = \sqrt{T / \rho},$

For flexural modes, the frequencies are

$$f_n^F = \pi n^2 c_L \kappa / 8L^2; n = 3.01, 5.00, 7, 9, 11$$

where L is the length of the bar,

c_L and c_T are the phase speed of longitudinal and torsional waves,

κ is the radius of the gyration, $\kappa^2 = \left(\frac{1}{S}\right) \iint y^2 dx dy$

E is the Young's modulus $\frac{F}{A} = -E \frac{\Delta L}{L}$

G is the shear modulus

ρ is the density of the bar.

Elastic Moduli in terms of Resonant Frequencies

So it is a rather simple matter to determine the elastic moduli from the resonance frequencies of a free-free bar

$$G = 4\rho L^2 (f_n^T / n)^2, \text{ from torsional mode,}$$

$$E = 4\rho L^2 (f_n^L / n)^2 \text{ from longitudinal mode,}$$

$$E = \frac{64}{\pi^2 K^2} \rho L^4 (f_n^F / n^2)^2 \text{ from the flexural mode.}$$

Complex Modulus and Q

Equation of motion for a damped driven oscillator

$$M \frac{\partial^2 x}{\partial t^2} + R \frac{\partial x}{\partial t} + K x = F(t)$$

If the applied force is sinusoidal of frequency ω ,

$$-\omega^2 M x + K \left(1 + j \frac{\omega R}{K} \right) x = F^*$$

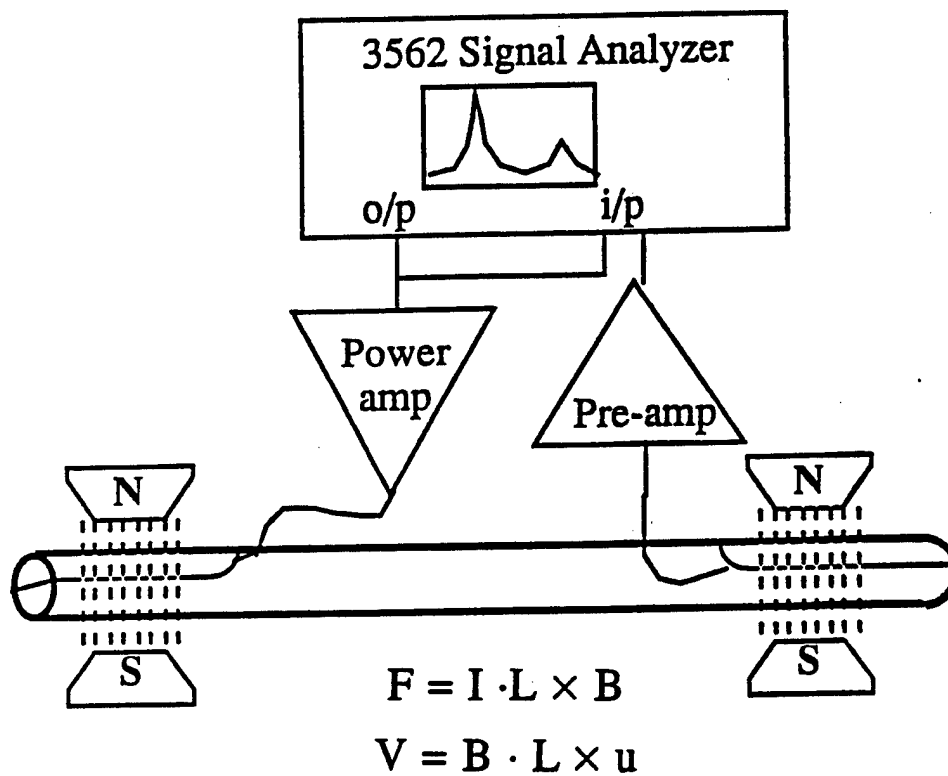
where the coefficient of the effective stiffness term can be expressed as

$$K^* = K \left(1 + j \frac{\omega R}{K} \right) = K (|1 + j \tan \delta|)$$

At resonance, $\omega = \omega_0 = \sqrt{K/M}$, the loss tangent is inversely related to the quality factor, Q by

$$\frac{1}{\tan \delta} = \frac{K}{\omega_0 R} = \frac{\sqrt{K M}}{R} = \frac{\omega_0 M}{R} = Q.$$

Transfer Function Method



$$\frac{u}{F} = \frac{V}{I} (BL)^2$$

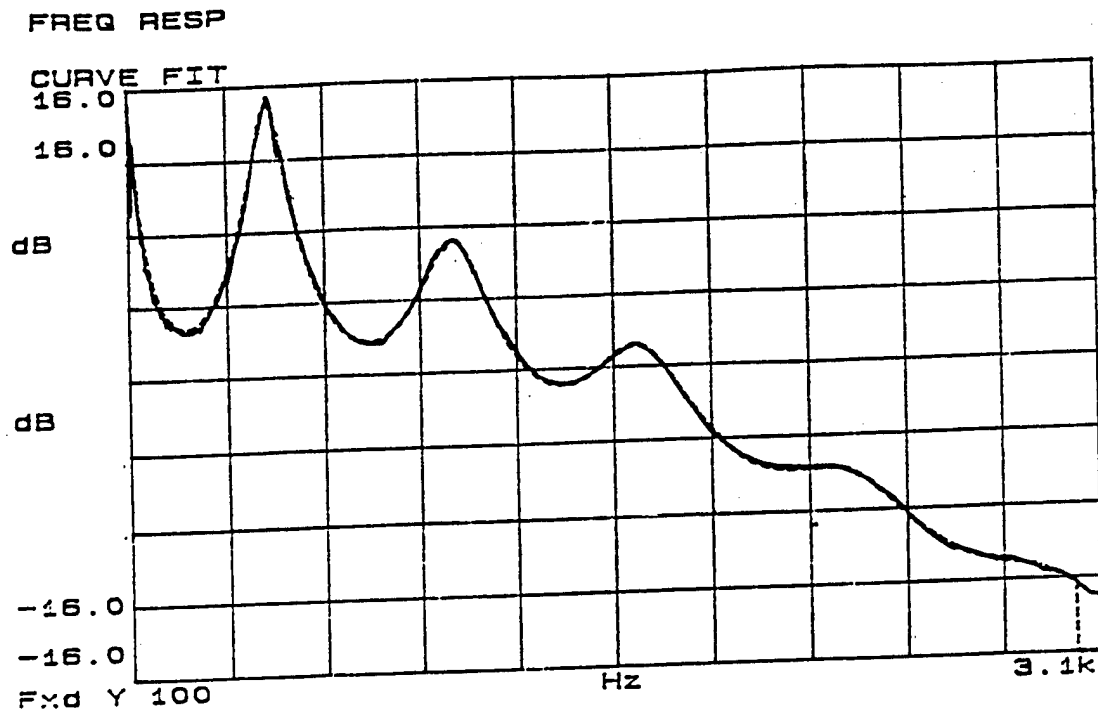
u = velocity
F = force

V = voltage
I = current

B = Magnetic field
L = length

Torsional Mode

Temp = 22.4 C , ASA Sample Y



Curve Fit				
Poles And Zeros				
POLES		ZEROS		
1	17.7601k	-297.82		
2	-18.9356 ±j 99.1363	-41.933		
3	-43.072 ±j 525.018	9.15551k		
4	-93.6262 ±j 1.1065k	757.879 ±j 545.197		
5	-150.887 ±j 1.68311k	-636.194 ±j 1.19935k		
6	410.367 ±j 2.172k	651.558 ±j 1.6757k		
7	-223.471 ±j 2.32244k	351.79 ±j 2.20706k		
8	-289.036 ±j 2.94456k	-732.629 ±j 2.42846k		
9		524.93 ±j 2.90327k		

Data Analysis Torsional Mode

Mode #	Frequency	Freq/Mode #	Quality factor
[n]	[fn] Hz	[fn/n]	[Q]
1	525	525	6.12
2	1106	553	5.93
3	1683	561	5.59
4	2322	580	5.22
5	2944	588	5.12

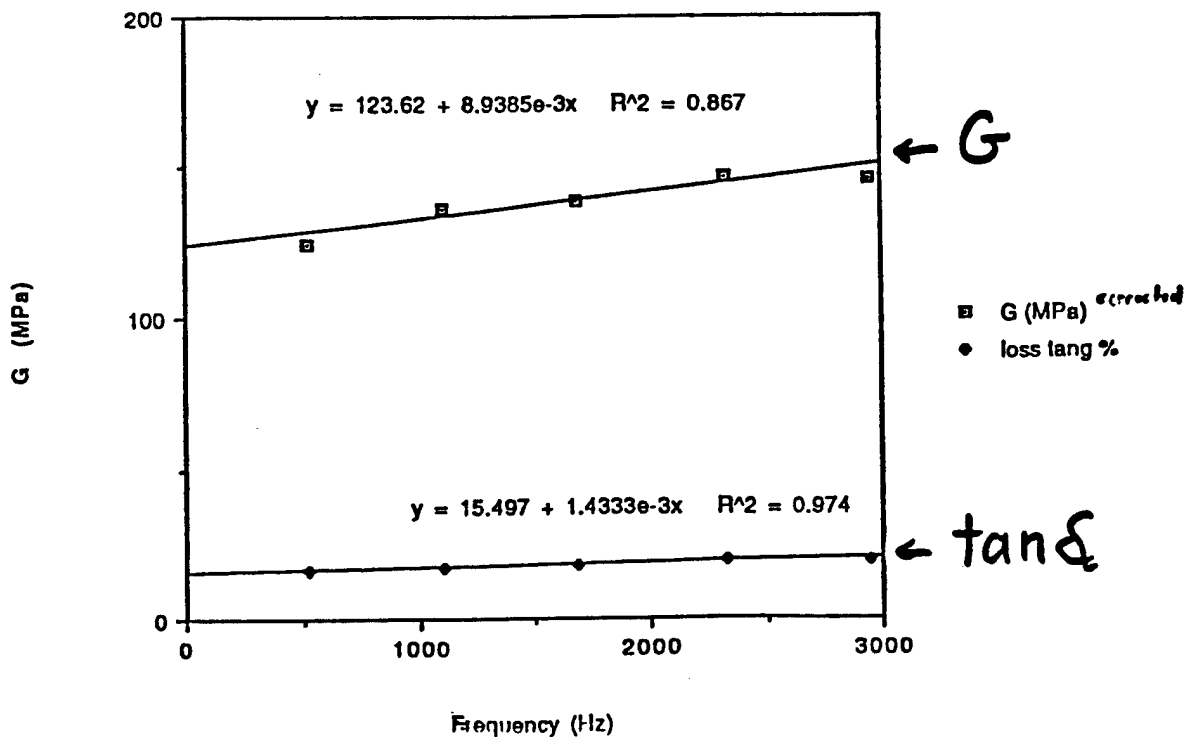
$$G = 4\rho L^2 \left(\frac{f_n^T}{n} \right)^2 \Omega_s \Omega_m$$

Ω_s = shape correction factor, 1 for a circular rod

Ω_m = transducer mass correction

$$G = 4(1025)(0.2733)^2 (525)^2 (1.20)(1.23) = 124 \text{ M PA}$$

525 Hz; 23 C

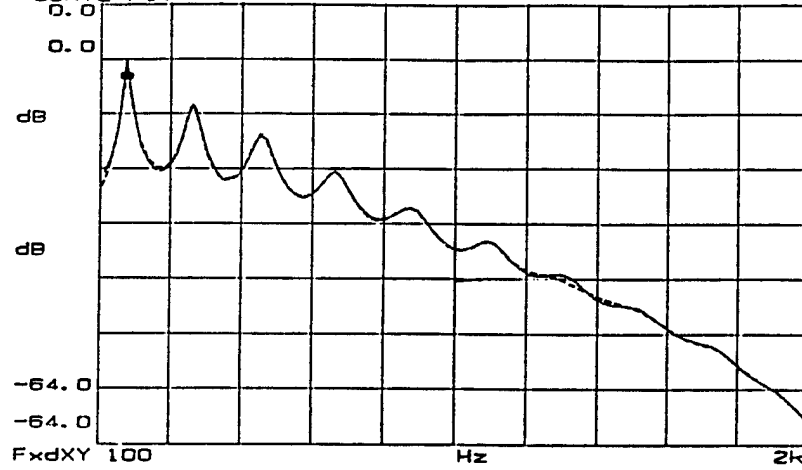


PR1592

X=189.6 Hz

FREQ RESP
Yb=-10.549 dB
CURVE FIT
0.0

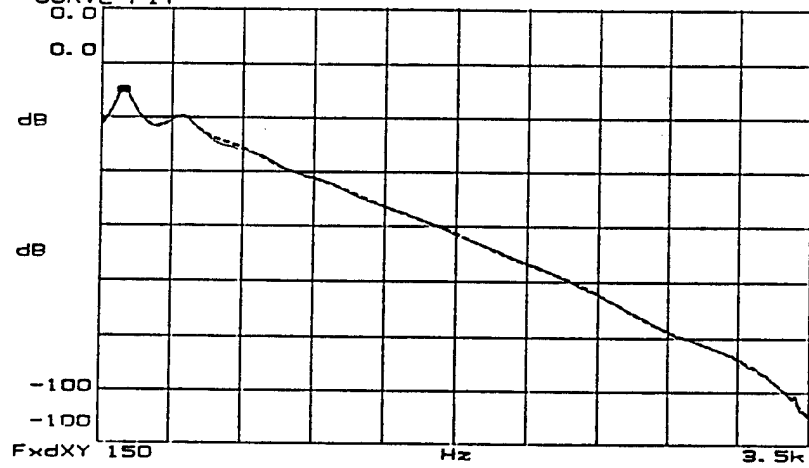
84.6°C



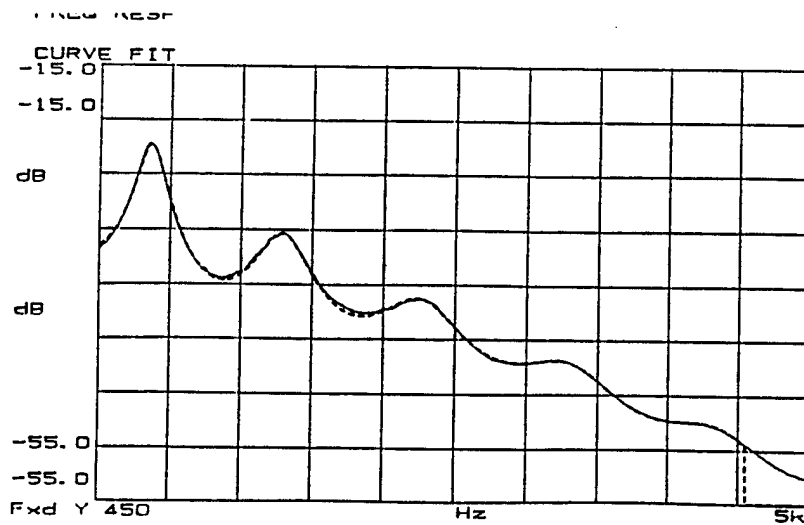
X=254.4 Hz

FREQ RESP
Yb=-18.783 dB
CURVE FIT
0.0

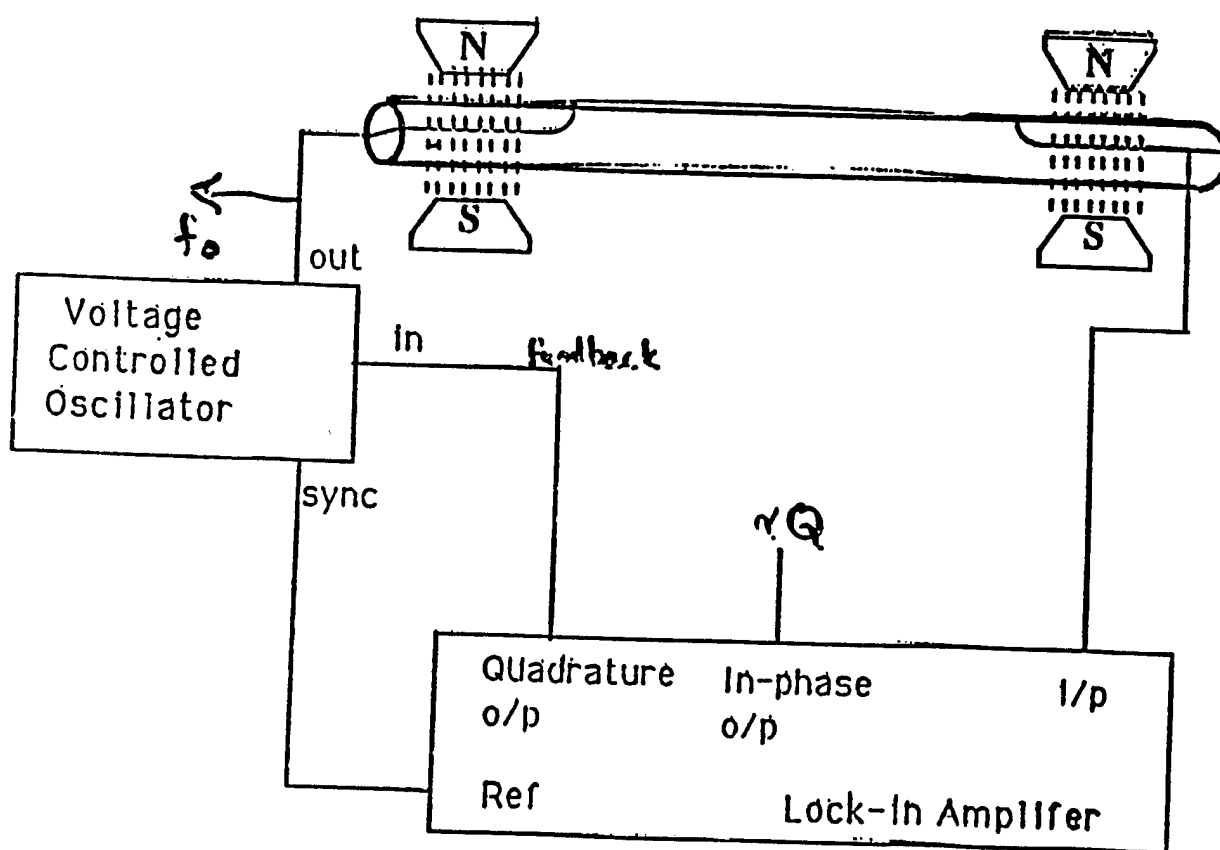
25°C

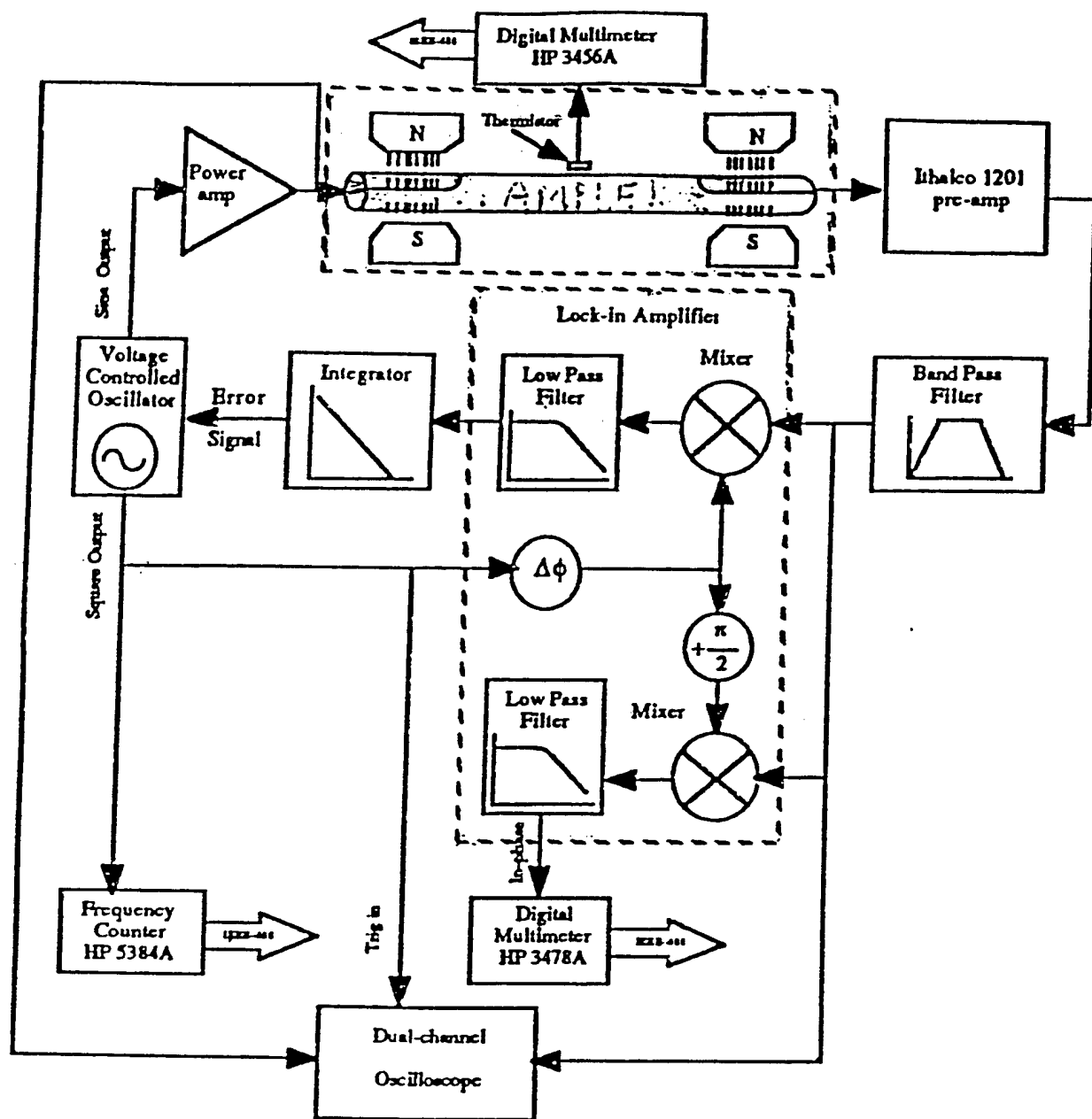


-16.8°C

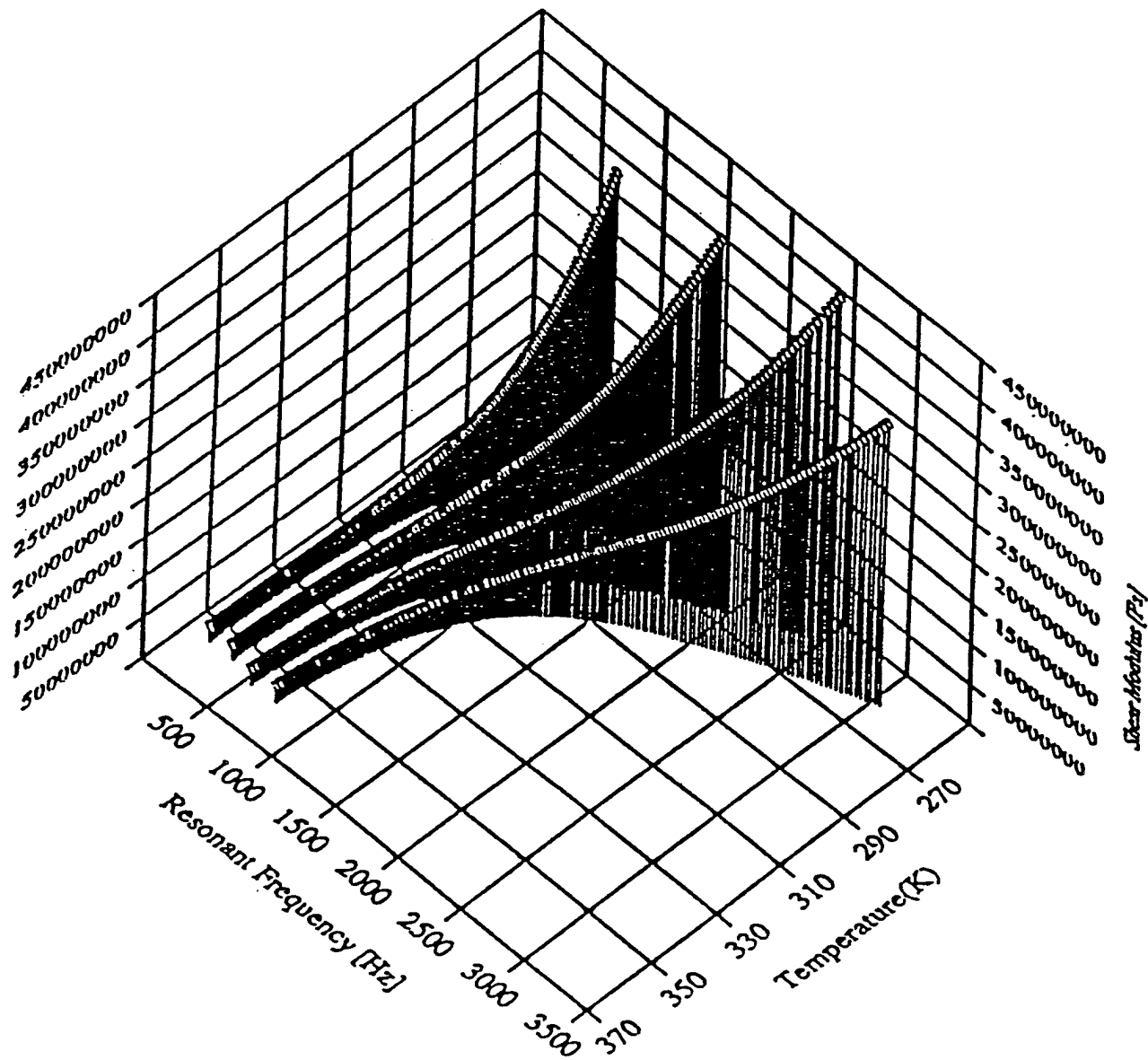


Phase Locked Loop Method





Block diagram of the instrumentation used to track the dynamic mode dependence on temperature and frequency.



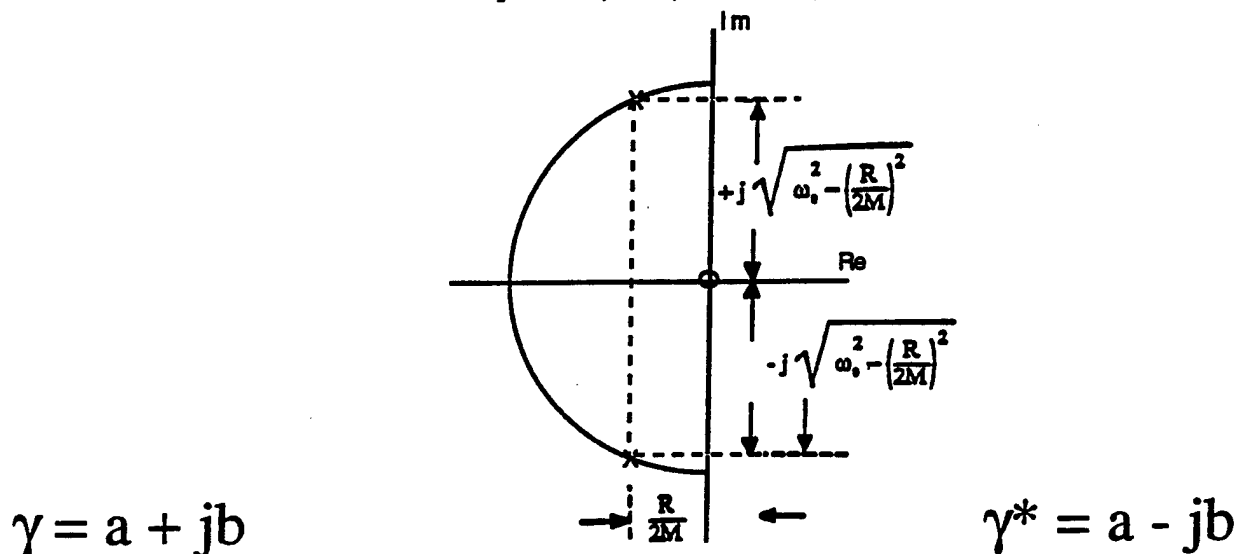
Shear modulus of PR1592 as a function of frequency and temperature.

$$Y^*(s) = \frac{1}{M} \left[\frac{s}{(s-\gamma)(s-\gamma^*)} \right]$$

Transfer function

$$\gamma = \frac{-R}{2M} + j \sqrt{\omega_0^2 - \left(\frac{R}{2M}\right)^2} \quad \text{and} \quad \gamma^* = \frac{-R}{2M} - j \sqrt{\omega_0^2 - \left(\frac{R}{2M}\right)^2}$$

Thus the transfer admittance function has poles at γ and γ^* and a single zero at $\omega = 0$.



Pole zero plot of complex admittance function.

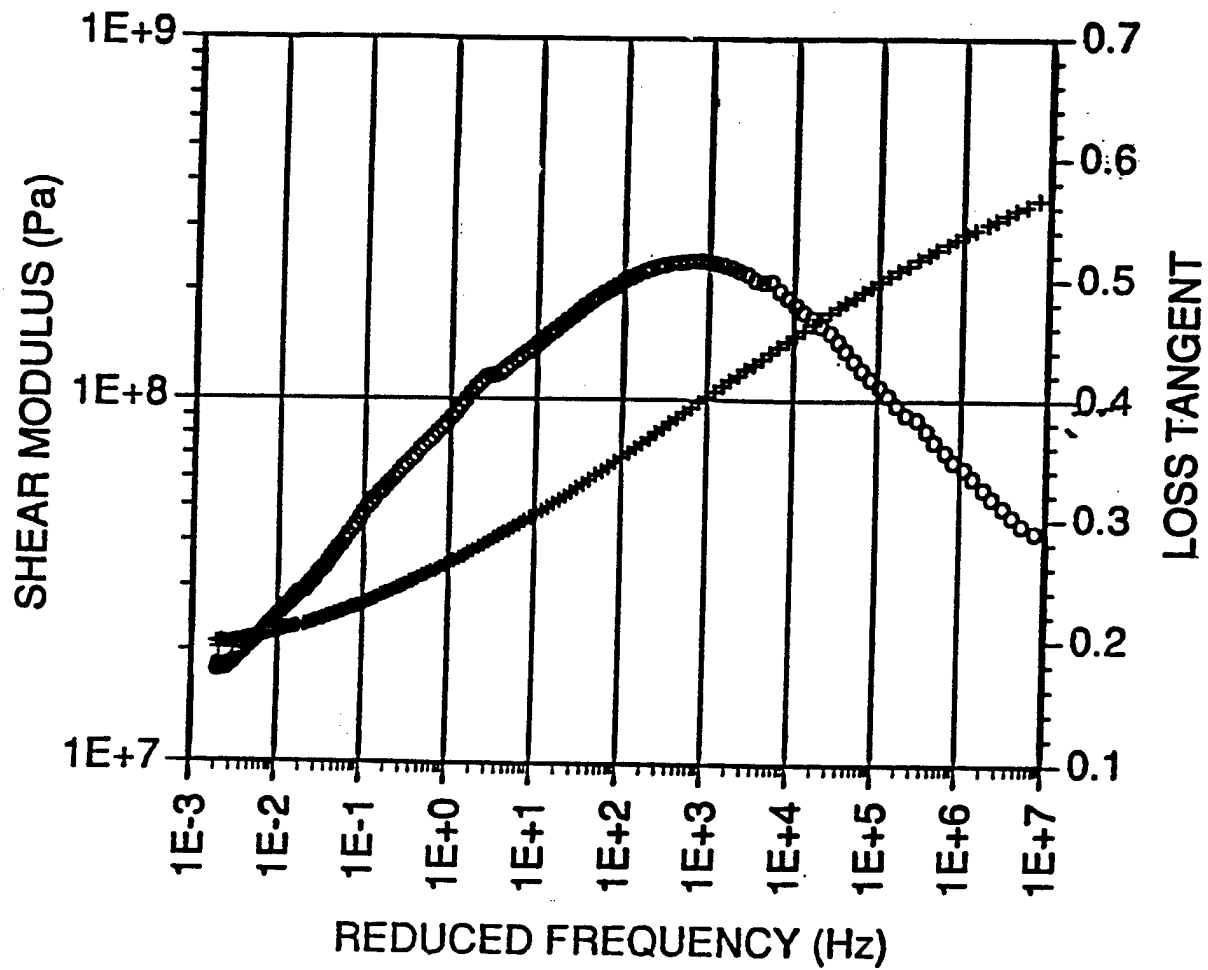
If we express the location of the poles as γ, γ^* , then Q can be expressed as follows

$$Q = \frac{\sqrt{b^2 + a^2}}{-2a} \quad (17)$$

and the resonance frequency is equal to

$$\omega_0 = \sqrt{b^2 + a^2} \cong b \left(1 + \frac{1}{2} \frac{a^2}{b^2} \right) \approx b \quad (18)$$

P R 1592



Complications associated with soft materials
Complications high loss materials

Correction factors due to added mass and stiffness of
Transducers becomes very important.

Materials can be so soft that they can't support a constant
shape

Losses can be so high that there is no apparent resonance

Corrections Factors

**The simple (thin bar) theory is often
not sufficiently accurate**

Corrections:

**due to coupled motion in a bar
(Saint Venant warping function).**

due to thick or short bar

due to added transducer mass

due to added stiffness of the transducers

Coupled motion in a bar correction factor (Saint Venant warping function).

When the bar is excited to a particular mode, any element in the bar moves mainly due to the particular mode. But still it has to move along the perpendicular direction because the volume is constant.

Longitudinal Mode: an element that is not at axis of the bar moves both along the axis and in the radial direction.

Torsional Mode: an element move both in the cross section plane and in the longitudinal direction.

The coupled motion and hence correction factor can be substantial as the elastic modulus or correctional area is increased.

[Ref Love, *A treatise on the mathematical theory of elasticity*].

Coupled motion case correction factors

When the coupled motion among different dimensions is considered, the resonant angular frequencies(ω) can be recalculated by the energy methods. The angular frequency change is $\Delta\omega$. And the angular frequency of the "bare" bar is ω_0 . M is the mass of unloaded bar. Δm is the added mass(include coils and glue). L is the length of the bar. Δl is the length of the transducer along the axis of the bar. The added mass is regarded as a point mass at the position away from the end by $\frac{\Delta l}{2}$. For torsional mode,

$$G = 4\rho L^2 \left(\frac{f_n^T}{n} \right)^2 \Omega_S \Omega'_L$$

$$\text{where } \Omega'_L = \left[1 + \frac{\Delta m \kappa^2}{M K_P^2} \cos^2 \left(\frac{n\pi \Delta l}{2L} \right) \right]^2,$$

which is slightly smaller than the above correction.
(Danielson)

Torsional Examples for different cross-sections

For a cylindrical symmetric bar,

the warping function $\Phi = 0$,

For an ellipsoidal cross-section bar

with semi-major a (along x axis) and semi-minor b ,

$$\Phi = -\frac{a^2 - b^2}{a^2 + b^2} xy$$

For a rectangular cross section bar of sides $2a$ (along x axis) and $2b$, (Ref. Spinner and Teft)

$$\Phi = -xy + 4b^2 \left(\frac{2}{\pi}\right)^3 \sum_{n=0}^{\infty} \frac{(-1)^n}{(2n+1)^3} \frac{\sinh \frac{(2n+1)\pi x}{2b}}{\cosh \frac{(2n+1)\pi a}{2b}} \sin \frac{(2n+1)\pi y}{2b}$$

Correction for shear modulus

For torsional mode, the corrected formula of shear modulus becomes:

$$G = 4\rho L^2 \left(\frac{f_n^T}{n} \right)^2 \Omega_S \Omega_L \Omega_m$$

For the ellipsoidal cross section bar, $\Omega_S = \frac{(a^2 + b^2)^2}{4a^2b^2}$.

Correction for Young's modulus

Young's modulus can be obtained either from flexural mode or from longitudinal mode. The corrected Young's modulus from flexural mode is

$$E = \frac{64}{\pi^2 \kappa^2} \rho L^4 \left(\frac{f_n^F}{n} \right)^2 \Omega_L$$

where Ω_L is the correction factor.

For rectangular cross section bar of sides $2a$ (along x direction) and $2b(=h)$, we have $\kappa = \frac{h}{\sqrt{12}}$ and the correction factor is,

$$\Omega_L = 1 + 6.585(1 + 0.0752\nu + 0.819\nu^2) \left(\frac{h}{L} \right)^2 - 0.868 \left(\frac{h}{L} \right)^4 - \left[\frac{8.340(1 + 0.2023\nu + 2.713\nu^2) \left(\frac{h}{L} \right)^4}{1 + 6.338(1 + 0.14081\nu + 1.536\nu^2) \left(\frac{h}{L} \right)^2} \right]$$

As an example if $\frac{h}{L} = 0.1$, $T \approx 1.07$, which represents 7% correction.

Wave equation (w/ Saint Venant warping)

For the torsional mode, the wave equation becomes,

$$\frac{c_T^2}{R_S} \frac{\partial^2 \Psi}{\partial z^2} = \frac{\partial^2 \Psi}{\partial t^2} - \mu^2 \frac{\partial^4 \Psi}{\partial z^2 \partial t^2}$$

One can see that there are 4th order derivative terms in the wave equation when coupling is considered.

Ψ is the angular displacement of a "disc" element at location z .

Ω_S and μ^2 are from the coupling effect.

$$\Omega_S = I_P / J \qquad \mu^2 = \frac{\iint \Phi^2 dx dy}{I_P},$$

J is the polar moment of inertia of the bar's cross section,

I_P is the polar moment of inertia of the bar's cross section when the Saint Venant warping function $\Phi(x, y)$ is zero.

$$J = \iint \left(x^2 + y^2 + x \frac{\partial \Phi}{\partial y} - y \frac{\partial \Phi}{\partial x} \right) dx dy,$$

$$I_P = \iint (x^2 + y^2) dx dy,$$

The solution to the wave equation takes on the wave number

$$k = \frac{\omega}{c'} = \frac{\omega}{\sqrt{c^2 - \mu^2 \omega^2}}$$

Correction for transducer mass

No coupling case (just added mass)

If the mass of transducers at the ends is considered, but the coupling motion among different dimensions is neglected, the formulas are the same except that the length of the bar is replaced by an effective length. For longitudinal and flexural mode, the effective length is

$$L_{\text{eff}}^L \cong L_{\text{eff}}^F \cong L(1 + m/M).$$

For torsional mode, the effective length is

$$L_{\text{eff}}^T \cong L(1 + 2m/M)$$

(After Garrett's JASA article circa 1990)

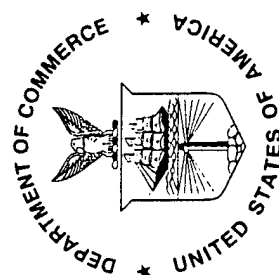
The correction can be obtained by means of Rayleigh's energy method. The effects of the transducer is only the effective increase of the length of the bar due to the increase of the mass of the bar. The resonant frequencies is less than that of the original bar. Because the mass increase is may or may not be a significant correction depending on experimental relative masses of the transducer and bar.

ACOUSTIC RESONANCE TECHNIQUES APPLIED TO METROLOGY

The universal gas constant R

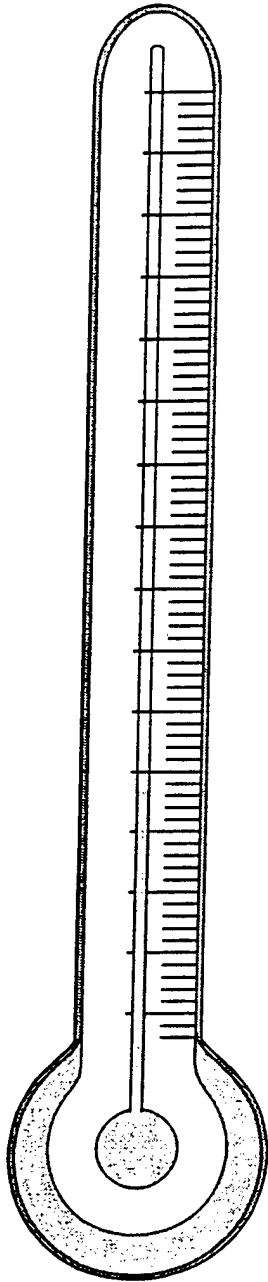
The thermodynamic temperature scale

NIST United States Department of Commerce
National Institute of Standards and Technology



MICHAEL R. MOLDOVER

**NIST Fellow
Physical and Chemical
Properties Division**



Why temperature scales?

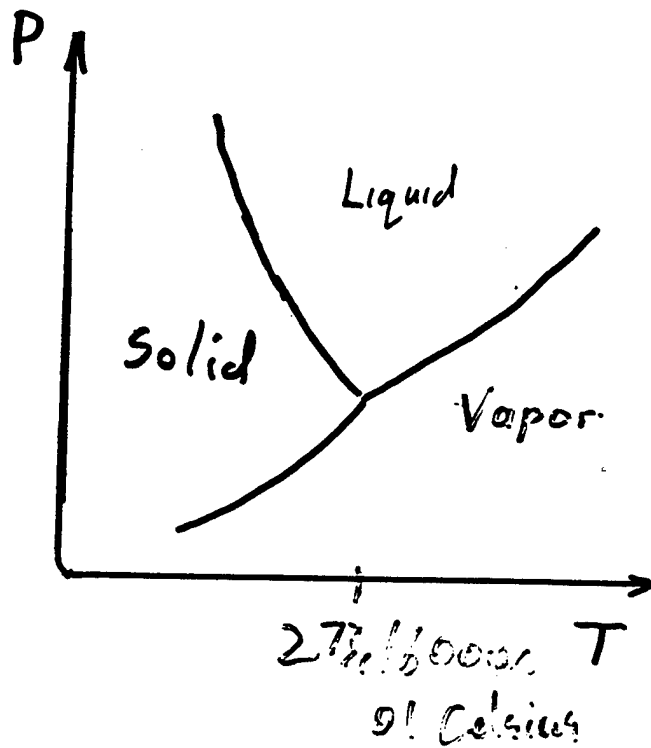
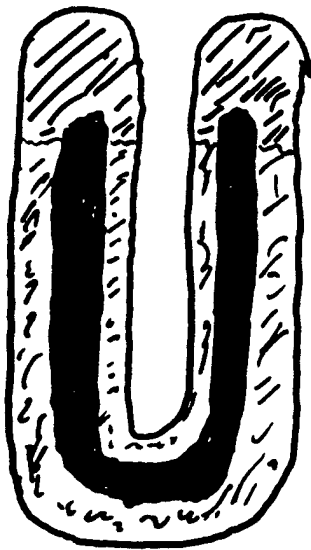
Why thermodynamic temperature scales?

What good is Boltzmann's constant k_B ?

What good is universal gas constant R ?

What is acoustic gas thermometry?

Why Temperature Scales?



$$\frac{\Delta T}{T} \sim 10^{-7} \quad (30 \mu\text{K near room temp})$$

instrumentation for $3 \mu\text{K}$ available

crystal size - strain

isotopic composition . . .

Why Thermodynamic Temperatures?

Latent Heat:
$$L = T \frac{dP}{dT} (V_{\text{gas}} - V_{\text{liquid}})$$

Heat of Electrochemical Reaction

$$Q = \Delta Z \left(\mathcal{E} - T \frac{d\mathcal{E}}{dT} \right)$$

Carnot Efficiency $\eta = 1 - \frac{T_{\text{COLD}}}{T_{\text{HOT}}}$

Examples of Primary Thermometers

Dilute Gas
(equation of state)

$$PV = nRT \left(1 + \frac{B}{V} + \dots \right)$$

Dilute Gas
(speed of sound)

$$Mc^2 = \frac{C_P^0}{C_V^0} RT \left(1 + A_1 P + \dots \right)$$

Black Body Radiation
(power / area)

$$\frac{P}{A} = \sigma T^4 = \frac{\pi^2}{60 \hbar^3 c^3} (k_B T)^4$$

Johnson Noise
(power)

$$P = \frac{\langle V^2 \rangle}{r} = 4k_B T \Delta f$$

Dipole in Field
(energy)

$$E = -\overline{\mu \cdot B} = -\mu B \left[\text{ctnh} \left(\frac{\mu B}{k_B T} \right) - \left(\frac{\mu B}{k_B T} \right) \right]$$

Acoustic Gas Thermometry

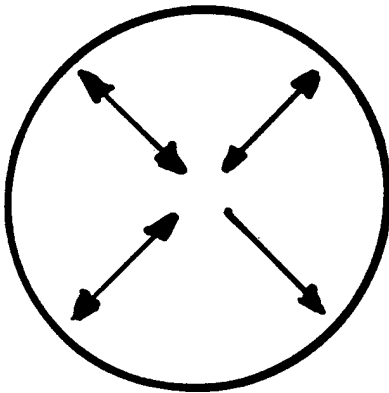
dilute monatomic gas

$$\frac{1}{2} m \overline{V^2} = \frac{3}{2} k_B T = \frac{1}{2} m \left(\frac{9}{5} c^2 \right) \quad k_B = \frac{3}{5} \frac{m c^2}{T}$$

$$R = N_A k_B = \frac{3}{5} \frac{M c^2}{T}$$

$$\frac{T}{T_W} = \frac{T}{273.16 \text{ K}} = \frac{c^2(T)}{c^2(T_W)}$$

Resonance Method

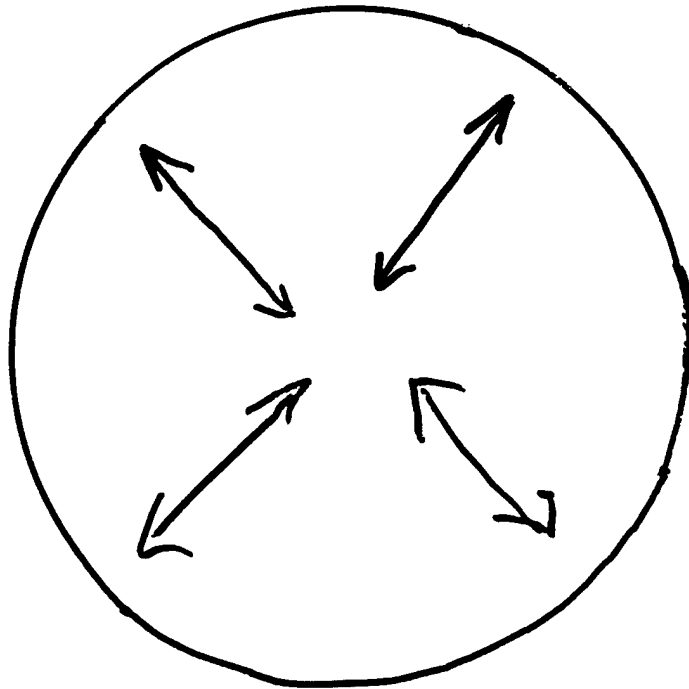


$$c = \frac{\text{length}}{\text{time}}$$

$$= V^{1/3} \times f \times \text{eigenvalue}$$

$$\frac{T}{T_W} = \left(\frac{V^{1/3} \times f}{V_W^{1/3} \times f_W} \right)^2 = \left(1 + \frac{\Delta V(T)}{V_W} \right)^{2/3} \times \left(\frac{f(T)}{f_W} \right)^2$$

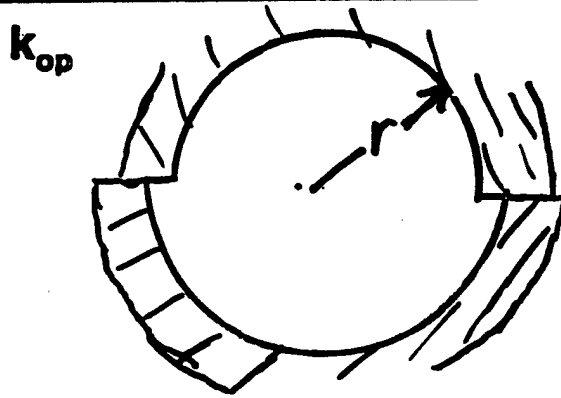
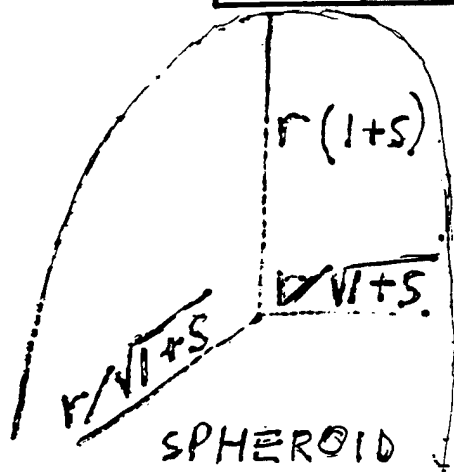
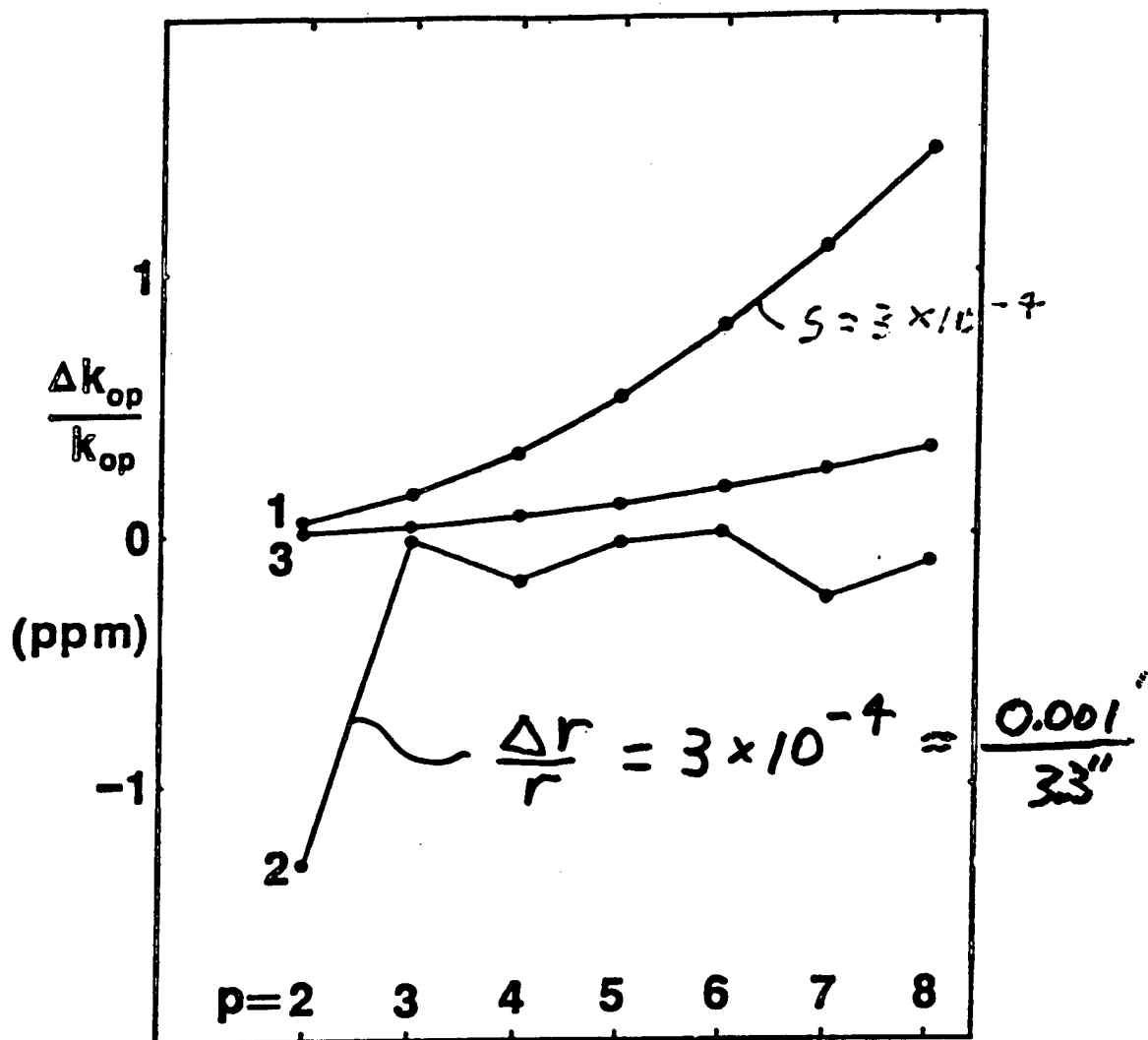
RADIAL RESONANCES IN A SPHERE



HIGHEST POSSIBLE Q AT LOW
DENSITY (NO VISCOUS DAMPING

NOT SENSITIVE TO SMALL ERRORS
IN CONSTRUCTION — NON-DEGENERATE
MODES

$\frac{\Delta f}{f}$



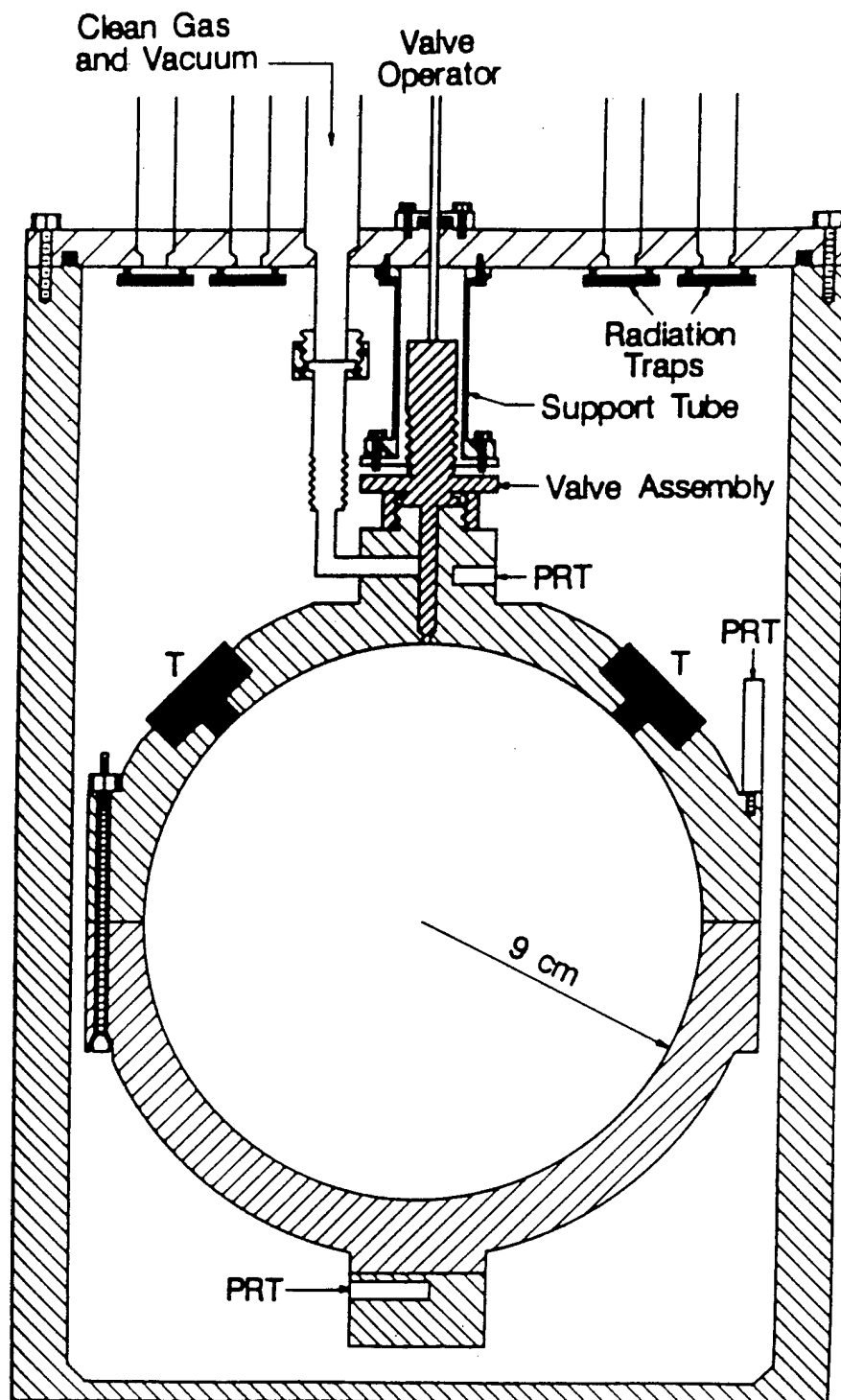
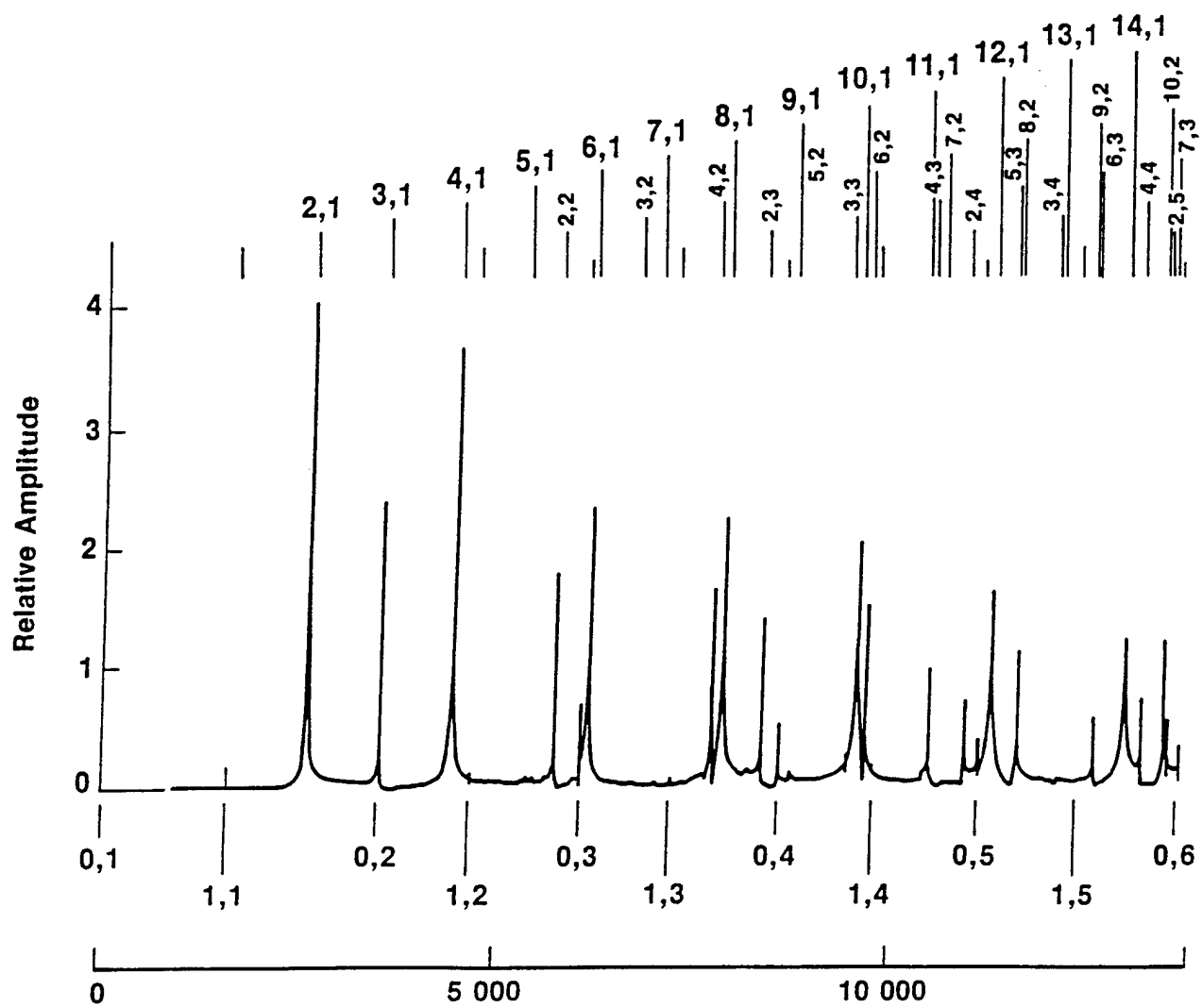
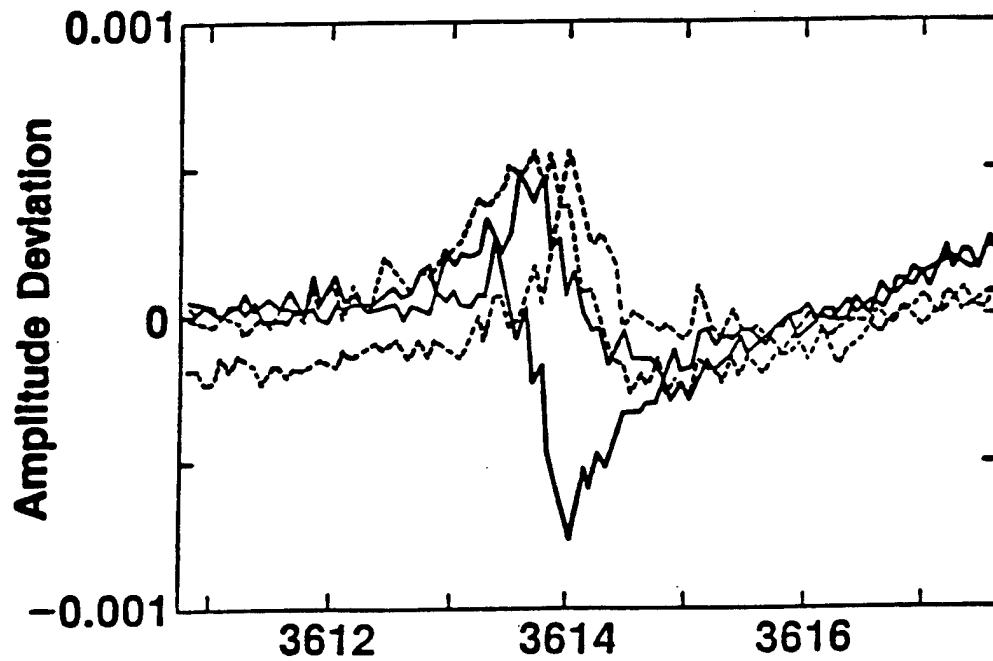
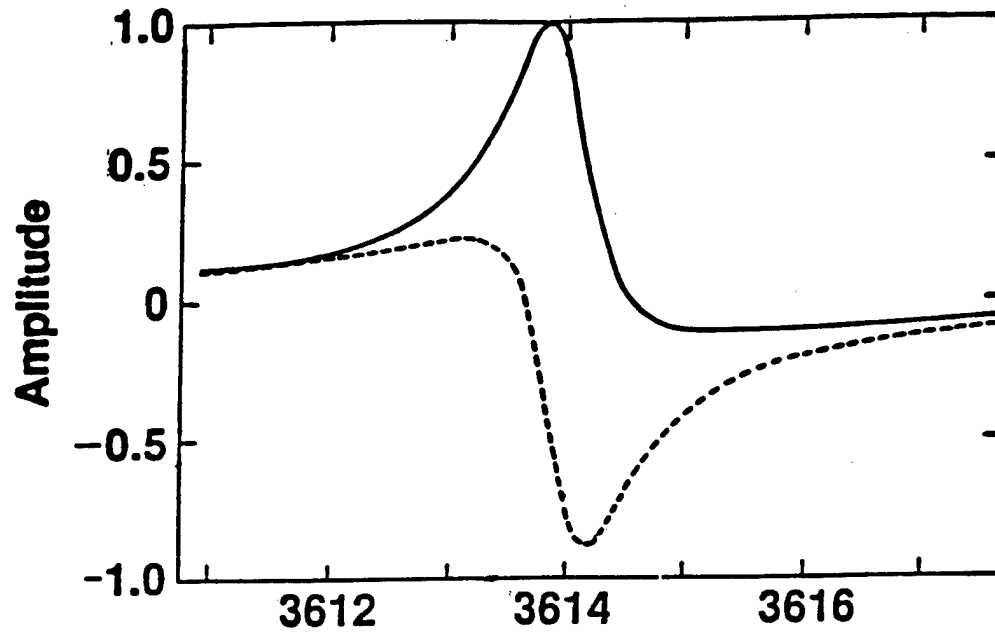


Figure 5. Cross-section of resonator and pressure vessel. The transducer assemblies are indicated by "T," and the locations of the capsule thermometers are indicated by "PRT."





Frequency (Hz)

$$Q \sim 5000 \quad \frac{\Delta f}{f} \sim 2 \times 10^{-7}$$

Lorentzian Line

$$\bar{V} = \frac{\bar{A} f}{(f_x + i g_x)^2 - f^2} + \bar{B} + \bar{C} f + \dots$$

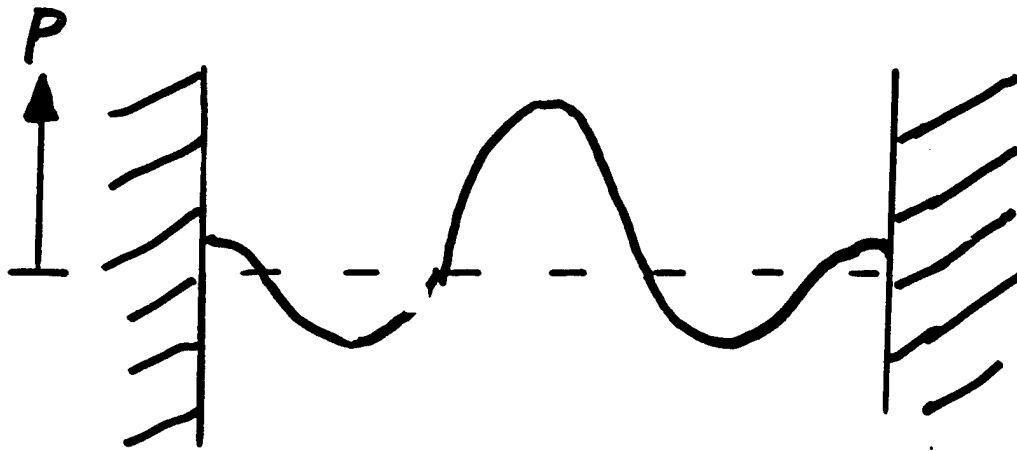
Precision

$$\frac{\delta g_x}{g_x} \sim \frac{\delta \bar{V}}{\bar{V}} \sim 10^{-3}$$

$$\frac{\delta f_x}{f_x} \sim \frac{\delta g_x}{f_x} \sim \frac{10^{-3} g_x}{f_x} = \frac{10^{-3} * 0.35}{3600} \sim 10^{-7}$$

Simplest Theory

Rigid spherical shell, ignore temperature


 j_n = n th spherical Bessel function

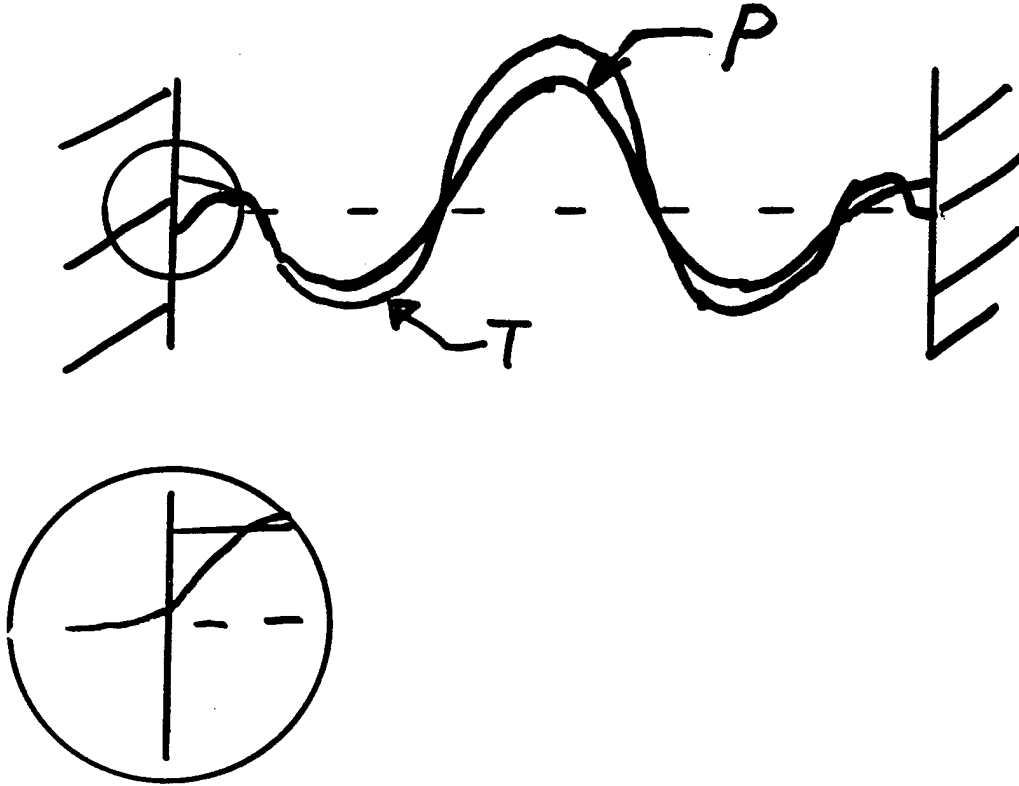
$$\frac{dj_n(\beta a)}{da} = 0 ; \quad \beta = \frac{2\pi f}{c}$$

 $\Rightarrow f(n, l)$

(Rayleigh)

l = # of root; $l = 0, 1, 2, \dots$
 n = # of Bessel function; $n = 0, 1, 2, \dots$

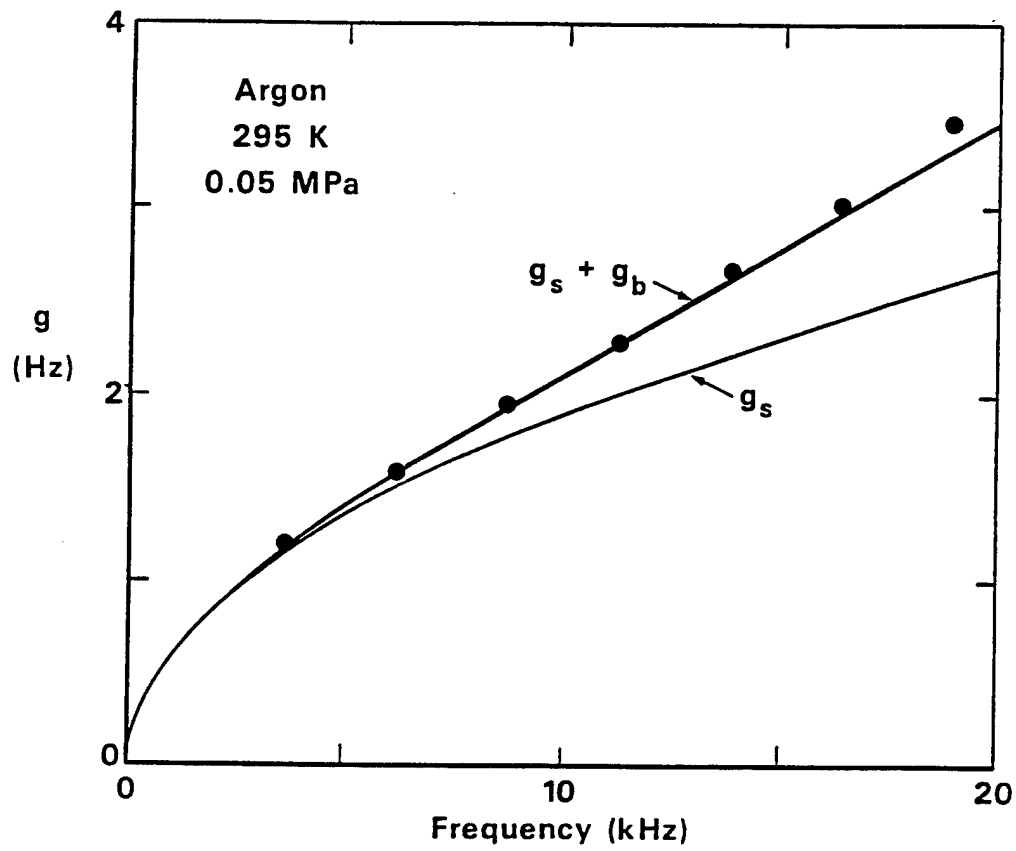
Heat Flow Between Gas and Shell



$$\left(\frac{\Delta f + ig}{f} \right)_{\text{heat flow}} = (-1 + i) \left(\frac{\gamma - 1}{2a} \right) \sqrt{\frac{D_T}{\pi f}}$$

$$= (-1 + i) (210 \times 10^{-6}) \sqrt{\frac{f_{0,1} \text{ 1 atm}}{f P}}$$

Note: $D_T = \frac{\lambda}{\rho C_P}$



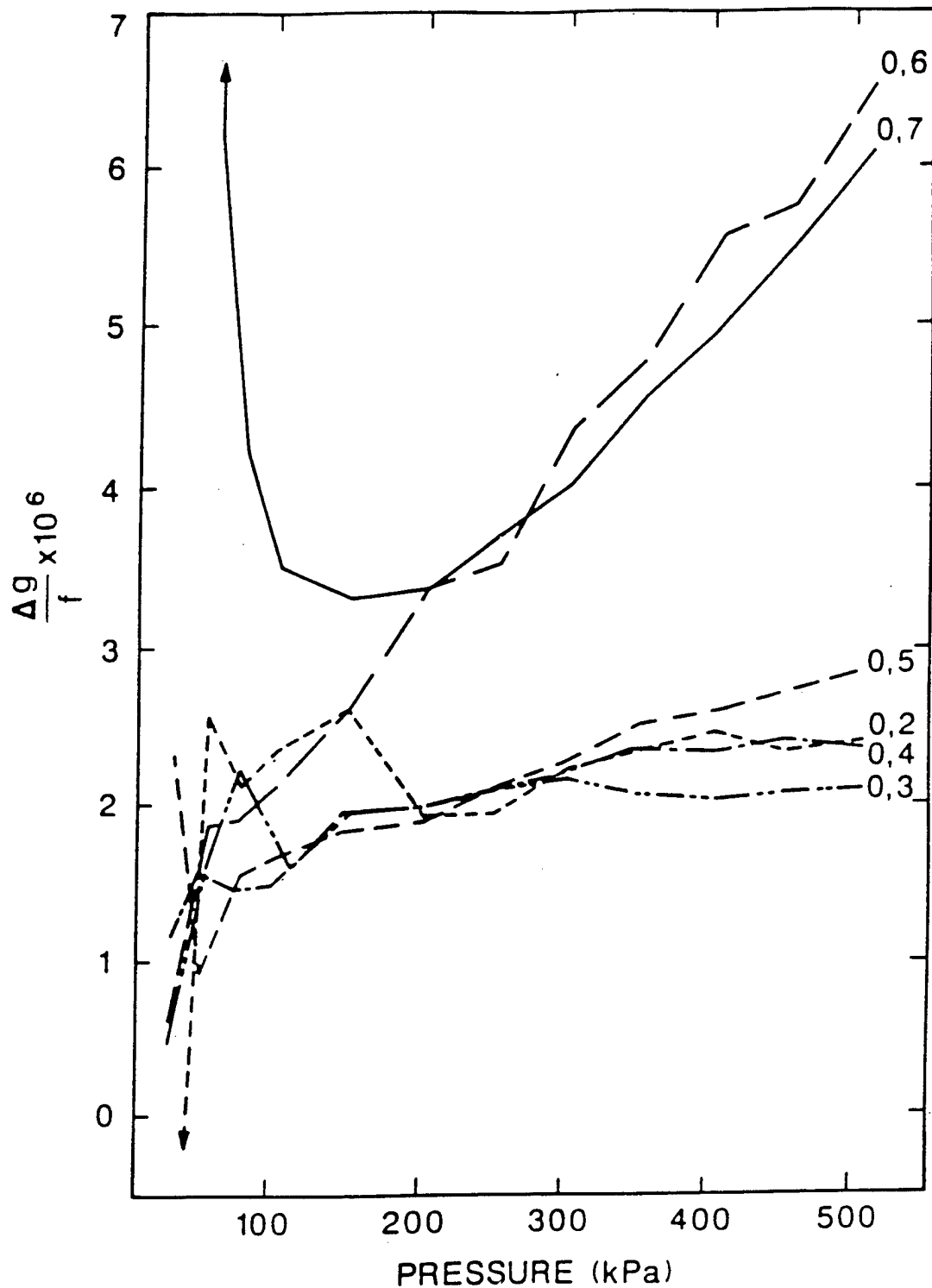
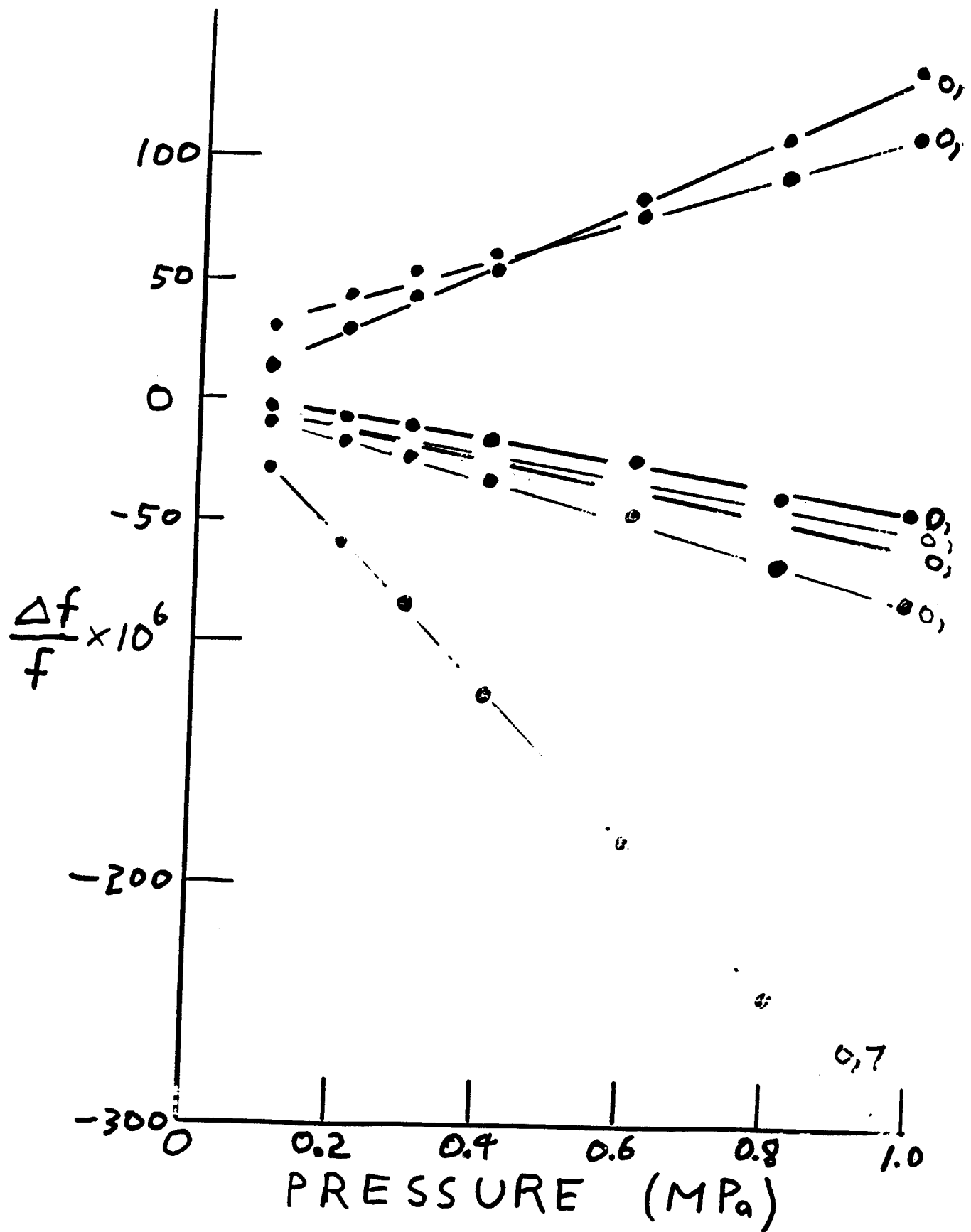
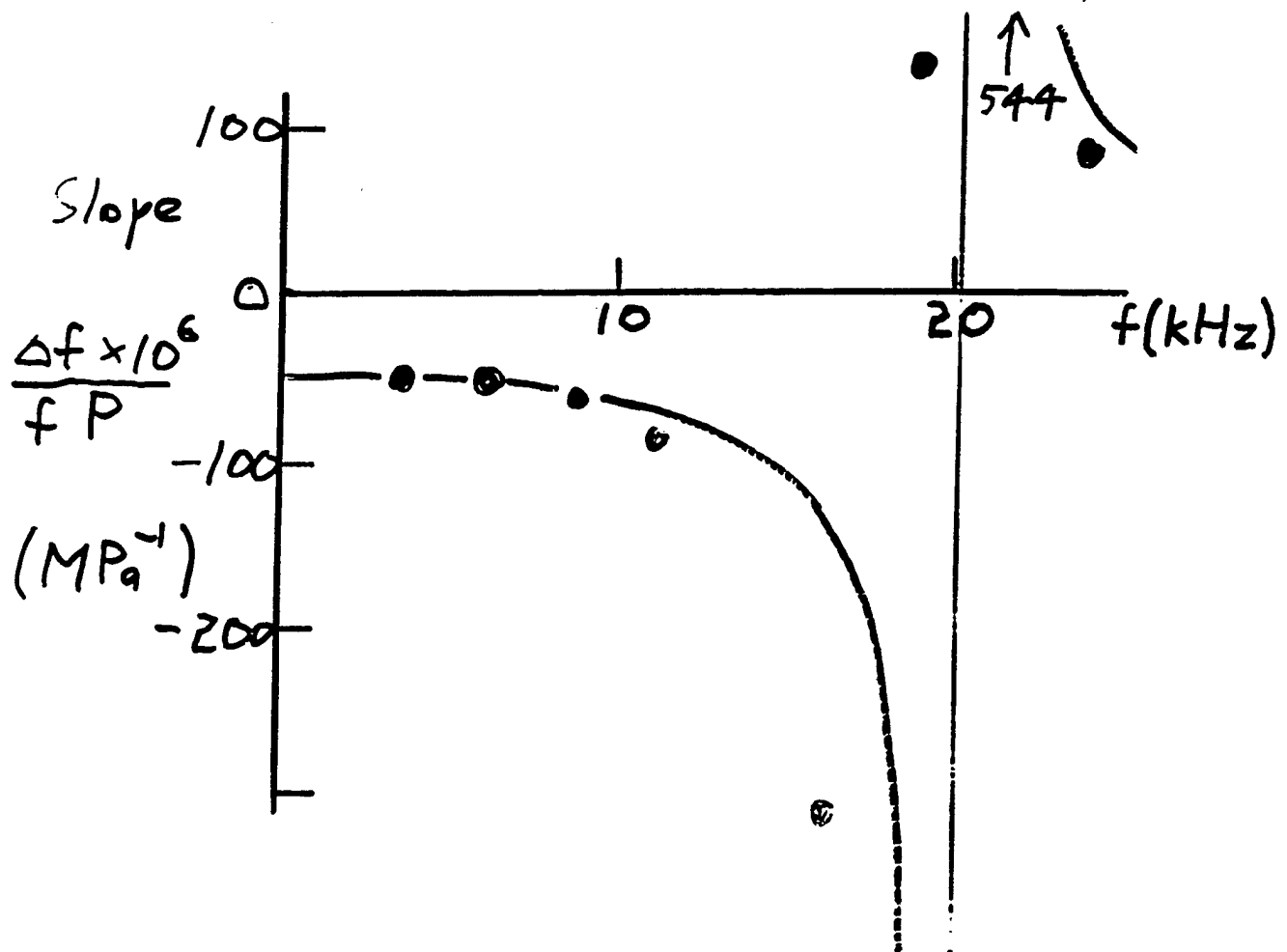
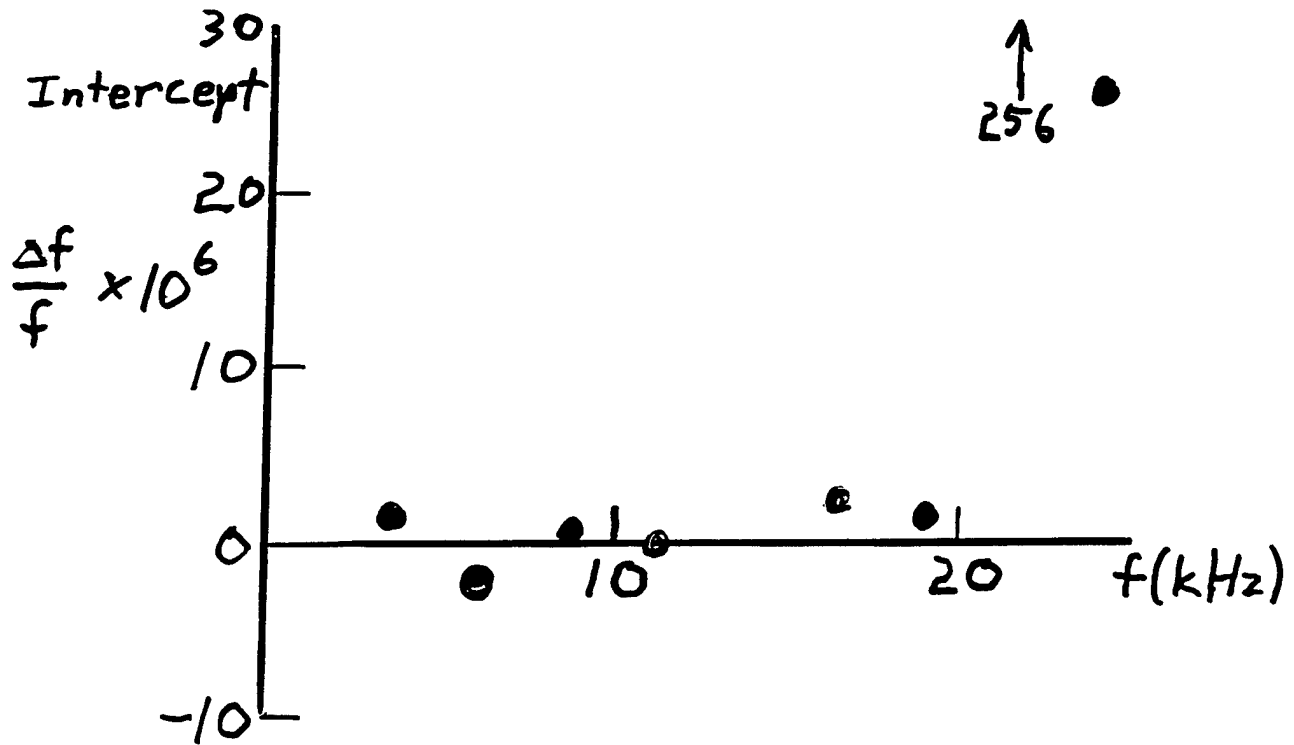
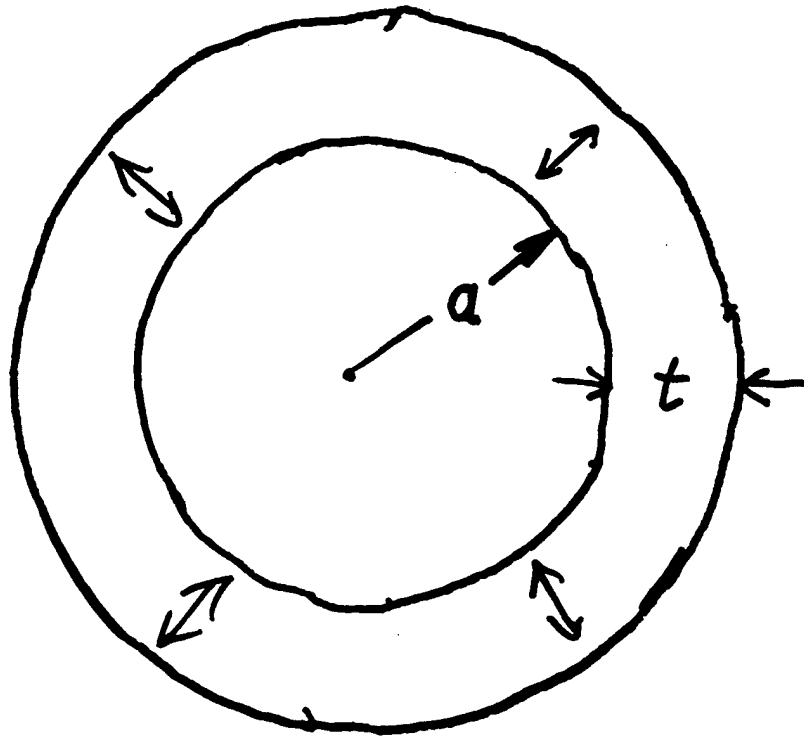


Figure 20. Excess half-widths of $(0,n)$ resonances with argon in the resonator scaled by $10^6/\text{frequency}$. $\Delta g = \text{measured } g \text{ minus calculated } g$.





THE SHELL BREATHES

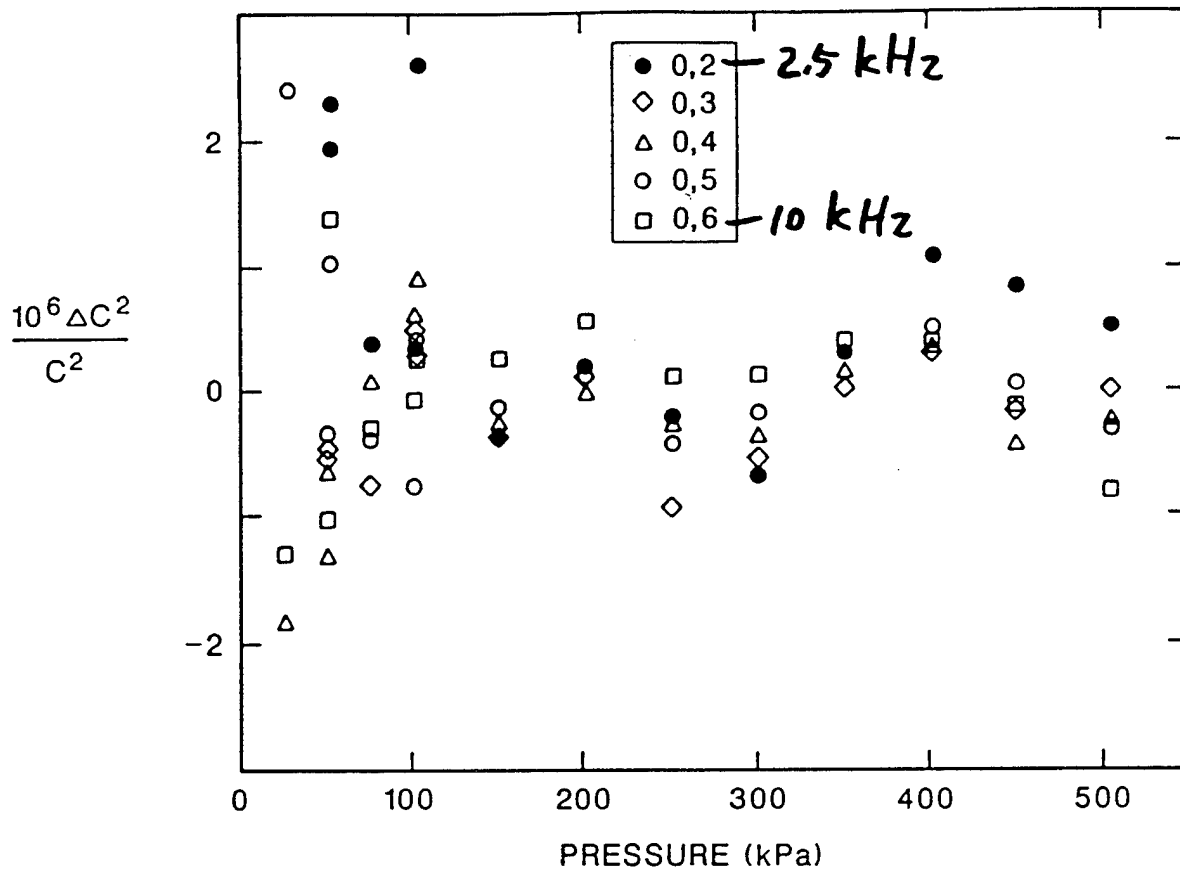


$$\frac{\Delta f}{f} = - \frac{(\rho c^2)_g}{(\rho c^2)_w} \left(\frac{a}{t} \right) \frac{1}{2 - (U_p C_g / C_w)^2}$$

$$U_p = 4.493, 7.725, 10.904, \dots$$

Argon, 295 K, 0.1 MPa, $p=1$

$$\frac{\Delta f}{f} = -5 \times 10^{-6}$$



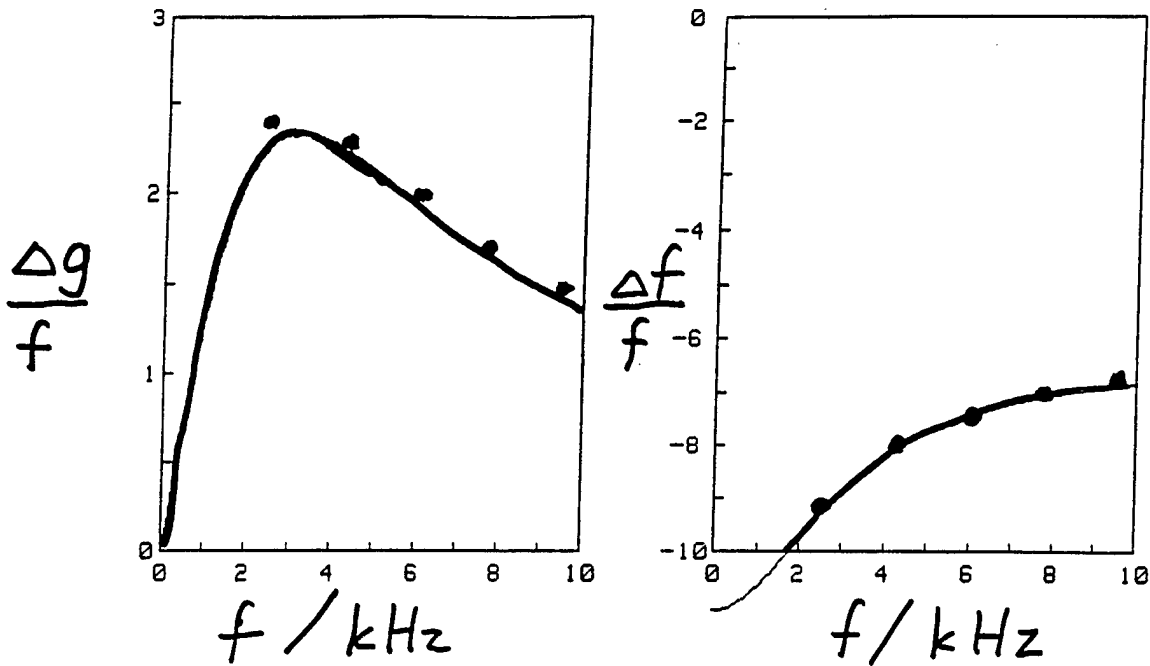
$$\frac{C^2}{a^2} - A_3 p^3 = A_0 + A_1 p + A_2 p^2 + A_{-1} p^{-1}$$

$\begin{matrix} & & 2 \text{ ppm} & & 1 & & 100 \text{ ppm} & & 10 \text{ ppm} & & 2 \text{ ppm} \\ & & \uparrow & & & & \updownarrow & & & & \updownarrow \\ \text{Goodwin, UCL} & & & & 5.40 \pm 0.01 \frac{\text{cm}^3}{\text{mol}} & & & & \text{acoustic elastic} & & \\ & & & & & & & & \text{coef} & & \\ & & & & 5.5 \pm 0.5 \text{ Theory} & & & & & & \\ & & & & 5.24 \pm 0.06 \text{ Data} & & & & & & h = 0.9 \pm 0.1 \end{matrix}$

From table 9 one can conclude, for example, that 1 ppm of water in helium will decrease c_0^2 by 3.93 ppm and that 1 ppm of water in argon will increase c_0^2 by 0.12 ppm.

Table 9. Sensitivity of c_0^2 to impurities

Impurity	M (g/mol)	γ_0	$\frac{1}{c_0^2} \frac{d(c_0^2)}{dx}$	
			in He	in Ar
H ₂	2	1.4	0.23	0.68
He	4	5/3		0.9
H ₂ O	18	1.32	-3.93	0.12
Ne	20	5/3	-4.0	0.5
N ₂	28	1.4	-6.27	0.03
O ₂	32	1.4	-7.3	-0.07
Ar	40	5/3	-9.0	
CO ₂	44	1.4	-10.3	-0.37
Kr	84	5/3	-20.0	-1.1
Xe	131	5/3	-31.8	-2.3
Hg	201	5/3	-49.0	-4.0



$$\frac{\Delta g}{f} = \frac{2X}{15} \frac{\omega\tau}{1 + (\omega\tau)^2}$$

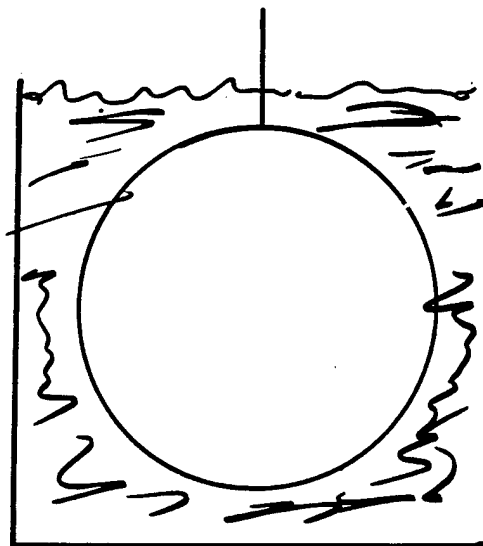
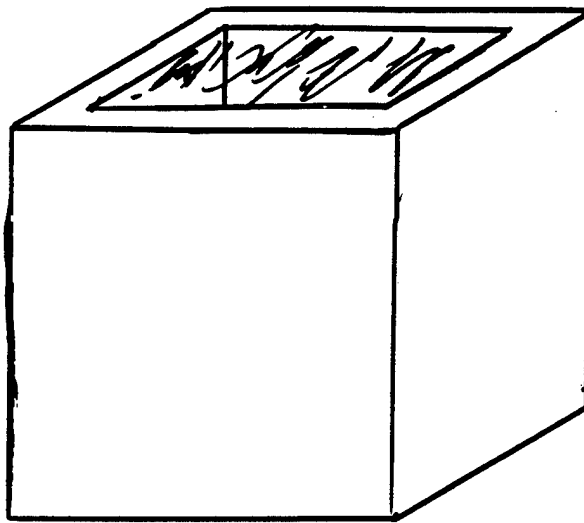
$$\frac{\Delta f}{f} = -\frac{2X}{15} \left[1 + \frac{1}{1 + (\omega\tau)^2} \right] - \frac{X}{20}$$

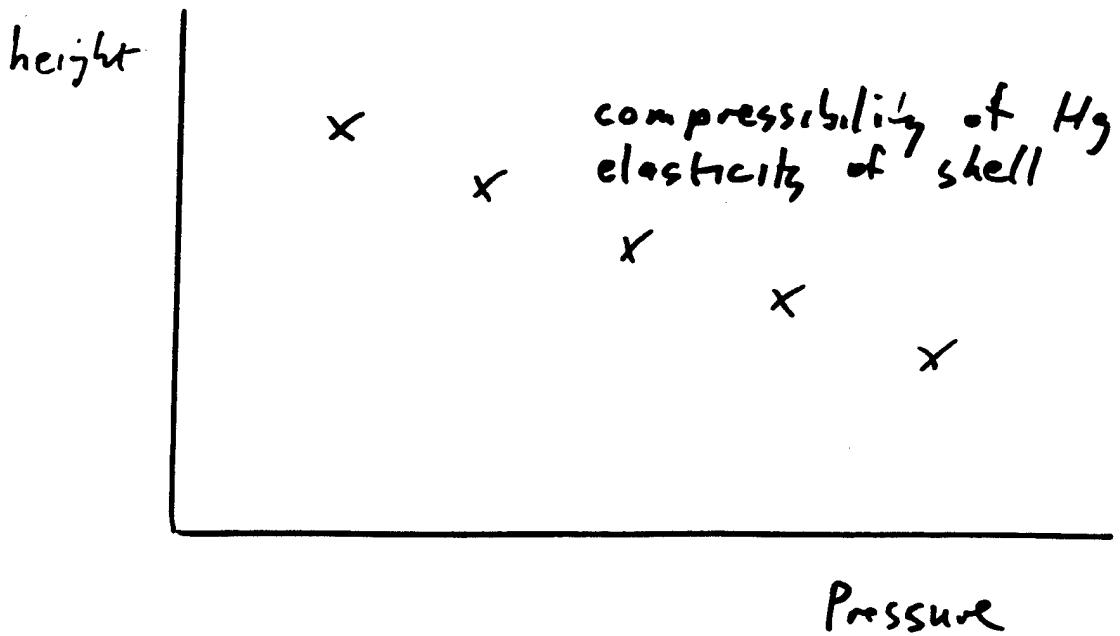
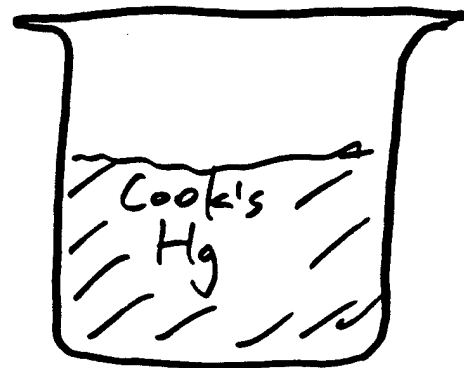
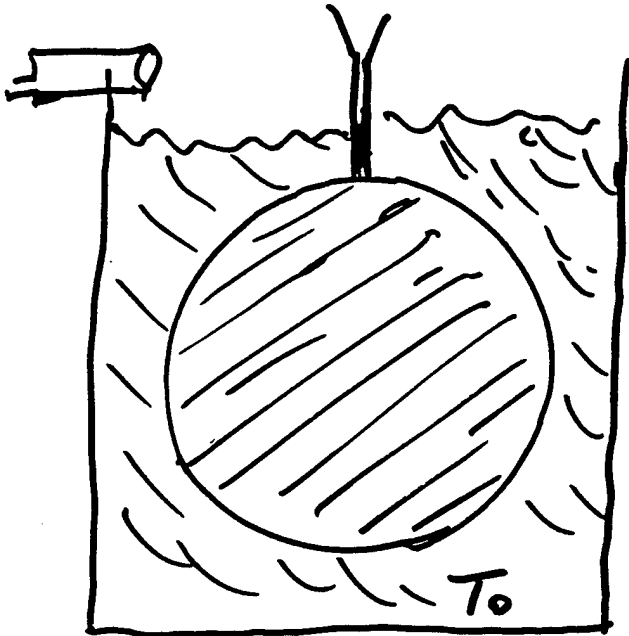
$$X = 35 \text{ ppm}$$

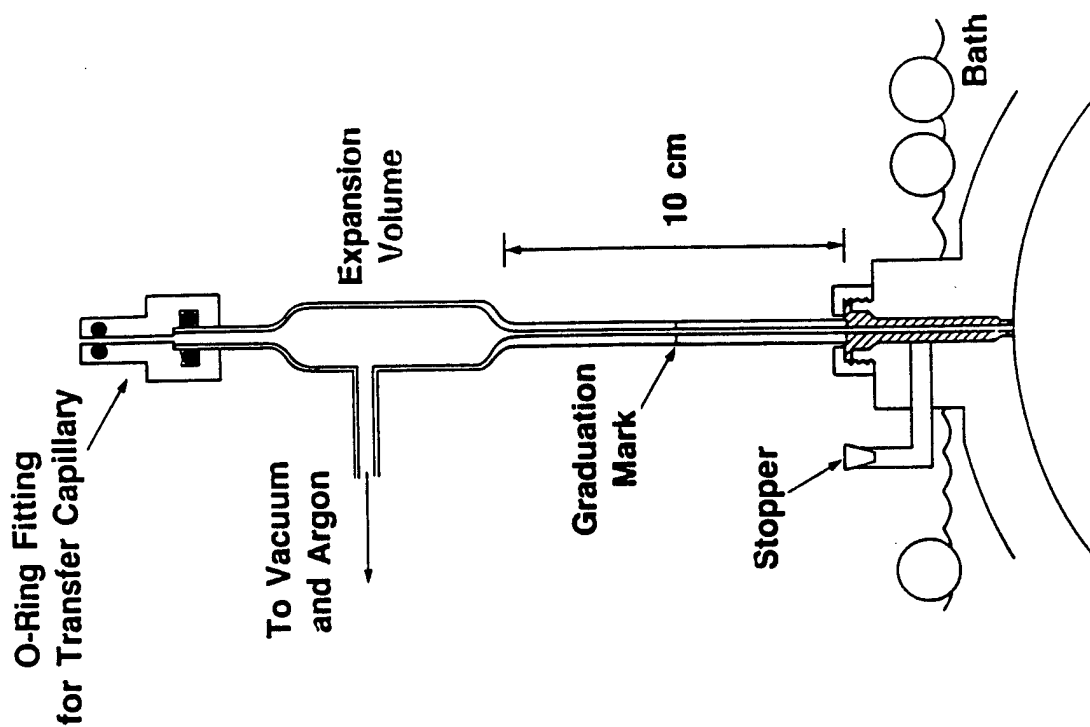
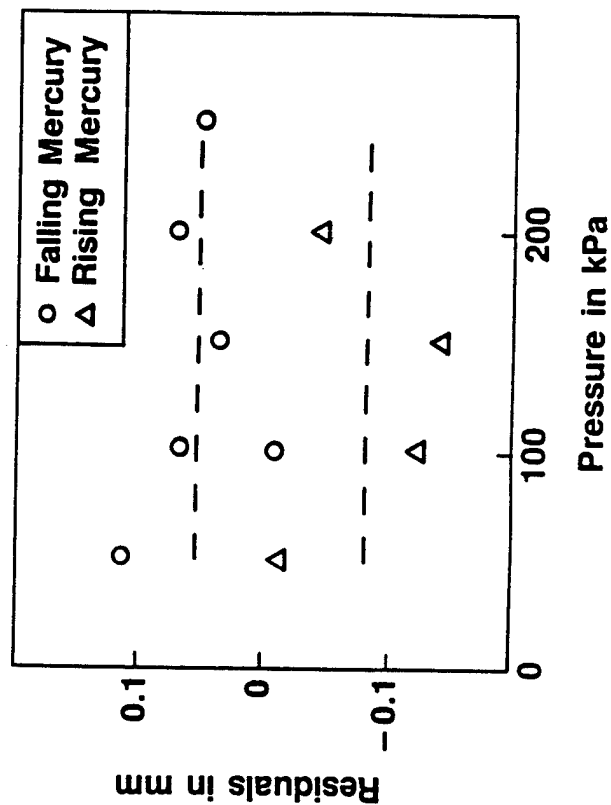
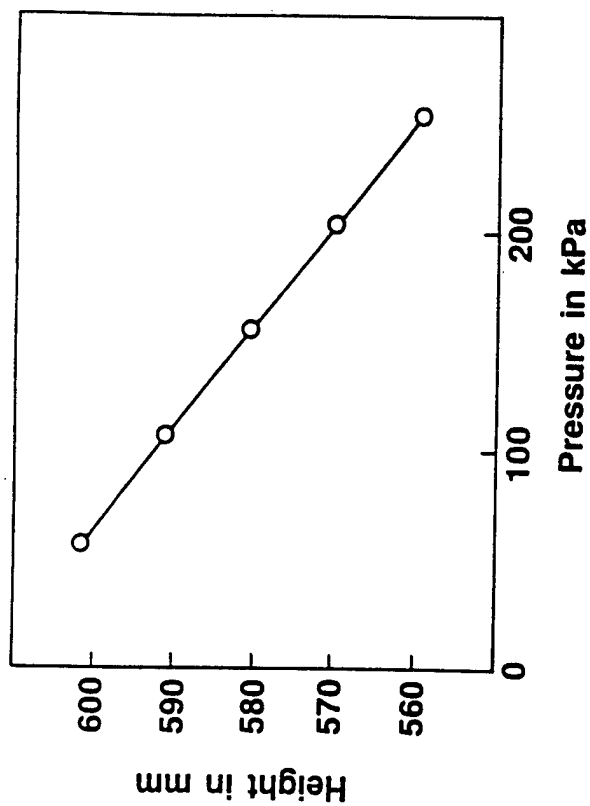
$$\frac{1}{\tau_m} = \frac{1-X}{\tau_{Ar}} + \frac{X}{\tau_{CO_2}}$$

\uparrow \uparrow
 $50 \mu s$ $8 \mu s$

Cook 1955 - 1961







dilute monatomic gas $T_w \equiv 273.16$ exact

$$\frac{1}{2} m \langle v^2 \rangle = \frac{3}{2} k_B T_w \quad \text{defines } k_B$$

$$\frac{1}{2} M \langle v^2 \rangle = \frac{3}{2} R T_w \quad \text{defines } R$$

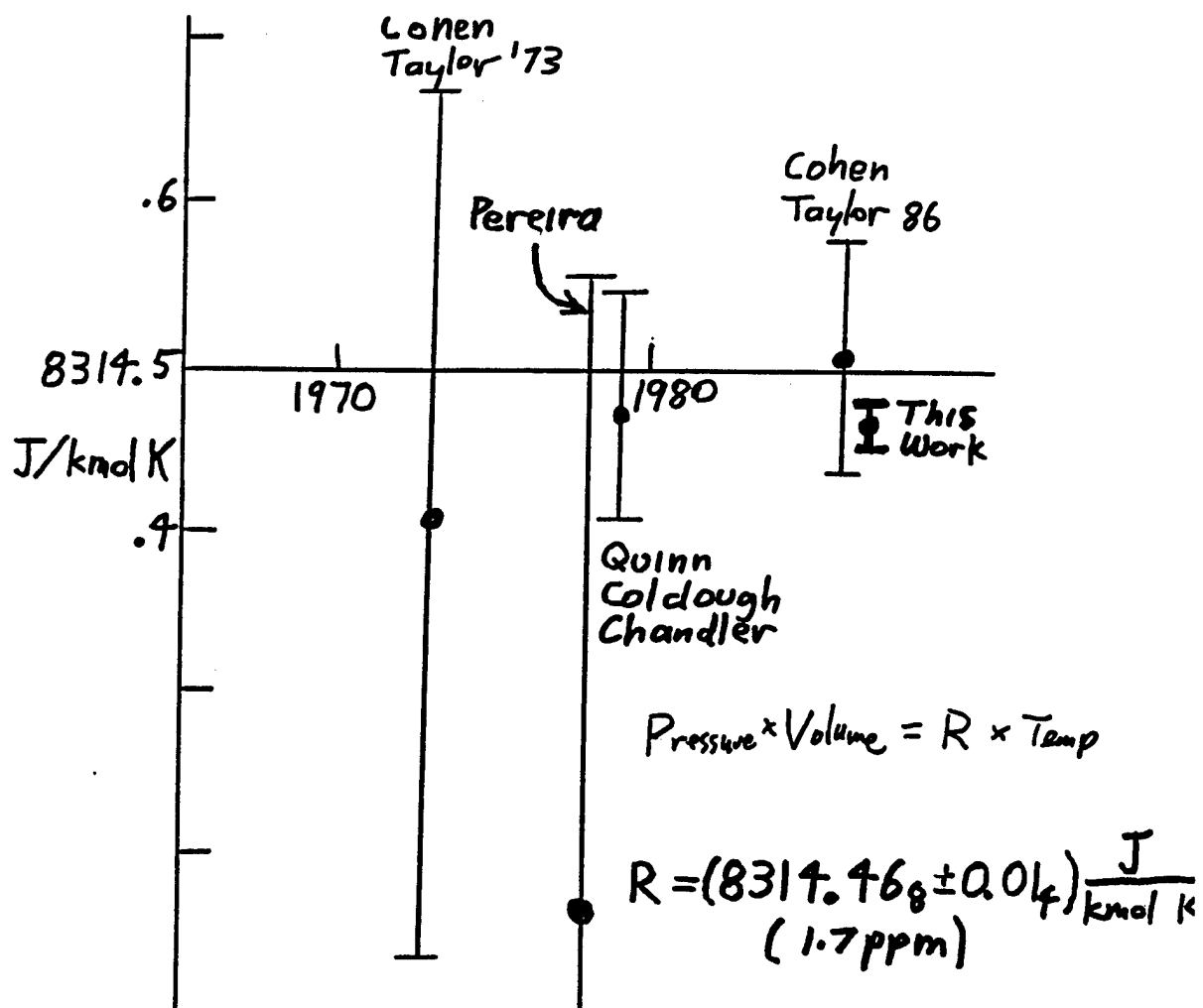
$$\langle v^2 \rangle = \frac{9}{5} c^2 \quad c = \text{speed of sound}$$

$$R = \frac{M c^2}{\frac{5}{3} T_w} = \frac{M (\text{Volume}) \left(\frac{f_n}{\lambda_n} \right)^2}{\frac{5}{3} 273.16000}$$

- ① f_n at T_w in limit $P \rightarrow 0$
- ② Volume at T_w in limit $P \rightarrow 0$
- ③ M
- ④ T_w

Table 1. One-sigma uncertainties (in parts per million) from various sources in the redetermination of R

<hr/>	
I	$(\text{Volume})^{2/3}$
	density of mercury at 20 °C 0.28
	storage and handling of mercury 0.20
	thermal expansion of mercury (0–20 °C) 0.67
	random error of volume measurements 0.20
	corrections from weighing configuration
	to acoustics configuration 0.10
	mass of counterweights 0.14
II	Temperature
	random error of calibrations 0.8
	temperature gradient 0.4
III	M/γ_0
	Ar-40 standard 0.7
	comparison of working gas to Ar-40 0.4
IV	Zero-pressure limit of $(f_{0n}/\nu_{0n})^2$
	s.d. of c_0^2 from 70 observations at 14 pressures 0.68
	thermal boundary layer correction (0.3% of
	thermal conductivity) 0.30
	possible error in location of transducers 0.55
<hr/>	
	Square root of the sum of the squares 1.7
<hr/>	



Asahi

June 13, 1988

気体定数Rの精度

実験で一ケタ向上



一モルの気
体定数Rの精
度がこれまで
よりもほぼ一

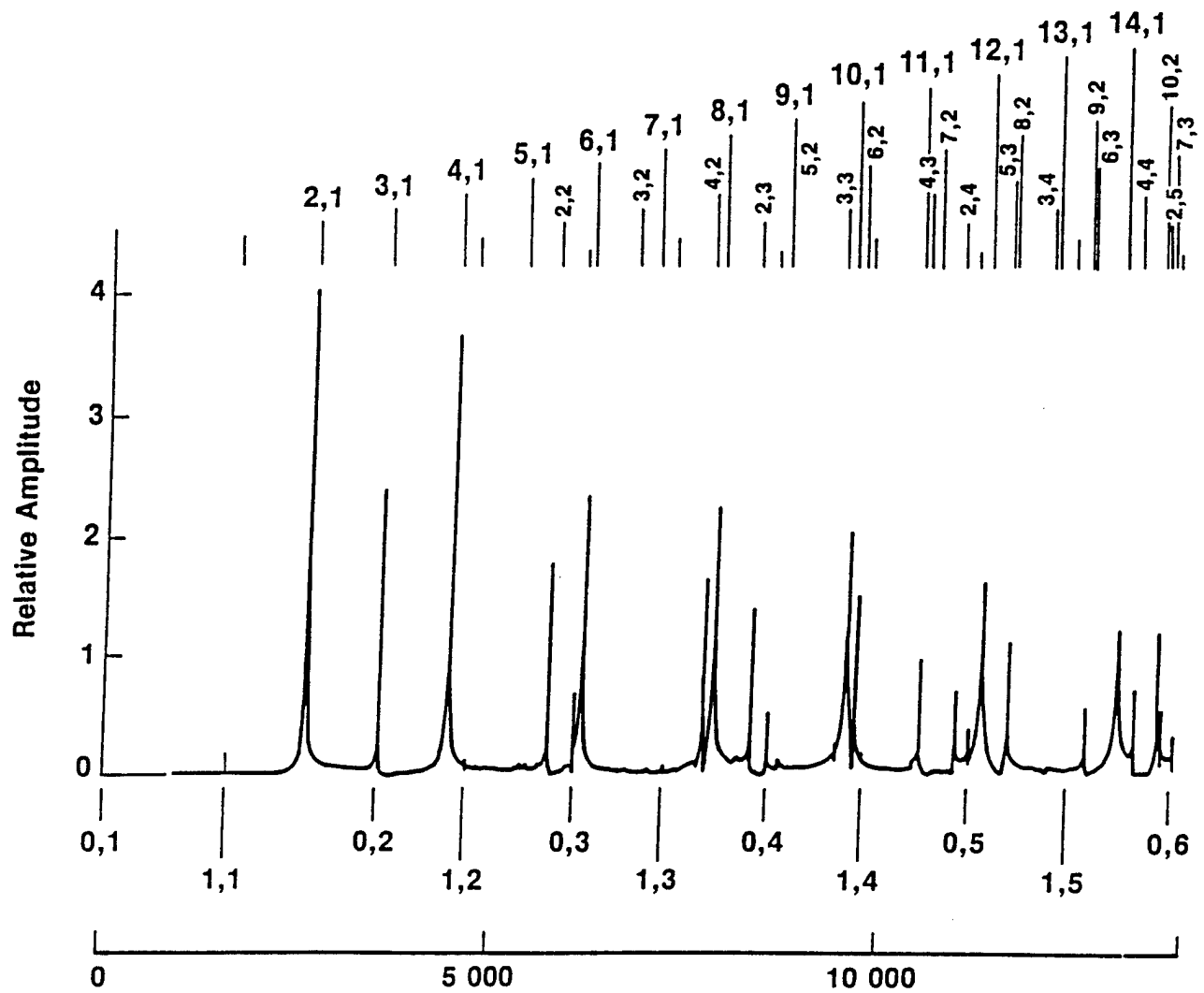
8.314472一ケタ向上し、
8.314472(1)プラスマイナ
ス0.000014(誤差百万
分の一・七)と実験で求められ
たことが、茨城県つくば市で開
かれた電気磁気精密測定会議で
明らかにされた。

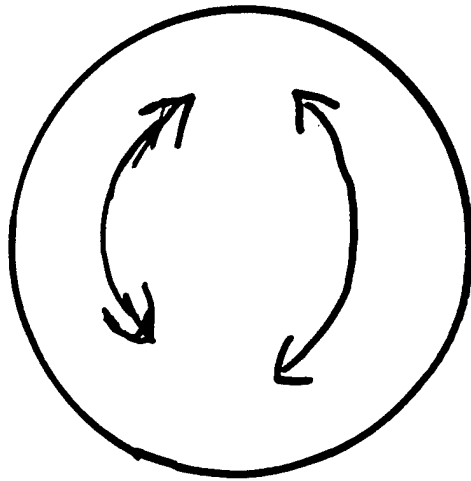
発表したのは米国立標局の
マイケル・R・モールドーバー
博士。三つの球形の器具に薄い
アルゴンガスを満たし、共振周
波数を測定する。ガス濃度をセ
ロに近づけた極限での共振周波
数を出し、正確な体積などとも
にRを求めたところ、一モル

・度あたりのジュール単位での
数値が得られた。

現在使われているRの値は八
・三二四五二〇プラスマイナス
〇・〇〇〇〇七〇(誤差百万分
の八・四)で、二年前に開かれ
た国際学術連合の科学技術諮
会で承認され、八八年版の理科
年表にも載っている。モールド
ーバー博士の求めたRの値は、
従来の値の五倍以上の精度を持
つ。

工業技術院計量研究所の増子
部長を「昨年退いた森村正臣さ
んは「基礎定数の精度を一ケタ
上げる、科学の立場からは画期
的な研究だ。ただし、他の基礎
定数との調整が必要。そのため
の科学技術諮議会が開かれるの
は十年近く先になろう。理科年
表の数値が改められるのも、そ
の後になると想」と語ってい
る。

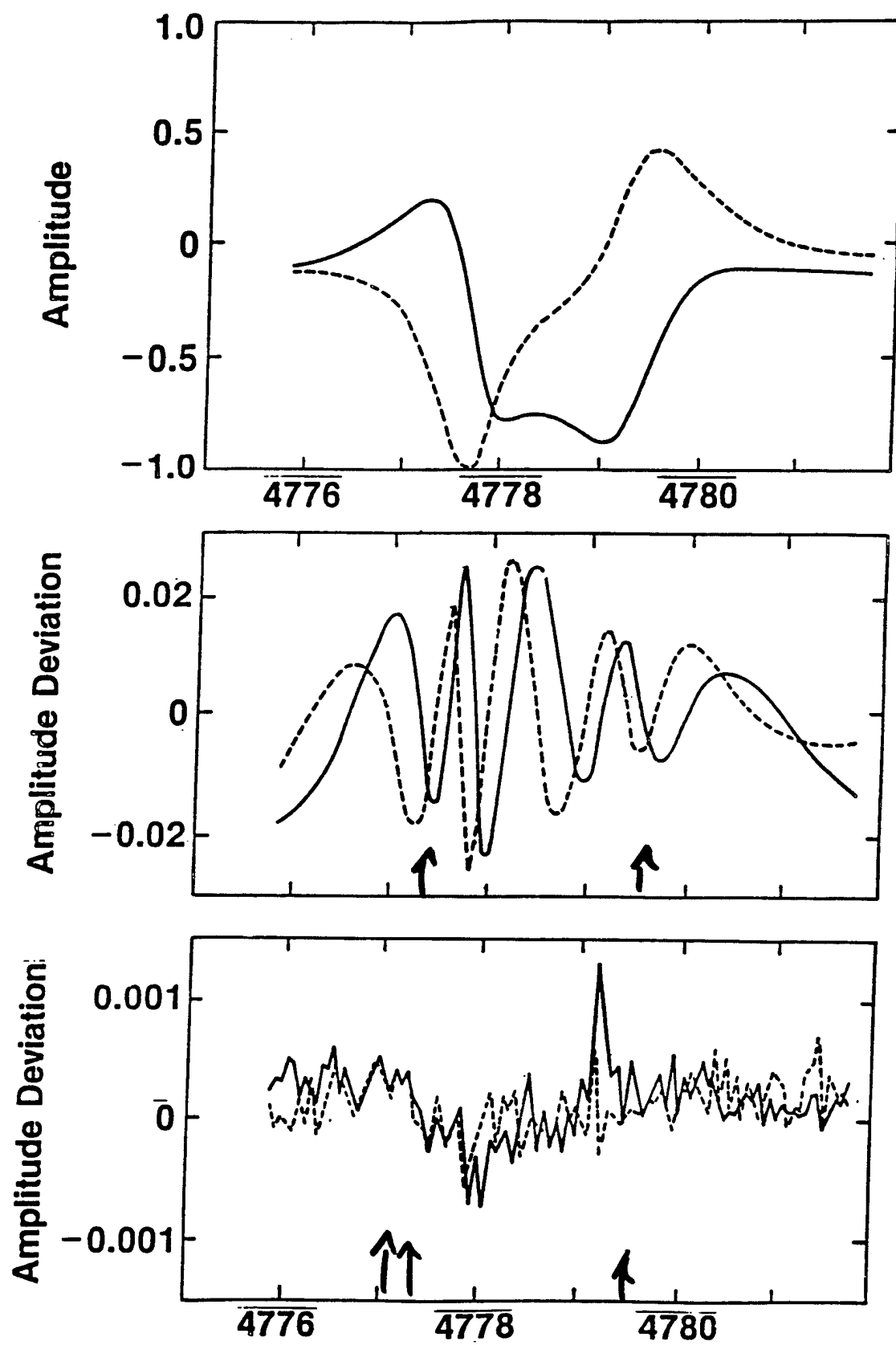


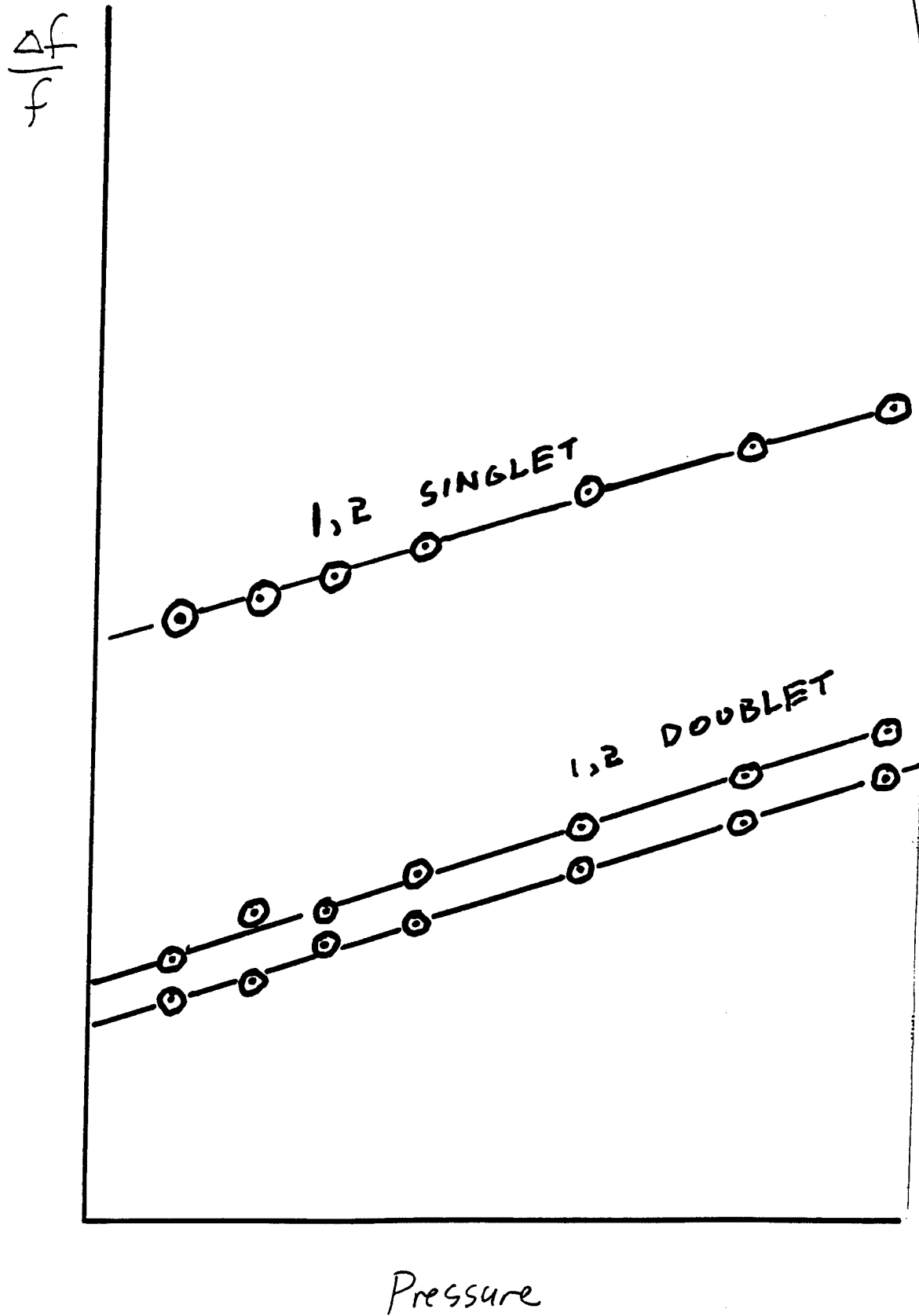


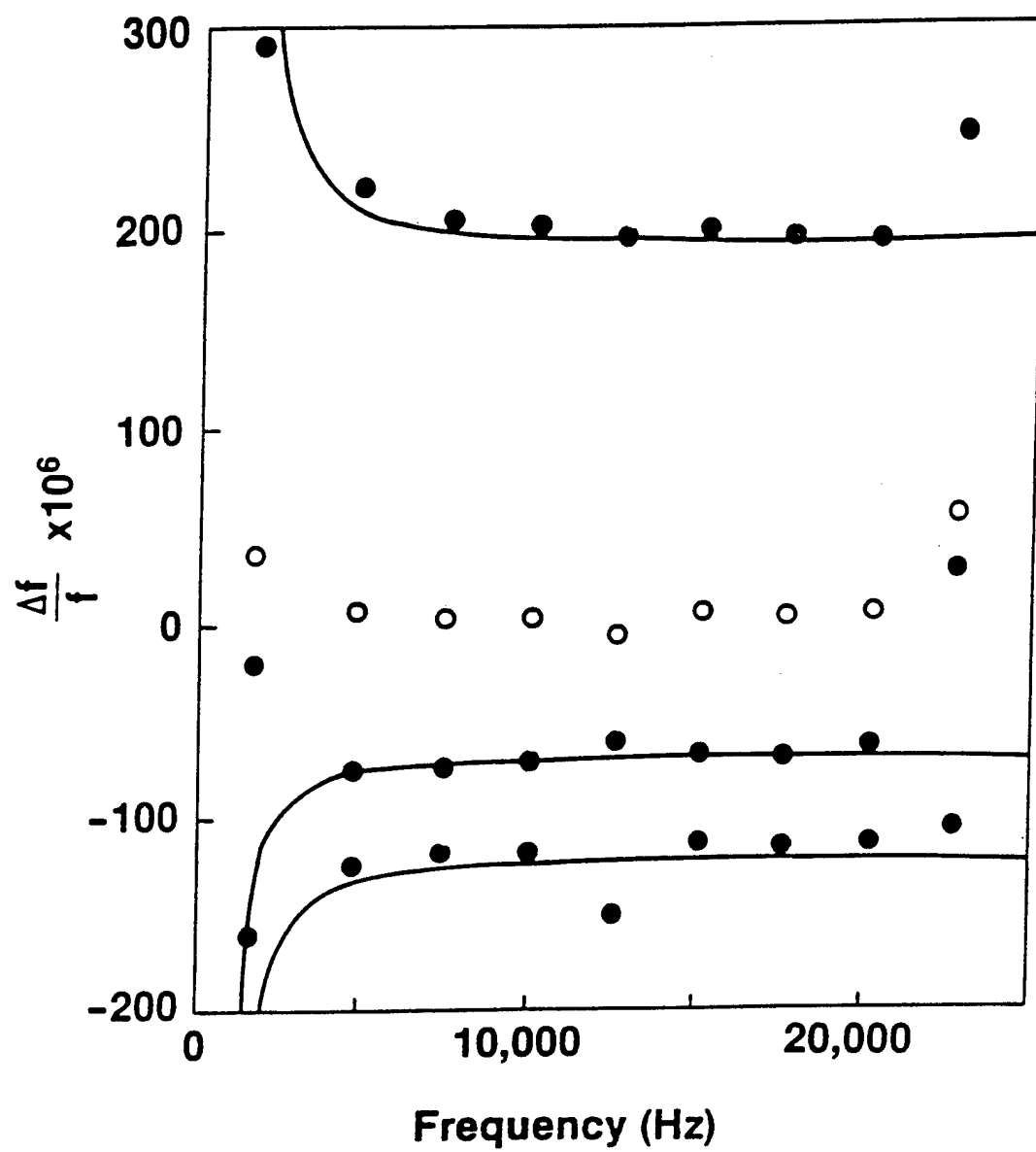
Symmetry of $P_1(\cos \theta)$

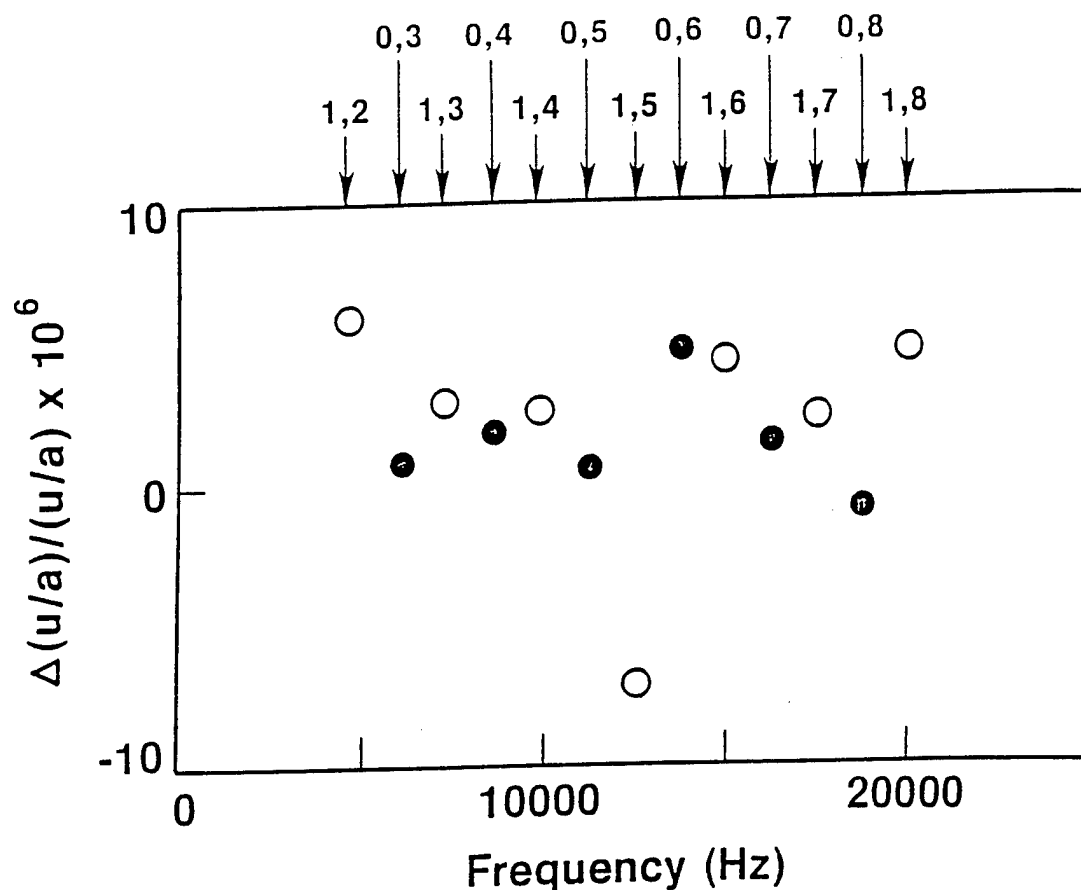
3 fold degenerate

Shell perturbation:
$$\frac{\Delta f}{f} = \frac{M_g}{M_s} \frac{3}{2(\Lambda^2 - 2)}$$









Measurement of the ratio of the speed of sound to the speed of light

James B. Mehl

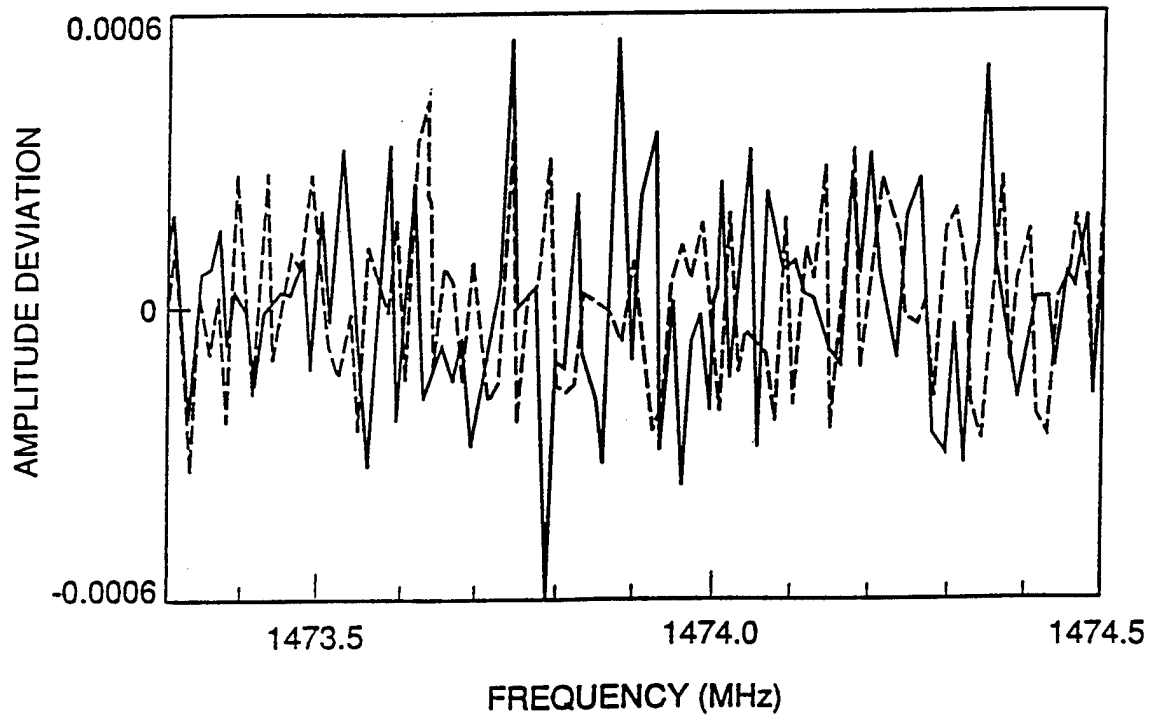
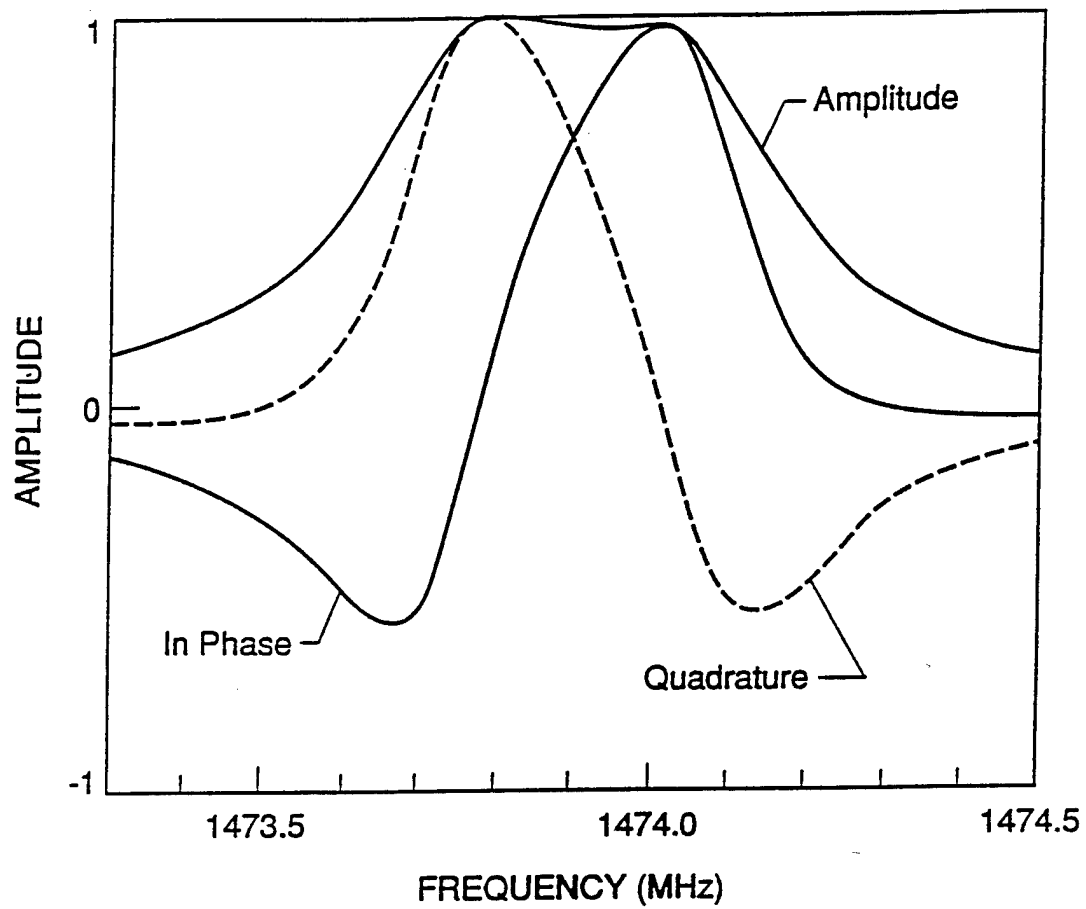
Physics Department, University of Delaware, Newark, Delaware 19716

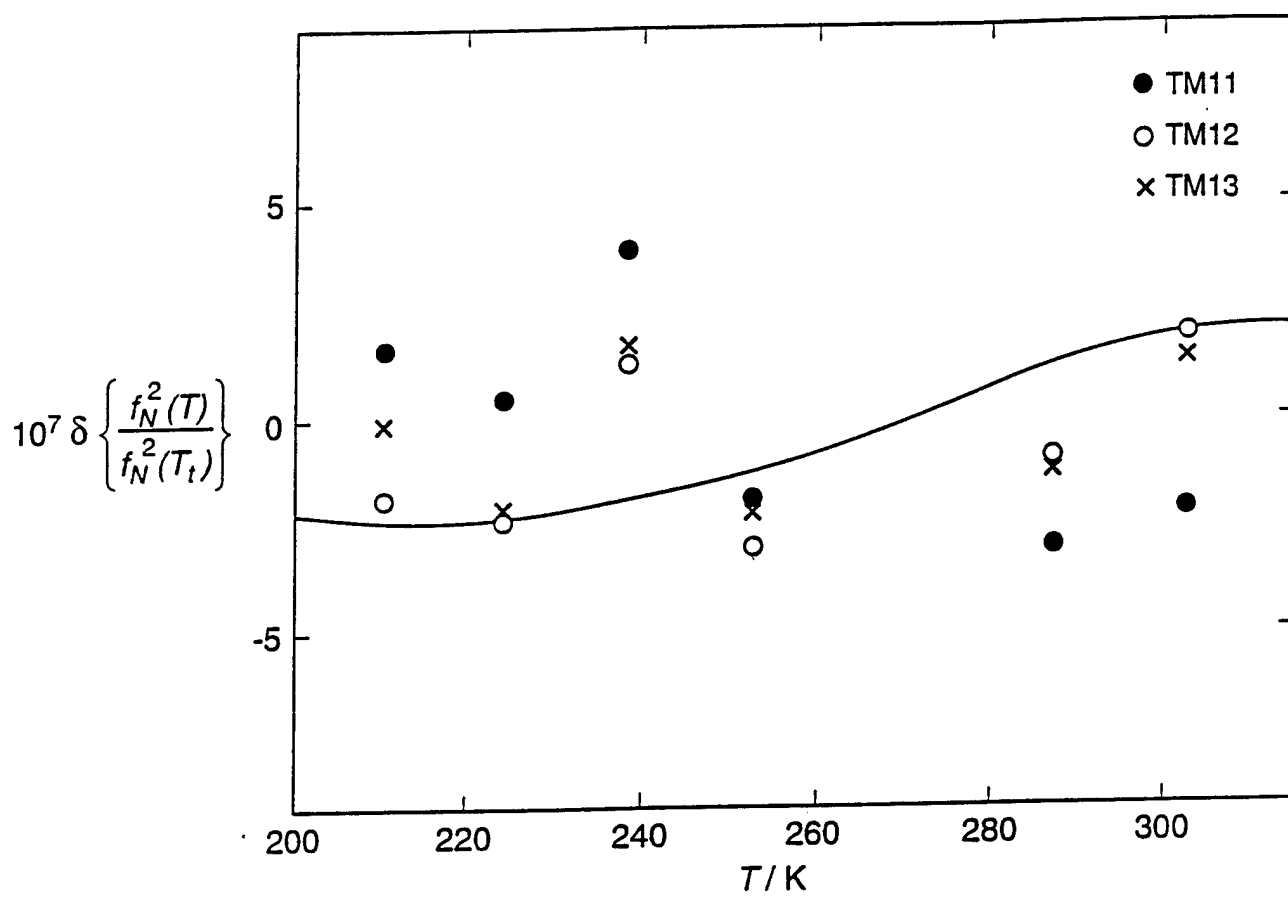
Michael R. Moldover

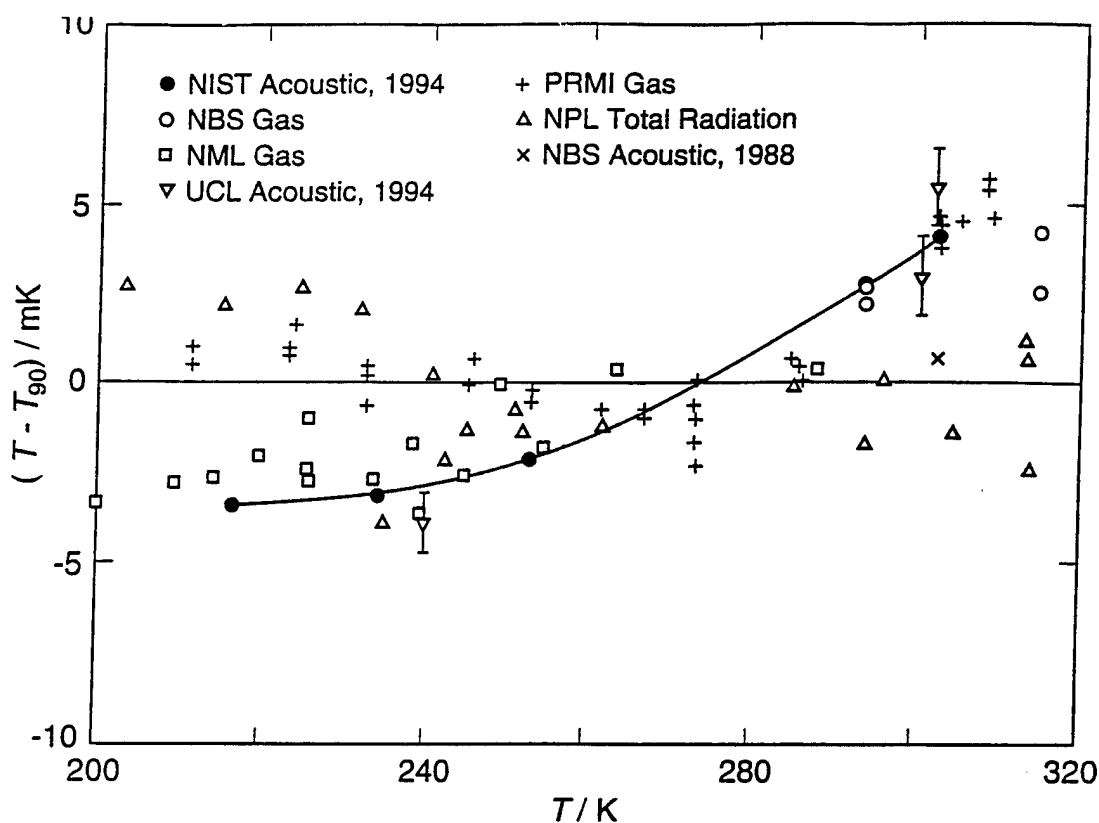
Thermophysics Division, National Bureau of Standards, Gaithersburg, Maryland 20899

(Received 2 June 1986)

Measurements of the resonance frequencies of the acoustic modes and of the microwave modes of a single cavity can determine u/c , the ratio of the speed of sound of a gas to the speed of light. Such measurements with a monatomic gas would determine the thermodynamic temperature T with unprecedented accuracy. By judicious choices of cavity geometry and resonance modes, u/c can be measured to part-per-million accuracy using cavities whose geometry is known only to parts per thousand. These techniques can also be applied to measurements of the universal gas constant R . A measurement of R would also require an accurate determination of the average atomic mass of the monatomic gas.





Table xx: The difference $T - T_{90}$.

T_{90}/K	$T - T_{90}/\text{mK}$ (isotherm fits)	$T - T_{90}/\text{mK}$ (surface fit)
Argon		
302.92	$3.9_3 \pm 0.5_2$	$4.4_6 \pm 0.3_6$
293.13	$2.7_9 \pm 0.4_4$	$3.0_6 \pm 0.2_8$
253.15	$-2.8_3 \pm 0.5_6$	$-2.5_7 \pm 0.2_2$
234.32	$-3.6_7 \pm 0.5_0$	$-3.1_7 \pm 0.2_2$
217.10	$-3.9_5 \pm 0.4_5$	$-3.7_8 \pm 0.2_3$
Xenon ^a		
302.9166	$3.5_2 \pm 0.9_5$	$3.5_3 \pm 0.8_6$

^aErrors for xenon include all of the items listed in Table 1 together with an allowance of 0.4_3 mK to account for the effects of the virtual leak and an allowance of 0.6 mK to account for uncertainty in the values of $A_3(T)$.

Sonic Gas Analyzers

Steven L. Garrett and Matt Golden
Penn State University
and
Robert Keolian
Naval Postgraduate School

OUTLINE

Non-specific gas analysis

Direct applications

Secondary applications (GC)

Historical Perspective

The *Schlagwetter-pfeife*

The rise of the Wheatstone Bridge

Resonator design

Isolate a single mode, suppress overtones

Sensor Applications

● Mine Safety

Mine sealed with 148 still inside

BY NIKOS KONSTANDARAS
Associated Press

KOZLU, Turkey — Despite appeals from weeping family members waiting at the surface, officials sealed off the Kozlu coal mine yesterday, ending all hope for 148 miners trapped one-third of a mile underground.

In Turkey's worst mine disaster,

mulation of poisonous gas made it perilous to enter the shaft.

"No one down there is alive. Yesterday, they brought some injured, but not today," said medic Sabahattin Oztas as he watched a truck dump tons of dirt on the steel-covered pit.

Miners took turns shoveling the dirt in order to starve the mine of oxygen.

Yesterday, headlines in Turkish newspapers said the disaster could have been averted. The stories said computers had showed increasing accumulation of methane gas at the pit, but that management failed to evacuate the mine.

State Minister Omer Barutcu said an early-warning system did not work because methane gas increased to the dangerous level just

● Agricultural Chemical

Methyl bromide warnings requested

BY BETSY LORDAN
Herald Staff Writer

A legal-aid group for farmworkers has sent a letter to Central Coast strawberry growers asking them to warn neighbors 21 days before they use the powerful soil fumigant methyl bromide.

Growers are not obligated legally to provide such warnings, said Michael Meuter, a lawyer in the Salinas office of California Rural Legal Assistance.

quent the area is part of being a good neighbor, Meuter said.

"I think if growers want to notify their neighbors and people that are nearby about their applications, they are free to do that," said Richard Nutter, Monterey County agricultural commissioner. "But there is no legal requirement that would make them responsible for doing that."

Because growers would warn their neighbors voluntarily, the Agricultural Commissioner's

Without H3rm, a group opposed to methyl bromide use. "People have the right to know that toxic chemicals are being used in their back yard."

The CRLA sent the letters to 375 Central Coast strawberry growers who have permits to use methyl bromide. Along with the letters, growers received a suggested warning that they can use or modify.

Included in the warning are:
■ A list of symptoms for those

local and state agencies that handle pesticide emergencies.

Growers also received a warning-zone table for methyl bromide developed by the California Department of Pesticide Regulation; the table is not used by regulators under current law. For example, if a grower treats 10 acres at a rate of 250 pounds per acre, the table recommends that anyone who frequents the zone within a 1-mile radius should be warned.

Meuter said that under Califor-

Pete Wilson's office. F advocates, environmentalists who oppose methyl bromide argue the use of growers is based on rather than scientific.

"That's probably true," said. "But (the dual) the reality of things."

As for the warning, Nutter said, "I don't know if information that would justify notification with"

Because it poses a use of methyl bromide

● Other obvious applications

Electric vehicles (H₂)

Chemical synthesis (e.g., H₂ in NH₃ or Cl₂)

Blast furnaces and metals processing (H₂)

Ethylene oxide in medical equip. sterilization

ARL - Penn State

S. Garrett

Sonic Gas Analysis

Sound Speed in Gas Mixtures

- Equipartition Theorem

Each quadratic degree of freedom gets $k_B T/2$

Communism is not dead!

Temperature is related to kinetic energy

Pythagorean sum: $\langle v^2 \rangle = \langle v_x^2 \rangle + \langle v_y^2 \rangle + \langle v_z^2 \rangle$

Symmetry: $\langle v_x^2 \rangle = \langle v_y^2 \rangle = \langle v_z^2 \rangle = (1/2)k_B T/m$

- Adiabatic Sound Speed

$$a^2 = \gamma \frac{RT}{M}$$

- Sound Speed in Gas Mixtures

Mean molecular mass

$$M_{\text{mix}} = x M_1 + (1-x) M_2$$

Mean polytropic coefficient

$$\gamma_{\text{mix}} = \frac{x C_{p,1} + (1-x) C_{p,2}}{x C_{v,1} + (1-x) C_{v,2}} \neq x \gamma_1 + (1-x) \gamma_2$$

Approximate sound speed ratio

$$\frac{a_{\text{mix}}^2}{a_1^2} \cong \frac{1 + [(\gamma_2 - \gamma_1)/\gamma_1]x}{1 + [(M_2 - M_1)/M_1]x}$$

Sensitivity analysis for resonance freq. shift, δx

$$\frac{\delta f}{f_1} = \frac{\delta a_{\text{mix}}}{a_1} \cong \left[\frac{(\gamma_2 - \gamma_1)}{\gamma_1} - \frac{(M_2 - M_1)}{M_1} \right] \frac{\delta x}{2} \equiv \beta \delta x$$

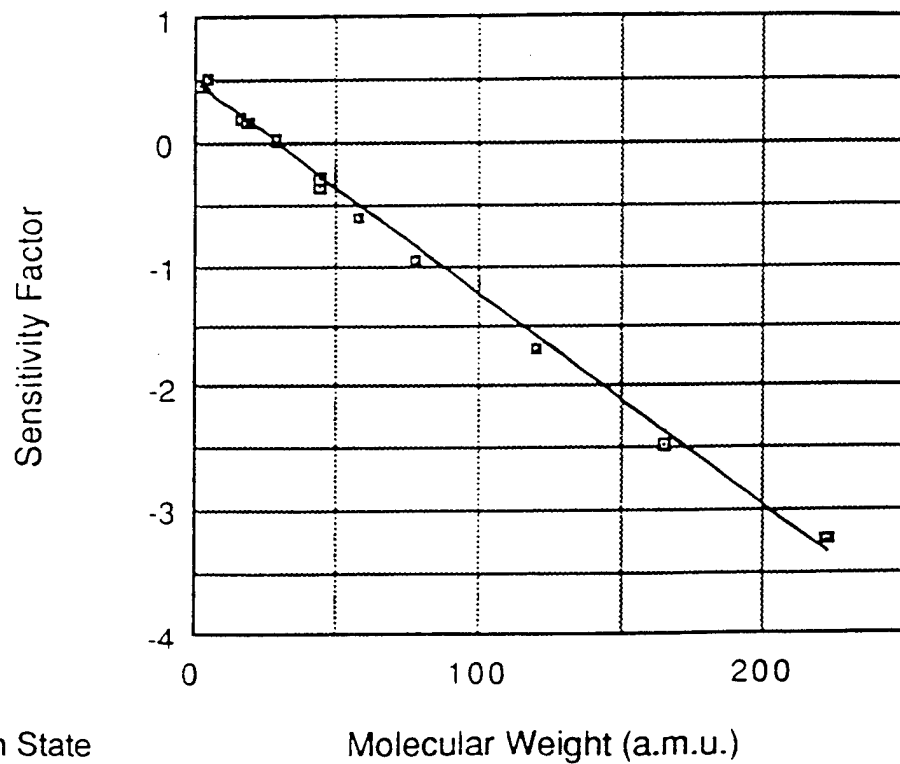
Sensitivity in Air

● Approximate sensitivity factor

Assume γ -factor is small

$$\beta = \frac{1}{f} \left(\frac{\partial f}{\partial x} \right)_{T,P} \cong \frac{M_2 - M_1}{2M_1}$$

Results for various gases in air



ARL - Penn State

Molecular Weight (a.m.u.)

S. Garrett

Sonic Gas Analysis

Schlagwetter-pfeife

- German mine safety whistle (1884)

Pump mine exhaust through a whistle

Wavelength, $\lambda = 2L$ for an open-open pipe

Frequency, $f_1 = a/\lambda = a/2L$

- Methane frequency shift

Molecular weights

$$\frac{M_{\text{methane}} - M_{\text{air}}}{M_{\text{air}}} = \frac{16.043 - 28.964}{28.964} = -0.446$$

Polytropic coefficients

$$\frac{\gamma_{\text{methane}} - \gamma_{\text{air}}}{\gamma_{\text{air}}} = \frac{1.31 - 1.403}{1.403} = -0.0663$$

Relative frequency shift

$$\frac{\delta f}{f_{\text{air}}} = \frac{\delta a_{\text{mix}}}{a_{\text{air}}} \approx 0.38 \frac{\delta x}{2} = 0.19 \delta x$$

Example: 1% Methane ($x = 0.01$)

Assume $f_{\text{air}} = 440$ Hz, $L = \lambda/2 = 39.2$ cm, $\delta f = 0.84$ Hz

What is x for an explosive mixture?

- Temperature compensation and “detection”

Use two whistles in good thermal contact

Listen for beat frequency $f_{\text{beat}} = f_{\text{mine}} - f_{\text{air}}$

S. Garrett

Sonic Gas Analysis

(Almost) Thermal Conductivity Theory

• Thermal Conductivity

Simple kinetic theory model

$$K = \frac{K_o}{\Omega \sigma^2} \sqrt{\frac{T}{M}}$$

Also related to thermal molecular speed

Square-root absolute temperature dependence

Pressure independence at "normal" pressures

Complex combination of constants

 σ = Characteristic molecular diameter (Angstroms) Ω = Collision function of $k_B T/\epsilon$ (tough calculation)

$$K_o = 1.9891 \times 10^{-4} \text{ cal } \text{\AA}^2 \text{ gm}^{1/2} \text{ sec}^{-1} \text{ } ^\circ\text{K}^{-3/2}$$

• Requires off-equilibrium measurement

Extremely dependent upon experimental conditions

"Probably the principal limitation upon the usefulness of the method is the fact that one can not calculate the significance of the indications obtained, but must, in every case, depend upon empirical calibration under conditions closely approximating those of actual service."

Nat. Bur. Standards, Tech. Paper No. 249 (1924)

Irreversible transport process

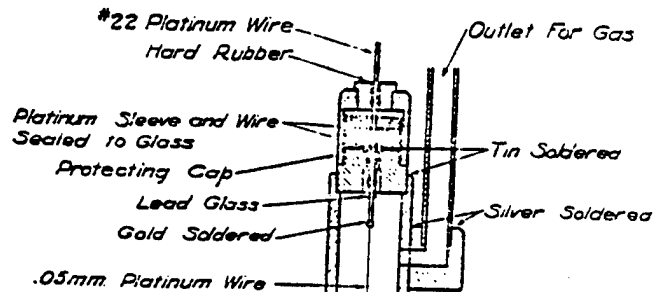
No resonant enhancement, $Q = 1/2$

S. Garrett

Sonic Gas Analysis

Gas Thermal Conductivity Sensor

- “Hot wire” cell at right



- Wheatstone Bridge detector below

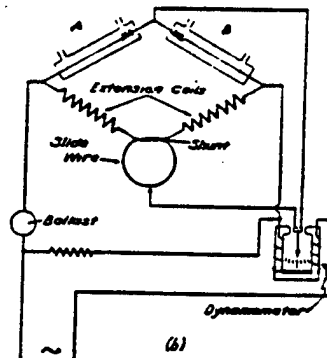
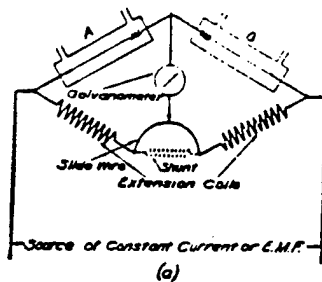


FIG. 21.—Balanced Wheatstone bridge.

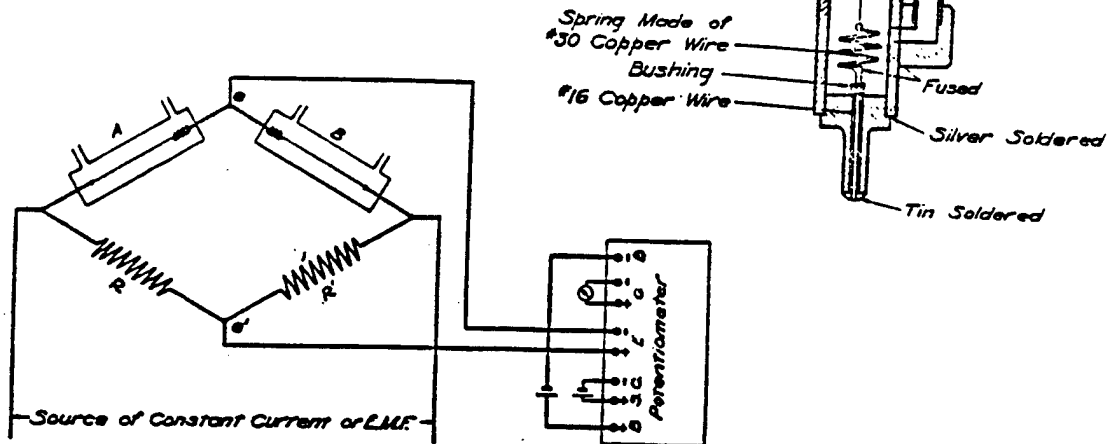


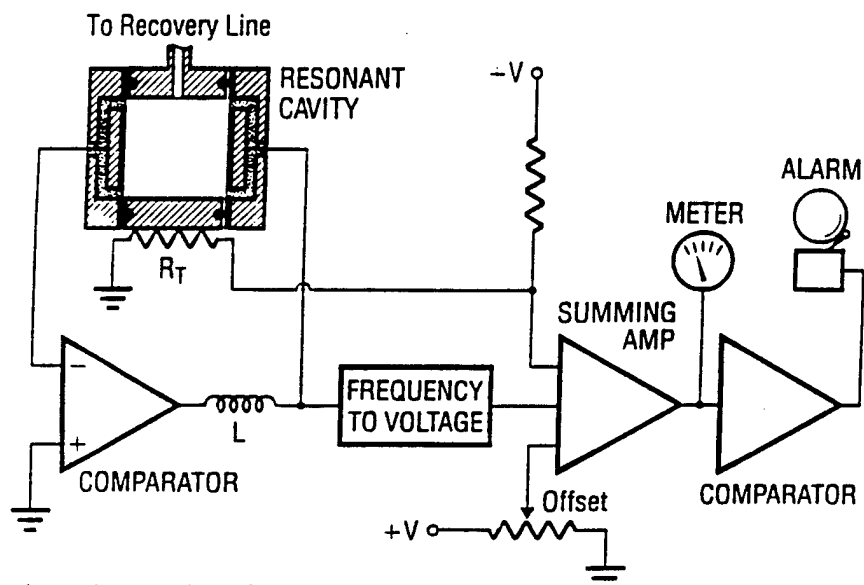
FIG. 20.—Unbalanced Wheatstone bridge with potentiometer.

S. Garrett

Sonic Gas Analysis

Resonant Sound Speed Measurement

- Complete system for Helium Recovery Air Alarm
Garrett, *et al.*, *Physica* **107B**, 601 (1981)

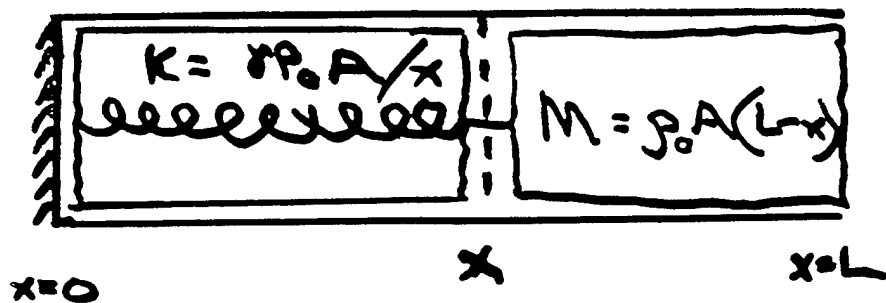


- "Technology Push"
 - Precision/Cost ratio
 - For frequency, 10 ppm \approx \$20, based on quartz watch
 - 5-digit voltmeter \approx \$1,000
 - Availability of cheap transducers
 - Electret microphone \approx \$0.59 (1000's)
 - Earphone sound source \approx \$0.20 (100's)
 - Availability of cheap circuit components
 - Voltage controlled oscillators \approx \$1.00 (1000's)
 - Multiplier chips (*e.g.*, AD633) \approx \$5.00 (100's)
 - Digital output (frequency)
 - More compatible with analysis and display hardware
 - No A/D conversion required

CHEAP RESONATORS



CHEAP THEORY

CLOSED - OPEN PLANE WAVE

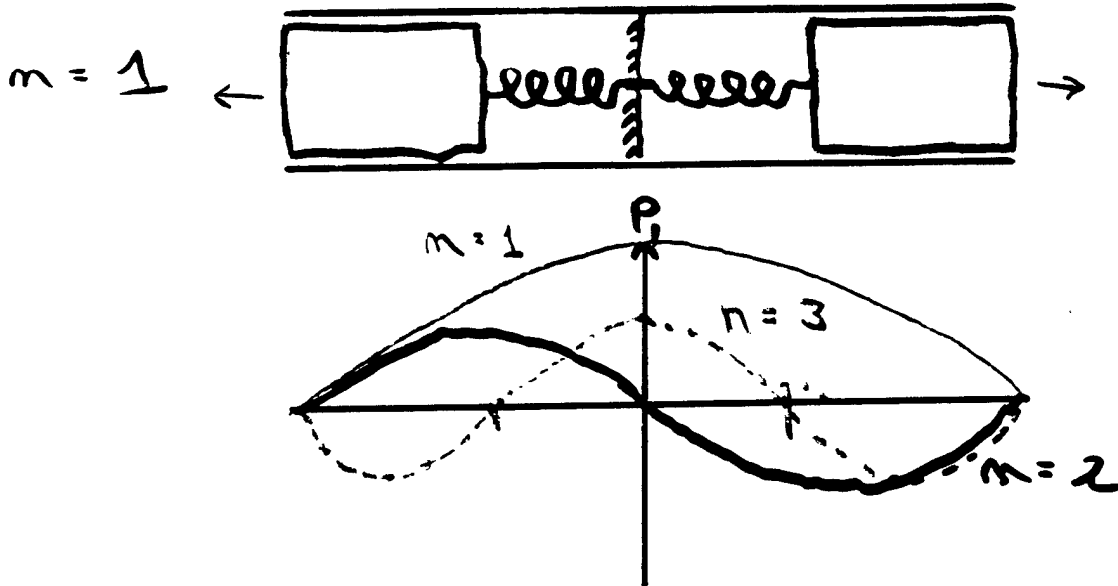
1. Stiffness depends only on P_0
2. Mass depends on molecular weight

$$\rho_0 = \frac{P_0 M}{RT}$$

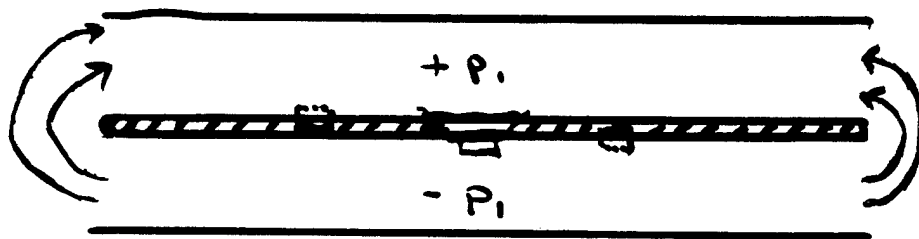
3. Frequency is independent of P_0
4. The "tip" is most sensitive

OPEN-OPEN DIPOLE

Open-open modes



Dual Resonator



No transducer pressure sensitivity

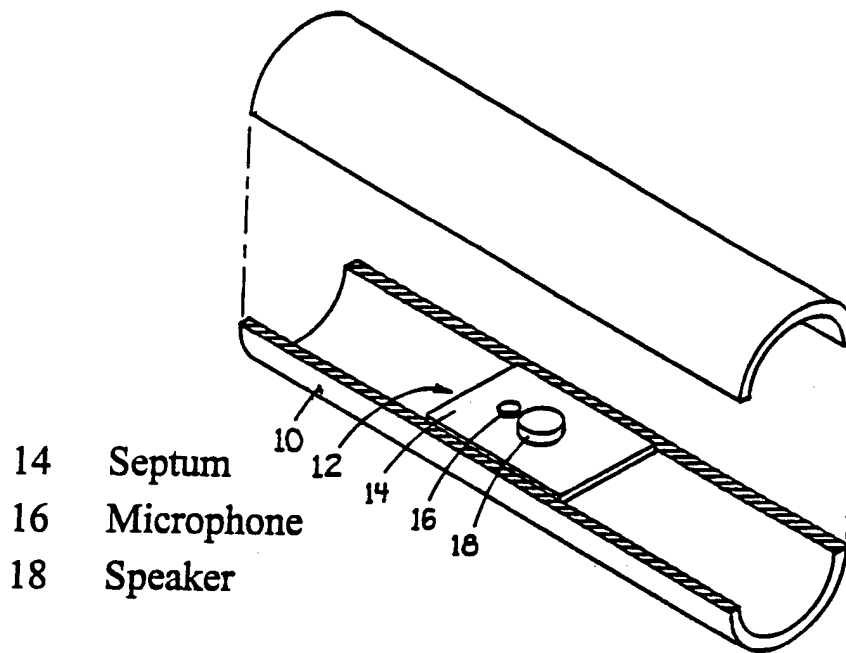
No "back volume" trapping

S. Garrett

Sonic Gas Analysis

Novel Resonator Geometries

- Basic Dual Half-Wavelength Dipole Design



- Mode suppression

Does not drive even modes

Mike located at pressure node for 3rd mode

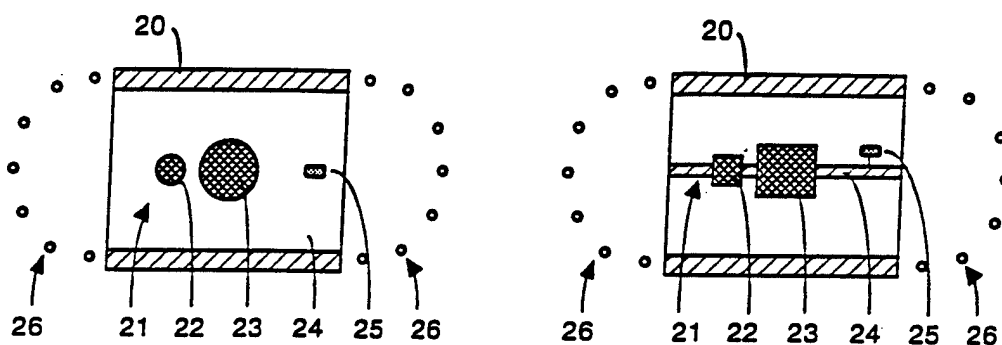
Dipole drive localizes flow at edge

Dipole gas motion is below cut-off for open tube

Dipole mike is insensitive to incident plane waves

*S. Garrett***Sonic Gas Analysis****Other Enhancements**

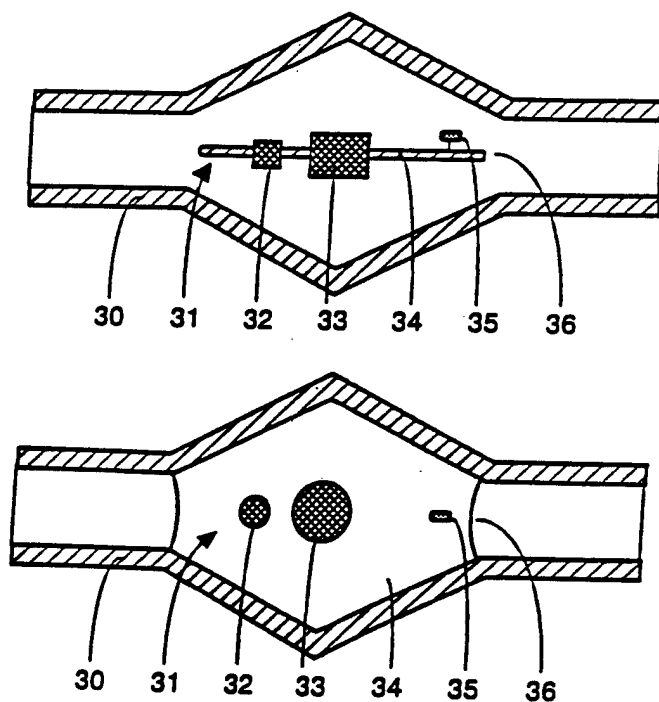
- **Short Screened End**



25 Electronic thermometer (e.g., thermistor)

26 Screen to prohibit physical frequency modification

- **Quasi-Helmholtz**



*S. Garrett***Sonic Gas Analysis**

Summary

- **Advantages of Sonic over TC gas analyzers**
 - Resonant signal enhancement
 - Quality factor, $10 > Q > 1000$
 - Calculable response independent of "drive level"
 - Gas flow rate is not a problem
 - Recent availability of new components/transducers
 - High precision-to-cost ratio
 - Intrinsically digital (frequency) output
 - Expanded processing and telemetry options
 - Infinite lifetime
 - No element burn-out or chemical regeneration
 - Pressure independent
 - Second virial coefficient gives 38 ppm/psi
 - Also advantage of thermal conductivity analyzers
- **Disadvantages of Sonic (also shared by TC)**
 - Non-specific
 - A problem if there are many possible "contaminants"
 - Humidity can be a problem
 - Requires active temperature compensation
 - Much easier for sonic, but still required
 - Humidity changes effect frequency
 - $\pm 20\%$ change in RH give ± 800 ppm in frequency
 - May require humidity compensation

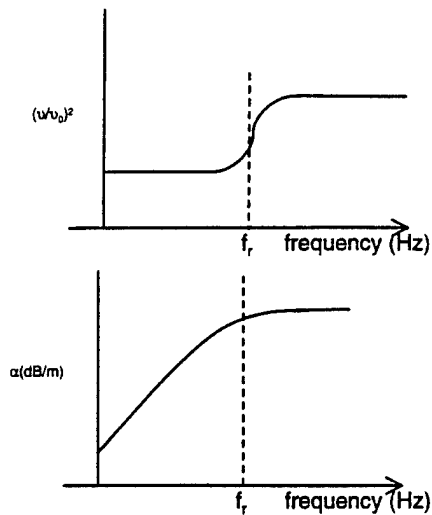
**Measurements of Relaxation Processes
in Gases and Liquids
Using Resonance Systems
by
Henry E. Bass**

**Jamie L. Whitten National Center for Physical Acoustics
The University of Mississippi
University, MS 38677**



*The
University of Mississippi*

Absorption and Dispersion Due to Microscopic Processes



f_r related to relaxation or reaction time/rate

Magnitude of dispersion/absorption related to concentration,
heat of reaction



The
University of Mississippi

Dispersion and Absorption Can be Small

$$\frac{\nabla v}{v} \text{ for } N_2 \approx 1 \times 10^{-4}$$

$$\alpha \text{ for air @ 1 kHz} \approx 2 \times 10^{-3} \text{ dB/meter}$$

$$\text{for seawater @ 10 kHz} \approx 10^{-3} \text{ dB/meter}$$



The
University of Mississippi

Resonators

Gases

Evans/Parker

Cylindrical Tube

Rectangular Room

Liquids

Fisher

Cylindrical Tube

Spherical Resonator



The
University of Mississippi

Definition of Terms

α Absorption/unit length

$\delta = \alpha c / \pi$ Width of Resonance Peak
(Half power points)

$Q = \frac{f_r}{2\delta}$ Quality of resonance

T Time required for Energy Density
to decay 60dB = $\frac{0.161V}{SA}$
Reverberation Time



The
University of Mississippi

Boundary Effects

- Absorption of Sound in Tube

Wall Loss Proportional to $\frac{1}{R} \cdot f^{\frac{1}{2}}$

- End Loss Few % of Wall Loss

$$\delta = B\sqrt{n}$$

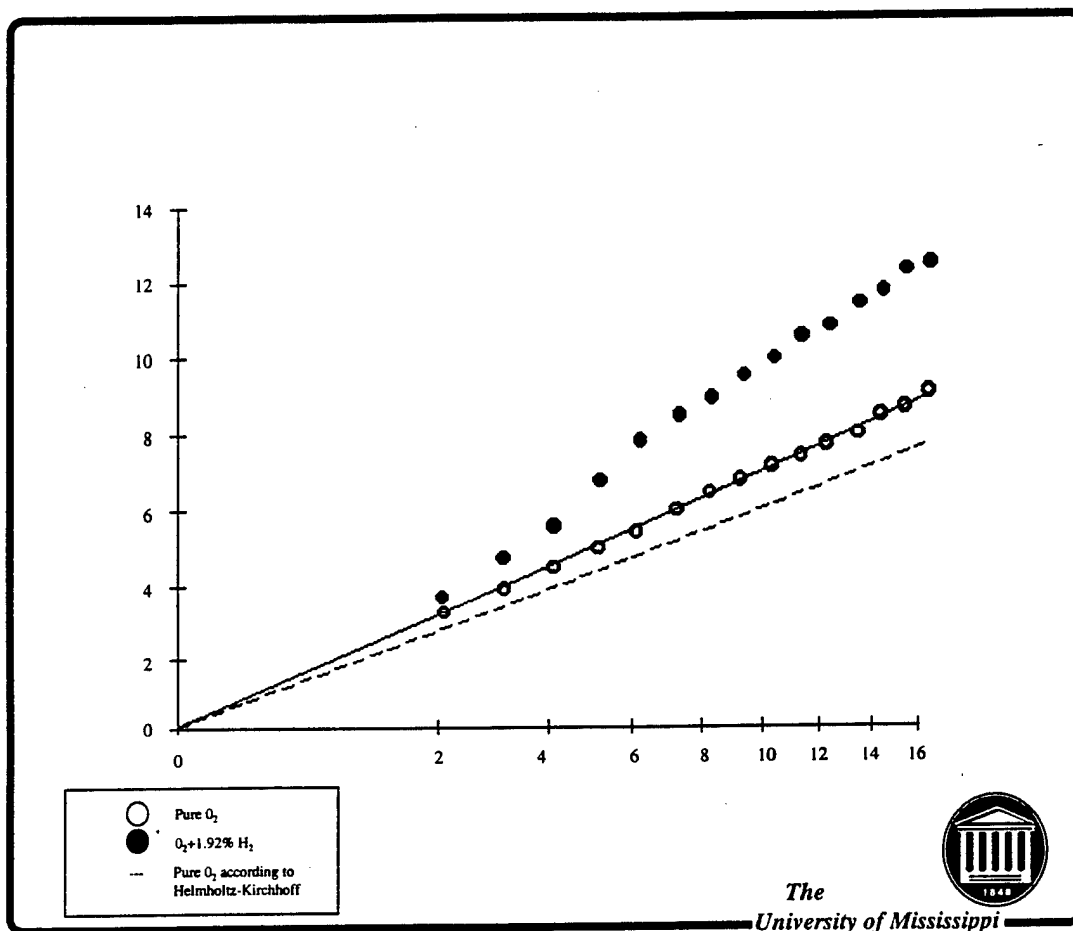
- Other Sources of Bulk Absorption

Viscosity and Thermal Conduction

$\delta_b / \delta_w \sim 10^{-3}$ Typical for Tubes - Larger for Sphere



The
University of Mississippi



Interpretation of Results

$$\delta = \delta_{\omega} + \delta_v$$

$$\delta_v = \left(RC_i / C_p^{\infty} C_v^{\infty} \right) \left[f_o f^2 / (f_o^2 + f^2) \right]$$

- Determine δ_{ω} from pure O_2 measurements
- Determine f_o from δ_v

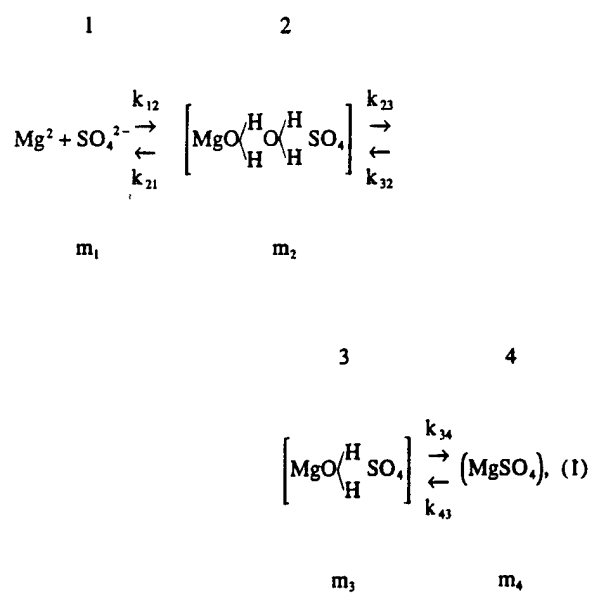
$$f_o = 1240 \text{ Hz for } X=1.92\%$$

$$\text{Collision number } 2 \times 10^3$$



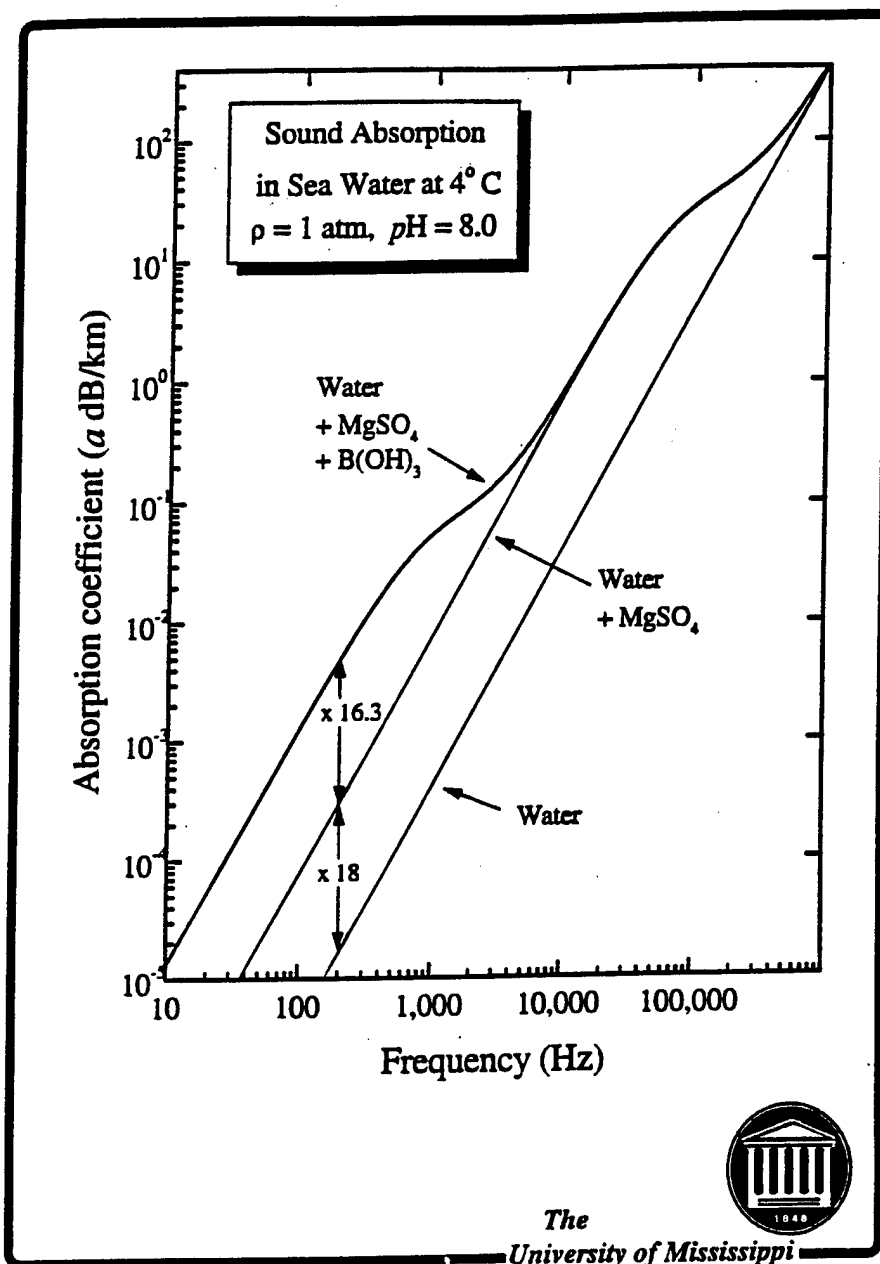
The
University of Mississippi

Relaxation in Sea Water



The
University of Mississippi







Design Considerations for Thermoacoustic Resonators

Thomas J. Hofler, Physics Department, Naval Postgraduate School

Presentation Outline

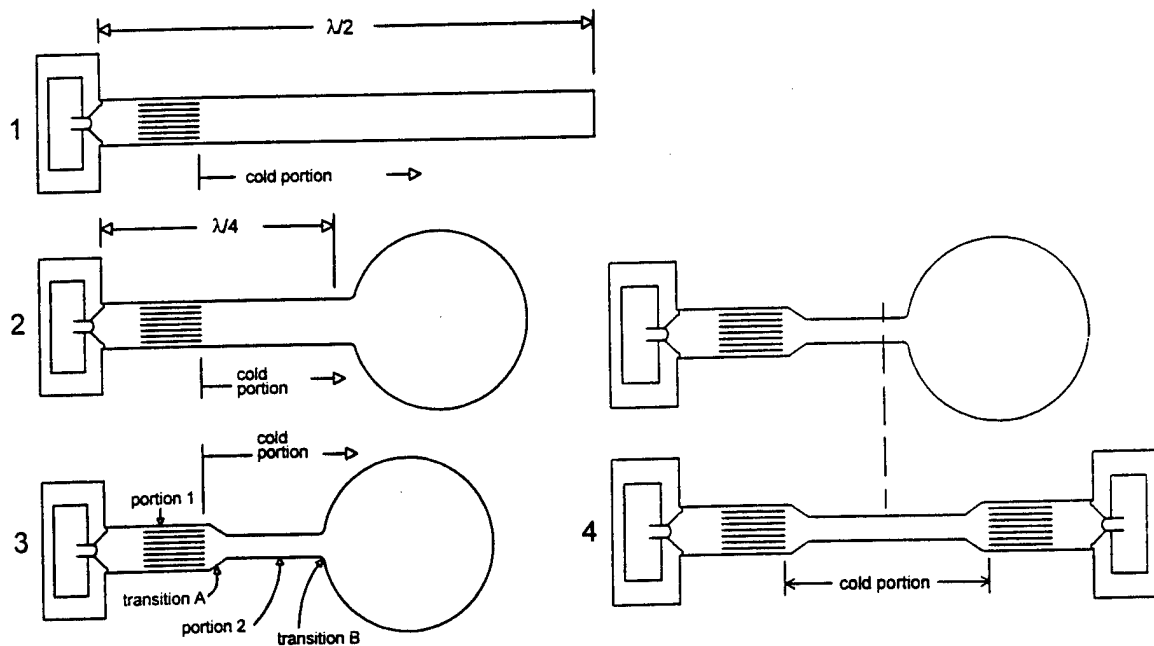
- **Resonator Topology & Efficient TA Refrigerators**
 - 4 resonator topologies
 - Some theory
 - Optimal dimensions
- **Suppressing Harmonic Distortion in TA Prime Movers**
 - An example prime mover apparatus
 - Suppression criteria & numerical determination
- **Amplitude Stability Issues in a Novel TA Prime Mover**
 - Thermal resonator tuning
 - Modest amplitude oscillations
 - Sudden large amplitude changes



Design Considerations for Thermoacoustic Resonators

Resonator Topology & Efficient TA Refrigerators

4 Thermoacoustic Refrigerator Resonator Topologies





Design Considerations for Thermoacoustic Resonators

Resonator Topology & Efficient TA Refrigerators

Cold Loss Calculation

Assume constant acoustic environment for the stack.

$$p_1 = p_{1o} \cos X_1$$

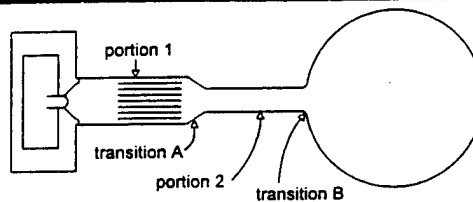
where $X_1 = kx_1 = 0$ at driver.

Match Z at transition A,

$$X_{2A} = \tan^{-1} \left(\left(\frac{D_1}{D_2} \right)^2 \tan X_{1A} \right).$$

Match p at transition A,

$$\frac{p_{2o}}{p_{1o}} = \frac{\cos X_{1A}}{\cos X_{2A}}.$$



Time averaged loss per unit area is,

$$\bar{w} = \frac{1}{4} \rho_m \omega \delta_v \left[|u|^2(x) + \left(\frac{\gamma-1}{\sqrt{\sigma}} \right) \frac{1}{a^2 \rho_m^2} |p|^2(x) \right].$$

Integrating, the total cold loss in portion 2 is,

$$W_{2N} = \frac{D_2}{D_1} \left(\frac{p_{2o}}{p_{1o}} \right)^2 \left[\left(1 + \frac{\gamma-1}{\sqrt{\sigma}} \right) \left(\frac{\pi}{2} - X_{2A} \right) + \frac{1}{2} \left(1 - \frac{\gamma-1}{\sqrt{\sigma}} \right) \sin 2X_{2A} \right],$$

where the sphere compliance is assumed infinite.

$$N = \frac{\pi D_1 \delta_v a p_{1o}^2}{8 \gamma p_m} \text{ is the power normalization.}$$

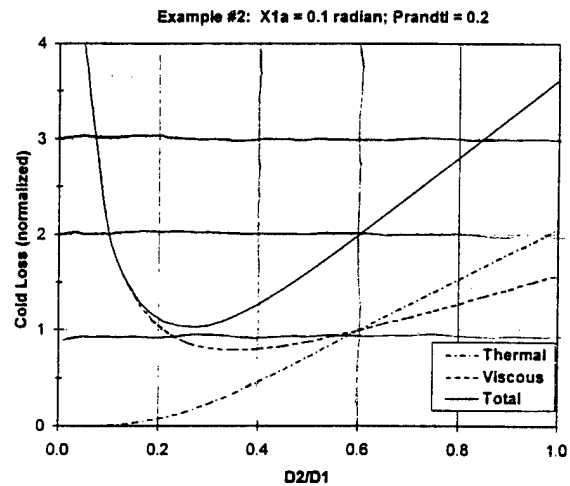
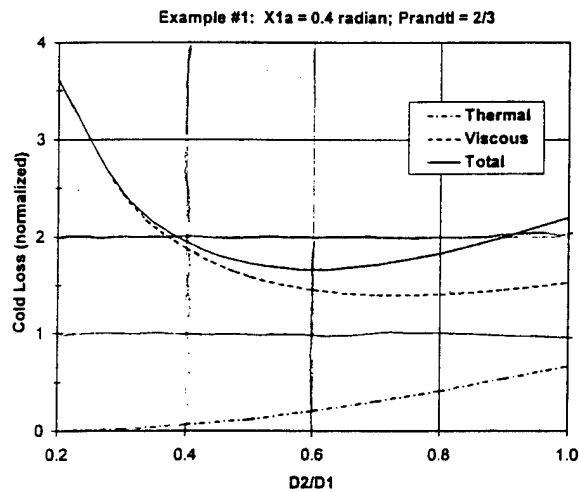


Design Considerations for Thermoacoustic Resonators

Resonator Topology & Efficient TA Refrigerators

Sample Loss Calculations

Two examples at the extremes of the resonator spectrum

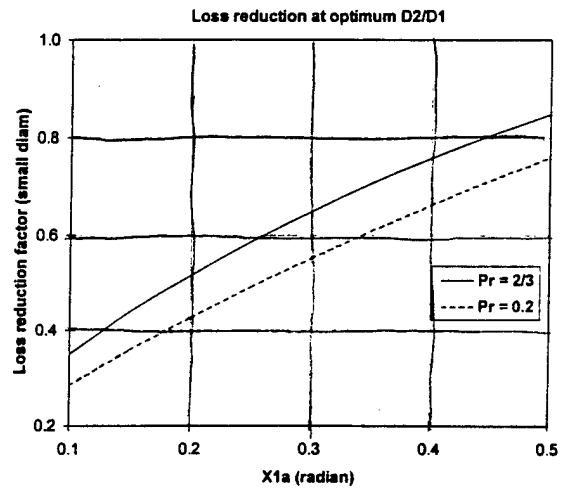
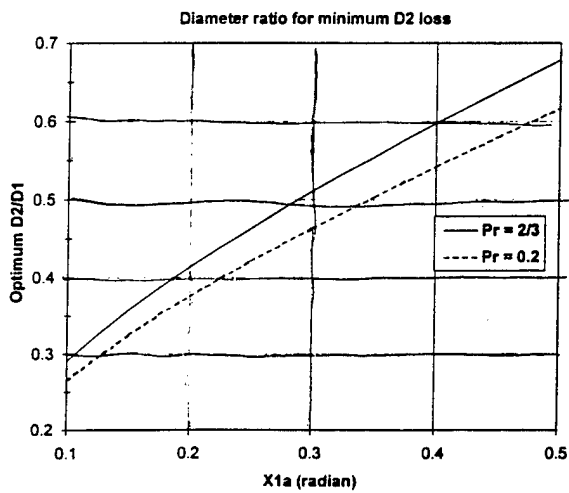




Design Considerations for Thermoacoustic Resonators

Resonator Topology & Efficient TA Refrigerators

Optimal diameter change & resulting reduction in loss

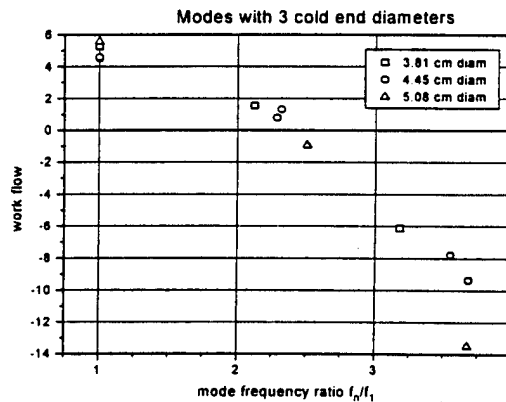
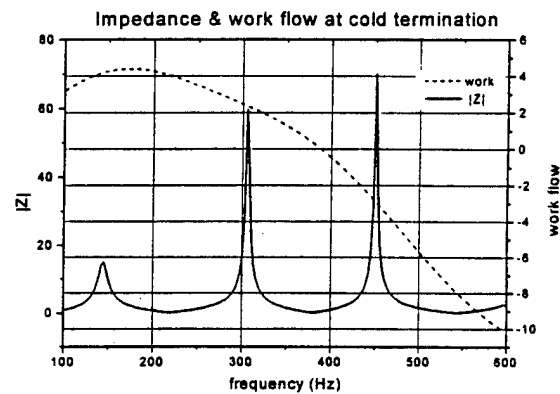
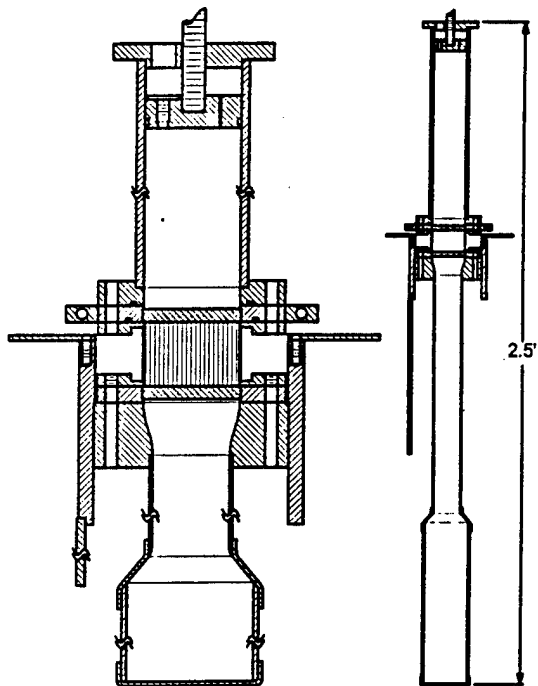




Design Considerations for Thermoacoustic Resonators

Suppressing Harmonic Distortion in TA Prime Movers

High-Amplitude Prime Mover Apparatus





Design Considerations for Thermoacoustic Resonators

Amplitude Stability in a Novel Prime Mover

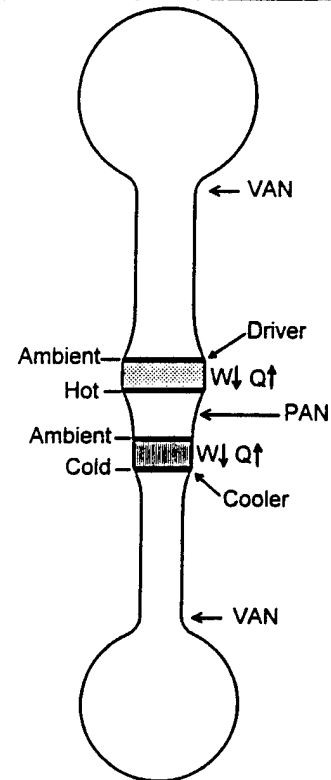
Half-wave TADTAR Design

Advantages

- High amplitudes possible with thermoacoustic driver
- Proper orientation of heat & work flow
 - Stirling cycle transport improves performance
- Good optimization freedom
 - Diameter & power of TAD & TAR are independent
 - Stack locations for TAD & TAR are independent
- Performance is very sensitive to location of Pressure AntiNode (PAN)
 - Can be thermally tuned for easy starting

Disadvantages

- Performance is very sensitive to location of PAN
 - Will the acoustic amplitude be stable?
- Unknown heat leak from hot heat exchanger



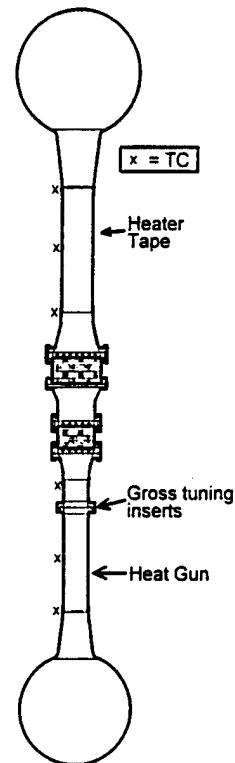


Design Considerations for Thermoacoustic Resonators

Amplitude Stability in a Novel Prime Mover

Preliminary Measurements

- Run driver only, with cooler sections empty
- Measure acoustic amplitude & maintain 400° C hot temperature via human controller
- Resonator tuning
 - Gross tuning with tube inserts
 - Fine tuning with heater tape on upper tube and heat gun on lower tube
 - 3 thermocouples were attached to each of the two small diam. tubes. Each triplet is averaged, converted to Kelvin, & the upper-to-lower ratio calculated. This "Temp. Ratio" indicates the level of fine tuning.

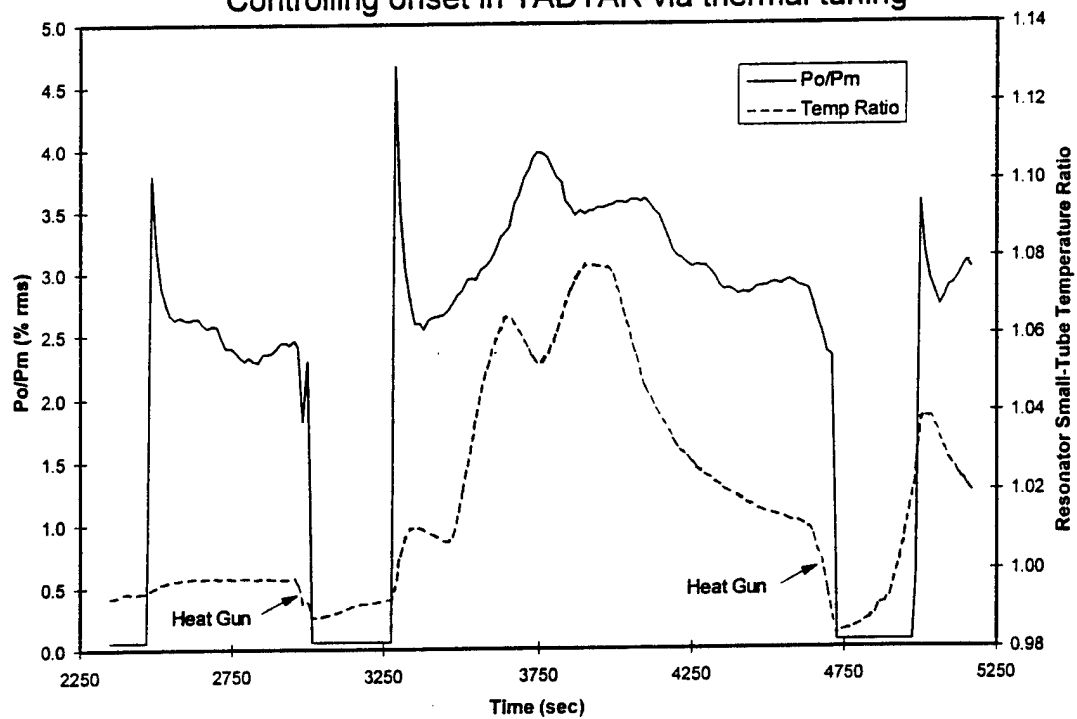




Design Considerations for Thermoacoustic Resonators

Amplitude Stability in a Novel Prime Mover

Controlling onset in TADTAR via thermal tuning

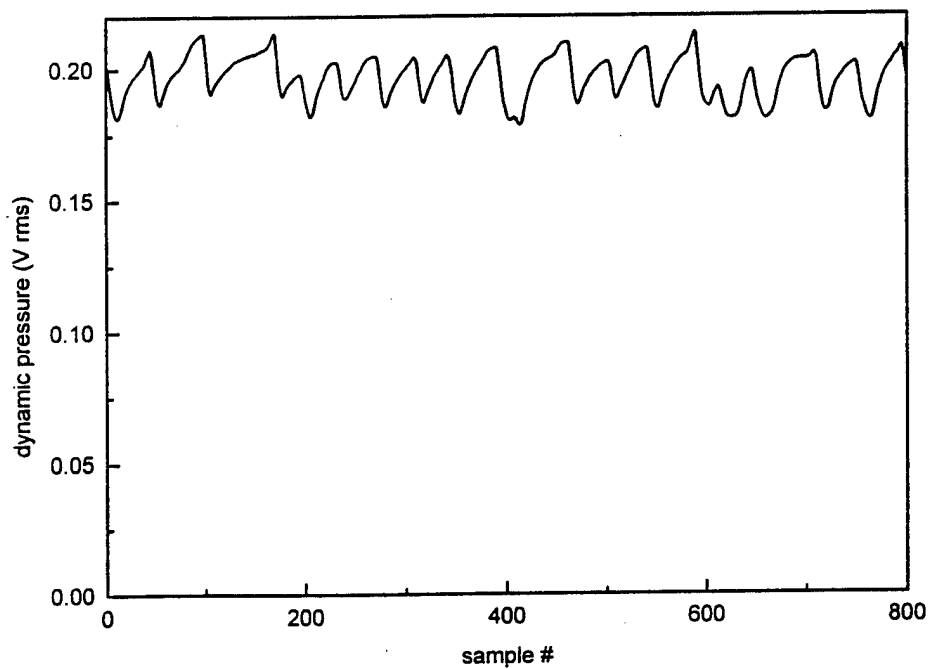




Design Considerations for Thermoacoustic Resonators

Amplitude Stability in a Novel Prime Mover

Oscillatory TADTAR amplitude (rms)
Period = 1 sec. approx.

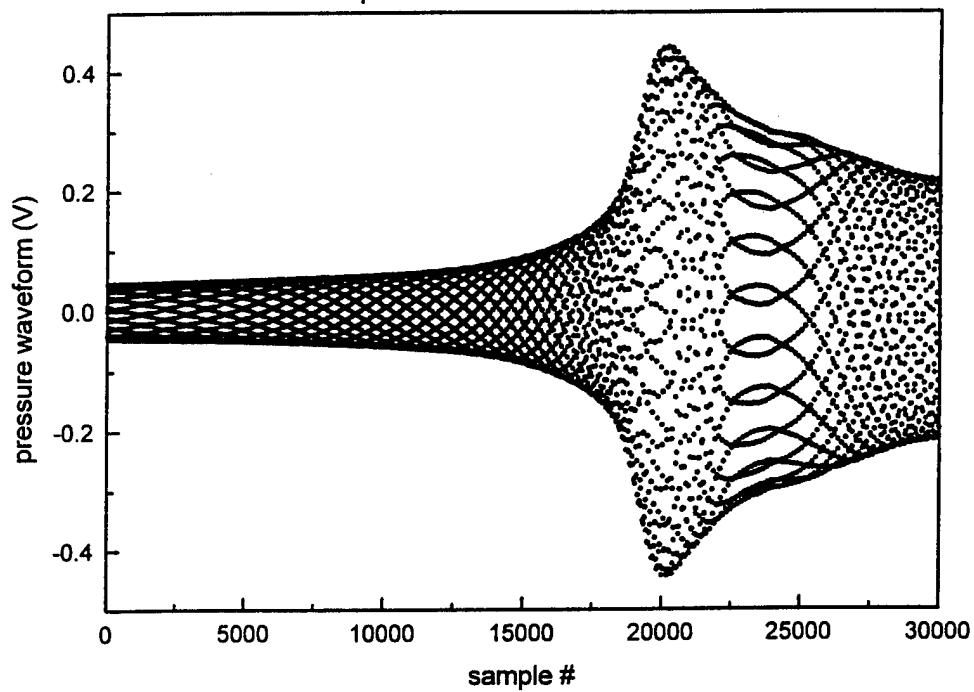




Design Considerations for Thermoacoustic Resonators

Amplitude Stability in a Novel Prime Mover

Sudden increase in TADTAR amplitude
sample interval = 0.4 ms



**ACOUSTIC MEASUREMENTS of THERMODYNAMIC
and TRANSPORT PROPERTIES in GASES**

NIST United States Department of Commerce
National Institute of Standards and Technology



MICHAEL R. MOLDOVER

**NIST Fellow
Physical and Chemical
Properties Division**

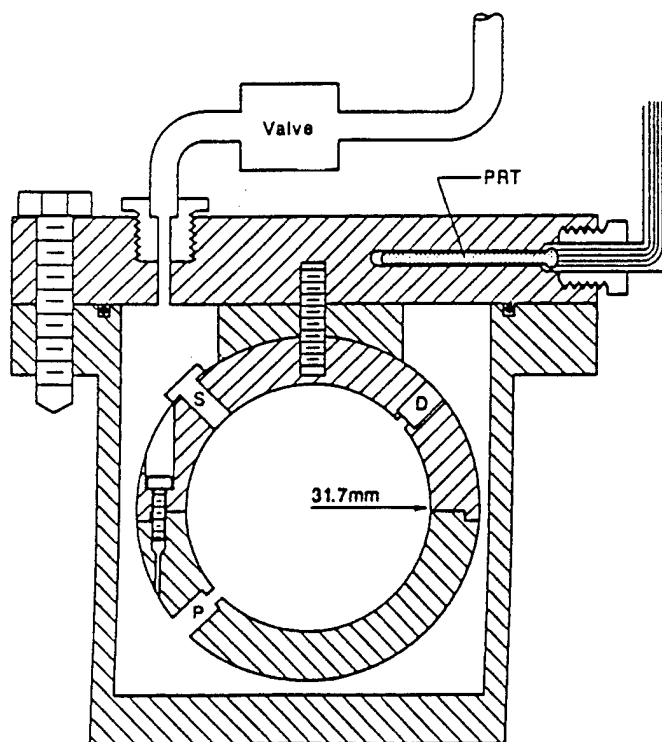
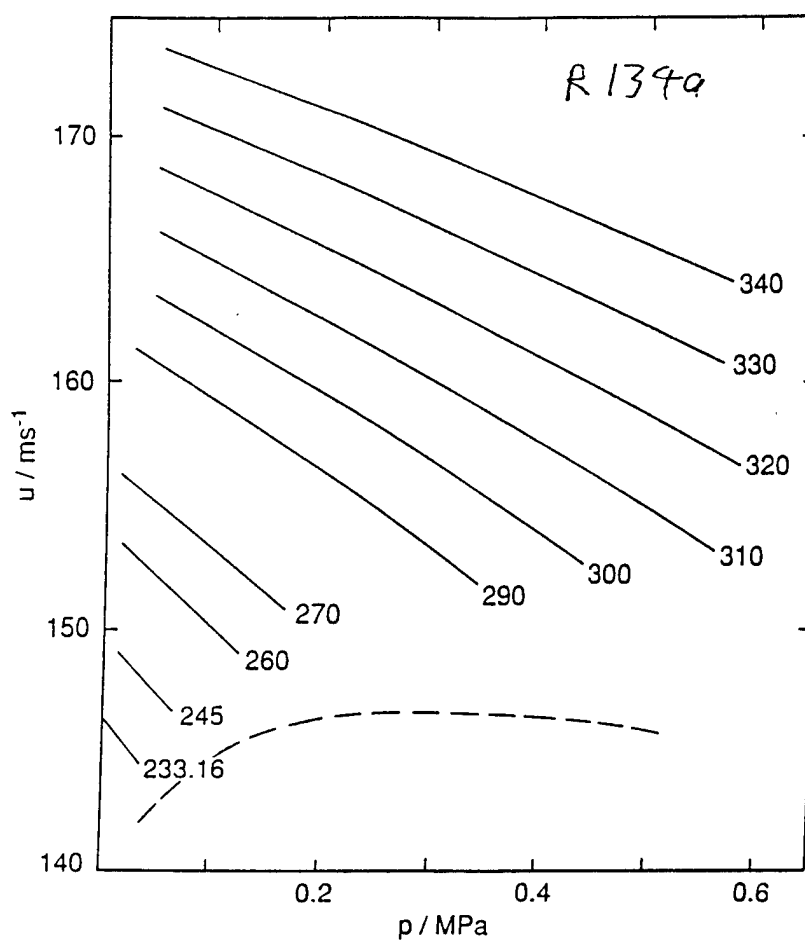
THERMODYNAMIC PROPERTIES

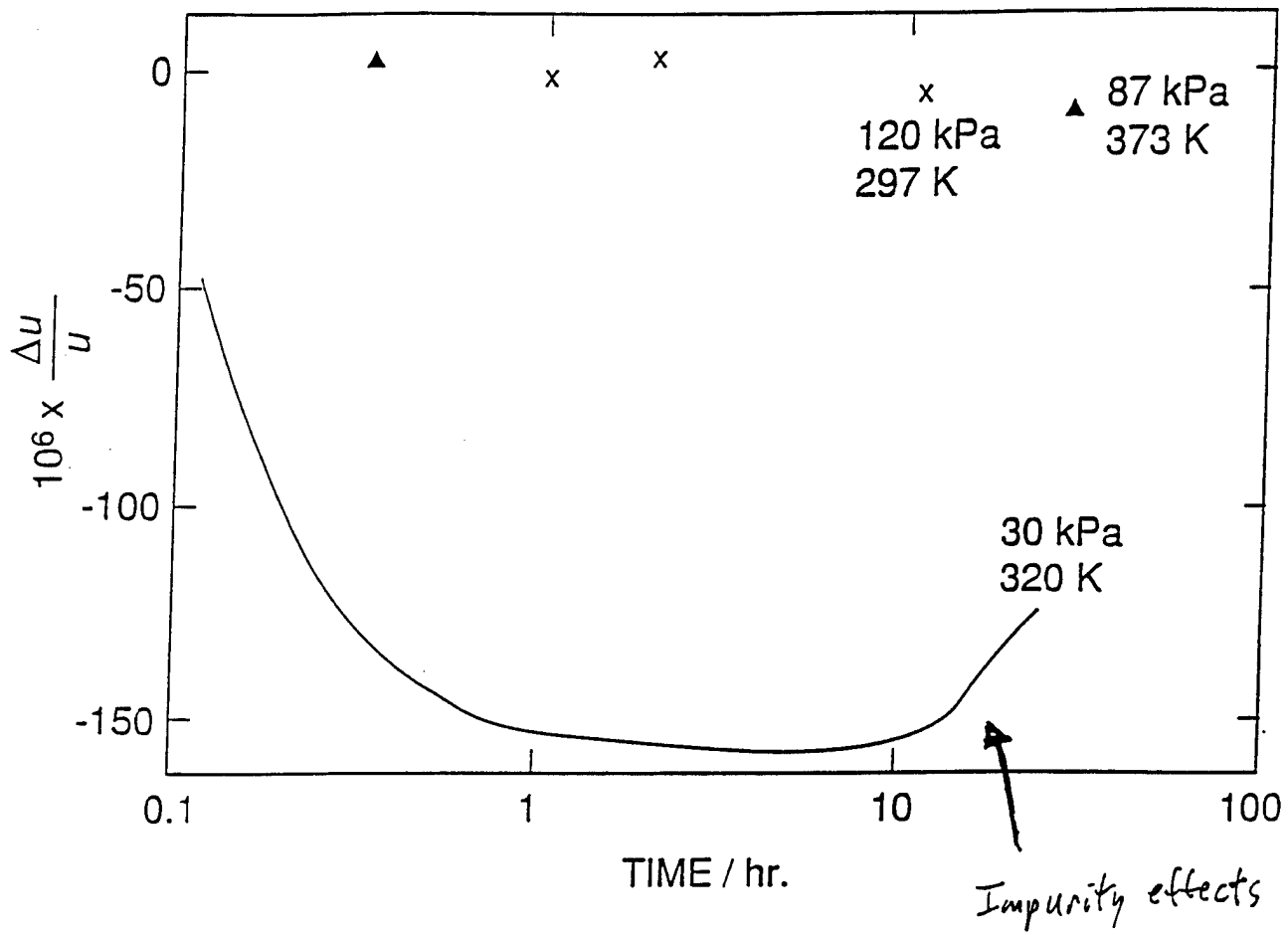
1. Ideal-gas heat-capacity: $C_p^0(T)$

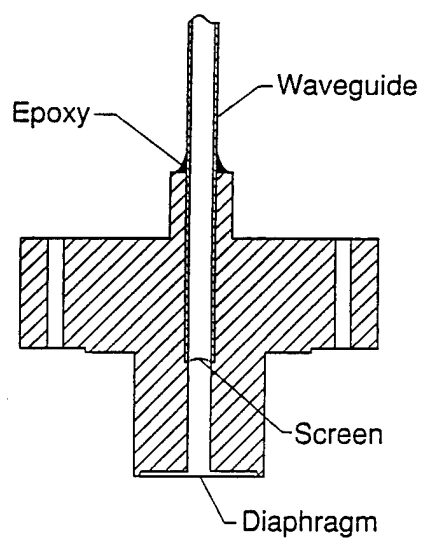
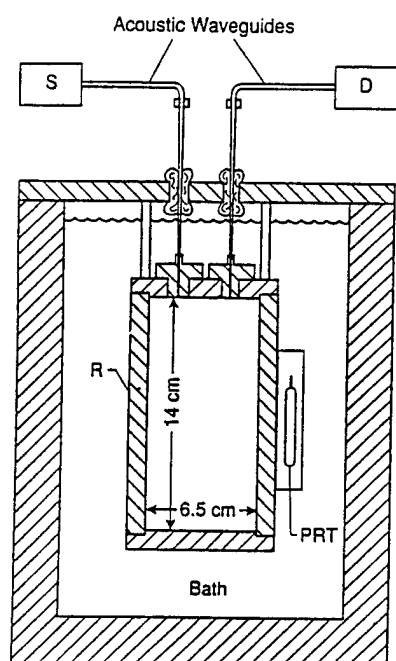
2. Virial equation of state:

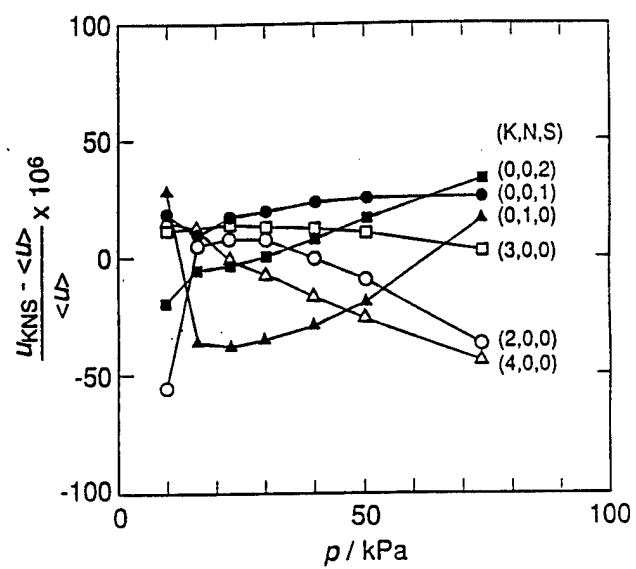
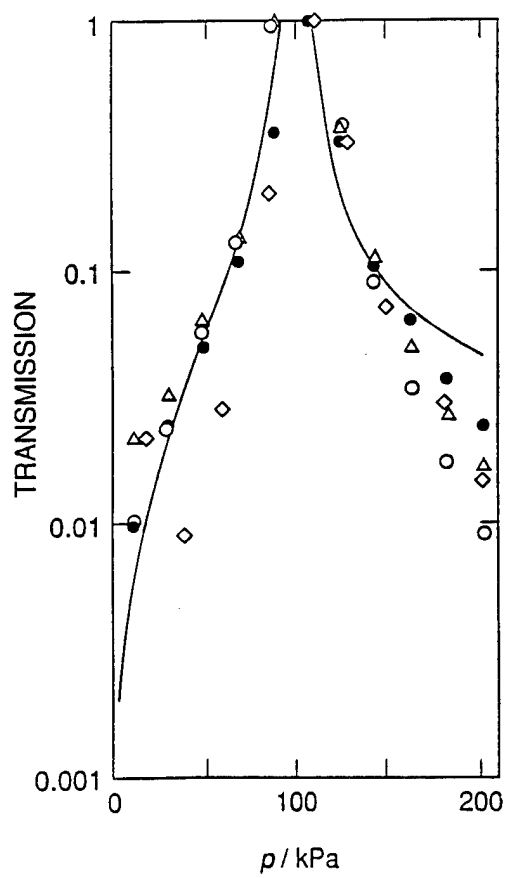
$$pV = RT(1 + B(T)\rho + C(T)\rho^2 + D(T)\rho^3 + \dots)$$

Note: Resonance techniques are not recommended for liquids because oscillations of container cannot be separated from oscillations of fluid









compound		temperature range K	maximum pressure kPa	number of isotherms
Candidate refrigerants for vapor compression cycles				
CF ₃ -CHF ₂	R134a	233 - 340	600	10
CFCI ₂ -CH ₃	R141b	260 - 315	70	5
CHCl ₂ -CF ₃	R123	260 - 335	80	6
CHFCI-CF ₂ -Cl	R123a	265 - 300	50	2
CHF ₂ -O-CHF ₂	E134	255 - 327	170	6
CHF ₂ -O-CHF ₂	E134	255 - 374	90	8
CF ₂ -O-CH ₂ -CF ₃	E245	278 - 384	50	5
CF ₃ -HF-CHF ₂	R236ea	267 - 380	600	8
CHFCI-CF ₃	R124	250 - 400	900	17
CHF ₂ -CF ₃	R125	240 - 400	1,000	9
CHF ₂ -CH ₃	R152a	240 - 400	1,000	9
CF ₃ -CH ₃	R143a	240 - 400	1,000	9
CF ₃ -CH ₂ -CF ₃	R236fa	276 - 400	1,000	7
CHF ₂ -CF ₂ -CH ₂ F	R245ca	311 - 400	900	5
CF ₃ -O-CF ₂ H	E125	260 - 400	1,000	13
1 composition	R134a/R32/R125	260 - 400	1,000	12
CF ₃ -CF ₂ -CF ₂ -CH ₂ F	R338mccq	300 - 400	400	6
Thermoacoustic Refrigeration				
5 compositions	He/Xe	210 - 400	1,500	42
Semiconductor Processing				
SF ₆		230 - 460	1,500	16
CF ₄		300 - 475	1,500	9
C ₂ F ₆		210 - 475	1,500	14
Cl ₂		planned		
HBr		planned		
BCl ₃		planned		
WF ₆		planned		

$$u^2 = \frac{\gamma^0 RT}{M} \left(1 + \frac{\beta_a p}{RT} + \frac{\gamma_a p^2}{RT} + \frac{\delta_a p^3}{RT} + \frac{\epsilon_a p^4}{RT} + \dots \right)$$

First, consider limit as $p \rightarrow 0$

$$\frac{C_p^0(T)}{R} = \frac{\gamma^0(T)}{\gamma^0(T) - 1} = \frac{Mu^2}{Mu^2 - RT}$$

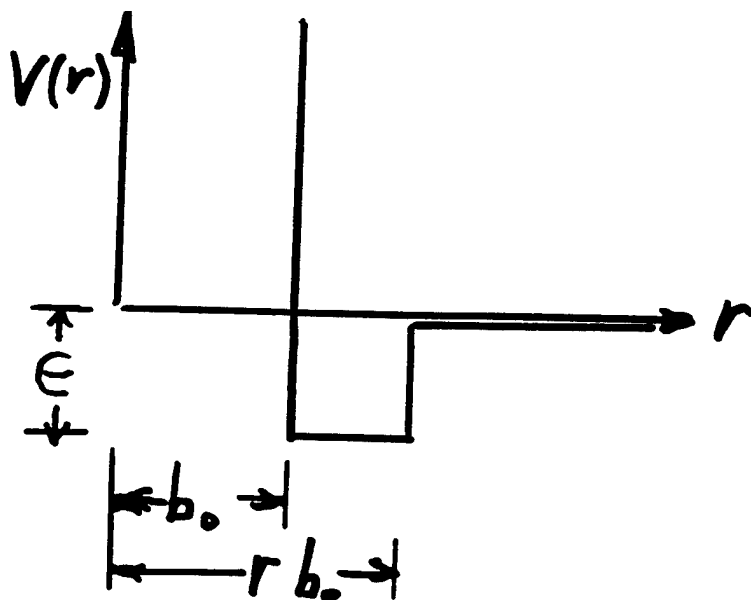
For polyatomic gases $\gamma^0 \rightarrow 1$.

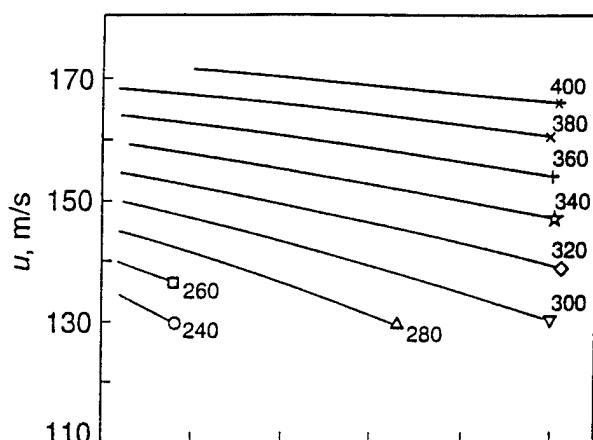
(e.g. SF_6 , $\gamma^0(298 \text{ K}) = 1.094$; $C_p/R = 1/10.6$)

Uncertainty of M from impurities amplified $10.6 \times$

$$\text{Ansatz: } B(T) = b_0 [1 + (r^3 - 1) (e^{\frac{\epsilon}{k_B T}} - 1)]$$

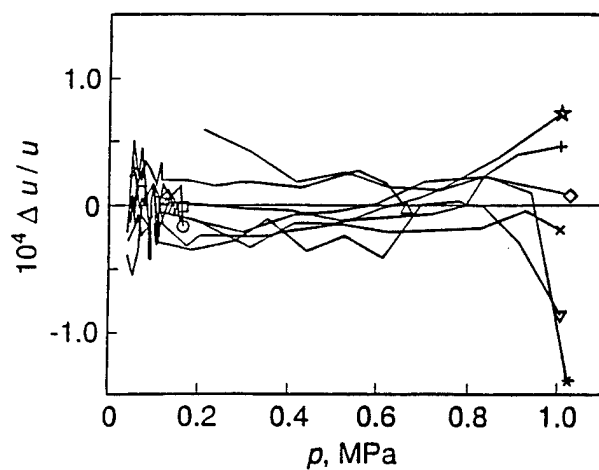
$$\beta_a = 2B + 2(\gamma_0 - 1)T \frac{dB}{dT} + \frac{(\gamma_0 - 1)^2}{\gamma_0} T^2 \frac{d^2 B}{dT^2}$$





Speed of sound data for $\text{CHF}_2\text{-CF}_3$.
Pentafluoroethane = refrigerant R125

Temperature range $0.71 \leq T/T_c \leq 1.18$

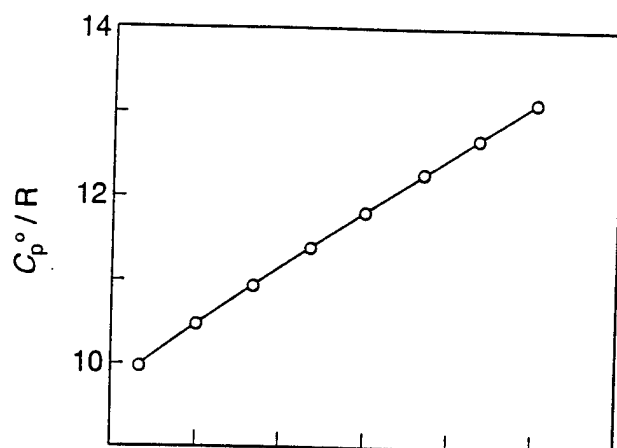


Deviations of data from $u(P, T)$ surface.

RMS deviations are $2 \times 10^{-5} \times u$.

Impurities cause larger systematic errors.

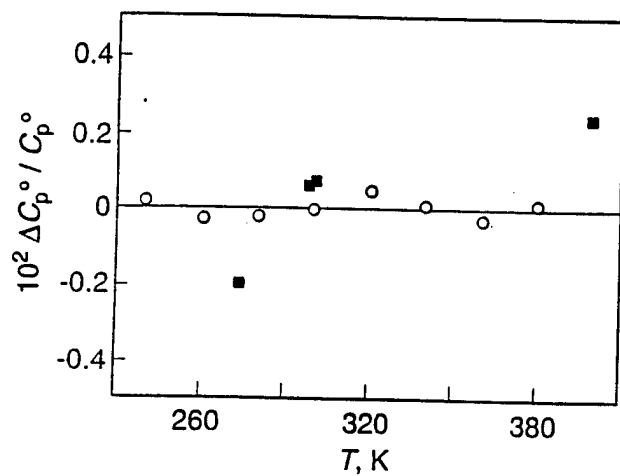
The surface uses 3 parameters for $C_p^0(T)$, (ideal-gas heat-capacity), 3 parameters for each of the virial coefficients $B(T)$ and $C(T)$ and 2 parameters for $D(T)$.



Ideal gas heat capacity of R125,
deduced from the speed of sound data
through the relation:

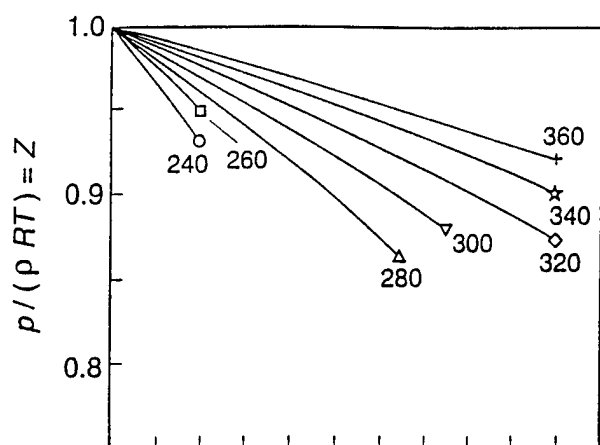
$$C_p^0(T)/R = Mu_0^2/(Mu_0^2 - RT).$$

R is the universal gas constant; M is the
molecular weight and u_0^2 is the zero-
pressure limit of $u^2(P, T)$

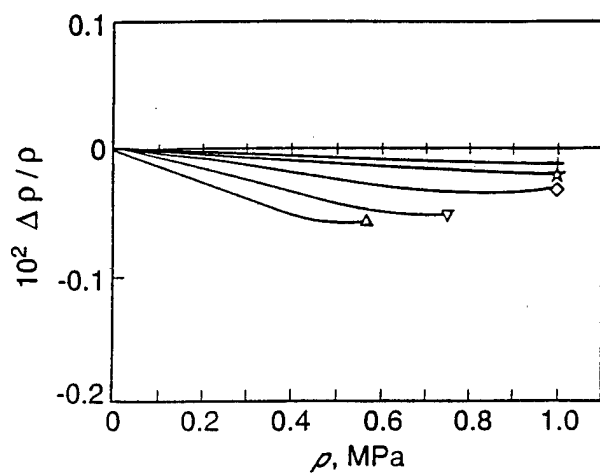


Deviations of $C_p^0(T)/R$ from a polynomial.

- present data
- independent spectroscopic
information (estimated)



Compression factor of R125 deduced from $u(P, T)$ data using the virial equation. The virial coefficients were assumed to have the temperature dependencies of a hard-core square-well intermolecular potential and the parameters in the potentials were fitted to the $u(P, T)$ data.



Fractional deviations of the density of R125 deduced from $u(P, T)$ data from independent density measurements by Boyes and Weber.

TRANSPORT PROPERTIES

1. Greenspan acoustic viscometer for η :

hard sphere of diameter σ

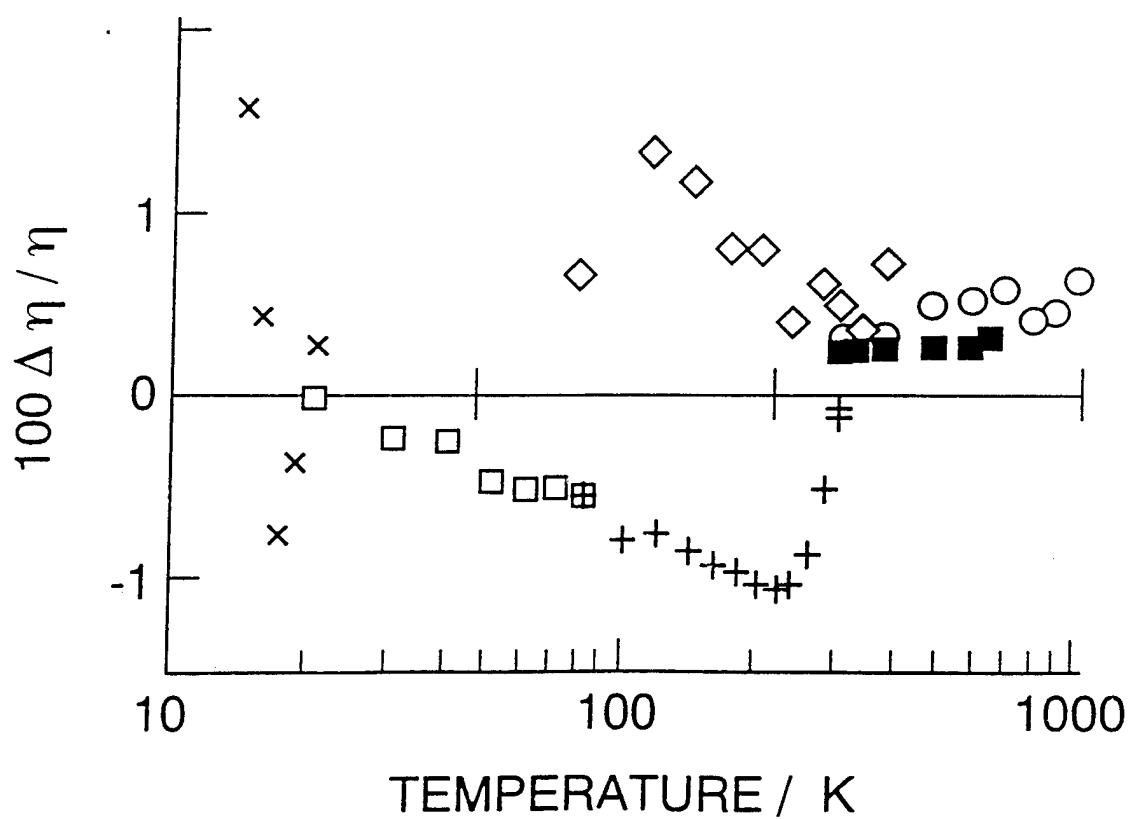
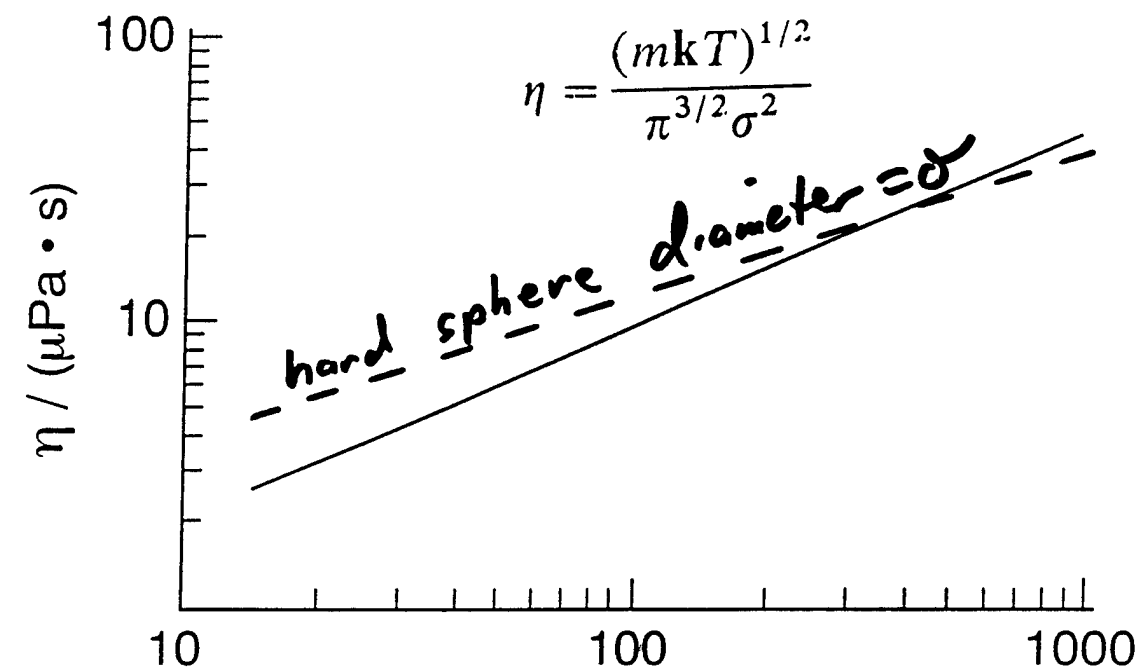
$$\eta = \frac{(mk_B T)^{1/2}}{\pi^{3/2} \sigma^2}$$

2. Prandtl number machine

$$\begin{aligned} Pr &= \frac{C_p \eta}{\lambda} = \frac{\text{viscous diffusivity}}{\text{thermal diffusivity}} \\ &= \frac{2}{3} \quad \text{for hard sphere} \end{aligned}$$

3. If time permits, electromagnetic equivalent of Greenspan viscometer: reentrant resonator

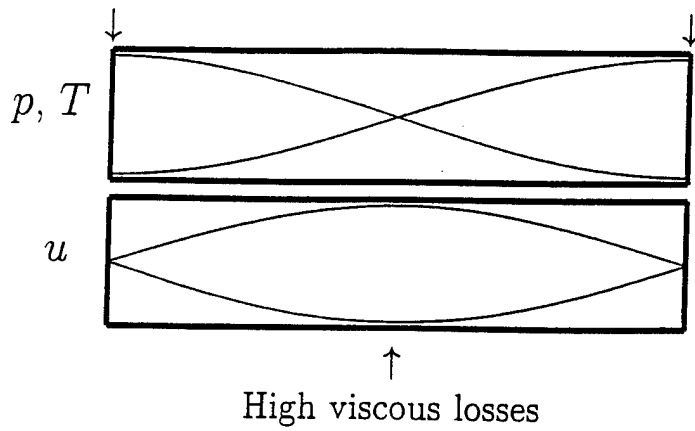
Helium



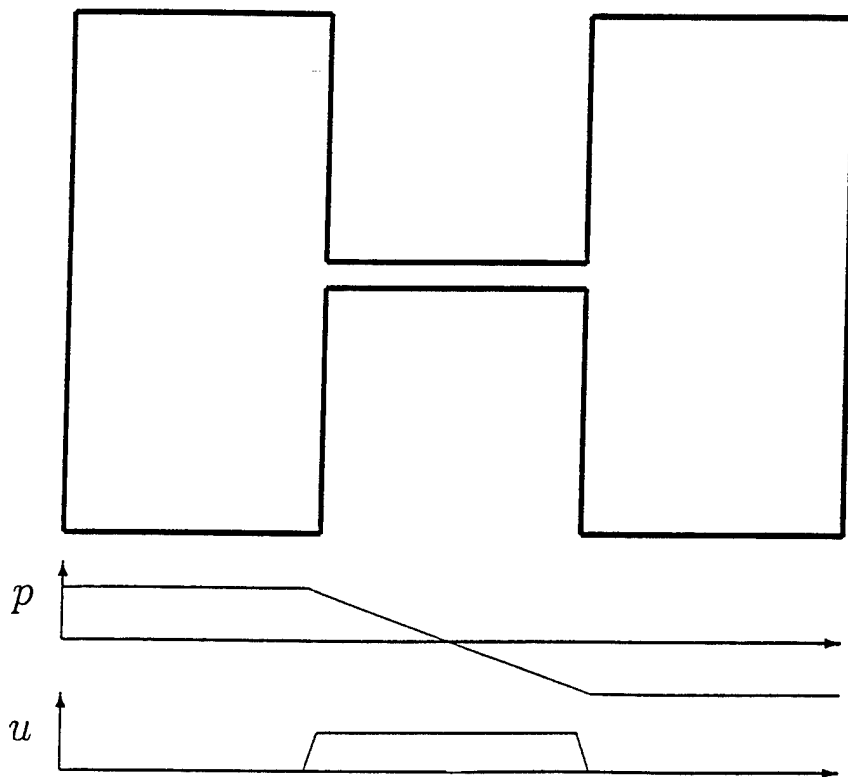
Loss mechanisms spatially separated in standing waves.

High thermal losses

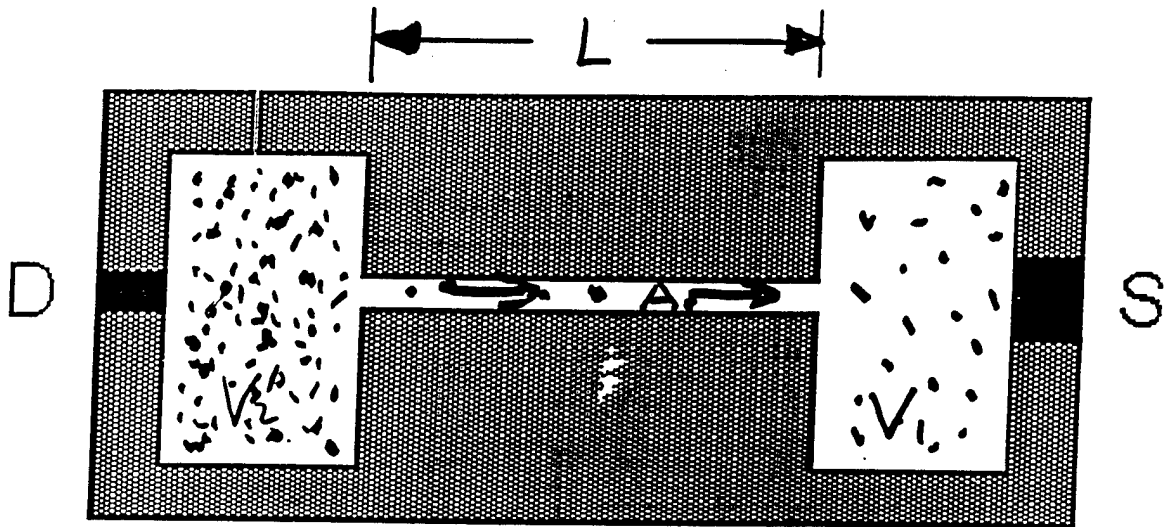
High thermal losses



Greenspan viscometer: $\lambda \gg \text{length}$

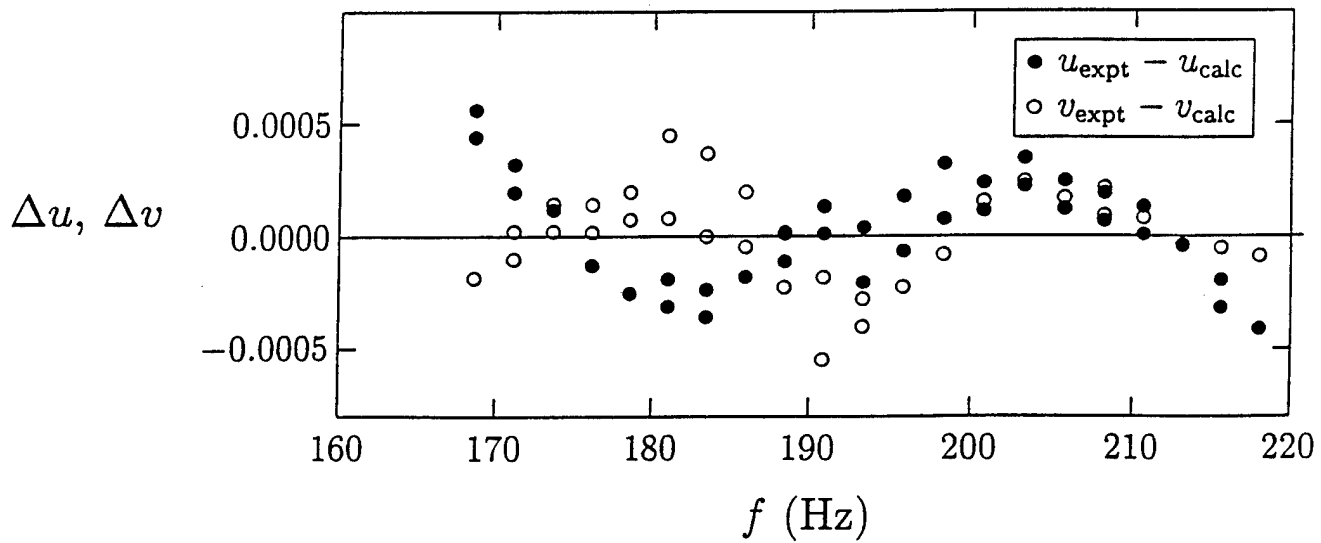
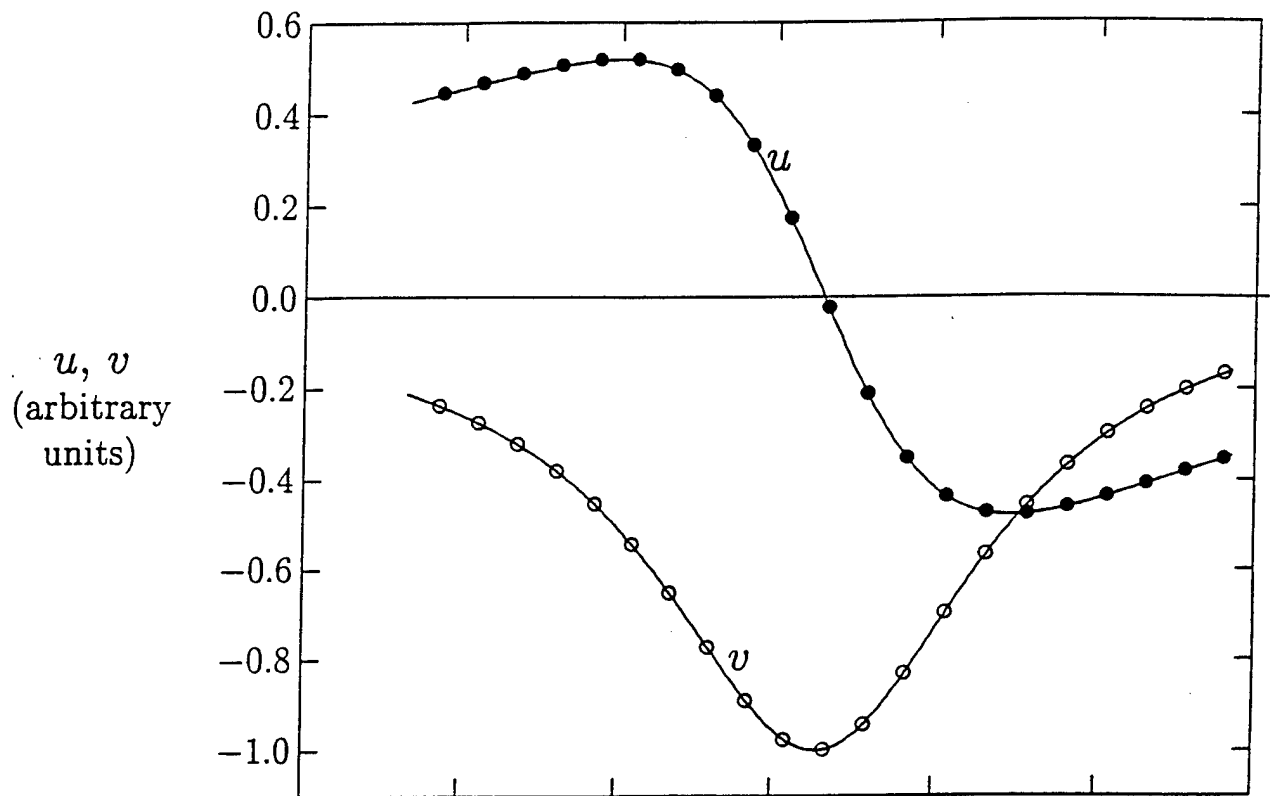


Double Helmholtz Resonator



$$\omega_0^2 = \frac{c^2 A}{L} \left[\frac{1}{V_1} + \frac{1}{V_2} \right]$$

$$\omega_1^2 = \frac{\omega_0^2 \left(1 - (1-i) \frac{\delta_v}{2a} \right)}{1 + (1-i)(\gamma-1) \frac{\delta_c S}{2V}} \left\{ 1 + \dots \right.$$

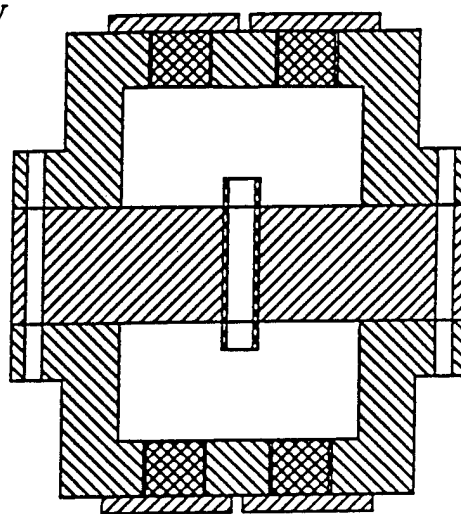
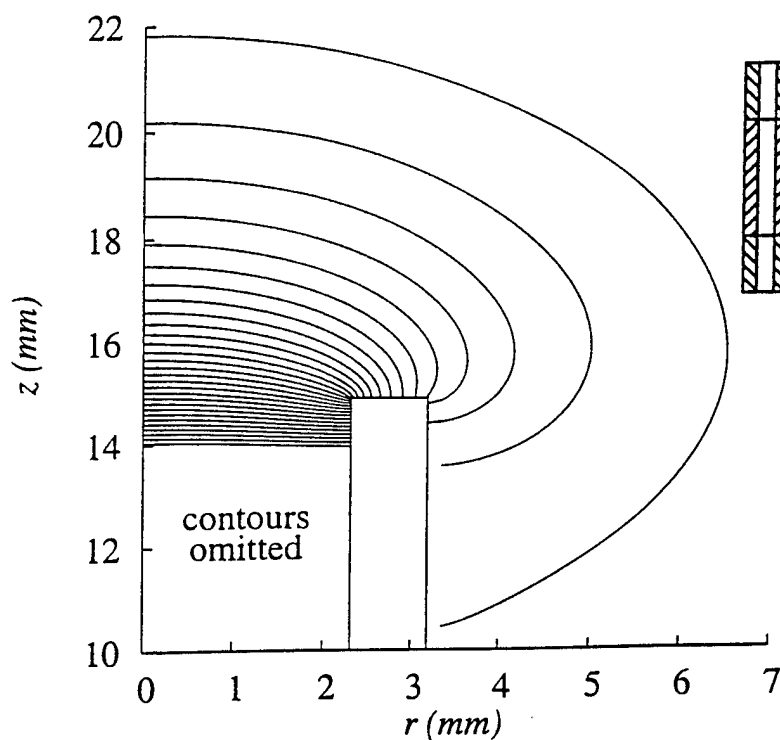


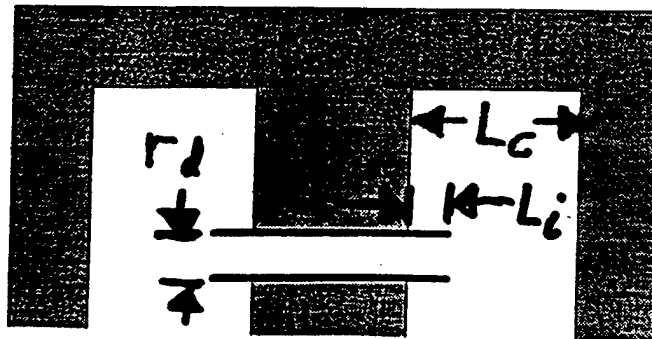
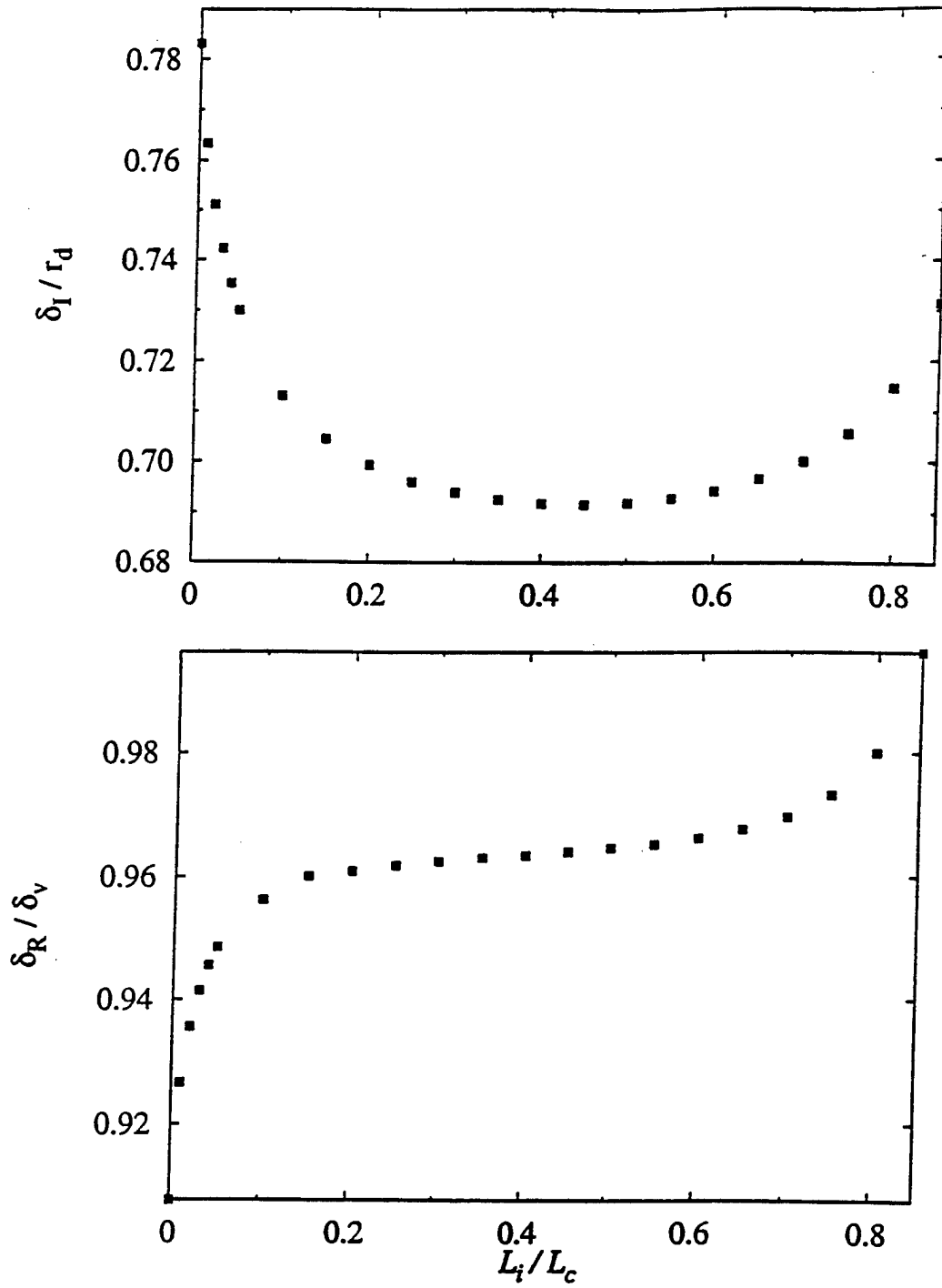
Acoustic pressure contours near duct end

Calculated from solutions of

$$(\nabla^2 + k^2)p(\mathbf{r}) = 0$$

$$\frac{\partial p}{\partial n} = 0 \quad \text{on boundary}$$

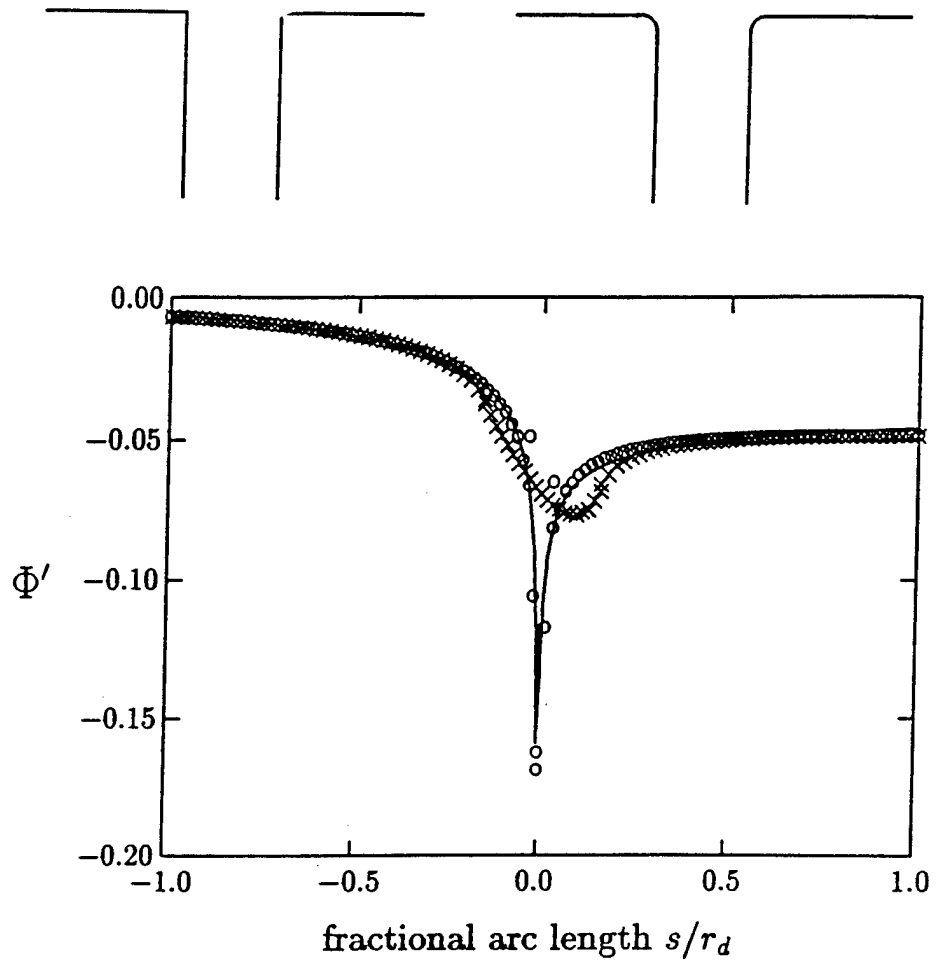




Orifice cross-sections

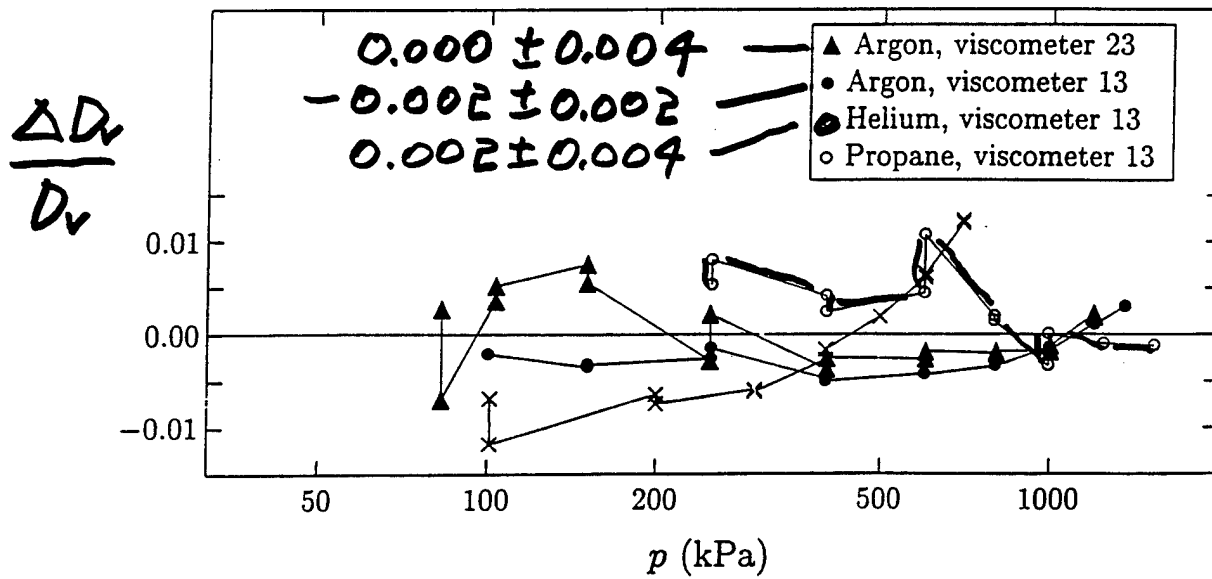
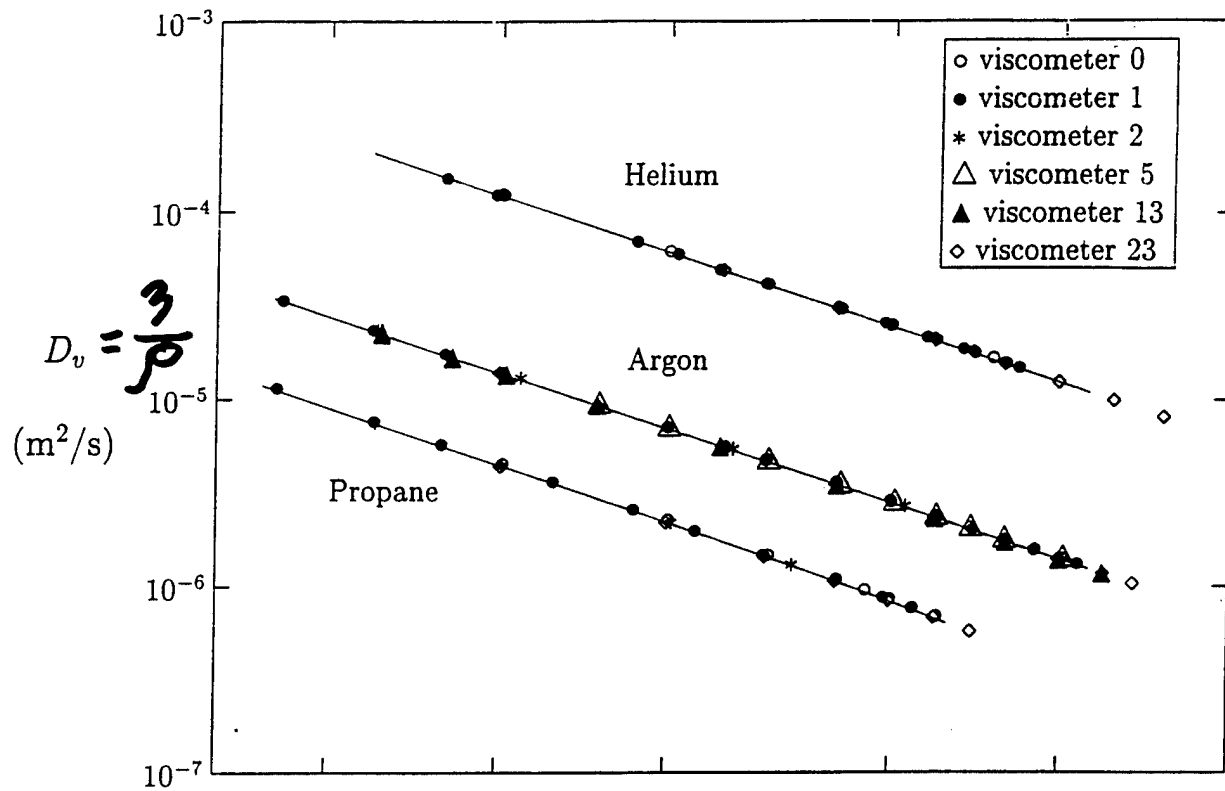
Sharp corners

Rounded corners



$$\frac{R(r_{ch})}{R(0)} = 1 - \frac{1}{3} \left(\frac{r_{ch}}{r_d} \right)^{(1/3)} ;$$

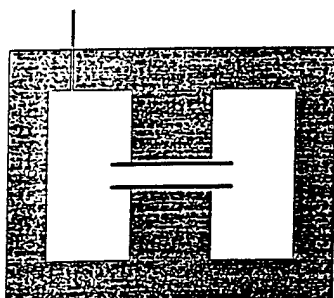
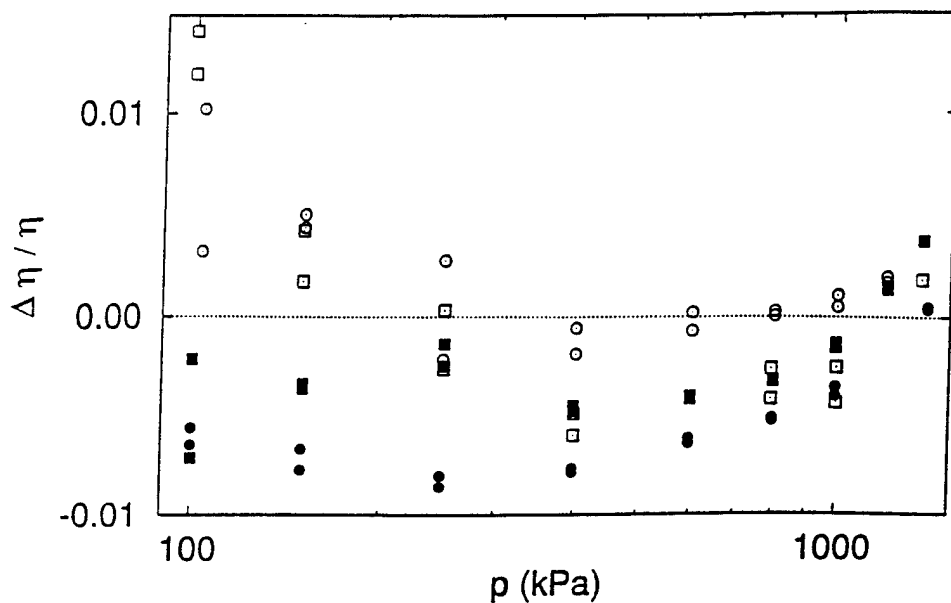
$$R(0) \approx 0.9\delta_v ; \quad R(r_d) \approx 0.6\delta_v$$



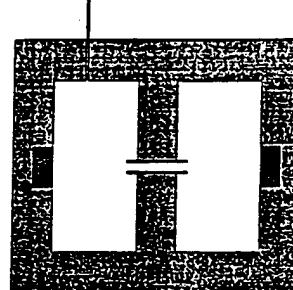
Greenspan viscometer as an absolute instrument
(no calibration)

Argon in 4 viscometers

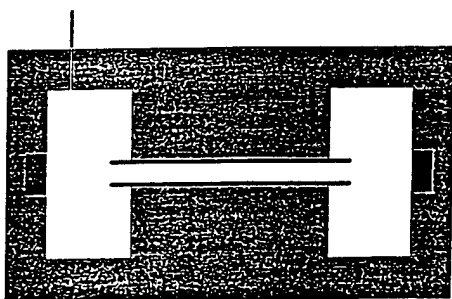
Experimental η compared with reference values



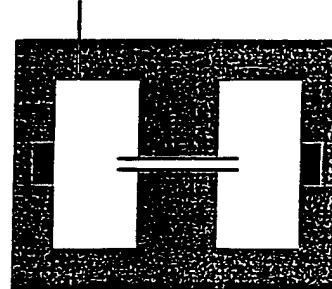
Viscometer 23 0.002 ± 0.003



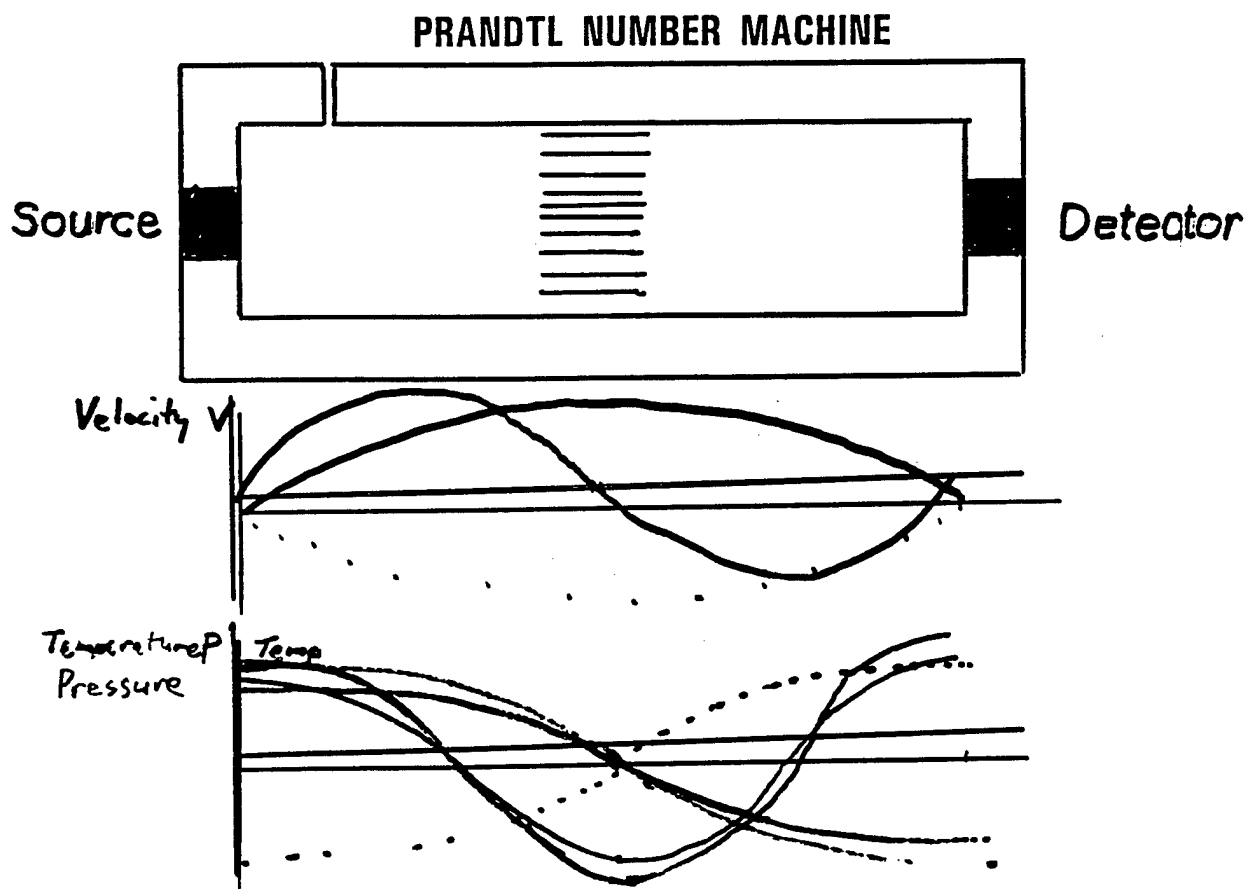
Viscometer 12 0.001 ± 0.006

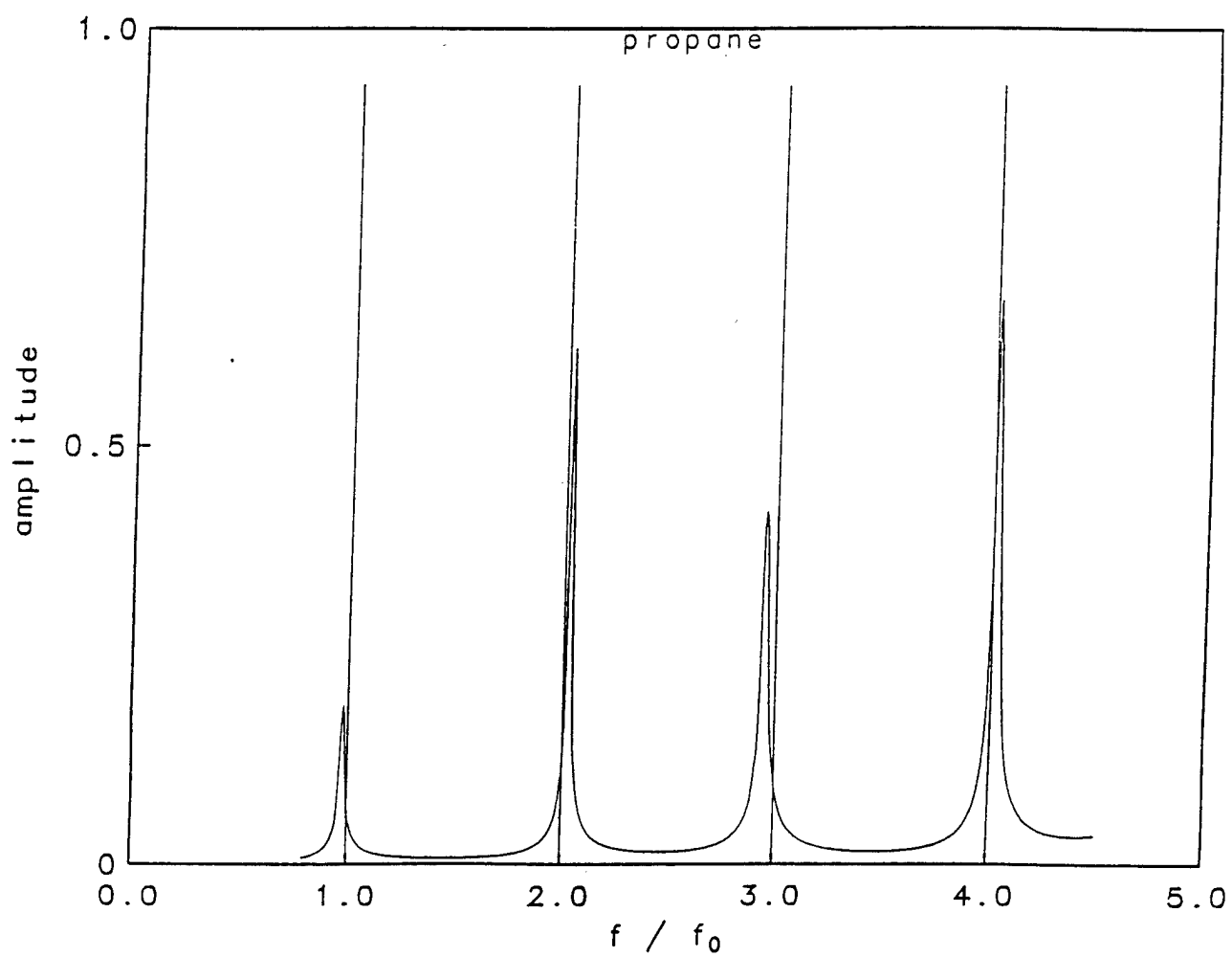
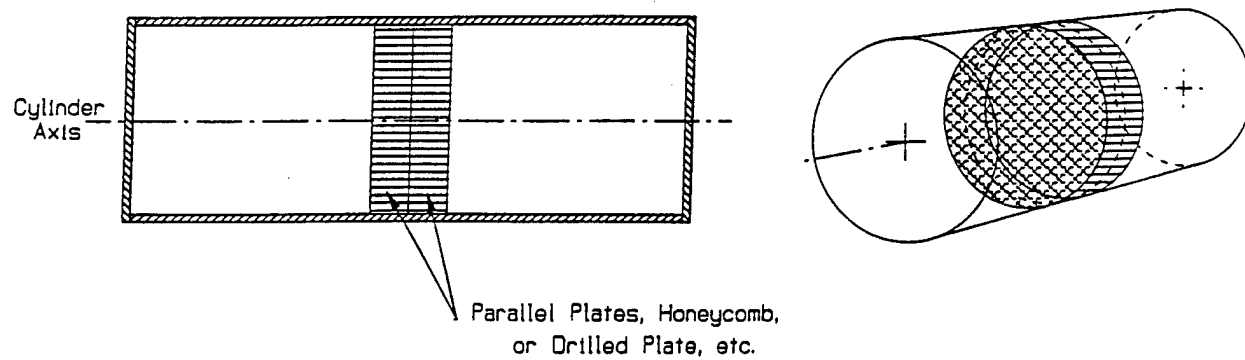


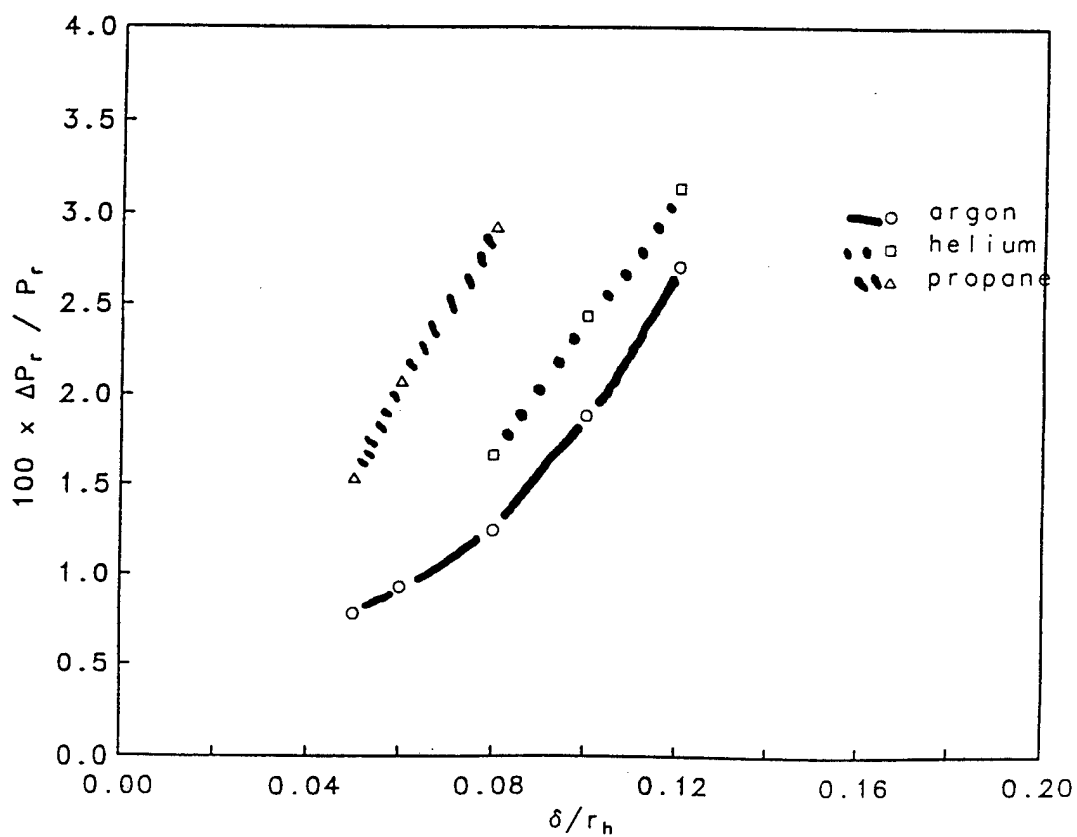
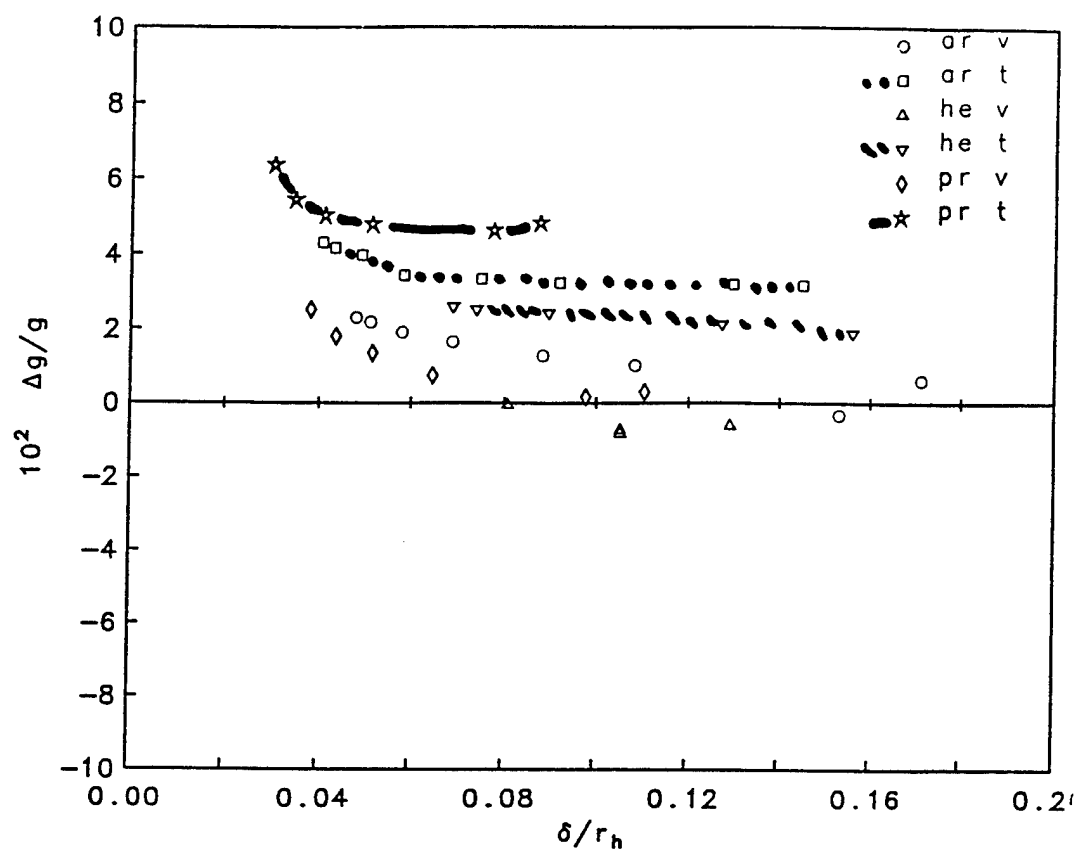
Viscometer 24 -0.005 ± 0.003

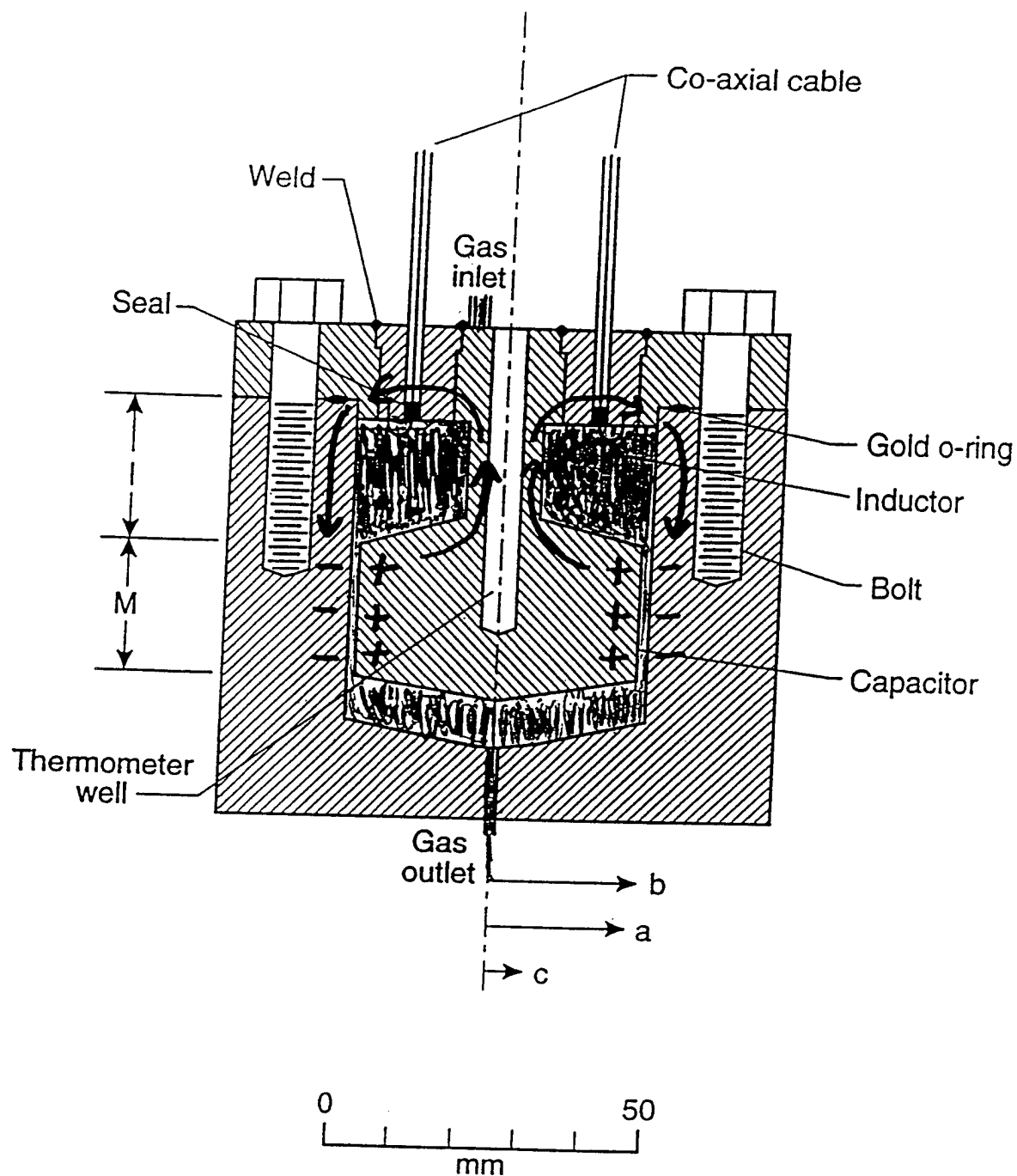


Viscometer 13 -0.002 ± 0.003



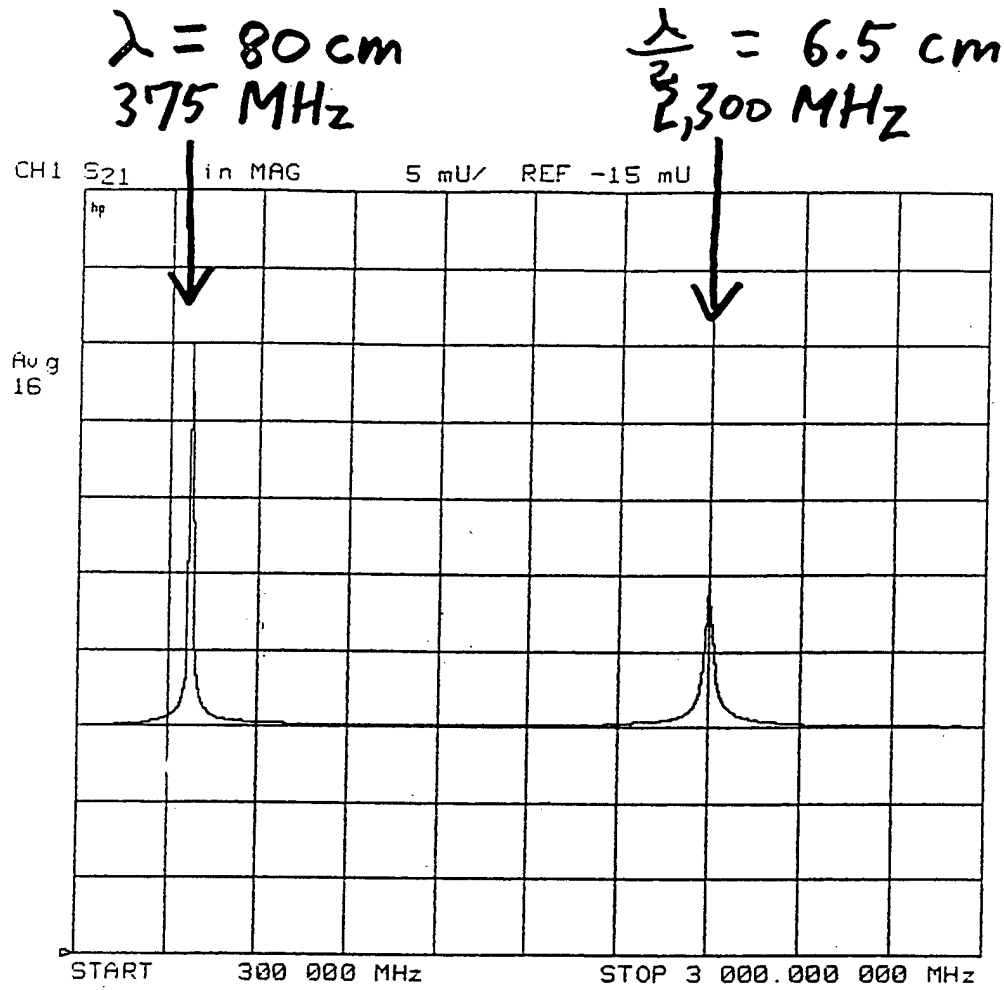




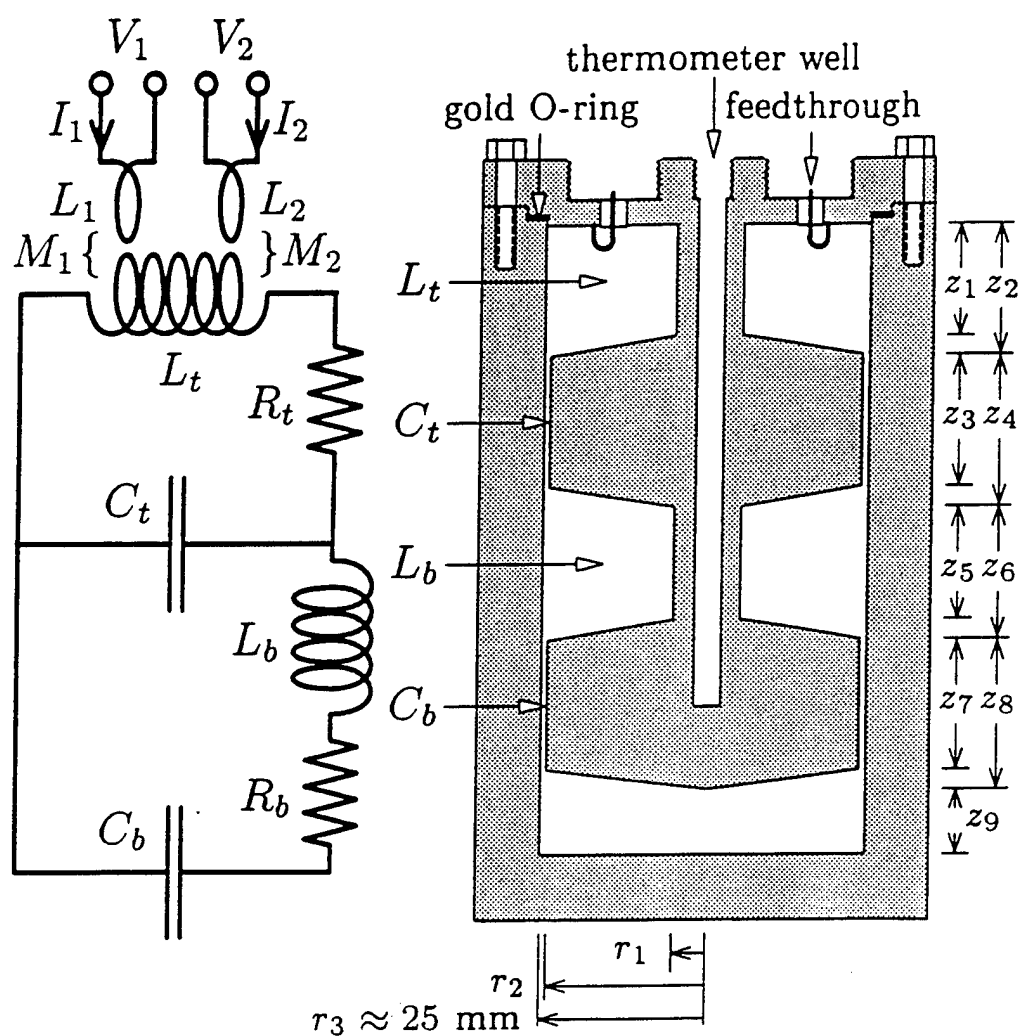


$$f = \frac{1}{2\pi} \sqrt{\frac{1}{LC}} \approx 350 \text{ MHz}$$

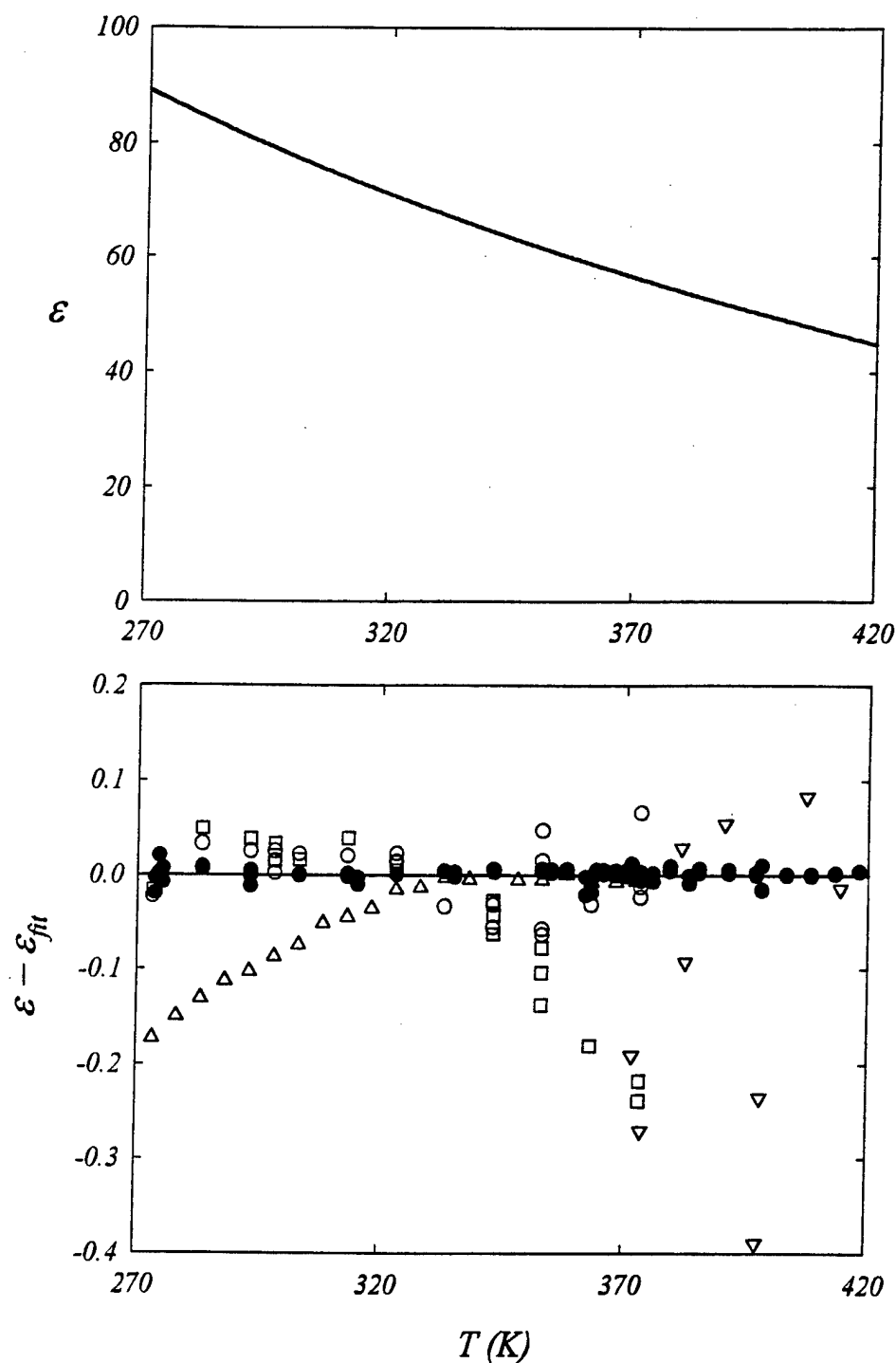
$C \propto$ dielectric constant of fluid in gap



Two-mode reentrant radio frequency resonator and equivalent circuit



Temperature dependence of the dielectric constant of water



- our data
- Fernández et al., *Int. J. Thermophysics* **16**, 929(1995) with LCR meter
- Fernández et al., *Int. J. Thermophysics* **16**, 929(1995) with transformer bridge
- △ Malmberg & Maryott, *J. Research Nat. Bur. Stds.* **56**, 1(1956)
- ▽ Oshry, Ph.D. Thesis, Univ. of Pittsburgh (1949)

$$\epsilon_{fit} = 296.3 \pm 0.5 - 1.219 \pm 0.005(T/K) + (2.03 \pm 0.01) \times 10^{-3}(T/K)^2 - (1.31 \pm 0.01) \times 10^{-6}(T/K)^3, s = 0.007 (1\sigma)$$

REPORT DOCUMENTATION PAGE			Form Approved OMB No. 0704-0188	
Public reporting burden for this collection of information is estimated to average 1 hour per response, including the time for reviewing instructions, searching existing data sources, gathering and maintaining the data needed, and completing and reviewing the collection of information. Send comments regarding this burden estimate or any other aspect of this collection of information, including suggestions for reducing this burden to Washington Headquarters Services, Directorate for Information Operations and Reports, 1215 Jefferson Davis Highway, Suite 1204, Arlington, VA 22202-4302, and to the Office of Management and Budget, Paperwork Reduction Project (0704-0188), Washington, DC 20503.				
1. AGENCY USE ONLY (Leave blank)	2. REPORT DATE 18 May 98	3. REPORT TYPE AND DATES COVERED Proceedings, 01 Mar 97 - 31 Oct 97		
4. TITLE AND SUBTITLE RESONANCE MEETING, VOLUME 2		5. FUNDING NUMBERS PE 61153N		
6. AUTHOR(S) H.E. Bass and E.F. Cauthen, eds.		G N00014-97-1-0270		
7. PERFORMING ORGANIZATION NAME(S) AND ADDRESS(ES) NATIONAL CENTER FOR PHYSICAL ACOUSTICS UNIVERSITY OF MISSISSIPPI UNIVERSITY MS 38677		8. PERFORMING ORGANIZATION REPORT NUMBER		
9. SPONSORING / MONITORING AGENCY NAME(S) AND ADDRESS(ES) OFFICE OF NAVAL RESEARCH ONR 331 800 NORTH QUINCY STREET ARLINGTON VA 22217-5660		10. SPONSORING / MONITORING AGENCY REPORT NUMBER		
11. SUPPLEMENTARY NOTES				
12a. DISTRIBUTION / AVAILABILITY STATEMENT Approved for public release: Distribution unlimited		12b. DISTRIBUTION CODE		
13. ABSTRACT (Maximum 200 words) The Resonance Meeting was held May 11-15, 1997 at the Asilomar Conference Center. The purpose of the Resonance Meeting was to cover a broad range of uses of acoustic resonances to determine physical properties of matter. The meeting grew out of prior meetings in 1994 and 1995 that were devoted entirely to Resonant Ultrasound Spectroscopy (RUS). The international list of participants included cutting-edge users of RUS and other resonance techniques, as well as researchers and graduate students who wanted to learn about and use these techniques. Universities from the United States and Japan, national laboratories and private research organizations were represented. The Resonance Meeting proved to stimulate extended discussions outside the scheduled sessions. The proceedings of the Resonance Meeting consist of two volumes. Volume 1 contains a verbatim transcript of each presentation. Volume 2 contains accompanying transparencies for each transcript. Anyone interested in obtaining more information on a particular presentation may contact the author(s). Volume 1 contains a complete list of participants and addresses.				
14. SUBJECT TERMS RESONANT ULTRASOUND SPECTROSCOPY, RUS, ACOUSTIC RESONANCE, ACOUSTIC SPECTROSCOPY		15. NUMBER OF PAGES 564		
		16. PRICE CODE		
17. SECURITY CLASSIFICATION OF REPORT UNCLASSIFIED	18. SECURITY CLASSIFICATION OF THIS PAGE UNCLASSIFIED	19. SECURITY CLASSIFICATION OF ABSTRACT UNCLASSIFIED	20. LIMITATION OF ABSTRACT	